Anomalous Hydrogen-Strontium Discharge

Randell L. Mills

Mark Nansteel

Ying Lu

BlackLight Power, Inc.
493 Old Trenton Road

Cranbury, NJ 08512

We report the observation of intense extreme ultraviolet (EUV) emission from incandescently heated atomic hydrogen and atomized Typically the emission of extreme ultraviolet light from hydrogen gas is achieved via a discharge at high voltage, a high power inductively coupled plasma, or a plasma created and heated to extreme temperatures by RF coupling (e.g. $> 10^6 K$) with confinement provided by a toroidal magnetic field. The observed plasma formed temperatures (e.g. $\approx 10^3 K$) from atomic hydrogen generated at a tungsten filament that heated a titanium dissociator and atomic strontium which was vaporized from the metal by heating. No emission was observed when sodium, magnesium, or barium replaced strontium or with hydrogen or strontium alone. The power balance of a gas cell having atomized hydrogen and strontium was measured by integrating the total light output corrected for spectrometer system response and energy over Control cell experiments were identical except that the visible range. sodium, magnesium, or barium replaced strontium. In the case of hydrogen-sodium, hydrogen-magnesium, and hydrogen-barium mixtures, 4000, 7000, and 6500 times the power of the hydrogen-strontium mixture was required, respectively, in order to achieve that same optically measured light output power. A plasma formed at a cell voltage of about 250 V for hydrogen alone and sodium-hydrogen mixtures, and 140-150 V for hydrogen-magnesium and hydrogen-barium mixtures; whereas, a plasma formed for hydrogen-strontium mixtures at an extremely low voltage of about 2 V.



A historical motivation to cause EUV emission from a hydrogen gas was that the spectrum of hydrogen was first recorded from the only known source, the Sun [1]. Developed sources that provide a suitable intensity are high voltage discharge, synchrotron, and inductively coupled plasma generators [2]. An important variant of the later type of source is a tokomak [3]. Fujimoto et al. [4] have determined the cross section for production of excited hydrogen atoms from the emission cross sections for Lyman and Balmer lines when molecular hydrogen is dissociated into excited atoms by electron collisions. This data was used to develop a collisional-radiative model to be used in determining the ratio of molecular-to-atomic hydrogen densities in tokomak plasmas. Their results indicate an excitation threshold of 17 eV for Lyman a emission. Addition of other gases would be expected to decrease the intensity of hydrogen lines which could be absorbed by the gas. Hollander and Wertheimer [5] found that within a selected range of parameters of a plasma created in a microwave resonator cavity, a hydrogen-oxygen plasma displays an emission that resembles the absorption of molecular oxygen. Whereas, a helium-hydrogen plasma emits a very intense hydrogen Lyman α radiation at 121.5 nm which is up to 40 times more intense than other lines in the spectrum. Lyman \alpha emission intensity showed a significant deviation from that predicted by the model of Fujimoto et al. [4] and from the emission of hydrogen alone.

It has been reported that intense EUV emission was observed at low temperatures (e.g. $\approx 10^3 \, K$) from atomic hydrogen and certain atomized elements or certain gaseous ions which singly or multiply ionize at integer multiples of the potential energy of atomic hydrogen, 27.2 eV [6-10]. Helium ions present in the experiment of Hollander and Wertheimer [5] ionize at a multiple of two times the potential energy of atomic hydrogen.

Kuraica and Konjevic [11] observed intense wing developments of hydrogen Balmer lines with argon present in the plasma of negative glow of a glow discharge of an argon-hydrogen mixture irrespective of cathode material (carbon, copper, and silver). An anomalous discharge was not observed in neon-hydrogen and pure hydrogen mixtures. The authors offer a tentative explanation for hydrogen line shapes in the presence of argon which is based on a quasiresonace charge transfer between metastable argon ions and hydrogen molecules and the formation of a hydrogen molecular ion. According to the authors,

"... it is essential that the H_2^+ or H_3^+ ion must gain energy in the electric field before dissociation. Otherwise, the large energy of excited hydrogen atoms (on the average 50 eV per atom) cannot be explained".

The source of $50 \, eV$ anomalous thermal broadening of the Balmer lines observed by Kuraica and Konjevic [11] may be dependent on the presence of an atom or ion which ionizes at about an integer multiple of $27.2 \, eV$ since Ar^+ ionizes at $27.6 \, eV$.

Strontium ionizes at integer multiples of the potential energy of atomic hydrogen; thus, a hydrogen-strontium mixture was tested for anomalous EUV emission and plasma formation relative to mixtures of hydrogen and chemically similar controls that do not have electron ionization energies which are a multiple of 27.2 eV.

We report that a hydrogen plasma is formed at low temperatures (e.g. $\approx 10^3 \, K$) by reaction of atomic hydrogen with strontium atoms, but not with magnesium, barium, or sodium atoms. In the case of EUV measurements, atomic hydrogen was generated by dissociation at a tungsten filament and at a transition metal dissociator that was incandescently heated by the filament. Strontium atoms were vaporized by heating to form a low vapor pressure (e.g. 1 torr). The kinetic energy of the thermal electrons at the experimental temperature of $\approx 10^3 \, K$ were about 0.1 eV, and the average collisional energies of electrons accelerated by the field of the filament were less than 1 eV. (No blackbody emission was recorded for wavelengths shorter than 400 nm.). Strontium atoms caused hydrogen EUV emission; whereas, the chemically similar atoms, magnesium and barium as well as sodium, caused no emission.

Furthermore, an anomalous hydrogen-strontium discharge was observed by visible emission. A cylindrical nickel mesh hydrogen dissociator of a gas cell also served as an electrode to produce an

essentially uniform radial electric field between the dissociator and the wall of the cylindrical stainless steel gas cell. Power was applied to the electrode to achieve a bright plasma which was recorded over the wavelength range $350 \le \lambda \le 750 \, nm$. The power balance of a gas cell having atomized hydrogen and strontium was measured by integrating the total light output corrected for spectrometer system response and energy over the visible range. Control experiments were identical except that sodium, magnesium, or barium replaced strontium. In the case of hydrogensodium, hydrogen-magnesium, and hydrogen-barium mixtures, 4000, 7000, and 6500 times the power of the hydrogen-strontium mixture was required, respectively, in order to achieve that same optically measured light output power.

II. EXPERIMENTAL

A. EUV spectroscopy

Due to the extremely short wavelength of this radiation, "transparent" optics do not exist for EUV spectroscopy. Therefore, a windowless arrangement was used wherein the source was connected to the same vacuum vessel as the grating and detectors of the EUV spectrometer. Windowless EUV spectroscopy was performed with an extreme ultraviolet spectrometer that was mated with the cell. Differential pumping permitted a high pressure in the cell as compared to that in the spectrometer. This was achieved by pumping on the cell outlet and pumping on the grating side of the collimator that served as a pin-hole inlet to the optics. The cell was operated under hydrogen flow conditions while maintaining a constant hydrogen pressure in the cell with a mass flow controller.

The experimental set up shown in Figure 1 comprised a quartz cell which was 500 mm in length and 50 mm in diameter. Three ports for gas inlet, outlet, and photon detection were on the other end of the cell. A tungsten filament (0.508 mm in diameter and 800 cm in length, total resistance ~2.5 ohm) and a titanium cylindrical screen (300 mm long and 40 mm in diameter) that performed as a hydrogen dissociator were inside the quartz cell. A new dissociator was used for each experiment.

The filament was coiled on a grooved ceramic tube support to maintain its shape when heated. The return lead passed through the inside of the The titanium screen was electrically floated. The power was applied to the filament by a Sorensen 80-13 power supply which was controlled by a constant power controller. The temperature of the tungsten filament was estimated to be in the range of 1100 to 1500 °C. The external cell wall temperature was about 700 °C. The hydrogen gas pressure inside the cell was maintained at about 300 mtorr with a hydrogen flow rate of 5.5 sccm controlled by a 20 sccm range mass flow controller (MKS 1179A21CS1BB) with a readout (MKS type 246). The entire quartz cell was enclosed inside an insulation package comprised of Zircar AL-30 insulation. Several K type thermocouples were placed in the insulation to measure key temperatures of the cell and insulation. thermocouples were read with a multichannel computer data acquisition system.

In the present study, the light emission phenomena was studied for hydrogen, argon, neon, and helium alone; hydrogen with strontium, magnesium, barium, and sodium metals, and strontium alone. The pure elements of magnesium, barium, and strontium were placed in the reservoir and volatized by the external heater. Magnesium, with a low vapor pressure (higher melting point), was volatilized by suspending a foil of the material (2 cm X 2 cm X 0.1 cm thick) between the filament and titanium dissociator and heating the test material with the filament. The power applied to the filament was 300 W in the case of strontium and up to 600 watts in the case of magnesium, barium, and sodium metals. The voltage across the filament was about 55 V and the current was about 5.5 ampere at 300 watts. For the controls, magnesium, barium, and sodium metals, the cell was increased in temperature to the maximum permissible with the power supply.

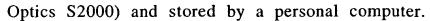
The light emission was introduced to an EUV spectrometer for spectral measurement. The spectrometer was a McPherson 0.2 meter monochromator (Model 302, Seya-Namioka type) equipped with a 1200 lines/mm holographic grating with a platinum coating. The wavelength region covered by the monochromator was $30-560 \, nm$. A channel electron multiplier (CEM) was used to detect the EUV light. The wavelength resolution was about $1 \, nm$ (FWHM) with an entrance and exit

slit width of $300 \, \mu m$. The vacuum inside the monochromator was maintained below $5 \, X \, 10^{-4}$ torr by a turbo pump. The EUV spectrum $(40-160 \, nm)$ of the cell emission with strontium present was recorded at about the point of the maximum Lyman α emission.

The UV/VIS spectrum (40-560 nm) of the cell emission with hydrogen alone was recorded with a photomultiplier tube (PMT) and a sodium salicylate scintillator. The PMT (Model R1527P, Hamamatsu) used has a spectral response in the range of 185-680 nm with a peak efficiency at about 400 nm. The scan interval was 0.4 nm. The inlet and outlet slit were $500 \mu m$ with a corresponding wavelength resolution of 2 nm.

B. Power cell apparatus and procedure

Plasma studies with hydrogen alone, or hydrogen with strontium, sodium, magnesium, or barium were carried out in the cylindrical stainless steel gas cell shown in Fig. 2. The experimental setup for generating a glow discharge hydrogen plasma and for optically measuring the power balance is shown in Fig. 3. The cell was heated in a 10 kW refractory brick kiln (L & L Kiln Model JD230) as shown in Fig. 3. The cell was evacuated and pressurized with hydrogen through a single 0.95 cm feed through. The discharge was started and maintained by an alternating current electric field in the 1.75 cm annular gap between an axial electrode and the cell wall. The cylindrical cell was 9.21 cm in diameter and 14.5 cm in height. The axial electrode was a 5.08 cm OD by 7.2 cm long stainless steel tube wound with several layers of nickel screen. The overall diameter of the axial electrode was 5.72 cm. A 1.6 mm thick UV-grade sapphire window with 1.5 cm view diameter provided a visible light path from inside the cell. The viewing direction was normal to the cell axis. A 1.27 cm diameter stainless steel tube passed through the furnace wall and connected to a view port welded to the cell wall at mid-height to provide an optical light path from the sapphire window to the furnace exterior. An 8 mm quartz rod channeled the light from the view port through the stainless tube to a collimating lens which was focused on a 100 µm optical fiber located outside the Spectral data was recorded with a visible spectrometer (Ocean furnace.



The field voltage was controlled by a variable voltage transformer operating from 115 VAC, 60 Hz. A step-up transformer was used when necessary. True rms voltage at the axial electrode was monitored by a digital multimeter (Fluke 8010 A or Tenma 726202). A second multimeter (Extech 380763) in series with the discharge gap was used to indicate the current. The cell temperature was measured by a thermocouple probe located in the cell interior approximately 2 cm from the discharge gap. The pressure in the hydrogen supply tube outside the furnace was monitored by 10 torr and 1000 torr MKS Baratron absolute pressure gauges. In the absence of hydrogen flow, the hydrogen supply tube pressure was essentially the cell hydrogen partial pressure.

Strontium (Aldrich Chemical Company 99.9 %), sodium (Aldrich Chemical Company 99.95 %), magnesium (Alfa Aesar 99.98 %), or barium (Aldrich Chemical Company 99.99 %) metals were loaded into the cell under a dry argon atmosphere. The cell was evacuated with a turbo vacuum pump to a pressure of 4 mtorr during most of the heating process. During the heat-up the cell was periodically pressurized with hydrogen (99.999% purity) to approximately 100 torr and subsequently evacuated to purge gaseous contaminants from the system. When the cell temperature stabilized hydrogen was added until the steady pressure The field voltage was increased until was approximately 1 torr. breakdown occurred. This was confirmed by the spectrometer response to visible light emitted from the cell. The hydrogen pressure was adjusted, as much as possible, to maximize the light emission from the The voltage was maintained at the minimum level which resulted in a stable discharge during data acquisition.

The spectrometer system comprised a 100 µm optical fiber and visible spectrometer (Ocean Optics S2000). To correct for the nonuniform response of the spectrometer system as a function of wavelength and the dependence of energy on wavelength, the system was calibrated against a reference light source (Ocean Optics LS-1-CAL). A spectral calibration factor was applied to the count rate data at each wavelength to yield the irradiation of the detector in units of energy/time/area/wavelength. The total visible radiant flux incident on the detector was calculated by integrating the spectral irradiation between 400 and 700 nm.

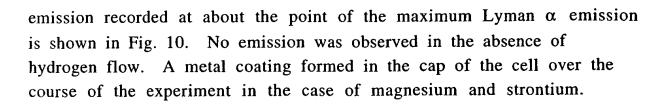
III. RESULTS

A. EUV spectroscopy

The cell without any test material present was run to establish the baseline of the spectrometer. The intensity of the Lyman α emission as a function of time from the gas cell at a cell temperature of 700 °C comprising a tungsten filament, a titanium dissociator, and 300 mtorr hydrogen with a flow rate of 5.5 sccm is shown in Fig. 4. The corresponding UV/VIS spectrum (40-560 nm) is shown in Fig. 5. The spectrum was recorded with a photomultiplier tube (PMT) and a sodium salicylate scintillator. No emission was observed except for the blackbody filament radiation at the longer wavelengths. No emission was also observed when argon, neon, or helium replaced hydrogen.

The intensity of the Lyman α emission as a function of time from the gas cell at a cell temperature of 700 °C comprising a tungsten filament, a titanium dissociator, sodium or barium metal in the catalyst reservoir, and 300 mtorr hydrogen with a flow rate of 5.5 sccm are shown in Figs. 6 and 7, respectively. Sodium or barium metal was volatized from the catalyst reservoir by heating it with an external heater. No emission was observed in either case. The maximum filament power was greater than 500 watts. A metal coating formed in the cap of the cell over the course of the experiment in both cases.

The intensity of the Lyman α emission as a function of time from the gas cell at a cell temperature of 700 °C comprising a tungsten filament, a titanium dissociator, a magnesium foil in the cell versus strontium metal in the catalyst reservoir, and 300 mtorr hydrogen with a flow rate of 5.5 sccm are shown in Figs. 8 and 9, respectively. No emission was observed with the magnesium foil and hydrogen. The maximum filament power was 500 watts. The temperature of the foil increased with filament power. At 500 watts, the temperature of the foil was 1000 °C which would correspond to a vapor pressure of about 100 mtorr. Strontium metal was volatized from the catalyst reservoir by heating it with an external heater. Strong emission was observed from strontium and hydrogen. The EUV spectrum (40–160 nm) of the cell



B. Optically measured power balance

Count rate and spectrometer system irradiation of the background spectrum of hydrogen and strontium vapor over the wavelength range $350 \le \lambda \le 750 \, nm$ in the absence of power applied to the electrode and in the absence of a discharge is shown in Fig. 11. This data was collected during cell evacuation following the test with strontium and hydrogen at a cell temperature of 664 °C. The maximum visible irradiation of $0.004 \, \mu W/cm^2 nm$ occurred at the red end of the visible spectrum. The results are summarized in Table I where T is the temperature, P_{hyd} is the hydrogen partial pressure, and P_{ν} is the equilibrium metal vapor pressure calculated from standard curves of the vapor pressure as a function of temperature [12].

Power was applied to the electrode to achieve a bright plasma in the strontium-hydrogen mixture and the controls of hydrogen alone, and sodium-hydrogen, magnesium-hydrogen, and barium-hydrogen mixtures for cell temperatures in the range 335-666 °C. In each case, the spectral radiant flux at the spectrometer system was recorded. If possible, the power driving the controls was adjusted such that the peak spectrometer system spectral irradiation was about $0.1 \,\mu W/cm^2 nm$ in each case. The integrated visible irradiation levels were of the order of $1 \,\mu W/cm^2$. One exception was the case of hydrogen-barium. In this case, the maximum spectral irradiation levels and integrated visible irradiation levels were only of the order of $0.01 \,\mu W/cm^2 nm$ and $0.03 \,\mu W/cm^2$, respectively.

The power required to maintain a plasma of equivalent optical brightness with strontium atoms present was 4000, 7000, and 6500 times less than that required for the sodium, magnesium, and barium control, respectively. A driving power of 33.7 W and 58 W was necessary to achieve a total visible radiant flux of about $1 \mu W/cm^2$ from a sodium-hydrogen mixture and a magnesium-hydrogen mixture, respectively. For a hydrogen-barium mixture, a power input of about 55



W was required to achieve a total visible irradiation of about $0.03 \,\mu\text{W/cm}^2$. Whereas, in the case of a strontium-hydrogen mixture, a power input of 8.5 mW resulted in a plasma with a total visible radiant flux of about the same optical brightness as sodium and magnesium. A plasma formed at a cell voltage of about 250 V for hydrogen alone and sodium-hydrogen mixtures, and 140-150 V for hydrogen-magnesium and hydrogen-barium mixtures; whereas, a plasma formed for hydrogen-strontium mixtures at the extremely low voltage of about 2 V. The results are summarized in Table I.

The count rate and the spectrometer system irradiation for a mixture of hydrogen and strontium vapor at 664 °C is shown in Fig. 12. Optimal light emission was observed after several hours of cell evacuation. The hydrogen partial pressure was unknown under these conditions. The calculated equilibrium vapor pressure of strontium at 664 °C is approximately 270 mtorr. The measured breakdown voltage was approximately 2 V. The maintenance voltage for a stable discharge was 2.2 V and input power was 8.5 mW. Spectral characteristics are noted in Table II. The hydrogen Balmer α and β peaks were obscured by strong strontium emission near 654.7 and 487.2 nm, respectively.

The spectrometer system irradiation for a hydrogen discharge at a cell temperature of 664 °C and 1 torr is shown in Fig. 13. The breakdown voltage was approximately 220 V. The field voltage required to form a stable discharge was 224 V. The input power was 24.6 W. Spectral features are tabulated in Table III. The peak at 589.1 nm may be due to sodium contamination from a previous experimental run. The minor peaks at 518.2 and 558.7 nm have not been identified.

The spectrometer system irradiation for mixtures of hydrogen and sodium vapor are shown in Figs. 14-16 for temperatures of 335, 516, and 664 °C, respectively. Corresponding hydrogen pressures are 1, 1.5, and 1.5 torr, respectively. The calculated sodium vapor pressure was 51 mtorr, 5.3 torr, and 63 torr at 335, 516, and 664 °C, respectively. At least 200 V was required to maintain a discharge. The input power for a stable discharge ranged from approximately 10 W at 664 °C to 34 W at 335 °C. Spectral features corresponding to 335 °C are summarized in Table IV. Strong emission observed near 656-657 nm was probably due, in-part, to hydrogen. The relative contribution to the intensity was



masked by strong sodium emission at a slightly shorter wavelength. The peak at 486.2 nm could only be due to hydrogen emission. Sodium does not have emission lines in the neighborhood of this wavelength. The intensity of this peak diminishes relative to the more prominent sodium peaks with increasing temperature as shown in Figs. 14-16. This may have been due to a decreasing hydrogen concentration as the sodium vapor pressure increased.

The spectral response for mixtures of magnesium vapor and hydrogen are shown in Figs. 17-19 for temperatures of 449, 582, and 654 °C, respectively. The corresponding hydrogen pressures are 4, 4.2, and 3 torr, respectively. A minimum of 150 V was required to maintain a discharge. The minimum input power required to maintain a stable discharge was 58 W at 449 °C. Spectral features corresponding to 449 °C are summarized in Table V. Both hydrogen and magnesium spectral features are observed. The modest sodium emission at 588 nm may be due to sodium contamination from previous control experiments.

The spectral response for a mixture of barium vapor and hydrogen at 666° C is shown in Fig. 20. The hydrogen partial pressure and barium vapor pressure are 2 torr and 25 mtorr, respectively. It was not possible to achieve a total visible irradiation level of $1 \,\mu W/cm^2$ even with voltages approaching 150 V. The voltage and power input corresponding to Fig. 20 are 138 V and 55 W, respectively. Spectral features are summarized in Table VI. Both barium and hydrogen spectral features are observed as well as sodium features which are presumably due to contamination. The peak at 493 nm has not been identified.

IV. DISCUSSION

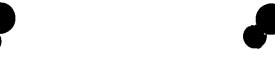
Intense EUV emission was observed at low temperatures (e.g. $\approx 10^3 \, K$) from atomic hydrogen and strontium which ionizes at integer multiples of the potential energy of atomic hydrogen. In the cases where Lyman α emission was observed, no possible chemical reactions of the tungsten filament, the dissociator, the vaporized test material, and 300 mtorr hydrogen at a cell temperature of 700 °C could be found which accounted for the hydrogen α line emission. In fact, no known chemical reaction releases enough energy to excite Lyman α emission from

hydrogen. The emission was not observed with hydrogen alone or with helium, neon, or argon gas. Intense emission was observed for strontium with hydrogen gas, but no emission was observed with hydrogen or strontium alone. This result indicates that the emission may be due to a reaction of hydrogen.

Other studies support the possibility of a novel reaction of atomic hydrogen which produces an anomalous discharge. It has been previously reported that intense extreme ultraviolet (EUV) emission was observed at low temperatures (e.g. $\approx 10^3 K$) from atomic hydrogen and certain atomized elements or certain gaseous ions [6-10]. The only pure elements that were observed to emit EUV were those wherein the ionization of t electrons from an atom to a continuum energy level is such that the sum of the ionization energies of the t electrons is approximately $m \cdot 27.2 \text{ eV}$ where t and m are each an integer. Strontium atoms ionize at integer multiples of the potential energy of atomic hydrogen and caused Whereas, the chemically similar atoms, magnesium and barium emission. as well as sodium, do not ionize at integer multiples of the potential energy of atomic hydrogen and caused no emission. The enthalpy of ionization of Sr to Sr^{5+} has a net enthalpy of reaction of 188.2 eV, which is equivalent to m=7.

The power balance of a gas cell having atomized hydrogen and strontium was measured by integrating the total light output corrected for spectrometer system response and energy over the visible range. A control cell was identical except that sodium, magnesium, or barium replaced strontium. In the controls, 4000-7000 times the power of the strontium cell was required in order to achieve the same optically measured light output power. A plasma formed at a cell voltage of about 250 V for hydrogen alone and sodium-hydrogen mixtures, and 140-150 V for hydrogen-magnesium and hydrogen-barium mixtures; whereas, a plasma formed for hydrogen-strontium mixtures at the extremely low voltage of about 2 V. This is two orders of magnitude lower than the starting voltages measured for gas glow discharges, cf. Table VII.

An anomalous plasma with hydrogen-potassium mixtures has been reported in an experiment identical to the present EUV experiments [9-10]. When the electric field was set to zero, the plasma decayed with a two second half-life which was the thermal decay time of the filament



which dissociated molecular hydrogen to atomic hydrogen. This experiment showed that hydrogen line emission was occurring even though the voltage between the heater wires was set to and measured to be zero and indicated that the emission was due to a reaction of potassium atoms with atomic hydrogen. Potassium atoms ionize at an integer multiple of the potential energy of atomic hydrogen, $m \cdot 27.2 \ eV$. The enthalpy of ionization of K to K^{3+} has a net enthalpy of reaction of 81.7426 eV, which is equivalent to m=3.

In the present experiments, it was determined that the presence of a weak electric field was necessary in order for strontium to produce an anomalous discharge of hydrogen. In the case that electrons are ionized to a continuum energy level, the presence of a low strength electric field alters the continuum energy levels. The minimum electric field in this experiment was about 2 V over the annular gap of about 2 cm. The ionization energy of $188.2 \, eV$ is 1% less than $m \cdot 27.2 \, eV$ where m = 7. In the anomalous discharge of hydrogen due to the presence of strontium, the weak field may adjust the energy of ionizing strontium to match the energy of $m \cdot 27.2 \, eV$ to permit a novel reaction of atomic hydrogen.

The formation of novel compounds would be substantial evidence supporting a novel reaction of hydrogen as the mechanism of the observed EUV emission and anomalous discharge. Novel hydrogen compounds have been isolated as products of the reaction of atomic hydrogen with atoms and ions identified as catalysts in the present EUV study [6-10, 16-21].

ACKNOWLEDGMENT

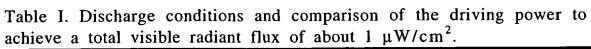
Special thanks to Jinquan Dong for preparing many of the cells comprising the test materials, to Takeyoshi Onuma for recording EUV and optical spectra and to Bala Dhandapani and Jiliang He for reviewing this manuscript.

REFERENCES

- 1. Phillips, J. H., Guide to the Sun, Cambridge University Press, Cambridge, Great Britain, (1992), pp. 16-20.
- 2. J. A. R. Sampson, Techniques of Vacuum Ultraviolet Spectroscopy, Pied

- Publications, (1980), pp. 94-179.
- 3. Science News, 12/6/97, p. 366.
- 4. T. Fujimoto, K. Sawada, and K. Takahata, J. Appl. Phys., Vol. 66 (6), (1989), pp. 2315-2319.
- 5. A. Hollander, and M. R. Wertheimer, J. Vac. Sci. Technol. A, Vol. 12 (3), (1994), pp. 879-882.
- 6. R. Mills, J. Dong, Y. Lu, "Observation of Extreme Ultraviolet Hydrogen Emission from Incandescently Heated Hydrogen Gas with Certain Catalysts", 1999 Pacific Conference on Chemistry and Spectroscopy and the 35th ACS Western Regional Meeting, Ontario Convention Center, California, (October 6-8, 1999).
- 7. R. Mills, J. Dong, Y. Lu, "Observation of Extreme Ultraviolet Hydrogen Emission from Incandescently Heated Hydrogen Gas with Certain Catalysts", Int. J. Hydrogen Energy, Vol. 25, (2000), pp. 919-943.
- 8. R. Mills, "Observation of Extreme Ultraviolet Emission from Hydrogen-KI Plasmas Produced by a Hollow Cathode Discharge", Int. J. Hydrogen Energy, in press.
- 9. R. Mills, "Temporal Behavior of Light-Emission in the Visible Spectral Range from a Ti-K2CO3-H-Cell", Int. J. Hydrogen Energy, in press.
- 10. R. Mills, M. Nansteel, and Y. Lu, "Observation of Extreme Ultraviolet Hydrogen Emission from Incandescently Heated Hydrogen Gas with Strontium that Produced an Anomalous Optically Measured Power Balance", Int. J. Hydrogen Energy, in press.
- 11. Kuraica, M., Konjevic, N., Physical Review A, Volume 46, No. 7, October (1992), pp. 4429-4432.
- 12. C. L. Yaws, Chemical Properties Handbook, McGraw-Hill, (1999).
- 13. David R. Linde, CRC Handbook of Chemistry and Physics, 79 th Edition, CRC Press, Boca Raton, Florida, (1998-9), pp. 10-1 to p. 10-87.
- 14. A. von Engel, Ionized Gases, American Institute of Physics, (1965).
- 15. M. S. Naidu and V. Kamaraju, High Voltage Engineering, McGraw-Hill, (1996).
- 16. R. Mills, B. Dhandapani, N. Greenig, J. He, "Synthesis and Characterization of Potassium Iodo Hydride", Int. J. of Hydrogen Energy, Vol. 25, Issue 12, December, (2000), pp. 1185-1203.
- 17. R. Mills, "Novel Inorganic Hydride", Int. J. of Hydrogen Energy, Vol. 25, (2000), pp. 669-683.

- 18. R. Mills, "Novel Hydrogen Compounds from a Potassium Carbonate Electrolytic Cell", Fusion Technology, Vol. 37, No. 2, March, (2000), pp. 157-182.
- 19. R. Mills, J. He, and B. Dhandapani, "Novel Hydrogen Compounds", 1999 Pacific Conference on Chemistry and Spectroscopy and the 35th ACS Western Regional Meeting, Ontario Convention Center, California, (October 6-8, 1999).
- 20. R. Mills, B. Dhandapani, M. Nansteel, J. He, T. Shannon, A. Echezuria, "Synthesis and Characterization of Novel Hydride Compounds", Int. J. of Hydrogen Energy, in press.
- 21. R. Mills, "Highly Stable Novel Inorganic Hydrides", Journal of Materials Research, submitted.



	T (°C)	P _{hyd.} (torr) ^a	P _v (Torr)	Voltage (V)	Current (mA)	Integ. time (ms)	Detector irradiation (μW/cm ²)	Power (W)
H ₂ +Sr	664		0.270	2.20	3.86	768	1.17	0.0085
H_2	664	1.0		224	110	1130	2.08	24.6
$H_2 + Na$	335	1.0	0.051	272	124	122	1.85	33.7
H_2 +Na	516	1.5	5.3	220	68	768	0.40	15.0
H_2 +Na	664	1.5	63	240	41	768	0.41	9.84
H_2+Mg	449	4.0	0.016	153	380	500	1.7	58
H_2+Mg	582	4.2	0.6	233	290	500	0.16	68
H_2+Mg	654	3.0	2.8	250	400	1000	0.18	100.0
H ₂ +Ba	666	2.0	0.025	138	730	716	0.03	55 ^b
Bkgnd.	664		0.270	0	0	768	0.20	0

^a Calculated [12]

TABLE II. Spectral features of hydrogen and strontium at 664 °C.

		7 V V
Measured Wavelength (nm)	Spectrometer System Irradiation (\(\muW/cm^2nm\)	Published Emission Data [13] (nm)
460.6	0.156	460.73 (Sr)
487.2	0.00290	487.25 (Sr), 486.13 (H ₂)
639.8	0.00813	638.82 (Sr)
654.7	0.0139	654.68 (Sr), 656.29 (H ₂)
689.4	0.0386	689.26 (Sr)

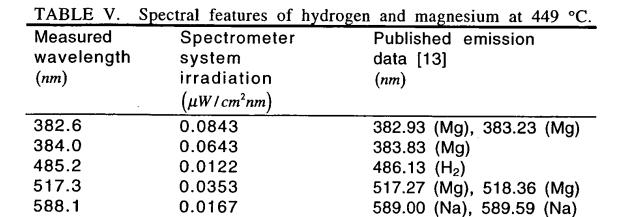
b Power input differs from volt-amperes due to non-unity power factor.

TABLE III. Spectral features of hydrogen at 664 °C.

Measured	Spectrometer	Published Emission
Wavelength	System	Data [13]
(nm)	Irradiation	(nm)
,	$(\mu W / cm^2 nm)$	
485.8	0.0165	486.13 (H ₂)
518.2	0.00894	
558.7	0.00694	
589.1	0.0174	589.00 (Na), 589.59 (Na)
656.7	0.0752	656.29 (H ₂)

TABLE IV. Spectral features of hydrogen and sodium at 335 °C.

Measured wavelength (nm)	Spectrometer System Irradiation (\(\muW/cm^2nm\)	Published emission data [13] (nm)
467.2	0.00400	466.86 (Na)
486.2	0.0055	486.13 (H ₂)
498.4	0.0176	498.28 (Na)
516.1	0.00380	515.34 (Na)
569.0	0.114	568.82 (Na)
589.3	0.302	589.00 (Na), 589.59 (Na)
615.9	0.0310	616.07 (Na)
656.0	0.0422	656.29 (H ₂), 655.24 (Na)
657.0	0.0421	656.29 (H ₂)



656.29 (H₂)

Table VI. Spectral features of hydrogen and barium at 666°C.

0.109

655.8

Measured	Spectrometer	Published emission
wavelength	system	data [13]
(nm)	irradiation	(nm)
	(mW/cm ² -nm)	
456.2	0.0021	455.40 (Ba)
492.6	0.002	, ,
552.7	8.4×10^{-4}	553.55 (Ba)
568.4	0.003	568.26 (Na)
588.8	0.006	589.00 (Na)
614.7	9.0×10^{-4}	614.17 (Ba)
655.9	0.002	656.29 (H ₂)

TABLE VII. Glow discharge parameters from von Engel [14] and Naidu Kamaraju [15].

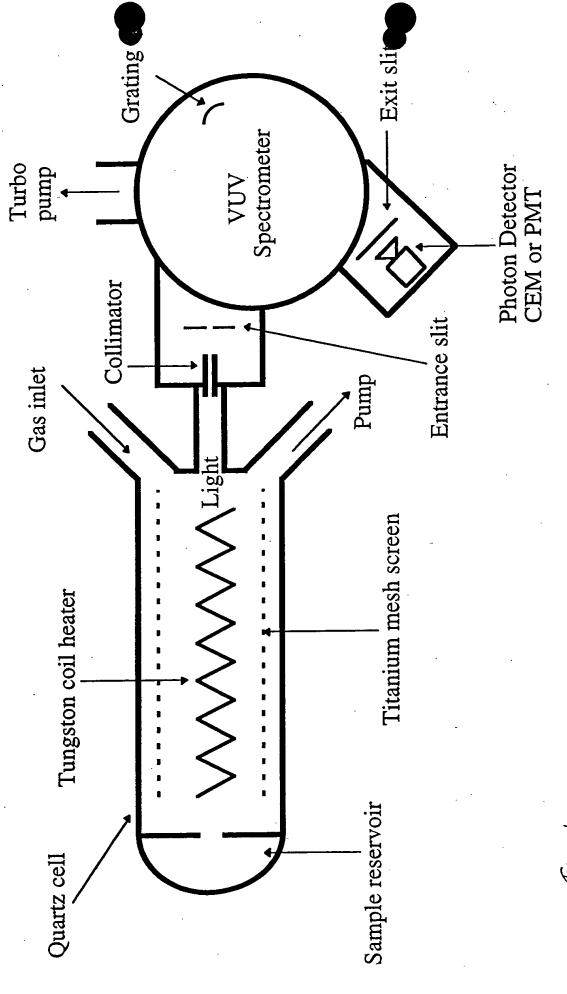
Gas	Minimum starting voltage	Pressure-discharge gap product at minimum starting
	(V)	voltage
		(cm-torr)
N ₂	251	0.67
H_2	273	1.15
Air	327	0.567
CO₂	420	0.51
Ar	137	0.9
He	156	4.0
Hg	520	2
<u>Na</u>	335	0.04

Figure Captions

- FIG. 1. The experimental set up comprising a gas cell light source and an EUV spectrometer which was differentially pumped.
- FIG. 2. Cylindrical stainless steel gas cell for plasma studies with hydrogen alone, or with hydrogen with strontium, sodium, or magnesium.
- FIG. 3. The experimental setup for generating a glow discharge hydrogen plasma and for optically measuring the power balance.
- FIG. 4. The intensity of the Lyman α emission as a function of time from the gas cell at a cell temperature of 700 °C comprising a tungsten filament, a titanium dissociator, and 300 mtorr hydrogen with a flow rate of 5.5 sccm.
- FIG. 5. The UV/VIS spectrum (40-560 nm) of the cell emission from the gas cell at a cell temperature of 700 °C comprising a tungsten filament, a titanium dissociator, and 300 mtorr hydrogen with a flow rate of 5.5 sccm that was recorded with a photomultiplier tube (PMT) and a sodium salicylate scintillator.
- FIG. 6. The intensity of the Lyman α emission as a function of time from the gas cell at a cell temperature of 700 °C comprising a tungsten filament, a titanium dissociator, sodium metal vaporized from the catalyst reservoir, and 300 mtorr hydrogen with a flow rate of 5.5 sccm.
- FIG. 7. The intensity of the Lyman α emission as a function of time from the gas cell at a cell temperature of 700 °C comprising a tungsten filament, a titanium dissociator, barium metal vaporized from the catalyst reservoir, and 300 mtorr hydrogen with a flow rate of 5.5 sccm.
- FIG. 8. The intensity of the Lyman α emission as a function of time from the gas cell at a cell temperature of 700 °C comprising a tungsten filament, a titanium dissociator, a magnesium foil, and 300 mtorr hydrogen with a flow rate of 5.5 sccm.
- FIG. 9. The intensity of the Lyman α emission as a function of time from the gas cell at a cell temperature of 700 °C comprising a tungsten filament, a titanium dissociator, strontium metal vaporized from the catalyst reservoir, and 300 mtorr hydrogen with a flow rate of 5.5 sccm.
- FIG. 10. The EUV spectrum (40-160 nm) of the cell emission recorded at about the point of the maximum Lyman α emission from the gas cell at a cell temperature of 700 °C comprising a tungsten filament, a

titanium dissociator, strontium metal vaporized from the catalyst reservoir, and 300 mtorr hydrogen with a flow rate of 5.5 sccm.

- FIG. 11. Count rate and spectrometer system irradiation of the background spectrum of hydrogen and strontium vapor over the wavelength range $350 \le \lambda \le 750 \, nm$ in the absence of power applied to the electrode and in the absence of a discharge.
- FIG. 12. The count rate and the spectrometer system irradiation for a mixture of hydrogen and strontium vapor at 664 °C.
- FIG. 13. The spectrometer system irradiation for a hydrogen discharge at a cell temperature of 664 °C and a hydrogen pressure of 1 torr.
- FIG. 14. The spectrometer system irradiation for a mixture of hydrogen and sodium vapor at 335 °C.
- FIG. 15. The spectrometer system irradiation for a mixture of hydrogen and sodium vapor at 516 °C.
- FIG. 16. The spectrometer system irradiation for a mixture of hydrogen and sodium vapor at 664 °C.
- FIG. 17. The spectrometer system irradiation for a mixture of hydrogen and magnesium vapor at 449 °C.
- FIG. 18. The spectrometer system irradiation for a mixture of hydrogen and magnesium vapor at 582 °C.
- FIG. 19. The spectrometer system irradiation for a mixture of hydrogen and magnesium vapor at 654 °C.
- Fig. 20. The spectrometer system irradiation for a mixture of hydrogen and barium vapor at 666 °C.



17. 1 M.115 Ars A

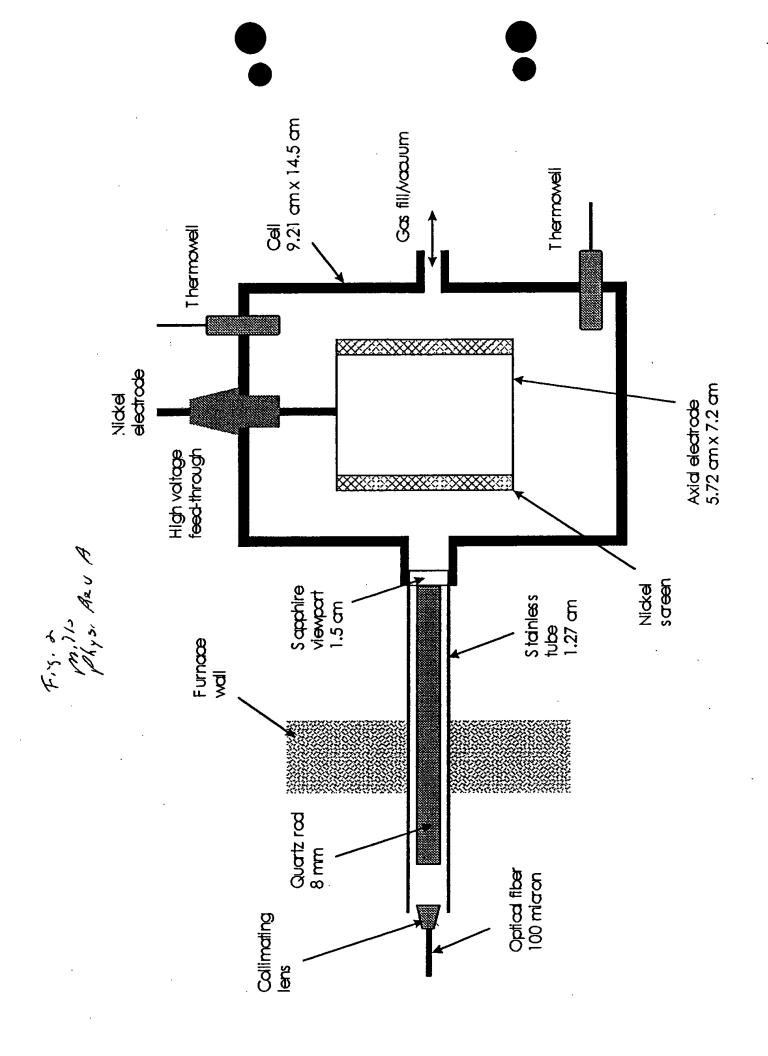
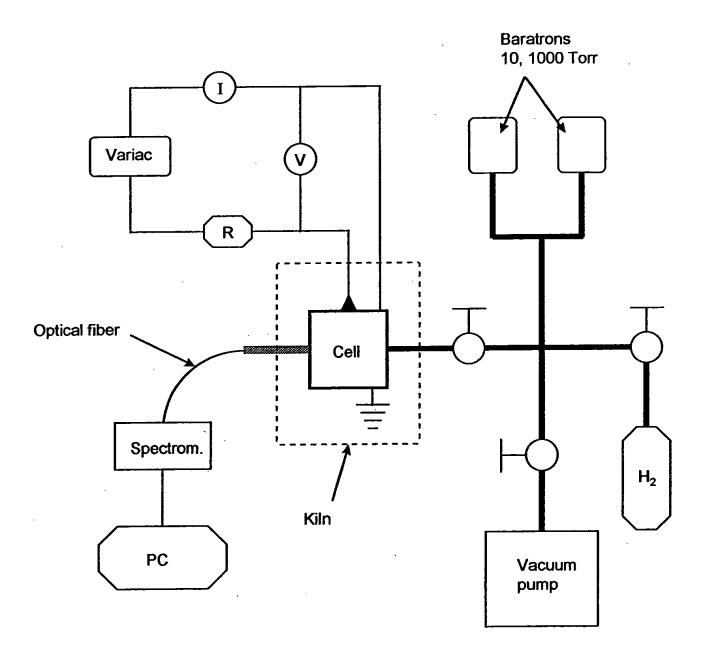
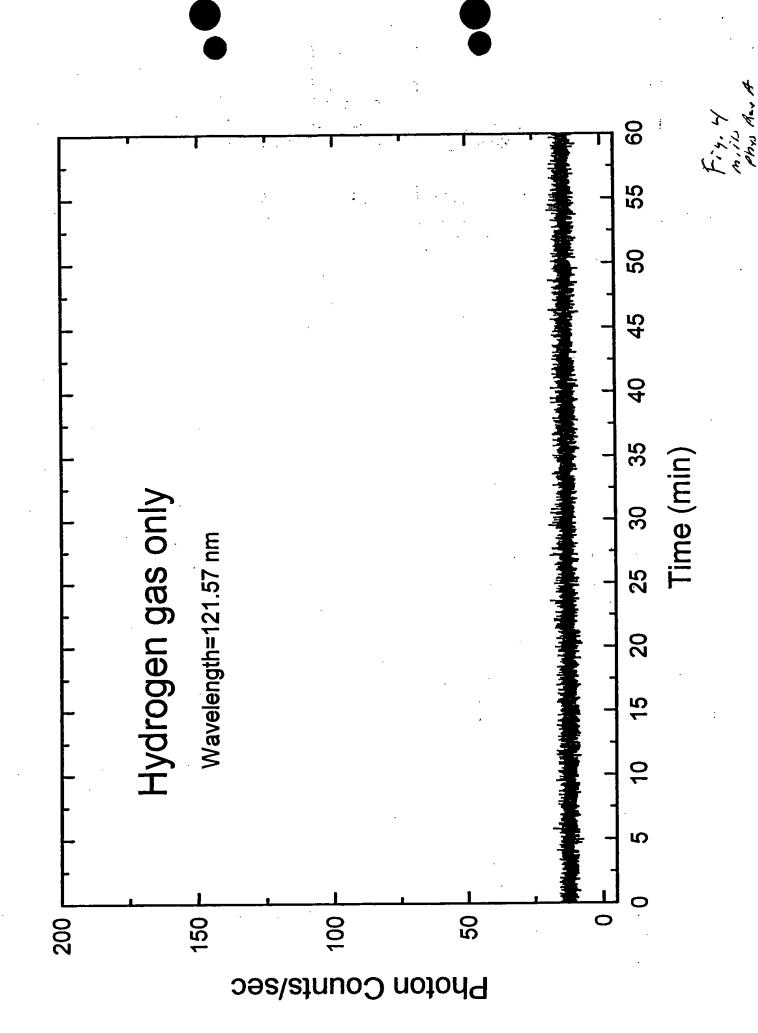
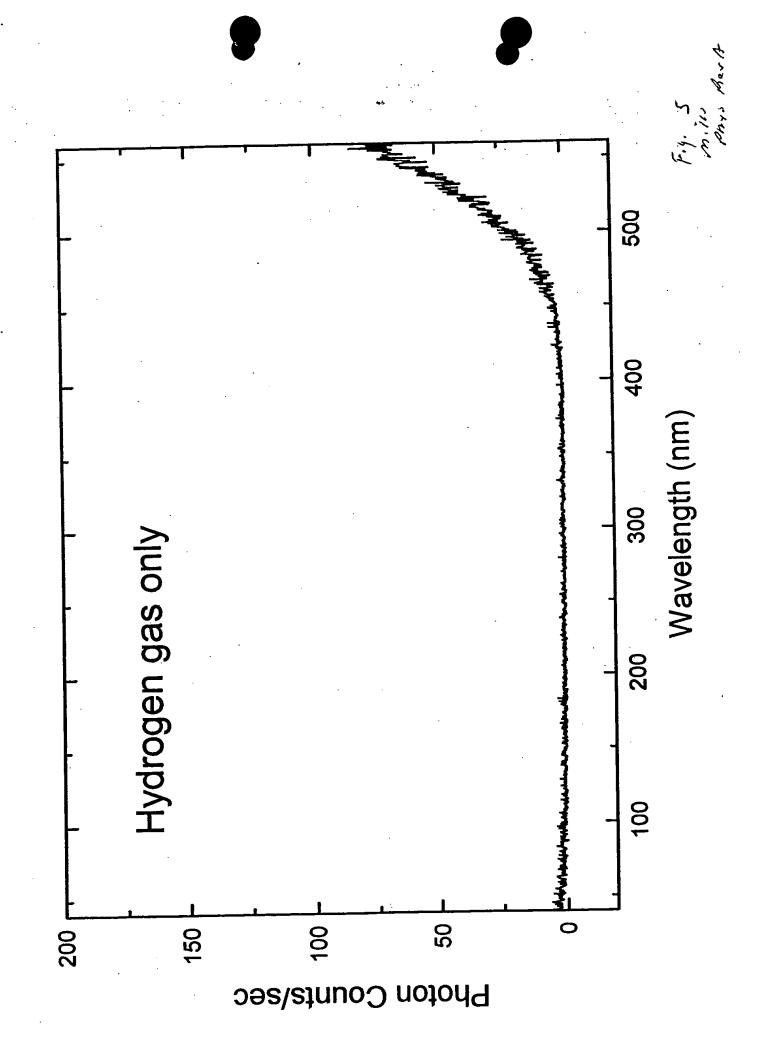
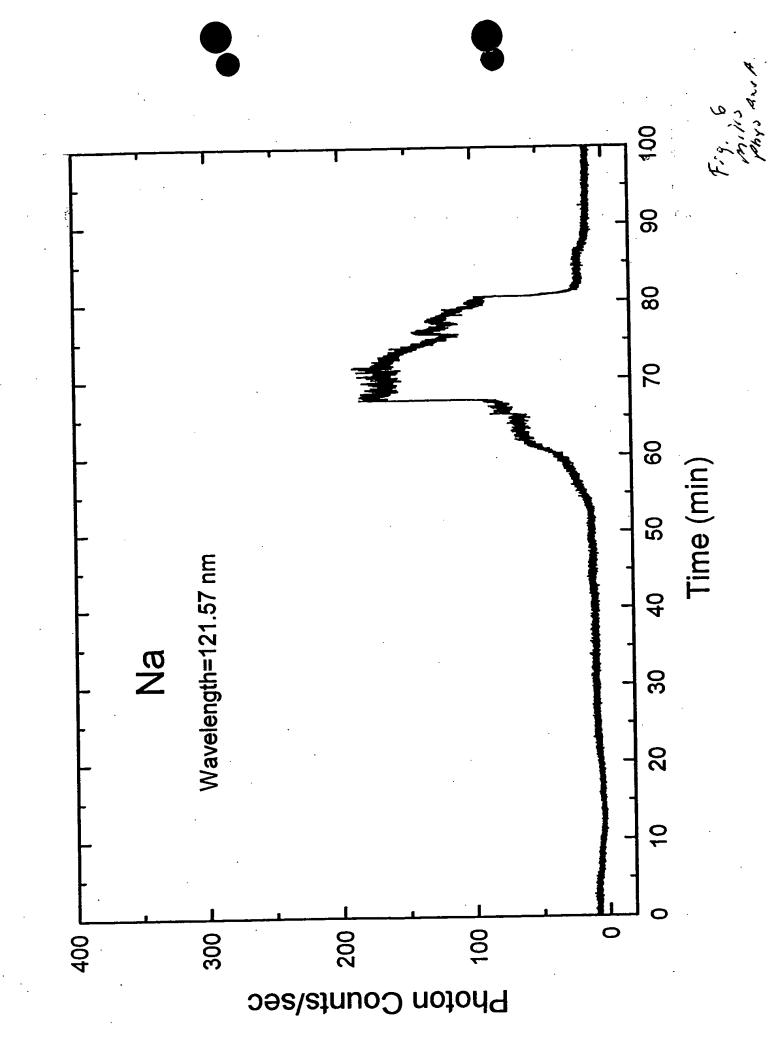


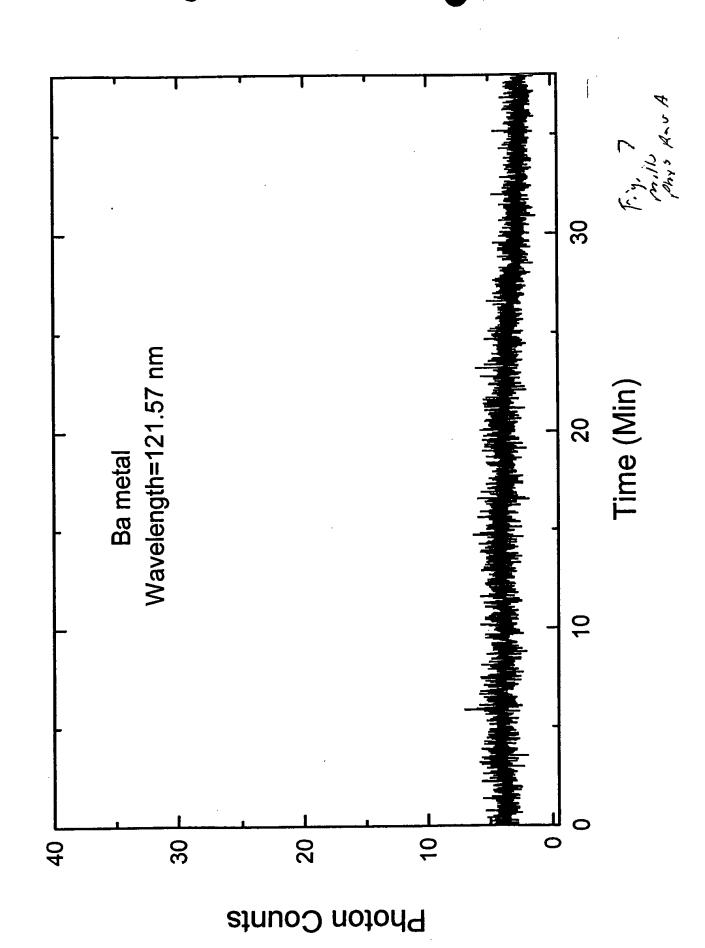
Fig. 3 Mills Ber A

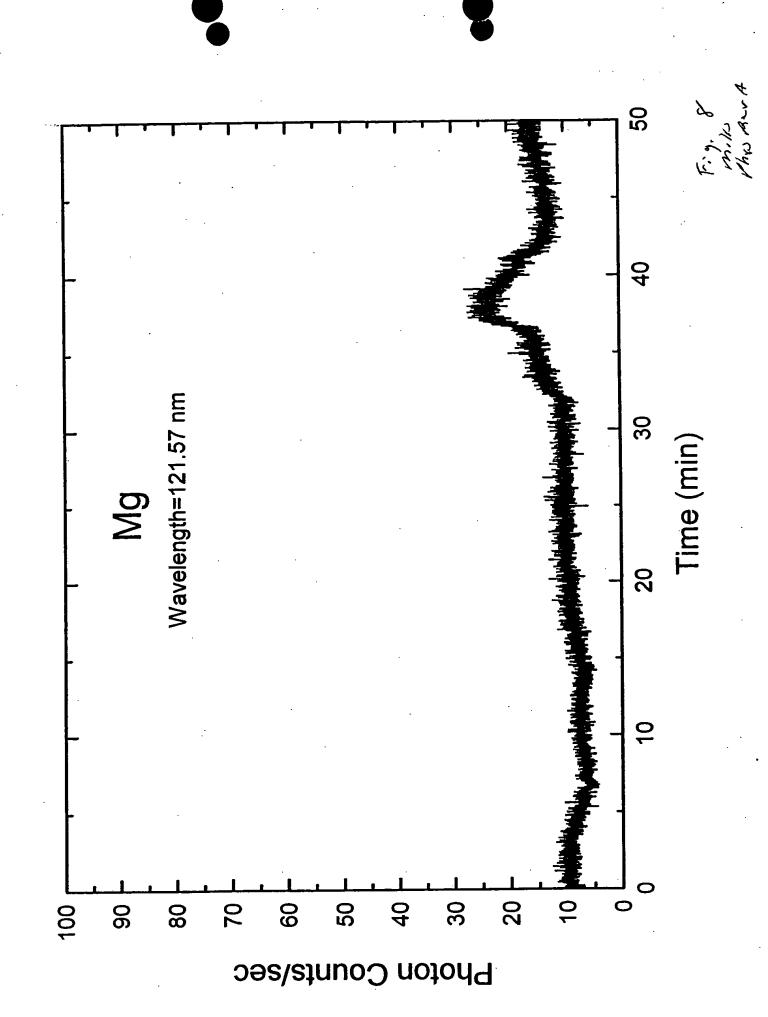


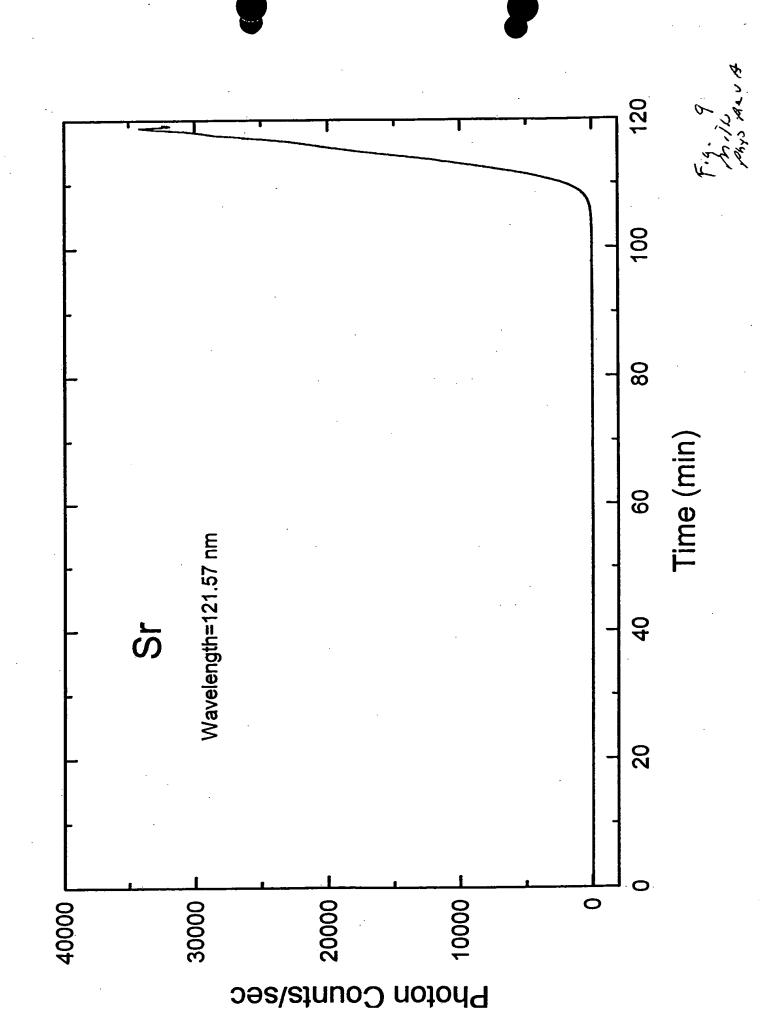












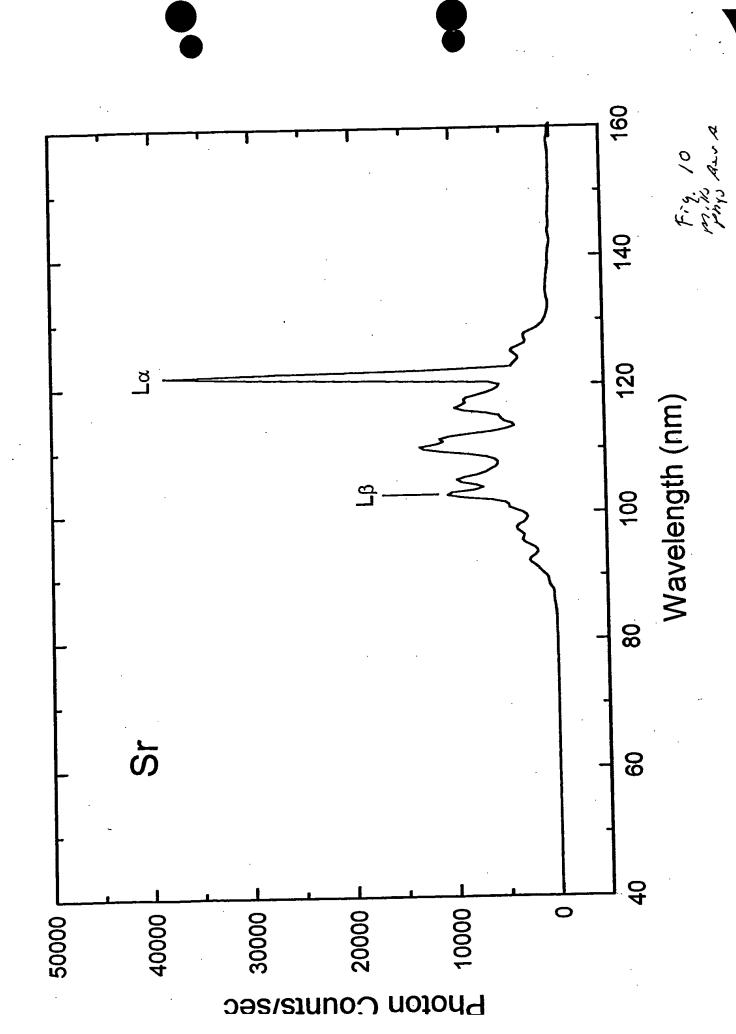
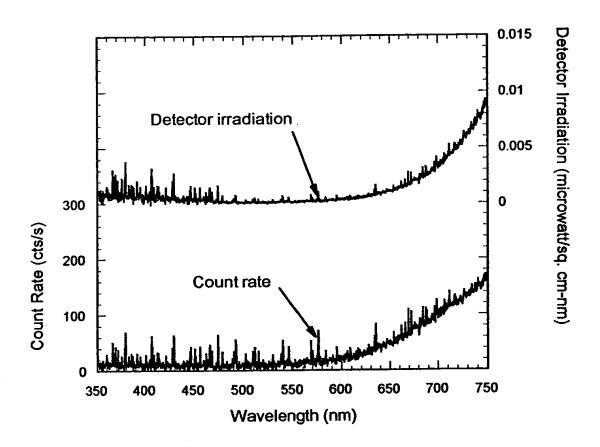


Fig. 11
miles Rev A



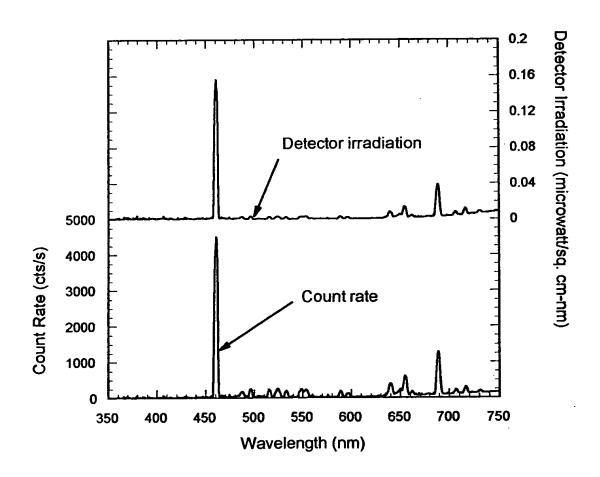


Fig. 13 Millard

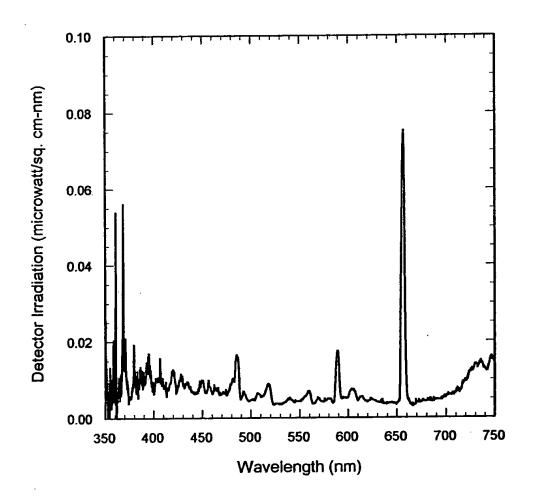


Fig. 14 Millson A

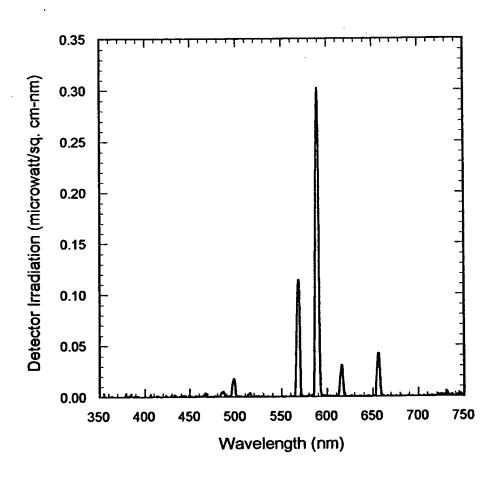


Fig. 15 Mills Phys Acr A

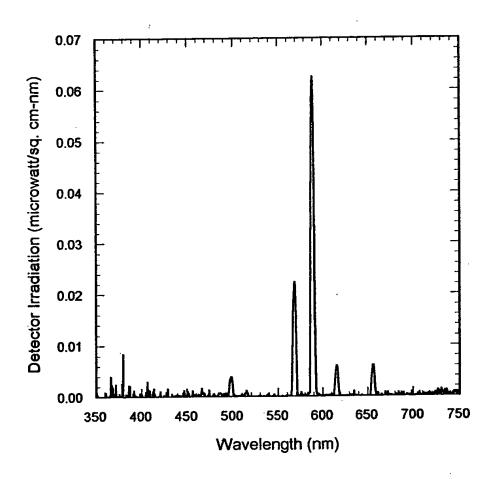


Fig. 16 Mills Phys Bev A

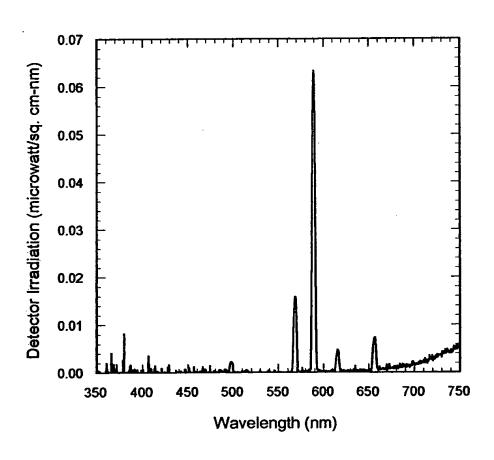


Fig. 17 mills phys Rev A

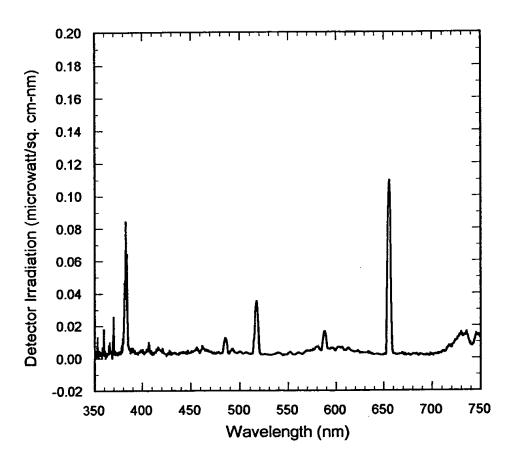


Fig. 18
milli
phys Azu A

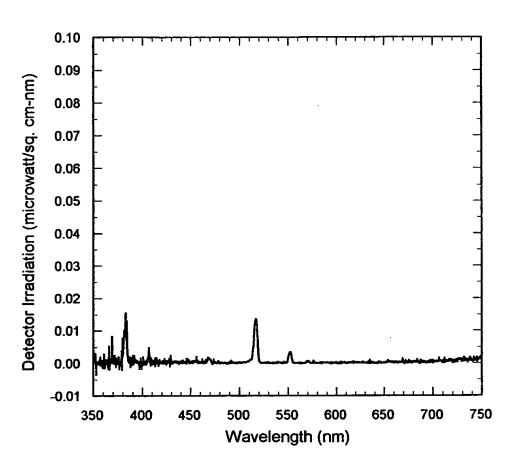


Fig. 19 Mills ARNA

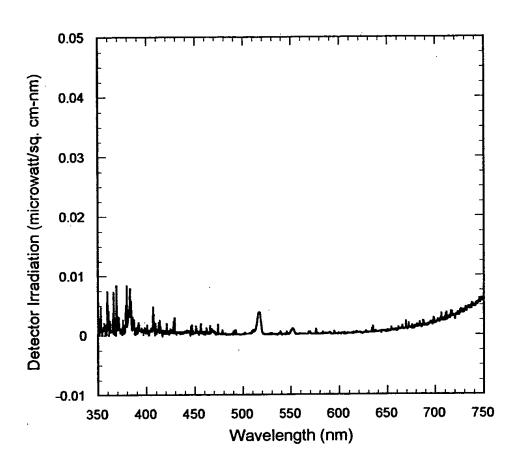
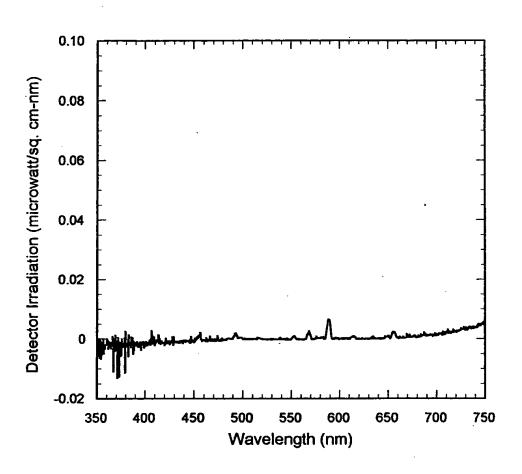


Fig. 20 Mills Bes A.





PERGAMON

International Journal of Hydrogen Energy 25 (2000) 919-943



www.elsevier.com/locate/ijhydene

Observation of extreme ultraviolet hydrogen emission from incandescently heated hydrogen gas with certain catalysts

Randell L. Mills*, Jinquan Dong, Ying Lu

BlackLight Power, Inc., 493 Old Trenton Road, Cranbury, NJ 08512, USA

Abstract

Typically the emission of extreme ultraviolet light from hydrogen gas is achieved via a discharge at high voltage, a high power inductively coupled plasma, or a plasma created and heated to extreme temperatures by RF coupling (e.g. $> 10^6$ K) with confinement provided by a toroidal magnetic field. We report the observation of intense extreme ultraviolet (EUV) emission at low temperatures (e.g. $< 10^3$ K) from atomic hydrogen and certain atomized pure elements or certain gaseous ions which ionize at integer multiples of the potential energy of atomic hydrogen. © 2000 International Association for Hydrogen Energy. Published by Elsevier Science Ltd. All rights reserved.

1. Introduction

A historical motivation to cause extreme ultraviolet (EUV) emission from a hydrogen gas was that the spectrum of hydrogen was first recorded from the only known source, the Sun [1]. Developed sources that provide a suitable intensity are high voltage discharge, synchrotron, and inductively coupled plasma generators [2]. An important variant of the latter type of source is a tokomak [3]. Fujimoto et al. [4] have determined the cross section for production of excited hydrogen atoms from the emission cross sections for Lyman and Balmer lines when molecular hydrogen is dissociated into excited atoms by electron collisions. This data was used to develop a collisional-radiative model to be used in determining the ratio of molecular-to-atomic hydrogen densities in tokomak plasmas. Their results indicate an excitation threshold of 17 eV

for Lyman α emission. Addition of other gases would be expected to decrease the intensity of hydrogen lines which could be absorbed by the gas. Hollander and Wertheimer [5] found that within a selected range of parameters of a plasma created in a microwave resonator cavity, a hydrogen-oxygen plasma displays an emission that resembles the absorption of molecular oxygen. Whereas, a helium-hydrogen plasma emits a very intense hydrogen Lyman α radiation at 121.5 nm which is up to 40 times more intense than other lines in the spectrum. The Lyman α emission intensity showed a significant deviation from that predicted by the model of Fujimoto et al. [4] and from the emission of hydrogen alone.

We report that EUV emission of atomic and molecular hydrogen occurs in the gas phase at low temperatures (e.g. $<10^3$ K) upon contact of atomic hydrogen with certain vaporized elements or ions. Atomic hydrogen was generated by dissociation at a tungsten filament and at a transition metal dissociator that was incandescently heated by the filament. Various elements or ions were atomized by heating to form a low vapor pressure (e.g. 1 torr). The kinetic

E-mail address: rmills@blacklightpower.com (R.L. Mills).

0360-3199/00/\$20.00 © 2000 International Association for Hydrogen Energy. Published by Elsevier Science Ltd. All rights reserved. PII: \$0360-3199(00)00018-5

^{*} Corresponding author. Tel.: +1-609-490-1090; fax: +1-609-490-1066

energy of the thermal electrons at the experimental temperature of <103 K was about 0.1 eV, and the average collisional energies of electrons accelerated by the field of the filament were less than 1 eV. (No blackbody emission was recorded for wavelengths shorter than 400 nm.) Atoms or ions which ionize at integer multiples of the potential energy of atomic hydrogen (e.g. cesium, potassium, strontium, and Rb⁺) caused emission; whereas, other chemically equivalent or similar atoms (e.g. sodium, magnesium, holmium, and zinc metals) caused no emission. Helium ions present in the experiment of Hollander and Wertheimer [5] ionize at a multiple of two times the potential energy of atomic hydrogen. The mechanism of EUV emission cannot be explained by the conventional chemistry of hydrogen, but it is predicted by a solution of the Schrodinger equation with a nonradiative boundary constraint put forward by Mills [6].

Mills predicts that certain atoms or ions serve as catalysts to release energy from hydrogen to produce an increased binding energy hydrogen atom called a hydrino atom having a binding energy of

Binding energy =
$$\frac{13.6 \text{ eV}}{n^2}$$
 (1)

where

$$n = \frac{1}{2}, \frac{1}{3}, \frac{1}{4}, \dots, \frac{1}{p}$$
 (2)

and p is an integer greater than 1, designated as $H_p^{(2n)}$ where a_H is the radius of the hydrogen atom. Hydrinos are predicted to form by reacting an ordinary hydrogen atom with a catalyst having a net enthalpy of reaction of about

$$m \cdot 27.2 \text{ eV}$$
 (3)

where m is an integer. This catalysis releases energy from the hydrogen atom with a commensurate decrease in size of the hydrogen atom, $r_n = na_H$. For example, the catalysis of H(n = 1) to H(n = 1/2) releases 40.8 eV, and the hydrogen radius decreases from a_H to $\frac{1}{2}a_H$.

The excited energy states of atomic hydrogen are also given by Eq. (1) except that

$$n=1,2,3,\ldots \tag{4}$$

The n=1 state is the 'ground' state for 'pure' photon transitions (the n=1 state can absorb a photon and go to an excited electronic state, but it cannot release a photon and go to a lower-energy electronic state). However, an electron transition from the ground state to a lower-energy state is possible by a nonradiative energy transfer such as multipole coupling or a resonant collision mechanism. These lower-energy states

have fractional quantum numbers, $n = \frac{1}{\text{integer}}$. Processes that occur without photons and that require collisions are common. For example, the exothermic chemical reaction of H + H to form H2 does not occur with the emission of a photon. Rather, the reaction requires a collision with a third body, M, to remove the bond energy — $H + H + M \rightarrow H_2 + M^*$ [7]. The third body distributes the energy from the exothermic reaction, and the end result is the H2 molecule and an increase in the temperature of the system. Some commercial phosphors are based on nonradiative energy transfer involving multipole coupling. For example, the strong absorption strength of Sb3+ ions along with the efficient nonradiative transfer of excitation from Sb³⁺ to Mn²⁺, are responsible for the strong manganese luminescence from phosphors containing these ions. Similarly, the n = 1 state of hydrogen and the n = 1integer states of hydrogen are nonradiative, but a transition between two nonradiative states is possible via a nonradiative energy transfer, say n = 1 to n = 1/2. In these cases, during the transition the electron couples to another electron transition, electron transfer reaction, or inelastic scattering reaction which can absorb the exact amount of energy that must be removed from the hydrogen atom. Thus, a catalyst provides a net positive enthalpy of reaction of $m \cdot 27.2$ eV (i.e. it absorbs $m \cdot 27.2$ eV where m is an integer). Certain atoms or ions serve as catalysts which resonantly accept energy from hydrogen atoms and release the energy to the surroundings to effect electronic transitions to fractional quantum energy levels.

An example of nonradiative energy transfer is the basis of commercial fluorescent lamps [8]. Consider Mn²⁺ which when excited sometimes emits yellow luminescence. The absorption transitions of Mn²⁺ are spin-forbidden. Thus, the absorption bands are weak, and the Mn²⁺ ions cannot be efficiently raised to excited states by direct optical pumping. Nevertheless, Mn²⁺ is one of the most important luminescence centers in commercial phosphors. For example, the double-doped phosphor Ca₅(PO₄)₃ F: Sb³⁺, Mn²⁺ is used in commercial fluorescent lamps where it converts mainly ultraviolet light from a mercury discharge into visible radiation. When 2536 Å mercury radiation falls on this material, the radiation is absorbed by the Sb³⁺ ions rather than the Mn2+ ions. Some excited Sb3+ ions emit their characteristic blue luminescence, while other excited Sb3+ ions transfer their energy to Mn2+ ions. These excited Mn2+ ions emit their characteristic yellow luminescence. The efficiency of transfer of ultraviolet photons through the Sb³⁺ ions to the Mn²⁺ ions can be as high as 80%. The strong absorption strength of Sb3+ ions along with the efficient transfer of excitation from Sb3+ to Mn2+ are responsible for the strong manganese luminescence from this material.

This type of nonradiative energy transfer is common.



R.L. Mills et al. | International Journal of Hydrogen Energy 25 (2000) 919-943

The ion which emits the light and which is the active :lement in the material is called the activator; and the on which helps to excite the activator and makes the naterial more sensitive to pumping light is called the ensitizer. Thus, the sensitizer ion absorbs the radiation

and becomes excited. Because of a coupling between sensitizer and activator ions, the sensitizer transmits its excitation to the activator, which becomes excited, and the activator may release the energy as its own characteristic radiation. The sensitizer to activator transfer is

able I lydrogen catalysts providing a net positive enthalpy of reaction of m-27.2 eV by one or more electron ionizations to the conti-

atalysts	IP ₁	IP ₂	IP ₃	IP ₄	IP ₅	IP ₆	IP ₇	IP ₈	Enthalpy	m
i	5.39172	75.6402			·	***	· · · · · ·		81.032	3
e	9.32263	18.2112					•		27.534	1
•	4.34066	31.63	45.806						81.777	3
'a	6.11316	11.8717	50.9131	67.27					136.17	5
i	6.8282	13.5755	27.4917	43.267	99.3				190.46	7
	6.7463	14.66	29.311	46.709	65.2817				162.71	6
r	6.76664	16.4857	30.96						54.212	2
ln	7.43402	15.64	33.668	51.2					107.94	4
e	7.9024	16.1878	30.652						54.742	2
8	7.9024	16.1878	30.652	54.8					109.54	4
0	7.881	17.083	33.5	51.3					109.76	4
0	7.881	17.083	33.5	51.3	79.5				189.26	7
i	7.6398	18.1688	35.19	54.9	76.06				191.96	7
i	7.6398	18.1688	35.19	54.9	76.06	108			299.96	11
u	7.72638	20.2924							28.019	1
1	9.39405	17.9644							27.358	i
1	9.39405	17.9644	39.723	59.4	82.6	108	134	174	625.08	23
3	9.8152	18.633	28.351	50.13	62.63	127.6			297.16	11
	9.75238	21.19	30.8204	42.945	68.3	81.7	155.4		410.11	15
£	13.9996	24.3599	36.95	52.5	64.7	78.5			271.01	10
5	13.9996	24.3599	36.95	52.5	64.7	78.5	111		382.01	14
)	4.17713	27.285	40	52.6	71	84.4	99.2		378.66	14
)	4.17713	27.285	40	52.6	71	84.4	99.2	136	514.66	19
	5.69484	11.0301	42.89	57	71.6				188.21	7
)	6.75885	14.32	25.04	38.3	50.55				134.97	5
0	7.09243	16.16	27.13	46.4	54.49	68.8276			151.27	. 8
9	7.09243	16.16	27.13	46.4	54.49	68.8276	125.664	143.6	489.36	18
	8.3369	19.43							27.767	1
	7.34381	14.6323	30.5026	40.735	72.28				165.49	6
	9.0096	18.6							27.61	ĩ
	9.0096	18.6	27.96						55.57	2
	3.8939	23.1575							27.051	i
	5.5387	10.85	20.198	36.758	65.55				138.89	5
	5.5387	10.85	20.198	36.758	65.55	77.6			. 216.49	8
	5.464	10.55	21.624	38.98	57.53				134.15	5
	5.6437	11.07	23.4	41.4					81.514	3
	6.15	12.09	20.63	44					82.87	3
	5.9389	11.67	22.8	41.47					81.879	3
	7.41666	15.0322	31.9373						54.386	2
+	8.9587	18.563							27.522	1
+		54.4178							54.418	2
+		47.2864	71.6200	98.91					217.816	8
+		27.285					•		27.285	ì
+ 2+				54.8					54.8	2
2+ 4+			27.13						27.13	ī
4+ +					54.49			•	54.49	2
•				54					54	2

not a radiative emission and absorption process, rather a nonradiative transfer. The nonradiative transfer may be by electric or magnetic multipole interactions. In the transfer of energy between dissimilar ions, the levels will, in general, not be in resonance, and some of the energy is released as a phonon or phonons. In the case of similar ions, the levels should be in resonance, and phonons are not needed to conserve energy.

Sometimes the host material itself may absorb (usually in the ultraviolet) and the energy can be transferred nonradiatively to dopant ions. For example, in YVO₄: Eu³⁺, the vanadate group of the host material absorbs ultraviolet light, then transfers its energy to the Eu³⁺ ions which emit characteristic Eu³⁺ luminescence.

The catalysis of hydrogen involves the nonradiative transfer of energy from atomic hydrogen to a catalyst which may then release the transferred energy by radiative and nonradiative mechanisms. As a consequence of the nonradiative energy transfer, the hydrogen atom becomes unstable and emits further energy until it achieves a lower-energy nonradiative state having a principal energy level given by Eq. (1).

For example, a catalytic system is provided by the ionization of t electrons from an atom each to a continuum energy level such that the sum of the ionization energies of the t electrons is approximately $m \cdot 27.2$ eV where t and m are each an integer. One such catalytic system involves cesium. The first and second ionization energies of cesium are 3.89390 eV and 23.15745 eV, respectively [9]. The double ionization (t = 2) reaction of Cs to Cs²⁺, then, has a net enthalpy of reaction of 27.05135 eV, which is equivalent to m = 1 in Eq. (3).

27.05135 eV + Cs(m) + H
$$\left[\frac{a_{\rm H}}{p}\right]$$
 \rightarrow Cs²⁺ + 2e⁻
+ H $\left[\frac{a_{\rm H}}{(p+1)}\right]$ + $\left[(p+1)^2 - p^2\right]$ × 13.6 eV (5)

$$Cs^{2+} + 2e^{-} \rightarrow Cs(m) + 27.05135 \text{ eV}$$
 (6)

And, the overall reaction is

$$H\left[\frac{a_{\rm H}}{p}\right] \rightarrow H\left[\frac{a_{\rm H}}{(p+1)}\right] + \left[(p+1)^2 - p^2\right] \times 13.6 \,\text{eV}$$
 (7)

Thermal energies may broaden the enthalpy of reaction. The relationship between kinetic energy and temperature is given by

$$E_{\rm kinetic} = \frac{3}{2}kT \tag{8}$$

For a temperature of 1200 K, the thermal energy is 0.16 eV, and the net enthalpy of reaction provided by

cesium metal is 27.21 eV which is an exact match to the desired energy.

Hydrogen catalysts capable of providing a net enthalpy of reaction of approximately $m \cdot 27.2$ eV where m is an integer to produce hydrino whereby telectrons are ionized from an atom or ion are given in Table 1. The atoms or ions given in the first column are ionized to provide the net enthalpy of reaction of $m \cdot 27.2$ eV given in the tenth column where m is given in the eleventh column. The electrons which are ionized are given with the ionization potential (also called ionization energy or binding energy). The ionization potential of the nth electron of the atom or ion is designated by IP_n and is given by the CRC [9]. That is, for example, $Cs + 3.89390 \text{ eV} \rightarrow Cs^+ + e^-$ and $Cs^+ +$ 23.15745 eV \rightarrow Cs²⁺+e⁻. The first ionization potential, $IP_1 = 3.89390$ eV, and the second ionization potential, $IP_2 = 23.15745$ eV, are given in the second and third columns, respectively. The net enthalpy of reaction for the double ionization of Cs is 27.05135 eV as given in the tenth column, and m = 1 in Eq. (3) as given in the eleventh column.

The energy released during catalysis may undergo internal conversion and ionize or excite molecular and atomic hydrogen resulting in hydrogen emission which includes well characterized ultraviolet lines such as the Lyman series. Lyman α emission was sought by EUV spectroscopy. Due to the extremely short wavelength of this radiation, 'transparent' optics do not exist. Therefore, a windowless arrangement was used wherein the source was connected to the same vacuum vessel as the grating and detectors of the EUV spectrometer. Windowless EUV spectroscopy was performed with an extreme ultraviolet spectrometer that was mated with the cell. Differential pumping permitted a high pressure in the cell as compared to that in the spectrometer. This was achieved by pumping on the cell outlet and pumping on the grating side of the collimator that served as a pin-hole inlet to the optics. The cell was operated under hydrogen flow conditions while maintaining a constant hydrogen pressure in the cell with a mass flow controller.

2. Experimental

The experimental set up, shown in Fig. 1, comprised a quartz cell which was 500 mm in length and 50 mm in diameter. A sample reservoir that was heated independently using an external heater powered by a constant power supply was on one end of the quartz cell. Three ports for gas inlet, outlet, and photon detection were on the other end of the cell. A tungsten filament (0.5 mm, total resistance ~2.5 ohm) and a titanium or nickel cylindrical screen (300 mm long and 40 mm in diameter) that performed as a hydrogen dissociator





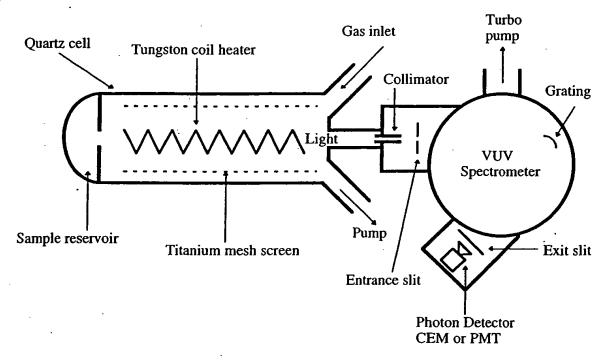


Fig. 1. The experimental set up comprising a gas cell light source and an EUV spectrometer which was differentially pumped.

were inside the quartz cell. The filament was 0.508 mm in diameter and 800 cm in length. The filament was coiled on a grooved ceramic support to maintain its shape when heated. The return lead ran through the middle of the ceramic support. The titanium screen was electrically floated. The power applied to the filament ranged from 300 to 600 W and was supplied by a Sorensen 80-13 power supply which was controlled by a constant power controller. The voltage across the filament was about 55 V and the current was about 5.5 A at 300 W. The temperature of the tungsten filament was estimated to be in the range of 1100 to 1500°C. The external cell wall temperature was about 700°C. The hydrogen gas pressure inside the cell was maintained at about 300 mtorr. The entire quartz cell was enclosed inside an insulation package comprised of Zircar AL-30 insulation. Several K type thermocouples were placed in the insulation to measure key temperatures of the cell and insulation. The thermocouples were read with a multichannel computer data acquisition system.

In the present study, the light emission phenomena was studied for more than 130 inorganic compounds and pure elements. The inorganic test materials were coated on a titanium or nickel screen dissociator by the method of incipient wetness. That is the screen was coated by dipping it in a concentrated deionized aqueous solution or suspension, and the crystalline ma-

terial was dried on the surface by heating for 12 h in a drying oven at 130°C. A new dissociator was used for each experiment. The chemicals on the screen were heated by the tungsten filament and vaporized. Pure elements with a high vapor pressure as well as inorganic compounds were placed in the reservoir and volatized by the external heater. Test chemicals with a low vapor pressure (high melting point) were volatilized by suspending a foil of the material (2 cm by 2 cm by 0.1 cm thick) between the filament and a titanium or nickel dissociator and heating the test material with the filament. The cell was increased in temperature to the maximum possible that was permissible with the power supply (about 300 W).

The light emission was introduced to a EUV spectrometer for spectral measurement. The spectrometer was a McPherson 0.2 m monochromator (Model 302, Seya-Namioka type) equipped with a 1200 lines/mm holographic grating. The wavelength region covered by the monochromator was 30–560 nm. A channel electron multiplier (CEM) was used to detect the EUV light. The wavelength resolution was about 12 nm (FWHM) with an entrance and exit slit width of 300 \times 300 μ m. The vacuum inside the monochromator was maintained below 5×10^{-4} torr by a turbo pump. The EUV spectrum (40–160 nm) of the cell emission was recorded at about the point of the maximum Lyman α emission.



tungsten filament and RbCl in the catalyst reser-

- In the case that a hazardous test material was run, the cell was closed, and the UV-VIS spectrum (300-560 nm) of the cell emission was recorded with a photomultiplier tube (PMT) and a sodium salicylate scintillator. The PMT (model R1527P, Hamamatsu) used has a spectral response in the range of 185-680 nm with a peak efficiency at about 400 nm. The scan interval was 0.4 nm. The inlet and outlet slit were 500-
- 500 μm. The UV-VIS emission from the gas cell was chan-

neled into the UV-VIS spectrometer using a 4 m long, five stand fiber optic cable (Edmund Scientific Model #E2549) having a core diameter of 1958 μm and a maximum attenuation of 0.19 dB/m. The fiber optic cable was placed on the outside surface of the top of the Pyrex cap of the gas cell. The fiber was oriented to maximize the collection of light emitted from inside the cell. The room was made dark. The other end of the fiber optic cable was fixed in a aperture manifold that attached to the entrance aperture of the UV-VIS spectrometer.

The experiments performed according to number

- 1. KCl/10% H₂O₂ treated titanium dissociator with tungsten filament
- 2. K₂CO₃/10% H₂O₂ treated titanium dissociator with tungsten filament and RbCl in the catalyst reservoir
- 3. K₂CO₃/10% H₂O₂ treated titanium dissociator with tungsten filament
- 4. Na₂CO₃/10% H₂O₂ treated titanium dissociator with tungsten filament
- 5. Rb₂CO₃/10% H₂O₂ treated titanium dissociator with tungsten filament
- 6. Cs₂CO₃/10% H₂O₂ treated titanium dissociator with tungsten filament
- 7. repeat Na₂CO₃/10% H₂O₂ treated titanium dissociator with tungsten filament
- 8. K₂CO₃ /10% H₂O₂ treated nickel dissociator with tungsten filament
- 9. KNO₃/10% H₂O₂ treated titanium dissociator with . tungsten filament
- 10. repeat K₂CO₃/10% H₂O₂ treated titanium dissociator with tungsten filament
- 11. K₂SO₄/10% H₂O₂ treated titanium dissociator with tungsten filament
- 12. LiNO₃/10% H₂O₂ treated titanium dissociator with tungsten filament
- 13. Li₂CO₃/10% H₂O₂ treated titanium dissociator with tungsten filament
- 14. MgCO₃/10% H₂O₂ treated titanium dissociator with tungsten filament
- 15. repeat RbCl/10% H₂O₂ treated titanium dissociator with tungsten filament; run at very high temperature to volatilize the catalyst
- 16. RbCl/10% H₂O₂ treated titanium dissociator with

- 17. K₂CO₃ coated on titanium dissociator with tung-
- sten filament
- 18. KHCO₃/10% H₂O₂ treated titanium dissociator with tungsten filament
- 19. CaCO₃/10% H₂O₂ treated titanium dissociator with tungsten filament
- 20. K₃PO₄/10% H₂O₂ treated titanium dissociator with tungsten filament
- 21. samarium foil with titanium dissociator and tungsten filament
- 22. zinc foil with titanium dissociator and tungsten filament
- 23. iron foil with titanium dissociator and tungsten filament
- 24. copper foil with titanium dissociator and tungsten filament
- 25. chromium foil with titanium dissociator and tungsten filament
- 26. holmium foil with titanium dissociator and tungsten filament
- 27. potassium metal in catalyst reservoir with titanium dissociator and tungsten filament
- 28. dysprosium foil with titanium dissociator and tungsten filament
- 29. magnesium foil with titanium dissociator and tungsten filament
- 30. sodium metal in catalyst reservoir with titanium dissociator and tungsten filament
- 31. rubidium metal in catalyst reservoir with titanium dissociator and tungsten filament
- 32, cobalt foil with titanium dissociator and tungsten filament
- 33. lead foil with titanium dissociator and tungsten filament; used closed cell with Balmer line detection by fiber optic cable as indication of EUV
- 34. manganese foil with titanium dissociator and tungsten filament
- 35. gadolinium foil with titanium dissociator and tungsten filament
- 36. lithium metal in catalyst reservoir with titanium dissociator and tungsten filament
- 37. praseodymium foil with titanium dissociator and tungsten filament
- 38. vanadium foil with titanium dissociator and tungsten filament
- 39. tin foil with titanium dissociator and tungsten filament
- 40. platinum foil with titanium dissociator and tungsten filament
- 41. palladium foil with titanium dissociator and tungsten filament
- 42. erbium foil with titanium dissociator and tungsten filament
- 43. aluminum foil with titanium dissociator and tung-



- sten filament
- 44. nickel foil with titanium dissociator and tungsten filament
- 45. molybdenum foil with titanium dissociator and tungsten filament
- 46. cerium foil with titanium dissociator and tungsten filament
- 47. repeat potassium metal in catalyst reservoir with titanium dissociator and tungsten filament at lower catalyst reservoir heater power to keep potassium metal in reaction zone longer
- 48. niobium foil with titanium dissociator and tungsten filament
- 49. tungsten filament with titanium dissociator and mixture of potassium metal and rubidium metal
- repeat cobalt foil with titanium dissociator and tungsten filament
- 51. silver foil with titanium dissociator and tungsten filament
- 52. calcium metal in catalyst reservoir with titanium dissociator and tungsten filament
- chromium foil with titanium dissociator and tungsten filament
- K₂CO₃ coated on nickel dissociator and tungsten filament
- 55. KHSO₄ coated titanium dissociator and tungsten filament
- 56. KHCO₃ coated titanium dissociator and tungsten filament
- 57. cesium metal in catalyst reservoir with titanium dissociator and tungsten filament
- 58. neon gas with titanium dissociator and tungsten filament
- 59. MoI₂ in catalyst reservoir with titanium dissociator and tungsten filament at low catalyst reservoir heater power to keep MoI₂ in reaction zone
- 60. repeat Cs₂CO₃ coated titanium dissociator and tungsten filament
- osmium foil with titanium dissociator and tungsten filament
- high purity carbon rod with titanium dissociator and tungsten filament
- repeat lithium metal in catalyst reservoir with titanium dissociator and tungsten filament
- tantalum foil with titanium dissociator and tungsten filament
- KH₂PO₄/10% H₂O₂ treated titanium dissociator and tungsten filament
- 66. etched germanium with titanium dissociator and tungsten filament
- 67. helium gas with titanium dissociator and tungsten filament
- etched silicon with titanium dissociator and tungsten filament
- 69. bismuth foil in catalyst reservoir with titanium dissociator and tungsten filament

- Strontium metal in catalyst reservoir with titanium dissociator and tungsten filament
- 71. etched gallium in catalyst reservoir with titanium dissociator and tungsten filament
- repeat iron foil with titanium dissociator and tungsten filament
- 73. argon gas with titanium dissociator and tungsten filament
- 74. selenium foil in catalyst reservoir with titanium dissociator and tungsten filament; used closed cell with Balmer line detection by fiber optic cable as indication of EUV
- RbI + KI coated titanium dissociator with tungsten filament
- SrCl₂ + FeCl₂ coated titanium dissociator with tungsten filament
- indium foil with titanium dissociator and tungsten filament
- zirconium foil with titanium dissociator and tungsten filament
- barium metal in catalyst reservoir with titanium dissociator and tungsten filament
- antimony foil in catalyst reservoir with titanium dissociator and tungsten filament
- ruthenium foil with titanium dissociator and tungsten filament
- yttrium foil in catalyst reservoir with titanium dissociator and tungsten filament
- 83. cadmium foil with titanium dissociator and tungsten filament
- 84. repeat samarium foil with titanium dissociator and tungsten filament
- 85. K₂HPO₄ coated titanium dissociator with tungsten filament
- SrCO₃ coated titanium dissociator with tungsten filament
- 87. ErCl₃ + MgCl₂ coated titanium dissociator with tungsten filament
- LiF + PdCl₂ coated titanium dissociator with tungsten filament
- EuCl₃ + MgCl₂ coated titanium dissociator with tungsten filament
- 90. La₂ (CO₃)₃ coated titanium dissociator with tungsten filament
- 91. Ag₂SO₄ coated titanium dissociator with tungsten filament
- Er₂(CO₃)₃ coated titanium dissociator with tungsten filament
- 93. repeat samarium foil third time with titanium dissociator and tungsten filament
- 94. Y₂(SO₄)₃ coated titanium dissociator with tungsten filament
- SiO₂ coated titanium dissociator with tungsten filament
- Zn(NO₃)₂ coated titanium dissociator with tungsten filament

Table 2

Extreme ultraviolet light emission from atomic hydrogen and atomized pure elements or gaseous inorganic compounds at low temperatures (e.g. < 10³ K)

Element*	Compound®	Experiment Gas number	Condensed metal vapor coating observed	Maximum intensity at zero order (counts/s)	Maximum intensity of hydrogen lyman α (counts/sec) ^b
	KCJ/H ₂ O ₂	1 H ₂	;	Presence of blue light by eye	
	K ₂ CO ₃ /H ₂ O ₂ and K _D C ₁ in reservoir K ₂ CO ₂ /H ₂ O ₂	3 H,	Yes	Daillet p 300	00009
	Na ₂ CO ₃ /H ₂ O ₂	4 H ₂	Yes		1
	Rb ₂ CO ₃ /H ₂ O ₂	5 H ₂	Yes		20000
	C ₃ CO ₃ /H ₂ O ₂	6 H ₂	Yes		30000
	Na ₂ CO ₃ /H ₂ O ₂	7 H ₂	Yes		1
	K ₂ CO ₃ /H ₂ O ₂ nickel dissociator	8 H ₂	Yes		10000
	KNO ₃ /H ₂ O ₂	9 H ₂	Yes		25000
	K ₂ CO ₃ /H ₂ O ₂	10 H ₂	Yes		30000
	K ₂ SO ₄ /H ₂ O ₂	11 H ₂	Yes		2000
	LiNO ₃ /H ₂ O ₂	12 H ₂	Š		2000
	Li ₂ CO ₃ /H ₂ O ₂	13 H ₂	8 Z		2500
	MgCO ₃ /H ₂ O ₂	14 H ₂	Š		150
	RbCl/H2O2	15 H ₂	ŝ		•
	RbCl/H2O2 and RbCl in reservoir	16 H ₂	Yes		1 0
	K ₂ CO,		Yes		2000
	KHCO ₃ /H ₂ O ₂		Yes		40000
	CaCO ₃ /H ₂ O ₂		Yes		7000
	K3PO4/H2O2	20 H ₂	Yes		000/
Samarium		_	Yes		3000
Zinc		22 H ₂	Yes		1 00
Iron		23 H ₂	ž		11000
Copper		24 H ₂	ž		ŧ.
Chromium			Š		1 5
Holmium		26 H ₂	Š		001
Potassium metal in reservoir			Yes		0009
Dysprosium		28 H ₂	Š		ı
Magnesium		29 H ₂	Yes		1
Sodium metal in reservoir		30 H ₂	Yes		170
Rubidium metal in reservoir			Yes		12000
Cobalt			N _o		ı
Lead		33 H ₂	Yes	Balmer β	1
Manganese		34 H ₂	Yes		•
Gadolinium			°		1
Lithium metal in reservoire			;		00%
Praseodymium		37 H ₂	o Z		0007



R.L. Mills et al. 1	International Journal	al of Hydrogen Energy 2	25 (2000) 919–943	927
12000	300 00009	40000 - 200 - 100	39000	continued on next page)

Balmer B

K₂CO₃^dnickel dissociator KHSO₄ KHCO₃ Mol₂ in reservoir Cs₂CO₃ Rbi + KI SrCi₂+ FeCi₂* KH2PO4/H2O2 Potassium and rubidium metals in reservoir

Potassium metal in reservoir

Niobium

Cobalt

Silver

Molybdenum

Cerium

Aluminum

Nickel

Palladium Platinum

Erbium

Calcium metal in reservoir Chromium

Cesium metal in reservoir

Neon gas

Strontium metal in reservoir Lithium metal in reservoir Barium metal in reservoir Antimony in reservoir Gallium in reservoir Germanium Helium gas Ruthenium Argon gas Selenium Zirconium. Tantalum Osmium Bismuth Carbon Indium Silicon Iron

),	Mills et al. International Journal of Hydrogen En	25	(2000) 919-943
•	Mills of al. I international Journal of Hydrogen Dis		(-000)

Table 2 (continued)					
Element	Compound*	Experiment Gas number	Condensed metal vapor coating observed	Maximum intensity at zero order (counts/s)	Maximum intensity of hydrogen lyman α (counts/sec) ^b
Yttrium metal in reservoir Cadmium		82 H ₂ 83 H ₂	No Yes		. 200
Samarium	K ₂ HPO ₄		% K & &		4000
	ErCl ₃ + MgCl ₂		S ₹ Z	·	1 1
	Lif + Facts EuCl ₃ + MgCl ₂		X X		- 0009
	La ₂ (CO ₃) ₃ Ag ₂ SO ₄	90 H ₂ 91 H ₂	X cs		
	Er ₂ (CO ₃),	92 H ₂ 93 H ₂	X Xº		3000
Samanum	Y2(SO4)3		ž:		i 1
	SiO ₂	95 H ₂	° နိ		1
	Ba(NO ₃)2		Š	-	400000
	Al ₂ O ₃		ž		1001
	CrPO.	99 H ₂	S X		00009
	Bi(NO ₃)		Yes		1
	$S_{c_2(CO_3)_3}$		%		r 1
Europium			2		
Rhenium		104 H ₂	2 Z		•
Lutetium	Mg(NO ₃),		Yes		1 000
	Sr(NO ₃) ₂		°Z :		3000
Neodymium		108 H ₂	۲ ج ۲ ج		
Ytterbium	, CX «X				
Thallium			Yes		00062
	R6NO3		Yes) I
Lanthanum	Ć	113 H ₂	o ¥		2000
	Sm(NO ₃)3		S &		1
Lerolum	La(NO ₃),		%		•
Hafnium			\$		1 1
	NaClO ₃	118 H ₂	° Š		2500
	NaNO		3		

|--|

	Sm ₂ (CO ₃) ₃	120 H ₂	Yes	2000
Scandium			×	
	NbO ₂		No	
	KCIO3		Yes	
	BaCO ₃		No	
	Yb(NO ₃)3		No	
Thulium			Yes	nie I
	Yb ₂ (CO ₃) ₃		No	rna I
	RbCIO ₃		Yes	1
	HU*		-	l
Rhodium				Jo
Iridium				nuri
Gold			No No	ıaı
Ytterbium				oj
Hafnium				пу
Potassium metal in reservoir			•	are
Potassium metal in reservoir)gei
	K ₂ CO ₃		Yes 30	n E
	NaI	138 H ₂		ner
				g.

Titanium screen dissociator and tungsten filament except where indicated.
 Lyman α was recorded except for toxic compounds wherein a window was used, and the maximum intensity of Balmer β emission was recorded in (counts/sec) where indi-

cated.

e Quartz cell failed due to reaction with lithium metal.

donly a small amount of K₂CO₃ on the titanium screen dissociator. Channel electron multiplier failed due to reaction with volatized compounds.

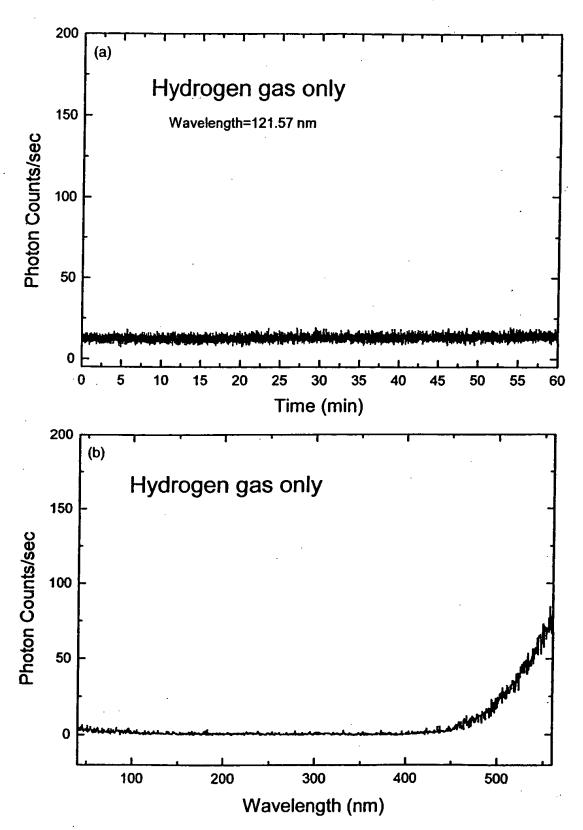
- 97. Ba(NO₃)₂ coated titanium dissociator with tungsten filament
- 98. Al₂O₃ coated titanium dissociator with tungsten filament
- 99. CrPO₄ coated titanium dissociator with tungsten filament
- 100. NaNO₃ coated titanium dissociator with tungsten filament
- 101. Bi(NO₃)₃ coated titanium dissociator with tungsten filament
- Sc₂(CO₃)₃ coated titanium dissociator with tungsten filament
- europium foil with titanium dissociator and tungsten filament
- 104. rhenium foil with titanium dissociator and tungsten filament
- 105. lutenium foil with titanium dissociator and tungsten filament
- 106. Mg(NO₃)₂ coated titanium dissociator with tungsten filament
- 107. Sr(NO₃)₂ coated titanium dissociator with tungsten filament
- 108. neodymium foil with titanium dissociator and tungsten filament
- 109. ytterbium foil with titanium dissociator and tungsten filament
- 110. NaNO₃ coated titanium dissociator with tungsten filament and helium (no hydrogen control)
- 111. thallium foil with titanium dissociator and tungsten filament
- 112. RbNO₃ coated titanium dissociator with tungsten filament
- 113. lanthanum foil with titanium dissociator and tungsten filament
- 114. Sm(NO₃)₃, coated titanium dissociator with tungsten filament
- 115. terbium foil with titanium dissociator and tungsten filament
- 116. La(NO₃)₃ coated titanium dissociator with tungsten filament
- 117. hafnium foil with titanium dissociator and tungsten filament
- 118. NaClO₃ coated titanium dissociator with tungsten filament
- 119. repeat NaNO₃ coated titanium dissociator with tungsten filament
- 120. Sm₂(CO₃)₃ coated titanium dissociator with tungsten filament
- 121. scandium foil with titanium dissociator and tungsten filament
- 122. NbO₂ coated titanium dissociator with tungsten filament
- 123. KClO₃ coated titanium dissociator with tungsten
- 124. BaCO₃ coated titanium dissociator with tungsten filament

- Yb(NO₃)₃ coated titanium dissociator with tungsten filament
- 126. thulium foil with titanium dissociator and tungsten filament
- 127. Yb₂(CO₃)₃ coated titanium dissociator with tungsten filament
- 128. RbClO₃ coated titanium dissociator with tungsten filament
- 129. Hfl₄ coated titanium dissociator with tungsten filament
- rhodium foil with titanium dissociator and tungsten filament
- 131. iridium foil with titanium dissociator and tungsten filament
- 132. gold foil with titanium dissociator and tungsten filament
- 133. repeat ytterbium foil with titanium dissociator and tungsten filament
- 134. repeat hafnium foil with titanium dissociator and tungsten filament
- 135. potassium metal in catalyst reservoir with tungsten filament, titanium dissociator, and neon (no hydrogen control)
- 136. potassium metal in catalyst reservoir with tungsten filament, titanium dissociator, and argon (no hydrogen control)
- 137. K₂CO₃ treated titanium foil with tungsten filament and argon (no hydrogen control)
- 138. NaI treated titanium foil with tungsten filament

3. Results

The results of the extreme ultraviolet (EUV) light emission from atomic hydrogen and atomized pure elements or gaseous inorganic compounds at low temperatures (e.g. $<10^3$ K) are summarized in Table 2. The EUV light emission measurements were performed on more than 100 elements and inorganic compounds comprising 138 experiments as given in the experimental section.

The cell without any test material present was run to establish the baseline of the spectrometer. The intensity of the Lyman α emission as a function of time from the gas cell comprising a tungsten filament, a titanium dissociator, and 0.3 torr hydrogen at a cell temperature of 700°C is shown in Fig. 2 (A). The UV-VIS spectrum (40-560 nm) of the cell emission from the gas cell comprising a tungsten filament, a titanium dissociator, and 0.3 torr hydrogen at a cell temperature of 700°C is shown in Fig. 2 (B). The spectrum was recorded with a photomultiplier tube (PMT) and a sodium salicylate scintillator. No emission was observed except for the blackbody filament radiation at the longer wavelengths.



ig. 2. (Caption overleaf).



The intensity of the Lyman a emission as a function of time from the gas cell comprising a tungsten filament, a titanium dissociator, cesium metal versus sodium metal in the catalyst reservoir, and 0.3 torr hydrogen at a cell temperature of 700°C are shown in Fig. 3 (A) and Fig. 4, respectively. Cesium metal or sodium metal was volatized from the catalyst reservoir by heating it with an external heater. Intense emission was observed from cesium metal starting after 35 min when the cell temperature rose from room temperature to approximately 700°C. The EUV spectrum (40-160 nm) of the cell emission recorded at about the point of the maximum Lyman α emission is shown in Fig. 3(B). In the case of the sodium metal, no emission was observed. The maximum filament power was 500 W. A metal coating formed in the cap of the cell over the course of the experiment in both cases.

The intensity of the Lyman a emission as a function of time from the gas cell comprising a tungsten filament, a titanium dissociator, strontium metal in the catalyst reservoir versus a magnesium foil in the cell, and 0.3 torr hydrogen at a cell temperature of 700°C are shown in Fig. 5 (A) and Fig. 6, respectively. Strontium metal was volatized from the catalyst reservoir by heating it with an external heater. The magnesium foil was volatilized by suspending a 2 cm by 2 cm by 0.1 cm thick foil between the filament and the titanium dissociator and heating the foil with the filament. Strong emission was observed from strontium. The EUV spectrum (40-160 nm) of the cell emission recorded at about the point of the maximum Lyman a emission is shown in Fig. 5 (B). In the case of the magnesium foil, no emission was observed. The maximum filament power was 500 W. The temperature of the foil increased with filament power. At 500 W, the temperature of the foil was 1000°C which would correspond to a vapor pressure of about 100 mtorr. A magnesium metal coating formed in the cap of the cell over the course of the experiment.

The intensity of the Lyman α emission as a function of time from the gas cell comprising a tungsten filament, a titanium dissociator treated with 0.6 M $K_2CO_3/10\%$ H_2O_2 before being used in the cell, and 0.3 torr hydrogen at a cell temperature of 700°C is shown in Fig. 7. The emission reached a maximum of 60,000 counts per second at a filament power of 300 W. At this power level, potassium metal was observed to condense on the wall of the top of the gas cell. The EUV spectrum (40–160 nm) of the cell emission recorded at about the point of the maximum Lyman α

emission is shown in Fig. 8 (A). The UV-VIS spectrum (40-560 nm) of the cell emission recorded with a photomultiplier tube (PMT) and a sodium salicylate scintillator from the gas cell comprising a tungsten filament, a titanium dissociator treated with 0.6 M K₂CO₃/10% H₂O₂ before being used in the cell, and 0.3 torr hydrogen at a cell temperature of 700°C is shown in Fig. 8(B). The visible spectrum is dominated by potassium lines. Hydrogen Balmer lines are also present in the UV-VIS region when the Lyman α emission is present in the EUV region. Thus, recording the Balmer emission corresponds to recording the Lyman α emission. The EUV spectrum (40-160 nm) of the cell emission recorded at about the point of the maximum Lyman a emission from the gas cell comprising a tungsten filament, a titanium dissociator treated with 0.6 M Na₂CO₃/10% H₂O₂ before being used in the cell, and 0.3 torr hydrogen at a cell temperature of 700°C is shown in Fig. 9. Essentially no emission was observed. Sodium metal was observed to condense on the wall of the top of the gas cell after the cell reached 700°C.

The results of the EUV light emission from atomic hydrogen and gaseous inorganic compounds at low temperatures (e.g. < 10³ K) are summarized in Table 2. Among the inorganic compounds tested, very strong hydrogen Lyman alpha line emissions were observed from Ba(NO₃)₂, RbNO₃, NaNO₃, K₂CO₃, KHCO₃, Rb₂CO₃, Cs₂CO₃, SrCO₃, and Sr(NO₃)₂. Fig. 8(A) shows a typical EUV emission spectrum obtained by heating K2CO3 coated on the titanium screen in presence of atomic hydrogen. The main spectral lines were identified as atomic hydrogen Lyman alpha (121.57 nm) and Lyman beta (102.57 nm) lines, and molecular hydrogen emission lines distributed in the region 80-150 nm. The potassium ionic lines (60.07 nm, 60.80 nm and 61.27 nm) were also observed in the spectrum, but they were not resolved. The spectra show that potassium ions were formed in the cell under the experimental conditions. Their actual intensity should be larger than the observed intensity because of the lower monochromator grating efficiency at shorter wavelength.

The results of the EUV light emission from atomic hydrogen and atomized pure elements at low temperatures (e.g. < 10³ K) are summarized in Table 2. Strong hydrogen Lyman alpha line emission was observed from Sr, Rb, Cs, Ca, Fe, and K.

The light emission usually occurred after the power of the filament was increased to above 300 W for about 20 min, and the light was emitted for a period

Fig. 2. (A). The intensity of the Lyman α emission as a function of time from the gas cell comprising a tungsten filament, a titanium dissociator, and 0.3 torr hydrogen at a cell temperature of 700°C. (B). The UV-VIS spectrum (40-560 nm) of the cell emission from the gas cell comprising a tungsten filament, a titanium dissociator, and 0.3 torr hydrogen at a cell temperature of 700°C that was recorded with a photomultiplier tube (PMT) and a sodium salicylate scintillator.



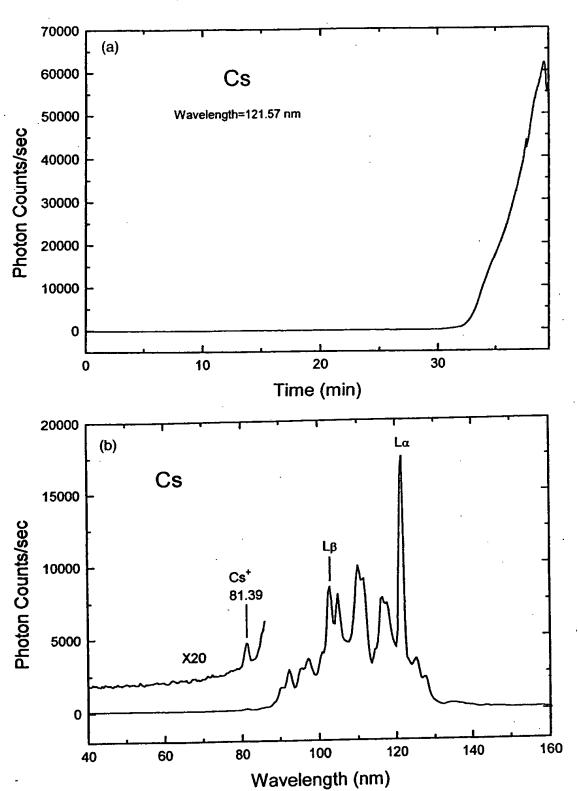


Fig. 3. (Caption overleaf).

depending on the temperature (heater power level), type and quantity of chemicals deposited in the cell. Higher power would cause higher temperature and higher emission intensity, but in the case of volatile chemicals, a shorter duration of emission was observed because the chemicals thermally migrated from the cell and condensed on the wall of the top of the cell. The appearance of a coating from this migration was noted in Table 2. The emission lasted from 1 h to 1 week depending on how much chemical was initially present in the cell and the power level which corresponded to the cell temperature.

4. Discussion

In the cases where Lyman α emission was observed, no possible chemical reactions of the tungsten filament, the dissociator, the vaporized test material, and 0.3 torr hydrogen at a cell temperature of 700°C could be found which accounted for the hydrogen a line emission. In fact, no known chemical reaction releases enough energy to excite Lyman a emission from hydrogen. In many cases such as the reduction of K₂CO₃ by hydrogen, any possible reaction is very endothermic. The emission was not observed with hydrogen alone or with helium, neon, or argon gas. The emission was not due to the presence of a particular anion. Ba is a very efficient source of electrons, and is commonly used to coat the cathode of a plasma discharge cell to improve the emission current [10,11]. No emission was observed with the titanium dissociator with Ba. Intense emission was observed for NaNO3 with hydrogen gas, but no emission was observed when hydrogen was replaced by helium. Intense emission was observed for potassium metal with hydrogen gas, but no emission was observed when hydrogen was replaced by argon. These latter two results indicate that the emission was due to a reaction of hydrogen. The emission of the Lyman lines is assigned to the catalysis of hydrogen which excites atomic and molecular hydrogen.

The only pure elements that were observed to emit EUV are each a catalytic system wherein the ionization of t electrons from an atom to a continuum energy level is such that the sum of the ionization energies of the t electrons is approximately $m \cdot 27.2$ eV where t and m are each an integer. These elements with the specific enthalpies of the

catalytic reactions appear in with the exception of neodymium metal since ionization data is unavailable.

Representative catalytic reactions appear in the balance equations infra. In the case that ordinary atomic hydrogen is the reactant, the parameter p which corresponds to Eq. (2) is one.

4.1. Strontium

One such catalytic system involves strontium. The first through the fifth ionization energies of strontium are 5.69484 eV, 11.03013 eV, 42.89 eV, 57 eV, and 71.6 eV, respectively [9]. The ionization reaction of Sr to Sr^{5+} , (t = 5), then, has a net enthalpy of reaction of 188.2 eV, which is equivalent to m = 7 in Eq. (3).

188.2 eV + Sr(m) + H
$$\left[\frac{a_{\rm H}}{p}\right]$$
 \rightarrow Sr⁵⁺ + 5e⁻
+ H $\left[\frac{a_{\rm H}}{(p+7)}\right]$ + $\left[(p+7)^2 - p^2\right]$ × 13.6 eV (9)

$$Sr^{5+} + 5e^{-} \rightarrow Sr(m) + 188.2 \text{ eV}$$
 (10)

And, the overall reaction is

$$H\left[\frac{a_{\rm H}}{p}\right] \rightarrow H\left[\frac{a_{\rm H}}{(p+7)}\right] + \left[(p+7)^2 - p^2\right] \times 13.6 \,\text{eV} \quad (11)$$

4.2. Praseodymium and neodymium metal

Another such catalytic system involves praseodymium metal. The first, second, third, fourth, and fifth ionization energies of praseodymium are 5.464 eV, 10.55 eV, 21.624 eV, 38.98 eV, and 57.53 eV, respectively [9]. The ionization reaction of Pr to Pr^{5+} , (t=5), then, has a net enthalpy of reaction of 134.148 eV, which is equivalent to m=5 in Eq. (3).

134.148 eV + Pr(m) + H
$$\left[\frac{a_{\rm H}}{p}\right]$$
 \rightarrow Pr⁵⁺ + 5e⁻
+ H $\left[\frac{a_{\rm H}}{(p+5)}\right]$ + $\left[(p+5)^2 - p^2\right] \times 13.6$ eV (12)

$$Pr^{5+} + 5e^{-} \rightarrow Pr(m) + 134.148 \text{ eV}$$
 (13)

And, the overall reaction is

Fig. 3. (A). The intensity of the Lyman α emission as a function of time from the gas cell comprising a tungsten filament, a titanium dissociator, cesium metal vaporized from the catalyst reservoir, and 0.3 torr hydrogen at a cell temperature of 700°C. (B). The EUV spectrum (40–160 nm) of the cell emission recorded at about the point of the maximum Lyman α emission from the gas cell comprising cesium metal vaporized from the catalyst reservoir, a tungsten filament, a titanium dissociator, and 0.3 torr hydrogen at a cell temperature of 700°C.

R.L. Mills et al. / International Journ
$$H\left[\frac{a_{\rm H}}{p}\right] \rightarrow H\left[\frac{a_{\rm H}}{(p+5)}\right] + \left[(p+5)^2 - p^2\right] \times 13.6 \text{ eV} \quad (14)$$

$$\frac{134.148 \text{ eV}}{5 \times 27.196 \text{ eV}} = \frac{134.148 \text{ eV}}{135.98 \text{ eV}} = 0.987$$

EUV emission was observed in the case of praseodymium metal (Pr(m)). The count rate was about 3000 counts/second. EUV emission was also observed in the case of neodymium metal (Nd(m)). The count rate was about the same as that of praseodymium metal, 3000 counts/second. Neodymium metal (Nd(m)) may comprise a catalytic system by the ionization of 5 electrons from each neodymium atom to a continuum energy level such that the sum of the ionization energies of the 5 electrons is approximately 5-27.2 eV. The first, second, third, and fourth ionization energies of neodymium are 5.5250 eV, 10.73 eV, 21.1 eV, and 40.41 eV, respectively [9]. The fifth ionization energy of neodymium should be about that of praseodymium, 57.53 eV, based on the close match of the first four ioniz-

ation energies with the corresponding ionization energies of praseodymium. In this case, the ionization reaction of Nd to Nd^{5+} , (t = 5), then, has a net enthalpy of reaction of 136.295 eV, which is equivalent to m = 5 in Eq. (3). The reaction is given by Eqs. (12)–(14) with the substitution of neodymium for praseodymium.

$$\frac{136.295 \text{ eV}}{5 \times 27.196 \text{ eV}} = \frac{136.295 \text{ eV}}{135.98 \text{ eV}} = 1.002$$

Furthermore, several cases of inorganic compounds were observed to emit EUV. The only ions that were observed to emit EUV are each a catalytic system wherein the ionization of t electrons from an ion to a continuum energy level is such that the sum of the ionization energies of the t electrons is approximately $m \cdot 27.2$ eV where m and t are each an integer. These ions with the specific enthalpies of the catalytic reactions appear in Table 1 with the exception of Ba^{2+} since ionization data is unavailable.

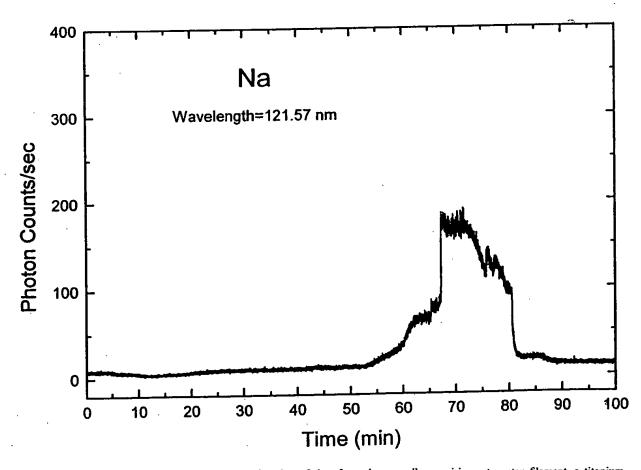


Fig. 4. The intensity of the Lyman α emission as a function of time from the gas cell comprising a tungsten filament, a titanium dissociator, sodium metal vaporized from the catalyst reservoir, and 0.3 torr hydrogen at a cell temperature of 700°C.

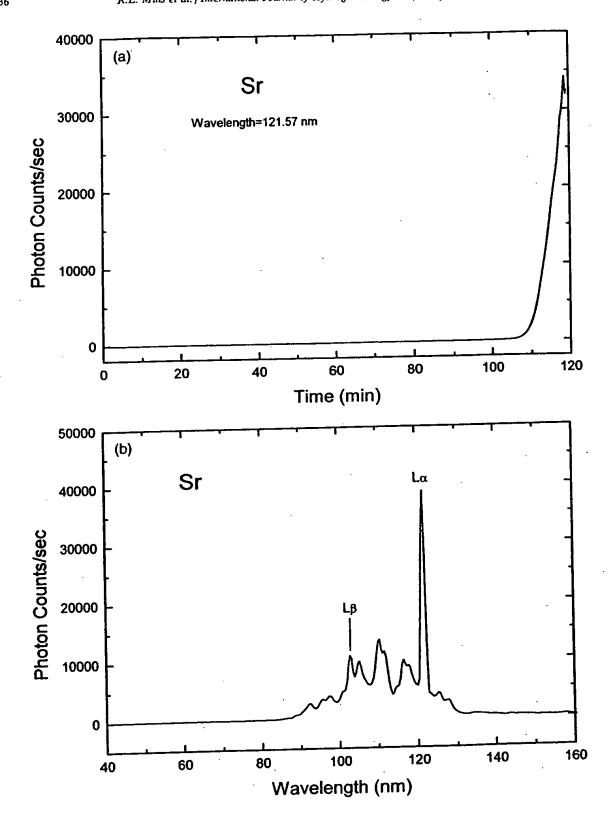


Fig. 5. (Caption opposite).

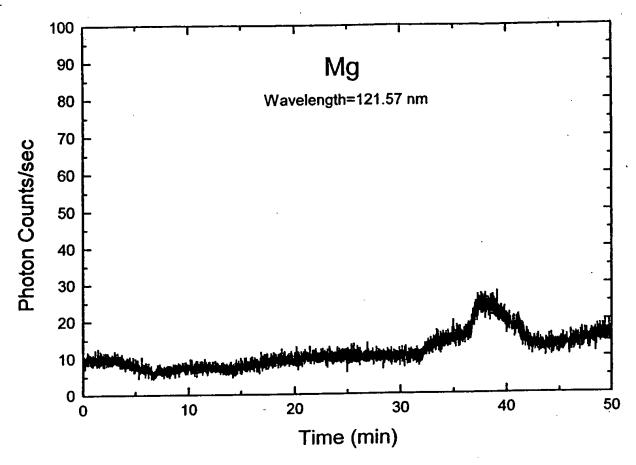


Fig. 6. The intensity of the Lyman α emission as a function of time from the gas cell comprising a tungsten filament, a titanium dissociator, a magnesium foil, and 0.3 torr hydrogen at a cell temperature of 700°C.

4.3. Rubidium

Rubidium ions can also provide a net enthalpy of a multiple of that of the potential energy of the hydrogen atom. The second ionization energy of rubidium is 27.28 eV. The reaction Rb^+ to Rb^{2+} has a net enthalpy of reaction of 27.28 eV, which is equivalent to m = 1 in Eq. (3).

27.28 eV + Rb⁺ + H
$$\left[\frac{a_{\rm H}}{p}\right]$$
 \rightarrow Rb²⁺ + e⁻
+ H $\left[\frac{a_{\rm H}}{(p+1)}\right]$ + $\left[(p+1)^2 - p^2\right] \times 13.6$ eV (15)

$$Rb^{2+} + e^- \rightarrow Rb^+ + 27.28 \text{ eV}$$
 (16)

The overall reaction is

$$H\left[\frac{a_{\rm H}}{p}\right] \rightarrow H\left[\frac{a_{\rm H}}{(p+1)}\right] + \left[(p+1)^2 - p^2\right] \times 13.6 \text{ eV} \quad (17)$$

The catalytic rate and corresponding intensity of EUV emission depends of the concentration of gas phase Rb⁺ ions. Rubidium metal may form RbH which may provide gas phase Rb⁺ ions, or rubidium metal may be ionized to provide gas phase Rb⁺ ions. Rb₂CO₃ comprises two Rb⁺ ions rather than one, and it is not as volatile. But, it may decompose to rubidium metal

Fig. 5. (A). The intensity of the Lyman α emission as a function of time from the gas cell comprising a tungsten filament, a titanium dissociator, strontium metal vaporized from the catalyst reservoir, and 0.3 torr hydrogen at a cell temperature of 700°C. (B). The EUV spectrum (40–160 nm) of the cell emission recorded at about the point of the maximum Lyman α emission from the gas cell comprising a tungsten filament, a titanium dissociator, strontium metal vaporized from the catalyst reservoir, and 0.3 torr hydrogen at a cell temperature of 700°C.



in which case the vapor pressure should be higher than that vaporized from the catalyst reservoir due to the large surface area of the rubidium coated titanium dissociator. Alkali metal nitrates are extraordinarily volatile and can be distilled at 350–500°C [12]. RbNO₃ is the favored candidate for providing gaseous Rb⁺ ions. The EUV spectrum (40–160 nm) of the cell emission recorded at about the point of the maximum Lyman α emission for rubidium metal, Rb₂CO₃, and RbNO₃ is shown in Fig. 10. RbNO₃ produced the highest intensity EUV emission.

4.4. Sodium iodide, sodium metal, sodium carbonate, sodium nitrate

No emission was observed in the case of NaI. No emission was observed in the case of KI either which indicates that iodides form a molecular bond in the gas phase. Essentially no EUV emission was observed

in the case of Na(m) and Na₂CO₃. What little was observed may be due to potassium contamination which was measured by time-of-flight-secondary-ionmass-spectroscopy. EUV emission was observed in the case of NaNO₃. Na(m) is not a catalyst. Na₂CO₃ decomposes to Na(m). Na₂CO₃ is further not a catalyst because two sodium ions are present rather than one, and Na₂CO₃ is not volatile. NaNO₃ is a catalyst which is volatile at the experimental conditions of the EUV experiment. The catalytic system is provided by the ionization of three electrons from Na+ to a continuum energy level such that the sum of the ionization energies of the three electrons is approximately m-27.2 eV where m is an integer. The second, third, and fourth ionization energies of sodium are 47.2864 eV, 71.6200 eV, and 98.91 eV, respectively [9]. The triple ionization reaction of Na⁺ to Na⁴⁺, then, has a net enthalpy of reaction of 217.8164 eV, which is equivalent to m = 8 in Eq. (3).

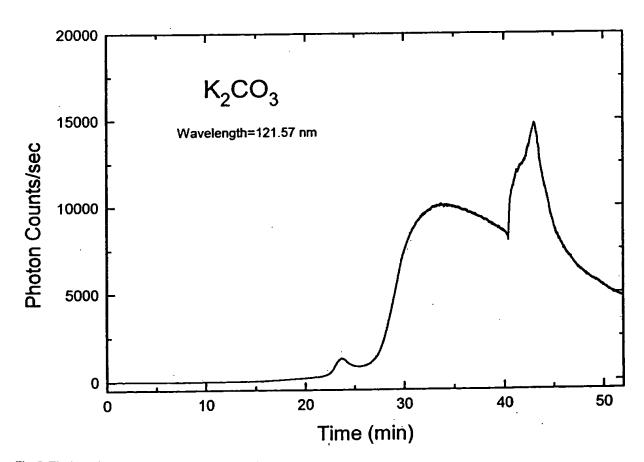


Fig. 7. The intensity of the Lyman α emission as a function of time from the gas cell comprising a tungsten filament, a titanium dissociator treated with 0.6 M K₂CO₃/10% H₂O₂ before being used in the cell, and 0.3 torr hydrogen at a cell temperature of 700°C.

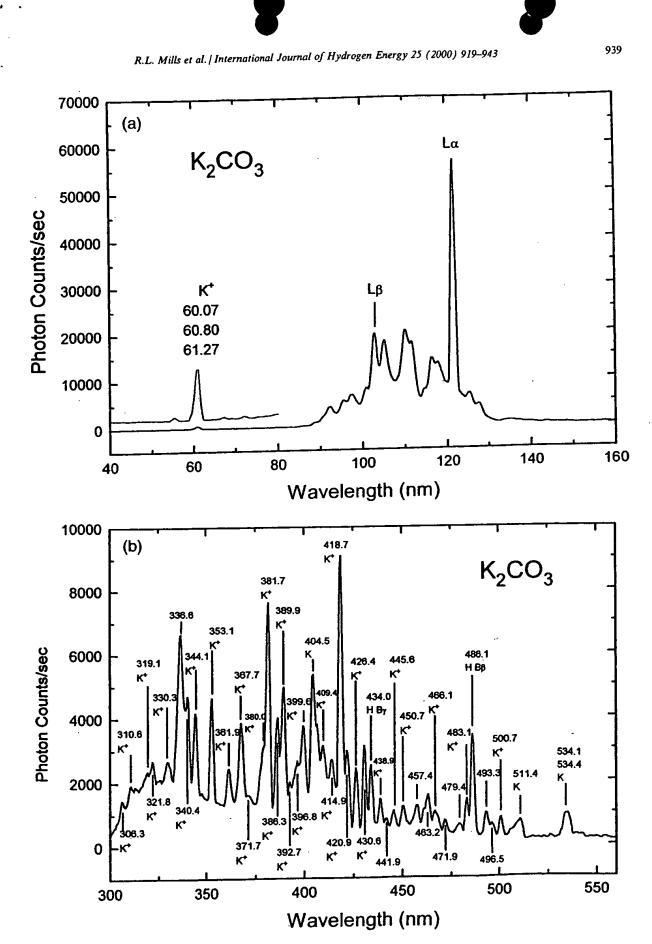


Fig. 8. (Caption overleaf).

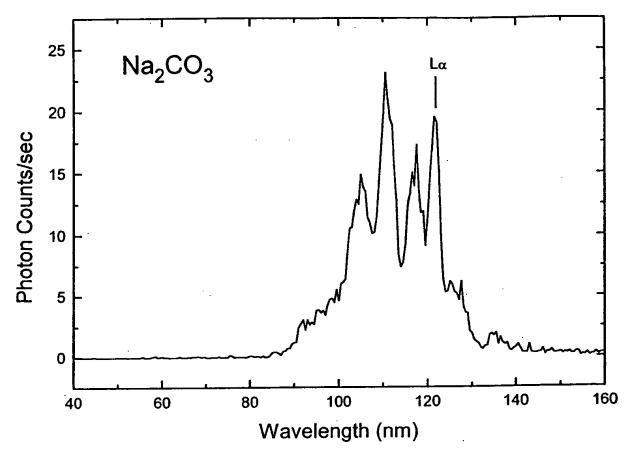


Fig. 9. The EUV spectrum (40–160 nm) of the cell emission recorded at about the point of the maximum Lyman α emission from the gas cell comprising a tungsten filament, a titanium dissociator treated with 0.6 M Na₂CO₃/10% H₂O₂ before being used in the cell, and 0.3 torr hydrogen at a cell temperature of 700°C.

217.8164 eV + Na⁺ + H
$$\left[\frac{a_{\rm H}}{p}\right]$$
 \rightarrow Na⁴⁺ + 3e⁻
+ H $\left[\frac{a_{\rm H}}{(p+8)}\right]$ + $\left[(p+8)^2 - p^2\right] \times 13.6$ eV (18)

$$Na^{4+} + 3e^- \rightarrow Na^+ + 217.8164 \text{ eV}$$
 (19)

And, the overall reaction is

$$H\left[\frac{a_H}{p}\right] \to H\left[\frac{a_H}{(p+8)}\right] + [(p+8)^2 - p^2] \times 13.6 \text{ eV}$$
 (20)

$$\frac{217.8164 \text{ eV}}{8 \times 27.196 \text{ eV}} = \frac{217.8164 \text{ eV}}{217.568 \text{ eV}} = 1.001$$

Very little mirroring was observed compared to that observed with the onset of EUV emission in the case of K₂CO₃ or KNO₃. This further supports the source of emission as NaNO₃ catalyst.

Fig. 8. (A). The EUV spectrum (40–160 nm) of the cell emission recorded at about the point of the maximum Lyman α emission from the gas cell comprising a tungsten filament, a titanium dissociator treated with 0.6 M $K_2CO_3/10\%$ H_2O_2 before being used in the cell, and 0.3 torr hydrogen at a cell temperature of 700°C. (B). The UV-VIS spectrum (300–560 nm) of the cell emission recorded with a photomultiplier tube (PMT) and a sodium salicylate-scintillator from the gas cell comprising a tungsten filament, a titanium dissociator treated with 0.6 M $K_2CO_3/10\%$ H_2O_2 before being used in the cell, and 0.3 torr hydrogen at a cell temperature of 700°C.





4.5 Barium nitrate

EUV emission was observed from Ba(NO₃)₂; whereas, no EUV emission was observed from Ba(m). Alkali metal nitrates are extraordinarily volatile and can be distilled 350-500°C, and barium nitrate can also be distilled at 600°C [12]. Ba(NO₃)₂ melts at 592°C; thus, it is stable and volatile at the operating temperature of the EUV experiment. Ba²⁺ may be a catalyst, but it is not possible to determine this since only the first two vacuum ionization energies of barium are published [9].

A catalysts may also be provided by the transfer of t electrons between participating ions. The transfer of t electrons from one ion to another ion provides a net enthalpy of reaction whereby the sum of the ionization energy of the electron accepting ion minus the ionization energy of the electron accepting ion equals approximately $m ext{-} 27.2 ext{ eV}$ where t and t are each an integer. Two K⁺ ions in one case and two La³⁺ ions in another were observed to serve as catalysts as indicated by the observed EUV emission. No other ion pairs caused EUV emission.

4.6. Potassium

Potassium ions can also provide a net enthalpy of a multiple of that of the potential energy of the hydrogen atom. The second ionization energy of potassium is 31.63 eV; and K^+ releases 4.34 eV when it is reduced to K. The combination of reactions K^+ to K^{2+} and K^+ to K, then, has a net enthalpy of reaction of 27.28 eV, which is equivalent to m=1 in Eq. (3)

27.28 eV + K⁺ + K⁺ + H
$$\left[\frac{a_{\rm H}}{p}\right]$$
 \rightarrow K + K²⁺
+ H $\left[\frac{a_{\rm H}}{(p+1)}\right]$ + $\left[(p+1)^2 - p^2\right]$ × 13.6 eV (21)

$$K + K^{2+} \rightarrow K^{+} + K^{+} + 27.28 \text{ eV}$$
 (22)

The overall reaction is

$$H\left[\frac{a_{\rm H}}{p}\right] \rightarrow H\left[\frac{a_{\rm H}}{(p+1)}\right] + \left[(p+1)^2 - p^2\right] \times 13.6 \text{ eV} \quad (23)$$

4,7. Lanthanum carbonate

EUV emission was observed from La₂(CO₃)₃; whereas, no emission was observed from lanthanum metal or La(NO₃)₃. Lanthanum metal is not a catalyst. A single La³⁺ corresponding to the case of La(NO₃)₃ is also not a catalyst. In another embodiment, a cataly-

tic system transfers two electrons from one ion to another such that the sum of the total ionization energy of the electron donating species minus the total ionization energy of the electron accepting species equals approximately $m \cdot 27.2$ eV where m is an integer. One such catalytic system involves lanthanum as $\text{La}_2(\text{CO}_3)_3$ which provides two La^{3+} ions. The only stable oxidation state of lanthanum is La^{3+} . The fourth and fifth ionization energies of lanthanum are 49.95 eV and 61.6 eV, respectively. The third and second ionization energies of lanthanum are 19.1773 eV and 11.060 eV, respectively [9]. The combination of reactions La^{3+} to La^{5+} and La^{3+} to La^{+} , then, has a net enthalpy of reaction of 81.3127 eV, which is equivalent to m=3 in Eq. (3).

81.3127 eV + La³⁺ + La³⁺ + H
$$\left[\frac{a_{\rm H}}{p}\right]$$
 \rightarrow La⁵⁺
+ La⁺ + H $\left[\frac{a_{\rm H}}{(p+3)}\right]$ + $\left[(p+3)^2 - p^2\right] \times 13.6$ eV (24)

$$La^{5+} + La^{+} \rightarrow La^{3+} + La^{3+} + 81.3127 \text{ eV}$$
 (25)

The overall reaction is

$$H\left[\frac{a_{\rm H}}{p}\right] \rightarrow H\left[\frac{a_{\rm H}}{(p+3)}\right] + \left[(p+3)^2 - p^2\right] \times 13.6 \,\text{eV} \quad (26)$$

$$\frac{81.3127 \text{ eV}}{3 \times 27.196 \text{ eV}} = \frac{81.3127 \text{ eV}}{81.588 \text{ eV}} = 0.997$$

4.8. Germanium

Weak (100 counts/sec) EUV emission was observed from Ge. The stable oxidation states of germanium are Ge^{2+} and Ge^{4+} . The catalytic system is provided by the ionization of two electrons from Ge^{2+} to a continuum energy level such that the sum of the ionization energies of the two electrons is approximately m-27.2 eV where m is an integer. The third and fourth ionization energies of germanium are 34.2241 eV, and 45.7131 eV, respectively [9]. The double ionization reaction of Ge^{2+} to Ge^{4+} , then, has a net enthalpy of reaction of 79.9372 eV, which is equivalent to m=3 in Eq. (3).

79.9372 eV + Ge²⁺ + H
$$\left[\frac{a_{\rm H}}{p}\right]$$
 \rightarrow Ge⁴⁺ + 2e⁻
+ H $\left[\frac{a_{\rm H}}{(p+3)}\right]$ + $\left[(p+3)^2 - p^2\right] \times 13.6$ eV (27)

$$Ge^{4+} + 2e^{-} \rightarrow Ge^{2+} + 79.9372 \text{ eV}$$
 (28)

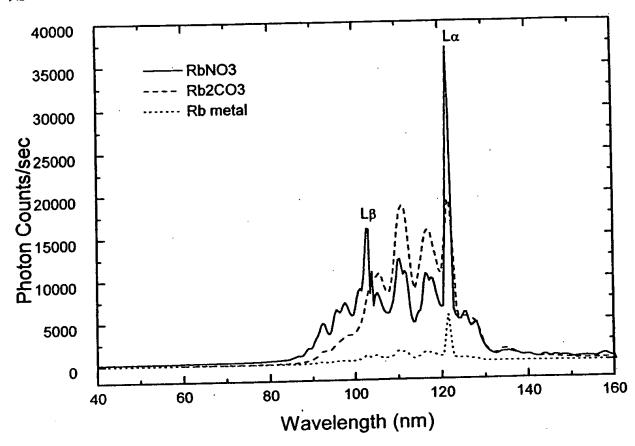


Fig. 10. The EUV spectrum (40–160 nm) of the cell emission recorded at about the point of the maximum Lyman α emission from the gas cell comprising rubidium metal, Rb₂CO₃, or RbNO₃, a tungsten filament, a titanium dissociator, and 0.3 torr hydrogen at a cell temperature of 700°C.

And, the overall reaction is

$$H\left[\frac{a_{\rm H}}{p}\right] \rightarrow H\left[\frac{a_{\rm H}}{(p+3)}\right] + \left[(p+3)^2 - p^2\right] \times 13.6 \text{ eV} \quad (29)$$

$$\frac{79.9372 \text{ eV}}{3 \times 27.196 \text{ eV}} = \frac{79.9372 \text{ eV}}{81.588 \text{ eV}} = 0.98$$

Very low level EUV emission with the presence of some of the elements in Table 1 may be explained by the presence of low levels of catalytic ions of a pure element such as the case of germanium or by contamination with catalytic reactants such as potassium in sodium.

5. Conclusions

Intense EUV emission was observed at low temperatures (e.g. < 10³ K) from atomic hydrogen and certain atomized pure elements or certain gaseous ions which ionize at integer multiples of the potential energy of atomic hydrogen. The release of energy from hydrogen as evidenced by the EUV emission must result in a lower-energy state of hydrogen. The lower-energy hydrogen atom called a hydrino atom by Mills [6] would be expected to demonstrate novel chemistry. The formation of novel compounds based on hydrino atoms would be substantial evidence supporting catalysis of hydrogen as the mechanism of the observed EUV emission. A novel hydride ion called a hydrino hydride ion having extraordinary chemical properties given by Mills [6] is predicted to form by the reaction of an electron with a hydrino atom. Compounds containing hydrino hydride ions have been isolated as products of the reaction of atomic hydrogen with atoms and ions identified as catalysts in the present EUV study [6,13,14]. Work is in progress to optimize the EUV emission and correlate the EUV emission with novel compound and heat production.

Billions of dollars have been spent to harness the energy of hydrogen through fusion using plasmas created and heated to extreme temperatures by RF coupling (e.g. > 10⁶ K) with confinement provided by a





toroidal magnetic field. The present study indicates that energy may be released from hydrogen at relatively low temperatures with an apparatus which is of trivial technological complexity compared to a tokomak. And, rather than producing radioactive waste, the reaction has the potential to produce compounds having extraordinary properties. The implications are that a vast new energy source and a new field of hydrogen chemistry have been discovered.

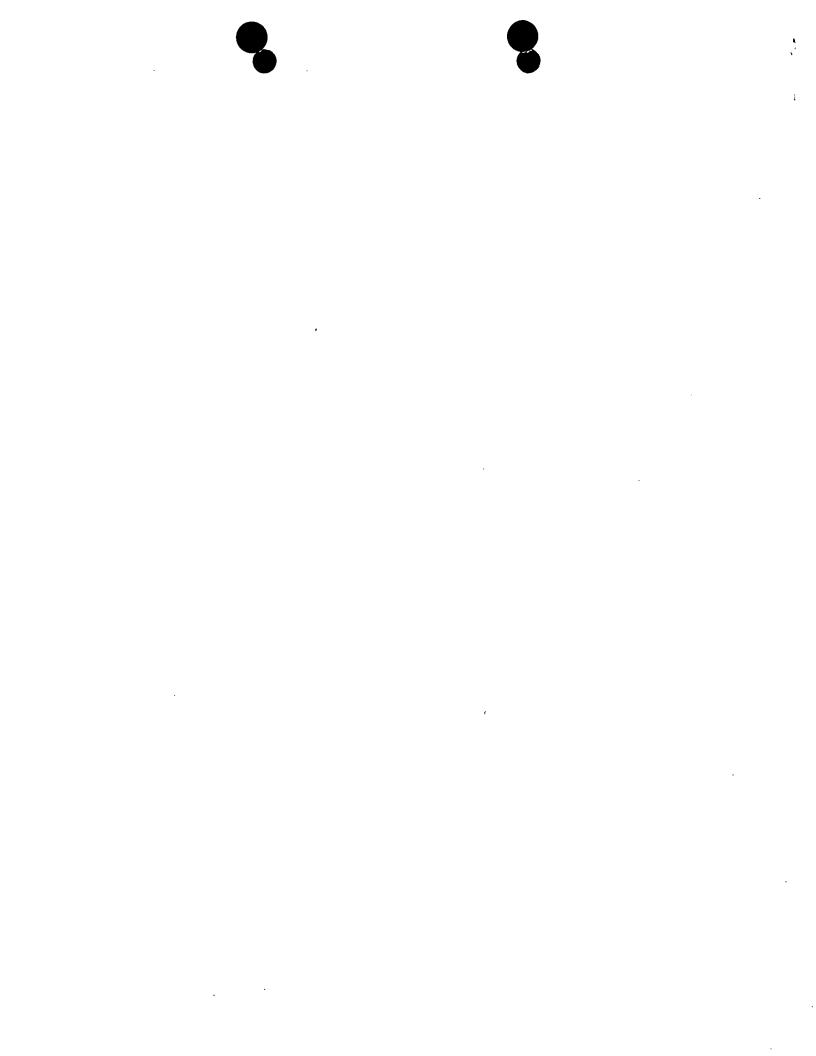
Acknowledgements

Special thanks to Nelson Greenig for designing the fiber optic system, to Grace Christ for preparing many of the cells comprising the test materials, and to Jiliang He for reviewing this manuscript.

References

- [1] Phillips JH. In: Guide to the Sun. Cambridge, UK: Cambridge University Press, 1992. p. 16-20.
- [2] Sampson JAR, Techniques of vacuum ultraviolet spectroscopy, Pied Publications, 1980, 94-179.

- [3] Science News, 12/6/97, 366.
- [4] Fujimoto T, Sawada K, Takahata K. J Appl Phys 1989;66(6):2315-9.
- [5] Hollander A, Wertheimer MR. J Vac Sci Technol A 1994;12(3):879-82.
- [6] Mills R. The Grand unified theory of classical quantum mechanics. January 1999 Edition. Cranbury, New Jersey: BlackLight Power, 1999 Distributed by Amazon.com.
- [7] Sidgwick NV. In: The chemical elements and their compounds, vol. I. Oxford: Clarendon Press, 1950. p. 17.
- [8] Lamb MD. In: Luminescence spectroscopy. London: Academic Press; 1978. p. 68.
- [9] David R Linde. In: CRC handbook of chemistry and physics. 79th Ed. Boca Raton, Florida: CRC Press, 1998-9. p. 10,175-10,1777.
- [10] Sampson, JAR, Techniques of vacuum ultraviolet spectroscopy, Pied Publications, (1980), 147.
- [11] M. Benjamin, The London, Edinburgh, and Dublin, Philosophical Magazine and Journal of Science 1935:July; 1-24.
- [12] C.J. Hardy, B.O. Field, J. Chem. Soc. 1963;5130-5134.
- [13] Mills R., Dhandapani B., Greenig N., He J, Synthesis and characterization of potassium iodo Hydride, Int. J. of Hydrogen Energy in Progress.
- [14] Mills R., Novel hydride compound, Int. J. of Hydrogen Energy, accepted.









International Journal of Hydrogen Energy 000 (2000) 000-000

www.elsevier.com/locate/ijhydene

Observation of extreme ultraviolet emission from hydrogen-KI plasmas produced by a hollow cathode discharge

Randell L. Mills *

BlackLight Power, Inc., 493 Old Trenton Road, Cranbury, NJ 08512, USA

Received 9 August 2000; accepted 24 October 2000

Abstract

A high-voltage discharge of hydrogen with and without the presence of a source of potassium, potal jum iodide, in the discharge was performed with a hollow cathode. It has been reported that intense extreme ultravillet (LJV) emission was observed from atomic hydrogen and certain elements or certain ions which ionize at intege multiples of the potential energy of atomic hydrogen, 27.2 eV (Mills et al., 1999 Pacific Conference on Chemistry and Spectroscopy and the 35th ACS Western Regional Meeting, Ontario Convention Center, California, October 6–8, 1999; Mills, at linearlydrogen Energy 25 (2000) 919; Mills, Int. J. Hydrogen Energy, in press; Mills et al., Int. J. Hydrogen Energy, in press, wills et al., June ACS Meeting, 29th Northeast Regional Meeting, University of Connecticut, Storrs, CT, June 18–3, 200. Two potassium ions or a potassium atom may each provide an electron ionization or transfer reaction that has a detect of halpy equal to an integer multiple of 27.2 eV. The spectral lines of atomic hydrogen were intense enough to be recorded on hotographic films only when KI was present. EUV lines not assignable to potassium, iodine, or hydrogen were objected on hotographic films only when KI was present. EUV lines not assignable to transitions of atomic hydrogen were objected at 733, 132.6, 513.6, 677.8, 885.9, and 1032.9 Å. The lines could be assigned to transitions of atomic hydrogen to lover-energy levels corresponding to lower-energy hydrogen atoms called hydrino atoms and the emission from the excitation of the corresponding hydride ions formed from the hydrino atoms. © 2000 International Association for Hydrogen Energy. Energy Energy Science Ltd. All rights reserved.

1. Introduction

The chemical interaction of potassium with hydrogen at temperatures below 1000 K has show suppristant results in terms of the emission of the Lyman and Ladmer lines [1-6] and the formation of novel drame compounds [1,6-12]. In searching for an explanation of themical reactions of unusually high energy which roduced hydrogen Lyman and Balmer series emission, a resonant electronic interaction between hydrogen and potassium at energy levels of a multiple of the ionication each of hydrogen, $nE_{\rm H}$, has been introduced into the discussion. This hypothesis is supported by the fact that being these elements such as potassium, cesium, and strophym which have bound electrons of energies of $E_{\rm m}E_{\rm H}$ show Lyman and Balmer emission during the chemical interaction with atomic hydrogen. Those elements will electronic states of $E_{\rm m} E_{\rm H}$ show no emission

* Tel.: +1-609-490-1040; fax: +1-609-490-1066. E-mail address: rmills@blacklightpower.com (R.L. Mills). under identical conditions. This paper addresses new electronic energy states of hydrogen. If such states are stable, spectral line emission should be observed in the EUV during their formation and during energetic electron excitation of compounds containing hydrogen in these states.

The following paper reports the first exploratory measurements in the EUV. For this experiment, a standard hollow cathode discharge in hydrogen was employed to generate atomic hydrogen and to provide the energetic electrons. This papers presents the experimental results and compares it with theoretical considerations.

A historical motivation to cause EUV emission from a hydrogen gas was that the spectrum of hydrogen was first recorded from the only known source, the Sun [13]. Developed sources that provide a suitable intensity are high-voltage discharge and inductively coupled plasma generators [14]. An important variant of the later type of source is a tokomak [15]. Fujimoto et al. [16] have determined the cross section for production of excited hydrogen atoms from the emission cross sections for Lyman and

Balmer lines when molecular hydrogen is dissociated into excited atoms by electron collisions. This data was used to develop a collisional-radiative model to be used in determining the ratio of molecular-to-atomic hydrogen densities in tokomak plasmas. Their results indicate an excitation threshold of 17 eV for Lyman a emission. Addition of other gases would be expected to decrease the intensity of hydrogen lines which could be absorbed by the gas. Hollander and Wertheimer [17] found that within a selected range of parameters of a plasma created in a microwave resonator cavity, a hydrogen-oxygen plasma displays an emission that resembles the absorption of molecular oxygen. Whereas, a helium-hydrogen plasma emits a very intense hydrogen Lyman a radiation at 121.5 nm which is up to 40 times more intense than other lines in the spectrum. The Lyman α emission intensity showed a significant deviation from that predicted by the model of Fujimoto et al. [16] and from the emission of hydrogen alone.

It has been reported [1-6] that EUV emission of atomic and molecular hydrogen occurs in the gas phase at low temperatures (e.g. $< 10^3$ K) upon contact of atomic hydrogen with certain vaporized elements or ions. Atomic hydrogen was generated by dissociation at a tungsten filament and at a transition metal dissociator that was incandescently heated by the filament. Various elements or ions were made gaseous by heating to form a low vapor pressure (e.g. 1 Torr). The kinetic energy of the thermal electrons at the experimental temperature of < 10³ K were about 0.1 eV, and the average collisional energies of electrons accelerated by the field of the filament were less than 1 eV. (No blackbody emission was recorded for wavelengths shorter than 400 nm.) Atoms or ions which ionize at integer multiples of the potential energy of atomic hydrogen (e.g. cesium, potage sium, strontium, and Rb+) caused hydrogen EUV emissi whereas, other chemically equivalent or similar atoms [e.g. sodium, magnesium, holmium, and zinc metals) aused no emission. Helium ions present in the experiment Holl der and Wertheimer [17] ionize at a multiple of the potential energy of atomic hydrogen. of EUV emission cannot be explained the chemistry of hydrogen, but it is predicted by a solution of the Schrodinger equation with numadiative boundary

constraint put forward by Mis [1].

Mills predicts that certain along or ions serve as catalysts to release energy from hydrogen to produce an increased binding energy hydrogen atomicalled a hydrino atom having a binding energy of

Binding energy,
$$\frac{13.6 \text{ eV}}{r^2}$$
, (1)

$$n = \frac{1}{2}, \frac{1}{2}, \frac{1}{4}, \dots, \frac{1}{p}$$
 (2)

and p is an integer greater than 1, designated as $H(a_H/p)$ where a_H is the radius of the hydrogen atom. Hydrinos are

predicted to form by reacting an ordinary hydrogen atom with a catalyst having a net enthalpy of reaction of about

$$m \times 27.2 \text{ eV}$$
 (3)

where m is an integer. This catalysis releases energy from the hydrogen atom with a commensurate decrease in size of the hydrogen atom, $r_n = na_H$. For example, the catalysis of H(n=1) to H(n=1/2) releases 40.8 eV, and the hydrogen radius decreases from a_H to $\frac{1}{2}a_H$.

The excited energy states of atomic hydrogen are also given by Eq. (1) except that

$$n=1,2,3,\ldots (4)$$

The n = 1 state is the "ground" state for "pure" photon transitions (the n = 1 state can absorb a photon and go to an excited electronic state, but it cannot release a photon and go to a lower-energy electronic state).

However, an electron transition from the ground state to a lower-energy state is possible a numadiative energy transfer such as multipole coupling over resonant collision mechanism. These lower-energy states love fractional quanturn numbers, n = 1/integer. Pocesses that occur without photons and that require collisions are common. For example, the exothermic familiary ction of H + H to form H_2 does not occur with the mission of a photon. Rather, the reaction requires a collision with a third body, M, to remove the bond energy $H + H + M \rightarrow H_2 + M^*$ [19]. The third body distribution is a second of the second body distribut the energy from the exothermic reaction, and the end result is the H_2 molecule and an increase in temperature of the system. Some commercial phosphors are bases on nonradiative energy transfer involving multiple compling. For example, the strong absorption strength of \$600 ions along with the efficient nonradiative transfer excitation from Sb³⁺ to Mn²⁺, are responsible for the strong manganese luminescence from phosphors containing these ions [20]. Similarly, the n = 1 state of hydrogen and the n = 1/integer states of hydrogen are nonradiative, but a transition between two nonradiative states is possible via a nonradiative energy transfer, say n=1 to 1/2. In these cases, during the transition the electron couples to another electron transition, electron transfer reaction, or inelastic scattering reaction which can absorb the exact amount of energy that must be removed from the hydrogen atom. Thus, a catalyst provides a net positive enthalpy of reaction of $m \times 27.2$ eV (i.e. it absorbs $m \times 27.2$ eV where m is an integer). Certain atoms or ions serve as catalysts which resonantly accept energy from hydrogen atoms and release the energy to the surroundings to effect electronic transitions to fractional quantum energy levels given by Eqs. (1) and (2).

2. Inorganic catalysts

A catalytic system is provided by the ionization of t electrons from an atom to a continuum energy level such that the sum of the ionization energies of the t electrons is

approximately $m \times 27.2$ eV where m is an integer. One such catalytic system involves potassium. The first, second, and third ionization energies of potassium are 4.34066, 31.63, 45.806 eV, respectively [21]. The triple ionization (t = 3) reaction of K to K³⁺, then, has a net enthalpy of reaction of 81.7426 eV, which is equivalent to m = 3 in Eq. (3):

81.7426 eV + K(m) + H
$$\left[\frac{a_{\rm H}}{p}\right]$$
 \rightarrow K³⁺ + 3e⁻

+H
$$\left[\frac{a_{\rm H}}{(p+3)}\right]$$
 + $[(p+3)^2 - p^2] \times 13.6 \text{ eV},$ (5)

$$K^{3+} + 3e^- \rightarrow K(m) + 81.7426 \text{ eV}$$
 (6)

and, the overall reaction is

$$H\left[\frac{a_{\rm H}}{p}\right] \to H\left[\frac{a_{\rm H}}{(p+3)}\right] + \left[(p+3)^2 - p^2\right] \times 13.6 \text{ eV}. \tag{7}$$

Potassium ions can also provide a net enthalpy of a multiple of that of the potential energy of the hydrogen atom. The second ionization energy of potassium is 31.63 eV; and K^+ releases 4.34 eV when it is reduced to K. The combination of reactions K^+ to K^{2+} and K^+ to K, then, has a net enthalpy of reaction of 27.28 eV, which is equivalent to m = 1 in Eq. (3):

27.28 eV + K⁺ + K⁺ + H
$$\left[\frac{a_{\rm H}}{p}\right] \to K + K^{2+}$$

+H
$$\left[\frac{a_{\rm H}}{(p+1)}\right]$$
+ $[(p+1)^2-p^2]$ × 13.6 eV, (8)

$$K + K^{2+} \rightarrow K^{+} + K^{+} + 27.28 \text{ eV}.$$

The overall reaction is

$$H\left[\frac{a_H}{p}\right] \to H\left[\frac{a_H}{(p+1)}\right] + [(p+1)^2 - p^2] \times 6 \text{ e}^{-1}$$

3. Hydrino catalysts

Lower-energy hydrogen atom hydrinos, can act as catalysts because each of the meastable excitation, resonance excitation, and ionizating energy of a hydrino atom is $m \times 27.2$ eV (Eq. (7). The tansition reaction mechanism of a first hydrino atom affected by a second hydrino atom involves the assonant soupling between the atoms of m degenerate robin are each having 27.21 eV of potential energy 18). The energy transfer of $m \times 27.2$ eV from the first hydrino atom to the second hydrino atom causes the central field. If the first atom to increase by m and its electron to drop m levels lower from a radius of $a_{\rm H}/p$ to a radius of $a_{\rm H}/(p+m)$. The second interacting lower-energy hydrogen is either excited to a metastable state, excited to a

resonance state, or ionized by the resonant energy transfer. The resonant transfer may occur in multiple stages. For example, a nonradiative transfer by multipole coupling may occur wherein the central field of the first increases by m, then the electron of the first drops m levels lower from a radius of a_H/p to a radius of $a_H/(p+m)$ with further resonant energy transfer. The energy transferred by multipole coupling may occur by a mechanism that is analogous to photon absorption involving an excitation to a virtual level. Or, the energy transferred by multipole coupling and during the electron transition of the first hydrino atom may occur by a mechanism that is analogous to two photon absorption involving a first excitation to a virtual level and a second excitation to a resonant or continuum level [22-24]. The transition energy greater than the energy transferred to the second hydrino atom may appear as a photon in a vacuum medium.

For example, the transition of $H[a_H, t_H]$ [teth[$a_H/(p+m)$] induced by a resonance transfer of m > 21 eV (Eq. (3)) with a metastable state excited in $H[a_H/p]$ is represented by

$$m \times 27.2 \text{ eV} + \text{H} \left[\frac{a_{\text{H}}}{p'} \right] + \text{H} \left[\frac{a_{\text{H}}}{p'} \right] + \left[\frac{a_{\text{H}}}{p'} \right] \times 13.6 \text{ eV}, \quad (11)$$

$$H + \begin{bmatrix} a_H \\ p \end{bmatrix} \rightarrow H \begin{bmatrix} a_H \\ p' \end{bmatrix} + m \times 27.2 \text{ eV}.$$
 (12)

And the everall reaction is

$$H\left[\frac{n}{p}\right] \to H\left[\frac{a_H}{p+m}\right] + [(p+m)^2 - p^2]$$
×13.6 eV, (13)

where p, p', and m are integers and the asterisk represents an excited metastable state.

The transition of H[$a_{\rm H}/p$] to H[$a_{\rm H}/(p+m)$] induced by a multipole resonance transfer of $m \times 27.21$ eV (Eq. (3)) and a transfer of [$(p')^2 - (p'-m')^2$] × 13.6 eV $-m \times 27.2$ eV with a resonance state of H[$a_{\rm H}/(p'-m')$] excited in H[$a_{\rm H}/p'$] is represented by

$$H\left[\frac{a_{H}}{p'}\right] + H\left[\frac{a_{H}}{p}\right] \rightarrow H\left[\frac{a_{H}}{p'-m'}\right] + H\left[\frac{a_{H}}{p+m}\right]$$
$$+\left[\left((p+m)^{2}-p^{2}\right)-(p'^{2}-(p'-m')^{2})\right] \times 13.6 \text{ eV},$$
(14)

where p, p', m, and m' are integers.

3.1. Hydride ions

A novel hydride ion having extraordinary chemical properties given by Mills [18] is predicted to form by the reaction

Table I The ionization energy of the hydrino hydride ion $H^{-}(n=1/p)$ as a function of p

Hydride ion	$(a_0)^a$	Calculated ionization energy ^b (eV)	Calculated wavelength (Å)
$H^-(n=1/2)$	0.9330	3.047	4070
$H^{-}(n=1/3)$	0.6220	6.610	1880
$H^{-}(n=1/4)$	0.4665	11.23	1100
$H^{-}(n=1/5)$	0.3732	16.70	742
$H^-(n=1/6)$	0.3110	22.81	544

From Eq. (17).

of an electron with a hydrino (Eq. (15)). The resulting hydride ion is referred to as a hydrino hydride ion, designated as $H^{-}(1/p)$:

$$H\left[\frac{a_{\rm H}}{p}\right] + e^- \to H^-(1/p). \tag{15}$$

The hydrino hydride ion is distinguished from an ordinary hydride ion having a binding energy of 0.8 eV. The latter is hereafter referred to as "ordinary hydride ion". The hydrino hydride ion is predicted [18] to comprise a hydrogen nucleus and two indistinguishable electrons at a binding energy according to the following formula:

Binding energy =
$$\frac{\hbar^2 \sqrt{s(s+1)}}{8\mu_e a_0^2 [(1+\sqrt{s(s+1))}/p]^2}$$
$$-\frac{\pi \mu_0 e^2 \hbar^2}{m_e^2 a_0^3} \left(1 + \frac{2^2}{[(1+\sqrt{s(s+1))}/p]^3}\right), \tag{16}$$

where p is an integer greater than one, s = 1/2, π is pice Planck's constant bar, μ_0 is the permeability of vacuum, m_e is the mass of the electron, μ_{t} is the reduced electron. ao is the Bohr radius, and e is the elementar ionic radius is

$$r_1 = \frac{a_0}{p}(1 + \sqrt{s(s+1)}), \quad s = \frac{1}{2}.$$
 (17)

From Eq. (17), the radius of the radius hydride ion $H^-(1/p)$; p = integer is 1/p time. But of ordinary hydride ion, $H^-(1/1)$. The predicted bilding energies and ionic radii for the first five hydring hydride ions are given in Table 1.

INP Greifswald, Germany scorded spectra of a hollow cathode plasma source in the range of 2.5–80 nm at the request of Blad Light lower, Inc. of Cranbury, NJ, USA [25]. This plasma source, called a BLP-source, consisted of a five way trace containing a hollow cathode discharge tube a five-way areas containing a hollow cathode discharge tube and a heart spipe comprising a reservoir for vaporizing KI. one ene of the reservoir was closed, and the other open was abounted close to the exit of the hollow cathode. The axis of both cylindrical pieces, the hollow cathode and the heated reservoir, were arranged almost perpendicular to each other.

A 4° grazing incidence spectrometer was attached to the BLP-source. At this shallow angle of incidence, a strong astigmatism stretches each point like a divergent light source at the entrance slit into a line in the focal plane. The spectrometer was filled with hydrogen during operation via the BLP source. Due to differential pumping a pressure drop was established between the source and the spectrometer.

The proper functioning of the spectrometer in the desired wavelengths range was demonstrated by using a known capillary discharge in high vacuum that emitted carbon and oxygen spectra of multiply ionized atoms down to 3.5 nm.

Potassium iodide was used as a source of potassium. Based on its reported exceptional emission [1-4,6], potassium was a good choice for a catalyst according to Eqs. (5) -(7) to cause transitions in hydrogen to lower energy levels to form hydrino atoms. The hydrino atoms then also served as catalysts according to Eqs. (11)-(13) and (14). Hydrino hydride ions formed by the reaction of assimple electrons with hydrino atoms. Compounds containing hydrino hydride ions were observed by their character tic emission when excited in the plasma discharge.

4. Methods

4.1. Standar en emission spectrum

A standard comic and molecular hydrogen extreme ulemission spectrum was obtained by BlackLight yer, R., Cranbury, NJ with a microwave discharge an EUV spectrometer. The microwave genera Opthos model MPG-4M generator (Frequency: MHz). The output power was set at 85 W. Hydrogen as was flowed through a half-inch diameter quartz tube at 550 mTorr. The tube was fitted with an Opthos coaxial microwave cavity (Evenson cavity). The EUV spectrometer was a McPherson model 302 (Seya-Namioka type) normal incidence monochromator. The monochromator slits was $30 \times 30 \ \mu m$. A sodium salicylate converter was used, and the emission was detected with a photomultiplier tube detector (Hamamatsu R1527P).

4.2. Capillary discharge

A certain discharge type has become very important for a couple of special applications. For example, in the field of radiation generation in the EUV or soft X-ray region the so-called capillary discharge is often used [26]. Several scientists have shown that it is possible to generate laser radiation at shorter wavelengths by means of a capillary discharge because fast capillary discharges with a large length-to-diameter ratio can generate highly ionized plasmas. The field is quite advanced [27,28] to the point that Rocca [27] has developed a table top laser using the 46.9 nm Argon line.

^bFrom Eq. (16).

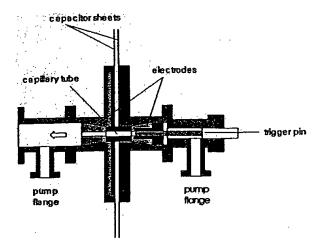


Fig. 1. Capillary discharge vessel.

A high electric power is required to excite atoms to high electronic energy levels. Since a high-energy input into a device is unwanted, a technically convenient energy has to be delivered to a plasma in a short time. The capillary discharge described by Bogen et al. [26] has an electric current rise time and an emission time of the hydrogen like carbon VII line that is shorter than 50 ns.

A cross-sectional view of the capillary discharge system is shown in Fig. 1. The capacitor, leads, capillary for plasma production, switch, and trigger were all integrated in a single unit in order to maintain a low inductance. The capacitor was a copper laminated plastic sheet with isolation gaps along the rim and in the center. A plastic dig with a plastic cylinder in the center provided additing high-voltage insulation. The plastic cylinder penetrated the capacitor and was encapsulated on each end by bra Hollow carbon electrodes were attached at each plastic cylinder by the brass pieces which trodes. The brass pieces were soldered to e carbon inate of the capacitor. The plastic ca the axis of the electrodes had a common borehold cylinder.

The plasma was observed and a spark one side. On the other side, a carbon trigger ph provided a spark when a sharply rising potentic was applied between this trigger pin and one of the carbon ele trodes. This spark triggered the discharge of the capacitor. A plasma was formed inside the plastic cylinter borehole which comprised the capillary. The plasma had an electron temperature of up to 50 each electron density of up to 10²⁵ particles per in 129. The brass pieces were connected to a vacuum system. This arrangement permitted the end-on observation of the generated spark. To avoid a pressure gradient, the trigger side of the discharge as well as the spectrograph side were evacuated by a pumping system shown in Fig. 1.

Table 2
Parameters used in the capillary discharge experiments

Discharge voltage V	6-10 kV
Discharge pressure p	≤ 10 ⁻⁵ mbar
Capacitor capacitance C	19 n F
Capacitor inductance I	19 nH
Thickness of the Makrolon foil b	200 nm
Number of single discharges n	About 500

4.3. System for EUV measurement of discharge

In order to protect the electronic devices from destruction and to avoid disturbances while measuring, the discharge source, the entire power supply, and the pumping system was placed in a grounded Faraday cage. The capacitor was charged via 1 M Ω resistor. The discharge was driven by a power supply in a voltage range between and 10 kV. In addition, a second power supply was used to provide a very fast high-voltage pulse (4 kV win a rise inne of 10 ns) to the trigger pin. This pulse provided a controlled ignition of the capillary discharge.

For more convenient operation, the EUV-spectrograph was located outside of the Faraday cage. In a capillary discharge, a spectrum is presented by excitation of atoms of an evaporated dielectric material. Polyethylene (PE) or polyacetal (PA) was justed in the present study. The discharge produced a spot dust. Therefore, a special Makrolon foil (polycarbonate with a thickness of about 200 nm that was transpal at to the soft X-ray and EUV region light of this study) was placed between the capillary discharge and the EUV-spectrograph to protect the grating. The spectrograph as well as the whole discharge vessel were connected with pumping system. The discharge was driven in vacuum at a working pressure of 10⁻⁵ mbar or less. For time-resolved measurements, the spectrograph was replaced by a fast photo multiplier that permitted examination of the temporal behavior of a single spark. Table 2 gives the main parameters of this experiment. The experimental setup is shown in Fig. 2.

4.4. EUV-spectrograph and photochemical detector

The spectrometer was a LSP-VUV 1-3S-M portable EUV grazing incidence spectrometer that used an off Rowland circle registration scheme wherein the diameter of the Rowland circle corresponded to the radius of curvature of the grating. In this study, the spectra were recorded in a single plane. Thus, the input slit was focused only for a single wavelength (center wavelength λ_0). The alignment to a different wavelength was produced by simply changing the distance between the focal plane and the grating. The spectra were detected using a special Russian EUV film.

The grazing angle of incidence to the grating was rated by the manufacturer to be 4°. The width of the entrance slit was chosen to be 100 μ m. The spectral resolution $\lambda/\Delta\lambda$ was better than 100. The grating parameters are shown in

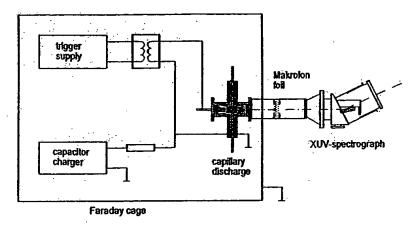


Fig. 2. Experimental setup for capillary discharge measurements.

Table 3

Grating parameters		
Radius of curvature (mm)	1000	
Size of ruled area (mm)	28×30	
Coating	Au 300 Å	
Number of grooves (mm)	1200	600 300
Blaze angle (deg)	1	3
Recommended spectral range (Å)	25-60	120-800

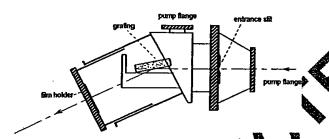


Fig. 3. Cross sectional view of the LSP-VUV 35.M stable EUV grazing incidence spectrometer.

Table 3. The cross sectional view of the spectrometer is shown in Fig. 3.

4.5. Measurements

The main purpose for the us of a capillary discharge was to demonstrate the spectral singe over which the system was capable of recording. The EUV spectrum of a capillary discharge of a pulyar steapillary tube was obtained with the results greatly in in Fig. 4 and in Table 4. The numbered specific lines (with respect to Fig. 4) are assigned to the corresponding wavelengths and energy levels. For an appropriate assignment, it was necessary to calculate the transformation from the plane of registration to the Rowland circle using the specific dispersion function of the grating. Emission could be observed down to 7 nm.

4.6. Experimental setup of the BLP source

Cranton, NJ) was investigated in the EUV and soft X-ray region. The plasma cell comprised a five-way stainless-steel sees. The plasma was generated at a hollow cathode inside the discharge cell. The hollow cathode was constructed of a stainless-steel rod inserted into a steel tube, and this assembly was inserted into an alumina tube. A flange opposite the end of the hollow cathode connected the spectrometer with the cell. It had a small hole that permitted radiation to pass to the spectrometer. In addition, a quartz tube positioned perpendicularly to the hollow cathode was attached to two copper high-voltage feedthroughs by means of a tungsten filament. The quartz tube served as a catalyst reservoir when filled with KI.

The electrical copper feedthroughs were connected to a power supply (U=0-6.3 V, I=0-40 A) to power the tungsten filament to heat the catalyst in the quartz tube. Some of the Kl was observed to vaporize when the filament glowed orange. Another power supply (U=0-20 kV, I=0-30 mA) was connected to the hollow cathode to generate a discharge. A Swagelok adapter at the very end of the steel cross provided a gas inlet and a connection with the pumping system. A diagram of the BLP plasma source is given in Fig. 5.

A high-speed shutter placed between the discharge cell and the spectrograph allowed for control of the detector

R.L. Mills | International Journal of Hydrogen Energy 000 (2000) 000-000

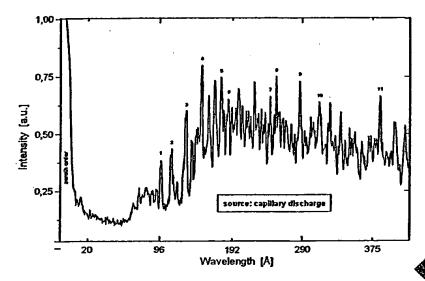


Fig. 4. Spectrum of a capillary discharge.

Table 4
Spectral lines of Fig. 4 with corresponding transitions and wavelengths

Number	lon	Energy level	Wavelength (Å)
1	O VII	1s2p-1s4d	96.1
2	O VI	1s ² 2p-19000	110
3	o vi	1s ² 2p-134d	130
<u> </u>	o VI	$1s^22p-1s^2$	150
5	0 VI	asap−1s²3d	173
6	O VI	$1s^2$ 2121 s^2 3s	184
7	CIV	Δ $s^2 2p = s^2 6d$	245
γ Q	CIV	△ 1820–18 ² 5d	259
9	CIV	Δ^2 2p-1s ² 4d	289
10	CIV		312
11	C IV	1s ² 2p-1s ² 3p 1s ² 2p-1s ² 3d	384

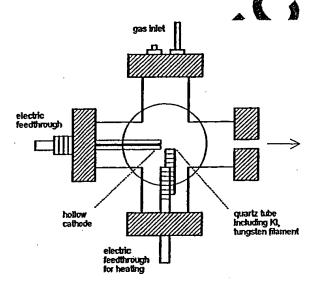


Fig. 5. Cross sectional view of the BLP discharge cell.

exposure time (see EUV-Spectrograph and Photochemical Detector Section). The hollow cathode, shutter, and EUV spectrograph were aligned on a common optical axis using a laser. The experimental setup for the BLP discharge measurements is illustrated in Fig. 6.

4.7. Measurements on the BLP source

The temperature of the tungsten filament which heated the quartz tube was determined by means of a special infrared camera system made by Jenoptic. The evaluation photos showed that the filament had a temperature of at least 1000 K, and the quartz tube was about 80 K colder. The temperature of 920 K was sufficient to melt and vaporize KI in the pressure range of the experiment.

The EUV emission spectrum of the BLP source was obtained during a plasma discharge in hydrogen with and without KI catalyst. Manipulated experimental parameters included the pressure, the temperature and position of the

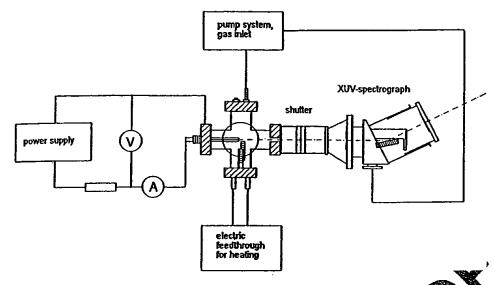


Fig. 6. Experimental setup for the BLP discharge measurements.

catalyst reservoir, the discharge voltage and current, the time of exposure of the detector film system, the particular grating, and the center wavelength λ_0 . The main parameter changes and basic spectrographic findings, are presented.

In order to make the wavelength assignments, all of the films were scanned, and the bitmap files were read out as shown in Fig. 4 for the case of the capillary discharge. The measured and calculated spectral lines were numbered from 1 (inside order) to 23. Corresponding lines of different films were assigned the same number based on the specific distances between the grating and the plane of the film that was a function of λ_0 . A first wavelength assignment was parformed by calculating the transformation from the plane of registration to the Rowland circle using the specific dispersion function of the particular grating.

A number of experiments proved that $\lim_{N \to \infty} N = 12$ as the Lyman alpha line with a known wavelengt of 1215.7 Å. This wavelength was used to determine the experimental angle of incidence. Thus, a slight disergence to the experiment was detected ($\Delta L = 0.33^{\circ}$), and the dispersion function was recalculated using the experimentally determined angle of grazing incidence of $1.5.54^{\circ}$.

5. Results

The standard in this en emission spectrum (850 and 1750 Å) obtained from a microwave plasma of hydrogen with a standard minibering order used in this analysis is shown in Fig. 7. The standard hydrogen spectrum was recorded by Blat Light Power Inc. using a photomultiplier tube detector. The EUV emission lines from hydrogen-KI plasmas produced by a hollow cathode discharge were recorded and identified on photographic films by INP Greifswald, Ger-

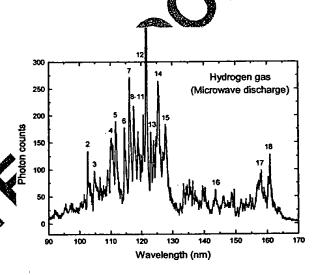


Fig. 7. Standard microwave discharge emission spectrum of hydrogen (900-1700 Å) recorded on the McPherson model 302 (Seya-Namioka type) EUV spectrometer.

many [25]. In order to make the wavelength assignments, all of the films were scanned, and the bitmap files were read out as shown in Figs. 8–12. Emission lines vs. scratches or other artifacts were determined from the films, and the wavelength assignments were based on the bitmap files shown in Figs. 8–12. A summary of the wavelength assignments and wavelength assignments based on the corrected calculated dispersion function are given in Table 5. Figs. 8–12 shows the observed spectral lines that are numbered on the respective numbered films as given in Table 5. Spectra were observed in the range around 100 nm only when K1 was present; otherwise, no lines were observed on the films. In addition, the discharge current and a special positioning of

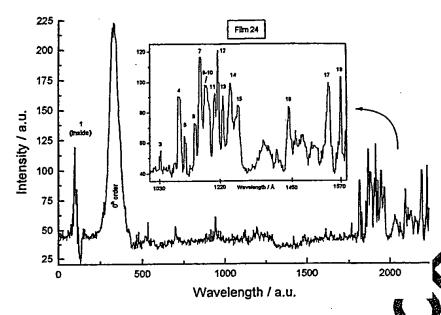


Fig. 8. The intensity of the scanned film 24 and the identified spectral lines recorded on the LSP-VLV scanned film 24 and the identified spectral lines recorded on the LSP-VLV scanned film 24 and the identified spectral lines recorded on the LSP-VLV scanned film 24 and the identified spectral lines recorded on the LSP-VLV scanned film 24 and the identified spectral lines recorded on the LSP-VLV scanned film 24 and the identified spectral lines recorded on the LSP-VLV scanned film 24 and the identified spectral lines recorded on the LSP-VLV scanned film 24 and the identified spectral lines recorded on the LSP-VLV scanned film 24 and the identified spectral lines recorded on the LSP-VLV scanned film 24 and the identified spectral lines recorded on the LSP-VLV scanned film 24 and the identified spectral lines recorded on the LSP-VLV scanned film 24 and the identified spectral lines recorded on the LSP-VLV scanned film 24 and the identified spectral lines recorded on the LSP-VLV scanned film 24 and the identified spectral lines recorded on the LSP-VLV scanned film 24 and the identified spectral lines recorded on the LSP-VLV scanned film 24 and the identified spectral lines recorded on the LSP-VLV scanned film 24 and the identified spectral lines recorded on the LSP-VLV scanned film 24 and the identified spectral lines recorded on the LSP-VLV scanned film 24 and the identified spectral lines recorded on the LSP-VLV scanned film 24 and the identified spectral lines recorded on the LSP-VLV scanned film 24 and the identified spectral lines recorded on the LSP-VLV scanned film 24 and the identified spectral lines recorded on the LSP-VLV scanned film 24 and the identified spectral lines recorded on the LSP-VLV scanned film 24 and the identified spectral lines recorded on the LSP-VLV scanned film 24 and the identified spectral lines recorded on the LSP-VLV scanned film 24 and the identified spectral lines recorded film 24 and the identified spectral lines recorded film 24 and the identified spectral lines recorded film 2

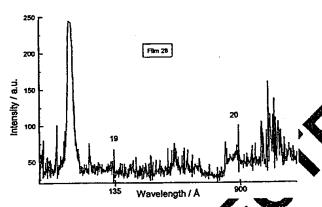


Fig. 9. The intensity of the scanned film 28 and the identified spectral lines recorded on the LSP-VUV 1-3S-1 portable EUV grazing incidence spectrometer.

the sufficiently heated KI reservoir clative to the powered hollow cathode seem to be essential. The exact positions of the spectral lines were dentified by using the Lyman-alpha line of hydrogen as a reference. The spectra comprised narrow and widefines.

The wavelengths of the standard hydrogen peaks and the experimental near numbered 4-18 are given in Table 6. These install peaks match closely the wavelengths and fit install peaks match closely the wavelengths and fit install peaks match closely the wavelengths and fit install peaks and atomic and molecular hydrogen peaks. However, the identification of peaks 2 and 3 was problemate. It is known from the standard hydrogen spectrum that the most intense peak in the wavelength region between 102 and 105 nm is the hydrogen Lyman beta line located at 102.6 nm as shown in Fig. 7. If peak 2 shown

in Fig. 11 is the Lyman beta line, then the experimental peak 3 shown Fig. 8 and 11 are different from the control since the peak 3 state most intense peak in the region rather than Lyman beta. Peak 3 could be assigned to $H^-(n=1/4)E_0 = 11.2$ eV as given in Table 7.

tines not assignable to potassium, iodine, or hydrogen were observed at 73.0, 132.6, 513.6, 677.8, 885.9, and 1032.

The lines could be assigned to transitions of hydrino atoms and the emission from the excitation of the responding hydrino hydride ions. The assignments are given in Table 7.

The line at 73 Å which appeared as an inside-order-line was reproducible and was probably real. But, it had to be questioned, because of the observation of bunching into the sagittal direction and interference patterns into the meridional direction. This line was produced by the grating and was not subject to reflections as were some "ghosts" appearing as "absorption-lines" independently of the grating rulings. This "inside-order-line" vanished, when gratings with double or quadruple rulings were used. It cannot be excluded, that stimulated emission at this wavelength occurred from the hydrogen-KI plasma inside the hollow cathode or the area in front of it. According to the characteristics of the grating, the true wavelength could also be one-half, one-third, or less likely one-forth of 73 Å. It must be regarded as belonging to the regular emission of EUV light of the BLP plasma source.

By measuring the distances between the spectral lines on the printed scans and comparing it to those on the films, the average error in the calculation of the assigned wavelengths was determined to be about 30 Å in the region above 800 Å. Line 12 was determined to be the Lyman alpha



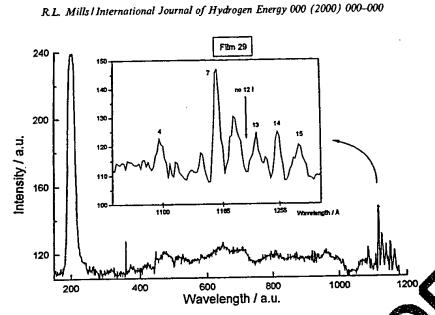


Fig. 10. The intensity of the scanned film 29 and the identified spectral lines recorded on the LSP-VUV (3S-M) ortable EUV grazing incidence spectrometer.

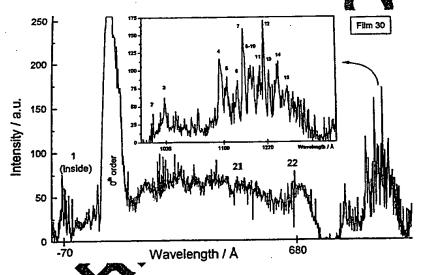


Fig. 11. The intensity of the scanner film to and the identified spectral lines recorded on the LSP-VUV 1-3S-M portable EUV grazing incidence spectrometer.

line of hydrogen ($\lambda = (215. \text{ Å})$ by comparing the structure of lines 3–15 with the known spectrum of hydrogen. This line was seed to 18 hellate the dispersion function of grating #3. The error in the corrected data was about $\pm 3 \text{ Å}$.

(Discussion

The results support that potassium atoms reacted with atomic hydrogen to form novel hydrogen energy states. Potassium iodide present in the discharge of hydrogen served

as a source of potassium metal which was observed to collect on the walls of the cell during operation. According to Eqs. (5)–(7), potassium metal reacts with atomic hydrogen present in the discharge and forms the hydrino atom $H[a_H/4]$. The energy released was expected to undergo internal conversion to increase the brightness of the plasma discharge since this is the common mechanism of relaxation. This is consistent with observation.

The product, $H[a_H/4]$ may serve as a catalyst to form $H[a_H/5]$ according to Eqs. (11)-(13). The transition of $H[a_H/4]$ to $H[a_H/5]$ induced by a resonance transfer of 27.21 eV, m=1 in Eq. (3) with a metastable state excited

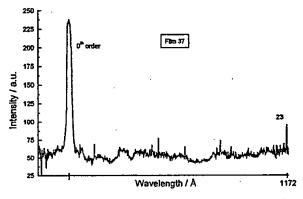


Fig. 12. The intensity of the scanned film 37 and the identified spectral lines recorded on the LSP-VUV 1-3S-M portable EUV grazing incidence spectrometer.

in $H[a_H/4]$ is represented by

27.2 eV + H
$$\left[\frac{a_{\rm H}}{4}\right]$$
 + H $\left[\frac{a_{\rm H}}{4}\right]$ \rightarrow H * $\left[\frac{a_{\rm H}}{4}\right]$ + H $\left[\frac{a_{\rm H}}{5}\right]$ +27.2 eV + 95.2 eV, (18)

$$H * \left[\frac{a_H}{4}\right] \rightarrow H\left[\frac{a_H}{4}\right] + 27.2 \text{ eV},$$
 (19)

$$H\left[\frac{\alpha_H}{4}\right] \to H\left[\frac{\alpha_H}{5}\right] + 95.2 \text{ eV} + 27.2 \text{ eV}.$$
 (20)

The energy emitted by a hydrino which has nonradiatively transferred $m \times 27.2$ eV of energy to a second hydrino may be emitted as a spectral line. Hydrinos may only accept energy by a nonradiative mechanism [18]; thus, rather than suppressing the emission through internal conversion they do not interact with the emitted radiation. The predicted 95.2 eV (130.3 Å) photon (peak # 19) shown in Fig. 9 is a close match with the observed 132.6 Å line. In Fig. 9, an additional peak (peak #20) was observed at 885.9 Å. It is proposed that peak #20 arises from inelastic hydrogen scattering of the metastable state $H * [a_H/4]$ formed by the resonant nonradiative energy transfer of 27.2 eV from a first $H[a_H/4]$ atom to a second as shown in Eq. (18). The metastable state then nonradiatively transfers part of the 27.2 eV excitation energy to excite atomic hydrogen initially in the state $1s^2S_{1/2}$ to the state $6h^2H_{11/2}$. This leaves a 13.98 eV (887.2 Å) photon, peak 20. The initial and final states for all hydrogen species and mixed photons are determined by the selection rule for deservation of angular momentum where the 1348 eventorian corresponds to $m_{\ell} = 0$ and the initial and mad states for the hydrino atom catalysts correspond to -2, respectively. In the case that the 95.25 V (13.3 Å) photon (peak # 19) conserved. The crite state hydrogen may then emit hydrogen lines that are observed in Fig. 9. Thus, the inelastic hydrogen scattering of the deexcitation of $H * [a_H/4]$ may be

Table 5
Wavelength assignments of identified emission peaks

Line no.	Average distance to zeroth order/mm on film no. #	Angle β/deg measured to zeros! order (grating #3)	Situance angle $\alpha = 4^{\circ}$	λ/\dot{A} (recalculated entrance angle with $\alpha = 3.56^{\circ}$)	Comments
l (inside)	-5.21/0	1.62	80	73.0	
2	35.9/#30	11.1	1070	1021.0	
3	36.2/#30	▲ .18	1081.9	1032.9	
4	37.5/#30	1 101	1148.5	1095.8	Wide
5	37.8/#30	7.72	1165.5	1114.4	
6	38.4/#30		1195.7	1143.7	
7	38.8/#30	12.03	1215	1162.1	Wide
8	39.1/#30	12.12	1229.6	1176.5	
9	39.2/#30	12.15	1234.3	1181.3	
10	39.3/#30	12.18	1239	1186.0	
11	39.7	12.30	1258.8	1204.8	
12	39.97#30	12.37	1270.3	1215.7	Strong, La
13	19.2	12.46	1284.9	1230.8	
14	40.7/#30	12.61	1309.9	1254.7	
15	41.2 30	12.76	1335	1279.2	
16	#30	13.74	1503	1443.7	
17	46.26/#24	14.30	1605.4	1541.9	Wide
18	46.78/#24	14.46	1633.7	1570.5	Wide
ka V	8.57/#28	2.66	144.1	132.6	Weak
2	32.68/#28	10.15	930.5	885.9	Weak
21	22.9/#30	7.12	544.8	513.6	Weak
22	27.5/#30	8.55	715.5	677.8	Weak
23	40.28/#37	12.09	1224	1171.8	

Table 6
Experimental peaks that matched the control hydrogen spectrum and are assigned to atomic and molecular hydrogen peaks

Peak number	Control hydrogen (Å)	Experimental (Å)
2	1025.4	1021.0
3	1047.0	_
4	1101.4	1095.8
5	1116.2	1114.4
6	1144.8	1143.7
7	1160.6	1162.1
8	1174.9	1176.5
9	.1188.4	1181.3
10	1198.6	1186.0
11	1205.8	1204.8
12	1215.7	1215.7
13	1229.6	1230.8
14	1253.4	1254.7
15	1277.8	1279.2
16	1436.2	1443.7
17	1577.9	1541.9
18	1607.9	1570.5
23	Same as peak 8	1171.8

represented by

$$H * \left[\frac{a_{H}}{4}\right] (m_{\ell} = 3) + H(n = 1; m_{\ell} = 0) \rightarrow$$

$$H \left[\frac{a_{H}}{4}\right] (m_{\ell} = -2) + H(n = 6; m_{\ell} = 5)$$

$$+13.98 \text{ eV} (m_{\ell} = 0). \tag{21}$$

The product of the catalysis of atomic hydrogen with potassium metal, $H[a_H/4]$ may serve as both a catalyst and a reactant to form $H[a_H/3]$ and $H[a_H/6]$ according to Eq. (14). The transition of $H[a_H/4]$ to $H[a_H/6]$ induced by a multipole resonance transfer of 54.4 eV, m=2 in Eq. (4) and a transfer of 40.8 eV with a resonance state of $H[a_H/4]$ is represented by

$$H\left[\frac{a_H}{4}\right] + H\left[\frac{a_H}{4}\right] \rightarrow H\left[\frac{a_H}{6}\right] + H\left[\frac{a_H}{3}\right] - 1$$
 (22)

The predicted 176.8 eV (70.2) shown is a close match with the observed 73.0 Å line

The hydrinos are predicted it form hydrino hydride ions. A novel inorganic hydride composaid KHI which comprises high binding energy hydride ions was synthesized by reaction of atomic hydrogen with potassium metal and potassium iodide [7]. The X-ray photoelectron spectroscopy (XPS) spectrum of the triffic ed from that of KI by having additional than 11.1 eV that do not correspond to any other printary element peaks may correspond to the $H^-(n=1/4)E_b = 1.2$ eV hydride ion predicted by Mills [18] (Eq. (16)) in two different chemical environments where E_b is the predicted vacuum binding energy. In this case, the reaction to form $H^-(n=1/4)$ is given by Eqs. (5)–(7) and

(15). Hydrino hydride ions $H^-(n=1/4)$, $H^-(n=1/5)$, and $H^{-}(n = 1/6)$ corresponding to the corresponding hydrino atoms were anticipated. The predicted energy of emission due to these ions in the plasma discharge was anticipated to be higher than that given in Table 1 due to the formation of stable compounds such as KHI comprising these ions. Emission peaks which could not be assigned to hydrogen, potassium, or iodine were observed at 1032.9 Å (12.0 eV), 677.8 Å (18.3 eV), and 513.6 Å (24.1 eV). The binding energies of hydrino hydride ions $H^{-}(n = 1/4)$, $H^{-}(n = 1/5)$, and $H^{-}(n = 1/6)$ corresponding to the corresponding hydrino atoms are 11.23, 16.7, and 22.81 eV. The emissions were 1-2 eV higher than predicted which may be due to the presence of these ions in compounds with chemical environments different from that of vacuum. The excitation was due to the plasma electron bombardment. Additional studies are in progress to collect the compound formed in the reaction chamber so that XPS may be performed and the XPS spectrum may be compared with the Europeaks.

7. Conclusion

Lines which could be assigned to all of the hydrino tran-sitions and hydrino hydride ions possible in the spectral range of 2.5-180 mestarting with a potassium catalyst (Eqs. (5)-(7)) are poserved. Intense EUV emission was obmic hydrogen in the presence of potassium served from which ionizes integer multiples of the potential energy atonia hydrogen (Eq. (3)). The release of energy from hydrogen as evidenced by the EUV emission must result a lever-energy state of hydrogen. The data supports that outsium metal reacts with atomic hydrogen present in the Scharge and forms the hydrino atom $H[a_H/4]$. The energy released undergoes internal conversion to increase the brightness of the plasma discharge. The product, $H[a_H/4]$ serves as both a catalyst and a reactant to form $H[a_H/5]$ with a 132.6 Å and 885.9 Å emission and $H(a_H/6)$ with a 73.0 Å emission according to Eqs. (18)-(21) and (22), respectively. Hydrino hydride ions $H^{-}(n=1/4)$, $H^{-}(n=1/5)$, and $H^-(n = 1/6)$ corresponding to the hydrino atoms of the same quantum state were formed in the plasma as evidenced by the emissions at 513.6, 677.8, and 1032.9 Å. respectively. The emissions were 1-2 eV higher than predicted which may be due to the presence of these ions in compounds with chemical environments different from that of vacuum. Novel compounds containing hydrino hydride ions have been isolated as products of the reaction of atomic hydrogen with potassium atoms and ions [6-12] identified as catalysts in a recent EUV study [1-4]. The formation of novel compounds based on hydrino atoms is substantial evidence supporting catalysis of hydrogen as the mechanism of the observed EUV emission.

J. J. Balmer showed in 1885 that the frequencies for some of the lines observed in the emission spectrum of atomic hydrogen could be expressed with a completely empirical

Table 7

Observed emission data from hydrogen-KI plasmas produced by a hollow cathode discharge that cannot be assigned to atomic or molecular hydrogen

Peak	#	Observed			Predicted	
		Wavelength (Å)	Energy (eV)	Peak assignment	Energy (eV)	Wavelength (Å)
	(inside)	73.0	169.9	1/4 → 1/6 H transition ^a	176.8	70.2
3	(#30)	1032.9	12.0	H ⁻ (1/4) ^{b,c}	11.23	1104
19	(#28)	132.6	93.5	1/4 → 1/5 H transition ^d	95.2	130.3
20	(#28)	885.9	14.0	Inelastic H scattering of H * $\left[\frac{\sigma_H}{4}\right]^e$	13.98	887.2
20 21	(#30)	513.6	24.15	H ⁻ (1/6) ^c	22.8	543
22	(#30) (#30)	677.8	18.30	H~(1/5)°	16.7	742

*Transition induced by a resonance state excited in H[aH/4]

$$H\left[\frac{a_H}{4}\right] + H\left[\frac{a_H}{4}\right] \rightarrow H\left[\frac{a_H}{6}\right] + H\left[\frac{a_H}{3}\right] + 176.8 \text{ eV}$$

b]+ has a peak at 1034.66 Å, [31] but none of the other iodine lines were detected including much stronger line. The hydride ion emission is anticipated to be shift to shorter wavelengths due to its presence in a chemical determinant of Transition induced by a metastable state excited in $H[a_H/4]$

27.2 eV + H
$$\left[\frac{a_{\rm H}}{4}\right]$$
 + H $\left[\frac{a_{\rm H}}{4}\right]$ \rightarrow H * $\left[\frac{a_{\rm H}}{4}\right]$ + H $\left[\frac{a_{\rm H}}{5}\right]$ + 27.2 eV + 95.2 eV,

$$H * \left[\frac{a_H}{4}\right] \rightarrow H \left[\frac{a_H}{4}\right] + 27.2 \text{ eV},$$

$$H\left[\frac{a_H}{4}\right] \rightarrow H\left[\frac{a_H}{5}\right] + 95.2 \text{ eV} + 27.2 \text{ eV}.$$

^cHydrogen inelastic scattered peak of H * $[a_H/4]$ deexcitation

$$H * \left[\frac{a_H}{4}\right] + H(n = 1; m_\ell = 0) \rightarrow H\left[\frac{a_H}{4}\right] + H(n = 6; m_\ell = 5)$$
 13.98 c

relationship. This approach was later extended by R. R. Radberg, who showed that all of the spectral lives a atom hydrogen were given by the equation

$$\vec{v} = R\left(\frac{1}{n_f^2} - \frac{1}{n_i^2}\right),\tag{23}$$

where $R = 109,677 \text{ cm}^{-1}$, $n_i = 12,3,...$, $n_i = 2,3,4,...$, and $n_i > n_f$.

Niels Bohr, in 1913 develope a theory for atomic hydrogen that gave energy levels in agreement with Rydberg's equation. An identical duation, based on a totally different theory for the hydrogen atom, was developed by E. Schrödingertand index indently by W. Heisenberg, in 1926:

$$E_n = \frac{2}{n^2 \cos(n)} - \frac{13.598 \text{ eV}}{n^2},$$
 (24a)

$$n = 1, 2, \dots$$
 (24b)

where $a_{\rm H}$ is the Bohr radius for the hydrogen atom (52.947 pm), e is the magnitude of the charge of the electron, and ϵ_0 is the vacuum permittivity. The EUV emission

of atomic hydrogen with a source of potassium indicates that Eq. (24b), should be replaced by Eq. (24c),

$$n = 1, 2, 3, ..., \text{ and, } n = \frac{1}{2}, \frac{1}{3}, \frac{1}{4}, ...$$
 (24c)

A number of independent experimental observations also lead to the conclusion that atomic hydrogen can exist in fractional quantum states that are at lower energies than the traditional "ground" (n = 1) state. The detection of atomic hydrogen in fractional quantum energy levels below the traditional "ground" state - hydrinos - was reported [18,30] by the assignment of soft X-ray emissions from the interstellar medium, the Sun, and stellar flares, and by assignment of certain lines obtained by the far-infrared absolute spectrometer (FIRAS) on the Cosmic Background Explorer. The assigned hydrogen transition reactions were similar to those shown in Table 7. The detection of a new molecular species - the diatomic hydrino molecule - was reported by the assignment of certain infrared line emissions from the Sun. The detection of a new hydride species --- hydrino hydride ion - was reported by the assignment of certain soft

X-ray, ultraviolet (UV), and visible emissions from the Sun. This has implications for several unresolved astrophysical problems such as the Solar neutrino paradox and the identity of dark matter. The present study also has the important technological implications of the discovery of a new energy source and a new field of hydrogen chemistry.

Acknowledgements

Special thanks to J. Conrads, S. Goetze, J. Schwartz, and H. Lange for performing the experiments and for identifying spectral lines to be assigned, to Ying Lu for reviewing the data and making the assignments to known transitions where possible, and J. Conrads for reviewing this manuscript and providing helpful comments.

References

- [1] Mills R, Dong J, Lu Y. Observation of extreme ultraviolet hydrogen emission from incandescently heated hydrogen gas with certain catalysts. 1999 Pacific Conference on Chemistry and Spectroscopy and the 35th ACS Western Regional Meeting, Ontario Convention Center, California, October 6-8, 1999.
- [2] Mills R, Dong J, Lu Y. Observation of extreme ultraviolet hydrogen emission from incandescently heated hydrogen gas with certain catalysts. Int J Hydrogen Energy 2000;25: 919 - 43.
- [3] Mills R. Temporal behavior of light-emission in the visible spectral range from a Ti-K2CO3-H-Cell. Int J Hydrogen Energy, in press.
- [4] Mills R, Lu Y, Onuma T. Formation of a hydrogen plasma from an incandescently heated hydrogen-potassing gas mixture and plasma decay upon removal of heater pos Int J Hydrogen Energy, in press.
- [5] Mills R, Nansteel M, Lu Y. Observation of extremeditraviolet hydrogen emission from incandescently heated hydrogen with strontium that produced an anomalous of power balance. Int J Hydrogen Energy, in
- [6] Mills R, Dhandapani B, Greenig N Conrads H. Formation of an engetig and novel hydrides from incandescently_ hydrogen gas with 250 Northeast Regional certain catalysts, June ACS Meeting, Meeting, University of Conectival, storrs, CT, June 18-21, 2000.
- [7] Mills R, Dhandapa een N. He J. Synthesis and characterization of transsium iodo hydride. Int J Hydrogen Energy, in pa
- el inomanic hydride. Int J Hydrogen Energy

- [9] Mills R. Novel hydrogen compounds from a potassium carbonate electrolytic cell. Fusion Technol 2000;37(2):157-82
- [10] Mills R, He J, Dhandapani B. Novel hydrogen compounds. 1999 Pacific Conference on Chemistry and Spectroscopy and the 35th ACS Western Regional Meeting, Ontario Convention Center, California, October 6-8, 1999.
- [11] Mills R, Dhandapani B, Nansteel M, He J. Synthesis and characterization of novel hydride compounds. Int J Hydrogen Energy, in press.
- [12] Mills R. Highly stable novel inorganic hydrides. J Mater Res., submitted for publication.
- [13] Phillips JH. Guide to the sun, Cambridge, Great Britain: Cambridge University Press, 1992. p. 16-20.
- [14] Sampson JAR. Techniques of vacuum spectroscopy. Pied Publications, 1980. p. 94-179.
- [15] Sci News, 12/6/97, p. 366.
- K. J Appl Phys [16] Fujimoto T, Sawada K, Takahata 1989;66(6):2315-9.
- [17] Hollander A, Wertheimer MR. J Sci Technol A 1994;12(3):879-82.
- [18] Mills R. The grand unified theory mechanics, January 2000 Edition, Bla kLight Power, Inc., Cranbury, New Jersey, State of Amazon.com.
 [19] Sidgwick NV. The chanical elements and their compounds,
- vol. 1. Oxford: Clasendo Press 1950. p. 17.
- [20] Lamb MD. Lumine sence spectroscopy. London: Academic Press, 1978. p. 38
- book of chemistry and physics, 79th ed. [21] Linde DR CRC II L: CRC Press, 1998-9. p. 10-175-7. Boca Kanon
- [22] Thompson J. Handbook of nonlinear optics. New York: acel Dekker, Inc., 1996. p. 497-548.
- Shell YR. The principles of nonlinear optics. New York: Wile 1984. p. 203–10.
- 24] de Beauvoir B, Nez F, Julien L, Cagnac B, Biraben F, Touahri Hilico L, Acef O, Clairon A, Zondy JJ. Phys Rev Lett 1997;78(3):440–3.
- [25] Conrads JPF, Goetze S, Schwartz J, Lange H. Investigation of hydrogen-KI plasmas produced by a hollow cathode discharge. December 18, 1998, Institut für Niedertemperatur-Plasmaphysik e.V., Friedrich-Ludwig-Jahn-Strasse 19, 17489 Greifswald, Germany.
- [26] Bogen P, Conrads H, Gatti G, Kohlhaas W. JOSA 1968:58(3):203-6.
- [27] Rocca JJ, Marconi MC, Tomasel FG. J Quant Electron 1983;29:180.
- [28] Kunze HJ, Koshelev KN, Steden C, Uskov D, Wiesebrink HT. Phys Rev A 1993;193:183.
- [29] Conrads JPF Institut für Niedertemperatur-Plasmaphysik e.V., personal communication.
- [30] Mills R. The hydrogen atom revisited. Int J Hydrogen Energy, in press.
- [31] NIST Atomic Spectra Database, www.physics.nist.gov/ cgibin/AtData/display.ksb.







International Journal of Hydrogen Energy 000 (2000) 000-000



www.elsevier.com/locate/ijhydene

Temporal behavior of light-emission in the visible spectral range from a Ti-K₂CO₃-H cell

Randell L. Mills *

Black Light Power, Inc., 493 Old Trenton Road, Cranbury, NJ 08512, USA

Abstract

We report the generation of a hydrogen plasma and extreme ultraviolet emission as recorded at the hydrogen Balmer emission in the visible range. Typically, a hydrogen plasma is generated and the emission of extrane ultraviolet light from hydrogen gas is achieved via a discharge at high voltage, a high-power inductively coupled plasma or plasma created and heated to extreme temperatures by RF coupling (e.g. $> 10^6$ K) with confinement provided by a to didal magnetic field. The observed plasma formed at low temperatures (e.g. $\approx 10^3$ K) from atomic hydrogen generated a magnetic field magnetic field. The attanium dissociator coated with potassium carbonate. The temporal behavior of the plasma was recorded via hydrogen Balmer α line emission when all power into the cell was terminated. A 2 s decay of the plasma was observed after a fast decay of the electric field to zero. The persistence of emission following the remova of a of the power to the cell indicates that a novel chemical power source is present that forms an energetic plasma in hydrogen. No unusual behavior was observed with the control sodium carbonate. © 2000 International Association for Hydrogen Energy. Published by Elsevier Science Ltd. All rights reserved.

1. Introduction

A historical motivation to cause extreme u (EUV) emission from a hydrogen gas was that trum of hydrogen was first recorded from source, the Sun [1]. Developed sources able intensity are high-voltage discharge inductively coupled plasma generator. variant of the later type of source is makonak [3]. Fujimoto et al. [4] have determined the section for production of excited hydrogen atoms irenatile smission cross sections for Lyman and Balmer lines when molecular hydrogen is dissociated into could always oy electron collisions. This data was used todevelon a collisional-radiative model to be used in determining the ratio of molecular-to-atomic hydrogen densities in tokomak plasmas. Their results indicate an excitation threshold of 17 eV for Lyman α emission. Addition of other gases would be expected to decrease the

* Tel.: +1-609-490-1040; fax: +1-609-490-1066. E-mail address: rmills@blacklightpower.com (R.L. Mills). intensity of hydrogen lines which could be absorbed by the gas. Hollander and Wertheimer [5] found that within a selected range of parameters of a plasma created in a microwave resonator cavity, a hydrogen—oxygen plasma displays an emission that resembles the absorption of molecular oxygen. Whereas, a helium—hydrogen plasma emits a very intense hydrogen Lyman α radiation at 121.5 nm which is up to 40 times more intense than other lines in the spectrum. The Lyman α emission intensity showed a significant deviation from that predicted by the model of Fujimoto et al. [4] and from the emission of hydrogen alone.

We report that a hydrogen plasma is formed at low temperatures (e.g. $\approx 10^3$ K) by reaction of atomic hydrogen with potassium atoms, but not with sodium atoms. Atomic hydrogen was generated by dissociation at a tungsten filament and at a transition metal dissociator that was incandescently heated by the filament. Potassium metal formed by thermal decomposition of K_2CO_3 and by reaction with hydrogen. Potassium atoms were vaporized by heating to form a low vapor pressure (e.g. 1 Torr). The kinetic energy of the thermal electrons at the experimental

temperature of $\approx 10^3$ K were about 0.1 eV, and the average collisional energies of electrons accelerated by the field of the filament were less than 1 eV. (No blackbody emission was recorded for wavelengths shorter than 400 nm.) Potassium atoms ionize at integer multiples of the potential energy of atomic hydrogen and caused hydrogen EUV emission; whereas, the chemically equivalent atom, sodium, caused no emission. Helium ions present in the experiment of Hollander and Wertheimer [5] ionize at a multiple of two times the potential energy of atomic hydrogen. The mechanism of EUV emission cannot be explained by the conventional chemistry of hydrogen, but it is predicted by a solution of the wave equation with a nonradiative boundary constraint put forward by Mills [6].

Mills predicts that certain atoms or ions serve as catalysts to release energy from hydrogen to produce an increased binding energy hydrogen atom called a *hydrino atom* having a binding energy of

Binding Energy =
$$\frac{13.6 \text{ eV}}{n^2}$$
, (1)

where

$$n = \frac{1}{2}, \frac{1}{3}, \frac{1}{4}, \dots, \frac{1}{p}$$
 (2)

and p is an integer greater than 1, designated as $H[a_H/p]$ with a_H being the radius of the hydrogen atom. Hydrinos are predicted to form by reacting an ordinary hydrogen atom with a catalyst having a net enthalpy of reaction of about

$$m \cdot 27.2 \text{ eV},$$
 (3)

where m is an integer. This catalysis releases energy from the hydrogen atom with a commensurate decrease in size of the hydrogen atom, $r_n = na_H$. For example, the catalysis of H(n = 1) to H(n = 1/2) releases 40.8 eV, and the hydrogen radius decreases from a_H to $\frac{1}{2}a_H$.

The excited energy states of atomic hydrogen are also given by Eq. (1) except that

$$n=1,2,3,\ldots$$

The n = 1 state is the "ground" state for transitions (the n=1 state can absorb a photon o to an release a photon and excited electronic state, but it cannot go to a lower-energy electronic state. However, an electron thower-energy state is transition from the ground start to possible by a nonradiative energy ansier such as multipole coupling or a resonant collision mechanism. These lower-energy states have fractional quantum numbers, n=1/integer. Processes that electr without photons and that require collisions are common. For example, the exothermic chemical scales of H + H to form H_2 does not occur with the doission of a photon. Rather, the reaction requir**ch**a ellision with a third body, M, to remove the bond energy- $H + H + M \rightarrow H_2 + M^*$ [7]. The third body distributes the energy from the exothermic reaction, and the end result is the H2 molecule and an increase in the temperature of the system. Some commercial phosphors

are based on nonradiative energy transfer involving multipole coupling. For example, the strong absorption strength of Sb3+ ions along with the efficient nonradiative transfer of excitation from Sb3+ to Mn2+, are responsible for the strong manganese luminescence from phosphors containing these ions [8]. Similarly, the n = 1 state of hydrogen and the n = 1/integer states of hydrogen are nonradiative, but a transition between two nonradiative states is possible via a nonradiative energy transfer, say $n = 1 - \frac{1}{2}$. In these cases, during the transition the electron couples to another electron transition, electron transfer reaction, or inelastic scattering reaction which can absorb the exact amount of energy that must be removed from the hydrogen atom. Thus, a catalyst provides a net positive enthalpy of reaction of $m \cdot 27.2$ eV (i.e. it absorbs $m \cdot 27.2$ eV where m is an integer). Certain atoms or ions serve as catalysts which resonantly accept energy from hydrogen atoms and release the energy to the surroundings to effect electronic transitions to fractional quantum energy levels.

The catalysis of hydrogen involves the hardiative transfer of energy from atomic hydrogen to alcatal at which may then release the transferred energy by radiative and nonradiative mechanisms. As a pine puer of the nonradiative energy transfer, the hydrogen atom becomes unstable and emits further energy antil tracks was a lower-energy nonradiative state having a frincipal energy level given by Eqs. (1) and (2).

The energy feliased during catalysis may undergo internal conversion and indize or excite molecular and atomic hydrogen resulting in hydrogen emission which includes well-characterized ultraviolet lines such as the Lyman series and the visible Balmer series. Balmer emission was sought by visible spectroscopy. The existence of Balmer emission requires that Lyman emission is also generated. This contrast that a hydrogen plasma exists. The temporal behavior of the light emission in the visible range was recorded when all of the power into the cell was removed. The persistence of visible emission when the field was zero was a means to determine whether the plasma was due to the externally applied power or whether a novel chemical source of power that required potassium and hydrogen was responsible.

2. Experimental

INP Greifswald, Germany recorded the temporal behavior of light-emission in the visible spectral range from a Ti- K_2CO_3 -H cell at the request of Black Light Power, Inc. of Cranbury, NJ, USA [9]. The quartz cell in the experimental set up, shown in Fig. 1, was provided by Black Light Power, Inc. Cranbury, NJ, USA. It comprised a quartz cell which was 500 mm in length and 50 mm in diameter. Two ports for gas inlet and outlet were on the end of the cell. A tungsten filament (0.5 mm, total resistance $\sim 2.5 \Omega$) and a titanium or nickel cylindrical screen (300 mm long and 40 mm in diameter) that performed as a hydrogen

Fiber optic

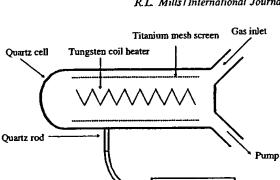


Fig. 1. Experimental setup for observing the UV/Vis spectrum and temporal behavior of light emission from a Ti-K₂CO₃-H cell.

UV/VIS

Spectrometer

dissociator were inside the quartz cell. The filament was 0.508 mm in diameter and 800 cm in length. The filament was coiled on a grooved ceramic support to maintain its shape when heated. The return lead ran through the middle of the ceramic support. The titanium screen was electrically floated. The power applied to the filament was 300 W and was supplied by a Sorensen 80-13 power supply which was controlled by a constant power controller. The voltage across the filament was about 55 V and the current was about 5.5 A at 300 W. The temperature of the tungsten filament was estimated to be in the range of 1100-1500°C. The external cell wall temperature was about 700°C. The hydrogen gas pressure inside the cell was maintained at about 500 mTorr. The entire quartz cell was enclosed inside an insulation package comprised of Zircar AL-30 insulation. Several K-type thermocouples were placed in the insulation to measure key temperatures of the cell and insulation. The thermocouples were read with a multichannel computer data acquisities system.

In the present study, the light-emission phenomena was studied for potassium carbonate and sodium carboi are. The inorganic test materials were coated on a tranium of dissociator by the method of wet impregnate. That is the screen was coated by dipping it in a M & C₃/10% H₂O₂ or 0.6 M Na₂CO₃/10% H₂C and the crystalline material was dried on the surface of lieiting for 12 h in a drying oven at 130°C. A new associator was used for each experiment. The alkali carbonate on the screen were heated by the tungsten filament with the way hydrogen to form the corresponding alkali metal which vaporized.

The light emission was introduced to a UV/Vis monochromator or spectral measurement. The wavelength region covered by the monochromator was 380-720 nm. The UV association (380-720 nm) of the cell emission was record with a photomultiplier tube (PMT) and a sodium strey are scintillator.

This UV Vis emission from the gas cell was channeled into the V/Vis spectrometer using a fiber optic cable. The observation of the plasma in the cell was "side-on". The

gap between the hot quartz wall of the cell and the glass cable was bridged by a quartz rod. The room was made dark. The other end of the fiber optic cable was fixed in an aperture manifold that attached to the entrance aperture of the UV/Vis spectrometer.

In order to study the temporal behavior of the cell, the current of the heater was interrupted by a commercial opener with an opening time of under 2 m which set the voltage to zero. The emission was filtered with an interference filter for the hydrogen Balmer alpha line (Model # λ_{max} = 652 nm; FWHM = 7 nm). The filtered emission was detected by a photomultiplier and recorded by a storing scope.

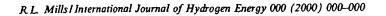
3. Results

Fig. 2 shows a spectrum recorded of a plasma that formed in the cell containing K2CO3. The nomic hydrogen Balmer series was observed such as Balmer at 656 nm, Balmer β at 486 nm, and Balmer γ at 450 nm. Molecular hydrogen emission was also observed arches the Fulcher band in the region 580-650 nm well potassium lines. The light-emission occurred formation of potassium metal was noted by the formation of a mirror on the walls of the top of the scharthis occurred after the power of the filament was increased to above 300 W for about 10 min. The light was emitted for a period depending on the eased to above 300 W for about temperature healer power level), and quantity of K2CO3 deposited on the titanium dissociator in the cell. Higher power would cause higher temperature and higher emission intensity, but a shorter duration of emission was observed n the cast because the potassium metal formed and migrated com the cell more quickly under these conditions. he mission lasted from 20 min to 6 h depending on how Mr K₂CO₃ was initially present in the cell and the power level which corresponded to the cell temperature.

The dissociator was present in all experiments. Spectra were recorded under identical conditions wherein (1) K_2CO_3 was present without hydrogen, (2) only hydrogen was present, (3) K_2CO_3 was present and hydrogen was absent, and (4) Na_2CO_3 replaced K_2CO_3 and hydrogen was present. In these cases, only the blackbody radiation of the filament was observed.

The temporal behavior of the plasma was studied following the interruption and restoration of the power. Only the cell containing K₂CO₃ with hydrogen was studied since this was the only case in which a plasma was formed. The monochromator was adjusted to the range around 670 nm, a part of the spectrum where no line radiation was observed, and the blackbody radiation from the heater was significant. It took about 10 min, before plasma was observed in the cell. Then, the heater current was interrupted several times. The recorded radiation decayed with a time constant of about 2 s.

Next, the hydrogen Balmer α line was selected using an interference filter at a wavelength of 652 nm with a full-width at half-maximum of 7 nm. It was determined



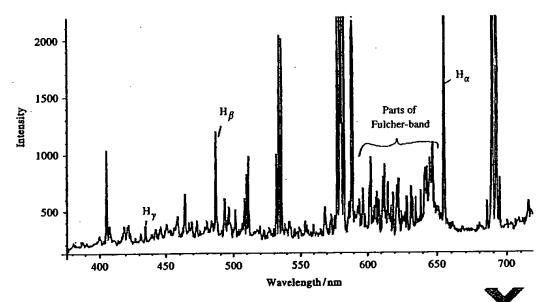


Fig. 2. A UV/Vis spectrum (380-720 nm) recorded of a plasma that formed in the cell containing K min.

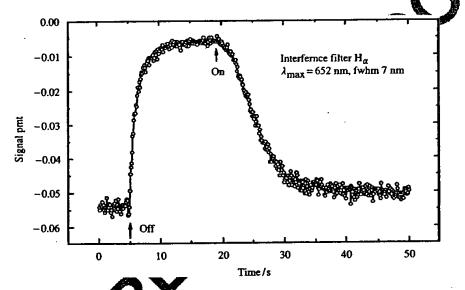


Fig. 3. The photomultiplier signal of the odrossu Balmer α line displayed as a negative signal as a function of time while the heater power was switched off and on.

that the amplitude of the signal of the Balmer α line was orders of magnitude higher that the signal from the black-body light of the later. In peater current was interrupted again several times with sufficient spacing between the interruptions, a that the line emission always returned to its previous lay. The emission of the cell as a function of time while the heater power was turned off and on is shown in Fig. 3. The signal is displayed as negative. It returns to baseline as a function of time with interruption, and the opposite occurs with a longer time constant upon restoration of the heater power. The time constant of the decay of the

hydrogen plasma following interruption of the heater power may be determined from the signal as a function of time which appears in Fig. 4. The time constant of the signal intensity change was about 2 s. The thermal decay of the filament was observed to have the same time constant.

4. Discussion

In the cases where plasma was observed, no possible chemical reactions of the tungsten filament, the titanium

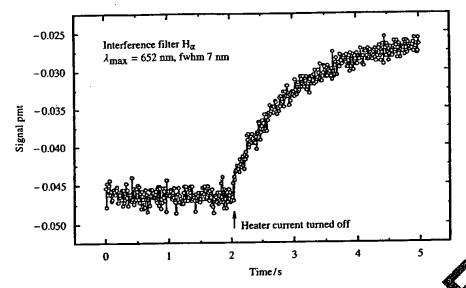


Fig. 4. The photomultiplier signal of the hydrogen Balmer α line displayed as a negative signal as a function of time all the heater power was switched off.

dissociator, potassium carbonate, and 300 mTorr hydrogen at a cell temperature of 700°C could be found which accounted for the plasma. In fact, no known chemical reaction releases enough energy to form a hydrogen plasma, and the reduction of K₂CO₃ by hydrogen is very endothermic. The dissociator was present in all experiments. The emission was not observed with the cell alone, with hydrogen alone, K₂CO₃ alone, or under identical conditions wherein Na₂CO₃ replaced K₂CO₃. No emission was observed until the cell temperature increased to a level that potassium metal was observed to form. Hydrogen line emission was occurring even though the voltage between the heater wires was set to and measured to be zero. These results indicate that the emission was due to a reaction of atomic hydrogen with potassium atoms.

According to Mills [6], a catalytic system is provided the ionization of t electrons from an atomic accontinuum energy level such that the sum of the inization energies of the t electrons is approximately t 27. Where t is an integer. One such catalytic system volves potassium. The first, second, and third ionization energies of potassium are 4.34066, 31.63, and 45.806 t, respectively [10]. The triple ionization (t = 3) rection of t to t in Eq. (3):

81.7426 eV
$$K(p) \rightarrow I\left[\frac{a_H}{p}\right] \rightarrow K^{3+} + 3e^{-}$$

 $+H\left[(p+3)^2 - p^2\right]X13.6 \text{ eV},$ (5)

$$K^{3+} + 3e^{-} \rightarrow K(m) + 81.7426 \text{ eV}.$$
 (6)

And, the overall reaction

$$H\left[\frac{a_{H}}{p}\right] \to H\left[\frac{1}{(p+3)^{2}-p^{2}]X13.6 \text{ eV}}.$$
(7)

No such reaction is possible for sodium.

We take power was interrupted, the hydrogen line emission decay hatched the thermal decay of the filament. It may be also tuned to chemical reactions because typically their mess are dependent on the temperature. Candidate chemical tractions are the hydrogen catalysis reaction, the dissociator of molecular hydrogen to atomic hydrogen, and the formation of potassium metal catalyst. (Atomic hydrogen and catalysts are required as reactants for hydrogen catalysis as given by Eqs. (5)-(7)).

Other studies support the possibility of a novel catalytic reaction of atomic hydrogen. It has been reported that intense EUV emission was observed at low temperatures (e.g. $\approx 10^3$ K) from atomic hydrogen and certain atomized elements or certain gaseous ions which ionize at integer multiples of the potential energy of atomic hydrogen, 27.2 eV [11–16].

5. Conclusions

Line radiation from hydrogen emitted by the cell loaded with K_2CO_3 on titanium and operated in hydrogen requires a minimum temperature. The heat from the filament and possibly the weak dipole field from the filament may sustain the hydrogen plasma; but, it is not essential because hydrogen lines are emitted during times when this voltage is set to zero.

The emission from a plasma was observed at low temperatures (e.g. $\approx 10^3$ K) from atomic hydrogen and potassium atoms which ionize at integer multiples of the potential energy of atomic hydrogen. The release of energy from hydrogen was evidenced by the hydrogen Balmer emission which identifies EUV emission and the presence of a hydrogen plasma. The persistence of emission following the removal of all of the power to the cell indicates that novel chemical power source is present.

Novel compounds containing hydrino hydride ions have been isolated as products of the reaction of atomic hydrogen with potassium atoms and ions [17–23] identified as catalysts in a recent EUV studies [11–16]. The formation of novel compounds based on hydrino atoms is substantial evidence supporting catalysis of hydrogen as the mechanism of the observed EUV emission. The implications are that a vast new energy source and a new field of hydrogen chemistry have been discovered.

Acknowledgements

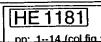
Special thanks to J. Conrads, S. Goetze, J. Schwartz, and H. Lange for performing the experiments and analysis.

References

- Phillips JH. Guide to the sun. Cambridge, UK: Cambridge University Press, 1992. p. 16-20.
- [2] Sampson JAR. Techniques of vacuum ultraviolet spectroscopy. Pied Publications, 1980. p. 94-179.
- [3] Science News, 12/6/97, p. 366.
- [4] Fujimoto T, Sawada K, Takahata K. J Appl Phys 1989;66(6):2315-9.
- [5] Hollander A, Wertheimer MR. J Vac Sci Technol 1994;12(3):879-82.
- [6] Mills R. The grand unified theory of classical quantum mechanics, January 2000 ed. Cranbury, NJ: BlackLight Power Inc., distributed by Amazon.com.
- [7] Sidgwick NV. The chemical elements and their compounds, vol. 1. Oxford: Clarendon Press, 1950, pp. 17.
- [8] Lamb MD. Luminescence spectroscopy. Academic Press, 1978, p. 68.
- [9] Conrads J, Goetze S, Schwartz, Lange H Temporal behavior of light-emission in the visible of the lange from a Ti-K₂CO₃-H cell. Institut for Negertemperatur-Plasmaphysik Friedrich-Ludwig-Jaho Strass, vol. 19, Greifswald, Germany, September 20, 1999. 17 48

- [10] Linde DR. CRC handbook of chemistry and physics, 79th Ed. Boca Raton, FL: CRC Press, 1998-9, p. 10-175, 10-177.
- [11] Mills R, Dong J, Lu Y. Observation of extreme ultraviolet hydrogen emission from incandescently heated hydrogen gas with certain catalysts. Int J Hydrogen Energy 2000;25:919-43.
- [12] Mills R. Observation of extreme ultraviolet hydrogen and hydrino emission from hydrogen-Kl plasmas produced by a hollow cathode discharge. Int J Hydrogen Energy, submitted for publication.
- [13] Mills R, Lu Y, Onuma T. Formation of a hydrogen plasma from an incandescently heated hydrogen-potassium gas mixture and plasma decay upon removal of heater power. Int J Hydrogen Energy, accepted for publication.
- [14] Mills R, Nansteel M, Lu Y. Observation of extreme ultraviolet hydrogen emission from incandescently heated hydrogen gas with strontium that produced an optically measured power balance that was 4000 times the control. Int J Hydrogen Energy, accepted for publication.
- [15] Mills R, Dhandapani B, Greenig N, He I, Dong J, Lu Y, Conrads H. Formation of an energetic plasma and novel hydrides from incandescently heaten hydrogen gas with certain catalysts. June ACS Meeting 29th ortheast Regional Meeting, University of Connectant, Stores, II, June 18-21, 2000
- [16] Mills R, Dong J, Lu Y
 hydrogen emission from incandescently heated hydrogen gas
 with certain catalysts 13 2 Pacific Conference on Chemistry
 and Spectroscopy and the 5th ACS Western Regional
 Meeting, Ontari Convention Center, CA, October 6-8, 1999.
 [17] Mills R, Dandaphi B, Greenig N, He J. Synthesis and
- [17] Mills R, Banda Shi B, Greenig N, He J. Synthesis and characterization of polassium iodo hydride. Int J Hydrogen Energy, as a ped for publication.
- [18] Mills R. Nove inorganic hydride. Int J Hydrogen Energy 2000, 669-83.
- Mills Novel hydrogen compounds from a potassium catorogie electrolytic cell. Fusion Technol 2000;37(2):
- 20 Aills R, Dhandapani B, Nansteel M, He J. Synthesis and characterization of novel hydride compounds. Int J Hydrogen Energy, submitted for publication.
- [21] Mills R. Highly stable novel inorganic hydrides. J Mater Res, submitted for publication.
- [22] Mills R, He J, Dhandapani B. Novel hydrogen compounds. 1999 Pacific Conference on Chemistry and Spectroscopy and the 35th ACS Western Regional Meeting, Ontario Convention Center, CA, October 6-8, 1999.
- [23] Mills R, Dhandapani B, Greenig N, He J, Dong J, Lu Y, Conrads H. Formation of an energetic plasma and novel hydrides from incandescently heated hydrogen gas with certain catalysts. June ACS Meeting, 29th Northeast Regional Meeting, University of Connecticut, Storrs, CT, June 18-21, 2000.





PROD. TYPE: COM

GN: VD - SCAN: Mout



International Journal of Hydrogen Energy 000 (2001) 000-000

HYDROGE

www.elsevier.com/locate/ijhydene

Formation of a hydrogen plasma from an incandescently heated hydrogen-catalyst gas mixture with an anomalous afterglow duration

Randell L. Mills *, Takeyoshi Onuma, Ying Lu

BlackLight Power, Inc., 493 Old Trenton Road, Cranbury, NJ 08512, USA

Abstract

We report the generation of a plasma of hydrogen and certain alkali ions as recorded via EUV spectroscopy and the hydrogen Balmer and alkali line emissions in the visible range. Typically, a hydrogen plasma is generated and the emission of extreme ultraviolet light from hydrogen gas is achieved via a discharge at high voltage, a high power inductively coupled plasma, or a plasma created and heated to extreme temperatures by RF coupling (e.g. $> 10^6$ K) with confinement provided by a toroidal magnetic field. The observed plasma formed at low temperatures (e.g. $\approx 10^3$ K) from a toling hydrogen generated at a tungsten filament that heated a titanium dissociator and a catalyst comprising one of potassium, pibidium, cesium, and their carbonates and nitrates. These atoms and ions ionize to provide a catalyst with a net cathain of reaction of an integer multiple of the potential energy of atomic hydrogen ($m \times 27.2$ eV m = integer) to within 0.17 and comprise only a single ionization in the potential energy of atomic hydrogen ($m \times 21.2$ eV m = integer) to within 0.1 / eV and comprise only a single ionization in the case of a potassium or rubidium ion. Whereas, the chemically similar atoms of sodium and sodium and lithium carbonates and nitrates which do not ionize with these constraints caused no emission. It test the electric dependence of the emission, the weak electric field of about 1 V/cm was set and measured to be error < 0.0000 s. An anomalous afterglow duration of about 1-2 s was recorded in the case of potassium, rubidium resign, (0.0000), RbNO₃, and CsNO₃. Hydrogen line or alkali line emission was occurring even though the voltage between the least wires was set to and measured to be zero. These atoms and ions ionize to provide a catalyst with a net enthalpy of reacher of an integer multiple of the potential energy of atomic hydrogen to within less than the thermal energies at ≈ 0.000 cand comprise only a single ionization in the case of a potassium or rubidium ion. Since the thermal decay time of the flament of release to the standard of release to the standard of release to the standard of release the standard of release to or rubidium ion. Since the thermal decay time of the filament for dissociation of molecular hydrogen to atomic hydrogen was similar to the anomalous plasma afterglow duration, the emission was determined to be due to a reaction of atomic hydrogen with a catalyst that did not require the presence of asselectric field to be functional. © 2001 International Association for Hydrogen Energy. Published by Elsevier State Ltd. All rights reserved.

1. Introduction

A historical motivation to Pause EUV emission from a hydrogen gas was that the spectrum of hydrogen was first recorded from the only known source, the Sun [1]. Developed sources that provide a suitable intensity are high voltage discharge. Vnchrotron, and inductively coupled plasma generators [2]. An important variant of the later type of source is a tokomak [3]. Fujimoto et al. [4] have deter-

* Corresponding author. Tel.: +1-609-490-1040; fax: +1-609-490-1066.

E-mail address: rmills@blacklightpower.com (R. L. Mills).

mined the cross section for production of excited hydrogen atoms from the emission cross sections for Lyman and Balmer lines when molecular hydrogen is dissociated into excited atoms by electron collisions. These data were used to develop a collisional-radiative model to be used in determining the ratio of molecular-to-atomic hydrogen densities in tokomak plasmas. Their results indicate an excitation threshold of 17 eV for Lyman a emission. Addition of other gases would be expected to decrease the intensity of hydrogen lines which could be absorbed by the gas. Hollander and Wertheimer [5] found that within a selected range of parameters of a plasma created in a microwave resonator cavity, a hydrogen-oxygen plasma displays an emission that resem-



bles the absorption of molecular oxygen. Whereas, a heliumhydrogen plasma emits a very intense hydrogen Lyman α radiation at 121.5 nm which is up to 40 times more intense than other lines in the spectrum. The Lyman α emission intensity showed a significant increase from that predicted by the model of Fujimoto et al. [4] and from the emission of hydrogen alone.

Observation of intense extreme ultraviolet (EUV) emission has been previously reported at low temperatures (e.g. ≈103 K) from atomic hydrogen and certain atomized elements or certain gaseous ions [6-17]. The only pure elements that were observed to emit EUV were those wherein the ionization of t electrons from an atom to a continuum energy level is such that the sum of the ionization energies of the t electrons is approximately $m \times 27.2$ eV where t and m are each an integer. Potassium, cesium, and strontium atoms and Rb+ ion ionize at integer multiples of the potential energy of atomic hydrogen and caused emission. Whereas, the chemically similar atoms, sodium, magnesium and barium, do not ionize at integer multiples of the potential energy of atomic hydrogen and caused no emission. Helium ions present in the experiment of Hollander and Wertheimer [5] ionize at a multiple of 2 times the potential energy of atomic hydrogen.

Prior studies support the possibility of a novel reaction of atomic hydrogen which produces an anomalous discharge and produces novel hydride compounds [6-31]. Experiments that confirm the novel hydrogen chemistry include extreme ultraviolet (EUV) spectroscopy, plasma formation, power generation, and analysis of chemical compounds. For examples: (1) Lines observed by EUV spectroscopy could be assigned to transitions of atomic hydrogen to lower energy levels corresponding to lower energy hydrogen atoms and the emission from the excitation of the corresponding hydride ions [8,11,13,15-17]. (2) The chemical intera of catalysts with atomic hydrogen at temperature 1000 K has shown surprising results in terms of the mission of the Lyman and Balmer lines [6-17] and the formation of novel chemical compounds [13,15-31]. An energetic plasma in hydrogen was generated by accatalysts reaction at 1% of the theoretical or prior known will be requirement and with 1000s of times less power imputin a system wherein the plasma reaction was controlled with a weak electric field [6,10]. (4) An anomalous plasma with hydrogen/potassium mixtures has been reported wherein the plasma decayed with a two second half-life which was the thermal decay time of the filament which dissociated molecular hydrogen to atomic hydrogen when the electric field was set to zero [9]. This experiment showed that hydrogen line emission was occurring even though the voltage between the heater wires was set to and ineasured to be zero and indicated that the emission was due to a reaction of potassium atoms with atomic hydrogen (5) Novel hydrogen compounds have been isolated as products of the reaction of atomic hydrogen with atoms and ions identified as catalysts in the reported EUV studies [6-31].

We report that a hydrogen plasma formed at low temperatures (e.g. $\approx 10^3$ K) by reaction of atomic hydrogen with a catalyst with a net enthalpy of reaction of an integer multiple of the potential energy of atomic hydrogen $(m \times 27.2 \text{ eV } m = \text{integer})$. Atomic hydrogen was generated by dissociation at a tungsten filament and at a transition metal dissociator that was incandescently heated by the filament. Catalyst atoms or ions were vaporized by heating to form a low vapor pressure (e.g. 1 Torr). The kinetic energy of the thermal electrons at the experimental temperature of $\approx 10^3$ K were about 0.1–0.2 eV, and the average collisional energies of electrons accelerated by the field of the filament were less than I eV. (No blackbody emission was recorded for wavelengths shorter than 400 nm.) Only blackbody radiation was observed at lower wavelengths unless an anomalous discharge formed. The mechanism of EUV emission cannot be explained by the conventional chemistry of hydrogen, but it is predicted by a solution of the Schrodinger equation with a nonradiative boundary instraint put forward by Mills [32].

Mills predicts that certain atoms or ions serve as catalysts to release energy from hydrogen caproduce an increased binding energy hydrogen atom cared a hydrino atom having a binding energy of a binding energy of

where

$$n = \frac{1}{2} \frac{1}{2} \dots$$
 (2)

In integer greater than 1, designated as $H(a_H/p)$ where is the radius of the hydrogen atom. Hydrinos are predicted to form by reacting an ordinary hydrogen atom In a catalyst having a net enthalpy of reaction of about

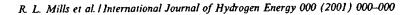
$$m \times 27.2 \text{ eV},$$
 (3)

where m is an integer. This catalysis releases energy from the hydrogen atom with a commensurate decrease in size of the hydrogen atom, $r_n = na_H$. For example, the catalysis of H(n=1) to H(n=1/2) releases 40.8 eV, and the hydrogen radius decreases from $a_{\rm H}$ to $\frac{1}{2}a_{\rm H}$.

The excited energy states of atomic hydrogen are also given by Eq. (1) except that

$$n=1,2,3,\ldots \tag{4}$$

The n = 1 state is the "ground" state for "pure" photon transitions (the n = 1 state can absorb a photon and go to an excited electronic state, but it cannot release a photon and go to a lower-energy electronic state). However, an electron transition from the ground state to a lower-energy state is possible by a nonradiative energy transfer such as multipole coupling or a resonant collision mechanism. These lowerenergy states have fractional quantum numbers, n =1/integer. Processes that occur without photons and that require collisions are common. For example, the exothermic chemical reaction of H + H to form H2 does not



occur with the emission of a photon. Rather, the reaction requires a collision with a third body, M, to remove the bond energy-H + H + M \rightarrow H₂ + M* [33]. The third body distributes the energy from the exothermic reaction, and the end result is the H2 molecule and an increase in the temperature of the system. Some commercial phosphors are based on nonradiative energy transfer involving multipole coupling. For example, the strong absorption strength of Sb3+ ions along with the efficient nonradiative transfer of excitation from Sb3+ to Mn2+, are responsible for the strong manganese luminescence from phosphors containing these ions [34]. Similarly, the n = 1 state of hydrogen and the n = 1/integer states of hydrogen are nonradiative, but a transition between two nonradiative states is possible via a nonradiative energy transfer, say n = 1-1/2. In these cases, during the transition the electron couples to another electron transition, electron transfer reaction, or inelastic scattering reaction which can absorb the exact amount of energy that must be removed from the hydrogen atom. Thus, a catalyst provides a net positive enthalpy of reaction of $m \times 27.2$ eV (i.e. it absorbs $m \times 27.2$ eV where m is an integer). Certain atoms or ions serve as catalysts which resonantly accept energy from hydrogen atoms and release the energy to the surroundings to effect electronic transitions to fractional quantum energy levels. Recent analysis of mobility and spectroscopy data of individual electrons in liquid helium show direct experimental evidence that electrons may have fractional principal quantum energy levels [35].

The catalysis of hydrogen involves the nonradiative transfer of energy from atomic hydrogen to a catalyst which may then release the transferred energy by radiative and nonradiative mechanisms. As a consequence of the nonradiative energy transfer, the hydrogen atom becomes unstable and emits further energy until it achieves a lower-energy nondiative state having a principal energy level given by Eqs. (1) and (2).

The energy released during catalysis may undergo internal conversion and cause alkali line emission. The dargy could also ionize or excite molecular and atomic hydrogen resulting in hydrogen emission which methods will characterized ultraviolet lines such as the lyman series and the visible Balmer series. The existence is Balmer emission requires that Lyman emission is also generated. This confirms that a hydrogen plasma exists. Lyman α emission was sought by EUV spectroscopy and Balmer and alkali line emission was sought to visible spectroscopy.

The temporal seriavior of the light emission in the visible range was recorded when all of the power into the cell was removed Typically, the temporal emission of a plasma is very short for example, the afterglow with decay to zero emission of cesium lines (e.g. 455.5 nm) of a high voltage pulse discharge is about 100 µs [36]. And, the duration of the afterglow of a neon plasma which was switched off from a stationary state was under 250 µs [37]. In the present study, the presence of EUV emission and the persistence of Balmer beta or alkali line emission when the field was zero

was a means to determine whether the plasma was due to the externally applied power or whether a novel chemical source of power that required a catalyst and hydrogen was responsible. The electric field dependence of the catalysts was also determined.

2. Experimental

Due to the extremely short wavelength of this radiation, "transparent" optics do not exist. Therefore, a windowless arrangement was used wherein the source was connected to the same vacuum vessel as the grating and detectors of the EUV spectrometer. Windowless EUV spectroscopy was performed with an extreme ultraviolet spectrometer that was mated with the cell. Differential pumping permitted a high pressure in the cell as compared to that in the spectrometer. This was achieved by pumping on the cell outlet and pumping on the grating side of the collimator that served as a pin-hole inlet to the optics. The cell was operated under hydrogen flow conditions while maintaining a constant hydrogen pressure in the cell with a mass flow controller.

The experimental set in showing Fig. 1 comprised a quartz cell which was 50 mm in length and 50 mm in diameter. Three ports for green and the cell. A transfer flower

tion were on the tither and of the cell. A tungsten filament (0.508 mm in diameter and 800 cm in length, total resistance ~ 2.5 2) and a litanium cylindrical screen (300 mm long and 40 min in diameter) that performed as a hydrogen_dissociator were inside the quartz cell. A new dissociatop was used for each experiment. The filament was coiled son agrowed ceramic support to maintain its shape when heated. The return lead ran through the middle of the cefamily support. The filament leads were covered by a alumina sheath which differed from the set up reported previously [7]. The titanium screen was electrically floated. The power was applied to the filament by a power supply (Sorensen 80-13) which was controlled by a constant power controller. The cell was operated with 300 W or less input power which corresponded to a cell wall temperature of about 700°C or less which was lower than the maximum power and temperature, respectively, reported in previous EUV studies [7]. This temperature was selected in order to maximize the vaporization of the catalyst while avoiding decomposition to the corresponding alkali metal in the case of alkali carbonates and nitrates. The temperature of the tungsten filament was estimated to be in the range of 1100-1500°C. The hydrogen gas pressure inside the cell was maintained at about 300 mTorr. The entire quartz cell was enclosed inside an insulation package (Zircar AL-30). Several K-type thermocouples were placed in the insulation to measure key temperatures of the cell and insulation. The thermocouples were read with a multichannel computer data acquisition system.

In the present study, the light emission phenomena was studied for (1) hydrogen, argon, neon, and helium alone, (2) all alkali metals except lithium which reacted with the quartz cell and all alkali carbonates

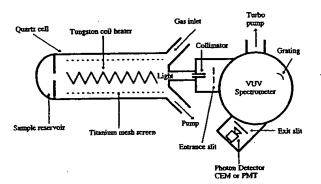


Fig. 1. The experimental set up comprising a gas cell light source and an EUV spectrometer which was differentially pumped.

and nitrates. The inorganic test materials were coated on a titanium screen dissociator by the method of wet impregnation. The screen was coated by dipping it in a $0.6~M~Na_{2}CO_{3}/10\%~H_{2}O_{2},~0.6~M~K_{2}CO_{3}/10\%~H_{2}O_{2},~~\text{or}~~$ 0.6 M RbNO₃/10% H₂O₂ solution, and the crystalline material was dried on the surface by heating for 12 h in a drying oven at 130°C. A new dissociator was used for each experiment. Alkali metals were placed in the bottom of the cell and volatized by the external heater.

The light emission was introduced to an EUV spectrometer for spectral measurement. The spectrometer was a McPherson 0.2 m monochromator (Model 302, Seya-Namioka type) equipped with a 1200 lines/mm holographic grating with a platinum coating. The wavelength region covered by the monochromator was 30-560 nm. The vacuum inside the monochromator was maintained below 5×10^{-4} Torr by a turbo pump.

The EUV spectrum (40-160 nm) of the cell emissions was recorded with a channel electron multiplier (CEM The wavelength resolution was about 1 nm (FWHM) with an entrance and exit slit width of 300 × 300 μm except for the Na₂CO₃ cell wherein an entrance and exit slie width of $500 \times 500 \ \mu m$ was used.

The EUV/UV/VIS spectrum (40-560) emission of hydrogen alone was recognitive photomultiplier tube (PMT) and a sodium satisfy intillator. The uppler tupe (PM1) and a sodrum satelylate antillator. The PMT (Model R1527P, Hamama 19) used has a spectral response in the range of 185-640 nm with a peak efficiency at about 400 nm. The scan interval was 0.4 nm. The inlet and outlet slit were 500 × 500 nm which corresponded to a wavelength resolution of about 2 nm (FWHM).

The UV/VIS pectrum (200-560 nm) of the cell emission was recorded with the photomultiplier tube (PMT) without the sodium satelylate scintillator. The scan interval was 0.4 nm 13 min and outlet slit were 500 × 500 nm

0.4 nm. The in thand outlet slit were 500 × 500 μm.

The emission in the region 560-900 nm was recorded with a 100 unit optical fiber and visible spectrometer (Ocean Oblics S2000). To correct for the nonuniform response of the spectrometer system as a function of wavelength and the dependence of energy on wavelength, the system was calibrated against a reference light source (Ocean Optics

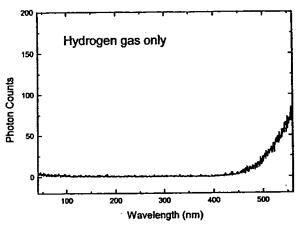


Fig. 2. The UV/VIS spectrum (40-560 nm) of the cell emission from the gas cell comprising a tungsten filament, a titanium dissociator, and 0.3 Torr hydrogen at a cell temperature of 700°C that was recorded with a PMT and a sodium salle tale scintillator with an increased slit width of 500 × 500 pins

LS-1-CAL). A spectral california factor was applied to the count rate data at each avelength to yield the irradiation

of the detector in units of energy time/area/wavelength.

In order to study the temporal behavior of the cell,

UV/VIS spectroming was set to the Balmer beta line or
a alkali line and the current of the heater was interrupted by a switch between the power supply and the filament. This switch see the voltage to zero in $< 0.5 \times 10^{-6}$ s as recorded by an oscilloscope (BK Precision Model 2120). The response time of the photomultiplier was also tested by switching off the room lights and recording the zero order as a fugiction of time. The emission in the 300-560 nm region was recorded as a function of time at 200 ms steps with the photomultiplier as the filament was switched on and off. The emission in the 560-900 nm region was recorded as a function of time at 200 ms steps with the Ocean Optics S2000 spectrometer as the filament was switched on and off.

3. Results

The cell without any test material present was run to establish the baseline of the spectrometer. The UV/VIS spectrum (40-560 nm) of the emission from the gas cell comprising a tungsten filament, a titanium dissociator, and 0.3 Torr hydrogen at a cell temperature of 700°C is shown in Fig. 2. No emission was observed except for the blackbody filament radiation at the longer wavelengths. No emission was also observed when argon, neon, or helium replaced hydrogen.

The EUV spectrum (40-160 nm) of the cell emission from the Na₂CO₃, K₂CO₃, and RbNO₃ gas cell is shown in Figs. 3-5, respectively. Even with the larger slit widths, essentially no EUV emission was observed in the case of Na₂CO₃ which is not a catalyst. The cause of the weak emission may have been due to potassium contamination

R. L. Mills et al. | International Journal of Hydrogen Energy 000 (2001) 000-000

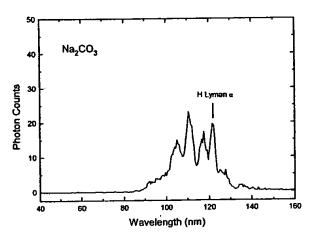


Fig. 3. The EUV spectrum (40–160 nm) of the cell emission from the gas cell comprising a tungsten filament, a titanium dissociator treated with 0.6 M $\rm Na_2CO_3/10\%~H_2O_2$ before being used in the cell, and 0.3 Torr hydrogen at a cell temperature of 700° C that was recorded with a CEM with an increased slit width of 500×500 μ m.

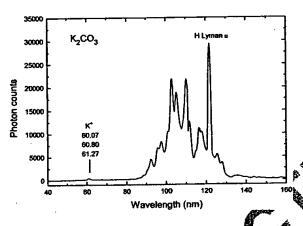


Fig. 4. The EUV spectrum (40–160 nm) of the cell emission from the gas cell comprising a tungsten filament, a titatium discretion treated with 0.6 M K₂CO₃/10% H₂O₂ before from used in the cell, and 0.3 Torr hydrogen at a cell term and 0.3 Torr hydrogen at a cell

which was observed by time of them secondary ion mass spectroscopy. Strong emission of hydrogen Lyman series and weak potassium and rubidium lines were observed in the cases of catalysts K₂C₀, and JbNO₃, respectively. In these cases, the EUV mission indicted that a plasma of hydrogen and alkali ion was present with emissions 10 times more energetic than landary chemical reactions.

The Spectrum (300-560 nm) of the cell emission from the Na₂CO₃, K₂CO₃, and RbNO₃ gas cell is shown in Figs. 6-8, respectively. No UV/VIS emission was observed in the case of Na₂CO₃ which is not a catalyst; whereas, strong emission was observed in the cases of catalysts K₂CO₃ and RbNO₃. In the case of K₂CO₃, the visible spectrum shown in Fig. 7 contains potassium lines

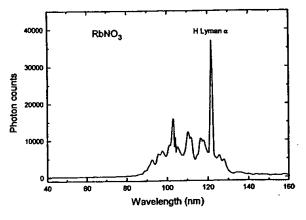


Fig. 5. The EUV spectrum (40-160 nm) of the cell emission from the gas cell comprising a tungsten filament, a titanium dissociator treated with 0.6 M RbNO₃/10% H₂O₂ before being used in the cell, and 0.3 Torr hydrogen at a cell temperature of 700°C that was recorded with a CEM.

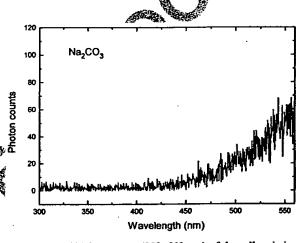


Fig. 6. The UV/VIS spectrum (300-560 nm) of the cell emission from the gas cell comprising a tungsten filament, a titanium dissociator treated with 0.6 M Na₂CO₃/10% H₂O₂ before being used in the cell, and 0.3 Torr hydrogen at a cell temperature of 700°C that was recorded with a PMT.

and hydrogen Balmer lines. Balmer beta was present at 486 nm, and Balmer gamma was present at 434 nm when the Lyman α emission was present in the EUV region. Thus, recording the Balmer emission corresponds to recording the Lyman α emission. The Balmer beta was selected and the temporal behavior of the light emission in the visible range was recorded when all of the power into the cell was removed. In the case of RbNO₃, the visible spectrum shown in Fig. 8 contains rubidium lines. The rubidium 550.0 nm was present when the Lyman α emission was present in the EUV region. Thus, recording the rubidium 550.0 nm corresponds to recording the Lyman α emission. The rubidium 550.0 nm was selected and the temporal behavior of the light emission



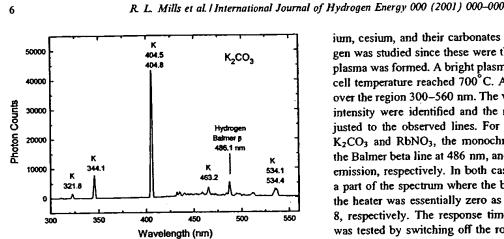


Fig. 7. The UV/VIS spectrum (300-560 nm) of the cell emission from the gas cell comprising a tungsten filament, a titanium dissociator treated with 0.6 M K2CO3/10% H2O2 before being used in the cell, and 0.3 Torr hydrogen at a cell temperature of 700°C that was recorded with a PMT.

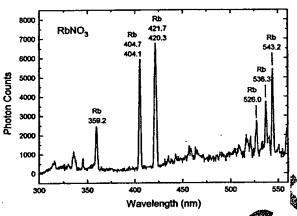


Fig. 8. The UV/VIS spectrum (300-560 nm) of the cell from the gas cell comprising a tungsten filament, sociator treated with 0.6 M RbNO₃/10% H₂O₂ <u>rafafe of</u> 700°C in the cell, and 0.3 Torr hydrogen at a cell tering that was recorded with a PMT.

in the visible range was recorded when all of the power into the cell was removed.

The temporal behavior of the filament was studied following the interruption and estoration of the power. The monochromator was adjusted the range around 670 nm, a part of the specifilm where no line radiation was observed, and the blackbody radiation from the heater was significant. It took about 10 time before the blackbody of the filament reached steady level. Then, the heater current was interrupted several times. The thermal decay time of the filament for dissociation of molecular hydrogen to atomic hydrogen was about 2 s.

Next the temporal behavior of the plasma was studied following the interruption of the heater power. Only the cell containing a catalyst comprising one of potassium, rubid-

ium, cesium, and their carbonates and nitrates with hydrogen was studied since these were the only cases in which a plasma was formed. A bright plasma formed by the time the cell temperature reached 700°C. A spectrum was obtained over the region 300-560 nm. The visible lines of maximum intensity were identified and the monochromator was adjusted to the observed lines. For example, in the case of K₂CO₃ and RbNO₃, the monochromator was adjusted to the Balmer beta line at 486 nm, and the rubidium 550.0 nm emission, respectively. In both cases, the line appeared as a part of the spectrum where the blackbody radiation from the heater was essentially zero as shown in Figs. 2, 7 and 8, respectively. The response time of the photomultiplier was tested by switching off the room lights and recording the zero order as a function of time. The results are shown in Fig. 9. The photomultiplier output went to zero within the sampling time (200 ms) of the photofaultiplier. With a faster rate, this time constant may be reduced. The heater current was interrupted several times with sufficient spacing between the interruptions, so that the line emission always returned to its previous level. The switch set the voltage to zero in a $< 0.5 \times 10^{-6}$ s as recorded by the oscilloscope (BK Precision Model 2220), and the output of the photomultiplier was recorded. In the case of K2CO3 and RbNO3, the emission of the cell as a function of time while the heater power was turned on and off is shown in Figs. 10(a)-(c) and 11, respectively. The observed decay time of the emission was about 1-2 s.

The atoms and ions which gave an anomalous discharge as determined by strong EUV and visible emission are given in table. The atoms and ions which gave an anomalous afterglaw duration of about 1-2 s are also given in Table 1 with the corresponding line emission(s).

4. Discussion

Only blackbody radiation was observed at lower wavelengths unless an anomalous discharge formed. In the cases where plasma was observed, no possible chemical reactions of the tungsten filament, the titanium dissociator, catalyst, and 0.3 Torr hydrogen at a cell temperature of 700°C could be found which accounted for the plasma. In fact, no known chemical reaction releases enough energy to form a hydrogen plasma. For examples, the enthalpy of formation ΔH_p of potassium, rubidium, and cesium hydride is -14.13, -13.00, and -13.50 kcal/mol [38]. Thus, the formation of potassium, rubidium, and cesium hydride releases 0.59, 0.54, and 0.56 eV/atom, respectively. The reduction of K2CO3 by hydrogen calculated from the heats of formation is very endothermic.

$$H_2 + K_2CO_3 \rightarrow 2K + H_2O + CO_2,$$

 $\Delta H = +122.08 \text{ kcal/mol } H_2.$ (5)



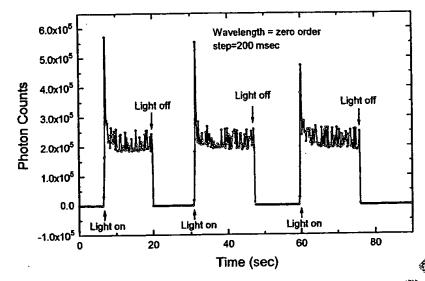


Fig. 9. The response time of the photomultiplier tested by switching off the room lights and recording the zero order as affunction of time.

The reaction absorbs 2.5 eV/hydrogen atom. The reduction of KNO₃ to water, potassium metal, and NH₃ calculated from the heats of formation only releases 0.3 eV/hydrogen atom.

$$9/2H_2 + KNO_3 \rightarrow K + 3H_2O + NH_3,$$

 $\Delta H = -14.2 \text{ kcal/mol H}_2.$ (6)

The most energetic reaction possible was the reaction of hydrogen to form water which releases 1.48 eV per atom of hydrogen; whereas, the energy of Lyman emission is greater than 10.2 eV/atom.

The dissociator was present in all experiments. The extin sion was not observed with the cell alone, with hydra helium, neon, or argon alone, or under identical conditions wherein a noncatalyst replaced a catalyst. power was interrupted, the emission decayed in about s. Decay was recorded over a time greater than the typical duration of a discharge plastin altergiow [36]. mission was occurring This experiment shows, that plasman even though the voltage between the water wires was set to and measured to be zero a direction which was cay time of the filament anomalous. Since the thermal for dissociation of molecular hydrogen to atomic hydrogen was similar to the animalous plasma afterglow duration which required the presence of a catalyst, the emission was determined to due to a reaction of catalyst with atomic hydrogen. hydrogen.

hydrogen.

In the present tudy, the filament leads were covered by a alchima sheath which differed from the set up reported previous [7]. It was found in previous studies that a weak electric field was required in order for a resonance energy match to be achieved between an atom of hydrogen and a catalyst atom or ion such as a strontium atom [6,10]. A further goal of the present study was to determine the field

dependence of EUV emission and to demonstrate an anomalous afterglow within field present. In previous studies [7] the maximum field was about 10 V/cm between the leads with a dipole field along the length of the filament of about 1 V/cm in the present cell only the weak dipole field of 1 V/cmi was present until the power to the filament was switched off. In either case, the field was negligible relative to that which causes an electrical discharge. At the same progen pressure as that of the present studies, breakdown did not secur for an applied voltage of less than 3000 V of about 1000 V/cm across the leads with the filament disconnected. In this case, only an arc formed versus a plasma which filled the entire cell when a catalyst and atomic hydrogen from the filament were present. With the field minimized, only those catalysts with a net enthalpy of reaction of an integer multiple of the potential energy of atomic hydrogen ($m \times 27.2$ eV m = integer) to within 0.17 eV and involve only a single ionization form in the case of a catalyst ion produced EUV and visible emission as shown in Table 1. And, only those catalysts with a net enthalpy of reaction of an integer multiple of the potential energy of atomic hydrogen to within less than the thermal energies at $\approx 10^3 \text{ K}$ and involve only a single ionization in the case of a catalyst ion produced an anomalous plasma afterglow duration as shown in Table 1.

4.1. Catalysts

The emission must have been due to a novel chemical reaction between catalyst and atomic hydrogen. According to Mills [32], a catalytic system is provided by the ionization of t electrons from an atom or ion to a continuum energy level such that the sum of the ionization energies of the t electrons is approximately $m \times 27.2$ eV where m is an

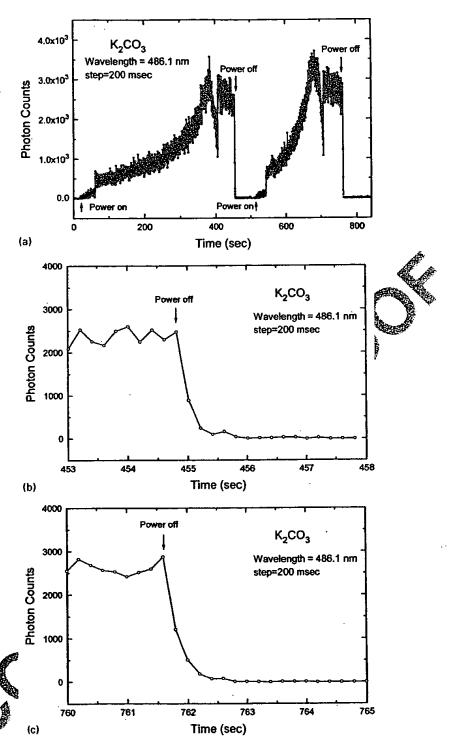


Fig. 11 (a) The emission of the 486.1 nm hydrogen Balmer β line as a function of time while the heater power was turned on and off. The gas belt comprised a tungsten filament, a titanium dissociator treated with 0.6 M K₂CO₃/10% H₂O₂ before being used in the cell, and 0.3 four hydrogen at a cell temperature of 700°C that was recorded at 200 ms intervals with a PMT. (b) The expanded region 453-458 s shown in Fig. 10(a) of the emission of the 486.1 nm hydrogen Balmer β line as a function of time showing the decay when the heater power was turned off. (c) The expanded region 760-765 s shown in Fig. 10(a) of the emission of the 486.1 nm hydrogen Balmer β line as a function of time showing the decay when the heater power was turned off.



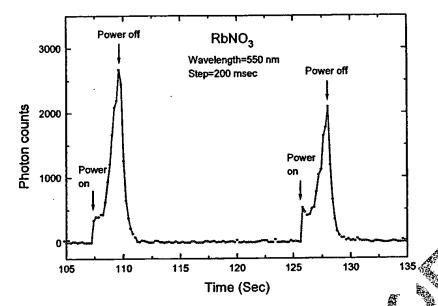


Fig. 11. The emission of the Rb 550.0 nm line as a function of time while the heater power was turned on and off. The gas cell comprised a tungsten filament, a titanium dissociator treated with 0.6 M RbNO₃/10% H₂O₂ before being used in the cell, and 0.3 Torr hydrogen at a cell temperature of 700°C that was recorded at 200 ms intervals with a PMT.

integer. A catalyst may also be provided by the transfer of t electrons between participating ions. The transfer of t electrons from one ion to another ion provides a net enthalpy of reaction whereby the sum of the ionization energy of the electron donating ion minus the ionization energy of the electron accepting ion equals approximately $m \times 27.2$ eV where t and m are each an integer.

4.2. Potassium metal

One such atomic catalytic system involves potassium metal. The first, second, and third ionization energies of potassium are 4.34066, 31.63, 45.806 eV respectively [39]. The triple ionization (t = 3) reaction of K to K^{3+} , then, has a net enthalpy of reaction of K, which is equivalent to m = 3 in Eq. (3).

81.7766 eV + K(m) + H
$$\begin{bmatrix} a_1 \\ b_2 \end{bmatrix}$$
 + $\begin{bmatrix} a_1 \\ b_2 \end{bmatrix}$ + $\begin{bmatrix} a_2 \\ b_1 \end{bmatrix}$ + $\begin{bmatrix} a_2 \\ b_2 \end{bmatrix}$ × 13.6 eV, (7)

$$K^{3+} + 3e^- \rightarrow (m) + 81.7766 \text{ eV}.$$
 (8)

The overall Perficient

H
$$\left[\frac{a_{\rm H}}{(p+3)}\right]$$
 + $\left[(p+3)^2 - p^2\right] \times 13.6 \text{ eV}.$ (9)

The anomalous afterglow of potassium metal may be possible since the triple ionization (t=3) reaction of K-K²⁺ has a net enthalpy of reaction of 81.7766 eV, which is within

thermal energies of \$2 \times 2.22 eV. And, the potassium atom is neutral so that a counter-ion would not effect the vacuum ionization energies.

Also, the antimalous afterglow of potassium metal may be dile to catalysis by potassium ions which provide an net centhality of reaction of 27.28 eV which is essentially resonant with the 27.2 eV from atomic hydrogen. Strong K⁺ emission was observed in the EUV spectrum.

Also, the identification of the predicted product of catalysis by potassium ions as well as by potassium metal [18] when only potassium metal was supplied as the catalyst provides support for the catalyst by potassium ions as the basis of the anomalous afterglow when potassium metal is supplied.

4.3. Potassium carbonate and potassium nitrate

Potassium ions can also provide a net enthalpy of a multiple of that of the potential energy of the hydrogen atom. The second ionization energy of potassium is 31.63 eV; and K^+ releases 4.34 eV when it is reduced to K. The combination of reactions K^+ to K^{2+} and K^+ to K, then, has a net enthalpy of reaction of 27.28 eV, which is equivalent to m = 1 in Eq. (3).

27.28 eV + K⁺ + K⁺ + H
$$\left[\frac{a_{\rm H}}{p}\right] \rightarrow$$
 K + K²⁺
+H $\left[\frac{a_{\rm H}}{(p+1)}\right]$ + $[(p+1)^2 - p^2] \times 13.6$ eV, (10)

(11)

 $K + K^{2+} \rightarrow K^{+} + K^{+} + 27.28 \text{ eV}.$



Table 1
Observation of EUV and visible emission and anomalous afterglow duration recorded on a hydrogen or alkali line from an incandescently heated gas mixture of hydrogen and an alkali metal, alkali carbonate, or alkali nitrate

Sample	EUV emission	Visible emission	Anomalous afterglow Lines (nm)
Li ₂ CO ₃	No	No	No
LiNO ₃	No	No	No
Na(m)	No	No	No
Na ₂ CO ₃	No	No	No
NaNO ₃	No	No	No
K(m)	Yes	Yes	Yes
rz(III)	2 60		K line
			536.1
r. co.	Yes	Yes	Yes
K₂CO₃	100		Balmer B
			486.1
KNO ₃	Yes	Yes	Ŋg₂
Rb(m)	Yes	Yes	√Y es,s
(U(III)			Rb lines
			420-6
			544.8
Rb ₂ CO ₃	Yes	Yes	, Ño
RbNO ₃	Yes	Yes	Yes
KUNO3	163		Rb line
			550.0
C=()	Yes	Yes Yes	Yes
Cs(m)	165		Cs line
			456.3
Cs ₂ CO ₃	Yes	Yes	No
Cs2CO3 CsNO3	Yes	Yes	Yes
CSNO3	1 60		Cs lines
			672.0
			852.0

The overall reaction is

$$H\left[\frac{a_H}{p}\right] \to H\left[\frac{a_H}{(p+1)}\right] + [(p+1)^2 - p^2] \times 16.6 \text{ eV}$$

An anomalous afterglow duration was observed in K_2CO_3 but not KNO₃ which indicates that the Talysis reaction given by Eqs. (10)–(12) is favored with K_2CO_3 which provides two potassium ions in the sange she file all environment. The EUV spectrum (40–160 int) of the cell emission for K_2CO_3 is shown in Fig. 4. Testable to K(m), K_2CO_3 , and KNO₃, K_2CO_3 produced the highest intensity EUV emission, and the anomalous afterglow duration of the Balmer β line which identified a plasma of hydrogen was present when the electric fields has zero shown in Figs. 10(A)–(C) was readily observable.

A.A. Rividium metal, rubidium carbonate, and rubidium ningge

Rubidium ions can also provide a net enthalpy of a multiple of that of the potential energy of the hydrogen atom. The second ionization energy of rubidium is 27.28 eV. The reaction Rb⁺ to Rb²⁺ has a net enthalpy of reaction of 27.28 eV, which is equivalent to m = 1 in Eq. (3).

27.28 eV + Rb⁺ + H
$$\left[\frac{a_{\rm H}}{p}\right]$$
 \to Rb²⁺ + e⁻

+H
$$\left[\frac{a_{\rm H}}{(p+1)}\right]$$
+ $[(p+1)^2-p^2]$ × 13.6 eV, (13)

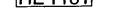
$$Rb^{2+} + e^- \rightarrow Rb^+ + 27.28 \text{ eV}.$$
 (14)

The overall reaction is

$$H\left[\frac{a_{\rm H}}{p}\right] \to H\left[\frac{a_{\rm H}}{(p+1)}\right] + [(p+1)^2 - p^2] \times 13.6 \text{ eV}.$$
(15)

The catalytic rate and corresponding intensity of EUV emission as well as the anomalous afterglow duration probably depends on the concentration of gas phase Rb⁺ ions. Rubidium metal may form RbH which may provide gas phase Rb⁺ ions, or rubidium metal may be ionized to provide gas phase Rb⁺ ions. EUV emission was observed from Rb₂CO₃





which may function as a catalyst. But, an anomalous afterglow duration was not observed possibly because two rubidium ions are present rather than one, and Rb₂CO₃ has a low volatility. In his case, gaseous rubidium from decomposition may be the main source. Rb⁺ ion emission was observed in the visible spectrum of rubidium metal and Rb₂CO₃.

Alkali metal nitrates are extraordinarily volatile and can be distilled at 350–500°C [40]. RbNO₃ is the favored candidate for providing gaseous Rb⁺ ions. The EUV spectrum (40–160 nm) of the cell emission for RbNO₃ is shown in Fig. 5. Relative to Rb(m), Rb₂CO₃, and RbNO₃, RbNO₃ produced the highest intensity EUV emission, and the anomalous afterglow duration shown in Fig. 11 was readily observable.

4.5. Cesium metal, cesium carbonate, and cesium nitrate

A catalytic system is provided by the ionization of two electrons from a cesium atom each to a continuum energy level such that the sum of the ionization energies of the two electrons is approximately 27.2 eV. The first and second ionization energies of cesium are 3.89390 and 23.15745 eV, respectively [39]. The double ionization reaction of Cs to Cs^{2+} , then, has a net enthalpy of reaction of 27.05135 eV, which is equivalent to m = 1 in Eq. (3).

27.05135 eV + Cs(m) + H
$$\left[\frac{a_{\rm H}}{p}\right] \rightarrow \text{Cs}^{2+} + 2e^{-}$$

+H $\left[\frac{a_{\rm H}}{(p+1)}\right]$ + $[(p+1)^2 - p^2] \times 13.6$ eV, (16)

$$Cs^{2+} + 2e^{-} \rightarrow Cs(m) + 27.05135 \text{ eV}.$$

The overall reaction is

$$H\left[\frac{a_H}{p}\right] \to H\left[\frac{a_H}{(p+1)}\right] + [(p+1)^2 - p^2] \times 2.6 \text{ eV}$$

The anomalous afterglow of cesium petin mather possible since the double ionization reaction of 2×10^{-2} has a net enthalpy of reaction of $2 \times 27.5 \times 10^{-2}$ which is within thermal energies of $2 \times 27.5 \times 10^{-2}$ which is essum atom is neutral so that a counter-ion would not effect the vacuum ionization energies.

neutral so that a counter ion would not effect the vacuum ionization energies.

EUV emission was also observed for Cs₂CO₃, and CsNO₃. Cs₂CO₄ and CsNO₃ are not catalysts, but they may readily decompose to csium metal under atomic hydrogen at the cell operating emperature. An anomalous afterglow duration was also observed in the case of CsNO₃, but not in the case of Cs₂CO₃. The anomalous afterglow duration of the CsNO₃ gas cell was observed only at long wavelengths indicating that a weak anomalous plasma was present after the heater was turned off. This is consistent with the greater rate of CsNO₃ decomposition relative to Cs₂CO₃. Strong cesium atom emission was observed in the visible spectrum.

4.6. Lithium metal, lithium carbonate, and lithium nitrate

No EUV emission was observed in the case of LiNO₃, and Li₂CO₃ which do not provide a reaction with a net enthalpy of a multiple of the potential energy of atomic hydrogen. Li(m) may function as a catalyst. The catalytic system is provided by the ionization of two electrons from Li to a continuum energy level such that the sum of the ionization energies of the two electrons is approximately 3×27.2 eV. The first and second ionization energies of lithium are 5.39172 eV and 75.64018 eV, respectively [39]. The double ionization reaction of Li to Li²⁺, then, has a net enthalpy of reaction of 81.0319 eV, which is equivalent to m = 3 in Eq. (3).

81.0319 eV + Li + H
$$\left[\frac{a_{\rm H}}{p}\right] \rightarrow {\rm Li}^{2+} + 2{\rm e}^{-}$$

+ H $\left[\frac{a_{\rm H}}{(p+3)}\right]$ + $\left[(p+3)^2 - p^2\right] \times 2.6$ eV, (19)

$$Li^{2+} + 2e^- \rightarrow Li + 81.0349 \text{ eV}.$$
 (20)

The overall reaction is

$$H\left[\frac{a_H}{p}\right] \to H\left[\frac{a_H}{(p+3)}\right] + \left[(p+3)^2 - p^2\right] \times 13.6 \text{ eV}.$$
(21)

Li₂CO₂ and Li₁CO₃ are not catalysts, but they may decompose to lithium metal under atomic hydrogen at high temperature. Weak emission was observed previously with the decomposition of Li₂CO₃ and LiNO₃ to lithium metal [7]. Lithium metal did not form to a significant extent in the desent study which may explain the absence of emission. Also, the presence of a field of about 10 V/cm may be required in order for a plasma to form in these cases since the mismatch between 81.0319 and 3 × 27.2 eV is 0.57 eV. In the case that electrons are ionized to a continuum energy level, the presence of a low strength electric field alters the continuum energy levels. In the anomalous discharge of hydrogen due to the presence of lithium, the weak field may adjust the energy of ionizing lithium to match the energy of 3 × 27.2 eV to permit a novel reaction of atomic hydrogen.

4.7. Sodium metal, sodium carbonate, and sodium nitrate

No EUV emission was observed in the case of Na(m) which does not provide a reaction with a net enthalpy of a multiple of the potential energy of atomic hydrogen. Na⁺ may serve as a catalyst. The catalytic system is provided by the ionization of three electrons from Na⁺ to a continuum energy level such that the sum of the ionization energies of the three electrons is approximately 8×27.2 eV. The second, third, and fourth ionization energies of sodium are 47.2864, 71.6200, and 98.91 eV, respectively [39]. The triple ionization reaction of Na⁺ to Na⁴⁺, then, has a net

enthalpy of reaction of 217.8164 eV, which is equivalent to m = 8 in Eq. (3).

217.8164 eV + Na⁺ + H
$$\left[\frac{a_{\rm H}}{p}\right] \rightarrow \text{Na}^{4+} + 3\text{e}^{-}$$

+H $\left[\frac{a_{\rm H}}{(p+8)}\right]$ + $[(p+8)^2 - p^2] \times 13.6 \text{ eV},$ (22)

$$Na^{4+} + 3e^{-} \rightarrow Na^{+} + 217.8164 \text{ eV}.$$
 (23)

The overall reaction is

$$H\left[\frac{a_H}{p}\right] \to H\left[\frac{a_H}{(p+8)}\right] + [(p+8)^2 - p^2] \times 13.6 \text{ eV}.$$
 (24)

No emission was observed from Na₂CO₃ which may not function as a catalyst because two sodium ions are present rather than one, and Na₂CO₃ is not volatile. NaNO₃ may function as a catalyst. However, no emission was observed with NaNO₃ which may have to be volatized in order to be functional as a catalyst. Of all the alkali nitrates, NaNO₃ is the least volatile [40].

Alternatively, based on the previously observed emission from NaNO₃ [7], the presence of a field of about 10 V/cm may be required in order for a plasma to form since the mismatch between 217.8164 and 8 × 27.2 eV is 0.22 eV. In the anomalous discharge of hydrogen due to the presence of NaNO₃, the weak field may adjust the energy of ionizing Na⁺ to Na⁴⁺ to match the energy of 8 × 27.2 eV to permit a novel reaction of atomic hydrogen.

Another possible explanation for the field dependence of the emission of NaNO₃ versus RbNO₃ is that the counter ion of the former influences the vacuum ionization energies to a significant extent. Thus, the counter ion may more sustantially alter the enthalpy of the triple ionization reaction of Na⁺ to Na⁴⁺, especially given the large enthalp of this reaction.

5. Conclusions

A plasma of hydrogen and certain all hiors was generated as recorded via EUV spectroscopy and hydrogen Balmer and alkali line emissions hathe visible range. The plasma formed at low temperatures (e.g. $\approx 10^3$ K) from atomic hydrogen and catalest comprising one of potassium, rubidium, cesium, and hier carbonates and nitrates. These atoms and formed to provide a catalyst with a net enthalpy of fraction of an integer multiple of the potential energy of atomic hydrogen ($m \times 27.2$ eV m = integer) to within the last way and comprise only a single ionization in the case of a potassium or rubidium ion. Whereas, the chemically similar atoms of sodium and sodium and lithium carbonates and nitrates which do not ionize with these constraints caused no emission. EUV radiation from hydrogen and alkali lines emitted by the cell loaded with catalyst and operated in hydrogen requires a minimum temperature and

atomic hydrogen produced by dissociation of molecular hydrogen by the hot filament. The heat from the filament and possibly the weak dipole field from the filament may sustain the hydrogen plasma, but it is not essential because in some cases, hydrogen lines or alkali lines were emitted during times when this voltage was set to zero. An anomalous afterglow duration of about 1-2 s was recorded in the case of potassium, rubidium, cesium, K2CO3, RbNO3, and CsNO3. These atoms and ions ionize to provide a catalyst with a net enthalpy of reaction of an integer multiple of the potential energy of atomic hydrogen to within less than the thermal energies at $\approx 10^3$ K and involve only a single ionization in the case of a potassium or rubidium ion. An electric field of about 10 V/cm may be required in order for NaNO3 to be catalytic. No unusual behavior was observed with the each control noncatalyst.

The release of energy from hydrogen has evidenced by the hydrogen Lyman and Balmer emission and alkali line emission which identifies the presence of a plasma. The persistence of emission following the removal of all of the power to the cell indicates that novel chemical power source is present.

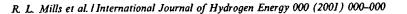
Reports of the formation of povel compounds provide

substantial evidence supporting a novel reaction of hydrogen as the mechanism of the observed EUV emission, anomalous discharge, and anomalous afterglow duration. Novel hydrogen compounds have been isolated as products of the reaction of atomic hydrogen with atoms and ions identified as catalysts in the reported EUV studies [6 31]. Novel inorganic alkali and alkaline earth hydrides of the formula MH* and MH*X wherein M is the metal, X, is a singly negatively charged anion, and H* comprises a hover high binding energy hydride ion were synthesized if a high temperature gas cell by reaction of atomic hydrogen with a catalyst such as potassium metal and MH, MX or MX₂ corresponding to an alkali metal or alkaline earth metal compound, respectively [18,21,31]. Novel hydride compounds were identified by (1) time of flight secondary ion mass spectroscopy which showed a dominate hydride ion in the negative ion spectrum, (2) X-ray photoelectron spectroscopy which showed novel hydride peaks and significant shifts of the core levels of the primary elements bound to the novel hydride ions, (3) proton nuclear magnetic resonance spectroscopy (NMR) which showed extraordinary upfield chemical shifts compared to the NMR of the corresponding ordinary hydrides, and (4) thermal decomposition with analysis by gas chromatography, and mass spectroscopy which identified the compounds as hydrides. The implications are that a vast new energy source and a new field of hydrogen chemistry have been discovered.

Acknowledgements

Special thanks to Bala Dhandapani and Jiliang He for reviewing this manuscript.





References

- [1] Phillips JH. Guide to the sun. Cambridge, Great Britain: Cambridge University Press, 1992. p. 16-20.
- [2] Sampson JAR. Techniques of vacuum ultraviolet spectroscopy. Pied Publications, 1980. p. 94-179.
- [3] Science News. 12/6/97. p. 366.
- [4] Fujimoto T, Sawada K, Takahata K. J Appl Phys 1989:66(6):2315-9.
- [5] Hollander A, Wertheimer MR. J Vac Sci Technol A 1994;12(3):879-82.
- [6] Mills R, Nansteel M, Lu Y. Anomalous hydrogen/strontium discharge. European J Phys D, submitted for publication.
- [7] Mills R, Dong J, Lu Y. Observation of extreme ultraviolet hydrogen emission from incandescently heated hydrogen gas with certain catalysts. Int J Hydrogen Energy 2000;25: 919-43.
- [8] Mills R. Observation of extreme ultraviolet emission from hydrogen-KI plasmas produced by a hollow cathode discharge. Int J Hydrogen Energy, in press.
- [9] Mills R. Temporal behavior of light-emission in the visible spectral range from a Ti-K2CO3-H-cell. Int J Hydrogen Energy, in press.
- [10] Mills R, Nansteel M, Lu Y. Observation of extreme ultraviolet hydrogen emission from incandescently heated hydrogen gas with strontium that produced an anomalous optically measured power balance. Int J Hydrogen Energy, in press.
- [11] Mills R, Dong J, Lu Y, Conrads J. Observation of extreme ultraviolet hydrogen emission from incandescently heated hydrogen gas with certain catalysts. 1999 Pacific Conference on Chemistry and Spectroscopy and the 35th ACS Western Regional Meeting, Ontario Convention Center, CA, October 6-8, 1999.
- [12] Mills R, Dong J, Greenig N, Lu Y. Observation of extreme ultraviolet hydrogen emission from incandescently heated hydrogen gas with certain catalysts. National Hydroge Association, 11th Annual US Hydrogen Meeting, Vienna February 29-March 2, 2000.
- [13] Mills R, Dhandapani B, Greenig N, He J, Dong J, Lu Conrads H. Formation of an energetic plasma hydrides from incandescently heated hydrogen certain catalysts. National Hydrogen Association 11th Annual US Hydrogen Meeting, Vienna, VA Pebruary 2000.
- [14] Mills R, Dong J, Greenig N, Lu Y Observation of extreme ultraviolet hydrogen emission from meandescently heated
- hydrogen gas with certain sates. 219th National ACS Meeting, San Francisco SA, March 26-30, 2000.

 [15] Mills R, Dhandapan B, Otenni N, He J, Dong J, Lu Y, Conrads H. Formation of an energetic plasma and novel hydrides from meaning entity heated hydrogen gas with certain catalogue. 219th National ACS Meeting, San Francisco, CA, Match 26, 30, 2600.

 [16] Mills R. Dhandapani B, Greenig N, He J, Dong J, Lu Y,
- Confairs II. Formation of an energetic plasma and novel hydrides from incandescently heated hydrogen gas with certain catalysts. June ACS Meeting, 29th Northeast Regional Meeting, University of Connecticut, Storrs, CT, June 18-21,
- [17] Mills R, Dhandapani B, Greenig N, He J, Dong J, Lu Y. Conrads H. Formation of an energetic plasma and

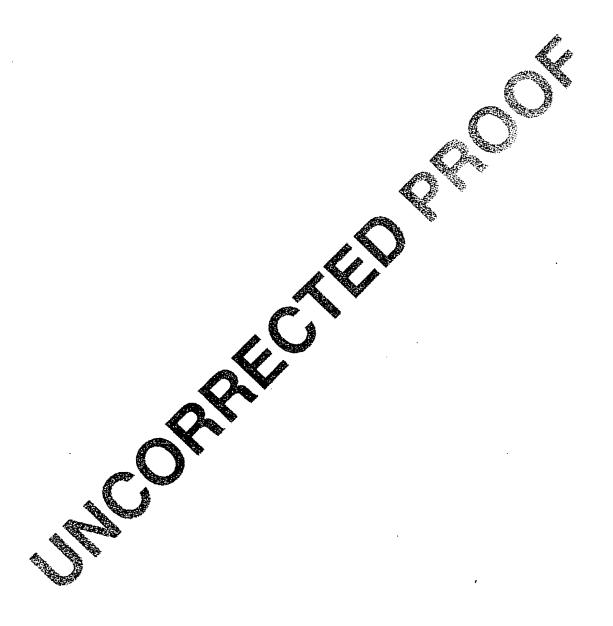
- novel hydrides from incandescently heated hydrogen gas with certain catalysts. August National ACS Meeting, 220th ACS National Meeting, Washington, DC, August 20-24, 2000.
- [18] Mills R, Dhandapani B, Greenig N, He J. Synthesis and characterization of potassium iodo hydride. Int J Hydrogen Energy 2000;25(12):1185-203.
- [19] Mills R. Novel inorganic hydride. Int J Hydrogen Energy 2000;25:669-83.
- [20] Mills R. Novel hydrogen compounds from a potassium carbonate electrolytic cell. Fusion Technol 2000;37(2): 157-82.
- [21] Mills R, Dhandapani B, Nansteel M, He J, Shannon T. Echezuria A. Synthesis and characterization of novel hydride compounds. Int J Hydrogen Energy, in press.
- [22] Mills R. Highly stable novel inorganic hydrides. J Mater Res, submitted for publication.
- [23] Mills R. Novel hydride compound. 1999 Pacific Conference on Chemistry and Spectroscopy and 15 35th ACS Western Regional Meeting, Ontario Convention Center, CA, October
- 6-8, 1999. [24] Mills R, Dhandapani B, Greenig N. He J. Synthesis and characterization of potassium jodo Bydride. 1999 Pacific Conference on Chemistry and Specific Scopy and the 35th ACS Western Regional Meeting, Onlario Convention Center, CA, October 6-8, 1999.

 [25] Mills R, He J, Dhahdapani B. Novel hydrogen compounds.
- 1999 Pacific Conference on Chemistry and Spectroscopy and the 35th ACS Western Regional Meeting, Ontario Convention Center, CA October 6-8, 1999.
- [26] Mills R. Jovel hydride compound. National Hydrogen American, 11th Annual US Hydrogen Meeting, Vienna, VA, February 29-March 2, 2000.
- [27]MillsR, He J, Dhandapani B. Novel alkali and alkaline earth hydrides. National Hydrogen Association, 11th Annual US Hydrogen Meeting, Vienna, VA, February 29-March 2, 2000. Mills R. Novel hydride compound. 219th National ACS Meeting, San Francisco, CA, March 26-30, 2000.
- [29] Mills R, He J, Dhandapani B. Novel alkali and alkaline earth hydrides. 219th National ACS Meeting, San Francisco, CA, March 26-30, 2000.
- [30] Mills R, He J, Dhandapani B. Novel alkali and alkaline earth hydrides. August National ACS Meeting, 220th ACS National Meeting, Washington, DC, August 20-24, 2000.
- [31] Mills R, Dhandapani B, Nansteel M, He J, Voigt A. Identification of compounds containing novel hydride ions by nuclear magnetic resonance spectroscopy. Int J Hydrogen Energy, submitted for publication.
- [32] Mills R. The grand unified theory of classical quantum mechanics, January 2000 ed. Cranbury, NJ: BlackLight Power, Inc. Distributed by Amazon.com.
- [33] Sidgwick NV. The chemical elements and their compounds, vol. I. Oxford: Clarendon Press, 1950. p. 17.
- [34] Lamb MD. Luminescence spectroscopy. London: Academic Press, 1978. p. 68.
- [35] Mills R. The nature of free electrons in superfluid heliuma test of quantum mechanics and a basis to review its foundations and make a comparison to classical theory. Int J Hydrogen Energy, submitted for publication.
- [36] Surmeian A, Diplasu C, Collins CB, Musa G, I-lovittz Popescu. J Phys D 1997;30:1755-8.



14

- [37] Bauer T, Gortchakov S, Loffhagen D, Pfau S, Winkler R. J Phys D 1997;30:3223-39.
- [38] Muller WM, Blackledge JP, Libowitz GG. Metal hydrides. New York: Academic Press, 1968. p. 201.
- [39] Linde DR. CRC handbook of chemistry and physics, 79th ed. Boca Raton, FL: CRC Press, 1998-9. p. 10-175-10-177.
- [40] Hardy CJ, Field BO. J Chem Soc 1963;5130-4.









HYDROGEN ENERGY

International Journal of Hydrogen Energy 000 (2000) 000-000

www.elsevier.com/locate/ijhydene

Observation of extreme ultraviolet hydrogen emission from incandescently heated hydrogen gas with strontium that produced an anomalous optically measured power balance

Randell L. Mills*, Mark Nansteel, Ying Lu

BlackLight Power, Inc., 493 Old Trenton Road, Cranbury, NJ 08512, USA

Abstract

We report the observation of intense extreme ultraviolet (EUV) emission from incandescriptly he ded atomic hydrogen and atomized strontium. It has been reported that intense EUV emission was observed at the temperatures (e.g. $\approx 10^3$ K) from atomic hydrogen and certain atomized elements or certain gaseous ions which ionize at integer multiples of the potential energy of atomic hydrogen, 27.2 eV [1-5]. Strontium ionizes at integer multiples of the potential energy of atomic hydrogen, 27.2 eV [1-5]. Strontium ionizes at integer multiples of the potential energy of atomic hydrogen, a high-power inductively coupled plasma, or a plasma created and heated to extreme temperatures by RF coupling (e.g. $> 10^6$ K) with confinement provided by a toroidal magnetic field. The observed plasma formed a low temperatures (e.g. $\approx 10^3$ K) from atomic hydrogen generated at a tangsten filament that heated a titanian dissociator and atomic strontium which was vaporized from the metal by heating. No emission was observed when solium magnesium, or barium replaced strontium or with hydrogen or strontium alone. The power balance of a gas cell having atomized hydrogen and strontium was measured by integrating the total light output corrected for spectrometer years results results and energy over the visible range. A control cell was identical except that sodium replaced strontium. In the case, 450 times the power of the strontium cell was required in order to achieve that same optically measured light output power. A plasma formed at a cell voltage of about 250 V in the cell with hydrogen alone and in the cell with hydrogen and sodium; whereas, a plasma formed in the strontium cell at the extremely low voltage of about 2 V. © 2000 laterational Association for Hydrogen Energy. Published by Elsevier Science Ltd. All rights reserved.

1. Introduction

A historical motivation to pane EUV emission from a hydrogen gas was that the spectrum of hydrogen was first recorded from the anown source, the Sun [6]. Developed sources that provide a suitable intensity are high-voltage listinger synchrotron, and inductively coupled plass to see a tors [7]. An important variant of the later type of source is a tokomak [8]. Fujimoto et al. [9] have

*Consequenting author. Tel.: +1-609-490-1040; fax:

E-mail address: rmills@blacklightpower.com (R.L. Mills).

determined the cross section for the production of excited hydrogen atoms from the emission cross sections for Lyman and Balmer lines when molecular hydrogen is dissociated into excited atoms by electron collisions. These data were used to develop a collisional-radiative model to be used in determining the ratio of molecular-to-atomic hydrogen densities in tokomak plasmas. Their results indicate an excitation threshold of 17 eV for Lyman α emission. Addition of other gases would be expected to decrease the intensity of hydrogen lines which could be absorbed by the gas. Hollander and Wertheimer [10] found that within a selected range of parameters of a plasma created in a microwave resonator cavity, a hydrogen-oxygen plasma displays an

emission that resembles the absorption of molecular oxygen. Whereas, a helium-hydrogen plasma emits a very intense hydrogen Lyman α radiation at 121.5 nm which is up to 40 times more intense than other lines in the spectrum. The Lyman α emission intensity showed a significant deviation from that predicted by the model of Fujimoto et al. [9] and from the emission of hydrogen alone.

We report that a hydrogen plasma is formed at low temperatures (e.g. $\approx 10^3$ K) by reaction of atomic hydrogen with strontium atoms, but not with magnesium, barium, or sodium atoms. In the case of EUV measurements, atomic hydrogen was generated by dissociation at a tungsten filament and at a transition metal dissociator that was incandescently heated by the filament. Strontium atoms were vaporized by heating to form a low vapor pressure (e.g. 1 torr). The kinetic energy of the thermal electrons at the experimental temperature of $\approx 10^3$ K were about 0.1 eV, and the average collisional energies of electrons accelerated by the field of the filament were less than 1 eV. (No blackbody emission was recorded for wavelengths shorter than 400 nm.) Strontium atoms ionize at integer multiples of the potential energy of atomic hydrogen and caused hydrogen EUV emission; whereas, the chemically similar atoms, magnesium and barium as well as sodium, caused no emission. Helium ions present in the experiment of Hollander and Wertheimer [10] ionize at a multiple of two times the potential energy of atomic hydrogen. The mechanism of EUV emission cannot be explained by the conventional chemistry of hydrogen, but it is predicted by a solution of the Schrodinger equation with a nonradiative boundary constraint put forward by Mills [11].

Mills predicts that certain atoms or ions serve as catalysts to release energy from hydrogen to produce an increased binding energy hydrogen atom called a *hydrino atom* having a binding energy of

Binding energy =
$$\frac{13.6 \text{ eV}}{n^2}$$
, (1)

where

$$n = \frac{1}{2}, \frac{1}{3}, \frac{1}{4}, \dots, \frac{1}{p}$$
 (2)

and p is an integer greater than 1, designate as $H[a_H/p]$ where a_H is the radius of the hydresen arm. Hydrinos are predicted to form by reacting an additional hydrogen atom with a catalyst having a present harm of reaction of about

$$m \cdot 27.2 \text{ eV},$$
 (3)

where m is an integer. This catalysis releases energy from the hydrogen atom with a commensurate decrease in size of the hydrogen atom, $\frac{1}{n} = na_{\rm H}$. For example, the catalysis of H(n=1) in $\frac{1}{n}$ releases 40.8 eV, and the hydrogen radius extrems from $a_{\rm H}$ to $\frac{1}{2}a_{\rm H}$.

the extred energy states of atomic hydrogen are also given by Eq. (1) except that

$$n=1,2,3,\ldots (4)$$

The n = 1 state is the "ground" state for "pure" photon transitions (the n=1 state can absorb a photon and go to an excited electronic state, but it cannot release a photon and go to a lower-energy electronic state). However, an electron transition from the ground state to a lower-energy state is possible by a nonradiative energy transfer such as multipole coupling or a resonant collision mechanism. These lower-energy states have fractional quantum numbers, n = 1/integer. Processes that occur without photons and that require collisions are common. For example, the exothermic chemical reaction of H + H to form H₂ does not occur with the emission of a photon. Rather, the reaction requires a collision with a third body, M, to remove the bond energy-H + H + M \rightarrow H₂ + M* [12]. The third body distributes the energy from the exothermic reaction, and the end result is the H₂ molecule and an increase in the temperature of the system. Some commercial phosphors are based on nomadiative energy transfer involving multipole coupling or xample, the strong absorption strength of Sb³⁺ join along with the efficient nonradiative transfer of excitation from Sb³⁺ to Mn^{2+} , are responsible for the strong manganese luminescence from phosphors containing the stons [13]. Similarly, the n=1 state of hydrogen and the n=1/integer states of hydrogen are nonrational but a transition between two nonradiative states is possible via a nonradiative energy transfer, say n = 1 is In these cases, during the transition the electron couples to another electron transition, electron transfer reaction or inelastic scattering reaction which can absorb the exact amount of energy that must be removed from the hydrogen atom. Thus, a catalyst provides a net positive eritalpy of reaction of $m \times 27.2$ eV (i.e. it absorbs $m \ge 2$ eV where m is an integer). Certain atoms or ions rve as catalysts which resonantly accept energy from warogen atoms and release the energy to the surroundings to effect electronic transitions to fractional quantum energy levels.

The catalysis of hydrogen involves the nonradiative transfer of energy from atomic hydrogen to a catalyst which may then release the transferred energy by radiative and nonradiative mechanisms. As a consequence of the nonradiative energy transfer, the hydrogen atom becomes unstable and emits further energy until it achieves a lower-energy nonradiative state having a principal energy level given by Eqs. (1) and (2).

1.1. Inorganic catalysts

A catalytic system is provided by the ionization of t electrons from an atom to a continuum energy level such that the sum of the ionization energies of the t electrons is approximately $m \times 27.2$ eV where m is an integer. One such catalytic system involves strontium. The first through the fifth ionization energies of strontium are 5.69484, 11.03013, 42.89, 57, and 71.6 eV, respectively [14]. The ionization reaction of Sr to Sr⁵⁺, (t = 5), then, has a net enthalpy of

reaction of 188.2 eV, which is equivalent to m=7 in Eq. (3).

188.2 eV + Sr(m) + H
$$\left[\frac{a_{\rm H}}{p}\right] \to \text{Sr}^{5+} + 5e^{-}$$

+H $\left[\frac{a_{\rm H}}{(p+7)}\right]$ + $[(p+7)^2 - p^2] \times 13.6$ eV, (5)

$$Sr^{5+} + 5e^{-} \rightarrow Sr(m) + 188.2 \text{ eV}.$$
 (6)

The overall reaction is

$$H\left[\frac{a_{\rm H}}{p}\right] \to H\left[\frac{a_{\rm H}}{(p+7)}\right] + \left[(p+7)^2 - p^2\right] \times 13.6 \text{ eV}. \tag{7}$$

The energy released during catalysis may undergo internal conversion and ionize or excite molecular and atomic hydrogen resulting in hydrogen emission which includes well-characterized ultraviolet lines such as the Lyman series. Lyman α emission was sought by EUV spectroscopy. Due to the extremely short wavelength of this radiation, "transparent" optics do not exist. Therefore, a windowless arrangement was used wherein the source was connected to the same vacuum vessel as the grating and detectors of the EUV spectrometer. Windowless EUV spectroscopy was performed with an extreme ultraviolet spectrometer that was mated with the cell. Differential pumping permitted a high pressure in the cell as compared to that in the spectrometer. This was achieved by pumping on the cell outlet and pumping on the grating side of the collimator that served as a pin-hole inlet to the optics. The cell was operated under hydrogen flow conditions while maintaining a constant hydrogen pressure in the cell with a mass flow controlled

The energy released during catalysis may also unerigo internal conversion and ionize or excite molecular an atomic hydrogen and the catalysts resulting in visibly emissional cylindrical nickel mesh hydrogen dissociated a gas cell also served as an electrode to produce a secondary and the wall of the cylindrical stainless steel gas and Power was applied to the electrode to achieve a bright plasts which was recorded over the wavelength range 350 \$\leq\$ 750 nm. The power balance of a gas cell having atomized hydrogen and strontium was measured by nucgrating the total light output corrected for spectrosteter system response and energy over the visible range. A deptrol cell was identical except that sodium replaced strontium to the case, 4000 times the power of the strontium cell will required in order to achieve the same optically the astrod light output power. A plasma formed at a cell voltage of about 250 V in the cell with hydrogen alone and the tell with hydrogen and sodium; whereas, a plasma formed if the strontium cell at the extremely low voltage of about 2 V.

2. Experimental

2.1. EUV spectroscopy

The experimental set up shown in Fig. 1 comprised a quartz cell which was 500 mm in length and 50 mm in diameter. A sample reservoir that was heated independently using an external heater powered by a constant power supply was on one end of the quartz cell. Three ports for gas inlet, outlet, and photon detection were on the other end of the cell. A tungsten filament (0.5 mm, total resistance \sim 2.5 Ω) and a titanium cylindrical screen (300 mm long and 40 mm in diameter) that performed as a hydrogen dissociator were inside the quartz cell. A new dissociator was used for each experiment. The filament was 0.508 millimeters in diameter and 800 cm in length. The filament was coiled on a grooved ceramic support to maintain its shape when heated. The return lead ran through the middle of the ramic support. The titanium screen was electrically floated. The power was applied to the filament by a Sorensen 80. It power supply which was controlled by a constant power entroller. The temperature of the tungsten filament was stimated to be in the range of 1100 to 1500° C. The hydrogen gas pressure inside the cell was maintained at a suit 400 mtorr with a hydrogen flow rate of 5.5 scent controlled by a MKS 1179A21CS1BB 20 sccm range mass flow controller with a MKS type 246 20 sccm range mass flow controller with a MKS type 246 readout. The entite quarte cell was enclosed inside an insulation package emprised of Zircar AL-30 insulation. Several K-type therm couples were placed in the insulation to me are key temperatures of the cell and insulation. The ber occurres were read with a multichannel computer data acquisitum system.

In the present study, the light emission phenomena was med for hydrogen, argon, neon, and helium alone; hydrogen with strontium, magnesium, barium, and sodium metals, and strontium alone. The pure elements of magnesium, barium, and strontium were placed in the reservoir and volatized by the external heater. Magnesium with a low vapor pressure (higher melting point) was volatilized by suspending a foil of the material (2 cm \times 2 cm \times 0.1 cm thick) between the filament and a titanium dissociator and heating the test material with the filament. The power applied to the filament was 300 W in the case of strontium and up to 600 W in the case of magnesium, barium, and sodium metals. The voltage across the filament was about 55 V and the current was about 5.5 A at 300 W. For the controls, magnesium, barium, and sodium metals, the cell was increased in temperature to the maximum permissible with the power supply.

The light emission was introduced to an EUV spectrometer for spectral measurement. The spectrometer was a McPherson 0.2 m monochromator (Model 302, Seya-Namioka type) equipped with a 1200 lines/mm holographic grating. The wavelength region covered by the monochromator was 30-560 nm. A channel electron multiplier (CEM) was used to detect the EUV light. The



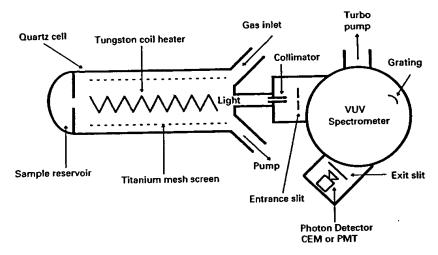


Fig. 1. The experimental set up comprising a gas cell light source and an EUV spectrometer which was differentially pumped.

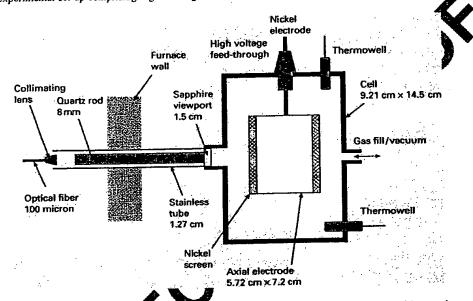


Fig. 2. Cylindrical stainless-steel gas cell plasma stotles with hydrogen alone, or with hydrogen with strontium or sodium.

wavelength resolution was about 12 im. HM) with an entrance and exit slit width of 300 365 im. The vacuum inside the monochromator was majurined below 5×10^{-4} torr by a turbo pump. The EUV pectrum (40–160 nm) of the cell emission with aronhum present was recorded at about the point of the maximum Lyman α emission.

The UV/VIS specifim (its 560 nm) of the cell emission with hydrogen alone we recorded with a photomultiplier tube (PMT) and a dism salicylate scintillator. The PMT (Model F 1872 Jamamatsu) used has a spectral response in the tangent [185–680 nm with a peak efficiency at about 400 nm. the sean interval was 0.4 nm. The inlet and outlet slift here 510–500 μm.

The V/VIS emission from the gas cell was channeled into the UV/VIS spectrometer using a 4 m long, five stand

fiber optic cable (Edmund Scientific Model #E2549) having a core diameter of 1958 µm and a maximum attenuation of 0.19 dB/m. The fiber optic cable was placed on the outside surface of the top of the Pyrex cap of the gas cell. The fiber was oriented to maximize the collection of light emitted from inside the cell. The room was made dark. The other end of the fiber optic cable was fixed in an aperture manifold that attached to the entrance aperture of the UV/VIS spectrometer.

2.2. Power cell apparatus and procedure

Plasma studies with hydrogen alone or hydrogen with strontium or sodium were carried out in the cylindrical stainless-steel gas cell shown in Fig. 2. The experimental





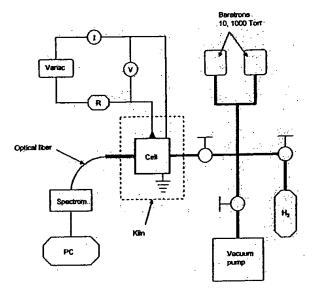


Fig. 3. The experimental setup for generating a glow discharge hydrogen plasma and for optically measuring the power balance.

setup for generating a glow discharge hydrogen plasma and for optically measuring the power balance is shown in Fig. 3. The cell was heated in a 10 kW refractory brick kiln (L & L Kiln Model JD230) as shown in Fig. 3. The kiln had three heating zones and a heated floor that were each heated by separate radiant elements. The zone temperatures were independently controlled by a Dynatrol controller using the temperatures read by 3 type-K thermocouples located adjacent to the kiln inner wall. The cell was evacuated and pressurized with hydrogen through a single 0.95 cm feed through. The discharge was started and maintained by alternating current electric field in the 1.75 cm annular between an axial electrode and the cell wall. The cylindrical cell was 9.21 cm in diameter and 14.5 cm in height. electrode was a 5.08 cm OD by 7.2 cm long tube wound with several layers of nickel set all diameter of the axial electrode w 1.6 mm thick UV-grade sapphire and view diameter provided a visible part path from inside the cell. The viewing direction was noticed to the cell axis. A 1.27 cm diameter stainless stee the passed through the w port welded to the furnace wall and connected to a cell wall at mid-height to provide an optical light path from the sapphir window the furnace exterior. An 8 mm quartz rod channed the light from the view port through the sample tube to a collimating lens which was focus 100 μm optical fiber located outside the furnace Spectral data were recorded with a visible spectrometer Ocean Optics S2000) and stored by a personal comp

The field voltage was controlled by a variable voltage transformer operating from 115 VAC, 60 Hz. A step-up

transformer was used when necessary. True rms voltage at the axial electrode was monitored by a digital multimeter (Fluke 8010 A or Tenma 726202). A second multimeter (Extech 380763) in series with the discharge gap was used to indicate the current. The cell temperature was measured by a thermocouple probe located in the cell interior approximately 2 cm from the discharge gap. The pressure in the hydrogen supply tube outside the furnace was monitored by 10 and 1000 torr MKS Baratron absolute pressure gauges. In the absence of hydrogen flow, the hydrogen supply tube pressure was essentially the cell hydrogen partial pressure.

Strontium (Aldrich Chemical Company 99.9%) or sodium (Aldrich Chemical Company 99.95%) metals were loaded into the cell under a dry argon atmosphere. The cell was evacuated with a turbo vacuum pump to a pressure of 4 mtorr during most of the heating process. During the heat-up the cell was periodically pressurized with hydrogen top and subse-(99.999% purity) to approximately 1455 quently evacuated to purge gaseous containants from the system. When the cell temperature stabilized hydrogen was added until the steady pressure as approximately 1 torr. The field voltage was increase unit reakdown occurred the ectrometer response to which was confirmed by The hydrogen pressure visible light emitted from the cal. The hydrogen pressure was adjusted as much a possible to maximize the light emission from the cal. The voltage was maintained at the minimum level which resulted in a stable discharge during data acquisition

Glow discharge were formed in pure control gases to determine their behavior as function of temperature and pressure for H6, N2, and H2 gases, the starting voltage to form a glow discharge, the voltage to maintain the discharge, and the light emitted were studied as a function of pressure at a mid 662°C. The discharged was formed in the cylindrical stainless-steel gas cell used for plasma studies with hydrogen alone, or with hydrogen with strontium or sodium as shown in Fig. 2. The experimental setup was identical to that used for generating a glow discharge hydrogen plasma and for optically measuring the power balance as shown in Fig. 3. The methods for forming a glow discharge and the procedure for measuring the voltage and current were as given previously. The presence or absence of light emission was observed visually.

After thorough evacuation, the cell was filled to the desired pressure with test gas. The electrode voltage was gradually increased until a rush of current (at least 3 mA) was observed in the circuit. The greatest voltage for which no current flowed was recorded as the starting voltage V_s . Once a discharge was present, the electrode voltage was slowly decreased until the current abruptly fell to zero. The lowest voltage for which current persisted was recorded as the maintenance voltage. Light emission from the discharge, if present, was noted. The results are given in the appendix.

R.L. Mills et al. International Journal of Hydrogen Energy 000 (2000) 000-000

Table 1 Reference source calibration data for Ocean Optics S2000 Spectrometer

λ (nm)	G _{λr} (μW/cm² nm)	λ (nm)	G _{λr} (μW/cm ² nm)	λ (nm)	G _{λr} (μW/cm ² nm)
300	0.0036	400	0.0194	650	0.502
	0.0023	420	0.031	700	0.697
310	0.0020	440	0.046	750	0.969
320	0.0021	460	0.065	800	1.344
330	0.0021	480	0.090	850	1.914
340	0.0028	500	0.118	900	2.742
350	0.0057	525	0.162	950	3.798
360	0.0037	550	0.214	1000	4.973
370 380	0.0082	575	0.274	1050	6.110
390	0.0148	600	0.342	_	

2.3. Spectrometer calibration for optical power balance measurement

Only a small portion of the light emission from the source was incident upon the spectrometer CCD detector since irradiation of the detector was dependent upon optical losses between the source and detector. The light of a small solid angle (1) passed through the sapphire window, (2) entered the quartz rod, (3) was channeled from the view port through the stainless-steel tube to the collimating lens, (4) was focused on the 100 µm optical fiber, (5) was carried on the optical fiber, (6) entered the spectrometer, and (7) ultimately was incident on the CCD detector. Attenuation occurred at each interface and along each optical element. To standardize these factors for the emission of strontium vapor with hydrogen, the control experiments of hydro gen alone and sodium vapor with hydrogen were run u der identical conditions. Thus, these experiments served as standard light sources. However, the spectra of each iment was unique. The spectrometer system comp 100 μm optical fiber and the visible spectrometer Optics S2000). To correct for the nonuniform the spectrometer system as a function was the dependence of energy on wavelength ystem was calibrated against a reference light our

During the recording of each spectrum, The spectrometer integration time was adjusted a maximize its sensitivity as recommended by the riantic ctuar (Ocean Optics). The recorded intensity versus wavelength was a rate; thus, it recorded intensity versus was independent of the maration time. And, all spectra were comparablesince they were acquired such that the

spectrometer was the rating in a linear response range.

The spectrometer system G_1 (energy time area-wavelength) was the rate at which energy in the wavelength interval $\lambda - \lambda + d\lambda$ was incident on c entrance of the spectrometer system per unit area are per unit wavelength interval dl. The corresponding spectrometer response or count rate S_{λ} (counts/s) was

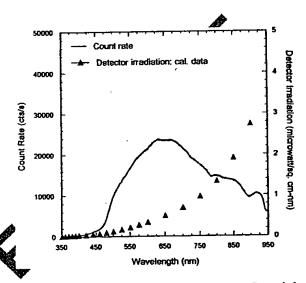


Fig. 4. The plot of the reference source count rate $S_{\lambda r}$ and the calibration data Ga.

proportional to spectrometer system irradiation,

$$S_{\lambda} = b_{\lambda} G_{\lambda}. \tag{8}$$

The spectral dependence of the proportionality factor b_{λ} arises from spectral bias of the spectrometer system. The radiant flux input to the spectrometer system was obtained by calibration with a reference light source (Ocean Optics LS-1-CAL) for which the radiant flux was known. The distribution of the spectrometer system irradiation by the reference light source $G_{lr}(\lambda)$ was supplied in tabular form by Ocean Optics as given in Table 1. The count rate due to irradiation by the reference source was

$$S_{k} = b_{\lambda} G_{k}, \tag{9}$$

where G_{kr} is the spectrometer system irradiation by the reference light source. Then the spectrometer system

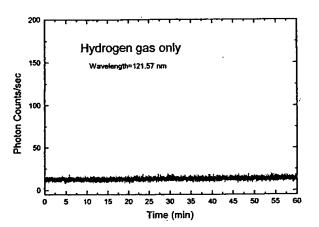


Fig. 5. The intensity of the Lyman α emission as a function of time from the gas cell at a cell temperature of 700° C comprising a tungsten filament, a titanium dissociator, and 300 mtorr hydrogen with a flow rate of 5.5 sccm.

irradiation by the source under study was given by

$$G_{\lambda} = S_{\lambda} \frac{G_{\lambda t}}{S_{\lambda t}}.$$
 (10)

The ratio

$$\frac{G_{b}}{S_{br}} = \left[\frac{\mu W/cm^2 nm}{cts/s}\right]$$
 (11)

was the spectral calibration factor for the system. This calibration approach holds regardless of whether the count rate is proportional to radiant energy/time or photons/time. In the latter case the proportionality factor b_{λ} accounts for the spectral bias of the photons as well as the spectral bias of the spectrometer system (i.e. b_{λ} includes the factor $(h\nu)^{-1}$). The reference source count rate $S_{\lambda r}$ and the calibration data G_{kr} are plotted in Fig. 4. The spectral bias of the sys tem which favored mid-range wavelengths (550-750 and is clear. Manual calibration of the raw count rate demonas carried out using calibration Eq. (10) for the harogen strontium mixture and background radiation tests. Il maining cases, the calibration was done in Ocean Optics spectrometer software OOllina ible radiant flux incident on the spe given by

$$G = \int_{\lambda = 400 \text{ nm}}^{\lambda = 700 \text{ nm}} G_{\lambda}(\lambda) d\lambda, \tag{12}$$

where $G_{\lambda}(\lambda)$ is the spectral irradiation. G_{λ} , S_{λ} , and G were each a rate, thus, they were independent of the integration time.

3. Result

3. A EU Spectroscopy

The cell without any test material present was run to establish the baseline of the spectrometer. The intensity of the

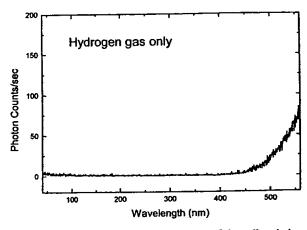


Fig. 6. The UV/VIS spectrum (40-560 nm) of the cell emission from the gas cell at a cell temperature of 700° C comprising a tungsten filament, a titanium dissociator, and 300 mtorr hydrogen with a flow rate of 5.5 sccm that was recorded with a photomultiplier tube (PMT) and a sodium salicylate scintiliant.

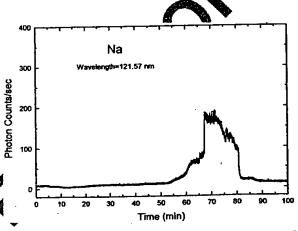


Fig. 7. The intensity of the Lyman α emission as a function of time from the gas cell at a cell temperature of 700° C comprising a tungsten filament, a titanium dissociator, sodium metal vaporized from the catalyst reservoir, and 300 mtorr bydrogen with a flow rate of 5.5 sccm.

Lyman α emission as a function of time from the gas cell at a cell temperature of 700°C comprising a tungsten filament, a titanium dissociator, and 300 mtorr hydrogen with a flow rate of 5.5 sccm is shown in Fig. 5. The UV/VIS spectrum (40–560 nm) of the emission from the gas cell at a cell temperature of 700°C comprising a tungsten filament, a titanium dissociator, and 300 mtorr hydrogen with a flow rate of 5.5 sccm is shown in Fig. 6. The spectrum was recorded with a photomultiplier tube (PMT) and a sodium salicylate scintillator. No emission was observed except for the blackbody filament radiation at the longer wavelengths. No emission was also observed when argon, neon, or helium replaced hydrogen.

The intensity of the Lyman α emission as a function of time from the gas cell at a cell temperature of 700° C com-

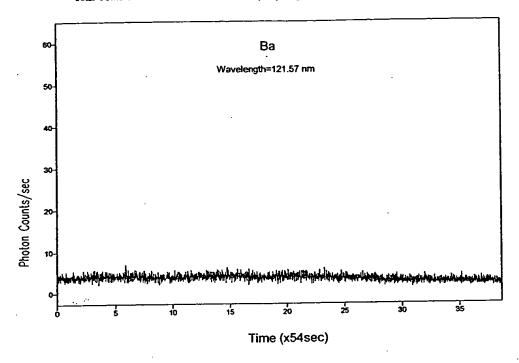


Fig. 8. The intensity of the Lyman α emission as a function of time from the gas cell at a cell emperature of 700°C comprising a tungsten filament, a titanium dissociator, barium metal vaporized from the catalyst reservoir, and 300 in a hydrogen with a flow rate of 5.5 secm.

prising a tungsten filament, a titanium dissociator, sodium or barium metal in the catalyst reservoir, and 300 mtorr hydrogen with a flow rate of 5.5 sccm are shown in Figs. 7 and 8, respectively. Sodium or barium metal was volatized from the catalyst reservoir by heating it with an external heater. No emission was observed in either case. The maximum filament power was over 500 W. A metal coating formed in the cap of the cell over the course of the aperiment in both cases.

The intensity of the Lyman a emission tion of time from the gas cell at a cell there erature of 700°C comprising a tungsten filament sociator, a magnesium foil in the l. mtorr hydrogen metal in the catalyst reservoir, win Figs. 9 and with a flow rate of 5.5 sccm 10, respectively. The magnesian for was volatilized by 0. In thick foil between suspending a 2 cm × 2 the filament and the tilinium issociator and heating the foil with the filater. inssion was observed with the magnesium oil and hydrogen. The maximum filament power was \$00 W. The temperature of the foil increased with lament power. At 500 W, the temper-V. The temperature of the foil the foil was 1000°C which would correspond to of about 100 mtorr. Strontium metal was ed ism the catalyst reservoir by heating it with an external scater. Strong emission was observed from strontium and hydrogen. The EUV spectrum (40-160 nm) of

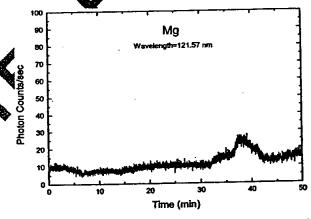


Fig. 9. The intensity of the Lyman α emission as a function of time from the gas cell at a cell temperature of 700° C comprising a tungsten filament, a titanium dissociator, a magnesium foil, and 300 mtorr hydrogen with a flow rate of 5.5 secm.

the cell emission recorded at about the point of the maximum Lyman α emission is shown in Fig. 11. No emission was observed when hydrogen was stopped. A metal coating formed in the cap of the cell over the course of the experiment in the case of magnesium and strontium.

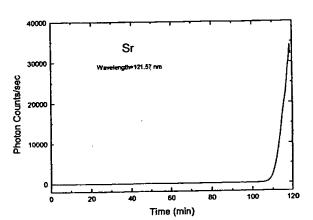


Fig. 10. The intensity of the Lyman α emission as a function of time from the gas cell at a cell temperature of 700° C comprising a tungsten filament, a titanium dissociator, strontium metal vaporized from the catalyst reservoir, and 300 mtorr hydrogen with a flow rate of 5.5 sccm.

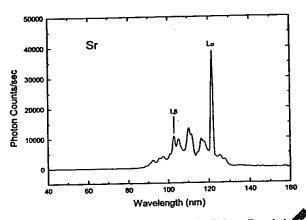


Fig. 11. The EUV spectrum (40–160 nm) of the cell emission recorded at about the point of the maximum Lyman α emission from the gas cell at a cell temperature of 700° C comparation to compare the catalyst reservoir, and 300 mtor hydrogen with a flow rate of 5.5 sccm.

3.2. Optically measured power balance

Count rate and spectrometer system infadiation of the background spectrum of hydrogen and strontium vapor over the wavelength range 35 \leq 00 nm in the absence of power applied to the electrode and in the absence of a discharge is shown in 12. The edata were collected during cell evacuation following the test with strontium and hydrogen at a cell tapp atta of 664° C. The maximum visible irradiation of 9.1° μ W/cm² nm occurred at the red end of the visible pectrum. The total visible radiant flux incident on the spectrometer system over the visible range 400 \leq λ 100 km was given by Eq. (12). The integral was approximated by rectangles with panel width $\Delta\lambda = 0.342$ nm. The results are summarized in Table 2 where T is the tem-

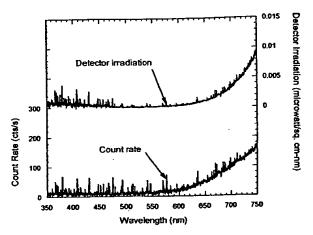


Fig. 12. Count rate and spectrometer system irradiation of the background spectrum of hydrogen and strontium vapor over the wavelength range $350 \le \lambda \le 750$ nm in the absence of power applied to the electrode and in the absence of discharge.

perature, P_{hyd} is the hydrogen partial pressure, and P_v is the equilibrium metal vapor pressure as a function of temperature [15].

Power was applied to the electrode to achieve a bright plasma in hydrogen with and in hydrogen with strontium or sodium vapa. For all temperatures in the range 335-664° C. In each case, the spectral radiant flux at the spectrometer system was recorded. The power driving the hydrogen alone and rydridgen plus sodium vapor controls was adjusted such that the pik spectrometer system spectral radiation was about $\mu W/cm^2$ nm in each case. The integrated visible tradiation levels (0.40 to 2.08 $\mu W/cm^2$) were of the same and of magnitude despite the differences in frequencies of the spectral lines recorded by the spectrometer system in the strontium case versus the controls.

The power required to maintain a plasma of equivalent optical brightness with strontium atoms present was 4000 times less than that required for the controls. For example, a driving power of 33.7 W was necessary to achieve a total visible radiant flux of about 1 μ W/cm² from a sodium hydrogen mixture; whereas, 8.5 mW formed a plasma with the same optical brightness in the case of a strontium hydrogen mixture. A plasma formed at a cell voltage of about 250 V in the cell with hydrogen alone and in the cell with hydrogen and sodium; whereas, a plasma formed in the strontium cell at the extremely low voltage of about 2 V. The results are summarized in Table 2.

The count rate and the spectrometer system irradiation for a mixture of strontium vapor and hydrogen at 664°C is shown in Fig. 13. Optimal light emission was observed after several hours of cell evacuation. The hydrogen partial pressure was unknown under these conditions. The calculated equilibrium vapor pressure of strontium at 664°C is approximately 270 mtorr. The measured breakdown volt-



Table 2	_
Discharge conditions and comparison of the driving power to achieve a total visible radiant flux of about	JμW/cm ²

	T (°C)	P _{byd} (Torr)	P _v (Torr) ^a	Voltage (V)	Current (mA)	Integration Time ^b (ms)	G (μW/cm²)	Power (W)
H ₂ + Sr	664	_	0.270	2.20	3.86	768	1.17	0.0085
H ₂ , 5.	664	1.0	_	224	110	1130	2.08	24.6
H ₂ + Na	335	1.0	0.051	272	124	122	1.85	33.7
$H_2 + Na$	516	1.5	5.3	220	68	768	0.40	15.0
$H_2 + Na$	664	1.5	63	240	41	768	0.41	9.84
Bkgnd.	664	_	0.270	0	0	768	0.20	0

^{*}Calculated [15].

^bG is independent of the integration time since it is a rate.

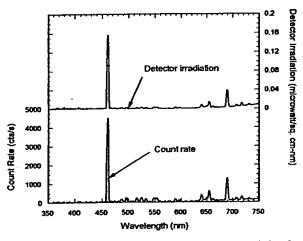


Fig. 13. The count rate and the spectrometer system irradiation for a mixture of strontium vapor and hydrogen at 664°C.

Table 3 Spectral features of hydrogen and strontium at 664°C

Measured wavelength (nm)	Spectrometer system irradiation (µW/cm² nm)	Published sprissridata [16]
460.6	0.156	466 (Sr)
487.2	0.00290	87.25 Sr), 486.13 (H ₂)
639.8	0.00813	63 32 (Sr)
654.7	0.0139	654.68 (Sr), 656.29 (H ₂)
689.4	0.0386	689.26 (Sr)

age was approximated V. The maintenance voltage for a stable discussed as 2.2 V and input power was 8.5 mW. Spectral characteristics are noted in Table 3. The hydrogen Balmer and peaks were obscured by strong strontium emission up at 654.7 and 487.2 nm, respectively.

The spectrometer system irradiation for a hydrogen discharge at a cell temperature of 664°C and 1 torr is shown in

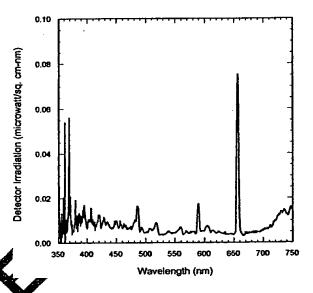


Fig. 14. The spectrometer system irradiation for a hydrogen discharge at a cell temperature of 664°C and a hydrogen pressure of 1 torr.

Fig. 14. The breakdown voltage was approximately 220 V. The field voltage required to form a stable discharge was 224 V. The input power was 24.6 W. Spectral features are tabulated in Table 4. The peak at 589.1 nm may be due to sodium contamination from a previous experimental run. The minor peaks at 518.2 and 558.7 nm have not been identified.

The spectrometer system irradiation for mixtures of sodium vapor and hydrogen are shown in Figs. 15-17 for temperatures of 335, 516, and 664°C, respectively. Corresponding hydrogen pressures are 1, 1.5, and 1.5 torr, respectively. The calculated sodium vapor pressure was 51 mtorr, 5.3 torr, and 63 torr at 335, 516, and 664°C, respectively. At least 200 V was required to maintain a discharge. The input power for a stable discharge ranged from approximately 10 W at 664°C to 34 W at 335°C. Spectral features corresponding to 335°C are summarized in Table 5. Strong emission observed near



Table 4 Spectral features of hydrogen at 664°C

HE 1143

Measured wavelength (nm)	Spectrometer system irradiation (µW/cm ² nm)	Published emission data [16] (nm)
485.8	0.0165	486.13 (H ₂)
518.2	0.00894	
558.7	0.00694	
589.1	0.0174	589.00 (Na), 589.59 (Na)
656.7	0.0752	656.29 (H ₂)

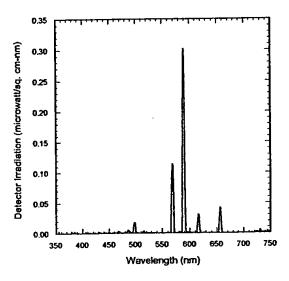


Fig. 15. The spectrometer system irradiation for a mixture of sodium vapor and hydrogen at 335°C.

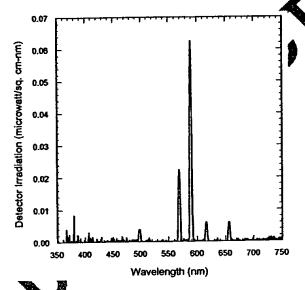


Fig. 10. The spectrometer system irradiation for a mixture of sodium vapor and hydrogen at 516°C.

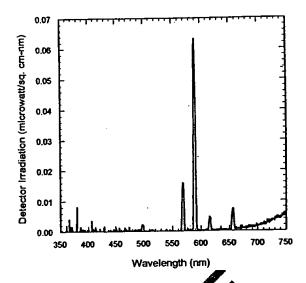


Fig. 17. The spectrometer system irradials a mixture of sodium vapor and hydrogen at 664°C

Table 5
Spectral features of hydrogen and softium at 335°C

Measured wavelength (nm)	Spectrose etc. stell in diation (W/cm² nm)	Published emission data [16] (nm)
467	0.00400	466.86 (Na)
48	0.0055	486.13 (H ₂)
498.4	0.0176	498.28 (Na)
540.1	0.00380	515.34 (Na)
69.6	0.114	568.82 (Na)
3	0.302	589.00 (Na), 589.59 (Na)
615.9	0.0310	616.07 (Na)
656.0	0.0422	656.29 (H ₂), 655.24 (Na)
657.0	0.0421	656.29 (H ₂)

656-657 nm was probably due, in-part, to hydrogen. The relative contribution to the intensity was masked by strong sodium emission at a slightly shorter wavelength. The peak at 486.2 nm could only be due to hydrogen emission. Sodium does not have emission lines in the neighborhood of this wavelength. The intensity of this peak diminishes relative to the more prominent sodium peaks with increasing temperature as shown in Figs. 15-17. This may have been due to a decreasing hydrogen concentration as the sodium vapor pressure increased.

The minimum starting voltage $V_{s\,min}$ determined with a variation of the discharge gas pressure and the corresponding pressure of the discharge gas defined as P_{min} are given in Table 6. The minimum voltage required to form a plasma in hydrogen at 662° C was about 200 V. Gas parameters from von Engel [17] and Naidu and Kamaraju [18] shown

Table 6 The minimum starting voltage $V_{\rm s\,min}$ determined with a variation of the discharge gas pressure and the corresponding pressure of the discharge gas defined as $P_{\rm min}$

	25°C		662°C	
Gas	V _{s min} (V)	P _{min} (torr)	V _{s min} (V)	P _{min} (torr)
He	162	2.20	145	7.37
N ₂	212	0.417	180	1.35
H ₂	185	0.70	195	2.44

in Table 7 indicate a minimum voltage of 273 V is required at 25°C. Further results of the behavior of glow discharges in control gases as a function of pressure and temperature are given in the appendix.

4. Discussion

In the cases where Lyman a emission was observed, no possible chemical reactions of the tungsten filament, the dissociator, the vaporized test material, and 300 mtom hydrogen at a cell temperature of 700°C could be found which accounted for the hydrogen a line emission. In fact, no known chemical reaction releases enough energy to excite Lyman a emission from hydrogen. The emission was not observed with hydrogen alone or with helium, neon, or argon gas. Intense emission was observed for strontium with hydrogen gas, but no emission was observed with hydrogen or strontium alone. This result indicates that the emission was due to a reaction of hydrogen. The emission of the Lyman lines is assigned to the catalysis of hydrogen which excites atomic at molecular hydrogen. Other studies support the possibility of a novel catalytic reaction of atomic hydrogen. It is been reported that intense extreme ultraviolet (EUX) was observed at low temperatures (e.g. 5 atomic hydrogen and certain atomized element gaseous ions [1-5]. The only pure elements the served to emit EUV were each a catavtic stem wherein the ionization of t electrons from a area to a continuum energy level is such that the and office ionization energies of the t electrons is approximate $n \times 27.2$ eV where t and m each are an integer from noms ionize at integer multiples of the potentia ener of atomic hydrogen and caused emission; mereas, the chemically similar atoms, magnesium and arium a well as sodium, caused no emission. The catalogic on sign for strontium are given by Eqs. (5)-(7) the enthalpy of ionization of Sr to then, has a net enthalpy of reaction of which is equivalent to m = 7 in Eq. (3).

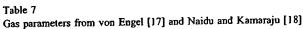
n power balance of a gas cell having atomized hydrogen and strontium was measured by integrating the total light output corrected for spectrometer system response and energy over the visible range. A control cell was identical except that sodium replaced strontium. In this case, 4000 times the power of the strontium cell was required in order to achieve that same optically measured light output power. A plasma formed at a cell voltage of about 250 V in the cell with hydrogen alone and in the cell with hydrogen and sodium; whereas, a plasma formed in the strontium cell at the extremely low voltage of about 2 V. The starting and maintenance discharge voltages were two orders of magnitude of that predicted by current theory or observed experimentally as shown in the appendix.

In the case of a potassium catalyst, a plasma was observed when the electric field was set to zero [4,5]. During the strontium catalysis reaction is given by Eqs. (5)–(7), the electrons are ionized to a continuum energy level. The presence of a low-strength electric field alters the continuum energy levels. The electric field in this experiment was about 2 V over the annular gap about 2 cm. A weak field may adjust the energy of the tonising strontium catalyst to match the energy released by a drogen to cause it to undergo catalysis to the lover-energy cate. In other words, the electric field may cause an energy resonance of the net enthalpies of reaction.

5. Conclusions

Intense EU mission was observed at low temperatures (e.g. \$103 K) hom atomic hydrogen and strontium which es attateger multiples of the potential energy of atomic gen. The release of energy from hydrogen by the catalis reasion with strontium atoms was evidenced by the UV mission and by the formation of an optically bright ma with 4000 times less input power and 2% of the voltage of that required to form an equivalent plasma with sodium and hydrogen. The energy release must result in a lower-energy state of hydrogen. The lower-energy hydrogen atom called a hydrino atom by Mills [11] would be expected to demonstrate novel chemistry. The formation of novel compounds based on hydrino atoms would be substantial evidence supporting catalysis of hydrogen as the mechanism of the observed EUV emission. A novel hydride ion called a hydrino hydride ion having extraordinary chemical properties given by Mills [11] is predicted to form by the reaction of an electron with a hydrino atom. Compounds containing hydrino hydride ions have been isolated as products of the reaction of atomic hydrogen with atoms and ions identified as catalysts in the present EUV study [1-5,11, 19-24].

Billions of dollars have been spent to harness the energy of hydrogen through fusion using plasmas created and heated to extreme temperatures by RF coupling (e.g. $> 10^6$ K) with confinement provided by a toroidal magnetic field. The present study indicates that energy may be released from hydrogen at relatively low temperatures with an apparatus



F						
Gas	A (cm ⁻¹ torr ⁻¹)	B (V/cm torr)	X/P (V/cm torr)	V _{s min} (V)	(Pd) _{min} (cm torr)	β
	12	342	100-600	251	0.67	3.24
N ₂		139	20-1000	273	1.15	3.90
H_2	5.4			327	0.567	4.94
Air	15	365	100-800			6.63
CO ₂	20	466	500-1000	420	0.51	
-	12	180	100-600	137	0.9	3.36
Аг		34	20-150	156	4.0	5.06
He	3	= :			2	10.3
Hg	20	370	200-600	520	-	10.5
Na	_			335	0.04	

which is of trivial technological complexity compared to a tokomak. And, rather than producing radioactive waste, the reaction has the potential to produce compounds having extraordinary properties. The implications are that a vast new energy source and a new field of hydrogen chemistry have been discovered. Work in progress includes synthesis and identification of novel compounds, spectroscopy of the plasma producing process, and energy balance measurements.

Acknowledgements

Special thanks are due to Nelson Greenig for designing the fiber optic system, to Jinquan Dong for preparing many of the cells comprising the test materials, to Takeyoshi Onuma for recording EUV and optical spectra and to Bala Dhandapani and Jiliang He for reviewing this manuscript.

Appendix A. Electrical breakdown and discharge interests

A.1. Summary of results

For He, N₂, and H₂ gases, the starting voltage to form a glow discharge, the voltage to maintain the discharge, and the light emitted were studied as a function of pressure at 25 and 662°C. A summary of the observations follows:

- 1. The starting voltage exhibited minimum with respect to the variation in pessure as redicted by Townsend theory. The minimum starting voltage, V_{s min}, occurred at a pressure defect as A_{min} shown in Table 6.
- 2. For helium, the minimum starting voltage was lower, and P_{\min} was inches that that observed for N_2 and H_2 .
- 3. For he man introgen, $V_{s min}$ decreases by less than 16% when the temperature was increased from 25 to 662 For H₂, $V_{s min}$ is almost independent of tempera-
- 4. For Me, N₂, and H₂ gases at 25°C, the measured values of the pressure-electrode gap spacing product

- corresponding to $V_{s \min}$, (Pd)_{min}, are in good agreement with published values.
- 5. For He, N₂, and H₂ gases, P_{min} shifts toward higher pressure with increasing temperature. For given gas, P_{min} occurs at approximately the same gas number density for 25 and 662°C, in agreement with the property of the proper
- 6. At room temperature, Towns of the V was a fair predictor of the starting voltage V and V and V and a good predictor of V min for V and V
- 7. For He, N₂, and H₂ gasts, a glo discharge was observed for a range of pressures at an P_{\min} . Light emission was greatest for pressure we near P_{\min} . For pressures substantially of the property o
- 8. N and H₂ are consumed when a discharge was present 662. This may result from nitride and hydride formation nuring the discharge.

4.2 Theoretical background

Consider a gas layer of thickness d bounded by plane electrodes. The gas pressure is P and the electrode potential is V. Electrons are periodically released from the cathode, perhaps due to ultraviolet irradiation, by cosmic radiation, etc. These primary electrons constitute a small current i_0 . The primary electrons experience numerous collisions as they accelerate toward the anode in the electric field. Two important types of collision, corresponding to ionization and excitation, are

$$e^- + N \rightarrow e^- + N^+ + e^-,$$
 (A.1)

$$e^- + N \rightarrow e^- + N^*, \tag{A.2}$$

where e^- , N, N^* and N^+ represent an electron, a neutral particle, an excited neutral particle, and a positive ion, respectively. Let α be the number of positive ion/electron pairs produced by a primary electron per unit length in the field direction. α is Townsend's first ionization coefficient. Ignoring recombination and the formation of negative ions, electron multiplication results in the current

$$i = i_0 e^{\alpha d} \tag{A.3}$$

at the anode [17]. The current at the anode is balanced by positive ions reaching the cathode where they combine with electrons and return to the gas as neutral particles.

Electrons are also released from the cathode due to bombardment by positive ions and excited neutral particles, and due to irradiation by excited particles in the gap [25]. These secondary electrons are accelerated in the field and result in electron multiplication just as the primary electrons. Eq. (A.3) for i ignores these secondary electrons. For simplicity, assume that the secondary electrons are produced at the cathode by positive ion impact alone. Denote by γ the number of secondary electrons produced by a positive ion arriving at the cathode. Common gases and cathode materials result in $0.001 < \gamma < 0.1$, approximately. γ is Townsend's second ionization coefficient. The current at the anode including multiplication by secondary electrons is [17]

$$i = \frac{i_0 e^{\alpha d}}{1 - \gamma (e^{\alpha d} - 1)}.$$
(A.4)

In this equation for current growth, the ionization coefficients for a particular gas and cathode material at a fixed temperature are functions of the field strength

$$X = \frac{V}{d} \tag{A.5}$$

and the gas pressure. More precisely

$$\frac{\alpha}{P} = f_1\left(\frac{X}{P}\right),\tag{A.6}$$

$$\gamma = f_2\left(\frac{X}{P}\right). \tag{A.7}$$

The physical basis for these relationships follows from the relationship between the mean free path of an electron in the gas, λ_e , and the gas pressure

$$P \propto \frac{1}{\lambda_e} = \frac{\text{collisions}}{\text{distance traveled}}$$
collisions

distance traveled in field direction

The second proportionality follows from p rate of frectron random velocity to drift velocity, v/v = constant [25]. The interpretations for α/P and X/P follows from the definitions of α and X:

$$\frac{\alpha}{P} = \alpha \frac{\text{ionizations}}{\text{collision}},$$
 (A.9)

$$\frac{X}{P} = \propto \frac{\text{potential}}{\text{collision}}$$
 (A.10)

For α/P , von tages 122 develops a semi-empirical approximation

$$\frac{\alpha}{P} = A e^{B(RP)} \tag{A.11}$$

where A are B are constants. The approximation is valid for a limited range of the reduced field strength X/P, shown in Table 7.

The current growth (Eq. (A.4)) indicates that current multiplication in the gas is infinite when

$$\gamma(e^{\alpha d} - 1) = 1. \tag{A.12}$$

This is the onset of breakdown. When this condition is reached the discharge becomes self-sustaining, requiring no flow of primary electrons from the cathode. Breakdown may occur for a fixed electrode spacing by increasing V. Introducing the functional expressions for the ionization coefficients and $X_s = V_s/d$ where V_s is the starting or breakdown voltage gives

$$f_2\left(\frac{V_s}{\mathrm{Pd}}\right)\left(e^{(\mathrm{Pd})f_1(V_s/\mathrm{Pd})}-1\right)=1. \tag{A.13}$$

Therefore, the breakdown voltage is a function of the product of the pressure and the electrode spacing,

$$V_{\rm s} = f(\rm Pd). \tag{A.14}$$

The product Pd is directly proportional to the number of particles in the electrode gap as shown who. The breakdown voltage is the same for a gap at the between electrodes with 1 mm spacing as it is for the same gas at 1 torr between electrodes with 10 mm spacing. In each case, the number of particles in the gap is the same, and the potential for acceleration of an electron between successive collisions at breakdown is also the same for both cases.

From the ideal w, the gas number density is given by

$$n = \frac{PN_a}{RT} \tag{A.15}$$

where N_{\bullet} . Avogadro's number, T is the absolute temperature and R is the ideal gas constant. The number of particles between electrodes of unit area is

$$\frac{PdN_{\bullet}}{RT}.$$
 (A.16)

Therefore, Pd is proportional to the number of particles between electrodes of unit area at a fixed temperature. Generalizing the functional relation (Eq. (A.14)) to account for temperature variations results in

$$V_{s} = \bar{f}(nd). \tag{A.17}$$

An approximation for the function f of Eq. (A.14) which ignores the temperature dependence is found by making the following substitutions into Eq. (A.13): (1) γ given by Eq. (A.7) where $X_s = V_s/d$ in Eq. (A.7) and the dependence of γ on X/P is ignored and (2) f_1 given by Eqs. (A.6) and (A.11) where $X_s = V_s/d$

$$\gamma[\exp\{A(Pd)e^{-B/(X_0/P)}\}-1]=1.$$
 (A.18)

Rearrangement leads to

$$\frac{X_s}{P} = \frac{B}{\log[A(Pd)/\log(1+1/\gamma)]}$$
 (A.19)

for the starting field strength or

$$V_{s} = \frac{B(Pd)}{\log[A(Pd)/\beta]},$$
(A.20)

where

$$\beta = \log(1 + 1/\gamma). \tag{A.21}$$

This is Paschen's law for the breakdown voltage in a gas that holds approximately for Pd < 1000 cm · torr. Because $\log x$ varies more slowly than x for large x and more rapidly than x for small x, a minimum value of V_s is expected where

$$\frac{\mathrm{d}V_{\mathrm{s}}}{\mathrm{d}(\mathrm{Pd})} = 0. \tag{A.22}$$

This minimum occurs for

$$Pd = (Pd)_{min} = \frac{e\beta}{A}$$
 (A.23)

and has the value

$$V_{\rm s min} = \frac{Be\beta}{4}.$$
 (A.24)

The minimum in starting voltage occurs because Pd is proportional to the number of particles between the electrodes. For small Pd, few ionizations take place, and the electron multiplication is low due to the small number of particles in the gap. A large Pd results in closely spaced neutral particles so that few electrons acquire sufficient energy for ionization between collisions. Measured values of the minimum breakdown voltage and $(Pd)_{min}$ are given in Table 7 along with the estimate for β

$$\beta = \frac{AV_{4 \text{ min}}}{Be}.$$
 (A.25)

Paschen's law also predicts that breakdown is impossible for values of Pd less than the limiting value $(Pd)_{\infty}$:

$$\frac{A(\mathrm{Pd})_{\infty}}{\beta} = 1, \quad V_s \to \infty, \tag{A.26}$$

$$(\mathrm{Pd})_{\infty} = \frac{\beta}{A} = \frac{(\mathrm{Pd})_{\min}}{e}.$$

That is, $(Pd)_{\infty}$ is slightly more than one-third the value of $(Pd)_{\min}$. Raizer [25] notes that breakdown does in factor $Pd < (Pd)_{\infty}$, resulting from field emission. The electrons from the cathode.

A.3. Measurements

The starting voltage was measured, and the light output was recorded when obseved quarty for discharges in He, N2, and H2. Measurements were made for varying gas pressures at room and elevated superatures. The experimental apparatus and see up and the apparatus and methods to provide the driving field and measure the voltage and current of the gas discharge are described in the power cell apparatus and procedure section.

The hande diameter of the stainless-steel cell which formed the outer electrode was $D_0 = 9.21$ cm. The overall diameter of the axial electrode was $D_i = 5.72$ cm. For an electrode potential V, the magnitude of the field strength at

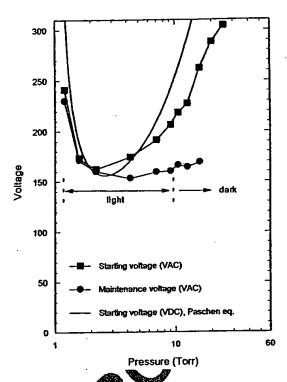


Fig. 18. The observed and theoretical (Paschen equation (Eqs. (A.18)-(A.19)) arting voltages and the observed maintenance voltages and that mission for helium at 25°C as a function of the helium dessare.

a canal distance r from the cell axis, ignoring end effects,

$$\frac{V}{r\log(D_0/D_i)}. (A.28)$$

The ratio of the field strengths at the cell wall and the axial electrode was

$$\frac{X_0}{X_i} = \frac{D_i}{D_0} = 0.621. \tag{A.29}$$

Thus, Paschen's law applied since the field strength did not vary significantly across the discharge gap. The mean field strength was

$$X = \frac{V}{d},\tag{A.30}$$

where $d = (D_0 - D_i)/2 = 1.75$ cm was the electrode spacing. The observed and theoretical (Paschen equation (Eqs. (A.20)-(A.21)) starting voltages and the observed maintenance voltages and light emission for helium at 25°C as a function of the helium pressure are shown in Fig. 18. The observed starting and maintenance voltages and light emission for helium at 662°C as a function of the helium pressure are shown in Fig. 19. The starting voltage exhibited the expected minimum with respect to pressure variation. At higher temperature, the starting voltages near the minimum were distributed over a broader range of pressure. By



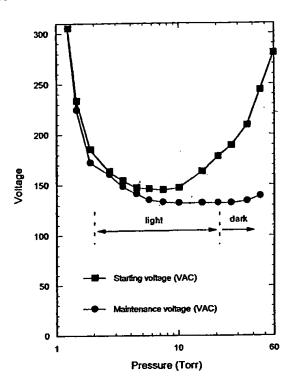


Fig. 19. The observed starting and maintenance voltages and light emission for helium at 662°C as a function of the helium pressure.

increasing temperature to 662° C, the minimum starting voltage, $V_{s \min}$, was diminished only about 10%. P_{\min} , the pressure corresponding to the minimum starting voltage, was shifted toward higher pressure with increasing temperature. However, P_{\min} occurred at nearly the same gas number density at 25°C as at 662° C which is in agreement with theory

$$\frac{n_{662}^{\circ} \text{C}}{n_{25}^{\circ} \text{C}} = 1.07. \tag{A.31}$$

At 25°C, (Pd)_{min} = 3.85 cm torr which was ment with the published value, (Pd)m in Table 7. The difference between and maingreater than P_{\min} . tenance voltage increased for p as a good predictor of From Fig. 18, the Paschen equation P_{\min} , but it under-predicted the sering voltage by a margin of 10-40%. The discremency was masked in Fig. 18 since $\sqrt{2}$ greater than the rms the peak voltage was a actor value shown. Subsequent reakdown, a glow discharge was observed for a range of pressures about Pmin. Light emission from the stage was greatest for pressures very near P_{\min} , a disnear P_{min} was significantly lower and light charge was formed (conducting gas) with little or no light engission. Similar effect was observed for pressures substantally greater than P_{\min} .

The observed and theoretical (Paschen equation (Eqs. (A.20)-(A.21)) starting voltages for nitrogen at 25°C

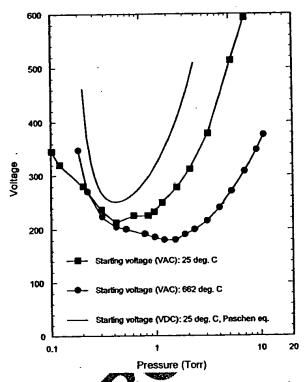


Fig. 20. The observed theoretical (Paschen equation (Eqs. (A.18)-(A.29)) Sarting voltages for nitrogen at 25°C as a function of the nitrogen pressure and the observed starting voltages for nitrogen at C as a function of the nitrogen pressure.

function of the nitrogen pressure and the observed starting vortages for nitrogen at 662°C as a function of gen pressure are shown in Fig. 20. The qualitative satures of the breakdown process and the discharge were similar to those of helium. The variation of V_s and P_{min} with temperature and the variation of light emission with pressure were similar. The minimum starting voltage was 35 -50 V higher than that of helium, and P_{\min} was smaller. At 25°C, (Pd)_{min} = 0.73 cm torr while from Table 7 (Pd)_{min} = 0.67 cm torr. The Paschen equation was again a good predictor of P_{\min} . For nitrogen, the starting voltage was also reasonably well predicted except near P_{\min} . The Paschen equation under-predicted the starting voltage by 15-20% when the nitrogen pressure was near P_{\min} considering that the actual voltage peaks exceeded the rms voltage by the factor $\sqrt{2}$. The gas number densities at $P = P_{\min}$ were in the ratio

$$\frac{n_{662} \circ c}{n_{25} \circ c} = 1.03. \tag{A.32}$$

At 662°C, the nitrogen pressure decreased steadily whenever a discharge was present in the cell. Perhaps the increased frequency of nitrogen ion collisions with the electrode surfaces enabled the formation of nitride compounds.

The observed and theoretical (Paschen equation (Eqs. (A.20)-(A.21)) starting voltages for hydrogen at 25°C as a



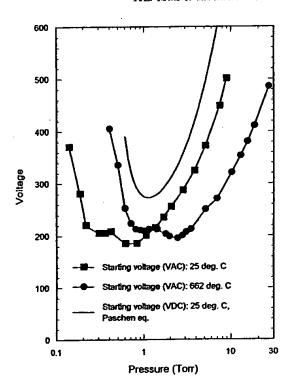


Fig. 21. The observed and theoretical (Paschen equation (Eqs. (A.18)-(A.19)) starting voltages for hydrogen at 25°C as a function of the hydrogen pressure and the observed starting voltages for hydrogen at 662°C as a function of the hydrogen pressure.

function of the hydrogen pressure and the observed starting voltages for hydrogen at 662°C as a function of the hydrogen pressure are shown in Fig. 21. The minimum starting voltages were similar to those observed for nitrogen. However, the variation of V_s with pressure differed from the behave observed for He and N2. A local minimum was observed the $V_s - P$ relation at a pressure slightly below P_{\min} havior may result from strong variation of the secon tion coefficient y for hydrogen near $X/P \approx$ [26]. Also, the broadening effect and the de he case with increased temperature were not chage was obof hydrogen. In fact, the minimum station served to increase slightly with to raise. As with He and N2, the V_s curve was shifted was higher pressure with greserve the number denincreasing temperature in order sity. The number density ratio

$$\frac{n_{662} \circ c}{n_{25} \circ c} = 1.11. \tag{A.33}$$

The Paschen sudies of predicted $P_{\rm min}$, but it predicted the startification reasonably well for pressures greater than $A_{\rm min}$ in emeasured value (Pd)_{min} = 1.23 cm torr at 25°C was again in good agreement with 1.15 cm torr given in table. As with nitrogen, the hydrogen pressure decreased steadily when a discharge was present. This effect was observed in hydrogen both at elevated temperature and

at room temperature. The pressure may have decreased due to hydride formation.

References

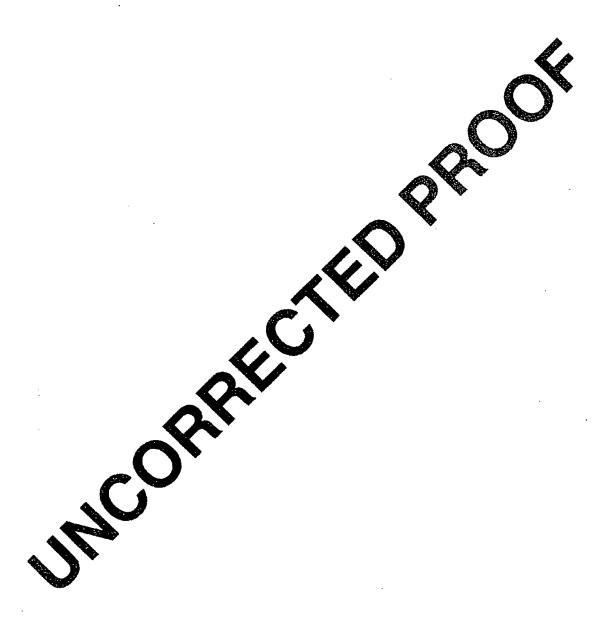
- Mills R, Dong J, Lu Y. Observation of extreme ultraviolet hydrogen emission from incandescently heated hydrogen gas with certain catalysts. 1999 Pacific Conference on Chemistry and Spectroscopy and the 35th ACS Western Regional Meeting, Ontario Convention Center, California, October 6-8, 1999.
- [2] Mills R, Dong J, Lu Y. Observation of extreme ultraviolet hydrogen emission from incandescently heated hydrogen gas with certain catalysts. Int J Hydrogen Energy 2000;25:919-43.
- [3] Mills R. Observation of extreme ultraviolet emission from hydrogen-KI plasmas produced by a hollow cathode discharge. Int J Hydrogen Energy, submitted for publication.
- [4] Mills R. Temporal behavior of light-emission in the visible spectral range from a Ti-K2CO3-H-O5H. Int J Hydrogen Energy, in press.
- [5] Mills R, Lu Y, Onuma T. Provided a hydrogen plasma from an incandescently heated hydrogen-potassium gas mixture and plasma decay upon reme al of heater power. Int J Hydrogen Energy, pre-
- [6] Phillips JH. Guide to the Sun Cambridge, Great Britain: Cambridge University July 1992. p. 16-20.
- [7] Sampson JAP The harders of vacuum ultraviolet spectroscopy Pre Arbitostions, 1980. p. 94-179.
- [8] Science News 12/6/15, p. 366.
- [9] Fujimoto T. Sawada K, Takahata K. J Appl Phys 1989;66(6): 15-9.
- [10] Hollander A, Wertheimer MR. J Vac Sci Technol A 1994 2(3):879-82.
- metanics, January 2000 ed. Cranbury, New Jersey:
 BackLight Power, Inc., Distributed by Amazon.com.
- Sidgwick NV. The chemical elements and their compounds, vol. I. Oxford: Clarendon Press, 1950. p. 17.
- [13] Lamb MD. Luminescence spectroscopy. London: Academic Press, 1978. p. 68.
- [14] Linde DR. CRC handbook of chemistry and physics, 79th ed., Boca Raton, Fl: CRC Press, 1998-9. p. 10-175-7.
- [15] Yaws CL. Chemical properties handbook. New York: McGraw-Hill, 1999.
- [16] Linde DR. CRC handbook of chemistry and physics, 79th ed. Boca Raton, FI: CRC Press, 1998-9. p. 10-1-87.
- [17] von Engel A. Ionized gases. American Institute of Physics, 1965.
- [18] Naidu MS, Kamaraju V. High voltage engineering. New York: McGraw-Hill, 1996.
- [19] Mills R, Dhandapani B, Greenig N, He J. Synthesis and characterization of potassium iodo bydride. Int J Hydrogen Energy, in press.
- [20] Mills R. Novel inorganic hydride. Int J Hydrogen Energy 2000;25:669-83.
- [21] Mills R. Novel hydrogen compounds from a potassium carbonate electrolytic cell. Fusion Technol 2000;37(2): 157-82.
- [22] Mills R, He J, Dhandapani B. Novel hydrogen compounds. 1999 pacific conference on chemistry and spectroscopy and

17

18

the 35th ACS Western Regional Meeting, Ontario Convention Center, California, October 6-8, 1999.

- [23] Mills R, Dhandapani B, Nansteel M, He J. Synthesis and characterization of novel hydride compounds. Int J Hydrogen Energy, submitted for publication.
- [24] Mills R. Highly stable novel inorganic hydrides. J Mater Res., submitted for publication.
- [25] Raizer YP. Gas discharge physics. Berlin: Springer, 1997.
- [26] Brown SC. Basic data of plasma physics. Cambridge, MA: MIT Press, 1959.





THE GRAND UNIFIED THEORY OF CLASSICAL QUANTUM MECHANICS

BY Section

Dr. Randell L. Mills

BLACKLIGHT POWER inc.

493 Old Trenton Road Cranbury, NJ 08512

January 2000 EDITION





the reflecting horizon, and is known as a horizontal event. On the other hand the arrival time of the diffracted pulse will be given by

$$t^2 - x/v^2 = vT_0^2,$$

where x is the horizontal distance from the shot-receiver location to the diffracting edge, and v is the wave speed. Therefore, on the seismic section, the diffracted pulse will appear as a hyperbolic trajectory, whose apex determines the edge of the truncated horizon. The amplitude of the reflection event is much greater than that of the diffraction event. Therefore, it is often extremely difficult to observe the diffraction in seismic reflection data, unless an amphi tude correction function is applied.

T. Young, Philos. Trans. R. Soc. London 12 (1802); T. Young, in Miscell laneous Works of the Late Thomas Young, Vol. 1 (Murray, London; England, 1855), p. 140.

²J. B. Keller, J. Opt. Soc. Am. 52, 116 (1962).

³J. J. Bowman, T. B. A. Senior, and P. L. E. Uslenghi, Electromagnetic and Acoustical Scattering by Simple Shapes (North-Holland, Amsterdam, 1969), pp. 308-345.

⁴H. S. Carslaw, Proc. London Math. Soc. 30, 121 (1899).

⁵P. C. Clemmow, Q. J. Mech. Appl. Math. 3, 241 (1950).

On the radiation from point charges

Department of Electrical Engineering and Computer Science and Research Laboratory of Electronics, H. A. Haus Massachusetts Institute of Technology, Cambridge, Massachusetts 02139

(Received 12 August 1985; accepted for publication 4 January 1986)

An alternative derivation of the radiation field of a point charge is presented. It starts with the Fourier components of the current produced by the moving charge. The electric field is found from the vector wave equation. Each step in the integration permits physical interpretation. The retarded time appears very naturally in this derivation. The interpretation of the present derivation is that a charge at constant velocity $\bar{v}(|\bar{v}| < c)$ does not radiate, not because it is unaccelerated, but because it has no Fourier components synchronous with waves traveling at the speed of light. Of course, Cherenkov radiation in a medium, in which the velocity of electromagnetic propagation is less than c, is the classic example of radiation by a charge moving at constant velocity.

I. INTRODUCTION

The equations of macroscopic electrodynamics attribute the rate of energy generation to the current density $\overline{J}(\overline{r},t)$. This fact is underscored by Poynting's theorem, in which the power delivered per unit volume is equated to the scalar product of the electric field and current density, $\widetilde{E}(\overline{r},t)\cdot \overline{J}(\overline{r},t)$. An oscillating dipole in the steady state radiates power that is equal to the time average of $\int \vec{E} \cdot \vec{J} dv$ integrated over the current distribution. On the other hand, it is well known that a single charged particle in uniform motion does not radiate in free space. The far field of a single particle derived from the Lienard-Wiechert potentials, which decays with distance from the particle as 1/r and thus accounts for radiation, is proportional to the acceleration of the particle. Thus the Poynting vector of the radiation fields is proportional to $[\overline{J}]^2$. This is one dilemma that faces the student of electrodynamics when he first sees the derivation from the Liénard-Wiechert potentials. Another new concept facing the student is the "retarded time" in the derivation of the Lienard-Wiechart potentials which does not enter explicitly into the discussion of macroscopic electrodynamics.

The usual derivation of the Lienard-Wiechert potentials is not conceptually simple. 12 It rests on the superposition. of the fields produced by different volume elements of the charge distribution representing the radiating particle,

which is treated for this purpose, and this purpose alone, as occupying a volume of finite size. An alternative derivation presented by Jackson3 rests on a careful evaluation of integrals of the spatial delta function. This derivation has much to recommend it. However, it does not provide a physical picture for the meaning of the mathematical development. Sommerfeld4 has presented two derivations of the potentials produced by a moving particle, both based on the Green's function and contour integration in the complex plane. His derivation is particularly elegant. Yet none of these three derivations bring out the dichotomy between $\overline{J}(\overline{r},t)$ as responsible for power transfer to the field accord ing to Poynting's theorem, and $\overline{J(7, t)}$ as responsible for radiation.

This paper is the outgrowth of work on the noise radiation from a "wiggled" electron beam in a waveguide' (free electron laser). The radiation in a waveguide is analyzed. most naturally in terms of the excitation of waveguide modes. The electric field of such a mode is proportional to the appropriate modal component of I (not wI). Yet when the analysis is taken to the limit of an infinite waveguide cross section, the same result is obtained as with the Lienard-Wiechert potentials. This suggests alternate interpretations of radiation of a moving particle

In Sec. II we summarize the spatial Fourier representation of a moving particle. In Sec. III we solve the vector wave equation in Fourier transform space (\vec{k}, ω) space). Then we perform the inverse Four analogue in two steps. First, the integral is carried over the magnitude of k. At this point, the expression assumes a particularly appealing form—the field is proportional to $J_1(k,\omega)$, where $J_1(k,\omega)$ is the Fourier transform of the current perpenditular to k and $\bar{n} \equiv k/|k|$. Further, this field appears summed over all the modes per unit volume and solid angle by the weighting factor

$$\rho(\omega,\Omega)d\omega d\Omega = \frac{4\pi\omega^2}{c^2} d\left(\frac{\omega}{c}\right) \frac{d\Omega}{4\pi}.$$

The integral over all angles brings in a factor of ω , i.e., $\omega \overline{J}_1$ can now be interpreted as containing the acceleration (but not evaluated with respect to retarded time). The analysis brings in the retarded time naturally, no factor $1-(\bar{v}\cdot\bar{n})/c$ appears in the expression for $E_1(\bar{r}, t)$. Finally, we obtain the well-known far field as a function of \bar{r} and t

II. THE SOURCE AND ITS FOURIER TRANSFORMS

Consider a charged particle of charge q and position $\overline{r}_0(t)$. The charge density of the particle is described by

$$\rho(\bar{r},t) = q\delta[\bar{r} - \bar{r}_0(t)] \tag{1}$$

where $\delta(\overline{r} - \overline{r}_0)$ is the spatial unit impulse function. The current density is

$$\overline{J}(\overline{r},t) = q\overline{r}_0(t)\delta[\overline{r} - \overline{r}_0(t)]. \tag{2}$$

The spatial Fourier transform represents the current density as a superposition of spatial exponentials, $\exp -i\vec{k} \cdot \vec{r}$.

$$\overline{J}(\overline{k},t) = \iiint d^{3}\overline{r}q\overline{r}_{0}(t)\delta[\overline{r} - \overline{r}_{0}(t)]e^{-i\overline{k}\cdot\overline{r}}$$

$$= q\overline{r}_{0}(t)e^{-i\overline{k}\cdot\overline{r}_{0}}.$$
(3)

The full space-time Fourier transform is of course,

$$\overline{J}(\overline{k},\omega) = \iiint \int dt d^{3}\overline{r} \, \overline{J}(\overline{r},t) e^{-i\overline{k}\cdot\overline{r}} e^{i\omega t} \,. \tag{4}$$

The inverse Fourier transform is

$$\overline{J}(\overline{r},t) = \left(\frac{1}{2\pi}\right)^4 \int d\omega \int \int \int d\overline{k} \, {}^{3}\overline{J}(\overline{k},\omega) e^{-i\omega t} e^{i\overline{k}\cdot\overline{r}}. \quad (5)$$

III. THE ELECTROMAGNETIC FIELD

The electric field obeys the vector wave equation

$$\nabla \times (\nabla \times \overline{E}) + \frac{1}{c^2} \frac{\partial^2 \overline{E}}{\partial t^2} = -\mu_0 \frac{\partial \overline{J}}{\partial t}.$$
 (6)

The space-time Fourier transform of the vector wave equation is

$$\bar{k} \times [\bar{k} \times \bar{E}(\bar{k},\omega)] + \frac{\omega^2}{c^2} \bar{E}(k,\omega)$$

$$= -i\omega \mu_0 \bar{J}(\bar{k},\omega) . \tag{7}$$

In the far field, only the component perpendicular to \bar{k} is of interest. Concentrating on this component one has

$$\overline{E}_{1}(\overline{k},\omega) = \frac{-i\omega \,\mu_{0}\overline{n} \times [\overline{n} \times \overline{J}(\overline{k},\omega)]}{k^{2} - (\omega^{2}/c^{2})},$$
(8)

with

$$\bar{n} = \frac{\bar{k}}{|\bar{k}|}. (9)$$

IV. THE INVERSE!

The inverse space-time Fourier transform involves the

$$= \int \frac{d\omega}{2\pi} e^{-i\omega t} \left(\frac{1}{2\pi}\right)^2 \int \int \int d^3 k e^{ik\cdot \frac{\pi}{2}}$$

We shall retain the Fourier transform with respect to time and thus not carry out the integration over ω . But we shall focus on a spectral width $d\omega$ of the field and thus write down expressions for $\overline{E}_1(\overline{r},\omega)(d\omega/2\pi)$. We separate the integrals into an integral over the magnitude of k, and into a double integral with respect to the angles θ and ϕ of k with respect to \overline{r} .

$$\overline{E}_{1}(\overline{r},\omega) \frac{d\omega}{2\pi} = -\frac{d\omega}{2\pi} \left(\frac{1}{2\pi}\right)^{3} \int \int d\phi d\theta \sin \theta$$

$$\times \int i\omega \,\mu_{0} k^{2} dk \, \frac{\overline{n} \times [\overline{n} \times \overline{J}(\overline{k},\omega)]}{k^{2} - (\omega^{2}/c^{2})} e^{i\overline{k} \cdot \overline{r}}.$$
(10)

The last integral can be carried out by contour integration. For $\bar{k} \cdot \bar{r} > 0$, the contour must be closed into the negative imaginary half plane of k with the result

$$\overline{E}_{1}(\overline{r},\omega) \frac{d\omega}{2\pi} = \left(\frac{1}{2\pi}\right)^{2} \frac{\omega^{2}}{c^{2}} d\left(\frac{\omega}{c}\right) \int \int \frac{d\phi d\theta \sin \theta}{4\pi} \\
\times \sqrt{\frac{\mu_{0}}{\epsilon_{0}}} c\overline{n} \times \left[\overline{n} \times \overline{J}\left(\frac{\omega}{c} \overline{n},\omega\right)\right] e^{i(\omega/c)\overline{n} \cdot \overline{r}}.$$
(11)

This expression may be rewritten in a way that lends itself to an appealing interpretation. The density of (linearly polarized) modes per unit volume and unit solid angle $\rho(\omega, \Omega)$ is

$$\rho(\omega,\Omega)d\omega d\Omega = \frac{1}{2\pi} \left(\frac{\omega}{c}\right)^2 d\left(\frac{\omega}{c}\right) \frac{d\Omega}{4\pi}.$$
 (12)

With this definition, one has

$$\overline{E}_{1}(\overline{r},\omega) \stackrel{d\omega}{=} = \frac{c}{2\pi} \int \rho(\omega,\Omega) d\omega d\Omega \sqrt{\frac{\mu_{0}}{\epsilon_{0}}} \times \overline{n} \times \left[\overline{n} \times \overline{J} \left(\frac{\omega}{c} \overline{n}, \omega \right) \right] e^{\mu(\omega/c)E \cdot \overline{r}} ... (13)$$

The field $E_1(7,\omega)(d\omega/2\pi)$ is proportional to $-\overline{J}_1((\omega/c)\overline{n},\omega)$ namely, the Fourier component for which $k=\omega/c$. Factors of ω that multiply the Fourier component of the current are due to the density of moder per unit volume and unit solid angle. An unaccelerated charge does not radiate in free space, not because it experiences no acceleration, but because it has no Fourier component

$$\overline{J}\left(\frac{\omega}{c}\,\overline{n},\omega\right)$$

Indeed, from (3)

$$J(\overline{k},\omega) = \int dt q \overline{v} e^{-i\overline{k} \cdot \overline{v}t + t\omega t}$$
$$= 2\pi q \overline{v} \delta(\omega - \overline{k} \cdot \overline{v}) . \tag{14}$$

The only nonzero Fourier components are for

$$k = \frac{\omega}{v \cos \theta} > \frac{\omega}{c} \,, \tag{15}$$



where θ is the angle between $\bar{\nu}$ and k. The reason for the radiation of an accelerated charge is that the Fourier decomposition of the current acquires Fourier components that are "synchronous" with the light velocity, i.e., with the propagation constant $|k| = \omega/c$. Thus, for example, an oscillating charge

$$\overline{r}_0(t) = \overline{d} \sin \omega_0 t, \qquad (16)$$

has a Fourier spectrum

$$\overline{J}(\overline{k},\omega) = \frac{q\omega_0 d}{2} J_m(k\cos\theta d) \{\delta[\omega - (m+1)\omega_0] + \delta[\omega - (m-1)\omega_0]\},$$
(17)

where the J_m s are Bessel functions of order m. These Fourier components can, and do, acquire phase velocities that are equal to the light velocity. For small kd only m=0remains and is approximately independent of k, $J_0[(\omega_0/c)\cos\theta d] \simeq 1.$

V. INTEGRATION OVER ANGLES

Starting with (11), we note that the exponential is a strong function of θ , whereas the component $\bar{n} \times [\bar{n} \times \bar{J}]$ varies much more slowly and thus can be pulled out from under the integration. We have to integrate an expression of the form

$$\frac{1}{2\pi} \frac{\omega^2 d\omega}{c^3} \int_0^{2\pi} \int_0^{\pi} \frac{d\phi d\theta \sin \theta}{4\pi} e^{i(\omega/c)\cos \theta r}$$

$$= -\frac{1}{2} i \frac{\omega}{c^2 r} \frac{d\omega}{2\pi} e^{i(\omega/c)r},$$

where the upper limit on θ is ignored because of the rapid variation of the exponent. With this result introduced in (11) one has

$$E_{1}(\bar{r},\omega)\frac{d\omega}{2\pi} = -\frac{d\omega}{2\pi}\frac{i}{4\pi}\sqrt{\frac{\mu_{0}}{\epsilon_{0}}}\frac{\omega}{cr}\bar{n}$$

$$\times \left[\bar{n}\times\bar{J}\left(\frac{\omega}{c}\bar{n},\omega\right)\right]e^{i(\omega/\epsilon)r}.$$
(18)

Here, \bar{n} is the direction of the radius vector \bar{r} . We note now that a factor of w appears in front of the current. One may therefore interpret the source as containing the acceleration although one must emphasize that multiplication by $-i\omega$ represents differentiation with respect to the time coordinate, not with respect to retarded time. The two are related by the factor $1 - \vec{n} \cdot \vec{v}/c$. It seems more natural to attribute the factor to the integration over all the modes, in particular because then Cherenkov radiation presents less of a mystery. Cherenkov radiation is produced by an unaccelerated particle, but since the velocity of light is less than c, the particle current can have Fourier components synchronous with $\omega/c\sqrt{\epsilon/\epsilon_0}$, where ϵ is the dielectric constant of the medium.

If one introduces (3), one finds from (18)

$$E_{1}(\bar{r},\omega) \frac{d\omega}{2\pi} = -\frac{iq}{4\pi} \sqrt{\frac{\mu_{0}}{\epsilon_{0}}} \frac{\omega}{cr} \left\{ \int dt' \bar{n} \times [\bar{n} \times \bar{r}_{0}(t')] \right\} \times \exp + i\omega \left(t' + \frac{r}{c} - \bar{n} \cdot \frac{\bar{r}_{0}(t')}{c} \right) \frac{d\omega}{2\pi}.$$
(19)

This expression has in it the retarder-time

It does not contain the factor 1 - (# v/c) which appears in the Lienard-Wiechert fields. However, we deal here with the Fourier transform in time of E. In the next section we show that the usual expression for the far field is obtained from the Fourier transform of (19).3

VI. THE ELECTRIC FIELD IN SPACE-TIME

The electric field in space-time is obtained by the inverse Fourier transform of (19)

Found: Consider
$$E_{\perp}(\bar{r},t) = \int_{-\infty}^{\infty} E_{\perp}(\bar{r},\omega)e^{-i\omega t} \frac{d\omega}{2\pi} = -\frac{q}{4\pi}\sqrt{\mu_0/\epsilon_0} \frac{1}{r}$$

$$\times \int_{-\infty}^{\infty} \frac{d\omega}{2\pi} \int dt' \bar{n} [\bar{n} \times \bar{r}_0(t')] i\omega$$

$$\times \exp{-i\omega \left(t - t' - \frac{r}{c} - \bar{n} \cdot \frac{\bar{r}_0(t')}{c}\right)}. \quad (21)$$

The factor iw can be replaced by a differentiation of the exponential

$$\frac{d}{dt'} \exp -i\omega \left(t - t' - \frac{r}{c} - \bar{n} \cdot \frac{\bar{r}_0(t')}{c}\right)
= i\omega \left(1 - \frac{\bar{n} \cdot \bar{r}_0}{c}\right) \exp -i\omega \left(t - t' - \frac{r}{c} - \bar{n} \cdot \frac{\bar{r}_0(t')}{c}\right). \tag{22}$$

In the notation of Jackson, we designate by κ the factor

$$1 - \frac{\overline{n} \cdot \overline{r}_0}{c} = \kappa, \tag{23}$$

and, by $\bar{\beta}$ the velocity normalized by the speed of light, \bar{r}_0 c. Introducing (22) and (23) into (21), and integrating by parts over 1', one has

$$\overline{E}_{1}(\overline{r},t) = \frac{q}{4\pi} \sqrt{\mu_{0}/\epsilon_{0}} \frac{1}{r} \int_{-\infty}^{\infty} \frac{d\omega}{2\pi} \int dt' \\
\times \exp -i\omega \left(t - t' - \frac{r}{c} - \frac{\overline{n} \cdot \overline{r}_{0}/t'}{c}\right) \\
\times \frac{d}{dt'} \left(\frac{\overline{n} \times [\overline{n} \times \overline{\beta}(t')]}{\kappa}\right).$$
(24)

In the far field, the time derivative of \bar{n} is negligible compared with the derivative of \overline{v} and \overline{r}_0 . In this limit, it is easy to show that3

$$\frac{d}{dt'} \left(\frac{\overline{n} \times [\overline{n} \times \overline{\beta}(t')]}{\kappa} \right) = \frac{\overline{n} \times [(\overline{n} - \overline{\beta}) \times \overline{\beta}]}{\kappa^2}.$$
 (25)

The integral over all ω of

$$\frac{1}{2\pi}\exp-i\omega\left(t-t'-\frac{r}{c}-\frac{\overline{n}\cdot\overline{r}_0(t')}{c}\right),\,$$

produces the delta function

$$\delta\left(t-t'-\frac{r}{c}-\frac{\overline{n}\cdot\overline{r}_0(t')}{c}\right).$$

When variab!

In the

f(t')

and

י Thus

 \overline{E}_{1} (

The e:

the re here v





Introducing these results into (24), gives

Introducing these reservoir

$$E_{1}(\bar{r},t) = \frac{q}{4\pi} \sqrt{\mu_{0}/\epsilon_{0}} \frac{1}{r} \int_{-\infty}^{\infty} dt' \times \delta\left(t - t' - \frac{r}{c} - \frac{\bar{n} \cdot \bar{r}_{0}(t')}{c}\right) \times \frac{\bar{n} \times \left[(\bar{n} - \bar{\beta}) \times \bar{\beta}\right]}{\kappa^{2}}.$$
(26)

When the argument of the delta function is a function of the variable of integration, the integration gives³

$$\int g(x)\delta[f(x)-\alpha]dx = \left(\frac{g(x)}{df/dx}\right)_{f(x)=\alpha}.$$
 (27)

$$f(t') = t' + \frac{r}{c} + \frac{\overline{n} \cdot \overline{r}_0(t')}{c}$$
 (28)

$$\frac{df}{dt} = 1 - \bar{n} \cdot \bar{\beta} = \kappa \,. \tag{29}$$

Thus we have from (26) the final result

$$\overline{E}_{1}(\bar{r},t) = \frac{q}{4\pi} \sqrt{\mu_{0}/\epsilon_{0}} \cdot \frac{1}{r\kappa^{3}} \{ \bar{n} \times [(\bar{n} - \bar{\beta}) \times \bar{\beta}] \}_{ret} . \tag{30}$$

The expression in brackets is evaluated at

$$t-\frac{r}{c}-\frac{\bar{n}\cdot\bar{r}_0(t)}{c},$$

the retarded time. Equation (30) is the standard result, here written in mks units.

VII. CONCLUSIONS

When the radiation field of a charged particle is evaluated by its inverse Fourier transform, the expressions resulting from successive integrals permit physically appealing interpretations. The integral over the magnitude of the propagation constant gives the Fourier component of the field that has the appearance (13)

held that has the appendix
$$\overline{E}_{1}(\bar{r},\omega) \frac{d\omega}{2\pi} = \frac{c}{2\pi} \int \int \rho(\omega,\Omega) d\omega d\Omega \sqrt{\frac{\mu_{0}}{\epsilon_{0}}} \bar{n} \times \left[\bar{n} \times \overline{J} \left(\frac{\omega}{c} \bar{n},\omega \right) \right] e^{i(\omega/c)\bar{n}\cdot\bar{r}}.$$
 (13)

Thus, radiation is produced by the Fourier component of \overline{J}_1 that has $\overline{k} = (\omega/c)\overline{n}$, i.e., that travels with the speed of light. Particles that are unaccelerated do not radiate, because their current density has no Fourier components synchronous with the light velocity. Thus the presence of Cherenkov radiation of particles moving in "slow" media, i.e., with light velocities in the medium less than c, is a natural consequence of this interpretation of (13) and does not present any conceptual difficulties.

The integral over the mode density produces a factor of ω multiplying \overline{J}_1 . Thus, one could interpret the expression for $\overline{E}_1(\overline{r},\omega)(d\omega/2\pi)$ as caused by acceleration, except of course that a multiplication by $-i\omega$ results via differentiation with respect to time—not retarded time. The Fourier $\overline{E}_1(\overline{r},\omega)$ contains an integrand expressed in terms of retarded time which came in quite naturally through the preceding integrations.

Equation (13) also makes plausible the appearance of $\overline{E}\cdot\overline{J}$ in Poynting's theorem. The \overline{E} field of the plane wave associated with a plane wave of current $\overline{J}_1(\overline{k},\omega)$, is proportional to \overline{J}_1 , not $\omega \overline{J}_1$ and 180 deg out of phase as required by power conservation. Factors of ω are the result of the superposition of plane waves at different angles of propaga. tion. Inverse Fourier transformation of $E_1(\overline{r},\omega)$ gives the usual expression for the far field in space-time. The deriva tion by this approach has much to recommend it because the successive mathematical steps permit physical interpretation. Further, the quantum analysis of photon detection7 uses as its starting part expressions that can be shown to be contained in the present analysis.

ACKNOWLEDGMENTS

The author is indebted to Dr. H. Motz for illuminating discussions. This work was supported, in part, by the National Science Foundation Grant ECE-8544345.

W. K. H. Panofsky and M. Phillips, Classical Electricity and Magnetism (Addison-Wesley, Reading, MA, 1956).

2R. D. Feynman, R. B. Leighton, and M. Sands, The Feynman Lectures on Physics (Addison-Wesley, Reading, MA, 1979), 6th printing, pp. 21-5. ³J. D. Jackson, Classical Electrodynamics (Wiley, New York, 1962).

Ph. Frank, R. v. Mises, Die Differential- and Integralgleichungen der Mechanik und Physik, Zweiter physikalischer Teil (Vieweg und Sohn, Braunschweig, 1935).

⁵H. A. Haus and M. N. Islam, J. Appl. Phys. 54, 4784 (1983). W. B. Colson, IEEE J. Quantum Electron. QE-17, 1417 (1981).

⁷R. J. Cook, Phys. Rev. A 25, 2164 (1982).



PERGAMON

International Journal of Hydrogen Energy 25 (2000) 1185-1203



www.elsevier.com/locate/ijhydene

Synthesis and characterization of potassium iodo hydride

Randell L. Mills *, Bala Dhandapani, Nelson Greenig, Jiliang He

BlackLight Power, Inc., 493 Old Trenton Road, Cranbury, NJ 08512, USA

Abstract

A novel inorganic hydride compound KHI which comprises a high binding energy hydride ion was synthesized by reaction of atomic hydrogen with potassium metal and potassium iodide. Potassium iodo hydride was identified by time-of-flight secondary ion mass spectroscopy, X-ray photoelectron spectroscopy, ¹H and ³⁹K nuclear magnetic resonance spectroscopy, Fourier transform infrared spectroscopy, electrospray ionization time-of-flight mass spectroscopy, liquid chromatography/mass spectroscopy, thermal decomposition with analysis by gas chromatography, and mass spectroscopy, and elemental analysis. Hydride ions with increased binding energies may form many novel compounds with broad applications. © 2000 International Association for Hydrogen Energy. Published by Elsevier Science Ltd. All rights reserved.

1. Introduction

Intense extreme ultraviolet (EUV) emission was observed at low temperatures (e.g. $< 10^3$ K) from atomic hydrogen and certain atomized elements or gaseous ions which ionize at integer multiples of the potential energy of atomic hydrogen [1–6]. Based on its exceptional emission, we used potassium metal as a catalyst to release energy from atomic hydrogen. Mills [7] predicts an exothermic reaction whereby certain atoms or ions serve as catalysts to release energy from hydrogen to produce an increased binding energy hydrogen atom called a hydrino having a binding energy of

Binding energy =
$$\frac{13.6 \text{ eV}}{(1/p)^2}$$
, (1)

where p is an integer greater than 1, designated as $H[a_H/p]$ where a_H is the radius of the hydrogen atom. Hydrinos are predicted to form by reacting an ordinary hydrogen atom with a catalyst having a net enthalpy of reaction of about

$$m \cdot 27.2 \text{ eV},$$
 (2)

where m is an integer. This catalysis releases energy from the hydrogen atom with a commensurate decrease in size of

E-mail address: rmills@blacklightpower.com (R.L. Mills).

the hydrogen atom, $r_n = na_H$. For example, the catalysis of H(n = 1) to $H(n = \frac{1}{2})$ releases 40.8 eV, and the hydrogen radius decreases from a_H to $\frac{1}{2}a_H$.

A catalytic system is provided by the ionization of t electrons from an atom each to a continuum energy level such that the sum of the ionization energies of the t electrons is approximately mX 27.2 eV where m is an integer. One such catalytic system involves potassium. The first, second, and third ionization energies of potassium are 4.34066, 31.63, 45.806 eV, respectively [8]. The triple ionization (t = 3) reaction of K to K^{3+} , then, has a net enthalpy of reaction of 81.7426 eV, which is equivalent to m = 3 in Eq. (2).

81.7426 eV + K(m) + H
$$\left[\frac{a_H}{p}\right] \to K^{3+} + 3e^-$$

+H $\left[\frac{a_H}{(p+3)}\right]$ + $[(p+3)^2 - p^2]X13.6$ eV, (3)

$$K^{3+} + 3e^{-} \rightarrow K(m) + 81.7426 \text{ eV}.$$
 (4)

The overall reaction is

$$H\left[\frac{a_{H}}{p}\right] \to H\left[\frac{a_{H}}{(p+3)}\right] + [(p+3)^{2} - p^{2}]X13.6 \text{ eV}.$$
(5)

Potassium ions can also provide a net enthalpy of a multiple of that of the potential energy of the hydrogen atom.

^{*} Corresponding author. Tel.: +001-609-490-1040; fax: +001-609-490-1066.

The second ionization energy of potassium is 31.63 eV; and K^+ releases 4.34 eV when it is reduced to K. The combination of reactions K^+ to K^{2+} and K^+ to K, then, has a net enthalpy of reaction of 27.28 eV, which is equivalent to m=1 in Eq. (2).

27.28 eV + K⁺ + K⁺ + H
$$\left[\frac{a_{\rm H}}{p}\right] \rightarrow K + K^{2+}$$

+H
$$\left[\frac{a_{\rm H}}{(p+1)}\right]$$
+ $[(p+1)^2-p^2]X13.6$ eV, (6)

$$K + K^{2+} \rightarrow K^{+} + K^{+} + 27.28 \text{ eV}.$$
 (7)

The overall reaction is

$$H\left[\frac{a_H}{p}\right] \to H\left[\frac{a_H}{(p+1)}\right] + [(p+1)^2 - p^2]X13.6 \text{ eV}.$$
 (8)

A novel hydride ion having extraordinary chemical properties given by Mills [7] is predicted to form by the reaction of an electron with a hydrino (Eq. (9)). The resulting hydride ion is referred to as a hydrino hydride ion, designated as $H^{-}(1/p)$.

$$H\left[\frac{a_{\rm H}}{p}\right] + e^- \to H^-(1/p). \tag{9}$$

The hydrino hydride ion is distinguished from an ordinary hydride ion having a binding energy of 0.8 eV. The latter is hereafter referred to as "ordinary hydride ion". The hydrino hydride ion is predicted [7] to comprise a hydrogen nucleus and two indistinguishable electrons at a binding energy according to the following formula:

Binding energy =
$$\frac{\hbar^2 \sqrt{s(s+1)}}{8\mu_e a_0^2 [(1+\sqrt{s(s+1)})/p]^2} - \frac{\pi\mu_0 e^2 \hbar^2}{m_e^2 a_0^3} \left(1 + \frac{2^2}{[(1+\sqrt{s(s+1)}/p]^3}\right),$$
(10)

where p is an integer greater than one, $s = \frac{1}{2}$, π is pi, \hbar is Planck's constant bar, μ_0 is the permeability of vacuum, m_e is the mass of the electron, μ_e is the reduced electron mass, a_0 is the Bohr radius, and e is the elementary charge. The ionic radius is

$$r_1 = \frac{a_0}{p}(1 + \sqrt{s(s+1)}); \ s = \frac{1}{2}.$$
 (11)

From Eq. (11), the radius of the hydrino hydride ion $H^-(1/p)$; p = integer is 1/p that of ordinary hydride ion, $H^-(1/1)$.

A novel inorganic hydride compound KHI which comprises high binding energy hydride ions was synthesized by reaction of atomic hydrogen with potassium metal and potassium iodide. Potassium iodo hydride was identified by time-of-flight secondary ion mass spectroscopy (ToF-SIMS), X-ray photoelectron spectroscopy (XPS), 'H and ³⁹K nuclear magnetic resonance spectroscopy (NMR), Fourier transform infrared (FTIR) spectroscopy, electrospray ionization time-of-flight mass spectroscopy (ES-ITOFMS), liquid chromatography/mass spectroscopy (LC/MS), thermal decomposition with analysis by gas chromatography (GC), and mass spectroscopy (MS), and elemental analysis.

Alkali and alkaline earth hydrides react violently with water to release hydrogen gas which subsequently ignites due to the exothermic reaction with water. Typically metal hydrides decompose upon heating at a temperature well below the melting point of the parent metal. These saline hydrides, so called because of their salt-like or ionic character, are the monohydrides of the alkali metals and the dihydrides of the alkaline-earth metals. Mills predicts a hydrogen-type molecule having a first binding energy of about

Binding energy =
$$\frac{15.5}{(1/p)^2} \text{ eV.}$$
 (12)

Dihydrino molecules may be produced by the thermal decomposition of hydrino hydride ions. $H^-(\frac{1}{2})$ may be less reactive and more thermally stable than ordinary potassium hydride, but may react at high temperature to form a hydrogen-type molecule. Potassium iodo hydride $KH(\frac{1}{2})I$ may be heated to release dihydrino by thermal decomposition

$$2KH(1/2)I \xrightarrow{\Delta} H_2^* \left[2c' = \frac{a_0}{\sqrt{2}} \right] + 2KJ, \tag{13}$$

where 2c' is the internuclear distance and a_0 is the Bohr radius [7]. The possibility of releasing dihydrino by thermally decomposing potassium iodo hydride with identification by gas chromatography was explored.

The first ionization energy, IP_1 , of the dihydrino molecule

$$H_2^* \left[2c' = \frac{\sqrt{2}a_0}{2} \right] \to H_2^* [2c' = a_0]^+ + e^-$$
 (14)

is $IP_1=62$ eV (p=2 in Eq. (12)); whereas, the first ionization energy of ordinary molecular hydrogen, $H_2[2c'=\sqrt{2}a_0]$, is 15.46 eV. Thus, the possibility of using mass spectroscopy to discriminate $H_2[2c'=\sqrt{2}a_0]$ from $H_2^*[2c'=a_0/\sqrt{2}]$ on the basis of the large difference between the ionization energies of the two species was explored. A novel high binding energy hydrogen molecule assigned to dihydrino $H_2^*[2c'=a_0/\sqrt{2}]$ was identified by the thermal decomposition of KHI with analysis by gas chromatography, and mass spectroscopy.

2. Experimental

2.1. Synthesis

Potassium iodo hydride was prepared in a stainless-steel gas cell shown in Fig. 1 comprising a Ti screen hydrogen



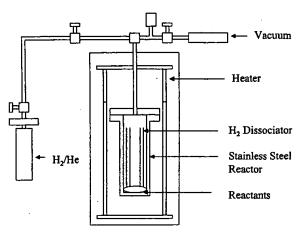


Fig. 1. Stainless-steel gas cell.

dissociator (Belleville Wire Cloth Co., Inc.), potassium metal catalyst (Aldrich Chemical Company), and KI (Aldrich Chemical Company 99.9%) as the reactant. The 304stainless-steel cell was in the form of a tube having an internal cavity of 359 mm in length and 73 mm in diameter. The top end of the cell was welded to a high-vacuum 4 5/8 in bored through conflat flange. The mating blank conflat flange contained a single coaxial hole in which was welded a 3/8 in diameter stainless-steel tube that was 100 cm in length and contained an inner coaxial tube of $\frac{1}{8}$ in diameter. A silver-plated copper gasket was placed between the two flanges. The two flanges are held together with 10 circumferential bolts. The bottom of the $\frac{3}{6}$ in tube was flush with the bottom surface of the top flange. The outer tube served as a vacuum line from the cell and the inner tube served as a hydrogen or helium supply line to the cell. The cell was surrounded by four heaters. Concentric to the heaters was high-temperature insulation (AL 30 Zircar). Each of the four heaters were individually thermostatically controlled.

The cylindrical wall of the cell was lined with two layers of Ti screen totaling 150 g. 75 g of crystalline KI was poured into the cell. About 0.5 g of potassium metal was added to the cell under an argon atmosphere. The cell was then continuously evacuated with a high-vacuum turbo pump to reach 50 mtorr measured by a pressure gauge (Varian Convector, Pirrani type). The cell was heated by supplying power to the heaters. The heater power of the largest heater was measured using a wattmeter (Clarke -Hess model 259). The temperature of the cell was measured with a type K thermocouple (Omega). The cell temperature was then slowly increased over 2 h to 300°C using the heaters that were controlled by a type 97 000 controller. The power to the largest heater and the cell temperature and pressure were continuously recorded by a DAS. The vacuum pump valve was closed. Hydrogen was slowly added to maintain a pressure within the range of 1000-1500 torr. The temperature of the cell was then slowly increased to 650°C over 5 h. The hydrogen valve was closed except to maintain the pressure at 1500 torr. After 24 h, the temperature of the cell was reduced to 400°C at a rate of 15°C/h. The hydrogen supply was switched to helium which was flowed through the inner supply line to the cell while a vacuum was pulled on the outer vacuum line to remove volatilized potassium metal at 400°C. The cell was then cooled and opened. About 75 g of blue crystals were observed to have formed in the bottom of the cell.

The synthesis was repeated with the exception that the hydrogen was slowly added to maintain a pressure within the range of 1-10 torr. About 75 g of green crystals were observed to have formed in the bottom of the cell.

2.2. ToF-SIMS characterization

The crystalline samples were sprinkled onto the surface of a double-sided adhesive tape and characterized using a Physical Electronics TFS-2000 ToF-SIMS instrument. The primary ion gun utilized a $^{69}\mathrm{Ga}^+$ liquid metal source. In order to remove surface contaminants and expose a fresh surface, the samples were sputter cleaned for 30 s using a 40 $\mu m \times$ 40 μm raster. The aperture setting was 3, and the ion current was 600 pA resulting in a total ion dose of 10^{15} ions/cm².

During acquisition, the ion gun was operated using a bunched (pulse width 4 ns bunched to 1 ns) 15 kV beam [9,10]. The total ion dose was 10^{12} ions/cm². Charge neutralization was active, and the post accelerating voltage was 8000 V. Three different regions on each sample of $(12 \ \mu m)^2$, $(18 \ \mu m)^2$, and $(25 \ \mu m)^2$ were analyzed. The positive and negative SIMS spectra were acquired. Representative post sputtering data are reported.

2.3. XPS characterization

A series of XPS analyses were made on the crystalline samples using a Scienta 300 XPS Spectrometer. The fixed analyzer transmission mode and the sweep acquisition mode were used. The step energy in the survey scan was 0.5 eV, and the step energy in the high-resolution scan was 0.15 eV. In the survey scan, the time per step was 0.4 s, and the number of sweeps was 4. In the high-resolution scan, the time per step was 0.3 s, and the number of sweeps was 30. C 1s at 284.5 eV was used as the internal standard.

The binding energies and features of core level electrons of control KI and the blue and green crystals comprising the alkali halido hydride KHI were analyzed by XPS. XPS analysis was conducted on a Kratos XSAM-800 spectrometer using nonmonochromatic Al K α (1468.6 eV) radiation. Samples were crushed in a glove box under argon and mounted on an analysis stub with copper tape. A piece of gold foil was stuck into the sample for calibration. The samples were transferred under an inert atmosphere. A survey spectrum was run from 1000 to 0 eV. For quantitative analysis, high-resolution spectra were run on core level electrons of interest, K 2p and I 3d electrons. A high-resolution

spectrum of the low binding energy region was also run from 100 to 0 eV that corresponded to the survey spectrum. Fixed analyzer transmission (FAT) mode was used in all measurements. For the survey scan, a pass energy of 320 eV was employed. A pass energy of 40 eV was used for high-resolution scans. In the cases where a charging effect was observed, the spectrum was corrected by using a calibration of the effect with the Au $4f_{7/2}$ peak at 84.0 eV as a first standard and the C 1s peak at 284.6 eV as a second standard.

2.4. NMR spectroscopy

 1H MAS NMR was performed on the blue crystals. The data were recorded on a Bruker DSX-400 spectrometer at 400.13 MHz. Samples were packed in zirconia rotors and sealed with airtight O-ring caps under an inert atmosphere. The MAS frequency was 4.5 kHz. During data acquisition, the sweep width was 60.06 kHz; the dwell time was 8.325 μs , and the acquisition time was 0.03415 s/scan. The number of scans was typically 32 or 64. Chemical shifts were referenced to external tetramethylsilane (TMS). The reference comprised KH (Aldrich Chemical Company 99%).

³⁹K MAS NMR was performed on the blue crystals. The data were recorded on a Bruker DSX-400 spectrometer at 18.67 MHz. Samples were packed in zirconia rotors and sealed with airtight O-ring caps under an inert atmosphere. The MAS frequency was 4.5 kHz. During data acquisition, the sweep width was 125 kHz; the dwell time was 4.0 μs, and the acquisition time was 0.01643 s/scan. The number of scans was 96. Chemical shifts were referenced to external KBr (Aldrich Chemical Company 99.99%). References comprised KI (Aldrich Chemical Company 99.99%) and the KH.

¹H MAS NMR was performed on the green crystals. The data were obtained on a custom built spectrometer operating with a Nicolet 1280 computer. Final pulse generation was from a tuned Henry radio amplifier. The ¹H NMR frequency was 270.6196 MHz. A 5 μs pulse corresponding to a 41° pulse length and a 3 s recycle delay were used. The window was ±20 kHz. The spin speed was 4.0 kHz. The number of scans was 600. The offset was 1541.6 Hz, and the magnetic flux was 6.357 T. The samples were handled under a nitrogen atmosphere. Chemical shifts were referenced to external tetramethylsilane (TMS). The reference comprised KH (Aldrich Chemical Company 99%) and equivalent molar mixtures of KH (Aldrich Chemical Company 99.99%) prepared in a glove box under argon.

2.5. FTIR spectroscopy

Samples were transferred to an infrared transmitting substrate and analyzed by FTIR spectroscopy using a Nicolet Magna 550 FTIR Spectrometer with a NicPlan FTIR microscope. The number of scans was 250 for both the sample and background. The resolution was 8.000/cm. A dry air purge was applied.

2.6. Electrospray-ionization-time-of-flight-mass-spectroscopy (ESITOFMS)

The data were obtained on a Mariner ESI TOF system fitted with a standard electrospray interface. The samples were submitted via a syringe injection system (250 μ l) with a flow rate of 5.0 μ l/min. The solvent was water/ethanol (1:1). A reference comprised KI (Aldrich Chemical Company 99.99%).

2.7. Liquid-chromatography/mass-spectroscopy(LC/MS)

Reverse phase partition chromatography was performed with a PE Sciex API 365 LC/MS/MS System. The column was a LC C18 column, 5.0 μ m, 150 \times 2 mm (Columbus 100 Å Serial #207679). 31.1 mg of blue crystals were dissolved in 6.2 ml solvent of 90% HPLC water and 10% HPLC methanol to give a concentration of 5 mg/ml. The sample was eluted using a gradient technique with the eluents of a solution A (water + 5 mM ammonium acetate + 1% formic acid) and a solution B (acetonitrile/water(90/10) + 5 mM ammonium acetate + 0.1% formic acid). The gradient profile was

Time (min):	0	3	18	27	28	30
%A	100	100	0	0	100	Stop
%B	0	0 .	100	100	0	Stop

The flow rate was 1 ml/min. The injection volume was $1\mu l$. The pump pressure was 110 psi.

A turbo electrospray ionization (ESI) and triple-quadrapole mass spectrometer was used. The turbo ESI converts the mobile phase to a fine mist of ions. These ions are then separated according to mass in a quadrapole radio frequency electric field. LC/MS provides information comprising (1) the solute polarity based on the retention time, (2) quantitative information comprising the concentration based on the chromatogram peak area, and (3) compound identification based on the mass spectrum or mass to charge ratio of a peak. The mass spectroscopy mode was positive. The selected ion mass to charge ratios (SIM) were m/e = 39.0, 204.8, 370.6, 536.8, and 702.6. The dwell time was 400 ms, and the pause was 2 ms. The turbo gas was 8 1/min (25 psi).

The controls comprised KI (Aldrich Chemical Company 99,99%) and sample solvent alone.

2.8. Elemental analysis

Elemental analysis was performed by Galbraith Laboratories, Inc., Knoxville, TN. Potassium was determined by Inductively Coupled Plasma using an ICP Optima 3000. Iodide



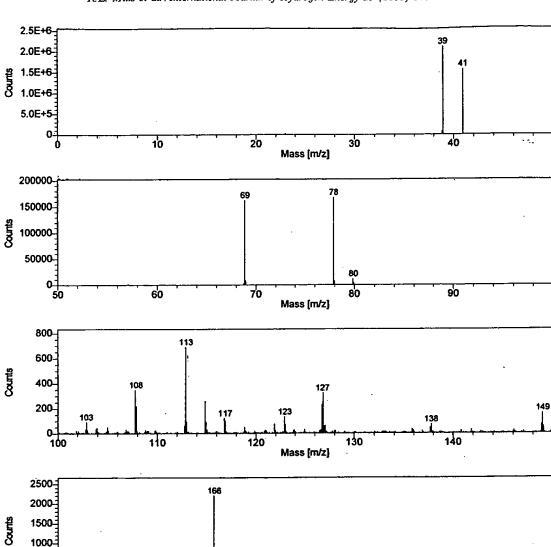


Fig. 2. The positive ToF-SIMS spectrum (m/e = 0-200) of the blue crystals.

Mass [m/z]

180

170

was determined volumetrically by iodometric titration with thiosulfate. The hydrogen was determined by a Perkin-Elmer elemental analyzer (#240) using ASTM D-5291 method wherein the sample was combusted in a tube furnace at 950°C and the water was measured by a thermal conductivity detector. The sample was handled in an inert atmosphere.

160

2.9. Thermal decomposition with analysis by gas chromatography

The gas cell sample comprised deep blue crystals that changed to white crystals upon exposure to air over about a

two week period. 0.5 g of the sample was placed in a thermal decomposition reactor under an argon atmosphere. The reactor comprised a 1/4" OD by 3" long quartz tube that was sealed at one end and connected at the open end with SwagelockTM fittings to a T. One end of the T was connected to a needle valve and a Welch Duo Seal model 1402 mechanical vacuum pump. The other end was attached to a septum port. The apparatus was evacuated to between 25 and 50 mtorr. The needle valve was closed to form a gas tight reactor. The sample was heated in the evacuated quartz chamber containing the sample with an external Nichrome wire heater using a Variac transformer. The sample was heated

190

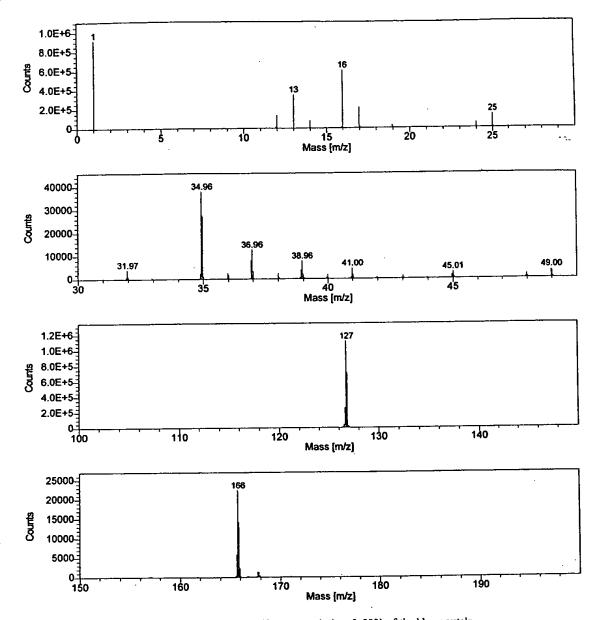


Fig. 3. The negative ToF-SIMS spectrum (m/e = 0-200) of the blue crystals.

to above 600°C by varying the transformer voltage supplied to the Nichrome heater until the sample melted. Gas released from the sample was collected with a 500 µl gas tight syringe through the septum port and immediately injected into the gas chromatograph. The reactor was cooled to room temperature, and a mixture of white and orange crystalline solid remained.

Gas samples were analyzed with a Hewlett Packard 5890 Series II gas chromatograph equipped with a thermal conductivity detector and a 60 m, 0.32 mm ID fused silica Rt-Alumina capillary PLOT column (Restek, Bellefonte,

PA). The column was conditioned at 200°C for 18-72 h before each series of runs. Samples were run at -196°C using Ne as the carrier gas. The 60 m column was run with the carrier gas at 3.4 psi with the following flow rates: carrier — 2.0 ml/min, auxiliary — 3.4 ml/min, and reference — 3.5 ml/min, for a total flow rate of 8.9 ml/min. The split rate was 10.0 ml/min.

The control hydrogen gas was of ultrahigh purity (MG Industries). Control KI (Aldrich Chemical Company ACS grade, 99+%,) was also treated by the same method as the blue crystals.



2.10. Thermal decomposition with analysis by mass spectroscopy

Mass spectroscopy was performed on the gases released from the thermal decomposition of the blue crystals. One end of a 4 mm ID fritted capillary tube containing about 5 mg of sample was sealed with a 0.25 in. Swagelock union and plug (Swagelock Co., Solon, OH). The other end was connected directly to the sampling port of a Dycor System 1000 quadrapole mass spectrometer (Model D200MP, Ametek, Inc., Pittsburgh, PA with a HOVAC Dri-2 Turbo 60 vacuum system). The capillary was heated with a Nichrome wire heater wrapped around the capillary. The mass spectrum was obtained at the ionization energy of 70 and 30 eV at different sample temperatures in the region m/e = 0-50. With the detection of hydrogen indicated by a m/e = 2 peak, the intensity as a function of time for masses m/e = 1, 2, 4, and 5 was obtained while changing the ionization potential (IP) of the mass spectrometer from 30 to 70 eV.

The control hydrogen gas was of ultrahigh purity (MG Industries).

3. Results and discussion

3.1. ToF-SIMS

The positive ToF-SIMS spectrum obtained from the blue crystals is shown in Fig. 2. The positive ion spectrum of the blue crystals and that of the KI control are dominated by the K⁺ ion. The comparison of the positive ToF-SIMS spectrum of the KI control with the blue crystals demonstrates that the 39 K⁺ peak of the blue crystals may saturate the detector and give rise to a peak that is atypical of the natural abundance of 41 K. The natural abundance of 41 K is 6.7%; whereas, the observed 41K abundance from the blue crystals is 73%. The high-resolution mass assignment of the m/z = 41 peak of the blue crystals was consistent with 41 K, and no peak was observed at m/z = 42.98 ruling out ⁴¹KH₂⁺. Moreover, the natural abundance of ⁴¹K was observed in the positive ToF-SIMS spectra of KHCO3, KNO3, and KI standards that were obtained with an ion current such that the 39K peak intensity was an order of magnitude higher than that given for the blue crystals. The saturation of the 39K peak of the positive ToF-SIMS spectrum by the blue crystals is indicative of a unique crystalline matrix

A small (50 counts) K^{2+} m/z = 19.48 ion was only observed in the positive ion spectrum of the blue crystals. Ga^+ m/z = 69, K_2^+ m/z = 78, $K(KCl^+$ m/z = (113), I^+ m/z = 127, KI^+ m/z = 166, and a series of positive ions $K[KI]_n^+$ m/z = (39 + 166n) are also observed.

The negative ion ToF-SIMS of the blue crystals shown in Fig. 3 was dominated by H⁻ and I⁻ peaks of about equal intensity. Iodide alone dominated the negative ion ToF-SIMS of the KI control. For both, O⁻ m/z = 16, OH⁻ m/z = 17,

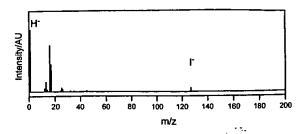


Fig. 4. The negative ToF-SIMS spectrum (m/e = 0-200) of the green crystals.

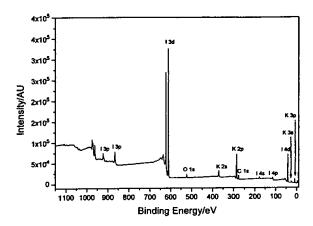


Fig. 5. The XPS survey scan of the blue crystals obtained on the Scienta instrument.

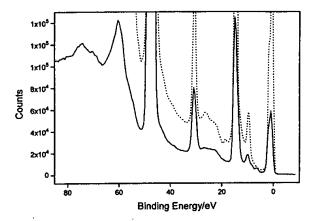


Fig. 6. The 0-85 eV binding energy region of a high-resolution XPS spectrum of the blue crystals (solid) and the control KI (dashed) obtained on the Scienta instrument.

 $Cl^- m/z = 35$, $Kl^- m/z = 166$, a series of negative ions $I[KI]_n^- m/z = (127 + 166n)$ are also observed.

The positive and negative ToF-SIMS spectrum obtained from the green crystals was similar to that obtained from the

Table 1
The results of the binding energies of selected core level electrons, full-width at half-maximum of the peaks, and energy of spin-orbit splitting for potassium iodo hydrides compared with KI

Compound	Peak	Binding energy (eV)	FWHM (eV)	S-O Splitting (eV)	Percentage (%)
KI	K 2p _{3/2}	294.44	1.84	2.75	
	K 2p _{1/2}	297.19	1.79		- 5.
	I 3d _{5/2}	620.37	2.07	11.53	
	I 3d _{3/2}	631.90	2.14		
Potassium	K 2p _{3/2}	294.44	1.77	2.81	68.8
iodo hydride	K 2p _{1/2}	297.21	1.69		
	K 2p _{3/2}	292.90	1.76		
(Blue)	K 2p _{1/2}	295.77	1.66	2.87	31.2
	I 3d _{5/2}	621.01	2.19	11.52	
	I 3d _{3/2}	632.53	2.30		
Potassium	K 2p _{3/2}	294.37	1.83	2.77	58.3
iodo hydride	K 2p _{1/2}	297.14	1.81		
	K 2p _{3/2}	292.51	1.87		
(Green)	K 2p _{1/2}	295.51	1.78	3.00	41.7
	I 3d _{5/2}	621.08	2.17	11.52	
	I 3d _{3/2}	632.60	2.20		

blue crystals except that the hydride ion peak of the negative ToF-SIMS spectrum obtained from the green crystals was much larger than that obtained from the blue crystals. The hydride peak of the green crystals was larger than the iodide peak as shown in Fig. 4; whereas, the hydride peak of the blue crystals was about equivalent to the iodide peak. These results are consistent with the formation of a higher hydride content or a higher hydride ion yield in the green crystals which may indicate that a higher binding energy hydride was formed by running the catalysis reaction at lower hydrogen pressure.

3.2. XPS

A survey spectrum was obtained over the region $E_b = 0-1200$ eV. The primary element peaks allowed for the determination of all of the elements present in the blue and green crystals and the control KI. The survey spectrum also detected shifts in the binding energies of the elements which had implications to the identity of the compound containing the elements.

The XPS survey scan of the blue crystals obtained on the Scienta instrument is shown in Fig. 5. The major species present in the blue crystals and the control are potassium and iodide. Small amounts of carbonate carbon and oxygen

were also identified in the blue crystals. The K 3p and K 3s peaks of the blue crystals were shifted relative to those of the control KI. The K 3p and K 3s of the blue crystals occurred at 17 and 33 eV, respectively. The K 3p and K 3s of the control KI occurred at 17.5 and 33.5 eV, respectively. Hydrogen is the only element which does not have primary element peaks; thus, it is the only candidate to produce the shifted peaks.

No elements were present in the survey scan which could be assigned to peaks in the low binding energy region with the exception of the K 3p and K 3s peaks at 17 and 33 eV, respectively, the O 2s at 23 eV, and the I 5s, I 4d_{5/2}, and I 4d_{3/2} peaks at 12.7, 51, and 53 eV, respectively. Accordingly, any other peaks in this region must be due to novel species. The 0-85 eV binding energy region of a high-resolution XPS spectrum of the blue crystals (solid) and the control KI (dashed) obtained on the Scienta instrument is shown in Fig. 6. The XPS spectrum of the blue crystals differs from that of KI by having additional features at 9.1 and 11.1 eV. The XPS peaks centered at 9.0 and 11.1 eV that do not correspond to any other primary element peaks may correspond to the H⁻ $(n=\frac{1}{4})E_b=11.2$ eV hydride ion predicted by Mills [7] (Eq. (10)) in two different chemical environments where E_b is the predicted vacuum binding energy. In this case, the reaction to form $H^-(n=1/4)$ is given by Eqs. (3)-(5) and



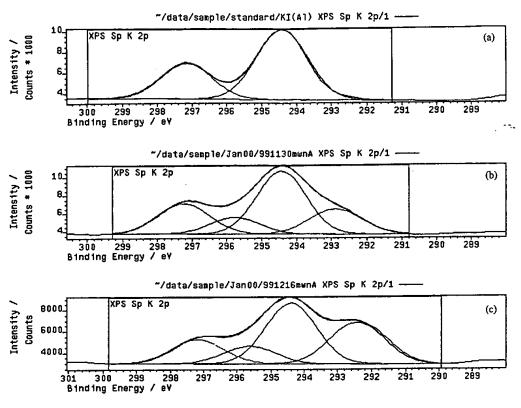


Fig. 7. (A) The XPS spectra of the K 2p core level in KI. (B) The XPS spectra of the K 2p core level in KHI (blue crystals). (C) The XPS spectra of the K 2p core level in KHI (green crystals).

Eq. (9). The hydride ion $H^-(n=\frac{1}{2})E_b=3.05$ eV may also be present in the XPS of the blue crystals under the valence peak at about 3.5 eV. The reaction to form $H^-(n=\frac{1}{2})$ is given by Eqs. (6)-(8) and Eq. (9).

The binding energies and features of core level electrons of control KI and the blue and green crystals comprising the alkali halido hydride KHI were analyzed by XPS. Kratos XPS was used to investigate the local structure of KI and KHI by studying the metal core level K 2p electrons and the iodine core level I 3d electrons. As atomic hydrogen undergoes reaction with potassium catalyst to form a lower-energy hydrogen species which subsequently reacts with the potassium center in KI, alterations in the electronic structure of potassium such as changes in core level binding energies and spin-orbital energies relative to the starting compound, KI, are expected. The results of the determination of the binding energies of selected core level electrons, full-width at half-maximum of the peaks (FWHM), and energy of spin-orbital splitting for the blue and green crystal comprising KHI compared with KI are listed in Table 1, respectively. The XPS spectra of the K 2p core level in KI, KHI, (blue crystals) and KHI (green crystals) appear in Figs. 7A, 7B, and 7C respectively. The XPS spectra of the I 3d core level in KI, KHI (blue crystals), and KHI (green crystals) appear in Figs. 8A, 8B, and 8C, respectively.

In contrast to the K 2p core level, the I 3d core level FWHM in both compounds is very similar to KI. Comparing the alterations in the K core levels versus the I core level indicates that the lower-energy hydrogen species is bound to the metal center of KI. This binding influences the metal core level with little perturbation of the halogen core level.

Each of the spectra of potassium iodo hydride were curve fit with one spin-orbit splitting component having a similar FWHM and energy separation as that of the starting material potassium iodide. An additional spin-orbit splitting component had to be added to each potassium iodo hydride in order to obtain a good curve fit of the K 2p spectra. In each case, the second component of spin-orbit splitting is assigned to the formation of the alkali metal halido hydride, KHI. The presence of the novel hydride ion shifts the K 2p peaks to lower binding energies relative to the corresponding peaks of KI.

The XPS data clearly indicate a change in the electronic structure at the K core level and different bonding in KHI relative to that in the corresponding KI. It strongly suggests the formation of a novel metal hydride which is consistent with the supporting data provided by XPS given above and NMR, ToF-SIMS, and gas chromatography/mass spectroscopy given in the respective sections. The change in electronic structure is greatest with the green crystals which

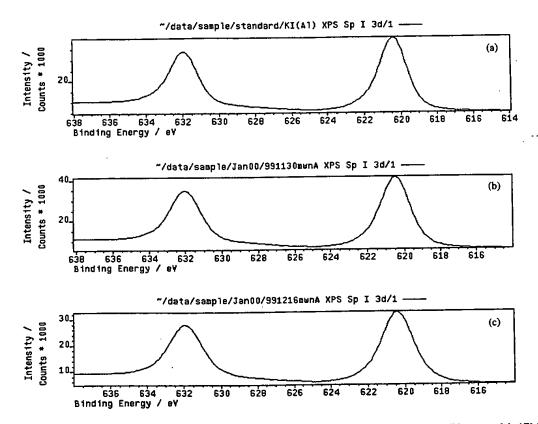


Fig. 8. (A) The XPS spectra of the I 3d core level in KI. (B) The XPS spectra of the I 3d core level in KHI (blue crystals). (C) The XPS spectra of the I 3d core level in KHI (green crystals).

indicates that a higher binding energy hydride is formed by running the catalysis reaction at lower hydrogen pressure.

The XPS survey scan of KI, the blue crystals, and the green crystals obtained on the Kratos instrument are shown in Figs. 9A-C, respectively. The 0-100 eV binding energy region of a high-resolution XPS spectrum of KI, the blue crystals, and the green crystals obtained on the Kratos instrument are shown in Figs. 10A-C, respectively. Peaks centered at 21 and 37 eV which do not correspond to any other primary element peaks were observed in the case of the green crystals. The intensity and shift match shifted K 3s and K 3p. Hydrogen is the only element which does not have primary element peaks; thus, it is the only candidate to produce the shifted peaks. These peaks may be shifted by a highly binding hydride ion $H^{-}(\frac{1}{6})$ with a binding energy of 22.8 eV given by Eq. (10) that bonds to potassium K 3p and shifts the peak to this energy. In this case, the K 3s is similarly shifted.

3.3. NMR

The ¹H MAS NMR spectra of the control KH and the blue crystals relative to external tetramethylsilane (TMS) are shown in Figs. 11 and 12, respectively. Three distinguishable

resonances at 3.65, 0.13 and -0.26 ppm, respectively, were found in the NMR of KH. The broad 3.65 ppm peak of KH is assigned to KOH formed from air exposure during sample handling. The peaks at 0.13 and -0.26 ppm are assigned to hydride H.

Three distinguishable resonances at 0.081, -0.376 and -1.209 ppm, respectively, were found in the NMR of the blue crystals. A fourth very broad resonance may be present at -2.5 ppm. The peaks at 0.081 and -0.376 ppm are within the range of KH and may be ordinary hydride H in two different chemical environments that are distinct from those of the control KH. The resonances at -1.209 ppm and possibly at -2.5 ppm may be due to novel hydride ions.

The color of the blue crystals was found to change to white over 2 weeks of exposure to air. The color-fade rate was greatly increased upon grinding the blue crystal into a fine powder. A dynamic ¹H NMR study following the possible oxidation or hydrolysis of the blue crystals when exposed to air is shown in Figs. 13A-D. The ¹H MAS NMR spectra from ground blue crystals relative to external tetramethylsilane (TMS) following air exposure times of 1, 20, 40, and 60 mins are shown in Figs. 13A-D. Downfield ¹H resonances shifted gradually to 3.861 and 4.444 ppm and then to 5.789. Upfield resonances shifted to 1.157 ppm, as the exposure to



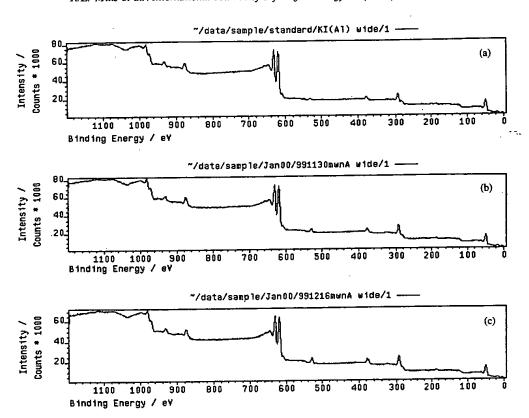


Fig. 9. (A) The XPS survey scan of KI obtained on the Kratos instrument. (B) The XPS survey scan of the blue crystals obtained on the Kratos instrument. (C) The XPS survey scan of the green crystals obtained on the Kratos instrument.

air was prolonged and the blue color concomitantly faded to white. The peak at 5.789 may be due to H of KOH in a chemical environment that is different from that of KOH formed by air exposure of KH. Since the downfield shift of the peak at 5.789 is substantially different from that observed for the control KH, 3.65 ppm, it may be due to KOH or a compound comprising KOH wherein H is increased binding energy hydrogen. The resonance at 1.157 comprises at least two peaks, one of which has a very broad upfield feature. These peaks may be novel hydride ions which are stable in air. In this case, the chemical environment is different from that of the blue crystals which showed potential novel hydride peaks at -1.209 ppm and possibly at -2.5 ppm. These observations strongly suggest that the H species in the blue crystals are new hydride species and may be responsible for the blue color. Decoupling studies are in progress to resolve the broad features of the blue crystal spectrum.

The ³⁹K MAS NMR spectra of KH, KI, and the blue crystals each showed a single resonance at 64.56, 52.71, and 53.32 ppm, respectively. The data indicate that the K local structure in the blue crystals is in between that of KI and KH.

To eliminate the possibility that KI influenced the local environment of the ordinary hydride of KH to produce an NMR resonance that was shifted upfield relative to KH alone, controls comprising KH and a KH/KI mixture were run. The ¹H MAS NMR spectra of the green crystals, the control comprising an equal molar mixture of KH and KI, and the control KH relative to external tetramethylsilane (TMS) are shown in Figs. 14A, 14B, and 14C, respectively. Ordinary hydride ion has a resonance at 1.1 and 0.8 ppm in the KH/KI mixture and in KH alone as shown in Figs. 14B and 14C, respectively. The additional peak at 4.5–4.6 ppm is assigned to KOH that formed by reaction of KH with air.

The presence of KI does not shift the resonance of ordinary hydride. The resonance at 1.1 ppm which is assigned to ordinary hydride ion was observed in the spectrum of the green crystals as shown in Fig. 14A. The 0.8 ppm resonance could not be resolved if it was present. A large distinct upfield resonance was observed at -2.5 ppm which was not observed in either control. This upfield shifted peak is consistent with a hydride ion with a smaller radius as compared with ordinary hydride since a smaller radius increases the shielding or diamagnetism. The -2.5 ppm peak is assigned to a novel hydride ion that has a smaller radius than that of the hydride ions observed in the case of the blue crystals since the upfield shift was larger in the case of the green crystals.

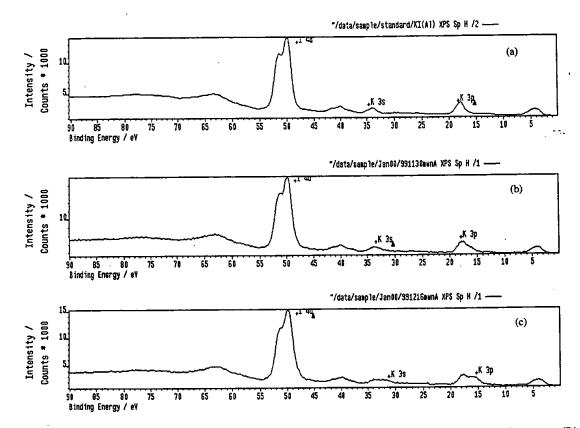


Fig. 10. (A) The 0-100 eV binding energy region of a high-resolution XPS spectrum of KI obtained on the Kratos instrument. (B) The 0-100 eV binding energy region of a high-resolution XPS spectrum of the blue crystals obtained on the Kratos instrument. (C) The 0-100 eV binding energy region of a high-resolution XPS spectrum of the green crystals obtained on the Kratos instrument.

3.4. FTIR

The FTIR spectra of KI (99.99%) was compared with that of the blue crystals. The FTIR spectra (45–3800/cm) of KI is given by Nyquist and Kagel [12]. The FTIR spectra (500–4000/cm) of the blue crystals is shown in Fig. 15. There are no vibrational bands in the 800–4000/cm region that can usually be assigned to covalent bondings. This eliminates the possibility of HI molecule embedded in KI crystals, since the H–I stretching mode is not observed at ~ 2309/cm. The FTIR spectra (500–1500/cm) of the blue crystals is shown in Fig. 16. Several bands shown in Fig. 16 such as 682, 712, 730/cm are found in the region assignable to ionic bonding or deformation vibration. The K–H vibrational band may be expected in this region. These bands are not present in pure KI. This implies that the compound of the blue crystals is ionic-like and contains different species from KI.

3.5. ESITOFMS

The positive ion ESITOFMS spectrum of the blue crystals and that of the KI control are dominated by the K^+ ion. A series of positive ions $K[KI]_n^+ m/z = (39 + 166n)$ were also

observed. In addition, KHI+ was only observed from the blue crystals.

3.6. LC/MS

No chromatographic peaks were observed of the selected ion monitoring LC/MS analysis of KI and sample solvent control.

Fig. 17A is the results of the selected ion monitoring LC/MS analysis of the blue crystals wherein the mass spectrum comprised the m/z = 204.6 ion signal. A chromatographic peak was observed at RT = 22.45 min. which corresponds to a nonpolar compound which gives rise to a $K(KI)^+$ mass fragment. The LC peak shown in Fig. 17A at RT = 2.21 min that comes out with the solvent front after injection corresponds to KI that gives rise to mass fragments K^+ and $K(KI)_x^+$.

Fig. 17B is the results of the Selected Ion Monitoring LC/MS analysis of the blue crystals wherein the mass spectrum comprised the m/z=370.6 ion signal. Chromatographic peaks were observed at RT=11.42 and 23.38 min. which correspond to a nonpolar compounds having the $K(KI)_2^+$ mass spectrum fragment. The LC peak shown in Fig. 17B

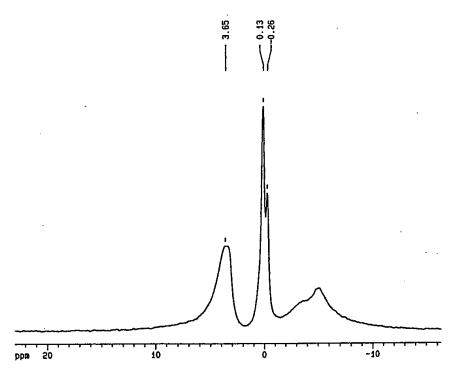


Fig. 11. The ¹H MAS NMR spectrum of the control KH relative to external tetramethylsilane (TMS).

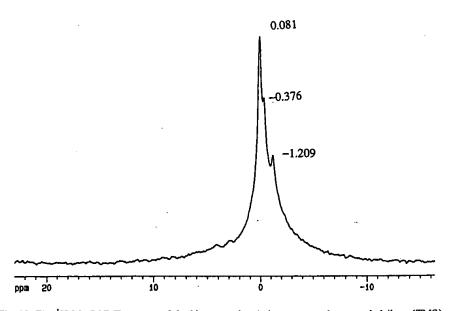


Fig. 12. The ¹H MAS NMR spectra of the blue crystals relative to external tetramethylsilane (TMS).

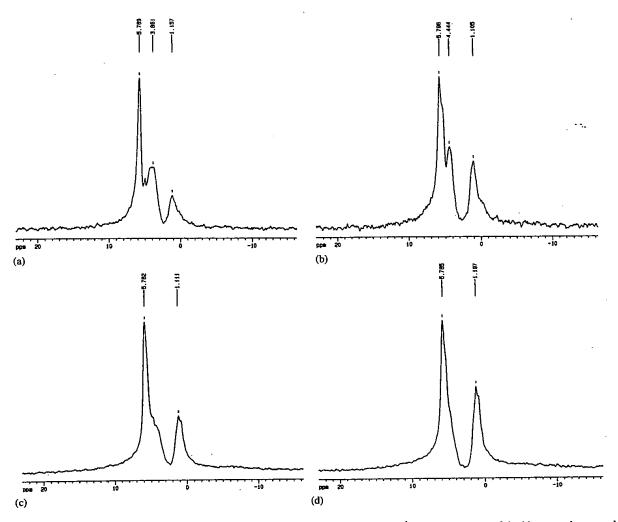


Fig. 13. (A) The ¹H NMR spectrum of the blue crystals exposed to air for 1 min. (B) The ¹H NMR spectrum of the blue crystals exposed to air for 20 min. (C) The ¹H NMR spectrum of the blue crystals exposed to air for 40 min. (D) The ¹H NMR spectrum of the blue crystals exposed to air for 60 min.

at RT = 2.21 min that comes out with the solvent front after injection corresponds to KI that gives rise to mass fragments K^+ and $K(KI)_x^+$.

The LC/MS data indicated that the blue crystal comprises a novel compound KHI which may contain two different hydride ions which gives rise to different mass fragmentation patterns. One KHI compound with a retention time of RT = 11.42 min may give rise to a $K(KI)_2^+$ mass fragment. Whereas, a second KHI compound with a retention time of about RT = 23 min may give rise to a $K(KI)_2^+$ and a $K(KI)_2^+$ mass fragment.

3.7. Gas chromatography

The gas chromatograph of the normal hydrogen gave the retention time for para hydrogen and ortho hydrogen as 22

and 24 min, respectively. Control KI and KI exposed to 500 mtorr of hydrogen at 600°C in the stainless-steel reactor for 48 h showed no hydrogen release upon heating to above 600°C with complete melting of the crystals. Dihydrino or hydrogen was released when the blue crystals were heated to above 600°C with melting which coincided with the loss of the dark blue color of these crystals.

The gas chromatograph of the dihydrino or hydrogen released from the blue crystals when the sample was heated to above 600°C with melting is shown in Fig. 18. The retention times drift with time due to conditioning of the column and absorption of contaminants. Thus, in previous studies [13], it was found that hydrogen must be present with dihydrino $H_2^*[n=\frac{1}{2};2c'=\sqrt{2}a_0/2]$ to identify the latter since the retention times are very close. But, these results confirm that the blue crystals are a hydride.

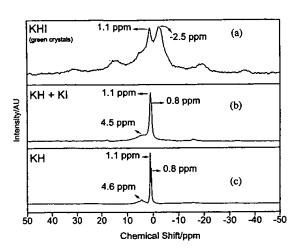


Fig. 14. (A) The ¹H MAS NMR spectrum of the green crystals relative to external tetramethylsilane (TMS). (B) The ¹H MAS NMR spectrum of the control comprising an equal molar mixture of KH and KI relative to external tetramethylsilane (TMS). (C) The ¹H MAS NMR spectrum of the control KH relative to external tetramethylsilane (TMS).

3.8. Mass spectroscopy

The dihydrino was identified by mass spectroscopy as a species with a mass to charge ratio of two (m/e=2) that has a higher ionization potential than that of normal hydrogen by recording the ion current as a function of the electron gun energy. The intensity as a function of time for masses m/e=1, 2, and 3 obtained while changing the ionization potential (IP) of the mass spectrometer from 30 to 70 eV is shown for gas released from thermal decomposition of the blue crystals and ultrapure hydrogen in Figs. 19A and 19B, respectively. Upon increasing the ionization potential from 30 to 70 eV, typically the m/e=2 ion current for the blue crystal sample increased by a factor of about 1000. Under the same pressure conditions, the m/e=2 ion current for the ultrapure hydrogen increased by a factor of less than 2.

The mass spectra (m/e=0-50) of the gases released from the thermal decomposition of the blue crystals at an ionization potential of 30 and 70 eV were recorded. As the ionization energy was increased from 30 to 70 eV m/e=4 and 5 peaks were observed that was assigned to $H_4^+(\frac{1}{2})$ and $H_5^+(\frac{1}{2})$, respectively. No helium was observed by gas chromatography as given above in gas chromatography section. The peaks serve as a signatures for the presence of dihydrino molecules.

3.9. Elemental analysis

The quantitative elemental analysis showed that the blue crystal consisted of 0.5 wt% H, 22.58 wt% K and 75.40 wt% I, or in equivalent $KI_{1.028}H_{0.865}$.

4. Discussion

The elemental analysis and the positive and negative ToF-SIMS results of the blue crystals are consistent with the proposed structure KHI. In the former analysis, the hydrogen content was determined by combustion analysis which identifies ordinary hydride. The presence of novel hydride ions present in this sample may stabilize ordinary hydride. This is consistent with the NMR of this sample shown in Fig. 12 as compared with the NMR of ordinary hydride shown in Fig. 11. Furthermore, the NMR, XPS, and LC/MS data indicate that two forms of novel hydride were present. The known compounds KI and KH have the potassium ion in a +1 state. The compound KHI is unknown and extraordinary. The implied valence of potassium is +2. A K²⁺ peak was observed in the positive ToF-SIMS which supports +2 as the valence state. High-resolution solids probe magnetic sector mass spectroscopy is in progress to confirm this state. The preliminary results are positive.

Another unusual feature of the blue crystals is their intense dark blue color. The blue color was found to be dependent on the presence of H in KHI. The intensity of the dark blue color was directly related to the amount of hydrogen which was determined by thermal decomposition with quantification by gas chromatography. The presence of some $H^-(\frac{1}{2})$ is indicated by the thermal decomposition with the identification of a hydrogen-type molecule assigned to $H_2^*[2c'=a_0/\sqrt{2}]$ with an ionization potential of 62 eV (Eq. (13)). The presence of some $H^-(1/4)$ is indicated by the new XPS peak at about 11 eV.

Potassium metal may be embedded in KI crystals wherein potassium metal ionizes into K⁺ and a free electron. This trapped free electron called an F-center may give rise to the blue color of the crystals. In contrast to other impurities such as OH⁻, the presence of ordinary hydrogen has a small influence on the emission lifetime of an F center in a similar alkali halide, KCl, which corresponds to a slight decrease in the coloration of F-centers by radiationless relaxation [14].

Coloration may occur by exposure of an alkali halide to alkali metal vapor at high temperature followed by thermal quenching. A nonhydrogen control was run under identical conditions used to synthesize the blue crystals except that helium replaced hydrogen. The resulting crystals appeared dirty brown with minimal coloring and contained inclusions of colloidal alkali metal.

An explanation of the absolutely reproducible homogeneous very dark blue coloration is required. Two mechanisms may explain the results. The catalysis of hydrogen creates an intense hydrogen plasma [1-6]. The predominant mechanism of forming F centers is by applying ionizing radiation. Thus, the extreme ultraviolet (EUV) radiation from the catalysis with the production of the hydrino hydride ions may be the source of F centers. In this case, the hydride content correlates with the color because the EUV emission corresponds to hydride production. Or, the hydrino hydride

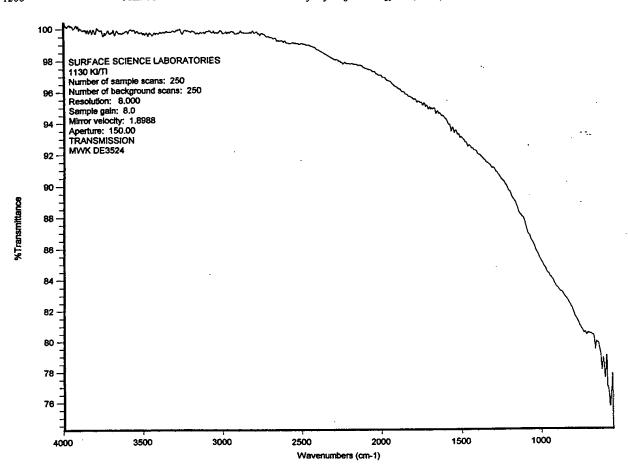


Fig. 15. The FTIR spectra (500-4000/cm) of the blue crystals.

ion assists in the formation, stability, or emission efficiency of F centers. To determine if the former explanation has merit, experiments are in progress whereby EUV emission of the gas cell reactor is correlated with the intensity of coloration of the blue crystalline product as determined by visible spectroscopy. To determine whether the latter explanation has merit, Raman spectroscopy experiments such as those of Gustin et al. [14] of the relaxation mechanism of excited F centers of the blue crystals are planned.

When the blue crystals were pulverized or exposed to air for a prolong period of about two weeks the blue color faded and white crystals formed. Investigations of these white crystals are in progress. Preliminary data indicate a hydride containing carbon dioxide, oxygen, and water-derived species. For example, the positive ToF-SIMS of the air-exposed crystals contained three new series of positive ions: $\{K[KH \ KHCO_3]_n^+ \ m/z = (39 + 140n), \ K_2OH[KH \ KHCO_3]_n^+ \ m/z = (95 + 140n),$ and $K_3O[KH \ KHCO_3]_n^+ \ m/z = (133 + 140n)\}$. These ions correspond to inorganic clusters containing novel hydride combinations (i.e. KH KHCO₃ units plus other positive fragments). The negative ion spectrum was dominated

by O⁻ and OH⁻ peaks as well as H⁻ and I⁻ peaks. A KHIO⁻ peak was present only in the negative spectrum of the air-exposed blue crystals and not in the spectrum of air-exposed KI control. The formation of the novel compound potassium hydride potassium hydrogen carbonate comprising H⁻($\frac{1}{2}$) and H⁻($\frac{1}{4}$) is consistent with the changes in the NMR observed with air exposure of the blue crystals. KH KHCO₃ has been made in an electrolytic cell reactor wherein potassium ions served as the catalysts according to Eqs. (6)-(8) [15]. KH KHCO₃ has also been synthesized in a gas cell energy reactor wherein potassium ions served as the catalyst according to Eqs. (3)-(5) [16,17].

An explanation for the color of the green crystals may be a charge transfer transition due to the presence of a K²⁺ in the crystal which is stabilized by a higher binding energy hydride ion relative to the blue crystals. The ToF-SIMS, XPS, and NMR results support this explanation.

The hydride peak of the green crystals was larger than the iodide peak; whereas, the hydride peak of the blue crystals was about equivalent to the iodide peak. These results are consistent with the formation of a higher hydride content or a higher hydride ion yield in the green crystals which may



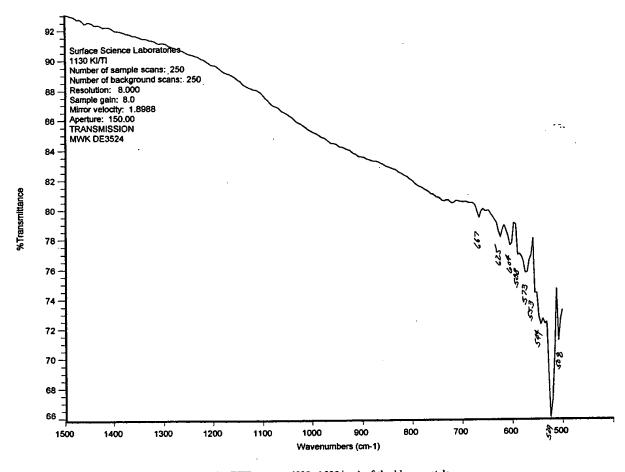


Fig. 16. The FTIR spectra (500-1500/cm) of the blue crystals.

indicate that a higher binding energy hydride was present in the green crystals.

The XPS data of the core levels clearly indicate a change in the electronic structure and different bonding in KHI relative to that in the corresponding KI. This binding influences the metal core level with little perturbation of the halogen core level. Comparing the alterations in the K core levels versus the I core level indicates that the lower-energy hydrogen species binds to the metal center of KI. An additional spin-orbit splitting component had to be added to each potassium iodo hydride in order to obtain a good curve fit of the K2p spectra. In each case, the second component of spin-orbit splitting is assigned to the formation of the alkali metal halido hydride, KHI. The presence of the novel hydride ion shifts the K2p peaks to lower binding energies relative to the corresponding peaks of KI. It strongly suggests the formation of a novel metal hydride which is consistent with the supporting data provided by XPS given above and NMR, ToF-SIMS, and gas chromatography/mass spectroscopy given in the respective sections. The change in electronic structure is greatest with the green crystals which indicates that a higher binding energy hydride is formed by running the catalysis reaction at lower hydrogen pressure.

The 0-100 eV binding energy region of a high-resolution XPS spectra of the blue and green crystals indicate the presence of the hydride ions $H^-(\frac{1}{2})$ and $H^-(\frac{1}{4})$ in the case of the blue crystals and the presence of the higher binding energy hydride ion $H^-(\frac{1}{6})$ in the case of the green crystals.

The upfield peak in the NMR spectrum of the green crystals at -2.5 ppm was assigned to a novel hydride ion that has a smaller radius than that of the hydride ions observed in the case of the blue crystals corresponding to resonances at -0.376 and -1.209 ppm since the upfield shift was larger in the case of the green crystals. A smaller radius corresponds to a higher binding energy.

5. Conclusions

The ToF-SIMS, XPS, NMR, FTIR, ESITOFMS, LC/MS, thermal decomposition with analysis by GC, and MS, and

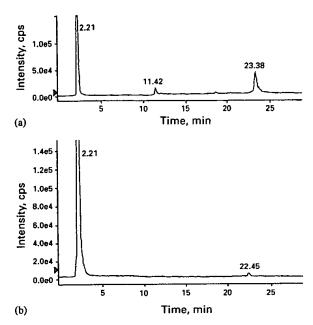


Fig. 17. (A) The results of the selected ion monitoring LC/MS analysis of the blue crystals wherein the mass spectrum comprised the m/z = 204.6 ion signal. (B) The results of the selected ion monitoring LC/MS analysis of the blue crystals wherein the mass spectrum comprised the m/z = 370.6 ion signal.

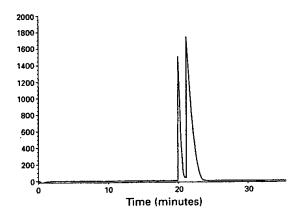


Fig. 18. The gas chromatograph of the dihydrino or hydrogen released from the blue crystals when the sample was heated to above 600°C with melting.

elemental analysis results confirm the identification of KHI having hydride ions, $H^-(\frac{1}{2})$, $H^-(\frac{1}{4})$, and $H^-(\frac{1}{6})$. Two forms of hydride ion $(H^-(\frac{1}{2})$ and $H^-(\frac{1}{4}))$ may be formed according to Eqs. (5), (8), and (9) which is supported by the XPS, NMR, and LC/MS data of the blue crystals. The thermal decomposition with mass spectroscopic analysis indicates that at least $H^-(\frac{1}{2})$ is present in KHI of the blue crystals.

The ToF-SIMS results of a more intense hydride peak, the NMR results of a greater upfield shifted peak, and the XPS results that the change in electronic structure was great-

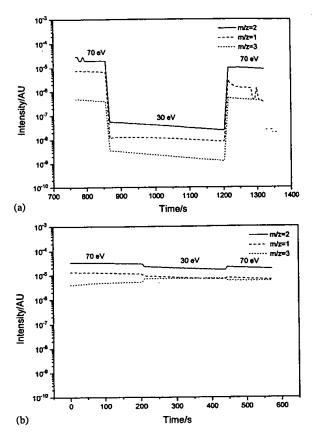


Fig. 19. (A) The intensity as a function of time for masses m/e=1, 2, and 3 obtained while changing the ionization potential (IP) of the mass spectrometer from 30 to 70 eV for gas released from thermal decomposition of the blue crystals. (B) The intensity as a function of time for masses m/e=1, 2, and 3 obtained while changing the ionization potential (IP) of the mass spectrometer from 30 to 70 eV for ultrapure hydrogen.

est with the green crystals relative to the blue crystals indicate that a higher binding energy hydride was formed by running the catalysis reaction at lower hydrogen pressure. The XPS results of the low binding energy region are consistent with the presence of $H^-(\frac{1}{6})$ in the green crystals. This product is predicted by an autocatalysis reaction of two $H(\frac{1}{4})$ atoms which has been confirmed by extreme ultraviolet spectroscopy [3].

The chemical structure and properties of KHI having a hydride ion with a high binding energy are indicative of a new field of hydride chemistry. The novel hydride ion may combine with other cations such as other alkali cations and alkaline earth, rare earth, and transition element cations. Numerous novel compounds may be synthesized with extraordinary properties relative to the corresponding compounds having ordinary hydride ions [15–19]. These novel compounds may have a breath of applications.



References

- [1] Mills R, Dong J, Lu Y. Observation of extreme ultraviolet hydrogen emission from incandescently heated hydrogen gas with certain catalysts. 1999 Pacific Conference on Chemistry and Spectroscopy and the 35th ACS Western Regional Meeting, Ontario Convention Center, California, October 6-8, 1999.
- [2] Mills R, Dong J, Lu Y. Observation of extreme ultraviolet hydrogen emission from incandescently heated hydrogen gas with certain catalysts. Int J Hydrogen Energy, 2000;25: 919-43.
- [3] Mills R. Observation of extreme ultraviolet hydrogen and hydrino emission from hydrogen-KI plasmas produced by a hollow cathode discharge. Int J Hydrogen Energy, submitted.
- [4] Mills R. Temporal behavior of light-emission in the visible —spectral range from a Ti-K2CO3-H-Cell. Int J Hydrogen Energy, in press.
- [5] Mills R, Lu Y, Onuma T. Formation of a hydrogen plasma from an incandescently heated hydrogen-potassium gas mixture and plasma decay upon removal of heater power. Int J Hydrogen Energy, submitted.
- [6] Mills R, Nansteel M, Lu Y. Observation of extreme ultraviolet hydrogen emission from incandescently heated hydrogen gas with strontium that produced an optically measured power balance that was 4000 times the control. Int J Hydrogen Energy, in press.
- [7] Mills R. The grand unified theory of classical quantum mechanics, January 2000 ed. Cranbury, New Jersey: BlackLight Power, Inc., Distributed by Amazon.com.

- [8] Linde DR. CRC handbook of chemistry and physics, 78th ed. Boca Raton, FL: CRC Press, 1997. p. 10-214-10-216.
- [9] Microsc Microanal Microstruct 1992;3:1.
- [10] For recent specifications see PHI Trift II, ToF-SIMS Technical Brochure, Eden Prairie, MN 55344, 1999.
- [11] Briggs D, Seah MP. editors. Ion and neutral spectroscopy. In Practical surface analysis, vol. 2. 2nd ed. New York: Wiley, 1992.
- [12] Nyquist RA, Kagel RO. Infrared spectra of inorganic compounds. New York: Academic Press, 1971. p. 464-5.
- [13] Mills R. NOVEL HYDRIDE COMPOUNDS. PCT US98/14029 filed on July 7, 1998.
- [14] E. Gustin, M. Leblans, A. Bouwen, D. Shoemaker, Phys Rev B 49 (2) (1994) 916-26.
- [15] R. Mills, Novel inorganic hydride, Int J Hydrogen Energy 25 (2000) 669-83.
- [16] Mills R, He J, Dhandapani B. Novel hydrogen compounds. 1999 Pacific Conference on Chemistry and Spectroscopy and the 35th ACS Western Regional Meeting, Ontario Convention Center, California, October 6-8, 1999.
- [17] Mills R, Dhandapani B, Nansteel M, He J. Synthesis and characterization of novel hydride compounds. Int J Hydrogen Energy, in press.
- [18] R. Mills, Novel hydrogen compounds from a potassium carbonate electrolytic cell, Fusion Technol 37 (2) (2000) 157-82.
- [19] Mills R. Highly stable novel inorganic hydrides. Int J Inorganic Mater., submitted.

THIS PAGE BLANK (USPTO)



PERGAMON

International Journal of

International Journal of Hydrogen Energy 25 (2000) 669-683

Novel inorganic hydride

Randell L. Mills*

BlackLight Power, Inc., 493 Old Trenton Road, Cranbury, NJ 08512, USA

Abstract

A novel inorganic hydride compound KH KHCO₃ which is stable in water and comprises a high binding energy hydride ion was isolated following the electrolysis of a K₂CO₃ electrolyte. Inorganic hydride clusters K[KH KHCO₃]¹, were identified by Time of Flight Secondary Ion Mass Spectroscopy. Moreover, the existence of a novel hydride ion has been determined using X-ray photoelectron spectroscopy, and proton nuclear magnetic resonance spectroscopy. Hydride ions with increased binding energies may be the basis of a high voltage battery for electric vehicles. © 2000 International Association for Hydrogen Energy. Published by Elsevier Science Ltd. All rights reserved.

1. Introduction

Evidence of the changing landscape for automobiles can be found in the recent increase in research into the next generation of automobiles. But, the fact that there is no clear front-runner in the technological race to replace the internal combustion (IC) engine can be attested to by the divergent approaches taken by the major automobile companies. Programs include various approaches to hybrid vehicles, alternative fueled vehicles such as dual-fired engines that can run on gasoline or compressed natural gas, and a natural gasfired engine. Serious efforts are also being put into a number of alternative fuels such as ethanol, methanol, propane, and reformulated gasoline. To date, the most favored approach is an electric vehicle based on fuel cell technology or advanced battery technology such as sodium nickel chloride, nickel-metal hydride, and lithium-ion batteries [1]. Although billions of dollars are being spent to develop an alternative to the IC engine, there is no technology in sight that can match the specifications of an IC engine system [2].

Fuel cells have advantages over the IC engine because they convert hydrogen to water at about 70% efficiency when running at about 20% below peak output [3]. But, hydrogen is difficult and dangerous to store. Cryogenic, compressed gas, and metal hydride storage are the main options. In the case of cryogenic storage, liquefaction of hydrogen requires an amount of electricity which is at least 30% of the lower heating value of liquid hydrogen [4]. Compressed hydrogen, and metal hydride storage are less viable since the former requires an unacceptable volume, and the latter is heavy and has difficulties supplying hydrogen to match a load such as a fuel cell [4]. The main challenge with hydrogen as a replacement to gasoline is that a hydrogen production and refueling infrastructure would have to be built. Hydrogen may be obtained by reforming fossil fuels. However, in practice fuel cell vehicles would probably achieve only 10-45% efficiency because the process of reforming fossil fuel into hydrogen and carbon dioxide requires energy [3]. Presently, fuel cells are also impractical due to their high cost as well as the lack of inexpensive reforming technology [5].

0360-3199/00/\$20.00 © 2000 International Association for Hydrogen Energy. Published by Elsevier Science Ltd. All rights reserved. PII: S0360-3199(99)00076-2

^{*} Tel.: +1-609-490-1040; fax: +1-609-490-1066. E-mail address: rmills@blacklightpower.com (R.L. Mills).

R.L. Mills | Inter-

In contrast, batteries are attractive because they can be recharged wherever electricity exists, which is ubiquitous. The cost of mobile energy from a battery powered car may be less than that from a fossil fuel powered car. For example, the cost of energy per mile of a nickel metal hydride battery powered car is 25% of that of a IC powered car [6]. However, current battery technology is trying to compete with something that it has little chance of imitating. Whichever battery technology proves to be superior, no known electric power plant will match the versatility and power of an internal combustion engine. A typical IC engine yields more than 10,000 W h kg⁻¹ of energy, while the most promising battery technology yields 200 W h kg⁻¹ [2].

A high voltage battery would have the advantages of much greater power and much higher energy density. The limitations of battery chemistry may be attributed to the binding energy of the anion of the oxidant. For example, the 2 V provided by a lead acid cell is limited by the 1.46 eV electron affinity of the oxide anion of the oxidant PbO2. An increase in the oxidation state of lead such as $Pb^{2+} \rightarrow Pb^{3+} \rightarrow Pb^{4+}$ is possible in a plasma. Further oxidation of lead could also be achieved in theory by electrochemical charging. However, higher lead oxidation states are not achievable because the oxide anion required to form a neutral compound would undergo oxidation by the highly oxidized lead cation. An anion with an extraordinary binding energy is required for a high voltage battery. One of the highest voltage batteries known is the lithium fluoride battery with a voltage of about 6 V. The voltage can be attributed to the higher binding energy of the fluoride ion. The electron affinity of halogens increases from the bottom of the Group VII elements to the top. A hydride ion may be considered a halide since it possesses the same electronic structure, and, according to the binding energy trend, it should have a high binding energy. However, the binding energy is only 0.75 eV which is much lower than the 3.4 eV binding energy of a fluoride ion.

An inorganic hydride compound having the formula KH KHCO₃ was isolated from an aqueous K₂CO₃ electrolytic cell reactor. Inorganic hydride clusters K[KH KHCO₃]⁺ were identified by Time of Flight Secondary Ion Mass Spectroscopy (ToF-SIMS). A hydride ion with a binding energy of 22.8 eV has been observed by X-ray photoelectron spectroscopy (XPS) having upfield shifted solid state magic-angle spinning proton nuclear magnetic resonance (¹H MAS NMR) peaks. Moreover, a polymeric structure is indicated by Fourier transform infrared (FTIR) spectroscopy. The discovery of a novel hydride ion with a high binding energy has implications for a new field of hydride chemistry with applications such as a high voltage battery. Such extremely stable hydride ions may stabilize positively charged ions in an unprecedented highly charged state. A battery may be possible having projected specifications that surpass those of the internal combustion engine.

Hydride ions having extraordinary binding energies may stabilize a cation M^{x+} in an extraordinarily high oxidation state such as +2 in the case of lithium. Thus, these hydride ions may be used as the basis of a high voltage battery of a rocking chair design wherein the hydride ion moves back and forth between the cathode and anode half cells during discharge and charge cycles. Exemplary reactions for a cation M^{x+} are:

Cathode reaction

$$MH_x + e^- \rightarrow MH_{x-1} + H^- \tag{1}$$

Anode reaction

$$MH_{x-2} + H^- \rightarrow MH_{x-1} + e^-$$
 (2)

Overall reaction

$$MH_x + MH_{x-2} \rightarrow 2MH_{x-1} \tag{3}$$

2. Experimental

2.1. Synthesis

An electrolytic cell comprising a K2CO3 electrolyte, a nickel wire cathode, and platinized titanium anodes was used to synthesize the KH KHCO3 sample [7]. Briefly, the cell vessel comprised a 10 gallon (33" x 15") Nalgene tank. An outer cathode comprised 5000 m of 0.5 mm diameter clean, cold drawn nickel wire (Ni 200 0.0197", HTN36NOAG1, A-1 Wire Tech, Inc., Rockford, Illinois, 61109) wound on a polyethylene cylindrical support. A central cathode comprised 5000 m of the nickel wire wound in a toroidal shape. The central cathode was inserted into a cylindrical, perforated polyethylene container that was placed inside the outer cathode with an anode array between the central and outer cathodes. The anode comprised an array of 15 platinized titanium anodes (ten Engelhard Pt/Ti mesh $1.6" \times 8"$ with one $3/4" \times 7"$ stem attached to the 1.6" side plated with 100 U series 3000; and five Engelhard 1" diameter × 8" length titanium tubes with one $3/4'' \times 7''$ stem affixed to the interior of one end and plated with 100 U Pt series 3000). Before assembly, the anode array was cleaned in 3 M HCl for 5 min and rinsed with distilled water. The cathode was cleaned by placing it in a tank of 0.57 M K₂CO₃/3% H₂O₂ for 6 h and then rinsing it with distilled water. The anode was placed in the support between the central and outer cathodes, and the electrode assembly was placed in the tank containing electrolyte. The electrolyte solution comprised 28 l of 0.57 M K_2CO_3 (Alfa K_2CO_3 99%). Electrolysis was performed at 20 A constant current with a constant current ($\pm 0.02\%$) power supply.

Samples were isolated from the electrolytic cell by concentrating the K_2CO_3 electrolyte about six-fold using a rotary evaporator at 50°C until a yellow-white polymeric suspension formed. Precipitated crystals of the suspension were then grown over 3 weeks by allowing the saturated solution to stand in a sealed round bottom flask at 25°C. Control samples utilized in the following experiments contained K_2CO_3

(99%), KHCO₃ (99.99%), HNO₃ (99.99%), and KH (99%).

2.2. ToF-SIMS characterization

The crystalline samples were sprinkled onto the surface of double-sided adhesive tapes and characterized using a Physical Electronics TFS-2000 ToF-SIMS instrument. The primary ion gun utilized a $^{69}\mathrm{Ga}^+$ liquid metal source. In order to remove surface contaminants and expose a fresh surface, the samples were sputter cleaned for 30 s using a 40 $\mu\mathrm{m}\times40~\mu\mathrm{m}$ raster.

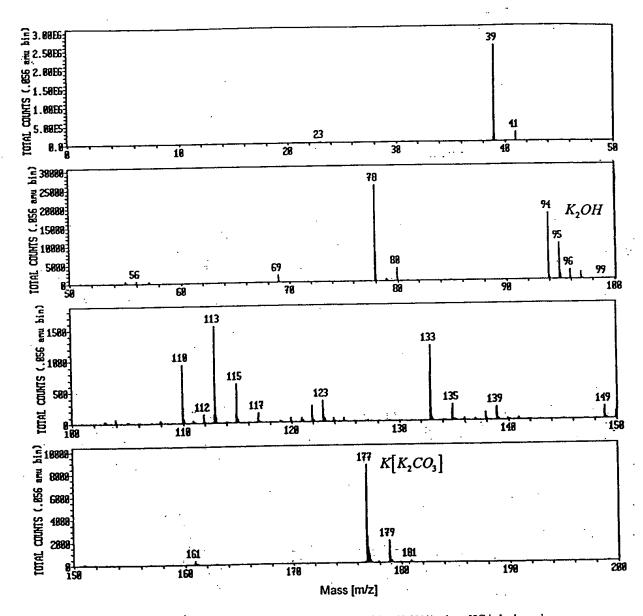


Fig. 1. The positive ToF-SIMS spectrum (m/e = 0-200) of KHCO₃ (99.99%) where HC is hydrocarbon.

The aperture setting was 3, and the ion current was 600 pA resulting in a total ion dose of 10¹⁵ ions/cm².

During acquisition, the ion gun was operated using a bunched (pulse width 4 ns bunched to 1 ns) 15 kV beam [8,9]. The total ion dose was 10¹² ions/cm². Charge neutralization was active, and the post accelerating voltage was 8000 V. Three different regions on each sample of (12 µm)², (18 µm)², and (25 µm)² were analyzed. The positive and negative SIMS spectra were acquired. Representative post sputtering data is reported.

2.3. XPS characterization

A series of XPS analyses were made on the crystalline samples using a Scienta 300 XPS Spectrometer. The fixed analyzer transmission mode and the sweep acquisition mode were used. The step energy in the survey scan was 0.5 eV, and the step energy in the high resolution scan was 0.15 eV. In the survey scan, the time per step was 0.4 s, and the number of sweeps was 4. In the high resolution scan, the time per step was 0.3 s, and the number of sweeps

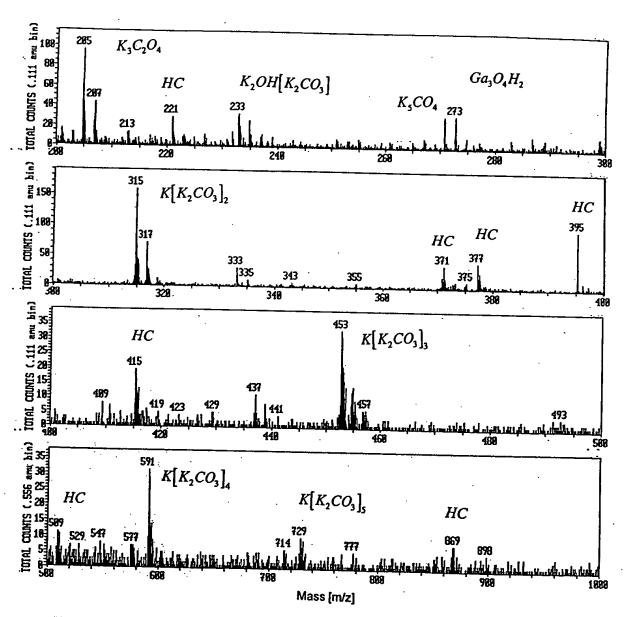


Fig. 2. The positive ToF-SIMS spectrum (m/e = 200-1000) of KHCO₃ (99.99%) where HC is hydrocarbon.





was 30. C is at 284.6 eV was used as the internal standard.

2.4. NMR spectroscopy

¹H MAS NMR was performed on the crystalline

samples. The data were obtained on a custom built spectrometer operating with a Nicolet 1280 computer. Final pulse generation was from a tuned Henry radio amplifier. The ¹H NMR frequency was 270.6196 MHz. A 2 μs pulse corresponding to a 15° pulse length and a 3-s recycle delay were used. The window was ±31 kHz. The spin speed was 4.5 kHz. The number of scans was

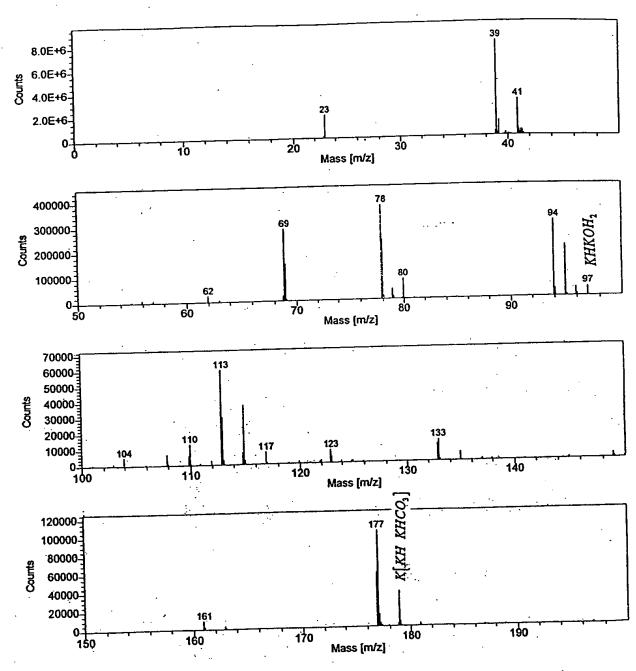


Fig. 3. The positive ToF-SIMS spectrum (m/e = 0-200) of an electrolytic cell sample where HC is hydrocarbon.

And the second s





Table 1
The respective hydride compounds and mass assignments (m/z) of the positive ToF-SIMS of an electrolytic cell sample

Hydrino hydride compound or fragment	Nominal mass m/z	Observed m/z	Calculated m/z	Difference between observed and calculated m/z
	40	39.97	39.971535	0.0015
KH	79	78.940	78.935245	0.004
K ₂ H	80	79.942	79.94307	0.001
(KH) ₂	97	96.945	96.945805	0.0008
KHKOH ₂	121	120.925	120.92243	0.003
$KH_2(KH)_2$	124	123.925	123.93289	0.008
KH KHCO₂	145	144.92	144.930535	0.010
KH ₂ KHO₄	151	150.90	150.8966	0.003
K(KOH) ₂	152	151.90	151.904425	0.004
KH(KOH) ₂	153	152.90	152.91225	0.012
KH ₂ (KOH) ₂	179	178.89	178.8915	0.001
K[KH KHCO ₃]	187	186.87	186.873225	0.003
KCO(KH) ₃	191	190.87	190.868135	0.002
K ₂ OHKHKOH	193	192.89	192.883785	0.006
KH ₂ KOHKHKOH	205	204.92	204.92828	0.008
K ₃ O(H ₂ O) ₄		234.86	234.857955	0.002
K ₂ OH[KH KHCO ₃]	235	256.89	256.8868	0.003
K[H ₂ CO ₄ KH KHCO ₃]	257 273	272.81	272.81384	0.004
K ₃ O[KH KHCO ₃]	303	302.88	302.89227	0.012
[KH ₂ CO ₃] ₃		316.80	316.80366	0.004
K[KH KHCO ₃ K ₂ CO ₃]	317 319	318.82	318.81931	0.001
K[KH KHCO ₃] ₂	329	328.80	328.7933	0.007
KH ₂ [KH KOH] ₃	337	336.81	336.82987	0.020
KOH ₂ [KH KHCO ₃] ₂		350.81	350.80913	0.001
KH KO, [KH KHCO][KHCO]	351 357	356.77	356.775195	0.005
KKHK ₂ CO ₃ [KH KHCO ₃]	359	358.78	358.790845	0.011
KKH[KH KHCO₃]₂		374.78	374.785755	0.005
K,OH[KH KHCO ₃] ₂	375 387	386.75	386.76238	0.012
K ₂ OH[KHKOH] ₂ [KHCO ₃]		404.79	404.80933	0.019
KKH KHTKH KHCO ³ P	405	410.75	410.72599	0.024
K ₃ O[K ₂ CO ₃] [KH KHCO ₃] or K[KH KOH(K ₂ CO ₃) ₂]	411 413	412.74	412.74164	0.002
K ₃ O[KH KHCO ₃] ₂	413	412.71		
K KH KOH (KH KHCO ₃) ₂	415	414.74	414.75729	0.017
	437	436.81	436.786135	0.024
KH2OKHCO3 [KH KHCO3]2	442	441.74	441.744375	0.004
KKHKCO2[KH KHCO3]2	459	458.72	458.74711	0.027
KIKH KHCO-P	469	468.70	468.708085	0.008
H[KH KOH] ₂ [K ₂ CO ₃] ₂ or K ₄ O ₂ H[KH KHCO ₃] ₂	477	476.72	476.744655	0.025
K[K ₂ CO ₃][KHCO ₃] ₃		514.72	514.713555	0.006
K ₂ OH[KH KHCO ₃] ₃	515	552.67	552.66944	0.001
K ₃ O(KH KHCO ₃) ₃	553 500	598.65	598.67491	0.025
K[KH KHCO ₃] ₄	599	654.65	654.641355	0.009
K ₂ OH[KH KHCO ₃] ₄	655	692.60	692.59724	0.003
K ₃ O[KH KHCO ₃] ₄	693	738.65	738.60271	0.047
KIKH KHCO3}5	739	832.50	832.52504	0.025
K ₃ O[KH KHCO ₃] ₅	833	832.50 878.50	878.53051	0.031
KIKH KHCO3%	879	972.50	972.45284	0.047
K ₃ O[KH KHCO ₃] ₆	973	912.30	712.43204	

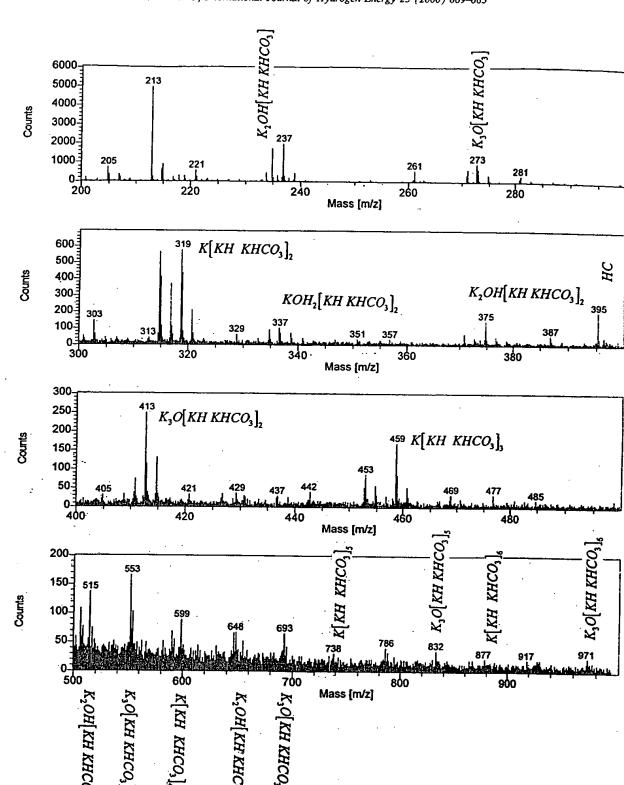


Fig. 4. The positive ToF-SIMS spectrum (m/e = 200-1000) of an electrolytic cell sample where HC is hydrocarbon.

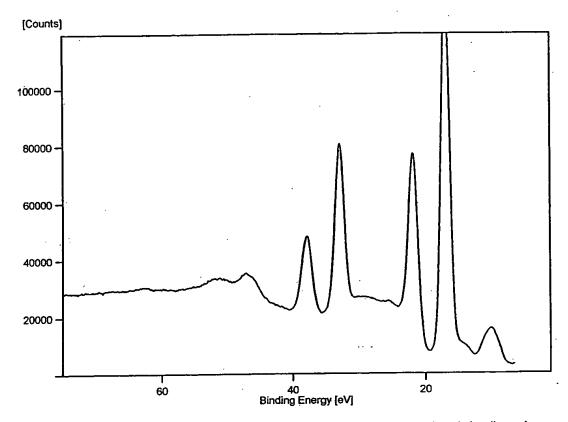


Fig. 5. The 0-80 eV binding energy region of a high resolution XPS spectrum of an electrolytic cell sample.

1000. Chemical shifts were referenced to external TMS. The offset was 1527.12 Hz, and the magnetic flux was 6.357 T.

2.5. FTIR spectroscopy

Samples were transferred to an infrared transmitting substrate and analyzed by FTIR spectroscopy using a Nicolet Magna 550 FTIR Spectrometer with a NicPlan FTIR microscope. The number of scans was 500 for both the sample and background. The number of background scans was 500. The resolution was 8.000. A dry air purge was applied.

3. Results and discussion

3.1. ToF-SIMS

The positive ToF-SIMS spectrum obtained from the KHCO₃ control is shown in Figs. 1 and 2. In addition, the positive ToF-SIMS of a sample isolated from the electrolytic cell is shown in Figs. 3 and 4. The respective hydride compounds and mass assignments appear in Table 1. In both the control and electrolytic

samples, the positive ion spectrum are dominated by the K⁺ ion. Two series of positive ions K[K₂CO₃]_n⁺ m/z = (39 + 138n), K₂OH[K₂CO₃]_n⁺ m/z = (95 + 138n)) are observed in the KHCO₃ control. Other peaks containing potassium include KC⁺, K_xO_y⁺, K_xO_yH_z⁺, KCO⁺, and K₂⁺. However, in the electrolytic cell sample, three new series of positive ions are observed at K[KH KHCO₃]_n⁺ m/z = (39 + 140n), K₂OH[KH KHCO₃]_n⁺, m/z = (133 + 140n)}. These ions correspond to inorganic clusters containing novel hydride combinations (i.e. KH KHCO₃ units plus other positive fragments).

The comparison of the positive ToF-SIMS spectrum of the KHCO₃ control with the electrolytic cell sample shown in Figs. 1 and 2, and 3 and 4, respectively, demonstrates that the $^{39}K^+$ peak of the electrolytic cell sample may saturate the detector and give rise to a peak that is atypical of the natural abundance of ^{41}K . The natural abundance of ^{41}K is 6.7%; whereas, the observed ^{41}K abundance from the electrolytic cell sample is 57%. This atypical abundance was also confirmed using ESIToFMS [10]. The high resolution mass assignment of the m/z = 41 peak of the electrolytic sample was consistent with ^{41}K , and no peak was observed at m/z = 42.98 ruling out $^{41}KH_2^+$. Moreover,





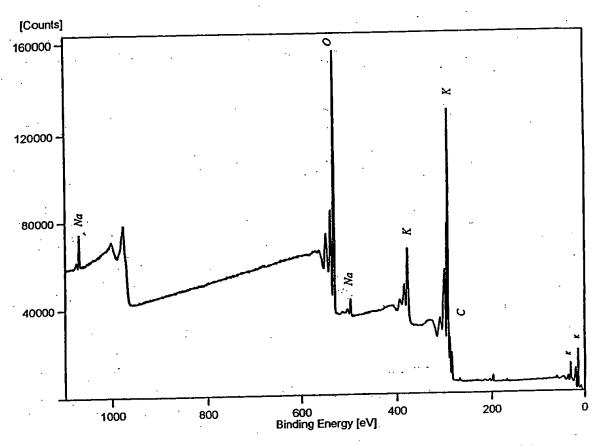


Fig. 6. The XPS survey spectrum of an electrolytic cell sample with the primary elements identified.

the natural abundance of ⁴¹K was observed in the positive ToF-SIMS spectra of KHCO₃, KNO₃, and KI standards that were obtained with an ion current such that the ³⁹K peak intensity was an order of magnitude higher than that given for the electrolytic cell sample. The saturation of the ³⁹K peak of the positive ToF-SIMS spectrum by the electrolytic cell sample is indicative of a unique crystalline matrix [11].

The negative ion ToF-SIMS of the electrolytic cell sample was dominated by H⁻, and much smaller O⁻, and OH⁻ peaks. A series of nonhydride containing negative ions $KCO_3[K_2CO_3]_n^-$ m/z = (99 + 138n) was also present which implies that H₂ was eliminated from KH KHCO₃ during fragmentation of the compound KH KHCO₃.

3.2. XPS

A survey spectrum was obtained over the region $E_b = 0-1200$ eV. The primary element peaks allowed for the determination of all of the elements present in each sample isolated from the K_2CO_3 electrolyte. The survey spectrum also detected shifts in the binding

energies of potassium and oxygen which had implications as to the identity of the compound containing the elements. A high resolution XPS spectrum was also obtained of the low binding energy region ($E_b = 0$ – 100 eV) to determine the presence of novel XPS peaks.

No elements were present in the survey scans which can be assigned to peaks in the low binding energy region with the exception of a small variable contaminant of sodium at 63 and 31 eV, potassium at 16.2 and 32.1 eV, and oxygen at 23 eV. Accordingly, any other peaks in this region must be due to novel species. The K 3s and K 3p are shown in Fig. 5 at 16.2 and 32.1 eV, respectively. A weak Na 2s is observed at 63 eV. The O 2s which is weak compared to the potassium peaks of K₂CO₃ is typically present at 23 eV, but is broad or obscured in Fig. 5. Peaks centered at 22.8 and 38.8 eV which do not correspond to any other primary element peaks were observed. The intensity and shift match shifted K 3s and K 3p. Hydrogen is the only element which does not have primary element peaks; thus, it is the only candidate to produce the shifted peaks. These peaks may be shifted by a highly binding hydride ion with a binding energy of

Table 2
The binding energies of XPS peaks of K₂CO₃ and an electrolytic cell sample

XPS	C 1s (eV)	O ls (eV)	K 3p (eV)	K 3s (eV)	K 2p _{3/2} (eV)	K 2p _{1/2} (eV)	K 2s (eV)
K₂CO₃	288.4	532.0	18	34	292.4	295.2	376.7
Electrolytic	288.5	530.4	16.2	32.1	291.5	293.7	376.6
Cell		537.5	22.8	38.8	298.5	300.4	382.6
Sample		547.8					
Min	280.5	529			292		
Max	293	535			293.2		

22.8 eV given in the Appendix that bonds to potassium K 3p and shifts the peak to this energy. In this case, the K 3s is similarly shifted. These peaks were not present in the case of the XPS of matching samples iso-

lated from an identical electrolytic cell except that Na_2CO_3 replaced K_2CO_3 as the electrolyte.

XPS further confirmed the ToF-SIMS data by showing shifts of the primary elements. The splitting of the principal peaks of the survey XPS spectrum is indicative of multiple forms of bonding involving the atom of each split peak. For example, the XPS survey spectrum shown in Fig. 6 shows extraordinary potassium and oxygen peak shifts. All of the potassium primary peaks are shifted to about the same extent as that of the K 3s and K 3p. In addition, extraordinary O 1s peaks of the electrolytic cell sample were observed at 537.5 and 547.8 eV; whereas, a single O is was observed in the XPS spectrum of K2CO3 at 532.0 eV. The results are not due to uniform charging as the internal standard C 1s remains the same at 284.6 eV. The results are not due to differential charging because the peak shapes of carbon and oxygen are normal, and no tailing of these peaks was observed. The binding

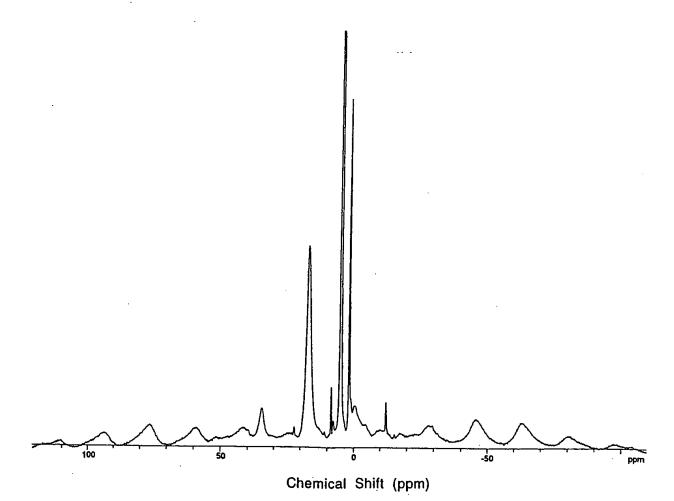


Fig. 7. The magic angle spinning proton NMR spectrum of an electrolytic cell sample.

Table 3
The NMR peaks of an electrolytic cell sample with their assignments

Peak at shift (ppm)	Assignment
+ 34.54	Side band of +17.163 peak
+ 22.27	Side band of +5.066 peak
+ 17.163	КН КНСО₃
+ 10.91	КН КНСО3
+ 8.456	KH KHCO ₃
+ 7.50	KH KHCO ₃
+ 5.066	H ₂ O
+ 1.830	KH KHCO ₃
	Side band of +17.163 peak
-0.59	KH KHCO ₃ *
12.05 15.45	KH KHCO3

 $^{^{}a}$ A small shoulder is observed on the -12.05 peak which is the side band of the +5.066 peak.

energies of the K₂CO₃ control and an electrolytic cell sample are shown in Table 2. The range of binding energies from the literature [12] for the peaks of interest are given in the final row of Table 2. The K 3p, K 3s, K 2p_{3/2}, K 2p_{1/2}, and K 2s XPS peaks and the O 1s XPS peaks shifted to an extent greater than those of known compounds may correspond to and identify KH KHCO₃.

3.3. NMR

The signal intensities of the ¹H MAS NMR spectrum of the K₂CO₃ reference were relatively low. It contained a water peak at 1.208 ppm, a peak at 5.604 ppm, and very broad weak peaks at 13.2 and 16.3 ppm. The ¹H MAS NMR spectrum of the KHCO₃ reference contained a large peak at 4.745 with a small shoulder at 5.150 ppm, a broad peak at 13.203 ppm, and small peak at 1.2 ppm.

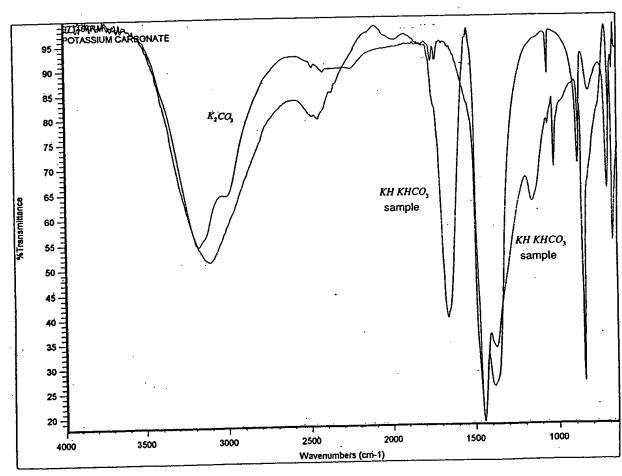


Fig. 8. The overlap FTIR spectrum of an electrolytic cell sample and the FTIR spectrum of the reference potassium carbonate.



The 1H MAS NMR spectra of an electrolytic cell sample is shown in Fig. 7. The peak assignments are given in Table 3. The reproducible peaks assigned to KH KHCO3 in Table 3 were not present in the controls except for the peak assigned to water at +5.066 ppm. The novel peaks could not be assigned to hydrocarbons. Hydrocarbons were not present in the electrolytic cell sample based on the ToF-SIMS spectrum and FTIR spectra which were also obtained (see below). The novel peaks without identifying assignment are consistent with KH KHCO3. The NMR peak of the hydride ion of potassium hydride was observed at -0.376 ppm relative to TMS. The upfield peaks of Fig. 7 are assigned to novel hydride ion (KH-) in different environments. The down field peaks are assigned to the proton of the potassium hydrogen carbonate species in different chemical environments (-KHCO₃).

3.4. FTIR

The FTIR spectra of K₂CO₃ (99%) and KHCO₃ (99.99%) were compared with that of an electrolytic cell sample. A spectrum of a mixture of the bicarbonate and the carbonate was produced by digitally adding the two reference spectra. The two standards alone and the mixed standards were compared with that of the electrolytic cell sample. From the comparison, it was determined that the electrolytic cell sample contained potassium carbonate but did not contain potassium bicarbonate. The unknown component could be a bicarbonate other than potassium bicarbonate. The spectrum of potassium carbonate was digitally subtracted from the spectrum of the electrolytic cell sample. Several bands were observed including bands in the 1400-1600 cm⁻¹ region. Some organic nitrogen compounds (e.g. acrylamides, pyrolidinones) have strong bands in the region 1660 cm⁻¹ [13]. However, the lack of any detectable C=H bands (≈2800-3000 cm⁻¹) and the bands present in the 700-1100 cm⁻¹ region indicate an inorganic material [14]. Peaks not assignable to potassium carbonate were observed at 3294, 3077, 2883, 1100, 2450, 1660, 1500, 1456, 1423, 1300, 1154, 1023, 846, 761, and 669 cm⁻¹.

The overlap FTIR spectrum of the electrolytic cell sample and the FTIR spectrum of the reference potassium carbonate appears in Fig. 8. In the 700-2500 cm⁻¹ region, the peaks of the electrolytic cell sample closely resemble those of potassium carbonate, but they are shifted about 50 cm⁻¹ to lower frequencies. The shifts are similar to those observed by replacing potassium (K₂CO₃) with rubidium (Rb₂CO₃) as demonstrated by comparing their IR spectra [15]. The shifted peaks may be explained by a polymeric structure for the com-

pound KH KHCO₃ identified by ToF-SIMS, XPS, and NMR.

3.5. Further analytical tests

X-ray diffraction (XRD), elemental analysis using inductively coupled plasma (ICP), and Raman spectroscopy were also performed on the electrolytic sample [10]. The XRD data indicated that the diffraction pattern of the electrolytic cell sample does not match that of either KH, KHCO3, K2CO3, or KOH. The elemental analysis supports KH KHCO3. In addition to the known Raman peaks of KHCO3 and a small peak assignable to K2CO3, unidentified peaks at 1685 and 835 cm⁻¹ were present. Work in progress [10] demonstrates that KH KHCO3 may also be formed by a reaction of gaseous KI with atomic hydrogen in the presence of K2CO3. In addition to the previous analytical studies, the fragment KK2CO1 corresponding to KH KHCO3 was observed by electrospray ionization time of flight mass spectroscopy as a chromatographic peak on a C18 liquid chromatography column typically used to separate organic compounds. No chromatographic peaks were observed in the case of inorganic compound controls KI, KHCO₃, K₂CO₃, and KOH.

4. Discussion

Álkali and alkaline earth hydrides react violently with water to release hydrogen gas which subsequently ignites due to the exothermic reaction with water. Typically metal hydrides decompose upon heating at a temperature well below the melting point of the parent metal. These saline hydrides, so called because of their saltlike or ionic character, are the monohydrides of the alkali metals and the dihydrides of the alkaline-earth metals, with the exception of beryllium. BeH2 appears to be a hydride with bridge type bonding rather than an ionic hydride. Highly polymerized molecules held together by hydrogen-bridge bonding is exhibited by boron hydrides and aluminum hydride. Based on the known structures of these hydrides, the ToF-SIMS hydride clusters such as K[KHKHCO₃], the XPS peaks observed at 22.8 and 38.8 eV, upfield NMR peaks assigned to hydride ion, and the shifted FTIR peaks, the present novel hydride compound may be a polymer, [KH KHCO₃]_n, with a structural formula which is similar to boron and aluminum hydrides. The reported novel compound appeared polymeric in the concentrated electrolytic solution and in distilled water. [KH KHCO₃], is extraordinarily stable in water; whereas, potassium hydride reacts violently with water.

(4)





As an example of the structures of this compound, the $K[KH \ KHCO_3]_n^+ \ m/z = (39+140n)$ series of fragment peaks is tentatively assigned to novel hydride bridged or linear potassium bicarbonate compounds having a general formula such as $[KH \ KHCO_3]_n \ n = 1,2,3 \dots$ General structural formulas may be

$$\begin{bmatrix} K^{\dagger} & HCO_3 \\ H & \end{bmatrix}_n$$

and

Liquid chromatography/ESIToFMS studies are in progress to support the polymer assignment.

The observation of inorganic hydride fragments such as K[KH KHCO₃] tin the positive ToF-SIMS spectra of samples isolated from the electrolyte following acidification indicates the stability of the novel potassium hydride potassium bicarbonate compound [10]. The electrolyte was acidified with HNO_3 to pH=2 and boiled to dryness to prepare samples to determine whether KH KHCO3 was reactive under these conditions. Ordinarily no K2CO3 would be present, and the sample would be converted to KNO3. Crystals were isolated by dissolving the dried crystals in water, concentrating the solution, and allowing crystals to precipitate. ToF-SIMS was performed on these crystals. The positive spectrum contained elements of the series of inorganic hydride clusters {K[KH KHCO₃]⁺_n m/ z = (39 + 140n), $K_2OH[KH KHCO_3]_n^+ m/z = (95 + 140n)$, and $K_3O[KH KHCO_3]_n^+$, m/z = (133 + 140n)} that were observed in the positive ToF-SIMS spectrum of the electrolytic cell sample as discussed in the ToF-SIMS Results Section and given in Figs. 3 and 4 and Table 1. The presence of bicarbonate carbon (C 1s≅289.5 eV) was observed in the XPS of the sample from the HNO₃ acidified electrolyte. In addition, fragments of compounds formed by the displacement of hydrogen carbonate by nitrate were observed [10]. A general structural formula for the reaction maybe

During acidification of the K_2CO_3 electrolyte the pH repetitively increased from 3 to 9 at which time additional acid was added with carbon dioxide release. The increase in pH (release of base by the titration reactant) was dependent on the temperature and concentration of the solution. A reaction consistent with this observation is the displacement reaction on NO_3^- for HCO_3^{2-} as given by Eq. (4).

5. Conclusions

The ToF-SIMS, XPS, and NMR results confirm the identification of KH KHCO3 with a new state of hydride ion. The chemical structure and properties of this compound having a hydride ion with a high binding energy are indicative of a new field of hydride chemistry. The novel hydride ion may combine with other cations such as other alkali cations and alkaline earth, rare earth, and transition element cations. Thousands of novel compounds may be synthesized with extraordinary properties relative to the corresponding compounds having ordinary hydride ions. These novel compounds may have a breath of applications. For example a high voltage battery (Eqs. (1-3)) according to the hydride binding energy of 22.8 eV observed by XPS may be possible having projected specifications that surpass those of the internal combustion engine.

Acknowledgements

Special thanks to Bala Dhandapani of BlackLight Power, Inc., for work on the Raman, FTIR, and XRD studies. Special thanks to Jiliang He of BlackLight Power, Inc., for obtaining the MAS NMR spectrum of potassium hydride. Special thanks to Robert Braun of BlackLight Power, Inc., Bala Dhandapani, and Jiliang He for helpful comments upon review of the manuscript.

Appendix A

A novel hydride ion having extraordinary chemical properties given by Mills [10] is predicted to form by the reaction of an electron with a hydrino (Eq. (A2)), a hydrogen atom having a binding energy given by

Binding energy =
$$\frac{13.6 \text{ eV}}{\left(\frac{1}{p}\right)^2}$$
 (A1)

where p is an integer greater than 1, designated as

$$H\left[\frac{a_H}{p}\right]$$

where $a_{\rm H}$ is the radius of the hydrogen atom. The resulting hydride ion is referred to as a hydrino hydride ion, designated as $H^{-}(1/p)$.

$$H\left[\frac{a_{\rm H}}{p}\right] + e^- \rightarrow H^-(1/p) \tag{A2}$$

The hydrino hydride ion is distinguished from an ordinary hydride ion having a binding energy of 0.8 eV. The latter is hereafter referred to as "ordinary hydride ion". The hydrino hydride ion is predicted [10] to comprise a hydrogen nucleus and two indistinguishable electrons at a binding energy according to the following formula:

Binding energy =
$$\frac{\hbar^2 \sqrt{s(s+1)}}{8\mu_e a_0^2 \left[\frac{1+\sqrt{s(s+1)}}{p}\right]^2} - \frac{\pi\mu_0 e^2 \hbar^2}{m_e^2 a_0^3} \left(1 + \frac{2^2}{\left[\frac{1+\sqrt{s(s+1)}}{p}\right]^3}\right)$$
(A3)

where p is an integer greater than one, s = 1/2, π is pi, \hbar is Planck's constant bar, μ_0 is the permeability of vacuum, m_e is the mass of the electron, μ_e is the reduced electron mass, a_0 is the Bohr radius, and e is the elementary charge. The ionic radius is

$$r_1 = \frac{a_0}{p}(1 + \sqrt{s(s+1)}; \quad s = \frac{1}{2}$$
 (A4)

From Eq. (A4), the radius of the hydrino hydride ion

H⁻ (1/p); p = integer is 1/p that of ordinary hydride ion, H⁻(1/1). The XPS peaks centered at 22.8 and 38.8 eV are assigned to shifted K 3s and K 3p. The anion does not correspond to any other primary element peaks; thus, it may correspond to the H⁻(n=1/6) E_b =22.8 eV hydride ion predicted by Mills [10] where E_b is the predicted binding energy.

Hydrinos are predicted to form by reacting an ordinary hydrogen atom with a catalyst having a net enthalpy of reaction of about

$$m \, 27.21 \, \text{eV}$$
 (A5)

where m is an integer [10]. This catalysis releases energy from the hydrogen atom with a commensurate decrease in size of the hydrogen atom, $r_n = na_H$. For example, the catalysis of H(n=1) to H(n=1/2) releases 40.8 eV, and the hydrogen radius decreases from a_H to $1/2a_H$. One such catalytic system involves potassium. The second ionization energy of potassium is 31.63 eV; and K^+ releases 4.34 eV when it is reduced to K. The combination of reactions K^+ to K^{2+} and K^+ to K, then has a net enthalpy of reaction of 27.28 eV, which is equivalent to m=1 in Eq. (A5).

27.28 eV + K + + K + + H
$$\left[\frac{a_{\rm H}}{p}\right]$$
 \rightarrow K + K ²⁺ + H $\left[\frac{a_{\rm H}}{(p+1)}\right]$ + $[(p+1)^2 - p^2]$ 13.6 eV (A6)

$$K + K^{2+} \rightarrow K^{+} + K^{+} + 27.28 \text{ eV}$$
 (A7)

The overall reaction is

$$H\left[\frac{a_{\rm H}}{p}\right] \rightarrow H\left[\frac{a_{\rm H}}{(p+1)}\right] + \left[(p+1)^2 - p^2\right] 13.6 \,\text{eV} \qquad (A8)$$

The energy given off during catalysis is much greater than the energy lost to the catalyst. The energy released is large as compared to conventional chemical reactions. For example, when hydrogen and oxygen gases undergo combustion to form water

$$H_2(g) + \frac{1}{2}O_2(g) \rightarrow H_2O(1)$$
 (A9)

the known formation enthalpy of water is $\Delta H_{\rm f} = -286$ kJ/mole or 1.48 eV per hydrogen atom. By contrast, each ordinary hydrogen atom (n=1) catalysis releases a net of 40.8 eV. The exothermic reactions Eqs. (A6)-(A8), Eq. (A2) and the enthalpy of formation of KH KHCO₃ could explain the observation of excess enthalpy of 1.6 × 10⁹ J that exceeded the total input enthalpy given by the product of the electrolysis voltage and current over time by a factor greater than 8 [7].





References

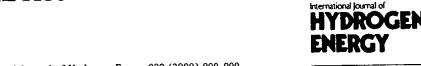
- [1] Uehara I, Sakai T, Ishikawa H. J Alloy Comp 1997;253/ 254:635-41.
- [2] Glanz J. Check the tires and charge her up, New Scientist, April 15, pp. 32-35, 1995.
- [3] Mulholland D. Defense News, Powering the Future Military, March 8, pp. 1 & 34, 1999.
- [4] Aceves SM, Berry GD, Rambach GD. Int J Hydrogen Energy 1998;23(7):583-91.
- [5] Ball J. Auto makers are racing to market "green" cars powered by fuel cells, The Wall Street Journal, March 15, p. 1, 1999.
- [6] National Technical Information Service, US Department of Commerce. Advanced automotive technology: visions of a super-efficient family car, US Office of Technology Assessment, Washington, DC PB96-109202, September 1995.
- [7] Mills R, Good W, Shaubach R. Fusion Technol 1994;25:103.
- [8] Microsc Microanal Microstruct, Vol. 3, 1, 1992.

- [9] PHI Trift II, ToF-SIMS Technical Brochure, Eden Prairie, MN 55344, 1999.
- [10] Mills R. The grand unified theory of classical quantum mechanics, January ed. Cranbury, New Jersey: BlackLight Power, Inc, 1999 Distributed by Amazon.com.
- [11] Practical surface analysis. In: Briggs D, Seah MP, editors. Ion and neutral spectroscopy, 2nd ed. Wiley and Sons, New York, 1992. 2.
- [12] Wagner CD, Riggs WM, Davis LE, Moulder JF, Mulilenberg GE, editors. Handbook of X-ray photo-electron spectroscopy. Eden Prairie, Minnesota: Perkin-Elmer Corp, 1997.
- [13] Lin-Vien D, Colthup NB, Fateley WG, Grassellic JG.
 The handbook of infrared and Raman characteristic frequencies of organic molecules. Academic Press, Inc, 1991.
- [14] Nyquist RA, Kagel RO, editors. Infrared spectra of inorganic compounds. New York: Academic Press, 1971.
- [15] Brooker MH, Bates JB. Spectrochimica Acta 1994;30A:2211-20.

THIS PAGE BLANK (USPTO)







International Journal of Hydrogen Energy 000 (2000) 000-000

www.elsevier.com/locate/ijhydene

Synthesis and characterization of novel hydride compounds

Randell L. Mills*, Bala Dhandapani, Mark Nansteel, Jiliang He, Tina Shannon, Alex Echezuria

BlackLight Power, Inc., 493 Old Trenton Road, Cranbury, NJ 08512, USA

Abstract

Novel inorganic alkali and alkaline earth hydrides of the formula MHX and MHMX wherein M is the metal X, is a singly negatively charged anion, and H comprises a novel high binding energy hydride ion were synthesized in whigh temperature gas cell by reaction of atomic hydrogen with a catalyst and MX or MX2 corresponding to an alkali metal or alkaline earth metal compound, respectively. Novel hydride compounds were identified by time of flight secondary ion mass spectroscopy, X-ray photoelectron spectroscopy, proton nuclear magnetic resonance spectroscopy, and thermal decomposition with analysis by gas chromatography, and mass spectroscopy. © 2000 International Association for Hydrogen Energy. Published by Elsevier Science Ltd. All rights reserved.

1. Introduction

Typically the emission of extreme ultraviolet light from hydrogen gas is achieved via a discharge at high voltage, a high power inductively coupled plasma, or a plasma created and heated to extreme temperatures by RF coupling (Eg. > 106 K) with confinement provided by a toroidal magnetic field. Intense extreme ultraviolet (EUV) emission was observed at low temperatures (e.g. $\approx 10^3$ K) from temperatures hydrogen and certain atomized elements or sertain gaseous ions which ionize at integer multiples of the ottential energy of atomic hydrogen [1-6]. For example, strontium ionizes at integer multiples of the noterital energy of atomic hydrogen. Intense EUV hydrogen plasma emission was observed at low temperatures (K) when atomic hydrogen was generated at a tungsten filament that heated a titanium dissociator and atomic strontium was vaporized from the metal by hearing No emission was observed when sodium, magnesium, or barium replaced strontium or when argon replaced hydrogen with strontium. Furthermore, the power balance of a gas cell having atomized hydrogen power balance of a gas cell having atomized hydrogen and strontium was measured by integrating the total light

• Corresponding author. Tel.: +1-609-490-1040; fax: +1-609-490-1066.

E-mail address: rmills@blacklightpower.com (R.L. Mills).

output corrected for detector response and energy over the visible range [6]. A control cell was identical except that sodium eplaced strontium. In this case, over 4000 times the power of the strontium cell was required in order to aeffect that same optically measured light output power. A plasma formed at a cell voltage of about 250 V in the cell with hydrogen alone and in the cell with hydrogen and sodium; whereas, a plasma formed in the strontium cell at the extremely low voltage of about 2 V.

Based on their exceptional emission, we used potassium, cesium, rubidium, calcium, and strontium metals as catalysts to release energy from atomic hydrogen to form novel compounds [1,2]. The theory is given in the Appendix.

Novel inorganic alkali and alkaline earth hydrides of the formula MHX and MHMX wherein M is the metal, X, is a singly negatively charged anion, and H comprises a novel high binding energy hydride ion were synthesized in a high-temperature gas cell by reaction of atomic hydrogen with a catalyst and MX or MX₂ corresponding to an alkali metal or alkaline earth metal compound, respectively. For example, atomic hydrogen was reacted with strontium vapor and SrBr₂ to form SrHBr. Novel hydride compounds such as SrHBr were identified by time of flight secondary ion mass spectroscopy, X-ray photoelectron spectroscopy, proton nuclear magnetic resonance spectroscopy, and thermal decomposition with analysis by gas chromatography,

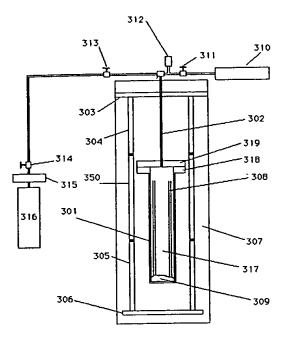


Fig. 1. Stainless steel gas cell comprising a screen dissociator, metal catalyst, and alkali or alkaline earth halide as the reactant. The components were: 301 — stainless steel cell; 317 — internal cavity of cell; 318 — high vacuum conflat flange; 319 — mating blank conflat flange; 302 — stainless steel tube vacuum line and gas supply line; 303 — lid to the kiln or top insulation, 304, 305, 350, and 306 — heaters; 307 — high temperature insulation; 308 — screen dissociator, 309 — powdered alkali or alkaline earth halide reactant; 310 — high vacuum turbo pump; 312 — pressure gauge; 311 — vacuum pump valve; 313 — valve; 314 — valve; 315 — regulator; 316 — hydrogen tank.

and mass spectroscopy. Hydride ions with increased binding energies form novel compounds with potential bread applications such as a high-voltage battery for consumer electronics and electric vehicles. In addition, they novel compositions of matter and associated technologic machave far-reaching applications in many integrals including chemical, electronics, computer, military energy, and aerospace in the form of products such as propellants, solid fuels, surface coatings, structural materials, and chemical processes.

2. Experimental

2.1. Synthesis

2.1.1. Potassium tidachi dride, KHI, synthesis in a 3.0 l stainless speckredstor

Potassium nodo hydride was prepared in a stainless steel gas cell hower in Fig. 1 comprising a Ni screen hydrogen dissociator (Belleville Wire Cloth Co., Inc.), potassium metal catalyst (Aldrich Chemical Company), and Kl (Aldrich Chemical Company 99.9%). The 316-stainless

steel cell was in the form of a tube having an internal cavity of 375 mm in length and 140 mm in diameter. The wall thickness was 6.35 mm. The bottom of the cell was closed by a 6.35 mm thick circular plate of 316 stainless steel that was welded to the cylinder. The top end of the cell was welded to a bored-through 304 stainless steel conflat-type flange with 8 in nominal diameter. A mating blank flange was bolted to the bored-through flange with 20 silver-plated bolts. A flange gasket was silver-plated copper. A 1.27 cm OD tube was welded into a hole at the center of the blank flange. This tube was closed at one end and extended 20 cm into the reactor, serving as a thermowell. A 9.5 mm OD stainless tube was welded to the flange approximately 4 cm from the flange center. This tube served as the vacuum line from the cell as well as a hydrogen or helium supply line to the cell.

The reactor was heated in a 10 kW refractory brick kiln (L & L Kiln Model JD230). The kiln had three heating zones and a heated floor that were each heated by separate radiant elements. The zone temperatures we independently controlled by a Dynatrol controlle. The reactor was instrumented with 5 type-K thermocouples. Two thermocouples were located in the central thermowell at approximately reactor mid-height and at flange-level. Three thermocouples were fixed to the external surface of the reactor and were located near the base, a mid-height, and near flange-level. The reactor was competed through bellows-type valves to a turbo vacuum pump. The vacuum level was measured by a 0-100 Torr Baratron vacuum gauge. Pressures above 100 Torr were measured by standard dial-type pressure gauges. Temperature and pressure data was logged to a data acquisition system at 5 min intervals.

Approximately 290 g of nickel screen (0.5 mm wire, 2 mm lesh was placed circumferentially around the reactor inner of the cell. 125 g of dry KI were placed in a stainless steel crucible on the reactor base. The reactor was flooded with argon gas. 1.7 g of metallic potassium was placed in a smaller stainless steel crucible and this crucible was placed in the larger one with the Kl crystals. The reactor was sealed and placed in the kiln. The system was evacuated for 2.5 h. The reactor was pressurized with hydrogen gas to a pressure of 10 Torr and sealed. The kiln was heated to 650°C at the rate of 300°C/h. The reactor was held at 650°C for 72 h. Hydrogen was added to the system periodically to maintain a pressure level of 10 Torr. The reactor was then evacuated for 1 h while at 650°C. The kiln and reactor were cooled to room temperature by forced convection in about 2 h while pumping continued. At room temperature the system was filled with helium gas to a pressure of 1.3 bar. The sealed reactor was then opened. About 125 g of green crystals were observed to have formed in the stainless steel crucible.

2.1.2. Strontium fluoro hydride synthesis in a 40 cm³ stainless steel gas cell reactor

Strontium fluoro hydride was prepared in a stainless steel gas cell shown in Fig. 1 comprising a Ti screen hydrogen





R.L. Mills et al. | International Journal of Hydrogen Energy 000 (2000) 000-000

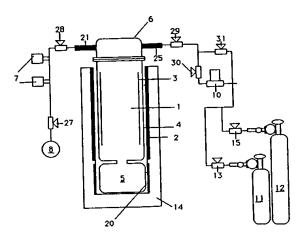


Fig. 2. Quartz gas cell comprising a Ni screen dissociator, potassium metal catalyst, and K_2CO_3 as the reactant. The components were: 1—internal cavity of cell; 3—nickel hydrogen dissociator; 4—quartz tube cell with Conflat style flange; 5—catalyst reservoir; 6—Pyrex cap with an identical Conflat style flange to the tube; 25—gas inlet line; 21—gas outlet line; 11—compressed gas cylinder of ultra high purity hydrogen; 13—hydrogen control valve; 12—compressed gas cylinder of ultrahigh purity helium; 15—helium control valve; 10—mass flow controller; 30—mass flow controller valve; 29—inlet valve; 31—mass flow controller bypass valve: 8—molecular drag pump; 27—vacuum pump valve; 28—outlet valve; 7—0 to 1000 torr Baratron pressure gauge and a 0 to 100 torr Baratron pressure gauge; 20—catalyst reservoir band heater; 14—Zircar AL-30 insulation package; 2—Mellen cell heater.

dissociator (Belleville Wire Cloth Co., Inc.), strontium metal catalyst (Alfa Aesar), and SrF₂ (Aldrich Chemical Company, 99.99%) as the reactant. The 304-stainless steel cell was fitted form of a tube having an internal cavity of 75 mm in length and 28 mm in diameter. The top end of the cell was welded to a high vacuum $2\frac{3}{4}$ in bored through conflit flange. The mating blank conflat flange contained a single optiming in which was welded a $\frac{1}{4}$ in diameter stainless steel tube that was 10 cm in length and contained a needle value to isolate the reactor from the rest of the gas manifold a silver plated copper gasket was placed between the two flanges. The two flanges are held together with 6 circumferential bolts. The bottom of the $\frac{1}{4}$ in tube was flush with the bottom surface of the top flange. The $\frac{1}{4}$ in tube served as a vacuum line and also as a hydrogen or helium supply line to the cell. The cell was surrounded by a claim shell heater (Mellen Company), which was in turns surrounded by insulation. The heater was controlled by a variate.

About 10 p. of Ti screen, 12 g of crystalline SrF2 and 0.6 g of strontium metal was added to the cell under an argon afficience. The cell was then continuously evacuated with the isolation needle valve open using a high vacuum turbo pump to reach 20 mTorr measured by a pressure gauge (MKS). The cell was heated by supply-

ing power to the heaters. The temperature of the cell was measured with a type K thermocouple (Omega). The cell temperature was then slowly increased to 100°C using the heaters. The vacuum pump valve was closed. Hydrogen was slowly added to maintain a pressure of 1 atm, and the needle valve was closed to isolate the reactor system. The temperature of the cell was then slowly increased to 650°C. Hydrogen was added periodically to maintain 1 atm using the needle valve. After 72 h, the temperature of the cell was reduced to room temperature. The reactor was flushed with helium and closed using the needle valve. It was then opened in an argon environment chamber to recover the strontium fluoro hydride. A white solid was obtained.

2.1.3. Potassium hydride potassium hydrogen carbonate synthesis in a quartz gas cell reactor

Potassium hydride potassium hydrogen carbonate was prepared in a quartz gas cell shown in Fig. 2 comprising a nickel screen hydrogen dissociator (Belleville Wire Cloth Co., Inc.), potassium metal catalys (Aldrich Chemical Company), and K₂CO₃ (Aldrich Chemical Company), and K₂CO₃ (Aldrich Chemical Company) 99.9%) as the reactant. The quartz cell was in the form of a tube having an internal cavity of fifty (50) millimeters in diameter and five hundred (500) millimeters in length. One end of the cell was necked down and attached to a fifty (50) cubic centimeter calalyst reservoir. The other end of the cell was fitted with a Comflat style high vacuum flange that was mated to a Pyrex cap with an identical Conflat style flange. A high vacuum seal was maintained with a Viton O-ring and stainless teel clamp. The Pyrex cap included two glass-to-metal tubes for the attachment of a gas inlet line and gas outlet

gas was supplied to the cell through the inlet from a compressed gas cylinder of ultra high-purity hydrogen controlled by a hydrogen control valve. Helium gas was supplied to the cell through the same inlet from a compressed gas cylinder of ultrahigh purity helium controlled by helium control valve. The flow of helium and hydrogen to the cell is further controlled by a mass flow controller, a mass flow controller valve, an inlet valve, and a mass flow controller bypass valve. The bypass valve was closed during filling of the cell. Excess gas was removed through the gas outlet by a molecular drag pump capable of reaching pressures of 10-4 Torr controlled by vacuum pump valve and outlet valve. Pressures were measured by a 0-10 Torr Baratron pressure gauge. The reactor and the catalyst reservoir, were heated independently using clam shell heaters (Mellen Company) powered by Variacs. The temperature was recorded using a K-type thermocouple placed close to the quartz reactor.

The cell was operated under flow conditions with a total pressure of less than two (2) Torr of hydrogen or control helium via mass flow controller. About 20 g of K₂CO₃ (Aldrich Chemical Company, 99.9%) was placed in the

catalyst reservoir and about 50 g, 12×12 cm of nickel screen dissociator (Belleville Wire Cloth Co., Inc.) was treated with 0.6 M K₂CO₃/10% H₂O₂ and dried at 130°C overnight and then placed in the center of the reactor. The reactor was evacuated to about 50 mTorr and hydrogen was introduced using the mass flow controller to maintain a pressure of about 2 Torr. The temperature of the reactor was increased to about 800-850°C to facilitate atomization of hydrogen, and the catalyst reservoir temperature was increased to 850°C to vaporize the catalyst. The reaction started when the catalyst vapor reached the hot zone of the reactor. The reaction was allowed to continue for about 120 h. The reaction was terminated by cooling the reactor and the catalyst reservoir to room temperature in hydrogen. The system was purged and back filled with helium and sealed. The reactor was opened in an argon environmental chamber and the samples were collected and analyzed. The compound was a white powder.

2.1.4. Synthesis of alkali halido hydrides and alkaline earth halido hydrides

A series of alkali and alkaline earth halido hydrides (KHF, KHCl, KHBr, KHI, RbHF, RbHCl, RbHBr, RbHl, CsHF, CsHCl, CsHBr, CsHl, CaHCl, CaHBr, CaHl, SrHF, SrHCl, and SrHBr) were synthesized in gas cells as described in the previous A-B Sections with the exception that the alkali or alkaline earth metal catalyst (rubidium metal (which is a catalyst as a hydride having Rb+) and potassium, cesium, calcium, and strontium metals) corresponded to the alkali or alkaline earth halide of the product alkali or alkaline earth halido hydride. RbHF was synthesized by the catalysis of atomic hydrogen with potassium metal catalyst followed by reaction with RbF wherein the hydrogen dissociator was a nickel screen. Reactants to form hydrides of these inorganic compounds obtained from Alfa A were KF (99.9%), KCl (ACS grade 99+(99.9%) Rbl (99.9%), CsF (99.9%), CsCl (99.9%), CsBr (99.9%) (99.9%), CaCl₂ (99.9%), CaBr₂ (99.9%), Cal₂ (SrF₂ (99.9%), SrCl₂ (99.9%), and SrBr₂ (99.9%). Iff the analytical analyses, each starting compound as a control.

2.2. ToF-SIMS characterization

The crystalline samples were spunkled onto the surface of a double-sided adhesive tape and characterized using a Physical Electronics TFS 2000 ToF-SIMS instrument. The primary ion gun utilized a $^{69}Ga^+$ liquid metal source. In order to remove surface contaminants and expose a fresh surface, the samples were sputter cleaned for 30 s using a 40 μ m x 30 μ m raster. The aperture setting was 3, and the ion current was 600 pA resulting in a total ion dose of 10^{12} lons/cm².

10¹⁴ ions/cin².

During acquisition, the ion gun was operated using a bunched (pulse width 4 ns bunched to 1 ns) 15 kV beam

[7,8]. ¹ The total ion dose was 10¹²ions/cm². Charge neutralization was active, and the post accelerating voltage was 8000 V. Three different regions on each sample of (12 µm)², (18 µm)², and (25 µm)² were analyzed. The positive and negative SIMS spectra were acquired. Representative post sputtering data is reported.

2.3. XPS characterization

A series of XPS analyses were made on the crystalline samples of KHCl and KCl using a Scienta 300 XPS Spectrometer. The fixed analyzer transmission mode and the sweep acquisition mode were used. The step energy in the survey scan was 0.5 eV, and the step energy in the high resolution scan was 0.15 eV. In the survey scan, the time per step was 0.4 s, and the number of sweeps was 4. In the high resolution scan, the time per step was 0.3 s, and the number of sweeps was 30. C 1s at 284.5 eV was used as the internal standard.

The binding energies and features of each level electrons of a series of alkali and alkaline earth halido in drides (KHCl, KHI, RbHCl, RbHI, CsHBr, CaHCl, CaHBr, CaHl, SrHF, SrHCl, and SrHBr) were analyzed by XPS. XPS analysis was conducted on a Krafos XSAM-800 spectrometer using nonmonochromatic AKK α (1468.6 eV) radiation. Samples were crushed in a glove box under argon and mounted on an analysis stub with copper tape. A piece of gold foil was stuck into the sample for calibration. The samples were transferred under an inert atmosphere. A survey spectrum was run from 1000 to 0 eV. For quantitative analysis, high resolution spectra were run on core level electrons of interstraigh as the Rb3d and Cs3d electrons. For KI and KHI, a high resolution spectrum of the low binding energy region was also run from 100 to 0 eV that corresponded to the surspectrum. Fixed analyzer transmission (FAT) mode was used in all measurements. For the survey scan, a pass energy of 320 eV was employed. A pass energy of 40 eV was used for high resolution scans. In the cases were a charging effect was observed, the spectrum was corrected by using a calibration of the effect with the Au4f_{1/2} peak at 84.0 eV as a first standard and the C1s peak at 284.6 eV as a second standard.

2.4. NMR spectroscopy

¹H MAS NMR was performed on solid samples of KHI, KHCI, KHBr, and RbHF. The data was obtained on a custom built spectrometer operating with a Nicolet 1280 computer. Final pulse generation was from a tuned Henry radio amplifier. The ¹H NMR frequency was 270.6196 MHz. A 5 μ s pulse corresponding to a 41° pulse length and a 3 recycle delay were used. The window was ± 20 kHz. The spin speed was 4.0 kHz. (The spin speed was varied to confirm real peaks versus side bands. The latter changed

¹ For recent specifications see Ref. [8].

position with spin speed, the former were independent of spin speed.) The number of scans was 600. The offset was 1541.6 Hz, and the magnetic flux was 6.357 T. The samples were handled under a nitrogen atmosphere. Chemical shifts were referenced to external tetramethylsilane (TMS). The reference of KHI comprised KH (Aldrich Chemical Company 99%) and equivalent molar mixtures of KH (Aldrich Chemical Company 99%) and KI (Aldrich Chemical Company 99.99%) prepared in a glove box under argon. The reference of KHCl comprised KH (Aldrich Chemical Company 99%) and equivalent molar mixtures of KH (Aldrich Chemical Company 99%) and KCl (Aldrich Chemical Company 99.99%) prepared in a glove box under argon. The reference of KHBr comprised KH (Aldrich Chemical Company 99%) and equivalent molar mixtures of KH (Aldrich Chemical Company 99%) and KBr (Aldrich Chemical Company 99.99%) prepared in a glove box under argon. The reference of RbHF comprised RbH (Aldrich Chemical Company 99%).

¹H MAS NMR was performed on a solid samples of SrHBr. The data were recorded on a Bruker DSX-300 spectrometer at 300.132 MHz. Samples were packed and sealed in 5 mm diameter NMR tubes under an inert atmosphere. The ¹H MAS NMR of strontium bromo hydride was run static. The MAS frequency was 4.1 kHz. During data acquisition, the 90° pulse length for a single pulse ¹H excitation was 3.4 μs; the sweep width was 147.058 kHz; the dwell time was 5.5 μs, and the acquisition time was 0.0139764 s/scan. The number of scans was typically 32.

The hydrogen composition of the samples was quantified by integrating the signal under each peak. In each case, the signal from an empty tube was baseline subtracted from the integral for each peak. The integration was calibrated using a polyethylene standard. From the sample weight, the wt% hydrogen was determined. The chemical shifts of the spectra were calibrated based on the chemical shift of H.O. The accuracy was determined to be within 0.1 ppm some samples were broadened due to ¹H-¹H dipole interaction. The broadening from a neighboring proton interaction was 120 kHz/r³. Given the NMR frequency of 300 MHz, there were 300 Hz per ppm. As an example, peak widths of 7 ppm correspond to 2.1 kHz. Based on this frequency, the distance to a neighboring proton.

2.5. Thermal decomposition with analysis by gas Chromatography

Solid samples were decomposed at high temperature and quantitatively analyzed for hydrogen using gas chromatography. Of professions placed in a thermal decomposition reactor under an argon atmosphere. The reactor comprised a 1/4" OD by 3" long quartz tube that was sealed at one end and connected at the open end with Swagelock titings to a T. One end of the T was connected to a needle valve and a HOVAC molecular drag pump. The other end

was attached to a septum port. The apparatus was evacuated to between 25 and 50 m Torr. The needle valve was closed to form a gas tight reactor. The sample was heated in the evacuated quartz chamber containing the sample with an external Nichrome wire heater using a Variac transformer. The sample was heated to above 600°C by varying the transformer voltage supplied to the Nichrome heater until the sample melted. Gas released from the sample was collected with a 500 µl gas tight syringe through the septum port and immediately injected into the gas chromatograph.

Gas samples were analyzed with a Hewlett Packard 5890 Series II gas chromatograph equipped with a thermal conductivity detector and a 60 m, 0.32 mm ID fused silica Rt-Alumina capillary PLOT column (Restek, Bellefonte, PA). The column was conditioned at 200° C for 18–72 h before each series of runs. Samples were run at -196° C using Ne as the carrier gas. The 60 m column was run with the carrier gas at 3.4 psi with the following flow rates: carrier -2.0 ml/min, auxiliary -3.4 ml/min and reference -3.5 ml/min, for a total flow rate of \$9 ml/min. The split rate was 10.0 ml/min.

The control hydrogen gas was ultrahigh purity (MG Industries). Control samples were also treated by the same method as the samples of the novel compounds.

2.6. Thermal decomposition with analysis by mass spectroscopy

Mass spectroscopy was performed on the gases released from the thermal decomposition of the samples. One end of a manal D fritted capillary tube containing about 5 mg of sample was sealed with a 0.25 in. Swagelock union and lug (Swelock Co., Solon, OH). The other end was conected directly to the sampling port of a Dycor System 1000 drapole Mass Spectrometer (Model D200MP, Ametek, Inc., Pittsburgh, PA with a HOVAC Dri-2 Turbo 60 Vacuum System). The capillary was heated with a Nichrome wire heater wrapped around the capillary. The mass spectrum was obtained at the ionization energy of 70 and 30 eV at different sample temperatures in the region m/e = 0-50. With the detection of hydrogen indicated by a m/e = 2 peak, the intensity as a function of time for masses m/e = 1, m/e = 2, m/e = 3, m/e = 4, m/e = 5, and m/e = 18 was obtained while changing the ionization potential (IP) of the mass spectrometer from 30 to 70 eV.

The control hydrogen gas was ultrahigh purity (MG lndustries).

3. Results and discussion

3.1. ToF-SIMS

3.1.1. ToF-SIMS of potassium iodo hydride sample

The positive ToF-SIMS spectrum (m/e = 0-140) of KHI, the positive ToF-SIMS spectrum (m/e = 0-140) of KI, the negative ToF-SIMS spectrum (m/e = 0-140) of KHI, and

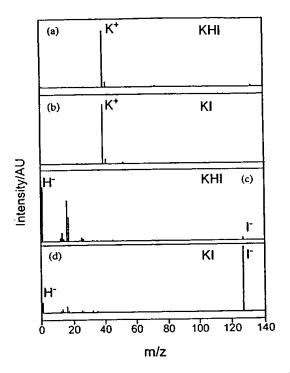


Fig. 3. (a) The positive ToF-SIMS spectrum (m/e = 0-140) of KHI. (b) The positive ToF-SIMS spectrum (m/e = 0-140) of KJ. (c) The negative ToF-SIMS spectrum (m/e = 0-140) of KHI. (d) The negative ToF-SIMS spectrum (m/e = 0-140) of KI.

the negative ToF-SIMS spectrum (m/e = 0-140) of K1 are shown in Figs. 3a-d, respectively. The positive ion spectrum of KH1 and that of the K1 control were dominated by the K⁺ ion. A K²⁺ ion was only observed in the positive spectrum of the KHI.

 Ga^+ m/z = 69, K_2^+ m/z = 78, $K(KCI)^+$ m/z (113), I^+ m/z = 127, KI^+ m/z = 166, and a series of positive ion $K[KI]_n^+$ m/z = (39 + 166n) were also observed the negative ion ToF-SIMS of KHI was dominated by H with a smaller I⁻ peak. Iodide alone dominated the negative ion ToF-SIMS of the KI control. For both, $O^ m_z = 6$ OH^- m/z = 17, CI^- m/z = 35, KI^- m/z = 160 a series of negative ions $I[KI]_n^-$ m/z = (127 + 166n) were also observed.

3.1.2. ToF-SIMS of polassium hydride potassium hydrogen carbonate saniple

The positive 10^{14} Simulation obtained from the KHCO₃ control is shown in Figs. 4 and 5. (KHCO₃ was used as a control versus 10^{14} because the former is more conservative in that 12 contains a larger source of H). In addition, the positive 10^{14} For SiMS of the KHKHCO₃ sample is shown in Figs. 6 and 7. In both the control and KHKHCO₃ samples the positive ion spectrum are dominated by the K⁺ ion. Two series of positive ions $\{K[K_2CO_3]_n^+ m/z = (39 + 138n)\}$ and $K_2OH[K_2CO_3]_n^+ m/z = (95 + 138n)\}$ are observed

in the KHCO₃ control. Other peaks containing potassium include KC⁺, $K_xO_y^+$, $K_xO_yH_z^+$, KCO⁺, and K_2^+ . However, in the KHKHCO₃ sample, three new series of positive ions are observed at $\{K[KHKHCO_3]_n^+ \ m/z = (39 + 140n), K_2OH[KHKHCO_3]_n^+ \ m/z = (133 + 140n)\}$. These ions correspond to inorganic clusters containing novel hydride combinations (i.e. KHKHCO₃ units plus other positive fragments). The same compound was seen previously in a sample isolated from a K_2CO_3 electrolytic cell [9].

The comparison of the positive ToF-SIMS spectrum of the KHCO₃ control with the KH KHCO₃ sample shown in Figs. 4 to 5 and 6, 7, respectively, demonstrates that the 39 K+ peak of the KH KHCO₃ sample may saturate the detector and give rise to a peak that is atypical of the natural abundance of 41 K. The natural abundance of 41 K is 6.7%; whereas, the observed 41 K abundance from the KH KHCO₃ sample is 53%. The high resolution mass assignment of the m/z = 41 peak of the KH KHCO₃ was consistent with 41 X, and no peak was observed at m/z = 42.98 ruling out 41 X, and no peak was observed at m/z = 42.98 ruling out 41 X. Moreover, the natural abundance of 41 K was observed at the positive ToF-SIMS spectra of KHCO₃, KhO₃, and KI standards that were obtained with an ion current such that the 39 K peak intensity was an order of magnitude higher than that given for the KH KHCO₃ sample. The saturation of the 39 K peak of the positive ToF-SIMS spectrum by the KH KHCO₃ sample is indicative of a unique crystalline matrix [10].

The negative 10F-SIMS spectrum (m/e = 0-100) of the KHCO₃ (39 9%) sample and the KH KHCO₃ sample

The negative 10F-SIMS spectrum (m/e = 0-100) of the KHCO₃ (29.99%) sample and the KHKHCO₃ sample are shown in Fig. 8 and 9, respectively. The negative ion TOF-SIME of the KHKHCO₃ sample was dominated by H, D, and OH peaks. A series of nonhydride containing negative ions { $KCO_3[K_2CO_3]_n^- m/z = (99 + 138n)$ } was also present which implies that H₂ was eliminated the KHKHCO₃ during fragmentation of the compound KHKHCO₃. Comparing the H to O ratio of the KHKHCO₃ sample to that of the KHCO₃ control sample, the H peak was about an order of magnitude higher in the KHKHCO₃ sample.

3.1.3. ToF-SIMS of rubidium fluoro hydride sample

The positive ToF-SIMS spectrum (m/e = 0-100) of RbHF, the positive ToF-SIMS spectrum (m/e = 0-100) of RbF, the negative ToF-SIMS spectrum (m/e = 0-100) of RbHF, and the negative ToF-SIMS spectrum (m/e = 0-100) of RbF are shown in Figs. 10a-d, respectively. The positive ion spectrum of RbHF and that of the RbF control were dominated by the Rb⁺ ion. Ga⁺ m/z = 69, Rb_2^+ m/z = 170, RbF⁺ m/z = 104, and a series of positive ions Rb[RbF]_n⁺ m/z = (85 + 104n) were also observed. The negative ion ToF-SIMS of RbHF was dominated by H⁻ with a smaller F⁻ peak. Fluorine alone dominated the negative ion ToF-SIMS of the RbF control. For both, O⁻ m/z = 16, OH⁻ m/z = 17, Cl⁻ m/z = 35, RbF⁻ m/z = 104, a series of negative ions $F\{RbF\}_n^-$ m/z = (19 + 104n) were also observed.

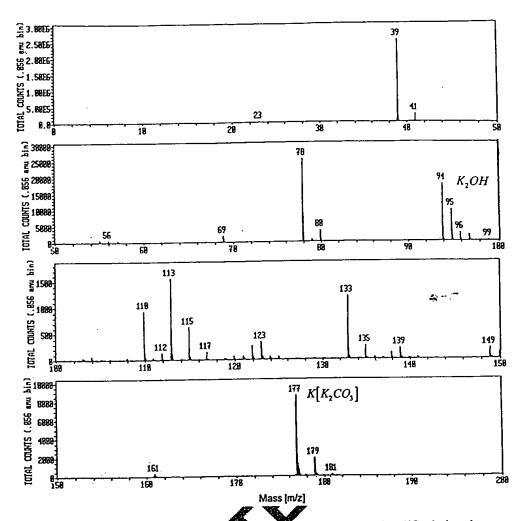


Fig. 4. The positive ToF-SIMS spectrum (m) 200) of KHCO₃ (99.99%) where HC = hydrocarbon.

3.1.4. ToF-SIMS of strontium fluoro hydride sample

The positive ToF-SIMS spectrum obtained from the SrHF sample is shown in Fig. 11. The positive spectrum was dominated by the strontium peal m/n = 88 and a 88 SrH+ m/z = 89 peak. Lithium sodiffication, potassium, small hydrocarbon fragments such a C_2H_3 m/z = 27 and C_2H_3 m/z = 29, 48 Ti+ 48 Ti+ 48 TiH+ 48 TiH+ 48 TiH+ 48 TiH 4

The positive spectrum of the SrF_2 control was also dominated by the by the montium peak Sr^+ m/z=88. A much smalled ⁸⁸ SrH m/z=89 peak was present. Lithium, sodium, potassium, hydrocarbon fragments, ⁸⁸ $SrOH^+$ m/z=105, ⁸⁸ SrF^+ m/z=107 were also observed. The hydrocarbon peaks were much more intense in the control sample than in the SrHF sample, and a large silicon peak was present.

The negative ion ToF-SIMS of SrHF shown in Fig. 12 was dominated by H⁻ and F⁻ m/z = 19 of equal inten-

sity. Fluoride alone dominated the negative ion ToF-SIMS of the SrF₂ control. For both samples, smaller $O^- m/z = 16$, $OH^- m/z = 17$, hydrocarbon fragment peaks such as $C^- m/z = 12$ and $CH^- m/z = 13$, $CI^- m/z = 35$, $SrF_2^- m/z = 126$, and $I^- m/z = 127$ were observed. A hydride peak which was significantly smaller than the $O^- m/z = 16$ peak was observed in the control. $Ti_xO_yH^-$ was observed in the SrHF sample. The hydrocarbon peaks were much more intense in the control.

The negative ToF-SIMS relative sensitivity factors (RSF) for the halides are all about equivalent. The hydrino hydride ion is in the same group as the halide ions. Thus, its RSF is projected to be equivalent to that of the halides. Therefore, the atomic percentage of hydrino hydride ion may be determined by comparison of its intensity with that of the fluoride ion of the product SrHF. The atomic percentage of hydrino hydride ion is equivalent to that of fluoride as shown in the negative ToF-SIMS. Since essentially no other cations are present, the positive and negative ToF-SIMS

Fig. 5. The positive ToF-SIMS spectrum (200-1000) of KHCO₃ (99.99%) where HC = hydrocarbon.

Mass [m/z]

indicates that SrHF is the product of the gas calification of SrF2 in the presence of atomic hydrogen and strongium metal catalyst.

3.2. XPS

8

3.2.1. XPS of potassium iodo hydride sample
A survey spectfull was attrained over the region $E_b = 0$ to 1200 eV. The primas element peaks allowed for the determination of all of the elements present in MHX and the control Marthe survey spectrum also detected shifts in the binding energies of the elements which had implications to the identity of the compound containing the elements.

XPS survey scan of KI and KHI are shown in Figs. 13a and b, respectively. C1s at 284.5 eV was used as the internal standard for KHI and the control KI. The

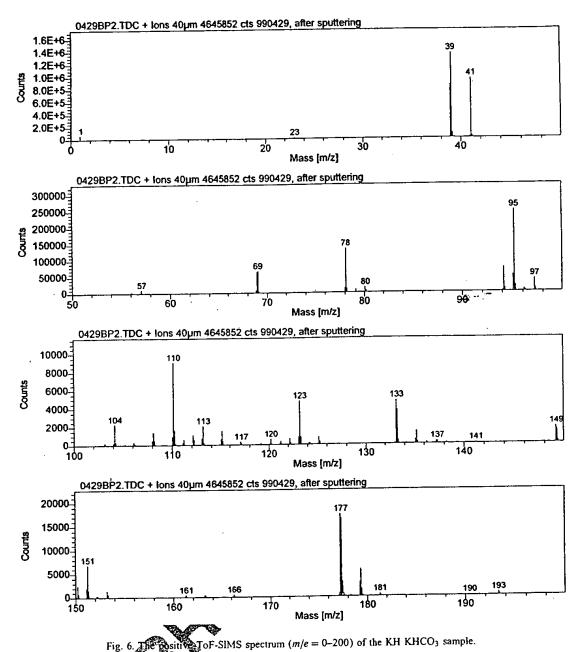
major species present in the KHl sample and the control are potassium and iodide. Trace small amounts of carbonate carbon and oxygen were also identified in the KHI sample.

The 0-100 eV binding energy region of a high resolution XPS spectrum of KI and KHI are shown in Figs. 14a and b, respectively. Peaks centered at 21 and 37 eV which do not correspond to any other primary element peaks were observed in the case of the KHI sample. The intensity and shift match shifted K3 s and K3 p. Hydrogen is the only element which does not have primary element peaks; thus, it is the only candidate to produce the shifted peaks. These peaks may be shifted by a highly binding hydride ion H⁻(1/6) with a binding energy of 22.8 eV given by Eq. (A.12) that bonds to potassium K3 p and shifts the peak to this energy. In this case, the K3 s is similarly shifted.

9

HE 1158

R.L. Mills et al. | International Journal of Hydrogen Energy 000 (2000) 000-000



3.2.2. XPS of potassium chloro hydride sample

A survey spectrum was obtained over the region $E_b = 0$ to 1200 eV. The primary element peaks allowed for the determination of all of the elements present in the magenta crystals of the KHCL sample and the control KCl. The survey spectrum also detected shifts in the binding energies of the elements which had implications to the identity of the compound containing the elements.

compound containing the elements.

The XPS survey scan of the KHCl sample and the KCl control sample are shown in Figs. 15 and 16, respectively.

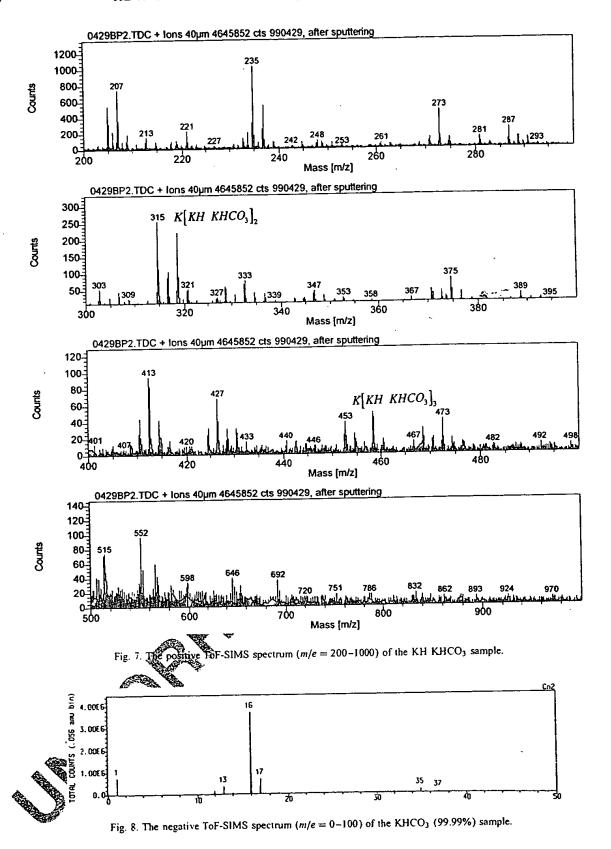
Cls at 284.6 eV was used as the internal standard for the

KHCl sample and the control KCl sample. The major species observed in the KHCl sample and the control were potassium and chlorine. Trace small amounts of carbon, oxygen, fluorine, iodine, and silicon were also identified in the KHCl sample. The identifying peaks of the primary elements and their binding energies are: FKL23L23 at 831.0 eV, F1s at 688.4 eV and at 682.8 eV, O1s at 530.6 eV, K2s at 377.2 eV, K2p1/2 at 295.4 eV, K2p3/2 at 292.5 V, C1s at 284.6 eV, C12s at 268.9 eV, C12p1/2 at 199.5 eV, C12p3/2 at 198.0 eV, Si2s at 152.4 eV, and Si2p3/2 at 101.9 eV. The K 3p and K 3s of the KHCl sample occurred at 16.7 and 32.8 eV,

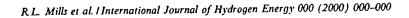




R.L. Mills et al. [International Journal of Hydrogen Energy 000 (2000) 000-000







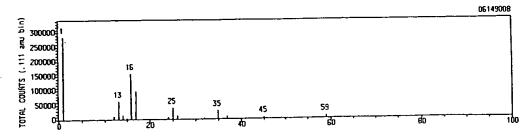


Fig. 9. The negative ToF-SIMS spectrum (m/e = 0-100) of the KH KHCO₃ sample.

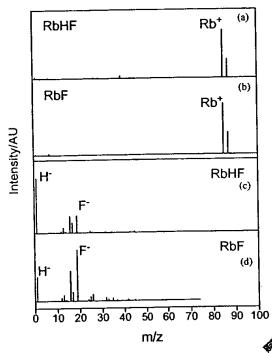


Fig. 10. (a) The positive ToF-SIMS spectrum (m/e = 0.400) of RbHF. (b) The positive ToF-SIMS spectrum (m/e=0-100) of Rb (c) The negative ToF-SIMS spectrum (m/e = 0 - 100)(d) The negative ToF-SIMS spectrum (m/e = 0)

respectively. The K3p and K3 s of the control KCl occurred at 17.0 and 32.8 eV, respectively.

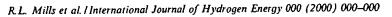
at 17.0 and 32.8 eV, respectively.

No elements were present in the survey scan which could be assigned to peaks in the low binding energy region with the exception of the K 3h and 8 3s peaks at 16.7 and 32.8 eV, respectively, and the 14ds, and 14ds/2 peaks at 51.8 and 49.7 eV respectively. Accordingly, any other peaks in this region must be due to novel species. The 0-125 eV binding energy region of a high resolution XPS spectrum of the KHCI sample and the control KCI sample are shown in 17 and 18, respectively. The XPS spectrum of the KHO sample differs from that of KCl by having an additional feature at 36.7 eV. The XPS peak centered at 36.7 eV that does not correspond to any other primary element peak

may correspond to the $H^-(n = 1/8)E_b = 36.1$ eV hydride ion given by Eq. (A.12) where E_b is the predicted vacuum binding energy. Also the K3s and K3 p peaks in the KHCl sample are wider when compared to the K3 s and K3 p of the KCl control. The Cl3p at 16 eV is merged with the K3 p of the KHCl sample, but the peaks are separated in the control taken at the same resolution. This clearly indicates that the environment of K in the KHC sample is different from that of KCl. The data further midicales the formation of a novel compound.

3.2.3. XPS of alkali halido hydrides and alkaline earth

halido hydrides samples halido hydrides samples halido hydrides (KHF, of a series of alkali and alkaline earth halido hydrides (KHF, KHCI, KHBE KHI, REHF, RbHCI, RbHBr, RbHI, CsHF, CsHCl, CsHB SHI, CaHCl, CaHBr, CaHI, SrHF, SrHCl, and SrHBr) were analyzed by XPS. The local structure of metal halides and metal halido hydrides was investigated by studying the metal core levels including K 2p, Rb 3d, Cs de Caro, and Sr 3d, and halogen core level including F , CD2p Br 2p, and I 3d. As atomic hydrogen undergoes tion with a catalyst to form a lower-energy hydrogen species which subsequently reacts with the metal center in a halide compound, alterations in the electronic structure of the metal such as changes in core level binding energies and spin-orbital energies relative to the starting halide are expected. In order to compare the full width at half maximum (FWHM) of the peaks, the difference between spin-orbit splitting in the core level was determined using curve fitting in the same or a close energy range. In some cases, the absolute core level binding energy was not calibrated, which did not affect the validity of the comparison of FWHM values. The results of the determination of the binding energies of selected core level electrons, full width at half maximum of the peaks, and energy of spin-orbital splitting for alkali halido hydrides, calcium halido hydrides, and strontium halido hydrides compared with the corresponding alkali halides, calcium halides, and strontium halides are listed in Tables 1-3, respectively. The XPS spectra of the K 2p core level in KI, KHI appear in Figs. 19a and b, respectively. The XPS spectra of the I 3d core level in KI and KHI appear in Figs. 20a and b, respectively. The XPS spectra of the Ca 2p core level in CaBr2 and CaHBr appear in Figs. 21a and



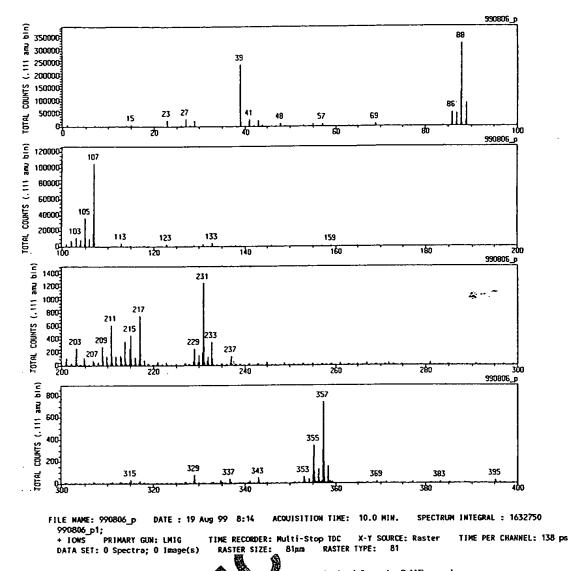


Fig. 11. The position To FSIMS spectrum obtained from the SrHF sample.

b, respectively. The XPS spectra of the School level in SrBr₂ and SrHBr appear in Figs 22a and b, respectively. The XPS spectra of the Br 2p core level in SrBr₂ and SrHBr appear in Figs. 23a and b. respectively.

appear in Figs. 23a and b. respectively.

It is clear that the FWHM of the metal core level peaks in alkali and alkaline earth halido hydrides is broader than that in the corresponding tables. The magnitude of broadening ranges from 0.3 to 0.9 eV, depending on compound. The trend for the troadening effect follows the sequence: iodo hydrides brome hydrides > fluoro hydrides chloro hydrides. In contrast, the halogen core level FWHM in both alkali and alkaline earth halido hydrides is broadened by only about 0.2 to 0.3 eV compared to the corresponding halide. Comparing the alterations in the metal core levels versus the halogen core level indicates that the lower-energy

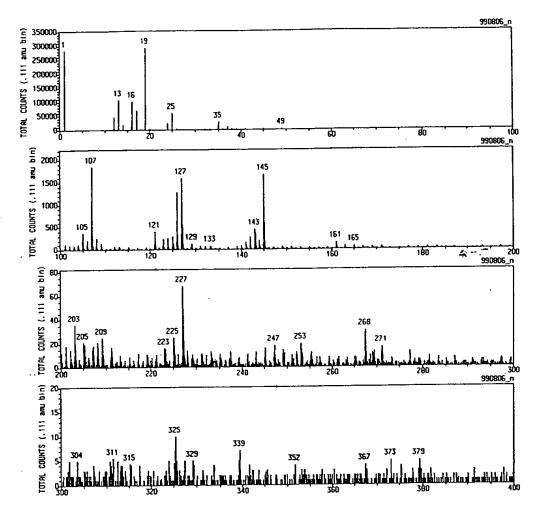
hydrogen species is bound to the metal center of the alkali or alkaline earth halide. This binding influences the metal core level with little perturbation of the halogen core level.

Each of the spectra of potassium iodo hydride, calcium bromo hydride, and strontium bromo hydride were curve fit with one spin-orbit splitting component having a similar FWHM and energy separation as that of the starting material potassium iodide, calcium bromide, and strontium bromide, respectively. An additional -spin-orbit splitting component had to be added to each of potassium iodo hydride, calcium bromo hydride, and strontium bromo hydride in order to obtain a good curve fit of the K 2p, Ca 2p, and Sr 3d spectra. In each case, the second component of spin-orbit splitting is assigned to the formation of the alkali or

HE 1158

R.L. Mills et al. | International Journal of Hydrogen Energy 000 (2000) 000-000

ANALYTICAL SERVICES GROUP SURFACE ANALYSIS LABORATORY T:609-490-1090 F:609-490-1066



FILE NAME: 990806_n DATE: 19 Aug 99 13:50 ACQUISITION TIME: 10.0 MIN. SPECTRUM INTEGRAL: 1247518

- IONS PRIMARY GUN: LMIG TIME RECORDER: Multi-Stop TDC X-Y SOURCE: Raster TIME PER CHANNEL: 138 DATA SET: 0 Spectra; 0 Image(s) ____ RASTER SIZE: 173дш RASTER TYPE: 173

Fig. 12. The negative ToF-SIMS spectrum obtained from the SrHF sample.

alkaline earth metal halido todride KHI, CaHBr, and SrHBr, respectively. The present of the novel hydride ion shifts the K 2p, Ca 2p and \$1,30 peaks to lower binding energies relative to the corresponding peaks of KI, CaBr₂, and SrBr₂, respectively.

The XPS data clearly indicates a change in the electronic structure at the metal-core level and different bonding in the metal halide by dides relative to that in the corresponding metal halide at strongly suggests the formation of a novel metal hydride which is consistent with the supporting data provided by XPS given above and NMR, ToF-SIMS, and gas chromatography/mass spectroscopy given in the respective sections.

3.3. NMR

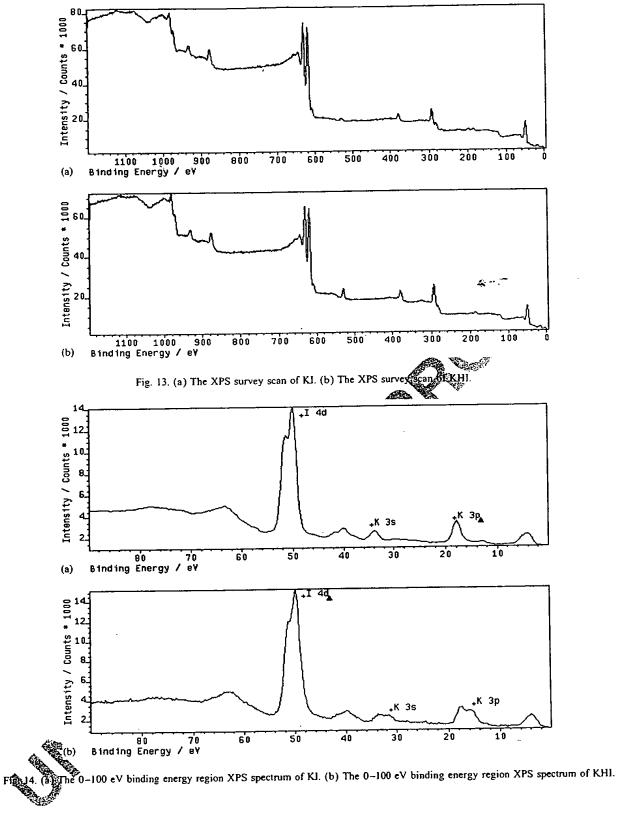
To eliminate the possibility that the alkali halide MX influenced the local environment of the ordinary alkali hydride MH to produce an NMR resonance that was shifted upfield relative to MH alone, controls comprising MH and a MH/MX mixture were run.

3.3.1. NMR of potassium iodo hydride sample

The ¹H MAS NMR spectra of the KHI sample, the control comprising an equal molar mixture of KH and KI, and control KH relative to external tetramethylsilane (TMS) are shown in Figs. 24a, b, and c, respectively. Ordinary hy-



R.L. Mills et al. I International Journal of Hydrogen Energy 000 (2000) 000-000



HE 1158

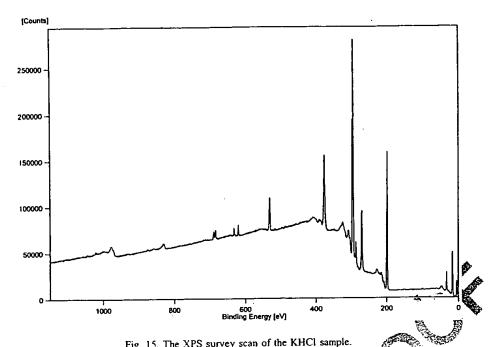


Fig. 15. The XPS survey scan of the KHCl sample.

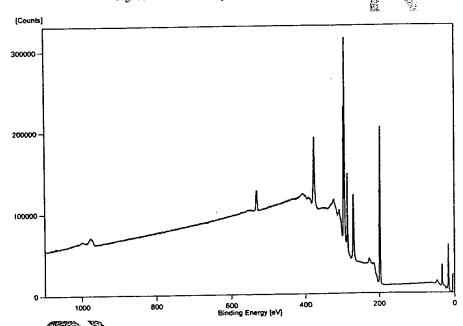


Fig. 16. The XPS survey scan of the KCl control sample.

dride ion has a resonance at 1.1 and 0.8 ppm in the KH/KI mixture and in KH alone as shown in Figs. 24b and c, respectively the additional peak at 4.5-4.6 ppm is assigned to KOH formed from air exposure of KH during sample handling. The spin speed was varied to confirm real peaks versus side bands. The latter changed position with spin speed, the former were independent of spin speed. The unlabeled peaks shown in Figure 24a were found to be side-

The presence of KI does not shift the resonance of ordinary hydride. The resonance at 0.9 ppm which is assigned to ordinary hydride ion was observed in the spectrum of the KHl sample as shown in Fig. 24a. The distinct 0.8 and 1.1 ppm resonances could not be resolved if they were present.





R.L. Mills et al. | International Journal of Hydrogen Energy 000 (2000) 000-000

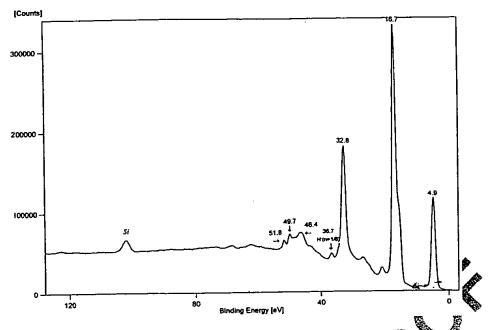


Fig. 17. The 0-125 eV binding energy region of a high resolution XPS spectrum of the KHC sample

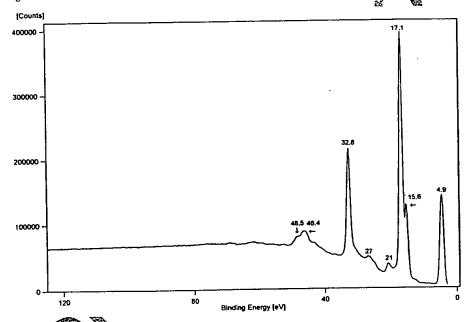


Fig. 18. The 0-125 V binding energy region of a high resolution XPS spectrum of the KCl control sample.

A large distinct upfield resonance was observed at -3.2 ppm which was not observed in either control. This upfield shifted peak is consisted with a hydride ion with a smaller radius as compared with ordinary hydride since a smaller radius increases the shielding or diamagnetism. The -3.2 ppm peak is a signed to a novel hydride ion that has a smaller radius than that of ordinary hydride ion since the shift was extraordinarily far upfield in the case of the KHI sample.

3.3.2. NMR of potassium chloro hydride sample

The ¹H MAS NMR spectra of the KHCl sample, the control comprising an equal molar mixture of KH and KCl, and the control KH relative to external tetramethylsilane (TMS) are shown in Figs. 25a, b, and c, respectively. Ordinary hydride ion has a resonance at 1.1 and 0.8 ppm in the KH/KCl mixture and in KH alone as shown in Figs. 25b and c, respectively. The additional peak at 6 ppm is assigned



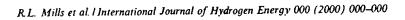


Table 1
The results of the determination of the binding energies of selected core level electrons, full width at half maximum of the peaks, and energy of spin-orbit splitting for alkali halido hydrides compared with the corresponding alkali halides

Compound	Peak	Binding energy (eV) ^a	Full width at half maximum (FWHM) (eV)	Energy of spin- orbit splitting (eV)
VE.	K 2p3/2	298.37	2.24	2.80
KF	K 2p3/2 K 2p1/2	301.11	2.27	
	F Is	688.97	2.33	
KHF	K 2p3/2	296.12	2.61	2.72
NJ1	K 2p1/2	298.84	2.61	
	Fis	687.60	2.20	
v.C1	K 2p3/2	296.87	1.88	2.75
(C)	K 2p3/2 K 2p1/2	299.62	1.97	•
		202.27	1.82	1.68
	Cl 2p3/2 Cl 2p1/2	203.95	1.58	A
			1.91	2.74
KHCI	K 2p3/2	297.09 299.85	1.98	
	K 2p1/2		A	
	Cl 2p3/2	202.57	1.77	.62
	Cl 2p1/2	204.19	1.60	
КВг	K 2p3/2	297.15	1.63	2.75
	K 2p1/2	299.90	1.72	7
	Br 3p3/2	186.34	2.55	6.87
	Br 3p1/2	193.07	2.39	
KIID-	K 2p3/2	296.90	2.10	2.76
KHBr	K 2p1/2	299.66	1.86	
	-	186.18		6.79
	Br 3p3/2 Br 3p1/2	192.87	99	
	-			2.75
K)	K 2p _{3/2}	294.44	1.84	2.75
	K 2p _{1/2}	297.19		
	1 3d _{3/2}	620.37	2.07	11.53
	1 3d _{3/2}	631.90	2.14	
кні	K 2p _{3/2}	294.37	1.83	2.77
	K 2p _{1/2}	297.14	1.81	
	K 2p _{3/2}	29:251	1.87	
	K 2p _{1/2}	295	1.78	3.00
	1 3d _{5/2}	621.08	2.17	11.52
	1 3d _{3/2}	632.60	2.20	
61.5		115.00	2.28	1.55
RbF	Rb 3ds _{/2}	116.55	2.08	
			2.30	
		688.35		1.56
RbHF	Rh 3d _{5/2}	114.65	1.95	1.55
4	R5/3d _{3/2}	116.37	1.56 2.24	
	Rb 3d _{5/2} Rb 3d _{3/2}	114.02 115.58	1.88	- 1.56
	Fls	688.35	2.10	
RbCl	Rb 3d _{5/2}	115.17	1.84	1.55
Carlot State	Rb 3d _{3/2}	116.72	1.77	

R.L. Mills et al. | International Journal of Hydrogen Energy 000 (2000) 000-000

Table 1. (Continued)

18

Compound	Peak	Binding energy (eV) ^a	Full width at half maximum (FWHM) (eV)	Energy of spin- orbit splitting (eV
	Cl 2p _{3/2}	203.39	1.75	1.66
	Cl 2p _{1/2}	205.05	1.69	
uuci	Rb 3d _{5/2}	114.30	2.17	1.56
кьнсі	Rb 3d _{3/2}	115.86	2.02	
			2.01	1.72
	Cl 2p _{3/2}	202.59 204.33	1.70	1.72
	Cl 2p _{1/2}			
lbBr	Rb 3d _{5/2}	114.46	1.76	1.51
	Rb 3d _{3/2}	115.97	1.83	
	Br 3p _{3/2}	186.56	2.88	6.66
	Br 3p _{1/2}	193.22	1.75	
вьнвг	Rb 3d _{5/2}	114.54	1.74	1.56
	Rb 3d _{3/2}	116.0	1.85	A
	Br 3p _{3/2}	186.65	2.70	3.63
	Br 3p _{1/2}	193.38	1.69	
кы	Rb 3d _{5/2}	114.54	1.99	N. 339
(01	Rb 3d _{3/2}	116.09	1.81	
	I 3d _{5/2}	623.72	2.04	11.49
	I 3d _{3/2}	635.21	2.07	3
		114.29	2.31	1.56
кьні	Rb 3d _{5/2} Rb 3d _{3/2}	115.85	1.89	
	•		2.10	11.50
	1 3d _{5/2}	623.28 634.78	2.17	
	1 3d _{3/2}			
CsF	Cs 3d _{5/2}	746.18		
	Fls	690.55		
CsHF	Cs 3d _{5/2}	741.30	22.2	
	Cs 3d _{5/2}	738.63		
	F Is	687.81	3.01	
	F 1s	684.23	2.60	
2-01	Cs 3d _{5/2}	74001	2.04	
CsC1	Cl 2p _{3/2}	205 45	1.65	1.50
	Cl 2p _{1/2}	20028	1.43	
2-1161	Cs 3d _{5/2}		2.35	
CsHCI	Cs 303/2 Cl 2p _{3/2}	203.60	1.73	1.56
	Cl 2p _{1/2}	205.24	1.58	
0 B	C 23	745.01	1.78	
CsBr	Control of the contro	743.01	,	
		100.22	2.25	6.68
	BrZp	188.33	2.35 2.13	0.00
<i>A</i> -	Br2p _{1/2}	195.01		
CsHBr 🎇	3d _{5/2}	728.79	2.40	~
	Cs 3d _{3/2}			
1 1 1 1 1 1 1 1 1 1 1 1 1 1 1 1 1 1 1	Br 2p _{3/2}	186.38	2.45	6.63
A A	Br 2p _{1/2}	193.01	2.08	

HE 1158





R.L. Mills et al. I International Journal of Hydrogen Energy 000 (2000) 000-000

Table 2
The results of the determination of binding energies of selected core level electrons, full width at half maximum of the peaks, and energy of spin-orbit splitting for calcium halido hydrides compared with the corresponding calcium halides

Compound	Peak	Binding energy (eV) ^a	Full width at Half Maximum (FWHM) (eV)	Energy of spin- orbit splitting (eV)
CaCl ₂	Ca 2p _{3/2}	352.18	2.25	3.51
	Ca 2p _{1/2}	355.69	2.19	
	Cl 2p _{3/2}	203.12	2.28	1.81
	Cl 2p _{1/2}	204.93	1.86	
CaHCl	Ca 2p _{3/2}	351.95	2.88	3.67
	Ca 2p _{1/2}	355.62	2.34	
	Cl 2p _{3/2}	202.75	2.25	1.57
	Cl 2p _{1/2}	204.32	2.01	
CaBr ₂	Ca 2p _{3/2}	348.24	1.79	3.51
•	Ca 2p _{1/2}	351.75	1.83	
	Br 3p _{3/2}	182.86	2.62	6.58
	Br 3p _{1/2}	189.54	2.36	
CaHBr	Ca 2p _{3/2}	347.36	2.38	3.59
	Ca 2p _{1/2}	350.95	2.02	
	Ca 2p _{3/2}	349.06	1.85	3.41
	Ca 2p _{1/2}	352.47	1.60	
	Br 3p _{3/2}	182.86	3.16	6.66
	Br 3p _{1/2}	189.52	2.97	
Cal ₂	Ca 2p _{3/2}	356.08	2 5	2.54
	Ca 2p _{1/2}	358.62	2.3	
	1 3d _{5/2}	624.27	2.38	11.51
	1 3đ _{3/2}	635.78	22.33	
CaHl	Ca 2p _{3/2}	352.05	3.08	3.86
	Ca 2p _{1/2}	355.91	2.63	
	1 3d _{5/2}	40	2.57	11.54
	I 3d _{3/2}		2.46	

^aUncalibrated, except for CaBr₂ and CaHBr

to KHCO3 formed from air exposure of K during sample handling. The additional sharp beak at 4.3 ppm shown in Fig. 25b is assigned to water in the KCl crystals. The additional broad peak at 46 ppm shown in Fig. 25c is assigned KOH formed from air exposure of KH during sample handling.

The presence of KCl does not shift the resonance of ordinary hydride. The resonance at 1.1 ppm which is assigned to ordinary hydride ion was observed in the spectrum of the KHCl sample as shown in Fig. 25a. The distinct 0.8 and 1.1 ppm resonances could not be resolved if they were

present. A large distinct upfield resonance was observed at -4.6 ppm which was not observed in either control. This upfield shifted peak is consistent with a hydride ion with a smaller radius as compared with ordinary hydride since a smaller radius increases the shielding or diamagnetism. The -4.6 ppm peak is assigned to a novel hydride ion that has a smaller radius than that of ordinary hydride ion since the shift was extraordinarily far upfield in the case of the KHCl sample. An additional water peak was found is other samples in which the novel hydride peak was observed. The presence of a water peak may demonstrate that the novel

Table 3

The results of the determination of the binding energies of selected core level electrons, full width at half maximum of the peaks, and energy of spin-orbit splitting for strontium halido hydrides compared with the corresponding strontium halides

Compound	Peak	Binding energy (eV) ^a	Full width at half maximum (FWHM) (eV)	Energy of spin- orbit splitting (eV)
C-E	Sr 3d _{5/2}	140.46	2.13	1.81
SrF ₂	Sr 3d _{3/2}	142.27	1.77	
	Fls	691.12	2.11	
SrHF	Sr 3d _{5/2}	139.20	2.48	1.91
3111	Sr 3d _{3/2}	141.11	1.95	
	Fis	689.88	2.42	
SrCl ₂	Sr 3d _{5/2}	139.45	2.36	1.86
SICI ₂	Sr 3d _{3/2}	141.31	1.88	•
	C1 2p _{3/2}	203.61	2.06	3 .70
	Cl 2p _{1/2}	205.31	1.95	
SrHC1	Sr 3d _{5/2}	138.71	2.61	Ju.87
Diffe.	Sr 3d _{3/2}	140.52	1.99	
	Cl 2p _{3/2}	202.98	2.06	1.72
	Cl 2p _{1/2}	204.70	1.89	#
SrBr ₂	Sr 3d _{5/2}	139.52	1.58	1.7
0.0.2	Sr 3d _{3/2}	141.22	1.65	
	Br 3p _{3/2}	187.45	2.50	6.77
	Br 3p _{1/2}	194.22	2	
SrHBr	Sr 3d _{5/2}	138.56		1.96
	Sr 3d _{3/2}	140.52	.62	
	Sr 3d _{5/2}	136.69	95	2.60
	Sr 3d _{3/2}	139.29	1.55	
	Br 3p _{3/2}	186.56	2.77	6.68
	Br 3p _{1/2}	19324	2.43	

^{*}Uncalibrated, except for SrBr2 and SrHE

hydride is stable to water, in the case that the water is not associated with unreacted KCl alone. This could partially explain why the KHCl sample was observed to be insoluble in water.

3.3.3. NMR of porassium momo hydride sample

The ¹H MAS NMR spectra of the KHBr sample, the control comprising an equation of mixture of KH and KBr, and the control KH relative to external tetramethylsilane (TMS) are shown in Figs. 26a, b, and c, respectively. Ordinary hydride ion has a resonance at 1.1 and 0.8 ppm in the KH/KBr mixture and in KH alone as shown in Figs. 26b and 26c, respectively. The additional sharp peaks at 4.3 and 5.9 ppm shown in Fig. 26a are assigned to water and KHCO₃ formed

from air exposure of K during sample handling. The additional sharp peak at 4.2 ppm shown in Fig. 26b is assigned to water in the KBr crystals. The additional broad peak at 4.6 ppm shown in Fig. 26c is assigned KOH formed from air exposure of KH during sample handling.

The presence of KBr does not shift the resonance of ordinary hydride. The resonance at 1.2 ppm which is assigned to ordinary hydride ion was observed in the spectrum of the KHBr sample as shown in Fig. 26a. The distinct 0.8 and 1.1 ppm resonances could not be resolved if they were present. A large distinct upfield resonance was observed at -4.1 ppm which was not observed in either control. This upfield shifted peak is consistent with a hydride ion with a smaller radius as compared with ordinary hydride since a

HE 1158





R.L. Mills et al. | International Journal of Hydrogen Energy 000 (2000) 000-000

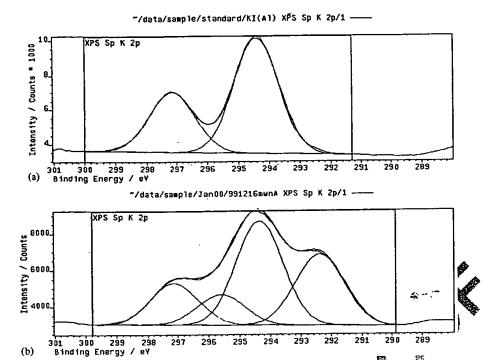


Fig. 19. (a) The XPS spectra of the K 2p core level in KI. (b) The XPS spectra of the K 2p core level in KHI.

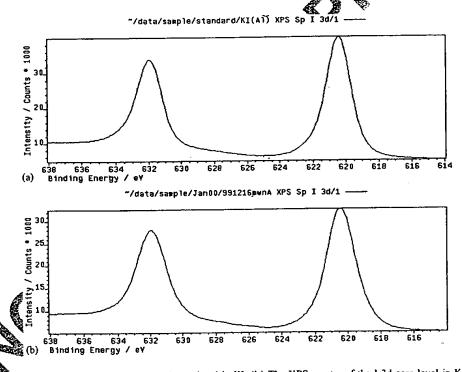
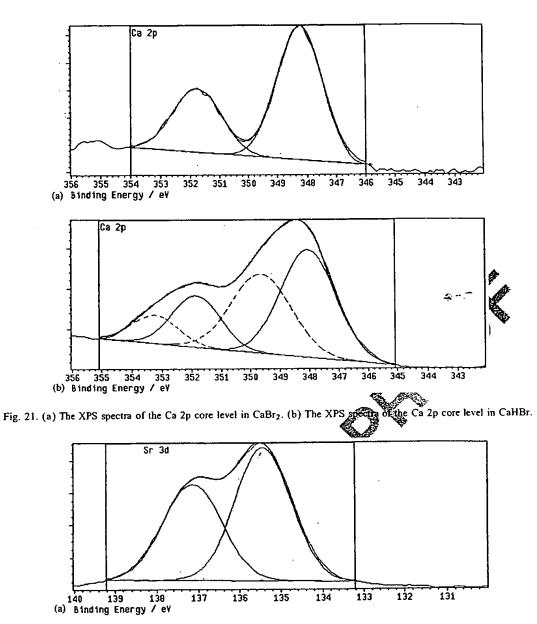


Fig. 20. (a) The XPS spectra of the I 3d core level in KI. (b) The XPS spectra of the I 3d core level in KHI.





R.L. Mills et al. | International Journal of Hydrogen Energy 000 (2000) 000-000



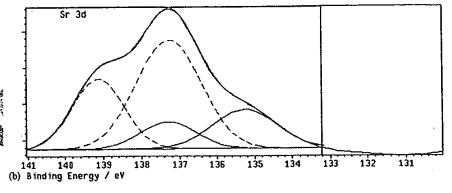
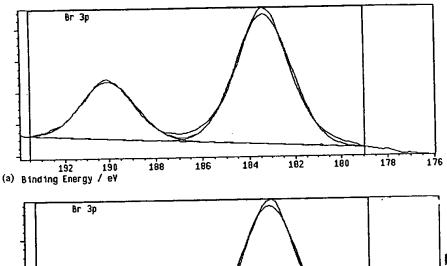


Fig. 22. (a) The XPS spectra of the Sr 3d core level in SrBr₂. (b) The XPS spectra of the Sr 3d core level in SrHBr.



194 192 190 188 186 184 182 180 178 (b) Binding Energy / eV

Fig. 23. (a) The XPS spectra of the Br 2p core level in SrBr₂. (b) The XPS spectra of the Br 2p core level in SrHBr.

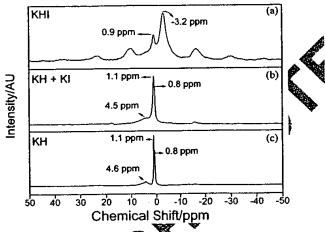


Fig. 24. (a) The ¹H MAS NAR spectrum of KHI relative to external tetramethylsilane (TMS). (b) The ¹H MAS NMR spectrum of the control comprising an equal modes mixture of KH and KI relative to external tetramethylsilane (TMS). (c) The ¹H MAS NMR spectrum of the control KH relative to external tetramethylsilane (TMS).

smaller radius increases the shielding or diamagnetism. The —A1 ppin peak is assigned to a novel hydride ion that has a smaller radius than that of ordinary hydride ion since the shift was extraordinarily far upfield in the case of the KHBr sample.

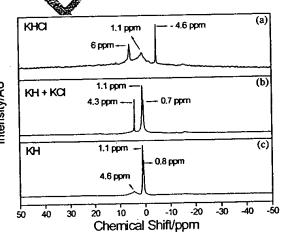


Fig. 25. (a) The ¹H MAS NMR spectrum of KHCl relative to external tetramethylsilane (TMS). (b) The ¹H MAS NMR spectrum of the control comprising an equal molar mixture of KH and KCl relative to external tetramethylsilane (TMS). (c) The ¹H MAS NMR spectrum of the control KH relative to external tetramethylsilane (TMS).

3.3.4. NMR of rubidium fluoro hydride sample

The ¹H MAS NMR spectrum of RbHF relative to external tetramethylsilane (TMS) is shown in Fig. 27a. Distinguishable resonances were observed at 1.2 and -4.4 ppm. The

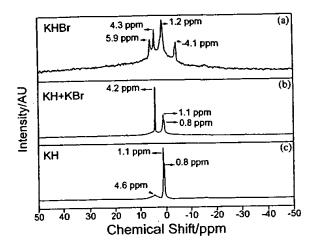


Fig. 26. (a) The ¹H MAS NMR spectrum of KHBr relative to external tetramethylsilane (TMS). (b) The ¹H MAS NMR spectrum of the control comprising an equal molar mixture of KH and KBr relative to external tetramethylsilane (TMS). (c) The ¹H MAS NMR spectrum of the control KH relative to external tetramethylsilane (TMS).

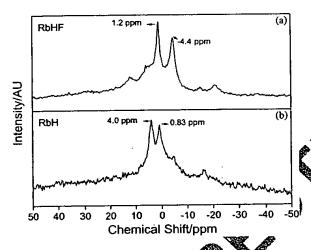


Fig. 27. (a) The ¹H MAS NMR spectrum of BhH relative to external tetramethylsilane (TMS). (b) The H MAS NMR spectrum of the control RbH relative to external tetramethylsilane (TMS).

upfield peak is assigned to a novel hydride ion of RbHF. The down field shifted peaksmay be ordinary hydride in a different chemical environment. The ¹H MAS NMR spectrum of the control Rolf relative to external tetramethylsilane (TMS riss shown in Fig. 27b. The 0.83 ppm peak is assigned to ordinary hydride ion of RbH. The peak at 4.0 ppm is assigned to RbOH formed from air exposure of RbH during sample handling.

The upfield shifted peak observed in the RbHF sample is consistent with a hydride ion with a smaller radius as

compared with ordinary hydride since a smaller radius increases the shielding or diamagnetism. The -4.4 ppm peak is assigned to a novel hydride ion that has a smaller radius than that of ordinary hydride ion since the shift was extraordinarily far upfield in the case of the RbHF sample.

3.3.5. NMR of strontium bromo hydride sample

The SrHBr sample was not spun; so, the hydride peaks were not resolved. Instead valuable ${}^{1}H^{-1}H$ separation data as well as ${}^{1}H$ content was obtained. The ${}^{1}H$ MAS NMR spectra of SrHBr relative to external $H_{2}O$ is shown in Fig. 28. The sample contained a significant amount of hydrogen with an integration of 0.0983 mmoles corresponding to about 0.02 wt% ${}^{1}H$ in the sample. There are two components: a narrow component with a peak at 6.3 ppm having an area of approximately 1/4th of the total signal, and a broad signal with a width of about 60 kHz The broadening of the peak corresponds to ${}^{1}H^{-1}H$ separation of under 1.5 Å. This is very significant given that the unit cell (orthorhombic P_{nma} form) parameters for ordinal stroptium hydride are a = 7.358 Å, b = 6.377 Å and c = 3.382 Å. The seven short M-H distances are 2.39 Å and c = 3.382 Å. The seven short M-H distances are 2.39 Å [11]. The data is consistent with a novel hydride ion of a greatly reduced radius.

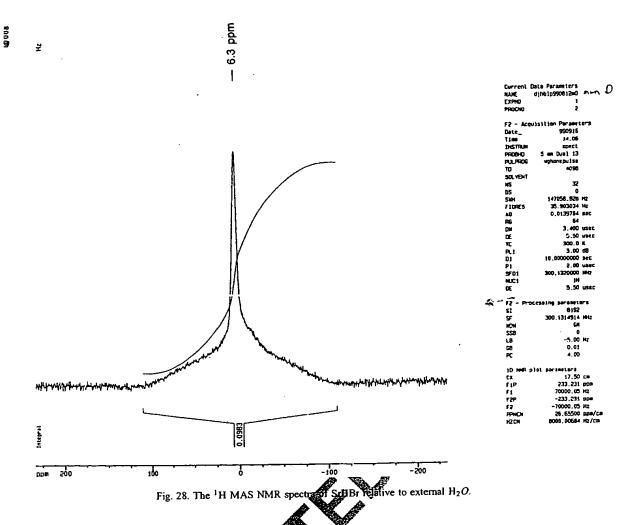
3.4. Gas chromatography (GC)

The gas chromatograph of the normal hydrogen gave the retention time for para hydrogen and ortho hydrogen as 14.5 and 5.5 min, respectively. Control SrBr2 showed no hytroger release upon heating to above 600°C. The gas chrohatograph of the dihydrino (see Appendix) or hydrogen resed from the SrHBr sample when it was heated to above 600°C is shown in Fig. 29. This chromatograph is representative of the results of the determination of dihydrino or hydrogen released from each sample of MHX or MHMX when heated to 600°C. In the case of a very stable hydride, no hydrogen may be released, thus, the amount observed in the minimum content. Table 4 gives a results which are representative of the minimum dihydrino or hydrogen content of novel hydride compounds determined by gas chromatograph of the gas released from each sample when it was heated to above 600°C. Each control, MX or MX2, showed no hydrogen release upon heating to above 600°C.

3.5. Mass spectroscopy (MS)

The dihydrino (see Appendix) was identified in the gas released by thermal decomposition of solid samples by mass spectroscopy. Dihydrino was detected as a species with a mass to charge ratio of two (m/e=2) that has a higher ionization potential than that of normal hydrogen by recording the ion current as a function of the electron gun energy. The intensity as a function of time for masses m/e=1, m/e=2,





and m/e = 3 obtained while changing the ionization potential (IP) of the mass spectrometer from 30 to 70 eV intrapure hydrogen is shown in Fig. 30. Upon the easing the ionization potential from 30 to 70 eV, the ally the n/e = 2 ion current for the ultrapure hydrogen uncertained by a factor of less than 2.

The intensity as a function of time for masses m/e = 1, m/e = 2, and m/e = 3 obtained while changing the ionization potential (IP) of the mass spectrometer from 30 to 70 eV for gas released from thermal decomposition of the KHI sample is shown in Fig. 31. Open increasing the ionization potential from 30 to 70 eV, typically the m/e = 2 ion current for the KHI sample increased by a factor of about 1000 under the same pressure conditions as those of the ultrapure hydrogen control. Fig. 31 is representative of the results of the determination of the increase in the m/e = 2 ion current for each sample of MHX or MHMX upon increasing the ionization potential from 30 to 70 eV under the same pressure conditions as those of the ultrapure hydrogen control.

The m/e = 2 ion current for the KHCl, KH KHCO₃, CsHI, SrHF, and SrHBr sample increased by a factor of about 400, 200, 400, 20, and 50, respectively, under the same pressure conditions as those of the ultrapure hydrogen control.

4. Conclusions

The ToF-SIMS, XPS, NMR, and thermal decomposition with analysis by GC, and MS results confirm the identification of novel hydride compounds MHX and MHMX wherein M is the metal, X, is a singly negatively charged anion, and H comprises a novel high binding energy hydride ion. The negative ToF-SIMS spectra of KHI, KH KHCO₃. RbHF, and SrHF were dominated by the hydride ion peak which identified the structures. The thermal decomposition with mass spectroscopic analysis indicated the minimum hydrogen or dihydrino content. At least H⁻(1/2) was observed to be present in KHX and KH KHCO₃.

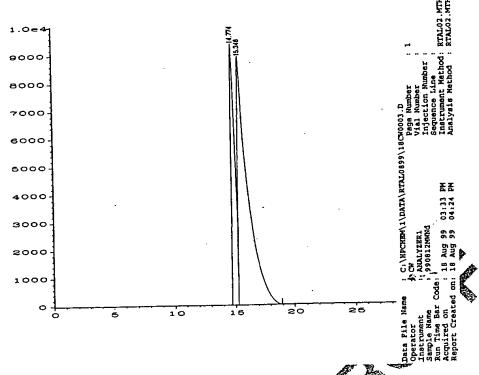


Fig. 29. The gas chromatograph of the dihydrino or hydrogen released from the SrHBr sample when it was heated to above 600°C.

Table 4

The minimum dihydrino or hydrogen content of novel hydride compounds determined by gas chromatograph of the gas released from each sample when it was heated to above 600° C

Novel hydride compound	Hydrogen or dihydrino content (µmol/g)				
KHI KHCI KHKHCO3 SrHF SrHBr	400 200 40 130				

The XPS of the low binding energy region of KHI is consistent with the presence of H (n=1/6) $E_b=22.8$ eV. This product is predicted by an autocatalysis reaction of two H(1/4) atoms formed via a potassium catalyst which has been confirmed by extreme ultraviolet spectroscopy [3]. The XPS of KHGI is consistent with the presence of a new policity of eV which is in agreement with the predicted binding energy of $H^-(n=1/8)$ $E_b=36.1$ eV. The bording of hydrino hydride ions with alkali and alkaline earth metals significantly broadens the metal core level peaks. The magnitude of broadening ranges from 0.3 to 0.9 eV, depending on compound. The

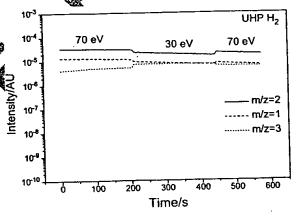


Fig. 30. The intensity as a function of time for masses m/e = 1, m/e = 2, and m/e = 3 obtained while changing the ionization potential (IP) of the mass spectrometer from 30 to 70 eV for ultrapure hydrogen.

trend for the broadening effect follows the sequence: iodo hydrides~bromo hydrides > fluoro hydrides~chloro hydrides. In particular, two additional spin-orbit splittings had to be added to each of potassium iodo hydride, calcium bromo hydride, and strontium bromo hydride in order to obtain a good curve fit of the K 2p, Ca 2p, and Sr 3d spectra, respectively.

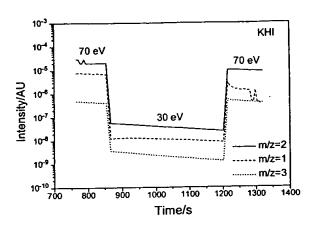


Fig. 31. The intensity as a function of time for masses m/e = 1, m/e = 2, and m/e = 3 obtained while changing the ionization potential (IP) of the mass spectrometer from 30 to 70 eV for gas released from thermal decomposition of the KHI sample.

Large distinct upfield resonances were observed at -3.2 ppm, -4.6 ppm, -4.1 ppm, -4.4 ppm in the case of KHI, KHCl, KHBr, and RbHF, respectively. The peaks are assigned to novel hydride ions that have substantially smaller radii than that of ordinary hydride ion since the shift was extraordinarily far upfield. The NMR peak of KHI at -3.2 ppm may be due to $H^-(n = 1/6)$ $E_b = 22.8$ eV observed by XPS. The NMR peak of KHCl at -4.6 ppm may be due to $H^-(n=1/8)$ $E_b = 36.1$ eV observed by XPS. The NMR of SrHBr showed a $^1H^{-1}H$ separation of under 1.5 Å. This is very significant compared to the atomic spacing parameters of ordinary strontium hydride and is consistent with a novel hydride ion of a greatly reduced radius.

The chemical structure and properties of the present novel compounds are indicative of a new field of hydrogy chemistry. Novel hydride ions may combine with other cations such as other alkali cations and alkaline early, rare and, and transition element cations. Numerous noted ompounds may be synthesized with extraordinant properties felative to the corresponding compounds having ridinary hydride ions. These novel compounds may have a breath of applications. For example, a high voltage lattery according to the hydride binding energies observed by XPS may be possible having projected specifications that surpass those of the internal combustion engine. The discovery of a novel hydride ion with a high binding energy has implications for a new field of hydride enemistry with applications such as a high voltage batter (19).

Hydride items laying extraordinary binding energies may stabilize a bion M^{x+} in an extraordinarily high oxidation state such as 12 in the case of lithium. Thus, these hydride ions may be used as the basis of a high voltage battery of a rocking chair design wherein the hydride ion moves back and forth between the cathode and anode half cells

during discharge and charge cycles. Exemplary reactions for a cation M^{r+} are:

Cathode reaction:

$$MH_x + e^- \rightarrow MH_{x-1} + H^-$$
 (1)

Anode reaction:

$$MH_{x-2} + H^- \rightarrow MH_{x-1} + e^-$$
 (2)

Overall reaction:

$$MH_x + MH_{x-2} \rightarrow 2MH_{x-1}. \tag{3}$$

Appendix A.

It has been reported that intense extreme ultraviolet (EUV) emission was observed at low temperatures (e.g. ≈ 10³ K) from atomic hydrogen and certain atomized elements or certain gaseous ions which ionize at integer multiples of the potential energy of atomic hydrogen, 27.2 eV [1-6]. The mechanism of EUV-emission can not be explained by the conventional chemistry of hydrogen, but it is predicted by a solution of the schrodinger equation with a nonradiative boundary constraint put forward by Mills [12,13]. The energy release must result in a lower-energy state of hydrogen. Mills predicts that certain atoms or ions serve as catalysts at release energy from hydrogen to produce an increased building energy hydrogen atom called a hydrino atom has ng a binding energy of

Binding Energy
$$\frac{13.6 \text{ eV}}{n^2}$$
 (A.1)

$$\frac{1}{2\sqrt{4}}, \frac{1}{\sqrt{4}}, \dots, \frac{1}{p} \tag{A.2}$$

where $a_{\rm H}$ is the radius of the hydrogen atom. Hydrinos are predicted to form by reacting an ordinary hydrogen atom with a catalyst having a net enthalpy of reaction of about

$$m \cdot 27.2 \text{ eV}$$
 (A.3)

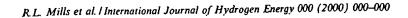
where m is an integer. This catalysis releases energy from the hydrogen atom with a commensurate decrease in size of the hydrogen atom, $r_n = na_H$. For example, the catalysis of H(n = 1) to H(n = 1/2) releases 40.8 eV, and the hydrogen radius decreases from a_H to $\frac{1}{2}a_H$.

The excited energy states of atomic hydrogen are also given by Eq. (A.1) except that

$$n = 1, 2, 3, \dots$$
 (A.4)

The n=1 state is the "ground" state for "pure" photon transitions (the n=1 state can absorb a photon and go to an excited electronic state, but it cannot release a photon and go to a lower-energy electronic state). However, an electron transition from the ground state to a lower-energy state is possible by a nonradiative energy transfer such as multipole coupling or a resonant collision mechanism. These

28



lower-energy states have fractional quantum numbers, n =1/integer. Processes that occur without photons and that require collisions are common. For example, the exothermic chemical reaction of H + H to form H2 does not occur with the emission of a photon. Rather, the reaction requires a collision with a third body, M, to remove the bond energy-H + H + $M \rightarrow$ H₂ + M* [14]. The third body distributes the energy from the exothermic reaction, and the end result is the H2 molecule and an increase in the temperature of the system. Some commercial phosphors are based on nonradiative energy transfer involving multipole coupling. For example, the strong absorption strength of Sb3+ ions along with the efficient nonradiative transfer of excitation from Sb3+ to Mn2+, are responsible for the strong manganese luminescence from phosphors containing these ions [15]. Similarly, the n = 1 state of hydrogen and the n=1/integer states of hydrogen are nonradiative, but a transition between two nonradiative states is possible via a nonradiative energy transfer, say n=1 to n=1/2. In these cases, during the transition the electron couples to another electron transition, electron transfer reaction, or inelastic scattering reaction which can absorb the exact amount of energy that must be removed from the hydrogen atom. Thus, a catalyst provides a net positive enthalpy of reaction of $m \cdot 27.2$ eV (i.e. it absorbs $m \cdot 27.2$ eV where m is an integer). Certain atoms or ions serve as catalysts which resonantly accept energy from hydrogen atoms and release the energy to the surroundings to effect electronic transitions to fractional quantum energy levels.

A.1. Inorganic catalysts

A catalytic system is provided by the ionization of t electrons from an atom to a continuum energy level such that the sum of the ionization energies of the t electrons is approximately $m \cdot 27.2$ eV where m is an integer. One such catalytic system involves strontium. The first through the fifth ionization energies of strontium are 5.69484, 11.0301, 42.89, 57, and 71.6 eV, respectively [16]. The ionization reaction of Sr to Sr^{5+} (t = 5), then, has a net enthalpy of eaction of 188.2 eV, which is equivalent to $m = 2m \cdot q$.

188.2 eV + Sr(m) + H
$$\left[\frac{a_{\rm H}}{p}\right]$$
 +5e⁻ + H $\left[\frac{a_{\rm H}}{(p+7)}\right]$ + [(p 7)² = p²] V 13.6 eV,
(A.5)

$$Sr^{5+} + 5e^- \rightarrow Sr(m) + 488.2 \text{ eV}$$
 (A.6)

And, the overall reaction is

$$H\left[\frac{a_{\rm H}}{p}\right] + [(p+7)^2 - p^2]X13.6 \text{ eV}.$$
(A.7)

Another catalytic system that is provided by the ionization of t electrons from an atom to a continuum energy level such

that the sum of the ionization energies of the t electrons is approximately mX27.2 eV where m is an integer involves potassium. The first, second, and third ionization energies of potassium are 4.34066, 31.63, 45.806 eV, respectively [16]. The triple ionization (t=3) reaction of K to, K^{3+} then, has a net enthalpy of reaction of 81.7426 eV, which is equivalent to m=3 in Eq. (A.3).

81.7426 eV + K(m) + H
$$\left[\frac{a_{\rm H}}{p}\right] \to \text{K}^{3+} + 3\text{e}^-$$

+H $\left[\frac{a_{\rm H}}{(p+3)}\right]$ + $[(p+3)^2 - p^2]X13.6$ eV, (A.8)

$$K^{3+} + 3e^{-} \rightarrow K(m) + 81.7426 \text{ eV}.$$
 (A.9)

And, the overall reaction is

$$H\left[\frac{a_H}{p}\right] \to H\left[\frac{a_H}{(p+3)}\right] + [(p+3)^2 - p^2]X13.6 \text{ eV}.$$
(A.10)

A novel hydride ion having extraordinar schemical properties given by Mills [12] is predicted to form by the reaction of an electron with a hydrim (Ed. (A.11)). The resulting hydride ion is referred to as a hydrino hydride ion, designated as $H^-(1/p)$.

$$H\left[\frac{a_{\rm H}}{p}\right] + e^- \to 0.07p \tag{A.11}$$

The hydrino hydride ion is distinguished from an ordinary hydride ion having a binding energy of 0.8 eV. The hydring hydride ion is predicted [12] to comprise a hydrogen nucleus and two indistinguishable electrons at a binding energy according to the following formula:

Binding Energy =
$$\frac{\hbar^2 \sqrt{s(s+1)}}{8\mu_e a_0^2 \left[\frac{1+\sqrt{s(s+1)}}{p}\right]^2}$$
$$-\frac{\pi\mu_0 e^2 \hbar^2}{m_e^2 a_0^3} \left(1 + \frac{2^2}{\left[\frac{1+\sqrt{s(s+1)}}{p}\right]^3}\right)$$
(A.12)

where p is an integer greater than one, s = 1/2, π is pi, \hbar is Planck's constant bar, μ_0 is the permeability of vacuum, m_e is the mass of the electron, μ_e is the reduced electron mass, a_0 is the Bohr radius, and e is the elementary charge. The ionic radius is

$$r_1 = \frac{a_0}{p}(1 + \sqrt{s(s+1)}); \quad s = \frac{1}{2}$$
 (A.13)

From Eq. (A.13), the radius of the hydrino hydride ion $H^-(1/p)$; p = integer is 1/p that of ordinary hydride ion, $H^-(1/1)$. Compounds containing hydrino hydride ions have been isolated as products of the reaction of atomic hydrogen with atoms and ions identified as catalysts by EUV emission [1-6,17-20].

Alkali and alkaline earth hydrides react violently with water to release hydrogen gas which subsequently ignites due to the exothermic reaction with water. Typically metal



hydrides decompose upon heating at a temperature well below the melting point of the parent metal. These saline hydrides, so called because of their saltlike or ionic character, are the monohydrides of the alkali metals and the dihydrides of the alkaline-earth metals. Mills predicts a hydrogen-type molecule having a first binding energy of about

Binding Energy =
$$\frac{15.5}{(\frac{1}{p})^2}$$
 eV. (A.14)

Dihydrino molecules may be produced by the thermal decomposition of hydrino hydride ions. KH⁻(1/2) may be less reactive and more thermally stable than ordinary potassium hydride, but may react at high temperature to form a hydrogen-type molecule. For example, potassium iodo hydride KH(1/2)1 may be heated to release dihydrino by thermal decomposition.

$$2KH(1/2)I \xrightarrow{\Delta} H_2^* \left[2c' = \frac{a_0}{\sqrt{2}}\right] + 2KI$$
 (A.15)

where 2c' is the internuclear distance and a_0 is the Bohr radius [12]. The possibility of releasing dihydrino by thermally decomposing alkali and alkaline earth halido hydrides and KH KHCO3 with identification by gas chromatography was explored.

The first ionization energy, IP1, of the dihydrino molecule

$$H_2^* \left[2c' = \frac{\sqrt{2}a_0}{2} \right] \to H_2^* [2c' = a_0]^+ + e^-$$
 (A.16)

is $IP_1=62 \text{ eV}(p=2 \text{ in Eq. (A.14)})$; whereas, the first ionization energy of ordinary molecular hydrogen, $H_2[2c'=\sqrt{2}a_0]$, is 15.46 eV. Thus, the possibility of using mass spectroscopy to discriminate $H_2[2c'=\sqrt{2}a_0]$ from $H_2^*[2c'=a_0/\sqrt{2}]$ on the basis of the large difference between the ionization energies of the two species was explored. A novel high binding energy hydrogen molecule assigned to dihydrino H2 [29 $a_0/\sqrt{2}$] was identified by the thermal decomposition of alkali and alkaline earth halido hydrides and KH KHCO3 with analysis by gas chromatography, and mass spe

References

[1] Mills R, Dong J, Lu, Y. Observation of extreme ultraviolet hydrogen emission from incondescently heated hydrogen gas extreme ultraviolet with certain catalysts. Pacific conference on Chemistry and Spectroscopy and the StracC Western Regional Meeting, nter, California, October 6-8, 1999. Ontario Convention

- [2] Mills R, Dong J, Lu Y. Observation of extreme ultraviolet hydrogen emission from incandescently heated hydrogen gas with certain catalysts. Int J Hydrogen Energy 2000;25:919-43.
- [3] Mills R. Observation of extreme ultraviolet emission from hydrogen-KI plasmas produced by a hollow cathode discharge. Int J Hydrogen Energy, submitted for publication.
- [4] Mills R. Temporal behavior of light-emission in the visible spectral range from a Ti-K2CO3-H-Cell. Int J Hydrogen Energy, accepted.
- [5] Mills R, Lu R, Onuma T. Formation of a hydrogen plasma from an incandescently heated hydrogen-potassium gas mixture and plasma decay upon removal of heater power. Int J Hydrogen Energy, accepted.
- [6] Mills R, Nansteel M, Lu Y. Observation of extreme ultraviolet hydrogen emission from incandescently heated hydrogen gas with strontium that produced an optically measured power balance that was 4000 times the control. Int J Hydrogen Energy, accepted.
- [7] Microsc. Microanal. Microstruct., 3(1) 1992.
- [8] PHI Trift II, ToF-SIMS Technical Brocker, Eden Prairie, MN 55344, USA, 1999.
- **Aydrogen** Energy [9] Mills R. Novel inorganic hydride 2000;25:669-83.
- [10] Briggs D, Seah MP, editors. Practical sur ice analysis. 2nd ed.
- lon and neutral spectroscopy vel. York: Wiley, 1992.
 [11] Mackay K.M. Hydroger Compounds of the metallic elements. London: E. & F. N. Sports 19665
 [12] Mills R. The grand unified theory of classical quantum
- Mechanics. Cranbur 10 BlackLight Power, Inc. January 2000. Distributed by Amazon.com.
- [13] Mills R the hidrogen atom revisited. Int J Hydrogen Energy, accepted.
- [14] Sidewick NV The chemical elements and their compounds, ol. E Oxford: Clarendon Press, 1950. p. 17.
- 5 Lamb MD. Luminescence spectroscopy. London: Academic Pre 978. p. 68.
- Linde DR. CRC handbook of chemistry and physics, 79th ed. Boca Raton, FL: CRC Press, (1998-9). pp. 10-175-10-177.
- [] Mills R, Dhandapani B, Greenig N, He J. Synthesis and characterization of potassium iodo hydride. Int J Hydrogen Energy, accepted.
- [18] Mills R. Novel hydrogen compounds from a potassium carbonate electrolytic cell. Fusion Technol 2000;37(2):157-
- [19] Mills R, He J, Dhandapani B. Novel hydrogen compounds. 1999 Pacific Conference on Chemistry and Spectroscopy and the 35th ACS Western Regional Meeting, Ontario Convention Center, California, October 6-8, 1999.
- [20] Mills R. Highly stable novel inorganic hydrides. J Mater Res, submitted for publication.

THIS PAGE BLANK (USPTO)

Highly Stable Novel Inorganic Hydrides

Randell L. Mills

BlackLight Power, Inc. 493 Old Trenton Road Cranbury, NJ 08512 USA

Novel inorganic hydride compounds $KHKHCO_3$ and KH were isolated following the electrolysis of a K_2CO_3 electrolyte. The compounds which comprised high binding energy hydride ions were stable in water, and KH was stable at elevated temperature (600 °C). Inorganic hydride clusters $K[KHKHCO_3]_n^+$ were identified by positive Time of Flight Secondary Ion Mass Spectroscopy (ToF-SIMS) of $KHKHCO_3$. The negative ToF-SIMS was dominated by hydride ion. The positive and negative ToF-SIMS of KH showed essentially K^+ and H^- only, respectively. Moreover, the existence of novel hydride ions was determined using X-ray photoelectron spectroscopy, and proton nuclear magnetic resonance spectroscopy. Hydride ions with increased binding energies may be the basis of a high voltage battery for electric vehicles.

INTRODUCTION

Evidence of the changing landscape for automobiles can be found in the recent increase in research into the next generation of automobiles. But, the fact that there is no clear front-runner in the technological race to replace the internal combustion (IC) engine can be attested to by the divergent approaches taken by the major automobile companies. Programs include various approaches to hybrid vehicles, alternative fueled vehicles such as dual-fired engines that can run on gasoline or compressed natural gas, and a natural gas-fired engine. Serious efforts are also being put into a number of alternative fuels such as ethanol, To date, the most favored methanol, propane, and reformulated gasoline. approach is an electric vehicle based on fuel cell technology or advanced battery technology such as sodium nickel chloride, nickel-metal hydride, and lithium-ion batteries [1]. Although billions of dollars are being spent to develop an alternative to the IC engine, there is no technology in sight that can match the specifications of an IC engine system [2].

Fuel cells have advantages over the IC engine because they convert hydrogen to water at about 70% efficiency when running at about 20% below peak output [3]. But, hydrogen is difficult and dangerous to store. Cryogenic, compressed gas, and metal hydride storage are the main options. In the case of cryogenic storage, liquefaction of hydrogen requires an amount of electricity which is at least 30% of the lower heating value of liquid hydrogen [4]. Compressed hydrogen, and metal hydride storage are less viable since the former requires an unacceptable volume, and the latter is heavy and has difficulties supplying hydrogen to match a load such as a fuel cell [4]. The main challenge with hydrogen as a replacement to gasoline is that a hydrogen production and refueling infrastructure would have to be built. Hydrogen may be obtained by reforming fossil fuels. However, in practice fuel cell vehicles would probably achieve only 10 to 45 percent efficiency because the process of reforming fossil fuel into hydrogen and carbon dioxide requires energy [3]. Presently, fuel cells are also impractical due to their high cost as well as the lack of inexpensive reforming technology [5].

In contrast, batteries are attractive because they can be recharged wherever electricity exists which is ubiquitous. The cost of mobile

energy from a battery powered car may be less than that from a fossil fuel powered car. For example, the cost of energy per mile of a nickel metal hydride battery powered car is 25% of that of a IC powered car [6]. However, current battery technology is trying to compete with something that it has little chance of imitating. Whichever battery technology proves to be superior, no known electric power plant will match the versatility and power of an internal combustion engine. A typical IC engine yields more than 10,000 watt-hours of energy per kilogram of fuel, while the most promising battery technology yields 200 watt-hours per kilogram [2].

A high voltage battery would have the advantages of much greater The limitations of battery power and much higher energy density. chemistry may be attributed to the binding energy of the anion of the oxidant. For example, the 2 volts provided by a lead acid cell is limited by the 1.46 eV electron affinity of the oxide anion of the oxidant PbO₂. An increase in the oxidation state of lead such as $Pb^{2+} \rightarrow Pb^{3+} \rightarrow Pb^{4+}$ is possible in a plasma. Further oxidation of lead could also be achieved in theory by electrochemical charging. However, higher lead oxidation states are not achievable because the oxide anion required to form a neutral compound would undergo oxidation by the highly oxidized lead cation. An anion with an extraordinary binding energy is required for a high voltage battery. One of the highest voltage batteries known is the lithium fluoride battery with a voltage of about 6 volts. The voltage can be attributed to the higher binding energy of the fluoride ion. electron affinity of halogens increases from the bottom of the Group VII elements to the top. Hydride ion may be considered a halide since it possess the same electronic structure. And, according to the binding energy trend, it should have a high binding energy. However, the binding energy is only 0.75 eV which is much lower than the 3.4 eV binding energy of a fluoride ion.

Novel inorganic hydride compounds having the formula $KH \ KHCO_3$ and KH were isolated from an aqueous K_2CO_3 electrolytic cell reactor. KH was stable at elevated temperature (600 °C). Inorganic hydride clusters $K[KH \ KHCO_3]_n^+$ were identified by positive Time of Flight Secondary Ion Mass Spectroscopy (ToF-SIMS) of $KH \ KHCO_3$. The negative ToF-SIMS was dominated by hydride ion. The positive and negative ToF-

SIMS of KH showed essentially K⁺ and H⁻ only, respectively. A hydride ion with a binding energy of 22.8 eV has been observed by X-ray photoelectron spectroscopy (XPS) of KH KHCO₃ having upfield shifted solid state magic-angle spinning proton nuclear magnetic resonance (¹H MAS NMR) peaks. Moreover, a polymeric structure is indicated by Fourier transform infrared (FTIR) spectroscopy. Hydride ions with a binding energies of 22.8 eV and 69.2 eV have been observed by XPS of KH. The discovery of novel hydride ions with high binding energies has implications for a new field of hydride chemistry with applications such as a high voltage battery. Such extremely stable hydride ions may stabilize positively charged ions in an unprecedented highly charged state. A battery may be possible having projected specifications that surpass those of the internal combustion engine.

Hydride ions having extraordinary binding energies may stabilize a cation M^{x+} in an extraordinarily high oxidation state such as +2 in the case of lithium. Thus, these hydride ions may be used as the basis of a high voltage battery of a rocking chair design wherein the hydride ion moves back and forth between the cathode and anode half cells during discharge and charge cycles. Exemplary reactions for a cation M^{x+} are:

Cathode reaction:

$$MH_x + e^- \to MH_{x-1} + H^- \tag{1}$$

Anode reaction:

$$MH_{x-2} + H^- \to MH_{x-1} + e^-$$
 (2)

Overall reaction:

$$MH_x + MH_{x-2} \rightarrow 2MH_{x-1} \tag{3}$$

EXPERIMENTAL

Synthesis

A. Potassium Hydride Potassium Hydrogen Carbonate, KH KHCO₃, Synthesis with an Electrolytic Cell

An electrolytic cell comprising a K_2CO_3 electrolyte, a nickel wire cathode, and platinized titanium anodes was used to synthesize the KH KHCO₃ sample [7]. Briefly, the cell vessel comprised a 10 gallon (33 in. x 15 in.) Nalgene tank. An outer cathode comprised 5000 meters of 0.5 mm diameter clean, cold drawn nickel wire (NI 200 0.0197", HTN36NOAG1, A-1 Wire Tech, Inc., 840-39th Ave., Rockford, Illinois, 61109) wound on a polyethylene cylindrical support. A central cathode comprised 5000 meters of the nickel wire wound in a toroidal shape. central cathode was inserted into a cylindrical, perforated polyethylene container that was placed inside the outer cathode with an anode array The anode comprised an array between the central and outer cathodes. of 15 platinized titanium anodes (ten - Engelhard Pt/Ti mesh 1.6" x 8" with one 3/4" by 7" stem attached to the 1.6" side plated with 100 U series 3000; and 5 - Engelhard 1" diameter x 8" length titanium tubes with one 3/4" x 7" stem affixed to the interior of one end and plated with 100 U Pt series 3000). Before assembly, the anode array was cleaned in 3 M HCl for 5 minutes and rinsed with distilled water. The cathode was cleaned by placing it in a tank of 0.57 M $K_2CO_3/3\%$ H_2O_2 for 6 hours and then rinsing it with distilled water. The anode was placed in the support between the central and outer cathodes, and the electrode assembly was placed in the tank containing electrolyte. The electrolyte solution comprised 28 liters of 0.57 M K_2CO_3 (Alfa K_2CO_3 99%). Electrolysis was performed at 20 amps constant current with a constant current (± 0.02%) power supply.

Samples were isolated from the electrolytic cell by concentrating the K_2CO_3 electrolyte about six fold using a rotary evaporator at 50 °C until a yellow white polymeric suspension formed. Precipitated crystals of the suspension were then grown over three weeks by allowing the saturated solution to stand in a sealed round bottom flask at 25°C.

Control samples utilized in the following experiments contained K_2CO_3 (99%), $KHCO_3$ (99.99%), HNO_3 (99.99%), and KH (99%).

B. Potassium Hydrino Hydride, KH, Synthesis with an Electrolytic Cell

An electrolytic cell comprising a K_2CO_3 electrolyte, a nickel wire cathode, and platinized titanium anodes described by Mills et al. [7] was used to synthesize potassium hydride, KH. The cell was equivalent to that described above except that it lacked the additional central cathode.

After 3 months of operation, the cathode wire obtained a graphite colored coating. The cathode was placed in 10 gallon (33 in. x 15 in.) Nalgene tank of 0.57 M $K_2CO_3/3\%$ H_2O_2 for 6 hours. A very vigorous exothermic reaction was observed during the six hours. The cathode was removed and placed in a second 10 gallon (33 in. x 15 in.) Nalgene tank NiO was observed to precipitate in the tank containing of distilled water. 0.57 M $K_2CO_3/3\%$ H_2O_2 . The coat was observed to be removed from the cathode when it was pulled from the distilled water bath. A white polymeric solid floated to the top of the water bath over 2 weeks. solid was collected by scooping it with a 250 ml beaker. The polymeric material was stable in water indefinitely (over a year with no observable The material was pure white and appeared like cotton Other samples were obtained which were thin films. suspended in water. The density was less than that of water. The material was observed to be weakly ferromagnetic. It collapsed along the magnet field lines and was attracted to a magnet in solution. It could be pulled out of water with a strong magnet. It was poured onto an evaporation dish, dried, and analyzed.

ToF-SIMS Characterization

The crystalline samples were sprinkled onto the surface of double-sided adhesive tapes and characterized using a Physical Electronics TFS-2000 ToF-SIMS instrument. The primary ion gun utilized a $^{69}Ga^+$ liquid metal source. In order to remove surface contaminants and expose a fresh surface, the samples were sputter cleaned for 30 seconds using a $40\mu m$ X $40\mu m$ raster. The aperture setting was 3, and the ion current was 600 pA resulting in a total ion dose of 10^{15} ions/cm².

During acquisition, the ion gun was operated using a bunched (pulse width 4 ns bunched to 1 ns) 15 kV beam [8-9]. The total ion dose was $10^{12} ions / cm^2$. Charge neutralization was active, and the post accelerating voltage was 8000 V. Three different regions on each sample of $(12\mu m)^2$, $(18\mu m)^2$, and $(25\mu m)^2$ were analyzed. The positive and negative SIMS spectra were acquired. Representative post sputtering data is reported.

XPS Characterization

A series of XPS analyses were made on the crystalline samples each mounted on a silicon wafer using a Scienta 300 XPS Spectrometer. fixed analyzer transmission mode and the sweep acquisition mode were used. A survey spectrum was obtained over the region $E_b = 0 \ eV$ to 1200 eV. The primary element peaks allowed for the determination of all of the elements present in each sample isolated from the K_2CO_3 electrolyte. survey spectrum also detected shifts in the binding energies of potassium and oxygen which had implications as to the identity of the compound containing the elements. A high resolution XPS spectrum was also obtained of the low binding energy region $(E_b = 0 \text{ eV} \text{ to } 100 \text{ eV})$ to determine the presence of novel XPS peaks. The step energy in the survey scan was 0.5 eV, and the step energy in the high resolution scan was 0.15 eV. In the survey scan, the time per step was 0.4 seconds, and the number of sweeps was 4. In the high resolution scan, the time per step was 0.3 seconds, and the number of sweeps was 30. C1s at 284.6 eV was used as the internal standard.

NMR Spectroscopy

"H MAS NMR was performed on the crystalline samples. The data were obtained on a custom built spectrometer operating with a Nicolet 1280 computer. Final pulse generation was from a tuned Henry radio amplifier. The "H NMR frequency was 270.6196 MHz. A 2 μsec pulse corresponding to a 15° pulse length and a 3 second recycle delay were used. The window was ±31 kHz. The spin speed was 4.5 kHz. The number of scans was 1000. The offset was 1527.12 Hz, and the magnetic flux was 6.357 T. Chemical shifts were referenced to external TMS.

FTIR Spectroscopy

Samples were transferred to an infrared transmitting substrate and analyzed by FTIR spectroscopy using a Nicolet Magna 550 FTIR Spectrometer with a NicPlan FTIR microscope. The number of scans was 500 for both the sample and background. The number of background scans was 500. The resolution was 8.000. A dry air purge was applied.

Thermal Decomposition with Analysis by Mass Spectroscopy

Mass spectroscopy was performed on the gases released from the thermal decomposition of the samples. One end of a 4 mm ID fritted capillary tube containing about 5 mg of sample was sealed with a 0.25 in. Swagelock union and plug (Swagelock Co., Solon, OH). The other end was connected directly to the sampling port of a Dycor System 1000 Quadrapole Mass Spectrometer (Model D200MP, Ametek, Inc., Pittsburgh, PA with a HOVAC Dri-2 Turbo 60 Vacuum System). The capillary was heated with a Nichrome wire heater wrapped around the capillary. The mass spectrum was obtained at the ionization energy of 70 eV at a sample temperature of 600 °C with the detection of hydrogen indicated by a m/e=2 peak.

The control hydrogen gas was ultrahigh purity (MG Industries).

RESULTS AND DISCUSSION

ToF-SIMS

A. ToF-SIMS of Potassium Hydride Potassium Hydrogen Carbonate, KH KHCO₃, Electrolytic Cell Sample

The positive ToF-SIMS spectrum obtained from the $KHCO_3$ control is shown in Figures 1 and 2. In addition, the positive ToF-SIMS of a sample isolated from the electrolytic cell is shown in Figures 3 and 4. The respective hydride compounds and mass assignments appear in Table 1. In both the control and electrolytic samples, the positive ion spectrum are dominated by the K^+ ion. Two series of positive ions $\{K[K_2CO_3]_n^+ \ m/z = (39+138n) \text{ and } K_2OH[K_2CO_3]_n^+ \ m/z = (95+138n)\}$ are observed in the $KHCO_3$ control. Other peaks containing potassium include

 KC^+ , $K_xO_y^+$, $K_xO_yH_z^+$, KCO^+ , and K_2^+ . However, in the electrolytic cell sample, three new series of positive ions are observed at $\{K[KH\ KHCO_3]_n^+\ m/z = (39+140n),\ K_2OH[KH\ KHCO_3]_n^+\ m/z = (95+140n),\ and\ K_3O[KH\ KHCO_3]_n^+\ m/z = (133+140n)\}$. These ions correspond to inorganic clusters containing novel hydride combinations (i.e. $KH\ KHCO_3$ units plus other positive fragments).

The comparison of the positive ToF-SIMS spectrum of the KHCO3 control with the electrolytic cell sample shown in Figures 1-2 and 3-4, respectively, demonstrates that the 39K+ peak of the electrolytic cell sample may saturate the detector and give rise to a peak that is atypical of the natural abundance of 41K. The natural abundance of 41K is 6.7%; whereas, the observed 41K abundance from the electrolytic cell sample is 57%. This atypical abundance was also confirmed using ESIToFMS [10]. The high resolution mass assignment of the m/z = 41 peak of the electrolytic sample was consistent with 41K, and no peak was observed at m/z = 42.98 ruling out ${}^{41}KH_2^+$. Moreover, the natural abundance of ${}^{41}K$ was observed in the positive ToF-SIMS spectra of KHCO3, KNO3, and KI standards that were obtained with an ion current such that the 39K peak intensity was an order of magnitude higher than that given for the electrolytic cell sample. The saturation of the 39K peak of the positive ToF-SIMS spectrum by the electrolytic cell sample is indicative of a unique crystalline matrix [11].

The negative ToF-SIMS spectrum (m/e=0-50) of the $KHCO_3$ (99.99%) sample and the negative ToF-SIMS spectrum (m/e=0-30) of the electrolytic cell sample are shown in Figures 5 and 6, respectively. The negative ion ToF-SIMS of the electrolytic cell sample was dominated by H^- , O^- , and OH^- peaks. A series of nonhydride containing negative ions $\{KCO_3[K_2CO_3]_n^T \ m/z = (99+138n)\}$ was also present which implies that H_2 was eliminated from $KH\ KHCO_3$ during fragmentation of the compound $KH\ KHCO_3$. Comparing the H^- to O^- ratio of the electrolytic cell sample to that of the $KHCO_3$ control sample, the H^- peak was about an order of magnitude higher in the electrolytic cell sample.

B. ToF-SIMS of Potassium Hydrino Hydride, KH, Electrolytic Cell Sample

The positive ToF-SIMS spectrum obtained from the KH electrolytic cell sample is shown in Figure 7. The positive spectrum was dominated by the potassium peak K^+ m/z = 39 followed by the proton peak. Small silicon, sodium, and hydrocarbon fragment peaks such as C_2H_3 m/z = 27 and C_2H_5 m/z = 29, K_2^+ m/z = 87, $K(KO)^+$ m/z = 94, and $K(KOH)^+$ m/z = 95 were also observed.

The positive spectrum of the $KHCO_3$ control shown in Figures 1 and 2 was also dominated by the potassium peak K^+ m/z = 39. Two series of positive ions $\{K[K_2CO_3]_n^+$ m/z = (39+138n) and $K_2OH[K_2CO_3]_n^+$ $m/z = (95+138n)\}$ were observed in the $KHCO_3$ control. Other peaks containing potassium included KC^+ m/z = 51, $K_xO_y^+$, $K_xO_yH_z^+$, KCO^+ m/z = 67, and K_2^+ m/z = 78.

The negative ion ToF-SIMS of KH shown in Figure 8 was dominated by H^- . Or m/z=16 and OH^- m/z=17 dominated the negative ion ToF-SIMS of the $KHCO_3$ control as shown in Figure 5. These peaks were present in the case of KH, but they were very small in comparison to the $KHCO_3$ control. For both samples smaller hydrocarbon fragment peaks such as C^- m/z=12 and CH^- m/z=13 were observed. A series of negative ions $\{KCO_3[K_2CO_3]_n^ m/z=(99+138n)\}$ was also present in the control which were not observed in the KH sample. A hydride peak probably due to OH^- m/z=17 which was significantly smaller than the O^- m/z=16 peak was observed in the control.

<u>XPS</u>

A. XPS of Potassium Hydride Potassium Hydrogen Carbonate, KH KHCO₃, Electrolytic Cell Sample

The 0 to 80 eV binding energy region of a high resolution XPS spectrum of the KH KHCO₃ electrolytic cell sample is shown in Figure 9. The XPS survey spectrum the KH KHCO₃ electrolytic cell sample with the primary elements identified is shown in Figure 10. No elements were present in the survey scans which can be assigned to peaks in the low binding energy region with the exception of a small variable contaminant

of sodium at 63 eV and 31 eV, potassium at 16.2 eV and 32.1 eV, and oxygen at 23 eV. Accordingly, any other peaks in this region must be due to novel species. The K3s and K3p are shown in Figure 9 at 16.2 eV and 32.1 eV, respectively. A weak Na2s is observed at 63 eV. The O2s which is weak compared to the potassium peaks of K_2CO_3 is typically present at 23 eV, but is broad or obscured in Figure 9.

Peaks centered at $22.8 \, eV$ and $38.8 \, eV$ which do not correspond to any other primary element peaks were observed. The intensity and shift match shifted K3s and K3p. Hydrogen is the only element which does not have primary element peaks; thus, it is the only candidate to produce the shifted peaks. These peaks may be shifted by a highly binding hydride ion with a binding energy of $22.8 \, eV$ given in the Appendix that bonds to potassium K3p and shifts the peak to this energy. In this case, the K3s is similarly shifted. These peaks were not present in the case of the XPS of matching samples isolated from an identical electrolytic cell except that Na_2CO_3 replaced K_2CO_3 as the electrolyte.

XPS further confirmed the ToF-SIMS data by showing shifts of the primary elements. The splitting of the principal peaks of the survey XPS spectrum is indicative of multiple forms of bonding involving the atom of each split peak. For example, the XPS survey spectrum shown in Figure 10 shows extraordinary potassium and oxygen peak shifts. All of the potassium primary peaks are shifted to about the same extent as that of the K3s and K3p. In addition, extraordinary O1s peaks of the electrolytic cell sample were observed at 537.5 eV and 547.8 eV; whereas, a single O 1s was observed in the XPS spectrum of K_2CO_3 at 532.0 eV. The results are not due to uniform charging as the internal standard C1s remains the same at 284.6 eV. The results are not due to differential charging because the peak shapes of carbon and oxygen are normal, and no tailing of these peaks was observed. The binding energies of the K,CO, control and the KH KHCO, electrolytic cell sample are shown in Table 2. The range of binding energies from the literature [12] for the peaks of interest are given in the final row of Table 2. The K3p, K3s, $K2p_{3/2}$, $K2p_{1/2}$, and K2s XPS peaks and the O 1s XPS peaks shifted to an extent greater than those of known compounds may correspond to and identify KH KHCO₃.

B. XPS of Poly-Potassium Hydrino Hydride, KH, Electrolytic Cell Sample

The XPS survey scan of the KH electrolytic cell sample is shown in Figure 11. C1s at $284.5 \, eV$ was used as the internal standard for the KH sample and the control K_2CO_3 . The major species present in the control are potassium and carbon and oxygen. The major species present in the KH sample was potassium. Large silicon, oxygen and graphitic and hydrocarbon carbon peaks were also seen that originated from the silicon wafer sample mount. Nitrogen was present, and trace magnesium and sodium may be present. The identifying peaks of the primary elements and their binding energies are: Na1s at $1072.2 \, eV$, O1s at $532.0 \, eV$, $Na KL_{23}L_{23}$ at $496.6 \, eV$, N1s at $399.3 \, eV$, K2s at $377.2 \, eV$, $Mg KL_{23}L_{23}$ at $305.9 \, eV$, $K2p_{1/2}$ at $295.4 \, eV$, $K2p_{3/2}$ at $292.5 \, eV$, C1s at $285.5 \, and 284.6 \, eV$, $Si2p_{3/2}$ at $156.7 \, eV$ and $153.4 \, eV$, Si2s at $105.7 \, eV$ and $102.1 \, eV$, and Mg2s at $88.5 \, eV$.

No elements were present in the survey scan which could be assigned to peaks in the low binding energy region with the exception of the K3p at 16.8 eV, K3s at 33.0 eV, O2s at 26.2 eV, and Mg2p at 49.6 eV. Accordingly, any other peaks in this region must be due to novel The 0-80 eV binding energy region of a high resolution XPS spectrum of the KH electrolytic cell sample is shown in Figure 12. Peaks of interest were observed in the valance band at 3.8 eV, 9.95 eV, and 13.7 eV which may be due to nitrogen, carbon, and oxygen, but the assignment can not be made with certainty. A 62.8 peak may be assigned to Na 2s. However, no peak is detectable above baseline at 29.8 eV which corresponds to $Na\ 2p_{1/2}$. Since the intensity of the $Na\ 2p_{1/2}$ peak is less than $Na\ 2s$, and the $Na\ 2s$ peak is weak, the $Na\ 2p_{1/2}$ may not be So, the assignment is uncertain. Novel peaks were observed in the KH sample at 19.5 eV, 36.0 eV, and 68.0 eV. The 68.0 eV peak may be assigned to Ni 3p, but the shape is incorrect. And, if the $Ni 2p_{3/2}$ at about 860 eV is present, it is smaller than the proposed Ni 3p. Thus, the 68.0 eV can not be assigned to Ni 3p.

The XPS peaks at 19.5 eV, 36.0 eV, and 68.0 eV do not correspond to any other primary element peaks. The 68.0 eV peak may correspond to a hydride ion with a binding energy of 69.2 eV given in the Appendix. Peaks at 19.5 eV and 36.0 eV which do not correspond to any other

primary element peaks were observed. The intensity and shift match shifted K3s and K3p. Hydrogen is the only element which does not have primary element peaks; thus, it is the only candidate to produce the shifted peaks. These peaks may be shifted by a highly binding hydride ion with a binding energy of $22.8 \, eV$ given in the Appendix that bonds to potassium K3p and shifts the peak to this energy. In this case, the K3s is similarly shifted. The shift of about 3 eV is greater than that of known potassium compounds. These peaks were not present in the case of the XPS of matching samples isolated from an identical electrolytic cell except that Na_2CO_3 replaced K_2CO_3 as the electrolyte.

The KH electrolytic cell sample was observed to be weakly ferromagnetic. The origin of the magnetism is from nonmetallic elements which were most likely potassium and hydrogen.

NMR

The signal intensities of the ^{1}H MAS NMR spectrum of the $K_{2}CO_{3}$ reference were relatively low. It contained a water peak at 1.208 ppm, a peak at 5.604 ppm, and very broad weak peaks at 13.2 ppm, and 16.3 ppm. The ^{1}H MAS NMR spectrum of the $KHCO_{3}$ reference contained a large peak at 4.745 with a small shoulder at 5.150 ppm, a broad peak at 13.203 ppm, and small peak at 1.2 ppm.

The ¹H MAS NMR spectra of the KHKHCO₃ electrolytic cell sample is shown in Figure 13. The peak assignments are given in Table 3. The reproducible peaks assigned to KHKHCO₃ in Table 3 were not present in the controls except for the peak assigned to water at +5.066 ppm. The novel peaks could not be assigned to hydrocarbons. Hydrocarbons were not present in the electrolytic cell sample based on the TOFSIMS spectrum and FTIR spectra which were also obtained (see below). The novel peaks without identifying assignment are consistent with KHKHCO₃. The NMR peak of the hydride ion of potassium hydride was observed at 0.8 and 1.1 ppm relative to TMS. The upfield peaks of Figure 13 are assigned to novel hydride ion (KH-) in different environments. The down field peaks are assigned to the proton of the potassium hydrogen carbonate species in different chemical environments (-KHCO₃).

FTIR

The FTIR spectra of K_2CO_3 (99%) and $KHCO_3$ (99.99%) were compared with that of the KHKHCO, electrolytic cell sample. A spectrum of a mixture of the bicarbonate and the carbonate was produced by digitally adding the two reference spectra. The two standards alone and the mixed standards were compared with that of the electrolytic cell From the comparison, it was determined that the electrolytic cell sample contained potassium carbonate but did not contain potassium The unknown component could be a bicarbonate other than The spectrum of potassium carbonate was potassium bicarbonate. digitally subtracted from the spectrum of the electrolytic cell sample. Several bands were observed including bands in the 1400-1600 cm⁻¹ Some organic nitrogen compounds (e.g. acrylamides, pyrolidinones) have strong bands in the region 1660 cm⁻¹ [13]. However, the lack of any detectable C-H bands ($\approx 2800-3000 \text{ cm}^{-1}$) and the bands present in the 700 to 1100 cm^{-1} region indicate an inorganic material [14]. Peaks are not assignable to potassium carbonate were observed at 3294, 3077, 2883, 1100 cm^{-1} , 2450, 1660, 1500, 1456, 1423, 1300, 1154, 1023, 846, 761, and $669 cm^{-1}$.

The overlap FTIR spectrum of the electrolytic cell sample and the FTIR spectrum of the reference potassium carbonate appears in Figure 14. In the 700 to $2500 \, cm^{-1}$ region, the peaks of the electrolytic cell sample closely resemble those of potassium carbonate, but they are shifted about $50 \, cm^{-1}$ to lower frequencies. The shifts are similar to those observed by replacing potassium (K_2CO_3) with rubidium (Rb_2CO_3) as demonstrated by comparing their IR spectra [15]. The shifted peaks may be explained by a polymeric structure for the compound $KH \, KHCO_3$ identified by ToF-SIMS, XPS, and NMR.

Mass Spectroscopy (MS)

The KH electrolytic cell sample did not decompose upon heating to 600 °C. Essentially no hydrogen was observed by mass spectroscopy. The sample changed very little which indicates no decomposition and extraordinary stability for a compound mainly comprised of hydrogen.

Further Analytical Tests

X-ray diffraction (XRD), elemental analysis using inductively coupled plasma (ICP), and Raman spectroscopy were also performed on the KH KHCO₃ electrolytic sample [10]. The XRD data indicated that the diffraction pattern of the electrolytic cell sample does not match that of either KH, KHCO₃, K₂CO₃, or KOH. The elemental analysis supports KH KHCO3. In addition to the known Raman peaks of KHCO3 and a small peak assignable to K_2CO_3 , unidentified peaks at 1685 cm⁻¹ and 835 cm⁻¹ were present. Work in progress [10] demonstrates that KH KHCO₃ may also be formed by a reaction of gaseous KI with atomic hydrogen in the presence of K_2CO_3 [16]. In addition to the previous analytical studies, the fragment KK, CO₃ corresponding to KH KHCO₃ was observed by electrospray ionization time of flight mass spectroscopy as a chromatographic peak on a C18 liquid chromatography column typically used to separate organic No chromatographic peaks were observed in the case of compounds. inorganic compound controls KI, KHCO3, K2CO3, and KOH

DISCUSSION

Alkali and alkaline earth hydrides react violently with water to release hydrogen gas which subsequently ignites due to the exothermic Typically metal hydrides decompose upon heating reaction with water. at a temperature well below the melting point of the parent metal. saline hydrides, so called because of their saltlike or ionic character, are the monohydrides of the alkali metals and the dihydrides of the alkalineearth metals, with the exception of beryllium. BeH2 appears to be a hydride with bridge type bonding rather than an ionic hydride. Highly polymerized molecules held together by hydrogen-bridge bonding is exhibited by boron hydrides and aluminum hydride. Based on the known structures of these hydrides, the ToF-SIMS hydride clusters such as $K[KHKHCO_3]_n^{\dagger}$, the XPS peaks observed at 22.8 eV and 38.8 eV, upfield NMR peaks assigned to hydride ion, and the shifted FTIR peaks, the present novel hydride compound of the KHKHCO3 electrolytic cell sample may be a polymer, [KH KHCO₃], with a structural formula which is similar to boron and aluminum hydrides. The reported novel compound

appeared polymeric in the concentrated electrolytic solution and in distilled water. $[KH\ KHCO_3]_n$ is extraordinarily stable in water; whereas, potassium hydride reacts violently with water.

As an example of the structures of this compound, the $K[KHKHCO_3]_n^+$ m/z = (39+140n) series of fragment peaks is tentatively assigned to novel hydride bridged or linear potassium bicarbonate compounds having a general formula such as $[KHKHCO_3]_n$ n=1,2,3... General structural formulas may be

and

Liquid chromatography/ESIToFMS studies are in progress to support the polymer assignment.

The observation of inorganic hydride fragments such as K[KHKHCO₃]⁺ in the positive ToF-SIMS spectra of samples isolated from the electrolyte following acidification indicates the stability of the novel potassium hydride potassium bicarbonate compound [10]. electrolyte was acidified with HNO_3 to pH=2 and boiled to dryness to prepare samples to determine whether KH KHCO3 was reactive under these conditions. Ordinarily no K_2CO_3 would be present, and the sample would be converted to KNO3. Crystals were isolated by dissolving the dried crystals in water, concentrating the solution, and allowing crystals to precipitate. ToF-SIMS was performed on these crystals. spectrum contained elements of the series of inorganic hydride clusters $\{K[KH\ KHCO_3]^{\dagger} \ m/z = (39+140n), \ K_2OH[KH\ KHCO_3]^{\dagger} \ m/z = (95+140n), \ \text{and}$ $K_3O[KH\ KHCO_3]_n^+$ m/z = (133+140n)} that were observed in the positive ToF-SIMS spectrum of the KH KHCO₃ electrolytic cell sample as discussed in the ToF-SIMS Results Section and given in Figures 3-4 and Table 1. presence of bicarbonate carbon (C1s = 289.5 eV) was observed in the XPS of the sample from the HNO₃ acidified electrolyte. In addition, fragments of compounds formed by the displacement of hydrogen carbonate by nitrate were observed [10]. A general structural formula for the reaction may be

During acidification of the K_2CO_3 electrolyte the pH repetitively increased from 3 to 9 at which time additional acid was added with carbon dioxide release. The increase in pH (release of base by the titration reactant) was dependent on the temperature and concentration of the solution. A reaction consistent with this observation is the displacement reaction of NO_3^- for HCO_3^{2-} as given by Eq. (4).

KH was stable at elevated temperature (600 °C). The positive and negative ToF-SIMS of the KH electrolytic sample showed essentially K^+ and H^- only, respectively. Hydride ions with a binding energies of 22.8 eV and 69.2 eV have been observed by XPS of KH. The former hydride ion with a binding energy of 22.8 eV was observed by X-ray photoelectron spectroscopy (XPS) of the KH KHCO₃ electrolytic sample. These compounds appear polymeric in aqueous solution. KH was observed to be weakly ferromagnetic; whereas, KH KHCO₃ was diamagnetic. The magnetism of KH may be due to mixed oxidation states due to the presence of two hydride ions with a substantially reduced radii to permit spin correlation.

CONCLUSIONS

The ToF-SIMS, XPS, and NMR results confirm the identification of KH KHCO₃ and KH with a new states of hydride ions. The chemical structure and properties of these compounds having hydride ions with high binding energies are indicative of a new field of hydride chemistry. The novel hydride ions may combine with other cations such as other alkali cations and alkaline earth, rare earth, and transition element cations. Thousands of novel compounds may be synthesized with extraordinary properties relative to the corresponding compounds having ordinary hydride ions. These novel compounds may have a breath of applications. For example, a high voltage battery (Eqs. (1-3)) according to the hydride binding energies of 22.8 eV and 69.2 eV observed by XPS may be possible having projected specifications that surpass those of the internal combustion engine.

ACKNOWLEDGMENTS

Special thanks to Bala Dhandapani for work on the Raman, FTIR, and XRD studies. Special thanks to Jiliang He for obtaining the MAS NMR spectrum of potassium hydride. Special thanks to Bala Dhandapani and Jiliang He for helpful comments upon review of the manuscript.

APPENDIX

A novel hydride ion having extraordinary chemical properties given by Mills [10] is predicted to form by the reaction of an electron with a hydrino (Eq. (6)), a hydrogen atom having a binding energy given by

Binding Energy =
$$\frac{13.6 \text{ eV}}{\left(\frac{1}{p}\right)^2}$$
 (5)

where p is an integer greater than 1, designated as $H\left[\frac{a_H}{p}\right]$ where a_H is the radius of the hydrogen atom. The resulting hydride ion is referred to as a hydrino hydride ion, designated as $H^-(1/p)$.

$$H\left[\frac{a_H}{p}\right] + e^- \to H^-(1/p) \tag{6}$$

The hydrino hydride ion is distinguished from an ordinary hydride ion having a binding energy of 0.8 eV. The latter is hereafter referred to as "ordinary hydride ion". The hydrino hydride ion is predicted [10] to comprise a hydrogen nucleus and two indistinguishable electrons at a binding energy according to the following formula:

Binding Energy =
$$\frac{\hbar^2 \sqrt{s(s+1)}}{8\mu_{\epsilon} a_0^2 \left[\frac{1+\sqrt{s(s+1)}}{p}\right]^2} - \frac{\pi \mu_0 e^2 \hbar^2}{m_{\epsilon}^2 a_0^3} \left(1 + \frac{2^2}{\left[\frac{1+\sqrt{s(s+1)}}{p}\right]^3}\right)$$
(7)

where p is an integer greater than one, s=1/2, π is pi, \hbar is Planck's constant bar, μ_o is the permeability of vacuum, m_e is the mass of the electron, μ_e is the reduced electron mass, a_o is the Bohr radius, and e is the elementary charge. The ionic radius is

$$r_1 = \frac{a_0}{p} \left(1 + \sqrt{s(s+1)} \right); \ s = \frac{1}{2}$$
 (8)

From Eq. (8), the radius of the hydrino hydride ion $H^-(1/p)$; p = integer is $\frac{1}{p}$ that of ordinary hydride ion, $H^-(1/1)$. The XPS peaks of $KH \ KHCO_3$ centered at 22.8 eV and 38.8 eV and the XPS peaks of KH centered at 19.5 eV and 36.0 eV are assigned to shifted $K \ 3s$ and $K \ 3p$. The anion does not correspond to any other primary element peaks; thus, it may correspond to the $H^-(n=1/6) E_b = 22.8 \ eV$ hydride ion predicted by Mills [10] where E_b is the predicted binding energy. The XPS peak of KH centered at 68.0 eV is assigned to $H^-(n=1/14) E_b = 69.2 \ eV$

Hydrinos are predicted to form by reacting an ordinary hydrogen atom with a catalyst having a net enthalpy of reaction of about

$$m \cdot 27.21 \text{ eV} \tag{9}$$

where m is an integer [10]. This catalysis releases energy from the hydrogen atom with a commensurate decrease in size of the hydrogen atom, $r_n = na_H$. For example, the catalysis of H(n=1) to H(n=1/2) releases $40.8 \, eV$, and the hydrogen radius decreases from a_H to $\frac{1}{2}a_H$. One such catalytic system involves potassium. The second ionization energy of potassium is $31.63 \, eV$; and K^+ releases $4.34 \, eV$ when it is reduced to K.

The combination of reactions K^+ to K^{2+} and K^+ to K, then, has a net enthalpy of reaction of 27.28 eV, which is equivalent to m=1 in Eq. (9).

27.28
$$eV + K^+ + K^+ + H\left[\frac{a_H}{p}\right] \to K + K^{2+} + H\left[\frac{a_H}{(p+1)}\right] + [(p+1)^2 - p^2] X 13.6 eV$$
 (10)

$$K + K^{2+} \rightarrow K^{+} + K^{+} + 27.28 \ eV$$
 (11)

The overall reaction is

$$H\left[\frac{a_H}{p}\right] \to H\left[\frac{a_H}{(p+1)}\right] + [(p+1)^2 - p^2] X 13.6 \ eV$$
 (12)

The energy given off during catalysis is much greater than the energy lost to the catalyst. The energy released is large as compared to conventional chemical reactions. For example, when hydrogen and oxygen gases undergo combustion to form water

$$H_2(g) + \frac{1}{2}O_2(g) \to H_2O(l)$$
 (13)

the known formation enthalpy of water is $\Delta H_f = -286 \, kJ \, l$ mole or 1.48 eV per hydrogen atom. By contrast, each ordinary hydrogen atom (n=1) catalysis releases a net of $40.8 \, eV$.

Calorimetry of pulsed current and continuous electrolysis of aqueous potassium carbonate at a nickel cathode were performed at Thermacore, Inc., Lancaster, PA [7]. This cell had produced an enthalpy of formation of novel hydride compounds of $1.6 \times 10^9 J$ that exceeded the total input enthalpy given by the product of the electrolysis voltage and current over time by a factor greater than 8. The exothermic reactions Eq. (10-12), Eq. (6) and the enthalpy of formation of $KH \times KHCO_3$ could explain the observation of excess enthalpy.

Calorimetry of pulsed current electrolysis of aqueous potassium carbonate at a nickel cathode was performed at Idaho National Engineering Laboratory. The cell was wrapped in a one-inch layer of urethane foam insulation about the cylindrical surface. The cell was operated in a pulsed power mode. A current of 10 amperes was passed through the cell for 0.2 seconds followed by 0.8 seconds of zero current for the current cycle. The cell voltage was about 2.4 volts, for an average input power of 4.8 W. The electrolysis power average was 1.84 W, and the stirrer power was measured to be 0.3 W. Thus, the total average net input power was 2.14 W. The cell was operated at various resistance heater settings, and the temperature difference between the cell and the

ambient as well as the heater power were measured. The results of the excess power as a function of cell temperature with the cell operating in the pulsed power mode at 1 Hz with a cell voltage of 2.4 volts, a peak current of 10 amperes, and a duty cycle of 20 % showed that the excess power is temperature dependent for pulsed power operation, and the maximum excess power was 18 W for an input electrolysis joule heating power of 2.14 W. Thus, the ratio of excess power to input electrolysis joule heating power was 850 % [17]. The exothermic reactions Eq. (10-12), Eq. (6) and the enthalpy of formation of KH could explain the observation of excess enthalpy.

REFERENCES

- 1. I. Uehara, T. Sakai, H. Ishikawa, J. Alloy Comp., 253/254, (1997), pp. 635-641.
- 2. J. Glanz, "Check the Tires and Charge Her Up", New Scientist, April 15, (1995) pp. 32-35.
- 3. D. Mulholland, Defense News, "Powering the Future Military", March 8, 1999, pp. 1&34.
- 4. S. M. Aceves, G. D. Berry, and G. D. Rambach, Int. J. Hydrogen Energy, Vol. 23, No. 7, (1998), pp. 583-591.
- 5. J. Ball, The Wall Street Journal, "Auto Makers Are Racing to Market "Green" Cars Powered by Fuel Cells", March 15, 1999, p. 1.
- 6. "Advanced Automotive Technology: Visions of a Super-Efficient Family Car", National Technical Information Service, US Department of Commerce, US Office of Technology Assessment, Washington, DC PB96-109202, September 1995.
- 7. R. Mills, W. Good, and R. Shaubach, Fusion Technol. 25, 103 (1994).
- 8. Microsc. Microanal. Microstruct., Vol. 3, 1, (1992).
- 9. For recent specifications see PHI Trift II, ToF-SIMS Technical Brochure, (1999), Eden Prairie, MN 55344.
- 10. R. Mills, The Grand Unified Theory of Classical Quantum Mechanics, January 1999 Edition, BlackLight Power, Inc., Cranbury, New Jersey, Distributed by Amazon.com.
- 11. Practical Surface Analysis, 2nd Edition, Volume 2, Ion and Neutral Spectroscopy, D. Briggs, M. P. Seah (Editors), Wiley & Sons, New York, (1992).
- 12. C. D. Wagner, W. M. Riggs, L. E. Davis, J. F. Moulder, G. E. Mulilenberg (Editor), *Handbook of X-ray Photoelectron Spectroscopy*, Perkin-Elmer Corp., Eden Prairie, Minnesota, (1997).
- 13. D. Lin-Vien, N. B. Colthup, W. G. Fateley, J. G. Grassellic, *The Handbook of Infrared and Raman Characteristic Frequencies of Organic Molecules*, Academic Press, Inc., (1991).
- 14. R. A. Nyquist and R. O. Kagel, (Editors), Infrared Spectra of Inorganic Compounds, Academic Press, New York, (1971).
- 15. M. H. Brooker, J. B. Bates, Spectrochimica Acta, Vol. 30A, (1994), pp. 2211-2220.

- 16. R. Mills, B. Dhandapani, M. Nansteel, J. He, "Synthesis and Characterization of Novel Hydride Compounds", Int. J. of Hydrogen Energy, submitted.
- 17. Jacox, M. G., Watts, K. D., "The Search for Excess Heat in the Mills Electrolytic Cell", Idaho National Engineering Laboratory, EG&G Idaho, Inc., Idaho Falls, Idaho, 83415, January 7, 1993.

Table 1. The respective hydride compounds and mass assignments (m/z) of the positive ToF-SIMS of the $KHKHCO_3$ electrolytic cell sample.

Hydrino Hydride Nominal Compound Observed Mass Calculated m/z Difference Between Observed and Calculate m/z KH 40 39.97 39.971535 0.0015 K2H 79 78.940 78.935245 0.004 (KH)2 80 79.942 79.94307 0.001 KHKOH2 97 96.945 96.945805 0.0008 KH2(KH)2 121 120.925 120.92243 0.003 KH KHCO2 124 123.925 123.93289 0.008 KH3,KHO4 145 144.92 144.930535 0.010 K(KOH)2 151 150.90 150.8966 0.003 KH(KOH)2 152 151.90 151.904425 0.004 KH2(KOH)2 153 152.90 152.91225 0.012 K[KH KHCO3] 179 178.89 178.8915 0.001 KCO(KH)3 187 186.87 186.873225 0.003 K1,2KOHKKOH 193 192.89 192.883785 0.006 K		
or Fragment m/z	Difference	
$\begin{array}{c ccccccccccccccccccccccccccccccccccc$	Between	
KH 40 39.97 39.971535 0.0015 K_2H 79 78.940 78.935245 0.004 $(KH)_2$ 80 79.942 79.94307 0.001 $KHKOH_2$ 97 96.945 96.945805 0.0008 $KH_2(KH)_2$ 121 120.925 120.92243 0.003 $KH KHCO_2$ 124 123.925 123.93289 0.008 KH_2KHO_4 145 144.92 144.930535 0.010 $K(KOH)_2$ 151 150.90 150.8966 0.003 $KH(KOH)_2$ 152 151.90 151.904425 0.004 $KH_2(KOH)_2$ 153 152.90 152.91225 0.012 $K[KH KHCO_3]$ 179 178.89 178.8915 0.001 $KCO(KH)_3$ 187 186.87 186.873225 0.003 $K_2OHKHKOH$ 191 190.87 190.868135 0.002 $KH_2KOHKHKOH$ 193 192.89 192.883785 0.006 $K_3O(H_2O)_4$ 205 204.92 204.92828 0.008 $K_2OH[KH KHCO_3]$		
KH 40 39.97 39.971535 0.0015 K_2H 79 78.940 78.935245 0.004 $(KH)_2$ 80 79.942 79.94307 0.001 $KHKOH_2$ 97 96.945 96.945805 0.0008 $KH_2(KH)_2$ 121 120.925 120.92243 0.003 $KH KHCO_2$ 124 123.925 123.93289 0.008 KH_2KHO_4 145 144.92 144.930535 0.010 $K(KOH)_2$ 151 150.90 150.8966 0.003 $KH(KOH)_2$ 152 151.90 151.904425 0.004 $KH_2(KOH)_2$ 153 152.90 152.91225 0.012 $K[KH KHCO_3]$ 179 178.89 178.8915 0.001 $KCO(KH)_3$ 187 186.87 186.873225 0.003 $K_2OHKHKOH$ 191 190.87 190.868135 0.002 $KH_2KOHKHKOH$ 193 192.89 192.883785 0.006 $K_3O(H_2O)_4$ 205 204.92 204.92828 0.008 $K_1CH_2CO_4$	ed	
K_2H 79 78.940 78.935245 0.004 $(KH)_2$ 80 79.942 79.94307 0.001 $KHKOH_2$ 97 96.945 96.945805 0.0008 $KH_2(KH)_2$ 121 120.925 120.92243 0.003 $KH KHCO_2$ 124 123.925 123.93289 0.008 KH_2KHO_4 145 144.92 144.930535 0.010 $K(KOH)_2$ 151 150.90 150.8966 0.003 $KH(KOH)_2$ 152 151.90 151.904425 0.004 $KH_2(KOH)_2$ 153 152.90 152.91225 0.012 $K[KH KHCO_3]$ 179 178.89 178.8915 0.001 $KCO(KH)_3$ 187 186.87 186.873225 0.003 $K_2OHKHKOH$ 191 190.87 190.868135 0.002 K_1 K_2 K_2 K_3 K_4		
$\begin{array}{c ccccccccccccccccccccccccccccccccccc$		
$KHKOH_2$ 97 96.945 96.945805 0.0008 $KH_2(KH)_2$ 121 120.925 120.92243 0.003 KH $KHCO_2$ 124 123.925 123.93289 0.008 KH_2KHO_4 145 144.92 144.930535 0.010 $K(KOH)_2$ 151 150.90 150.8966 0.003 $KH(KOH)_2$ 152 151.90 151.904425 0.004 $KH_2(KOH)_2$ 153 152.90 152.91225 0.012 $K[KH \ KHCO_3]$ 179 178.89 178.8915 0.001 $KCO(KH)_3$ 187 186.87 186.873225 0.003 $K_2OHKHKOH$ 191 190.87 190.868135 0.002 $KH_2KOHKHKOH$ 193 192.89 192.883785 0.006 $K_3O(H_2O)_4$ 205 204.92 204.92828 0.008 $K_2OH[KH \ KHCO_3]$ 235 234.86 234.857955 0.002 $K[H_2CO_4 \ KH \ KHCO_3]$ 257 256.89 256.8868 0.003 $K[KH \ KHCO_3]_3$ 303 302.88 302.89227 0.012 <td></td>		
$KH_2(KH)_2$ 121 120.925 120.92243 0.003 $KH KHCO_2$ 124 123.925 123.93289 0.008 KH_2KHO_4 145 144.92 144.930535 0.010 $K(KOH)_2$ 151 150.90 150.8966 0.003 $KH(KOH)_2$ 152 151.90 151.904425 0.004 $KH_2(KOH)_2$ 153 152.90 152.91225 0.012 $K[KH KHCO_3]$ 179 178.89 178.8915 0.001 $KCO(KH)_3$ 187 186.87 186.873225 0.003 $K_2OHKHKOH$ 191 190.87 190.868135 0.002 $KH_2KOHKHKOH$ 193 192.89 192.883785 0.006 $K_3O(H_2O)_4$ 205 204.92 204.92828 0.008 $K_2OH[KH KHCO_3]$ 235 234.86 234.857955 0.002 $K[H_2CO_4 KH KHCO_3]$ 257 256.89 256.8868 0.003 $K_3O[KH KHCO_3]$ 273 272.81 272.81384 0.004 $[KH_2CO_3]_3$ 303 302.88 302.89227 0.012		
$KH\ KHCO_2$ 124 123.925 123.93289 0.008 KH_2KHO_4 145 144.92 144.930535 0.010 $K(KOH)_2$ 151 150.90 150.8966 0.003 $KH(KOH)_2$ 152 151.90 151.904425 0.004 $KH_2(KOH)_2$ 153 152.90 152.91225 0.012 $K[KH\ KHCO_3]$ 179 178.89 178.8915 0.001 $KCO(KH)_3$ 187 186.87 186.873225 0.003 $K_2OHKHKOH$ 191 190.87 190.868135 0.002 $KH_2KOHKHKOH$ 193 192.89 192.883785 0.006 $K_3O(H_2O)_4$ 205 204.92 204.92828 0.008 $K_2OH[KH\ KHCO_3]$ 235 234.86 234.857955 0.002 $K[H_2CO_4\ KH\ KHCO_3]$ 257 256.89 256.8868 0.003 $K_3O[KH\ KHCO_3]$ 273 272.81 272.81384 0.004 $[KH_2CO_3]_3$ 303 302.88 302.89227 0.012 $K[KH\ KHCO_3K_2CO_3]$ 317 316.80 316.80366 0.004		
KH_2KHO_4 145 144.92 144.930535 0.010 $K(KOH)_2$ 151 150.90 150.8966 0.003 $KH(KOH)_2$ 152 151.90 151.904425 0.004 $KH_2(KOH)_2$ 153 152.90 152.91225 0.012 $K[KH\ KHCO_3]$ 179 178.89 178.8915 0.001 $KCO(KH)_3$ 187 186.87 186.873225 0.003 $K_2OHKHKOH$ 191 190.87 190.868135 0.002 $KH_2KOHKHKOH$ 193 192.89 192.883785 0.006 $K_3O(H_2O)_4$ 205 204.92 204.92828 0.008 $K_2OH[KH\ KHCO_3]$ 235 234.86 234.857955 0.002 $K[H_2CO_4\ KH\ KHCO_3]$ 257 256.89 256.8868 0.003 $K_3O[KH\ KHCO_3]$ 273 272.81 272.81384 0.004 $[KH_2CO_3]_3$ 303 302.88 302.89227 0.012 $K[KH\ KHCO_3K_2CO_3]$ 317 316.80 316.80366 0.004		
$K(KOH)_2$ 151150.90150.89660.003 $KH(KOH)_2$ 152151.90151.9044250.004 $KH_2(KOH)_2$ 153152.90152.912250.012 $K[KH\ KHCO_3]$ 179178.89178.89150.001 $KCO(KH)_3$ 187186.87186.8732250.003 $K_2OHKHKOH$ 191190.87190.8681350.002 $KH_2KOHKHKOH$ 193192.89192.8837850.006 $K_3O(H_2O)_4$ 205204.92204.928280.008 $K_2OH[KH\ KHCO_3]$ 235234.86234.8579550.002 $K[H_2CO_4\ KH\ KHCO_3]$ 257256.89256.88680.003 $K_3O[KH\ KHCO_3]$ 273272.81272.813840.004 $[KH_2CO_3]_3$ 303302.88302.892270.012 $K[KH\ KHCO_3K_2CO_3]$ 317316.80316.803660.004		
$KH(KOH)_2$ 152151.90151.9044250.004 $KH_2(KOH)_2$ 153152.90152.912250.012 $K[KH\ KHCO_3]$ 179178.89178.89150.001 $KCO(KH)_3$ 187186.87186.8732250.003 $K_2OHKHKOH$ 191190.87190.8681350.002 $KH_2KOHKHKOH$ 193192.89192.8837850.006 $K_3O(H_2O)_4$ 205204.92204.928280.008 $K_2OH[KH\ KHCO_3]$ 235234.86234.8579550.002 $K[H_2CO_4\ KH\ KHCO_3]$ 257256.89256.88680.003 $K_3O[KH\ KHCO_3]$ 273272.81272.813840.004 $[KH_2CO_3]_3$ 303302.88302.892270.012 $K[KH\ KHCO_3K_2CO_3]$ 317316.80316.803660.004		
$KH_2(KOH)_2$ 153152.90152.912250.012 $K[KH\ KHCO_3]$ 179178.89178.89150.001 $KCO(KH)_3$ 187186.87186.8732250.003 $K_2OHKHKOH$ 191190.87190.8681350.002 $KH_2KOHKHKOH$ 193192.89192.8837850.006 $K_3O(H_2O)_4$ 205204.92204.928280.008 $K_2OH[KH\ KHCO_3]$ 235234.86234.8579550.002 $K[H_2CO_4\ KH\ KHCO_3]$ 257256.89256.88680.003 $K_3O[KH\ KHCO_3]$ 273272.81272.813840.004 $[KH_2CO_3]_3$ 303302.88302.892270.012 $K[KH\ KHCO_3K_2CO_3]$ 317316.80316.803660.004		
$K[KH\ KHCO_3]$ 179 178.89 178.8915 0.001 $KCO(KH)_3$ 187 186.87 186.873225 0.003 $K_2OHKHKOH$ 191 190.87 190.868135 0.002 $KH_2KOHKHKOH$ 193 192.89 192.883785 0.006 $K_3O(H_2O)_4$ 205 204.92 204.92828 0.008 $K_2OH[KH\ KHCO_3]$ 235 234.86 234.857955 0.002 $K[H_2CO_4\ KH\ KHCO_3]$ 257 256.89 256.8868 0.003 $K_3O[KH\ KHCO_3]$ 273 272.81 272.81384 0.004 $[KH_2CO_3]_3$ 303 302.88 302.89227 0.012 $K[KH\ KHCO_3K_2CO_3]$ 317 316.80 316.80366 0.004		
$KCO(KH)_3$ 187 186.87 186.873225 0.003 $K_2OHKHKOH$ 191 190.87 190.868135 0.002 $KH_2KOHKHKOH$ 193 192.89 192.883785 0.006 $K_3O(H_2O)_4$ 205 204.92 204.92828 0.008 $K_2OH[KH KHCO_3]$ 235 234.86 234.857955 0.002 $K[H_2CO_4KH KHCO_3]$ 257 256.89 256.8868 0.003 $K_3O[KH KHCO_3]$ 273 272.81 272.81384 0.004 $[KH_2CO_3]_3$ 303 302.88 302.89227 0.012 $K[KH KHCO_3K_2CO_3]$ 317 316.80 316.80366 0.004		
$K_2OHKHKOH$ 191190.87190.8681350.002 $KH_2KOHKHKOH$ 193192.89192.8837850.006 $K_3O(H_2O)_4$ 205204.92204.928280.008 $K_2OH[KHKHCO_3]$ 235234.86234.8579550.002 $K[H_2CO_4KHKHCO_3]$ 257256.89256.88680.003 $K_3O[KHKHCO_3]$ 273272.81272.813840.004 $[KH_2CO_3]_3$ 303302.88302.892270.012 $K[KHKHCO_3K_2CO_3]$ 317316.80316.803660.004		
$KH_2KOHKHKOH$ 193192.89192.8837850.006 $K_3O(H_2O)_4$ 205204.92204.928280.008 $K_2OH[KH KHCO_3]$ 235234.86234.8579550.002 $K[H_2CO_4KH KHCO_3]$ 257256.89256.88680.003 $K_3O[KH KHCO_3]$ 273272.81272.813840.004 $[KH_2CO_3]_3$ 303302.88302.892270.012 $K[KH KHCO_3K_2CO_3]$ 317316.80316.803660.004		
$K_3O(H_2O)_4$ 205 204.92 204.92828 0.008 $K_2OH[KH\ KHCO_3]$ 235 234.86 234.857955 0.002 $K[H_2CO_4\ KH\ KHCO_3]$ 257 256.89 256.8868 0.003 $K_3O[KH\ KHCO_3]$ 273 272.81 272.81384 0.004 $[KH_2CO_3]_3$ 303 302.88 302.89227 0.012 $K[KH\ KHCO_3K_2CO_3]$ 317 316.80 316.80366 0.004		
$K_2OH[KH\ KHCO_3]$ 235 234.86 234.857955 0.002 $K[H_2CO_4\ KH\ KHCO_3]$ 257 256.89 256.8868 0.003 $K_3O[KH\ KHCO_3]$ 273 272.81 272.81384 0.004 $[KH_2CO_3]_3$ 303 302.88 302.89227 0.012 $K[KH\ KHCO_3K_2CO_3]$ 317 316.80 316.80366 0.004		
$K[H_2CO_4 KH KHCO_3]$ 257 256.89 256.8868 0.003 $K_3O[KH KHCO_3]$ 273 272.81 272.81384 0.004 $[KH_2CO_3]_3$ 303 302.88 302.89227 0.012 $K[KH KHCO_3K_2CO_3]$ 317 316.80 316.80366 0.004		
$K_3O[KH\ KHCO_3]$ 273 272.81 272.81384 0.004 $[KH_2CO_3]_3$ 303 302.88 302.89227 0.012 $K[KH\ KHCO_3K_2CO_3]$ 317 316.80 316.80366 0.004		
[KH ₂ CO ₃] ₃ 303 302.88 302.89227 0.012 K[KH KHCO ₃ K ₂ CO ₃] 317 316.80 316.80366 0.004		
$K[KH \ KHCO_3K_2CO_3]$ 317 316.80 316.80366 0.004		
K[KH KHCO ₃ K ₂ CO ₃] 317 316.80 316.80366 0.004		
V[VH VHCO] 040 040 040 040 040 040 040 040 040 04		
$K[KH \ KHCO_3]_2$ 319 318.82 318.81931 0.001		
KH ₂ [KH KOH] ₃ 329 328.80 328.7933 0.007		
KOH ₂ [KH KHCO ₃] ₂ 337 336.81 336.82987 0.020		
KH KO ₂ 351 350.81 350.80913 0.001		
[KH KHCO ₃][KHCO ₃]		
KKHK ₂ CO ₃ 357 356.77 356.775195 0.005		
[KH KHCO ₃]		





Mills

$KKH[KH\ KHCO_3]_2$	359	358.78	358.790845	0.011
$K_2OH[KH\ KHCO_3]_2$	375	374.78	374.785755	0.005
$K_2OH[KHKOH]_2$	387	386.75	386.76238	0.012
[KHCO ₃]				
$KKH_3KH_5[KH\ KHCO_3]_2$	405	404.79	404.80933	0.019
$K_3O[K_2CO_3]$	411	410.75	410.72599	0.024
[KH KHCO ₃] or				
$K[KH\ KOH(K_2CO_3)_2]$				
$K_3O[KH\ KHCO_3]_2$	413	412.74	412.74164	0.002
KH KOH	415	414.74	414.75729	0.017
$\left[\left(KH \ KHCO_{3} \right)_{2} \right]$			·	
KH ₂ OKHCO ₃	437	436.81	436.786135	0.024
$[KH\ KHCO_3]_2$				
$KKHKCO_2[KH KHCO_3]_2$	442	441.74	441.744375	0.004
$K[KH \ KHCO_3]_3$	459	458.72	458.74711	0.027
$H[KH KOH]_2[K_2CO_3]_2$	469	468.70	468.708085	0.008
or		·		
$K_4O_2H[KH\ KHCO_3]_2$				
$K[K_2CO_3][KHCO_3]_3$	477	476.72	476.744655	0.025
$K_2OH[KH\ KHCO_3]_3$	515	514.72	514.713555	0.006
$K_3O[KH\ KHCO_3]_3$	553	552.67	552.66944	0.001
$K[KH \ KHCO_3]_4$	599	598.65	598.67491	0.025
$K_2OH[KH\ KHCO_3]_4$	655	654.65	654.641355	0.009
$K_3O[KH\ KHCO_3]_4$	693	692.60	692.59724	0.003
$K[KH \ KHCO_3]_5$	739	738.65	738.60271	0.047
$K_3O[KH\ KHCO_3]_5$	833	832.50	832.52504	0.025
K[KH KHCO ₃] ₆	879	878.50	878.53051	0.031
$K_3O[KH\ KHCO_3]_6$	973	972.50	972.45284	0.047

Mills

Table 2. The binding energies of XPS peaks of K_2CO_3 and the KH KHCO₃

electrolytic cell sample.

electrolytic	CCII	sampic					
XPS	C 1s	O 1s	K 3p	K 3s	$K2p_3$	$K2p_1$	K 2s
#	(eV)	(eV)	(eV)	(eV)	(eV)	(eV)	(eV)
K_2CO_3	288.4	532.0	18	34	292.4	295.2	376.7
KH KHCO ₃	288.5	530.4	16.2	32.1	291.5	293.7	376.6
Electrolytic		537.5	22.8	38.8	298.5	300.4	382.6
Cell		547.8					
Sample							
Min	280.5	529			292		
Max	293	535			293.2		



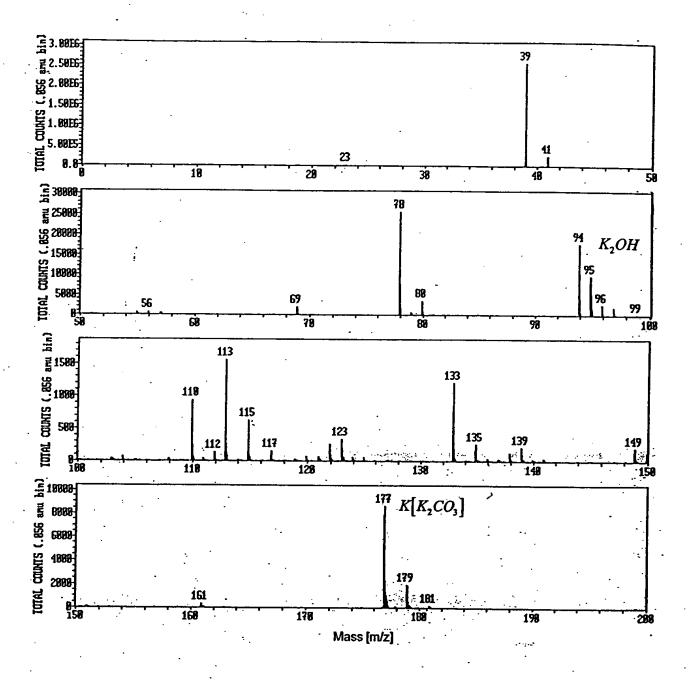
Table 3. The NMR peaks of the KH KHCO₃ electrolytic cell sample with their assignments.

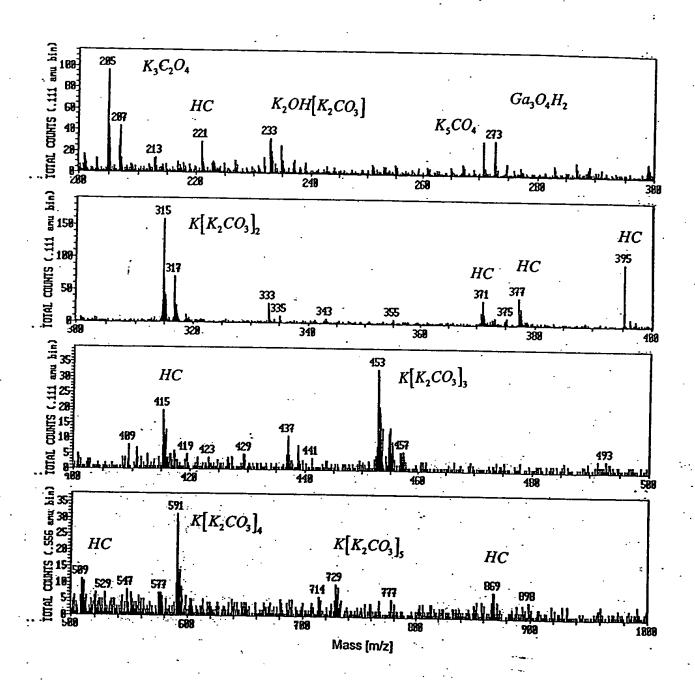
initents.			
Peak at Shift	Assignment		
(ppm)			
+34.54	side band of		
İ	+17.163 peak		
+22.27	side band of +5.066		
	peak		
+17.163	KH KHCO ₃		
+10.91	KH KHCO ₃		
+8.456	KH KHCO ₃		
+7.50	KH KHCO ₃		
+5.066	H_2O		
+1.830	KH KHCO ₃		
-0.59	side band of		
	+17.163 peak		
-12.05	<i>КН КНСО</i> 3 а		
-15.45	KH KHCO ₃		

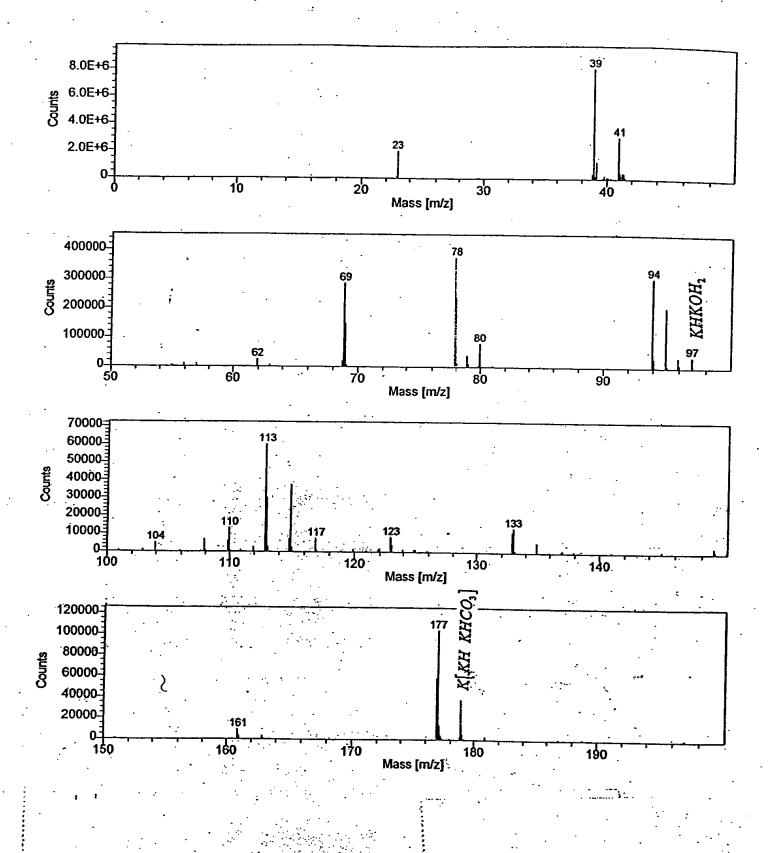
a small shoulder is observed on the -12.05 peak
 which is the side band of the +5.066 peak

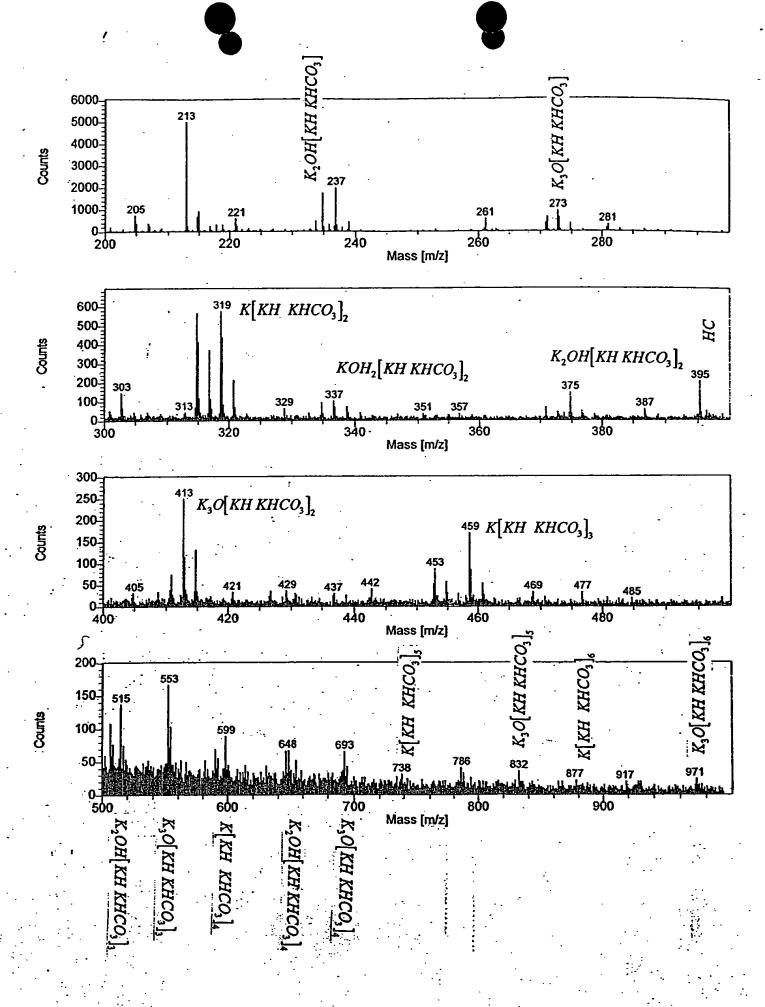
Mills

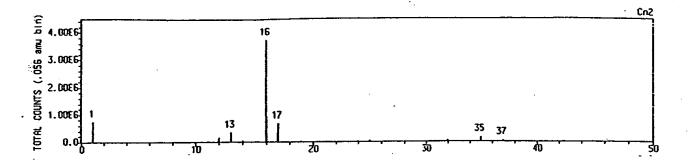
- Figure 1. The positive ToF-SIMS spectrum (m/e = 0 200) of KHCO₃ (99.99%) where HC = hydrocarbon.
- Figure 2. The positive ToF-SIMS spectrum (m/e = 200 1000) of $KHCO_3$ (99.99%) where HC = hydrocarbon.
- Figure 3. The positive ToF-SIMS spectrum (m/e = 0 200) of the $KH\ KHCO_3$ electrolytic cell sample where HC = hydrocarbon.
- Figure 4. The positive ToF-SIMS spectrum (m/e = 200 1000) of the $KH KHCO_3$ electrolytic cell sample where HC = hydrocarbon.
- Figure 5. The negative ToF-SIMS spectrum (m/e = 0 50) of the KHCO₃ (99.99%) sample.
- Figure 6. The negative ToF-SIMS spectrum (m/e = 0 30) of the $KH\ KHCO_3$ electrolytic cell sample.
- Figure 7. The positive ToF-SIMS spectrum of the KH electrolytic cell sample.
- Figure 8. The negative ToF-SIMS spectrum of the KH electrolytic cell sample.
- Figure 9. The 0 to 80 eV binding energy region of a high resolution XPS spectrum of the KH KHCO₃ electrolytic cell sample.
- Figure 10. The XPS survey spectrum of the KH KHCO₃ electrolytic cell sample with the primary elements identified.
 - Figure 11. The XPS survey scan of the KH electrolytic cell sample.
- Figure 12. The 0-80 eV binding energy region of a high resolution XPS spectrum of the KH electrolytic cell sample.
- Figure 13. The magic angle spinning proton NMR spectrum of the KH KHCO₃ electrolytic cell sample.
- Figure 14. The overlap FTIR spectrum of the KH KHCO₃ electrolytic cell sample and the FTIR spectrum of the reference potassium carbonate.











F19.5

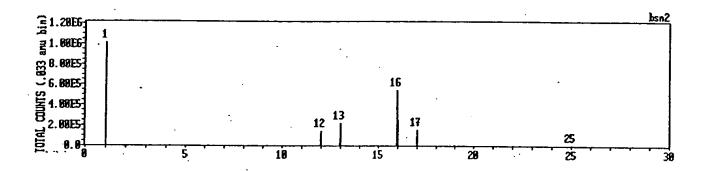
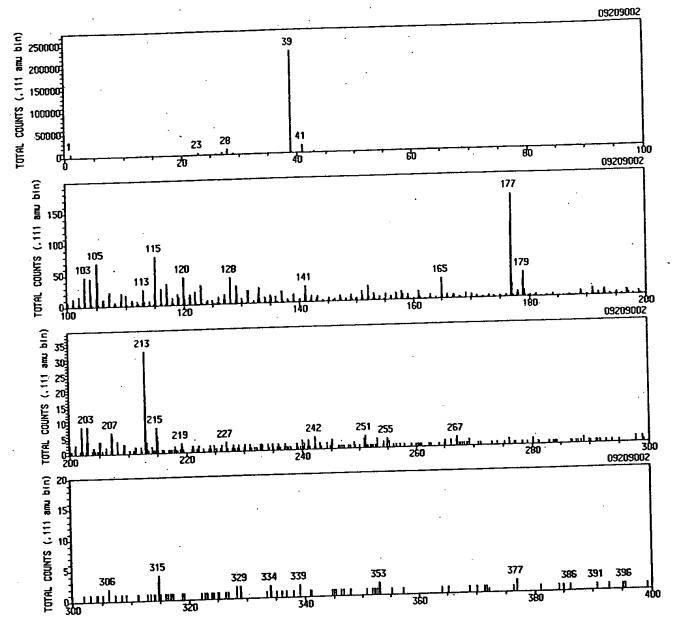


Fig. 6



BLACKLIGHT POWER, INC. ANALYTICAL SERVICES GROUP SURFACE ANALYSIS LABORATORY 1:609-490-1090 F:609-490-1066

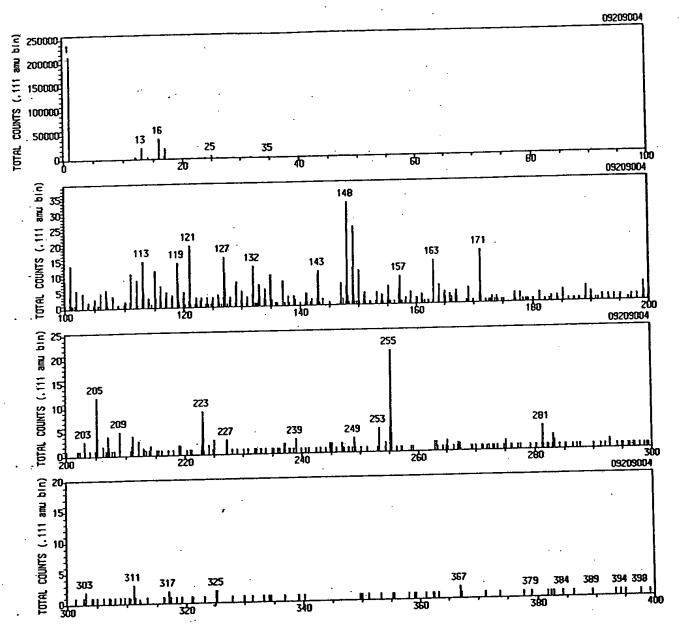


FILE NAME: 09209002 DATE: 20 Sep 99 16:53 ACQUISITION TIME: 5.0 MIN. SPECTRUM INTEGRAL: 319972 990917rm,+, 7ns, e-on, buch805, 5 minAqt, non-sput,(another spot; + IONS PRIMARY GUN: LMIG TIME RECORDER: Multi-Stop TDC X-Y SOURCE: RAE TIME PER CHANNEL: 138 ps DATA SET: 1 Spectra; 0 image(s) RASTER SIZE: 61µm RASTER TYPE: Full NI FlyBack

990912AN HXHY ZNEU

Fig. 7

BLACKLIGHT POWER, INC. ANALYTICAL SERVICES GROUP SURFACE ANALYSIS LABORATORY 1:609-490-1090 F:609-490-1066

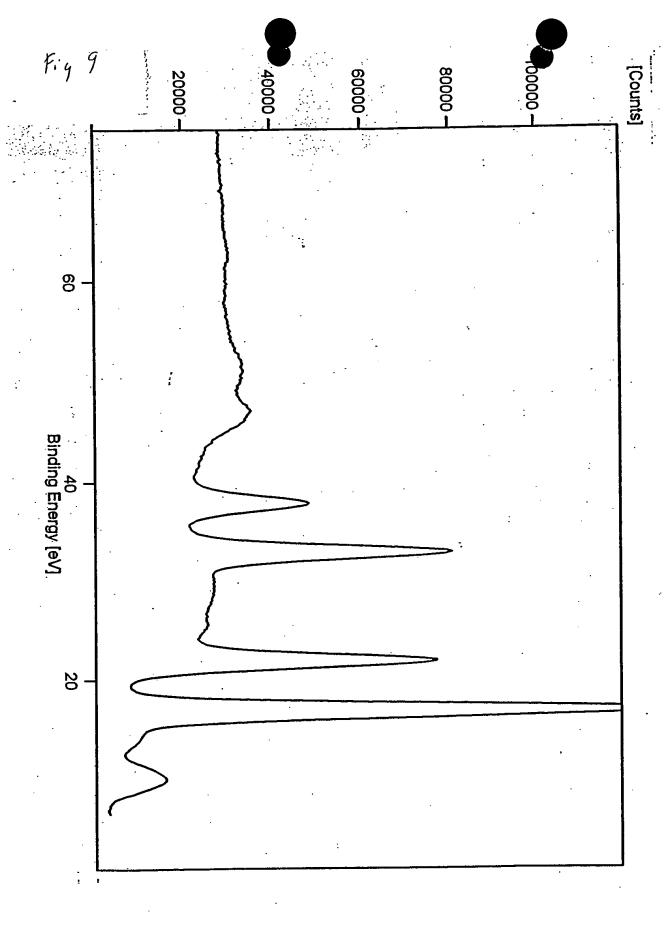


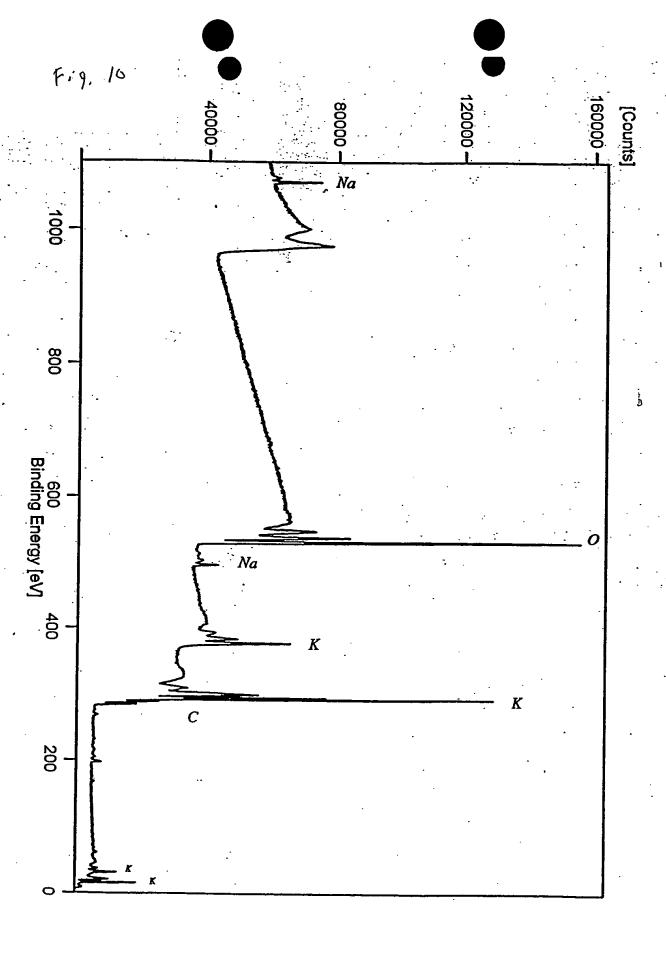
SPECTRUM INTEGRAL : 343853 ACQUISITION TIME: 5.0 MIN. DATE: 20 Sep 99 17:10 .FILE NAME: 09209004 990917rm, -, 7ns, e-on, buch805, 5 minAqt, 30s-sput,; TIME PER CHANNEL: 138 ps TIME RECORDER: Multi-Stop TDC X-Y SOURCE: RAE PRIMARY GUN: LMIG - IONS

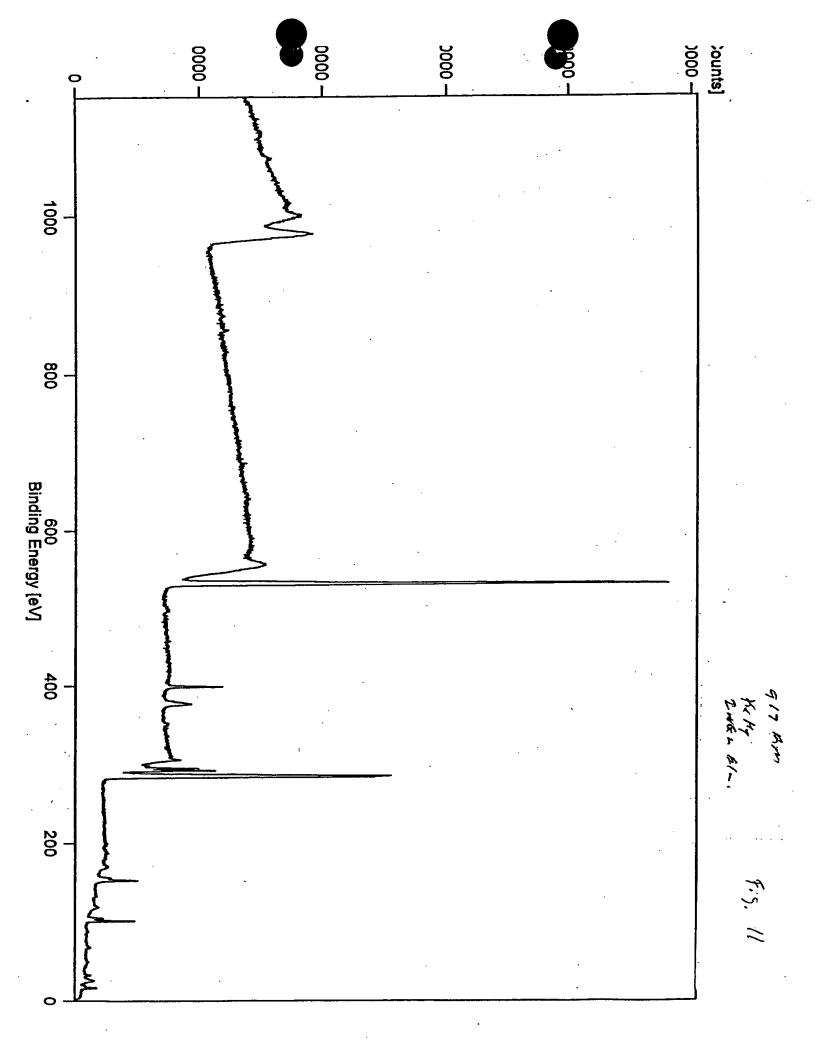
RASTER TYPE: Full NI FlyBack 61µm RASTER SIZE: DATA SET: 1 Spectra; 0 Image(s)

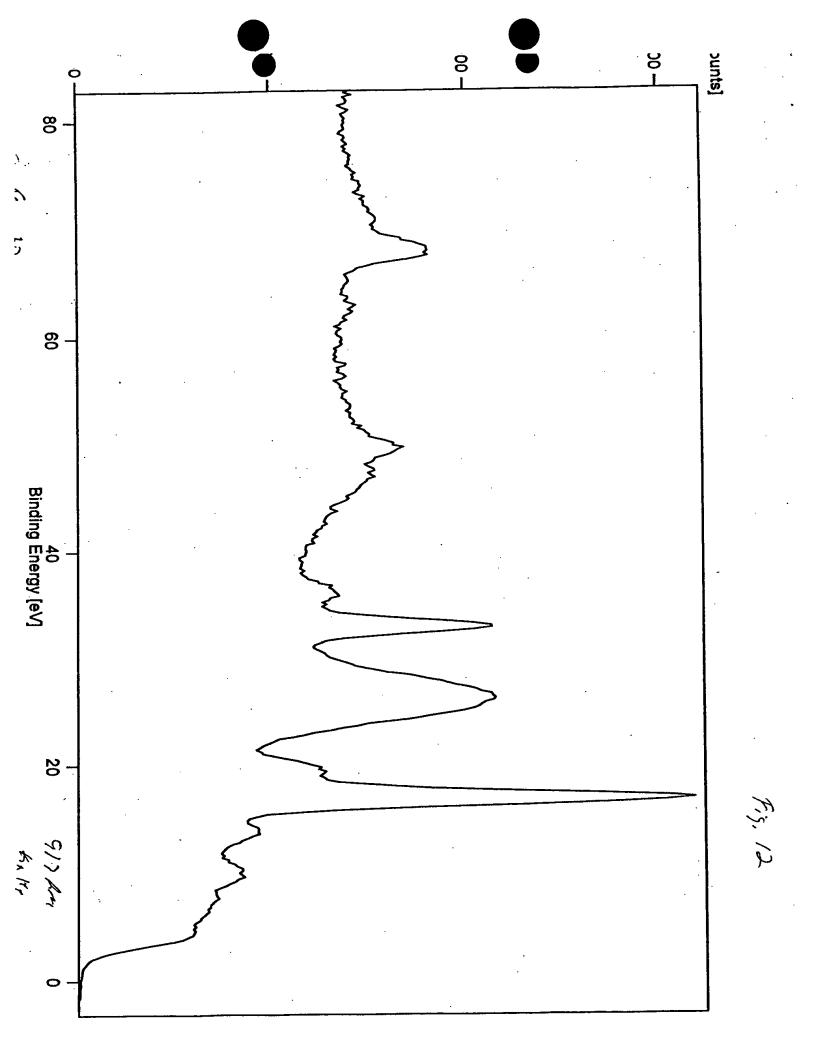
1909 DAM Harry INSL

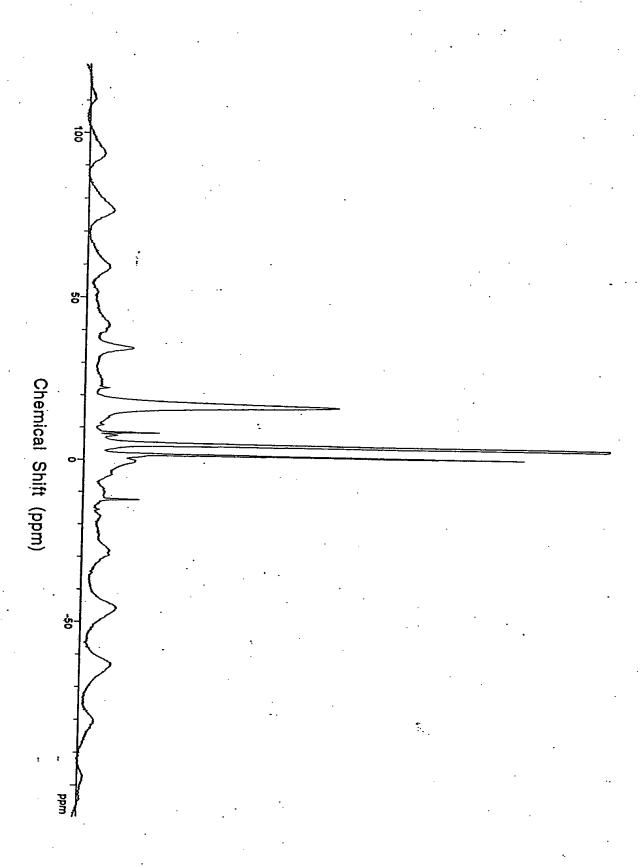
Fig. Y

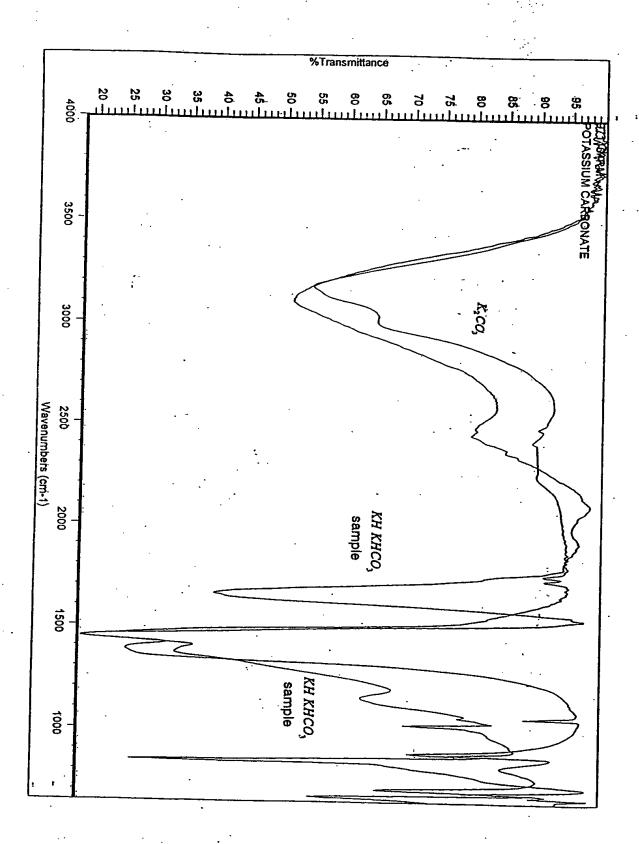
















ELECTROLYTIC DEVICES

KEYWORDS: novel hydrogen compounds, hydrogen catalysis, electrolytic cell

NOVEL HYDROGEN COMPOUNDS FROM A POTASSIUM CARBONATE ELECTROLYTIC CELL

RANDELL L. MILLS* BlackLight Power
493 Old Trenton Road, Cranbury, New Jersey 08512

Received March 24, 1999 Accepted for Publication August 4, 1999

Novel compounds containing hydrogen in new hydride and polymeric states that demonstrate novel hydrogen chemistry have been isolated following the electrolysis of a K_2CO_3 electrolyte with the production of excess energy. Inorganic hydride clusters $K[KH\ KHCO_3]_{\pi}^+$ and hydrogen polymer ions such as OH_{23}^+ and H_{16}^- were identified by time-of-flight secondary ion mass spectroscopy. The presence of compounds containing new states of hydrogen was confirmed by X-ray photoelectron spectroscopy, X-ray diffraction, Fourier transform infrared spectroscopy, Raman spectroscopy, and proton nuclear magnetic resonance spectroscopy.

I. INTRODUCTION

A hydride ion comprises two indistinguishable electrons bound to a proton. Alkali and alkaline earth hydrides react violently with water to release hydrogen gas that subsequently ignites because of the exothermic reaction with water. Typically, metal hydrides decompose upon heating at a temperature well below the melting point of the parent metal. These saline hydrides, so called because of their saltlike or ionic character, are the monohydrides of the alkali metals and the dihydrides of the alkaline-earth metals.

A novel hydride ion having extraordinary chemical properties, given by Mills, is predicted to form by the reaction of an electron with a hydrino [Eq. (2)], a hydrogen atom having a binding energy given by

Binding Energy =
$$\frac{13.6 \text{ eV}}{\left(\frac{1}{p}\right)^2}$$
, (1)

where p is an integer >1, designated as $H[a_H/p]$ where a_H is the radius of the hydrogen atom. The resulting hydride ion is referred to as a hydrino hydride ion, designated as $H^-(1/p)$:

$$H\left[\frac{a_H}{\frac{p}{p}}\right] + e^- \to H^-(1/p) \tag{2}$$

The hydrino hydride ion is distinguished from an ordinary hydride ion having a binding energy of 0.8 eV. The latter is hereafter referred to as "ordinary hydride ion." The hydrino hydride ion is predicted to comprise a hydrogen nucleus and two indistinguishable electrons at a binding energy according to the following formula:

Binding Energy =
$$\frac{\hbar^{2}\sqrt{s(s+1)}}{8\mu_{e}a_{0}^{2}\left[\frac{1+\sqrt{s(s+1)}}{p}\right]^{2}} - \frac{\pi\mu_{0}e^{2}\hbar^{2}}{m_{e}^{2}a_{0}^{3}} \times \left(1 + \frac{2^{2}}{\left[\frac{1+\sqrt{s(s+1)}}{p}\right]^{3}}\right), \quad (3)$$

where

$$p = integer > 1$$

$$s = \frac{1}{2}$$

$$\pi = p_1$$

 \hbar = Planck's constant bar

 μ_0 = permeability of vacuum

 $m_e = \text{mass of the electron}$

^{*}E-mail: rmills@blacklightpower.com

 μ_e = reduced electron mass

 $a_0 = Bohr radius$

e = elementary charge.

The ionic radius is

$$r_1 = \frac{a_0}{p} (1 + \sqrt{s(s+1)}), s = \frac{1}{2}$$
 (4)

From Eq. (4), the radius of the hydrino hydride ion $H^-(1/p)$, p = integer, is 1/p that of the ordinary hydride ion, $H^-(1/1)$. The binding energies and radii of the first 16 hydride ions, $H^-(n = 1/p)$ as a function of p, where p is an integer, are shown in Table I.

Hydrinos are predicted to form by reacting an ordinary hydrogen atom with a catalyst having a net enthalpy of reaction of about

$$m \cdot 27.21 \text{ eV}$$
 , (5)

where m is an integer. This catalysis releases energy from the hydrogen atom with a commensurate decrease in size of the hydrogen atom, $r_n = na_H$. For example, the catalysis of H(n = 1) to $H(n = \frac{1}{2})$ releases 40.8 eV, and the hydrogen radius decreases from a_H to $\frac{1}{2}a_H$. One such catalytic system involves potassium. The second ionization energy of potassium is 31.63 eV, and K^+ releases

TABLE I

The Representative Radius and Binding Energy of the Hydrino
Hydride Ion $H^-(n = 1/p)$ as a Function of p

	7 to the total of p							
Hydride Ion	$r_1 (a_0)^a$	Binding Energy (eV) ^b	Wavelength (nm)					
$H^{-}(n = \frac{1}{1})$ $H^{-}(n = \frac{1}{2})$ $H^{-}(n = \frac{1}{3})$ $H^{-}(n = \frac{1}{4})$ $H^{-}(n = \frac{1}{6})$ $H^{-}(n = \frac{1}{6})$ $H^{-}(n = \frac{1}{8})$ $H^{-}(n = \frac{1}{10})$ $H^{-}(n = \frac{1}{11})$ $H^{-}(n = \frac{1}{12})$	1.8660 0.9330 0.6220 0.4665 0.3732 0.3110 0.2666 0.2333 0.2073 0.1866 0.1696 0.1555	0.7540 3.047 6.610 11.23 16.70 22.81 29.34 36.08 42.83 49.37 55.49 60.97	1644 407 188 110 74.2 54.4 42.3 34.4 28.9 25.1 22.3					
H ⁻ $(n = \frac{1}{13})$ H ⁻ $(n = \frac{1}{14})$ H ⁻ $(n = \frac{1}{15})$ H ⁻ $(n = \frac{1}{16})$	0.1435 0.1333 0.1244 0.1166	65.62 69.21 71.53 72.38	20.3 18.9 17.9 17.3 17.1					

^aEquation (4).

4.34 eV when it is reduced to K. The combination of reactions K^+ to K^{2+} and K^+ to K, then, has a net enthalpy of reaction of 27.28 eV, which is equivalent to m = 1 in Eq. (5):

27.28 eV + K⁺ + K⁺ + H
$$\left[\frac{a_{H}}{p}\right]$$

 \rightarrow K + K²⁺ + H $\left[\frac{a_{H}}{(p+1)}\right]$
+ $[(p+1)^{2} - p^{2}] \times 13.6$ eV (6)

and

$$K + K^{2+} \rightarrow K^{+} + K^{+} + 27.28 \text{ eV}$$
 (7)

The overall reaction is

$$H\left[\frac{a_{\rm H}}{p}\right] \to H\left[\frac{a_{\rm H}}{(p+1)}\right] + \left[(p+1)^2 - p^2\right] \times 13.6 \text{ eV} . \tag{8}$$

The energy given off during catalysis is much greater than the energy lost to the catalyst. The energy released is large as compared to conventional chemical reactions. For example, when hydrogen and oxygen gases undergo combustion to form water.

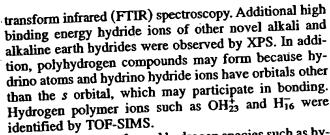
$$H_2(g) + \frac{1}{2}O_2(g) \to H_2O(l)$$
, (9)

the known enthalpy of formation of water is $\Delta H_f = -286$ kJ/mol or 1.48 eV per hydrogen atom. By contrast, each (n=1) ordinary hydrogen atom undergoing catalysis releases a net of 40.8 eV. Moreover, further catalytic transitions may occur: $n=\frac{1}{2}\to\frac{1}{3},\,\frac{1}{3}\to\frac{1}{4},\,\frac{1}{4}\to\frac{1}{5}$, and so on. Once catalysis begins, hydrinos autocatalyze further in a process called disproportionation. This mechanism is similar to that of an inorganic ion catalysis. But, hydrino catalysis should have a higher reaction rate than that of the inorganic ion catalyst because of the better match of the enthalpy to $m \times 27.2$ eV.

Hydrino hydride ions may react with cations to produce compounds such as alkali and alkaline earth hydrides. A representative compound has the formula $MH_mM'X$, wherein m is an integer, M and M' are each an alkali or alkaline earth cation, X is a singly or doubly negative charged anion, and the hydrogen content H_m of the compound comprises at least one hydrino hydride ion. For example, an inorganic hydride compound having the formula KH KHCO3 was isolated from an aqueous K₂CO₃ electrolytic cell reactor. Inorganic hydride clusters K[KH KHCO₃], were identified by timeof-flight secondary ion mass spectroscopy (TOF-SIMS). A hydride ion with a binding energy of 22.8 eV has been observed by X-ray photoelectron spectroscopy (XPS) and has upfield shifted solid-state magic-angle spinning proton nuclear magnetic resonance (1H MAS NMR) peaks. Moreover, a polymeric structure is indicated by Fourier

^bEquation (3).





The discovery of novel hydrogen species such as hydride ions with high binding energies has implications for a new field of hydrogen chemistry. These novel compositions of matter and associated technologies may have far-reaching applications in many industries, including chemical, electronics, computer, military, energy, and aerospace, in the form of products such as batteries, propellants, solid fuels, munitions, surface coatings, structural materials, and chemical processes.

II. EXPERIMENTAL

II.A. Electrolytic Cells

Thermacore (Lancaster, Pennsylvania) operated a ' K2CO3 electrolytic cell consisting of a nickel wire cathode and platinized titanium anodes described by Mills et al.2 and herein referred to as the Thermacore electrolytic cell. This cell had produced an enthalpy of formation of increased binding energy hydrogen compounds of 1.6×10^9 J that exceeded the total input enthalpy given by the product of the electrolysis voltage and current over time by a factor >8. Briefly, the cell vessel comprised a 10-gal (33-×15-in.) Nalgene tank. An outer cathode consisted of 5000 m of 0.5-mm-diam clean, cold drawn nickel wire wound on a polyethylene cylindrical support. A central cathode comprised 5000 m of the nickel wire wound in a toroidal shape. The central cathode was inserted into a cylindrical, perforated polyethylene container that was placed inside the outer cathode with an anode array between the central and outer cathodes. The anode comprised an array of 15 platinized titanium anodes.^b Before assembly, the anode array was cleaned in 3 M HCl for 5 min and rinsed with distilled water. The cathode was cleaned by placing it in a tank of 0.57 M K₂CO₃/3% H₂O₂ for 6 h and then by rinsing it with distilled water. The anode was placed in the support between the central and outer cathodes, and the electrode assembly was placed in the tank containing electrolyte. The electrolyte solution comprised 28 ℓ of 0.57 M K₂CO₃ (Alfa K₂CO₃ 99%).

aNI 2000.0197 in., HTN36NOAG1, from A-1 Wire Tech, Inc., 840-39th Avenue, Rockford, Illinois 61109.

Electrolysis was performed at 20-A constant current with a constant current (±0.02%) power supply.

A cell that produced 6.3×10^8 J of enthalpy of formation of increased binding energy hydrogen compounds was operated by BlackLight Power (Malvern, Pennsylvania), herein referred to as the BLP electrolytic cell. The cell description is also given in Ref. 2 except that it lacked the additional central cathode.

Idaho National Engineering Laboratory (INEL) operated a cell,3 herein referred to as the INEL electrolytic cell, identical to the Thermacore electrolytic cell except that it lacked the central cathode and that the cell was wrapped in a 1-in. layer of urethane foam insulation about the cylindrical surface. The cell was operated in a pulsed power mode. A current of 10 A was passed through the cell for 0.2 s followed by 0.8 s of zero current for the current cycle. The cell voltage was ~2.4 V, for an average input power of 4.8 W. The electrolysis power average was 1.84 W, and the stirrer power was measured to be 0.3 W. Thus, the total average net input power was 2.14 W. The cell was operated at various resistance heater settings, and the temperature difference between the cell and the ambient as well as the heater power was measured. The results of the excess power as a function of cell temperature with the cell operating in the pulsed power mode at 1 Hz with a cell voltage of 2.4 V, a peak current of 10 A, and a duty cycle of 20% showed that the excess power is temperature dependent for pulsed power operation, and the maximum excess power was 18 W for an input electrolysis joule heating power of 2.14 W. Thus, the ratio of excess power to input electrolysis joule heating power was 850%.

11.B. Sample Preparation

Sample 1: The sample was prepared by concentrating the K₂CO₃ electrolyte from the Thermacore electrolytic cell using a rotary evaporator at 50°C until a yellow-white polymeric suspension formed. The polymeric material was observed after the volume had been reduced from 3000 to 150 cm³. The inorganic polymeric material was centrifuged to form a pellet that was collected following decanting of the concentrated electrolyte.

Sample 2: The sample was prepared by concentrating the K₂CO₃ electrolyte from the Thermacore electrolytic cell at room temperature using an evaporation dish until a yellow-white solid containing a polymeric material just formed. The remaining electrolyte was decanted, and the solid was dried and collected.

Sample 3: The sample was prepared by concentrating $300 \, \mathrm{cm}^3$ of the $\mathrm{K}_2\mathrm{CO}_3$ electrolyte from the BLP electrolytic cell using a rotary evaporator at $50^{\circ}\mathrm{C}$ until a precipitate just formed. The volume was $\sim 50 \, \mathrm{cm}^3$. Additional electrolyte was added while heating at $50^{\circ}\mathrm{C}$ until the crystals disappeared. Crystals were then grown over 3 weeks by allowing the saturated solution to stand in a sealed round-bottom flask at $25^{\circ}\mathrm{C}$. The yield was 1 g.

bTen of the anodes were Engelhard Pt/Ti mesh, 1.6×8 in. with one $\frac{3}{4} \times 7$ -in. stem attached to the 1.6-in. side plated with 100 U series 3000; five of the anodes were Engelhard 1-in.-diam $\times 8$ -in.-long titanium tubes with one $\frac{3}{4} \times 7$ -in. stem affixed to the interior of one end and plated with 100 U Pt series 3000.

Sample 4: The cathode of the INEL electrolytic cell was placed in 28ℓ of $0.6 M \text{ K}_2\text{CO}_3/10\% \text{ H}_2\text{O}_2$; 200 cm^3 of the solution was acidified with HNO₃. The solution was allowed to stand open for 3 months at room temperature in a 250-ml beaker. White nodular crystals formed on the walls of the beaker by a mechanism equivalent to thin layer chromatography involving atmospheric water vapor as the moving phase and the Pyrex silica of the beaker as the stationary phase.

Sample 5: The sample was prepared by filtering the K₂CO₃ electrolyte from the BLP electrolytic cell with a Whatman 110-mm filter paper.^c

Sample 6: The reference consisted of K₂CO₃ (99%). Sample 7: The reference consisted of KHCO₃ (99.99%).

Sample 8: The reference consisted of HNO₃ (99.99%).

II.C. TOF-SIMS Characterization

Samples were sent to Evans East (East Windsor, New Jersey) for TOF-SIMS analysis. The crystalline samples were sprinkled onto the surface of double-sided adhesive tapes and characterized using a Physical Electronics TFS-2000 TOF-SIMS instrument. The primary ion gun utilized a 69 Ga⁺ liquid metal source. To remove surface contaminants and expose a fresh surface, the samples were sputter cleaned for 30 s using a $40-\times40-\mu\mathrm{m}$ raster. The aperture setting was 3, and the ion current was 600 pA, resulting in a total ion dose of 10^{15} ions/cm².

During acquisition, the ion gun was operated using a bunched (pulse width 4 ns bunched to 1 ns) 15-kV beam. ^{4,5d} The total ion dose was 10^{12} ions/cm². Charge neutralization was active, and the postaccelerating voltage was 8000 V. Three different regions on each sample of $(12 \ \mu m)^2$, $(18 \ \mu m)^2$, and $(25 \ \mu m)^2$ were analyzed. The positive and negative TOF-SIMS spectra were acquired. Representative postsputtering data are reported except where indicated.

II.D. XPS Characterization

The binding energy of various hydrino hydride ions may be obtained according to Eq. (3), as given in Table I. XPS was used to confirm the TOF-SIMS data showing production of the increased binding energy hydrogen compounds. This was achieved by identifying component hydrino hydride ions such as $n = \frac{1}{2}$ to $n = \frac{1}{16}$, $E_b = 3$ to 73 eV. The identities of the other elements of the samples were confirmed via the shifts of the primary element peaks of the component atoms due to binding with increased binding energy hydrogen species such as hydrino hydride ions. The hydrino hydride ion, $n = \frac{1}{16}$, is the most stable hydrino hydride ion. Thus, XPS of the energy range $E_b = 3$ to 73 eV detects these states. Compared to the

^cThe Whatman filter paper is catalog number 1450110.

surface of a cathode as the sample, isolation of pure hydrino hydride compounds from the electrolyte is a means of eliminating impurities so that impurities are eliminated as an alternative assignment to the hydrino hydride ion peaks. The absence of impurities was determined from the survey spectrum over the region $E_b = 0$ to 1200 eV. The survey spectrum also detected shifts in the binding energies of elements bound to hydrino hydride ions.

A series of XPS analyses was made by the Zettlemoyer Center for Surface Studies, Sinclair Laboratory, Lehigh University, on the crystalline samples using a Scienta 300 XPS spectrometer. The fixed analyzer transmission mode and the sweep acquisition mode were used. The step energy in the survey scan was 0.5 eV, and the step energy in the high-resolution scan was 0.15 eV. In the survey scan, the time per step was 0.4 s, and the number of sweeps was 4. In the high-resolution scan, the time per step was 0.3 s, and the number of sweeps was 30. As the internal standard, C 1s at 284.6 eV was used.

II.E. Characterization by XRD

The X-ray diffraction (XRD) patterns were obtained by IC Laboratories (Amawalk, New York) using a Phillips 547 diffractometer tuned for CuK_{α} (1.540590-Å) radiation generated at 45 kV and 35 mA. The sample was scanned from 8 to 68 2-theta with a step size of 0.02 deg and 1 s/step.

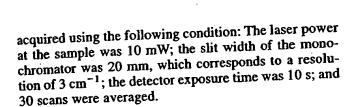
II.F. FTIR Spectroscopy

Samples were transferred to an infrared transmitting substrate and analyzed by FTIR spectroscopy by Surface Science Laboratories (Mountain View, California) using a Nicolet Magna 550 FTIR spectrometer with a Nic-Plan FTIR microscope. The number of scans was 500 for both the sample and background. The number of background scans was 500. The resolution was 8.000. A dry air purge was applied.

II.G. Raman Spectroscopy

Experimental and control samples were analyzed blindly by the Environmental Catalysis and Materials Laboratory of Virginia Polytechnic Institute. Raman spectra were obtained with a Spex 500 M spectrometer coupled with a liquid nitrogen-cooled charge coupled device detector (Spectrum One, Spex). An Ar⁺ laser (Model 95, Lexel) with a light wavelength of 514.5 nm was used as the excitation source, and a holographic filter (Super-Notch Plus, Kaiser) was employed to effectively reject the elastic scattering from the sample. The spectra were taken at ambient conditions, and the samples were placed in capillary glass tubes (0.8- to 1.1-mm outside diameter, 90 mm long, Kimble) on a capillary sample holder (Model 1492, Spex). Spectra of the powder samples were

dRecent specifications are listed in Ref. 5.



II.H. NMR Spectroscopy

The ¹H MAS NMR was performed on the crystalline samples by Spectral Data Services (Champaign, Illinois). The data were obtained on a custom-built spectrometer operating with a Nicolet 1280 computer. Final pulse generation was from a tuned Henry radio amplifier. The ¹H NMR frequency was 270.6196 MHz. A 2-μs pulse corresponding to a 15-deg pulse length and a 3-s recycle delay was used. The window was ±31 kHz. The spin speed was 4.5 kHz. The number of scans was 1000. Chemical shifts were referenced to external TMS. The offset was 1527.12 Hz, and the magnetic flux was 6.357 T.

III. RESULTS AND DISCUSSION

III.A. TOF-SIMS

The positive TOF-SIMS spectrum obtained from the KHCO₃ control is shown in Figs. 1 and 2. Moreover, the positive TOF-SIMS of sample 1 isolated from the electrolytic cell is shown in Figs. 3 and 4. The respective hydride compounds and mass assignments appear in Table II. In both the control and sample 1, the positive ion spectrum is dominated by the K⁺ ion. Two series of positive ions $\{K[K_2CO_3]_n^+ m/z = (39 + 138n)\}$ and $K_2OH[K_2CO_3]_n^+ m/z = (95 + 138n)\}$ are

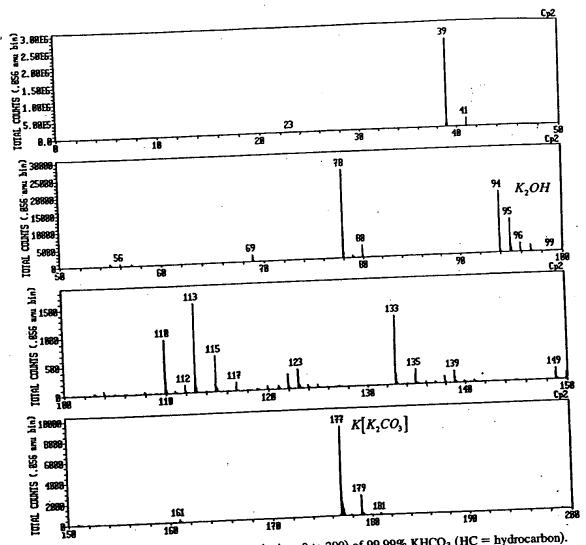


Fig. 1. The positive TOF-SIMS spectrum (m/e = 0 to 200) of 99.99% KHCO₃ (HC = hydrocarbon).

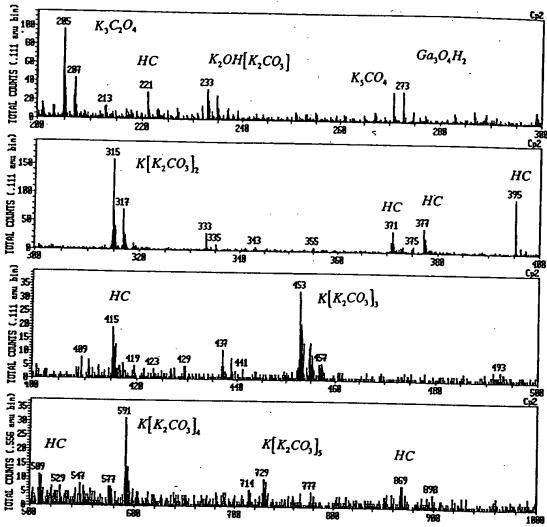


Fig. 2. The positive TOF-SIMS spectrum (m/e = 200 to 1000) of 99.99% KHCO₃ (HC = hydrocarbon).

observed in the KHCO₃ control. Other peaks containing potassium include KC⁺, $K_xO_y^+$, $K_xO_yH_z^+$, KCO⁺, and K_2^+ . However, in sample 1, three new series of positive ions are observed at {K[KH KHCO₃] $_n^+$ m/z = (39 + 140n), $K_2OH[KH KHCO_3]_n^+$ m/z = (95 + 140n), and $K_3O[KH KHCO_3]_n^+$ m/z = (133 + 140n)}. These ions correspond to inorganic clusters containing novel hydride combinations (i.e., KH KHCO₃ units plus other positive fragments). These 140 series peaks were also present in the positive TOF-SIMS spectrum of samples 2 and 3. The TOF-SIMS peaks of sample 1 were much more intense because of purification.

The comparison of the positive TOF-SIMS spectrum of the KHCO₃ control with the electrolytic cell sample shown in Figs. 1 and 2, and 3 and 4, respectively, demonstrates that the ³⁹K⁺ peak of sample 1 may saturate the detector and give rise to a peak that is atypical of the natural abundance of ⁴¹K. The natural abundance of ⁴¹K is 6.7%, whereas the observed ⁴¹K

abundance from sample 1 is 57%. This atypical abundance was also confirmed using electrospray ionization time of flight mass spectroscopy¹ (ESITOFMS). The high-resolution mass assignment of the m/z = 41 peak of the electrolytic sample was consistent with ⁴¹K, and no peak was observed at m/z = 42.98, ruling out ⁴¹KH₂. Moreover, the natural abundance of ⁴¹K was observed in the positive TOF-SIMS spectra of KHCO₃, KNO₃, and KI standards that were obtained with an ion current such that the ³⁹K peak intensity was an order of magnitude higher than that given for sample 1. The saturation of the ³⁹K peak of the positive TOF-SIMS spectrum by the electrolytic cell sample 1 is indicative of a unique crystalline matrix.⁶

The respective hydride compounds and mass assignments of the negative ion TOF-SIMS of electrolytic cell sample 1 appear in Table III. The spectrum was dominated by H⁻ with much smaller O⁻, and OH⁻ peaks. A series of nonhydride-containing negative ions



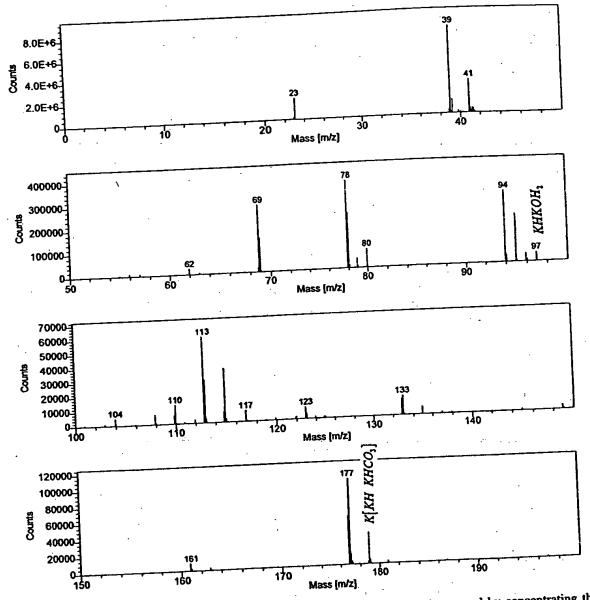


Fig. 3. The positive TOF-SIMS spectrum (m/e = 0 to 200) of the polymeric material prepared by concentrating the K_2CO_3 electrolyte from the Thermacore electrolytic cell with a rotary evaporator and centrifuging the polymeric material (sample 1) (HC = hydrocarbon).

 $\{KCO_3[K_2CO_3]_n^- m/z = (99 + 138n)\}$ was also present, which implies that the hydride is lost with the proton during fragmentation of the compound KH KHCO₃. A photograph of the inorganic polymeric material suspended in distilled water is shown in Fig. 5.

Magnesium hydrino hydride ions MgH_3^- (m/e = 27.008515) and $Mg_2H_4^-$ (m/e = 52.00138) were observed in the negative TOF-SIMS spectrum of sample 1. In sample 1, MgH_3^- (m/e = 27.008515) was observed in the TOF-SIMS spectrum with a hydrocarbon peak at m/e = 27.03, and CN⁻ was observed at m/e = 26.00, as shown in Fig. 6. Sample 1 was sput-

tered to remove hydrocarbons. The postsputtering negative TOF-SIMS spectrum m/e = 20 to 30 of sample 1 is shown in Fig. 7. The hydrino hydride compounds NaH₃ (m/e = 26.013275) and MgH₃ (m/e = 27.008515) were observed at m/e = 26.01 and m/e = 27.01, respectively.

The negative TOF-SIMS spectrum (m/e = 10 to 20) of 99.99% KHCO₃ is shown in Fig. 8. The negative TOF-SIMS spectrum (m/e = 10 to 20) of sample 1 is shown in Fig. 9. The negative TOF-SIMS spectrum (m/e = 10 to 20) of sample 4 is shown in Fig. 10. A peak with a high nominal mass that does not match any known compound

Mills

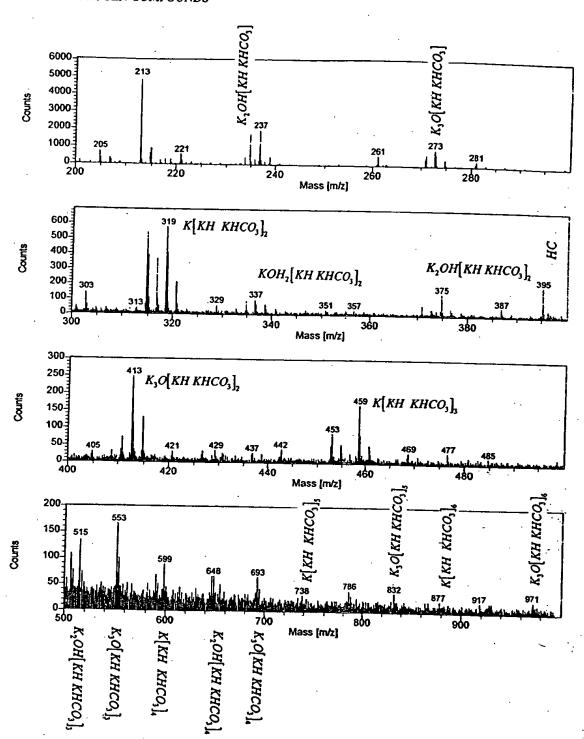


Fig. 4. The positive TOF-SIMS spectrum (m/e = 200 to 1000) of polymeric material prepared by concentrating the K_2CO_3 electrolyte from the Thermacore electrolytic cell with a rotary evaporator and centrifuging the polymeric material (sample 1) (HC = hydrocarbon).

or fragment was observed at m/e = 16.125 in the case of sample 1 and at m/e = 16.130 in the case of sample 4. Each mass excess peak has the same width as the oxygen peak; thus, each is not a metastable peak. Each peak is

not due to detector ringing because no such peak with a high nominal mass is seen at the position of any of the other identifiable peaks such as hydroxyl (OH) at m/e = 17.003, which has a greater intensity, and the peaks were



TABLE II The Respective Hydride Compounds and Mass Assignments (m/z) of the Positive TOF-SIMS of Sample 1

Hydrino Hydride Compound or Fragment	Nominal Mass m/e	Observed m/e	Calculated m/e	Difference Between Observed and Calculated m/e		
Hydrino Hydride Compound of Fragment		23.180	23.179975	0.000		
H ₂₃	23 24		23.997625	0.008		
17_17		23.99		0.003		
Nam OH ₂₃	39 [39.178	39.174885	0.0015		
	40	39.97	39.971535	0.0013		
KH NaHKH	64	63.96	63.96916	0.009		
vankn	· 79	78.940	78.935245	0.004		
K ₂ H	80	79.942	79.94307	0.001		
(KH) ₂		82.96	82,966545	0.007		
K ₂ H ₅	83	96.945	96,945805	0.0008		
KHKOH₂	97		102.93287	0.003		
KKHNaH	· 103	102.93	102.33207			
	121	120.925	120.92243	0.003		
KH ₂ (KH) ₂	124	123.925	123.93289	0.008		
KH KHCO ₂	145	144.92	144.930535	0.010		
KH ₂ KHO₄	151	150.90	150.8966	0.003		
K(KOH) ₂	151	151.90	151.904425	0.004		
KH(KOH) ₂	134			1		
	153	152.90	152.91225	0.012		
KH ₂ (KOH) ₂	179	178.89	178.8915	0.001		
K[KH KHCO3]	187	186.87	186.873225	0.003		
KCO(KH) ₃	191	190.87	190.868135	0.002		
K ₂ OHKHKOH	193	192.89	192.883785	0.006		
кн₂конкнкон	1	204.00	204.92828	0.008		
K ₃ O(H ₂ O) ₄	205	204.92		0.002		
K3O(1120)4 K2OH[KH KHCO3]	235	234.86	234.857955	0.002		
K ₂ OA[KA KHCO3] K[H ₂ CO ₄ KH KHCO ₃]	. 257	256.89	256.8868	- I		
	273	272.81	272.81384	0.004		
K ₃ O[KH KHCO ₃]	303	302.88	302.89227	0.012		
[KH ₂ CO ₃] ₃	210	316.80	316.80366	0.004		
K[KH KHCO ₃ K ₂ CO ₃]	317	318.82	318.81931	0.001		
K[KH KHCO₃]	319		328.7933	0.007		
KH ₂ [KH KOH] ₃	329	328.80	336.82987	0.020		
KOH ₂ [KH KHCO ₃] ₂	337	336.81		0.001		
KH KO ₂ [KH KHCO ₃][KHCO ₃]	351	350.81	350.80913			
	357	356.77	356.775195	0.005		
KKHK ₂ CO ₃ [KH KHCO ₃]	359	358.78 ::	358,790845	0.011		
KKH[KH KHCO ₃] ₂		374.78	374.785755	0.005		
K ₂ OH[KH KHCO ₃] ₂	375	386.75	386.76238	0.012		
K ₂ OH[KHKOH] ₂ [KHCO ₃]	387	404.79	404.80933	0.019		
KKH ₃ KH ₅ [KH KHCO ₅] ₂	405	404.79	1	s <mark>f</mark> ile i de la companya di angle de la companya di		
	411	410.75	410.72599	0.024		
K ₃ O[K ₂ CO ₃][KH KHCO ₃] or K[KH KOH(K ₂ CO ₃) ₂]	413	412.74	412.74164	0.002		
K ₃ O[KH KHCO ₃] ₂	415	414.74	414.75729	0.017		
K[KH KOH(KH KHCO ₃) ₂]	437	436.81	436.786135	0.024		
KH ₂ OKHCO ₃ [KH KHCO ₃] ₂		I .		0.004		
KKHKCO ₂ [KH KHCO ₃] ₂	442	441.74	441.744375	0.027		
KKHKCO ₂ [KH KHCO ₃] ₃	459	458.72	458.74711			
$K[KH KHCO_3]_3$ $H[KH KOH]_2[K_2CO_3]_2$ or $K_4O_2H[KH KHCO_3]_2$	469	468.70	468.708085	0.008		
MINU VOUISIES OF MACAMINA PROPERTY	477	476.72	476.744655	0.025		
K[K ₂ CO ₃][KHCO ₃] ₃	-,-	514.72	514,713555	0.006		
K,OH[KH KHCO ₃] ₃	515		552.66944	0.001		
K ₃ O[KH KHCO ₃] ₃	553	552.67	598.67491	0.025		
K[KH KHCO ₃] ₄	599	598.65		0.009		
K ₂ OH[KH KHCO ₃] ₄	655	654.65	654.641355	0.003		
K ₂ On(KH KHCO ₃) ₄	693	692.60	692.59724			
	739	738.65	738.60271	0.047		
K[KH KHCO ₃] ₅		832.50	832.52504	0.025		
K ₃ O[KH KHCO ₃] ₅	833	878.50	878.53051	0.031		
K[KH KHCO ₃] ₆	879		972.45284	0.047		
K ₃ O[KH KHCO ₃] ₆	973	972.50	714.43404	1 0.0.1		

TABLE III

The Respective Hydride Compounds and Mass Assignments (m/z) of the Negative TOF-SIMS of Sample 1

Hydrino Hydride Compound or Fragment	Nominal Mass m/e	Observed m/e	Calculated m/e	Difference Between Observed and Calculated m/e		
H ₁₆	16	16.130	16.1252	0.005		
H ₂₄	24	24.181	24.1878	0.007		
H ₂₅	25	25.195	25.195625	0.001		
NaH ₃	26	26.01	26.013275	0.003		
MgH ₃	27	27.01	27.008515	0.001		
CH ₂₃	35	35.183	35.179975	0.003		
NH ₂₃	37	37.185	37.183045	0.002		
KH ₃	42	42.00	41.987185	0.013		
(NaH) ₂	48	48.00	47,99525	0.005		
Na ₂ H ₃	49	49.00	49.003075	0.003		
Mg ₂ H ₄	52	52.00	52.00138	0.001		
КН ОН	57	56.98	56,97427	0.006		
NaH ₃ NaO	65	65.00	64.997985	0.002		
NaH ₂ KH ₅	. 69	69.00	69.008285	0.002		
(KH) ₂	80	79.95	79.94307	0.007		
KH KO	95	94.93	94.930155	0.007		
KH ₂ KOH	97	96.945	96.945805	0.0008		
GaKH	109	108.895	108.897235	0.003		
KH KNO	109	108.923	108.933225	0.010		
KH ₃ KCl ·	116	115.92	115.919745	0.000		
KOHNO ₃	118.	117.95	117.954245	0.004		
H ₂ I	129	128.92	128.92005	0.000		

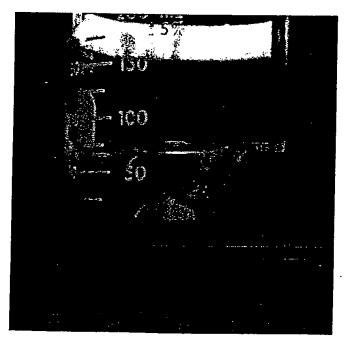


Fig. 5. Photograph of polymeric material comprising sample 1 suspended in distilled water.

repeatable using two different detectors. Also, they cannot be explained as an instrument artifact since each is present at the earliest times of acquisition. In both samples, the unidentifiable peak is assigned to polyhydrogen negative ion H_{16}^- , which is consistent with $H^-(\frac{1}{16})$ as the most stable hydrino hydride ion according to Eq. (3). The principal quantum number p=16 provides 16 multipoles (l=0 to l=n-1) comprising the molecular orbitals of $H^-(\frac{1}{16})$. The agreement between the observed mass and the calculated mass (m/e=16.125) is excellent. No other compound of this mass is possible.

Other positive and negative TOF-SIMS peaks observed for samples 1 and 4 confirm polyhydrogen compounds and ions. The positive TOF-SIMS spectrum (m/e = 0 to 50) of sample 4 is shown in Fig. 11. The positive TOF-SIMS spectrum (m/e = 20 to 30) of sample 1 is shown in Fig. 12. The presputtering negative TOF-SIMS spectrum (m/e = 20 to 30) of sample 1 is shown in Fig. 6. The postsputtering negative TOF-SIMS spectrum (m/e = 30 to 40) of sample 1 is shown in Fig. 13. The peak assigned to $OH_{23}^+(m/e = 39.174885)$ is shown in the positive TOF-SIMS spectrum of sample 4 (Fig. 11). The experimental mass is 39.175, which is in excellent agreement with the

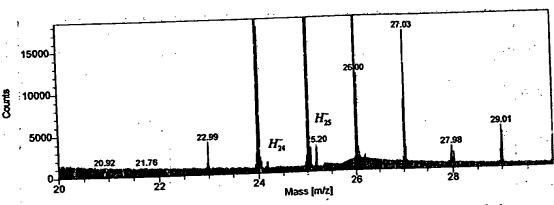


Fig. 6. The presputtering negative TOF-SIMS spectrum (m/e = 20 to 30) of sample 1.

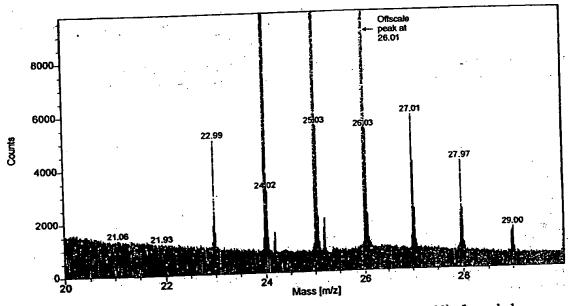


Fig. 7. The postsputtering negative TOF-SIMS spectrum (m/e = 20 to 30) of sample 1.

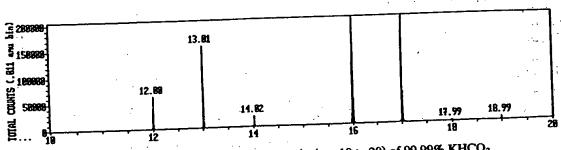


Fig. 8. The negative TOF-SIMS spectrum (m/e = 10 to 20) of 99.99% KHCO₃.

calculated mass. The peak assigned to H_{23}^+ (m/e = 23.179975) is shown in the positive TOF-SIMS spectrum of sample 1 (Fig. 12). The experimental mass is 23.180. This peak is assigned to a fragment of a parent

polyhydrogen molecule containing 24 hydrogen atoms. The corresponding negative ion, H_{24}^- , is shown in Fig. 6 with the M+1 peak, H_{25}^- . These peaks are also observed in Fig. 7. Figures 11 and 14 show OH_{23}^+ , which

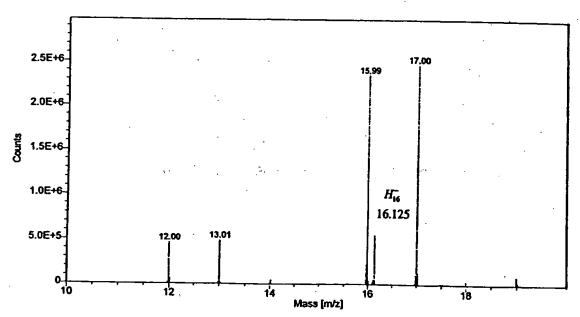


Fig. 9. The negative TOF-SIMS spectrum (m/e = 10 to 20) of polymeric material prepared by concentrating the K_2CO_3 electrolyte from the Thermacore electrolytic cell with a rotary evaporator and centrifuging the polymeric material (sample 1).

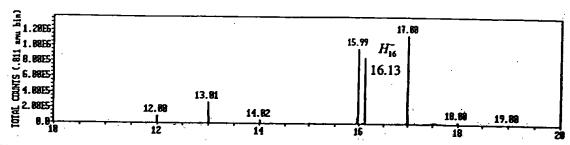


Fig. 10. The negative TOF-SIMS spectrum (m/e = 10 to 20) of crystals isolated from the cathode of the K_2CO_3 INEL electrolytic cell (sample 4).

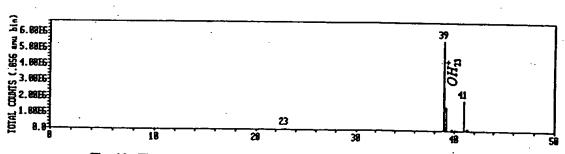


Fig. 11. The positive TOF-SIMS spectrum (m/e = 0 to 50) of sample 4.

may be a fragment of OH_{24} , and OH^- may also be a fragment. The OH^- (m/e = 17.002735) peak intensity of the negative spectrum of sample 4 shown in Fig. 10 is at least twice that of the control. The increased intensity is as-

signed to the fragmentation of OH_{24} to OH^- . In addition to substitution reactions with oxygen, the 24-atom polyhydrogen molecule may react with carbon and nitrogen. The negative ions CH_{23}^- and NH_{23}^- are shown in Fig. 13.



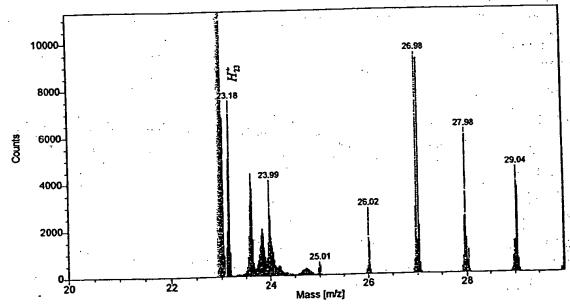


Fig. 12. The positive TOF-SIMS spectrum (m/e = 20 to 30) of sample 1.

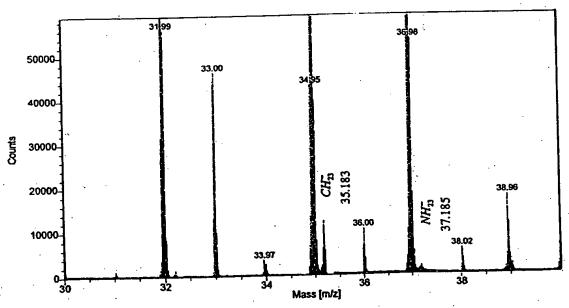


Fig. 13. The postsputtering negative TOF-SIMS spectrum (m/e = 30 to 40) of sample 1.

Polymer compounds and ions comprising 24 hydrogen atoms may form because H_{24}^- is the last stable hydride ion of the series 1/p = 1 to 1/24 given by Eq. (3). The most stable hydride ion that may give rise to compounds and ions containing 16 hydrogen atoms is H_{16}^- . Positive polyhydrogen ion peaks observed from the TOF-SIMS spectrum of sample 1 are given in Table II. Negative polyhydrogen ion peaks observed from the TOF-SIMS spectrum of sample 1 are given in Table III.

III.B. X-Ray Photoelectron Spectroscopy

A survey spectrum was obtained over the region $E_b = 0$ to 1200 eV. The primary element peaks allowed for the determination of all of the elements present in each sample isolated from the K_2CO_3 electrolyte. The survey spectrum also detected shifts in the binding energies of the elements, which had implications as to the identity of the compound containing the elements. A high-resolution XPS

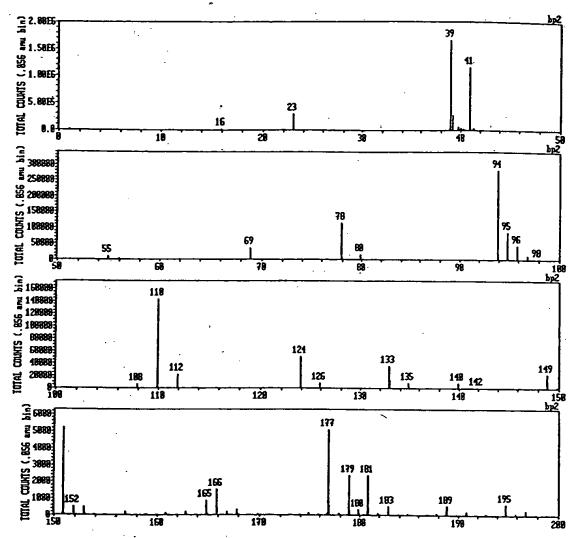


Fig. 14. The positive TOF-SIMS spectrum (m/e = 0 to 200) of crystals isolated from the cathode of the K_2CO_3 INEL electrolytic cell (sample 5).

spectrum was also obtained of the low binding energy region ($E_b = 0$ to 100 eV) to determine the presence of novel XPS peaks.

Samples 2 and 3 were purified from the K_2CO_3 electrolyte of the Thermacore and BLP electrolytic cells, respectively. No elements are present in the survey scans that can be assigned to peaks in the low binding energy region with the exception of a small variable contaminant of sodium at 64 and 31 eV, potassium at 16.2 and 32.1 eV, and oxygen at 23 eV. Accordingly, any other peaks in this region must be due to novel compositions. The theoretical positions of hydrino hydride ion peaks $H^-(n = 1/p)$ for p = 2 to p = 16 are identified for each of samples 2 and 3 in Figs. 15 and 16, respectively. The O 2s, which is weak compared to the potassium peaks of K_2CO_3 , is typically present at 23 eV but is broad or obscured in Figs. 15 and 16. In addition, the sodium peaks

Na of sample 3 are identified in Fig. 16. The K 3s and K 3p, K, are shown in Figs. 15 and 16 at 16.2 and 32.1 eV, respectively. Peaks centered at 22.8 and 38.8 eV, which do not correspond to any other primary element peaks, were observed. The intensity and shift match shifted K 3s and K 3p. Hydrogen is the only element that does not have primary element peaks; thus, it is the only candidate to produce the shifted peaks. These peaks may be shifted by a novel hydride ion with a high binding energy of 22.8 eV that bonds to potassium K 3p and shifts the peak to this energy. In this case, the K 3s is similarly shifted. The XPS peaks centered at 22.8 and 38.8 eV are assigned to shifted K 3s and K 3p. The anion does not correspond to any other primary element peaks; thus, it may correspond to the H⁻ $(n = \frac{1}{6})E_b = 22.8$ eV hydride ion predicted by Mills, where E_b is the predicted binding energy. These peaks were not present in the case of





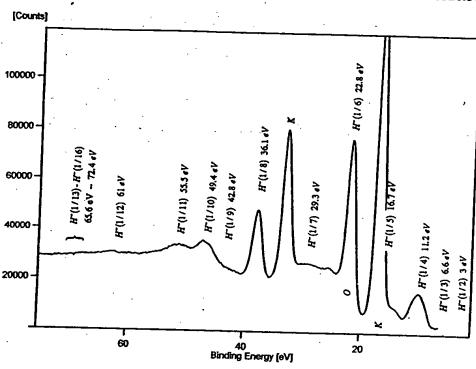


Fig. 15. The 0- to 80-eV binding energy region of a high-resolution XPS of polymeric material prepared by concentrating the K₂CO₃ electrolyte from the Thermacore electrolytic cell until a precipitate just formed (sample 2) with the primary elements identified.

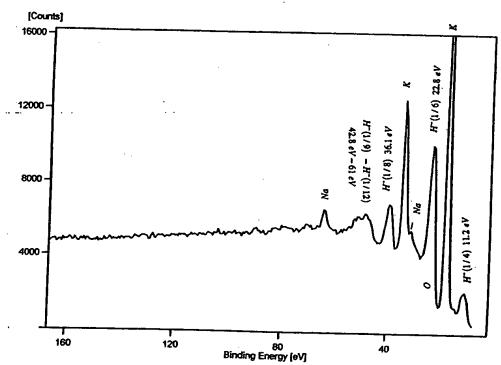


Fig. 16. The 0- to 165-eV binding energy region of the survey XPS of crystals prepared by concentrating the K₂CO₃ electrolyte from the BLP electrolytic cell with a rotary evaporator and allowing crystals to form on standing at room temperature (sample 3) with the primary elements identified.

the XPS of matching samples isolated from an identical electrolytic cell except that Na₂CO₃ replaced K₂CO₃ as the electrolyte.

XPS further confirmed the TOF-SIMS data by showing shifts of the primary elements. The splitting of the principal peaks of the survey XPS spectrum of samples 2 and 3 indicative of multiple forms of bonding involving the atom of each split peak appear in Table IV. The selected survey spectra with the corresponding figures of the high-resolution spectra of the low binding energy region are given as (#/#). The latter contain hydrino hydride ion peaks. And, several of the shifts of the peaks of elements given in Table IV and shown in the survey spectra are greater than those of known compounds. For example, the XPS survey spectrum of sample 3, which appears in Fig. 17, shows extraordinary potassium and oxygen peak shifts. All of the potassium primary peaks are shifted to about the same extent as that of the K 3s and K 3p. In addition, extraordinary O 1s peaks of the electrolytic cell sample were observed at 537.5 and 547.8 eV, whereas a single O 1s was observed in the XPS spectrum of K₂CO₃ at 532.0 eV. The results are not due to uniform charging as the internal standard C 1s remains the same at 284.6 eV. Also, the results are not due to differential charging because the peak shapes of carbon and oxygen are normal, and no tailing of these peaks was observed. The range of binding energies from the literature⁷ for the peaks of interest is given in the final row of Table IV. The peaks shifted to an extent that they are without identifying assignment correspond to and identify compounds containing hydrino hydride ions. For example, the positive and negative TOF-SIMS spectra of sample 3 were similar to that of sample 1 (Tables II and III). The spectrum contained inorganic hydride clusters

$$(K[KH KHCO_3]_n^+ m/e = (39 + 140n),$$
 $K_2OH[KH KHCO_3]_n^+ m/e = (95 + 140n),$

and

$$K_3O[KH\ KHCO_3]_n^+\ m/e = (133 + 140n))$$

observed in the positive TOF-SIMS spectrum of sample 1. In addition, the positive TOF-SIMS spectra of sample 3 showed large peaks, which were identified as KHKOH and KHKOH₂, as shown in Fig. 18. The extraordinary shifts of the K 3p, K 3s, K $2p_3$, K $2p_1$, and K 2s XPS peaks and the O 1s XPS peak shown in Fig. 17 are assigned to novel hydride compounds. TOF-SIMS and XPS taken together provide substantial support of hydrino hydride compounds as assigned herein.

The 0- to 60-eV binding energy region of a high-resolution XPS spectrum of crystals isolated from the INEL electrolytic cell (sample 4) with the primary element peaks identified appears in Fig. 19. No elements were present in the survey scan that can be assigned to

TABLE IV

The Binding Energies of XPS Peaks of K₂CO₃ and Electrolytic Cell Samples

VDC #	FIG#	C 1s (eV)	. N 1s (eV)	O 1s (eV)	Na 1s (eV)	K 3p (eV)	K 3s (eV)	K 2p ₃ (eV)	K 2p ₁ (eV)	K 2s (eV)
XPS # K ₂ CO ₃	F10 #	284.6		532.0		18	34	292.4	295.2	376.7
2	15	288.4 284.6 288.8	~390 Very broad	530.7 537.3 547.5	1070.0	16.2 22.8	32.1 38.8	291.5 298.5	293.7 300.4	376.6 382.6
3	17 16	284.6 288.5	393.6	530.9 537.5 547.8	1070.0	16.2 22.8	32.1 38.8	291.5 298.5	293.7 300.4	376.6 382.6
4	19	284.6 288.2	403.2 407.4	530.3 532.2 540.6 545.2	1070.8	16.8	32.7	295.3	292.6	377.5
5	20 21	284.6 285.7 287.4 288.7	403.2 407.0	532.1 535.7 563.8	1070.9 1077.5			·		
Minimum Maximum		280.5 293	398 407.5	529 535	1070.4 1072.8			292 293.2		



800

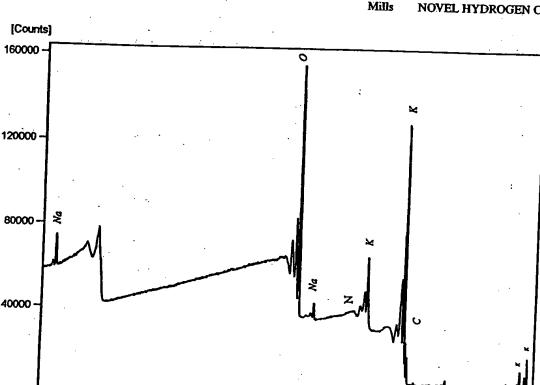
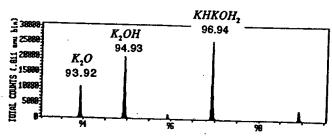


Fig. 17. The survey XPS of crystals prepared by concentrating the K₂CO₃ electrolyte from the BLP electrolytic cell with a rotary evaporator and allowing crystals to form on standing at room temperature (sample 3) with the primary elements

600

Binding Energy [eV]

400



1000

Fig. 18. The TOF-SIMS spectra (m/e = 94 to 99) of sample 3.

peaks in the low binding energy region with the exception of sodium at 64 and 31 eV, potassium at 16.8 and 32.7 eV, and oxygen at 23 eV. Accordingly, any other peaks in this region must be due to novel compositions. The theoretical positions of hydrino hydride ion peaks $H^-(\frac{1}{2})$ to H⁻ $(\frac{1}{11})$, as well as the weak oxygen peak, O 23 eV, sodium peaks, Na 31 eV and Na 64 eV, and the potassium peaks, K 3p and K 3s, are identified for sample 4 in Fig. 19. The hydrino hydride peak $H^{-}(\frac{1}{5})$ 16.7 eV is

under the K 3p peak. The hydrino hydride peak $H^{-}(\frac{1}{7})$ 29.3 eV is under the Na 31 eV peak. These hydrino hydride ion features were not present in the case of the XPS of matching samples except that Na₂CO₃ replaced K₂CO₃ as the electrolyte. The XPS data confirm the TOF-SIMS data of increased binding energy hydrogen compounds.

200

The survey scan of sample 5 is shown in Fig. 20 with the primary elements identified. No elements are present in the survey scan that can be assigned to peaks in the low binding energy region, with the exception of sodium at 64 and 31 eV and oxygen at 23 eV. Accordingly, any other peaks in this region must be due to novel compositions. The theoretical positions of hydrino hydride ion peaks $H^-(n = 1/p)$ for p = 2 to p = 16 and the oxygen peak O and sodium peaks Na are identified for sample 5 in Fig. 21. These peaks were not present in the case of the XPS of matching samples except that Na₂CO₃ replaced K₂CO₃ as the electrolyte.

The data provide the identification of hydrino hydride ions whose XPS peaks cannot be assigned to impurities. Several of the peaks are split, such as the $H^{-}(n = \frac{1}{4})$, $H^{-}(n = \frac{1}{5})$, $H^{-}(n = \frac{1}{8})$, $H^{-}(n = \frac{1}{10})$, and $H^{-}(n = \frac{1}{11})$ peaks shown in Fig. 21. The splitting

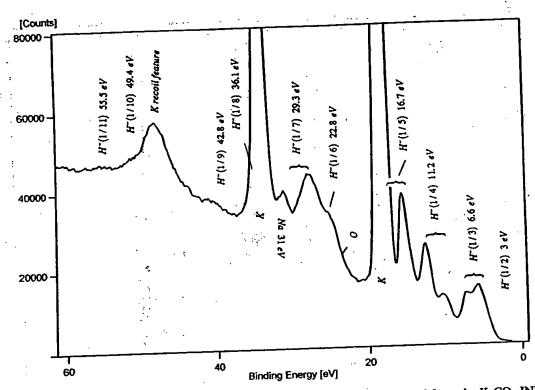


Fig. 19. The 0- to 60-eV binding energy region of a high-resolution XPS of crystals isolated from the K₂CO₃ INEL electrolytic cell (sample 4) with the primary element peaks identified.

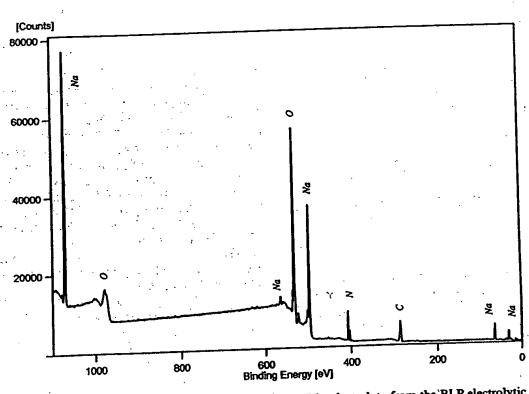


Fig. 20. The survey spectrum of crystals prepared by filtering the K₂CO₃ electrolyte from the BLP electrolytic cell (sample 5) with the primary elements identified.





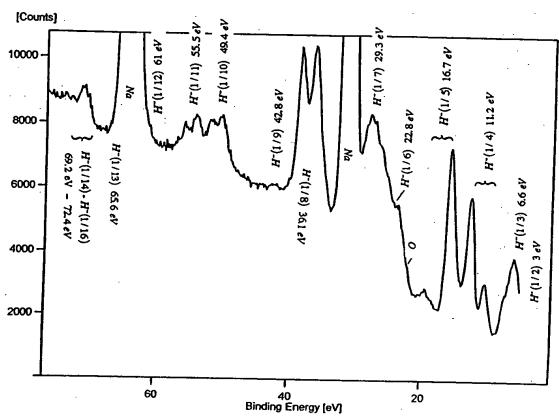


Fig. 21. The 0- to 75-eV binding energy region of a high-resolution XPS of crystals prepared by filtering the K₂CO₃ electrolyte from the BLP electrolytic cell (sample 5).

indicates that several compounds comprising the same hydrino hydride ion are present and that they may have different chemical environments.

The intensities of the corresponding peaks of the positive and negative TOF-SIMS were consistent with the majority compound and fragments comprising fragments of NaNO₂ > NaNO₃ and sodium hydrides. For example, NaH (m/e = 23.997625) and NaH₃ (m/e = 26.013275) were observed in the positive and negative TOF-SIMS, respectively, at (m/e = 23.99) and (m/e = 26.01). The observation by TOF-SIMS that the majority compound and fragments contain NaNO₂ > NaNO₃ is further confirmed by the presence of nitrite and nitrate nitrogen in the XPS spectrum (XPS sample 5 summarized in Table IV). The XPS Na 1s peak and the intensities of the N 1s peaks as nitrite (403.2 eV) greater than nitrate (407.4 eV) confirm the majority species as NaNO₂ > NaNO₃.

Sample 5 was filtered from an initially $0.57 \, M \, \text{K}_2 \text{CO}_3$ electrolyte. The solubility of NaOH is $42^{\text{orc}} \cdot \text{g}/100 \, \text{cm}^3$ (10.5 M). The solubility of NaNO₂ is $81.5^{15^{\circ}\text{C}} \cdot \text{g}/100 \, \text{cm}^3$ (11.8 M), and the solubility of NaNO₃ is $92.1^{25^{\circ}\text{C}} \cdot \text{g}/100 \, \text{cm}^3$ (10.8 M), whereas the solubility of $\text{K}_2 \text{CO}_3$ is $112^{25^{\circ}\text{C}} \cdot \text{g}/100 \, \text{cm}^3$ (8.1 M) and the solubility of KHCO₃

is 22.4 coldwater g/100 cm³ (2.2 M) (Ref. 8). Thus, NaNO₂ and NaNO₃ as the filtered precipitate is unexpected. The solubility, TOF-SIMS, and XPS results support the assignment of sodium nitrite and nitrate hydrino hydride compounds that are less soluble than KHCO₃. General structures for these compounds are given by substitution of sodium for potassium in the structures given in Eq. (10).

III.C. X-Ray Diffraction

The X-ray diffraction (XRD) pattern of sample 2 is shown in Fig. 22. The XRD data indicated that the diffraction pattern of sample 2 does not match that of either KH, KHCO₃, K_2CO_3 , or KOH. The identifiable peaks corresponded to a mixture of $K_4H_2(CO_3)_3 \cdot 1.5 H_2O$ and $K_2CO_3 \cdot 1.5 H_2O$. In addition, the spectrum contained a number of peaks that could not be assigned. The 2-theta and d-spacings of the unidentified XRD peaks of sample 2 are given in Table V.

In addition, the elemental analysis of the crystals was obtained at Galbraith Laboratories. The atomic hydrogen percentage was in excess even if the compound were considered 100% $K_4H_2(CO_3)_3 \cdot 1.5 H_2O$, which would have the most hydrogen.

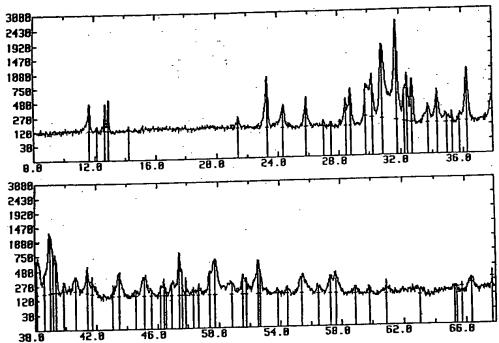


Fig. 22. The XRD pattern of polymeric material prepared by concentrating the K₂CO₃ electrolyte from the Thermacore electrolytic cell until a precipitate just formed (sample 2).

TABLE V

The 2-Theta and d-Spacings of the Unidentified XRD Peaks of the Crystals from K₂CO₃ Electrolytic Cell (Sample 2)

Peak Number	2-Theta (deg)	, (Å)
2	12.15	7.2876
4	12.91	6.8574
8	24.31	3.6614
12	28.46	3.1362
15	30.20	2.9594
31	39.34	2.2906
	40.63	2.2206
33 36	43.10	2.0991
• -	45.57	1.9905
40 42	46.40	1.9570
-	47.59	1.9141
46 47	47.86	1.9006
47 50	50.85	1.7958
52	51.75	1.7665
54 56	52.65	1.7386
	53.81	1.7037
57	54.46	1.6850
58		1.6292
60	56.49	1.5685
63	58.88	1.5207
65	60.93	1.4747
66	63.04	1.4/4/

III.D. Fourier Transform Infrared Spectroscopy

The FTIR spectra of K₂CO₃ (99%) and KHCO₃ (99.99%) were compared with that of sample 2. A spectrum of a mixture of the bicarbonate and the carbonate was produced by digitally adding the two reference spectra. The two standards alone and the mixed standards were compared with that of sample 2. From the comparison, it was determined that sample 2 contained potassium carbonate but did not contain potassium bicarbonate. The unknown component could be a bicarbonate other than potassium bicarbonate. The spectrum of potassium carbonate was digitally subtracted from the spectrum of sample 2. The subtracted spectrum appears in Fig. 23. Several bands were observed including bands in the 1400- to 1600-cm⁻¹ region. Some organic nitrogen compounds (e.g., acrylamides and pyrolidinones) have strong bands in the region 1660 cm⁻¹ (Ref. 9). However, the lack of any detectable C-H bands (≈2800 to 3000 cm⁻¹) and the bands present in the 700- to 1100-cm⁻¹ region indicate an inorganic material.10 Peaks that are not assignable to potassium carbonate were observed at 3294, 3077, 2883, 1100, 2450, 1660, 1500, 1456, 1423, 1300, 1154, 1023, 846, 761, and 669 cm⁻¹.

The overlap FTIR spectrum of sample 2 and the FTIR spectrum of the reference potassium carbonate appear in Fig. 24. In the 700- to 2500-cm⁻¹ region, the peaks of electrolytic cell sample 2 closely resemble those of





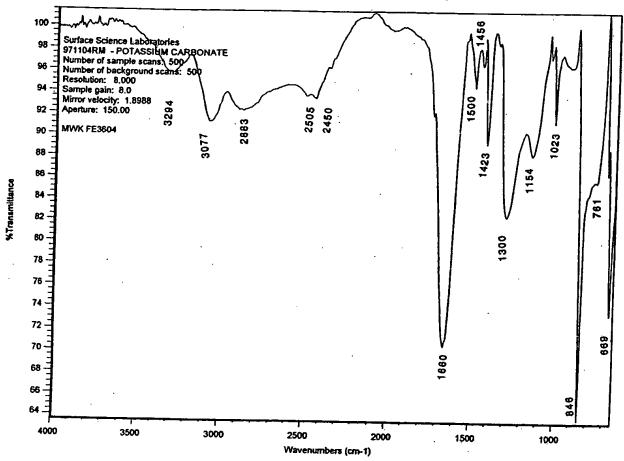


Fig. 23. The FTIR spectrum of polymeric material prepared by concentrating the K₂CO₃ electrolyte from the Thermacore electrolytic cell until a precipitate just formed (sample 2) from which the FTIR spectrum of the reference potassium carbonate was digitally subtracted.

potassium carbonate, but they are shifted ~50 cm⁻¹ to lower frequencies. The shifts are similar to those observed by replacing potassium (K2CO3) with rubidium (Rb₂CO₃), as demonstrated by comparing their infrared spectra. 11 The shifted peaks may be explained by a polymeric structure for the compound KH KHCO3 identified by TOF-SIMS, XPS, and NMR.

III.E. Raman

The Raman spectrum of sample 3 appears in Fig. 25. In addition to the known peaks of KHCO3 and a small peak assignable to K₂CO₃, unidentified peaks at 1685 and 835 cm⁻¹ are present. The unidentified Raman peak at 1685 cm⁻¹ is in the region of the N-H bonds. The FTIR spectrum of sample 2 also contains unidentified bands in the 1400- to 1600-cm⁻¹ region. Samples 3 and 2 do not contain N-H bonds by XPS studies. The N 1s XPS peak of the former is at 393.6 eV, and the N 1s XPS peak of the latter is a very broad peak at \sim 390 eV, whereas the N 1s XPS peak of compounds containing a N-H bond is

seen at \sim 399 eV, and the lowest energy N 1s XPS peak for any known compound is ~398 eV.

The 835-cm⁻¹ peak of Raman sample 2 is in the region of the bridged and terminal metal-hydrogen bonds. The novel peaks without the identifying assignment correspond to and identify hydrino hydride compounds.

III.F. Nuclear Magnetic Resonance

The signal intensities of the ¹H MAS NMR spectrum of the K₂CO₃ reference were relatively low. It contained a water peak at 1.208 ppm, a peak at 5.604 ppm, and very broad weak peaks at 13.2 and 16.3 ppm. The ¹H MAS NMR spectrum of the KHCO3 reference contained a large peak at 4.745 with a small shoulder at 5.150 ppm, a broad peak at 13.203 ppm, and small peak at 1.2 ppm.

The 'H MAS NMR spectrum of electrolytic cell sample 2 is shown in Fig. 26. The peak assignments are given in Table VI. The reproducible peaks assigned to KH KHCO3 in Table VI were not present in the controls except for the peak assigned to water at

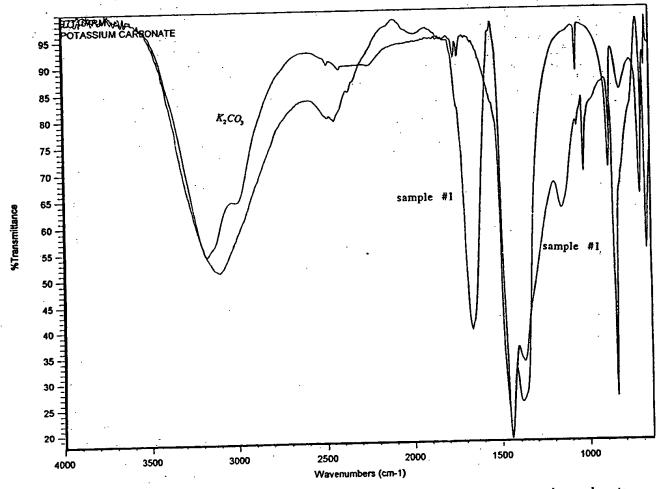


Fig. 24. The overlap FTIR spectrum of sample 2 and the FTIR spectrum of the reference potassium carbonate.

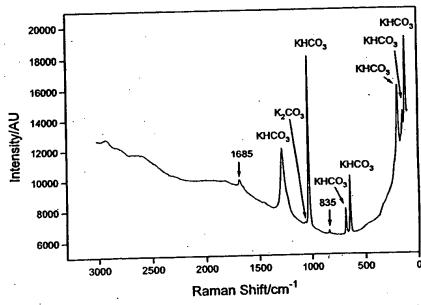


Fig. 25. The Raman spectrum of polymeric material prepared by concentrating the K₂CO₃ electrolyte from the Thermacore electrolytic cell until a precipitate just formed (sample 2).





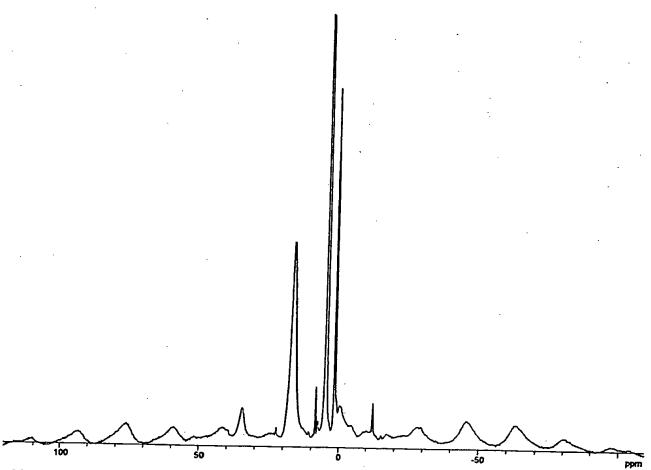


Fig. 26. The magic angle solid NMR spectrum of polymeric material prepared by concentrating the K₂CO₃ electrolyte from the Thermacore electrolytic cell until a precipitate just formed (sample 2).

+5.066 ppm. The novel peaks could not be assigned to hydrocarbons. Hydrocarbons were not present in the electrolytic cell sample 2 based on the TOF-SIMS spectrum and FTIR spectra. The novel peaks without identifying assignment are consistent with KH KHCO₃. The NMR peaks of the hydride ion of control potassium hydride were observed at 1.192 and 0.782 ppm relative to Tetra Methyl Silane (TMS). The upfield peaks of Fig. 26 are assigned to novel hydride ion (KH-) present in different environments. The downfield peaks are assigned to the proton of the potassium hydrogen carbonate species in different chemical environments (-KHCO₃).

IV. DISCUSSION

Alkali and alkaline earth hydrides react violently with water to release hydrogen gas, which subsequently ignites because of the exothermic reaction with water. Typically, metal hydrides decompose upon heating at a temperature well below the melting point of the parent

metal. These saline hydrides, so called because of their saltlike or ionic character, are the monohydrides of the alkali metals and the dihydrides of the alkaline-earth metals, with the exception of beryllium. BeH $_2$ appears to be a hydride with bridge-type bonding rather than an ionic hydride. Highly polymerized molecules held together by hydrogen-bridge bonding are exhibited by boron hydrides and aluminum hydride. Based on the known structures of these hydrides, the TOF-SIMS hydride clusters such as K[KH KHCO₃], the XPS peaks observed at 22.8 and 38.8 eV, the upfield NMR peaks assigned to hydride ion, and the shifted FTIR peaks, the present novel hydride compound may be a polymer, [KH KHCO₃]_n, with a structural formula that is similar to boron and aluminum hydrides. The reported novel compound appeared polymeric in the concentrated electrolytic solution and in distilled water. Whereas potassium hydride reacts violently with water, [KH KHCO₃]_n is extraordinarily stable in water.

As an example of the structures of this compound, the K[KH KHCO₃]⁺_n m/z = (39 + 140n) series of fragment peaks is tentatively assigned to novel hydride







TABLE VI The NMR Peaks of Sample 2 with Their Assignments

Peak at Shift (ppm)	Assignment
+34.54 +22.27 +17.163 +10.91 +8.456 +7.50 +5.066 +1.830 -0.59 -12.05 -15.45	Side band of +17.163 peak Side band of +5.066 peak KH KHCO ₃ Side band of +17.163 peak KH KHCO ₃ KH KHCO ₃

^aSmall shoulder is observed on the -12.05 peak, which is the side band of the +5.066 peak.

bridged or linear potassium bicarbonate compounds having a general formula such as $[KHKHCO_3]_n$ n =1,2,3.... General structural formulas may be

$$\begin{bmatrix} K^+ - H^- - K^+ - HCO_3^- \end{bmatrix}_n \xrightarrow{NO_3^-}$$

$$\begin{bmatrix}
K^{+} - H^{-} - K^{+} - NO_{3}^{-} \\
 & \\
K^{+} - H^{-}
\end{bmatrix}_{n}^{OT} + nHCO_{3}^{-}$$
(10)

During acidification of the K₂CO₃ electrolyte, the pH repetitively increased from 3 to 9, at which time additional acid was added with a carbon dioxide release. The increase in pH (release of base by the titration reactant) was dependent on the temperature and concentration of the solution. A reaction consistent with this observation is the displacement reaction of NO₃ for HCO₃²⁻, as given by Eq. (10).

and

$$\left[\begin{array}{c} K^{+} - K^{-} - K^{-} - K^{-} \end{array} \right]_{n}^{n}$$

Liquid chromatography/ESITOFMS studies are in progress to support the polymer assignment.

The observation of inorganic hydride fragments such as K[KH KHCO₃]+ in the positive TOF-SIMS spectra of samples isolated from the electrolyte following acidification indicates the stability of the novel potassium hydride potassium bicarbonate compound.1 The electrolyte was acidified with HNO₃ to pH = 2 and boiled to dryness to prepare samples to determine whether KH KHCO3 was reactive under these conditions. Ordinarily, no K₂CO₃ would be present, and the sample would be converted to KNO₃. Crystals were isolated by dissolving the dried crystals in water, concentrating the solution, and allowing crystals to precipitate. TOF-SIMS was performed on these crystals. The positive spectrum contained elements of the series of inorganic hydride clusters {K[KH KHCO₃]* $m/z = (39 + 140n), K_2OH[KH KHCO_3]_n^+ m/z = (95 + 140n)$ 140n), and $K_3O[KH \ KHCO_3]_n^+ \ m/z = (133 + 140n)$, which were observed in the positive TOF-SIMS spectrum of electrolytic cell sample 1 as discussed in Sec. III.A and given in Figs. 3 and 4 and Table I. The presence of bicarbonate carbon (C 1s = 289 eV) was observed in the XPS of the sample from the HNO3 acidified electrolyte. In addition, fragments of compounds formed by the displacement of hydrogen carbonate by nitrate were observed. A general structural formula for the reaction may be





Mills NOVEL HYDROGEN COMPOUNDS

V. CONCLUSION

The TOF-SIMS, XPS, and NMR results confirm the identification of KH KHCO3 with a new state of hydride ion. The chemical structure and properties of this compound having a hydride ion with a high binding energy as well as the observation of additional high binding energy hydride ions by XPS are indicative of a new field of hydride chemistry. Novel hydride ions may combine with other cations such as other alkali cations and alkaline earth, rare earth, and transition element cations. Thousands of novel compounds may be synthesized with extraordinary properties relative to the corresponding compounds having ordinary hydride ions if they exist. These novel compounds may have a breadth of applications. For example, according to the hydride binding energies observed as high as 70 eV by XPS, a high-voltage battery having projected specifications that surpass those of the internal combustion engine may be possible.

The TOF-SIMS, XPS, XRD, FTIR, Raman, and NMR results confirm the identification of hydrogen in new states: hydride ions of increased binding energy, inorganic hydrogen polymers, and hydrogen polymers. Work in progress demonstrates that bulk, pure compounds comprising new states of hydrogen may be formed by reaction of a gaseous catalyst with atomic hydrogen. In addition to TOF-SIMS, inorganic hydrogen compounds, alkali and alkaline earth hydrides, and polyhydrogen species were observed by ESITOFMS, solids-probemagnetic-sector-mass spectroscopy, and solids-probequadrupole mass spectroscopy. Novel inorganic hydrogen compounds were also identified by liquid chromatography/mass spectroscopy. The chemical structures and properties of compounds comprising these new states of hydrogen are indicative of a new field of hydrogen chemistry.

Novel hydride and novel hydrogen chemistry also represents a new energy source. The exothermic reactions Eqs. (6), (7), (8), and (2), and the enthalpy of formation of KH KHCO₃ could explain the observation of excess enthalpy of 1.6×10^9 J that exceeded the total input enthalpy given by the product of the electrolysis voltage and current over time by a factor >8 reported previously.² Since the author's original publication of the possibility of producing atomic hydrogen energy states below the 13.6-eV level with the release of heat ¹² followed by a report of lower energy molecular hydrogen, ^{2,13} other researchers have considered the possibility of sub-13.6-eV-state hydrogen. ¹⁴⁻¹⁷ The author's prediction and confirmation of novel hydride ions whereby the corresponding novel hydride compounds can be reproducibly made in bulk may lead to an explosion of development in this field.

ACKNOWLEDGMENTS

Special thanks to B. Dhandapani for work on the Raman, FTIR, and XRD studies. Special thanks to J. He for obtaining

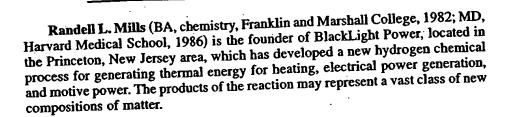
the MAS NMR spectrum of potassium hydride. Special thanks to R. Braun, B. Dhandapani, and J. He for helpful comments upon review.

REFERENCES

- 1. R. MILLS, The Grand Unified Theory of Classical Quantum Mechanics, BlackLight Power (Jan. 1999).
- 2. R. MILLS, W. R. GOOD, and R. M. SHAUBACH, "Dihydrino Molecule Identification," Fusion Technol., 25, 103 (1994).
- 3. M. G. JACOX and K. D. WATTS, "The Search for Excess Heat in the Mills Electrolytic Cell," Idaho National Engineering Laboratory (Jan. 7, 1993).
- 4. Microsc. Microanal. Microstruct., 3, 1 (1992).
- 5. "PHI Trift II," TOF-SIMS Technical Brochure, Physical Electronics, Eden Prairie, Minnesota.
- 6. "Practical Surface Analysis," *Ion and Neutral Spectroscopy*, Vol. 2, 2nd ed., D. BRIGGS and M. P. SEAH, Eds., John Wiley & Sons, New York (1992).
- 7. Handbook of X-Ray Photoelectron Spectroscopy, C. D. WAGNER, W. M. RIGGS, L. E. DAVIS, J. F. MOULDER, and G. E. MULILENBERG, Eds., Physical Electronics, Eden Prairie, Minnesota (1997).
- 8. CRC Handbook of Chemistry and Physics, 58th ed., pp. B-143 and B-161, R. C. WEAST, Ed., CRC Press, Boca Raton, Florida (1977).
- 9. D. LIN-VIEN, N. B. COLTHUP, W. G. FATELEY, and J. G. GRASSELLIC, The Handbook of Infrared and Raman Characteristic Frequencies of Organic Molecules, Academic Press, New York (1991).
- 10. Infrared Spectra of Inorganic Compounds, R. A. NYQUIST and R. O. KAGEL, Eds., Academic Press, New York (1971).
- 11. M. H. BROOKER and J. B. BATES, Spectrochim. Acta, 30A, 2211 (1994).
- 12. R. L. MILLS and S. P. KNEIZYS, "Excess Heat Production by the Electrolysis of an Aqueous Potassium Carbonate Electrolyte and the Implications for Cold Fusion," *Fusion Technol.*, 20, 65 (1991).
- 13. R. MILLS and W. R. GOOD, "Fractional Quantum Energy Levels of Hydrogen," Fusion Technol., 28, 1697 (1995).
- 14. J. P. VIGIER, "New Hydrogen Energies in Specially Structured Dense Media: Capillary Chemistry and Capillary Fusion," *Proc. 3rd Annual Conf. Cold Fusion*, Nagoya, Japan, October 21–25, 1992, p. 325, H. IKEGAMI, Ed., Universal Academy Press, Tokyo (1992).
- 15. J. P. VIGIER, "New Hydrogen (Deuterium) Bohr Orbits," *Proc. ICCF4*, Vol. 4, p. 7-1 (1994).
- 16. J. A. MALY and J. VÁVRA, "Electron Transitions on Deep Dirac Levels I," Fusion Technol., 24, 307 (1993).
- 17. J. DUFOUR, J. FOOS, J. P. MILLOT, and X. DUFOUR, "Interaction of Palladium/Hydrogen and Palladium/Deuterium to Measure the Excess Energy per Atom for Each Isotope," Fusion Technol., 31, 198 (1997).



Mills









International Journal of Hydrogen Energy 25 (2000) 1171-1183

www.elsevier.com/locate/ijhydene

The hydrogen atom revisited

Randell L. Mills *

BlackLight Power, Inc., 493 Old Trenton Road, Cranbury, NJ 08512, USA

Abstract

Several myths about quantum mechanics exist due to a loss of awareness of its details since its inception in the beginning of the last century or based on recent experimental evidence. It is taught in textbooks that atomic hydrogen cannot go below the ground state. Atomic hydrogen having an experimental ground state of 13.6 eV can only exist in a vacuum or in isolation, and atomic hydrogen cannot go below this ground state in isolation. However, there is no known composition of matter containing hydrogen in the ground state of 13.6 eV. It is a myth that hydrogen has a theoretical ground state based on first principles. Historically, there were many directions in which to proceed to solve a wave equation for hydrogen. The Schrodinger equation gives the observed spontaneously radiative states and the nonradiative energy level of atomic hydrogen. On this basis alone, it is justified despite its inconsistency with physical laws as well as with many experiments. A solution compatible with first principles and having first principles as the basis of quantization was never found. Scattering results required the solution to be interpreted as probability waves that give rise to the uncertainty principle which in turn forms the basis of the wave particle duality. The correspondence principal predicts that quantum predictions must approach classical predictions on a large scale. However, recent data has shown that the Heisenberg uncertainty principle as the basis of the wave particle duality and the correspondence principle taught in textbooks are experimentally incorrect. Recently, a reconsideration of the postulates of quantum mechanics, has given rise to a closed form solution of a Schrodinger-like wave equation based on first principles. Hydrogen at predicted lower energy levels has been identified in the extreme ultraviolet emission spectrum from interstellar medium. In addition, new compositions of matter containing hydrogen at predicted lower energy levels have recently been observed in the laboratory, which energy levels are achieved using the novel catalysts. © 2000 International Association for Hydrogen Energy. Published by Elsevier Science Ltd. All rights reserved.

1. Introduction

J.J. Balmer showed, in 1885, that the frequencies for some of the lines observed in the emission spectrum of atomic hydrogen could be expressed with a completely empirical relationship. This approach was later extended by J.R. Rydberg, who showed that all of the spectral lines of atomic hydrogen were given by the equation

$$\vec{v} = R \left(\frac{1}{n_f^2} - \frac{1}{n_i^2} \right), \tag{1}$$

where $R = 109,677 \text{ cm}^{-1}$, $n_f = 1,2,3,...,n_i = 2,3,4,...$, and $n_i > n_f$. Niels Bohr, in 1913, developed a theory for atomic hydrogen based on an unprecedented postulate of

stable circular orbits that do not radiate. Although no explanation was offered for the existence of stability for these orbits, the results gave energy levels in agreement with Rydberg's equation

$$E_n = -\frac{e^2}{n^2 8\pi \varepsilon_0 a_{\rm H}} = -\frac{13.598 \text{ eV}}{n^2},$$
 (2)

$$n=1,2,3,\ldots, \tag{3}$$

where $a_{\rm H}$ is the Bohr radius for the hydrogen atom (52.947 pm), e is the magnitude of the charge of the electron, and ϵ_0 is the vacuum permittivity. Bohr's theory was a straightforward application of Newton's laws of motion and Coulomb's law of electric force — both pillars of classical physics and is in accord with the experimental observation that atoms are stable. However, it is not in accord with electromagnetic theory — another pillar of classical physics which predicts that accelerated charges radiate energy in the form

^{*} Tel.: 00-1-609-490-1090; fax: 00-1-609-490-1066. E-mail address: rmills@blacklightpower.com (R.L. Mills).

of electromagnetic waves. An electron pursuing a curved path is accelerated and therefore should continuously lose energy, spiraling into the nucleus in a fraction of a second. The predictions of electromagnetic theory have always agreed with experiment, yet atoms do not collapse. To the early 20th century theoreticians, this contradiction could mean only one thing: The laws of physics that are valid in the macroworld do not hold true in the microworld of the atom. In 1923, de Broglie suggested that the motion of an electron has a wave aspect $-\lambda = h/p$. This concept seemed unlikely according to the familiar properties of electrons such as charge, mass and adherence to the laws of particle mechanics. But, the wave nature of the electron was confirmed by Davisson and Germer in 1927 by observing diffraction effects when electrons were reflected from metals. Schrödinger reasoned that if electrons have wave properties, there must be a wave equation that governs their motion. And in 1926, he proposed the Schrödinger equation, $H\Psi = E\Psi$, where Ψ is the wave function, H is the wave operator, and E is the energy of the wave. This equation, and its associated postulates, is now the basis of quantum mechanics, and it is the basis for the world view that the atomic realm including the electron and photon cannot be described in terms of "pure" wave and "pure" particle but in terms of a wave-particle duality. The wave-particle duality based on the fundamental principle that physics on an atomic scale is very different from physics on a macroscopic scale is central to present day atomic theory [1].

2. Development of atomic theory

2.1. Bohr theory

In 1911, Rutherford proposed a planetary model for the atom where the electrons revolved about the nucleus (which contained the protons) in various orbits to explain the spectral lines of atomic hydrogen. There was, however, a fundamental conflict with this model and the prevailing classical physics. According to classical electromagnetic theory, an accelerated particle radiates energy (as electromagnetic waves). Thus, an electron in a Rutherford orbit, circulating at constant speed but with a continually changing direction of its velocity vector is being accelerated; thus, the electron should constantly lose energy by radiating and spiral into the nucleus.

An explanation was provided by Bohr in 1913, when he assumed that the energy levels were quantized and the electron was constrained to move in only one of a number of allowed states. Niels Bohr's theory for atomic hydrogen was based on an unprecedented postulate of stable circular orbits that do not radiate. Although no explanation was offered for the existence of stability for these orbits, the results gave energy levels in agreement with Rydberg's equation. Bohr's theory was a straightforward application of Newton's laws

of motion and Coulomb's law of electric force. According to Bohr's model, the point particle electron was held to a circular orbit about the relatively massive point particle nucleus by the balance between the coulombic force of attraction between the proton and the electron and centrifugal force of the electron.

$$\frac{e^2}{4\pi\varepsilon_0 r^2} = \frac{m_e v^2}{r}.$$

Bohr postulated the existence of stable orbits in defiance of classical physics (Maxwell's equations), but he applied classical physics according to Eq. (4). Then Bohr realized that the energy formula (Eqs. (2) and (3)) was given by postulating nonradiative states with angular momentum

$$L_z = m_e v r = n\hbar, \quad n = 1, 2, 3 \dots$$
 (5)

and by solving the energy equation classically. The Bohr radius is given by substituting the solution of Eq. (5) for v into Eq. (4).

$$r = \frac{4\pi\varepsilon_0 \hbar^2 n^2}{m_e e^2} = n^2 a_0, \quad n = 1, 2, 3 \dots$$
 (6)

The total energy is the sum of the potential energy and the kinetic energy. In the present case of an inverse squared central field, the total energy (which is the negative of the binding energy) is one-half the potential energy [2]. The potential energy, $\phi(\mathbf{r})$, is given by Poisson's equation

$$\phi(\mathbf{r}) = -\int_{\mathbf{r}'} \frac{\rho(\mathbf{r}') \, \mathrm{d}\mathbf{r}'}{4\pi\epsilon_0 |\mathbf{r} - \mathbf{r}'|}.$$
 (7)

For a point charge at a distance r from the nucleus the potential is

$$\phi(r) = -\frac{e^2}{4\pi\varepsilon_0 r}. ag{8}$$

Thus, the total energy is given by

$$E = -\frac{Z^2 e^2}{8\pi \varepsilon_0 r},\tag{9}$$

where Z = 1. Substitution of Eq. (6) into Eq. (9) with the replacement of the electron mass by the reduced electron mass gives Eqs. (2) and (3).

Bohr's model was in agreement with the observed hydrogen spectrum, but it failed with the helium spectrum, and it could not account for chemical bonds in molecules. The prevailing wisdom was that the Bohr model failed because it was based on the application of Newtonian mechanics for discrete particles. Its limited applicability was attributed to the unwarranted assumption that the energy levels are quantized.

Bohr's theory may also be analyzed according to the corresponding energy equation. Newton's differential equations of motion in the case of the central field such as a gravitational or electrostatic field are

$$m(\ddot{r} - r\dot{\theta}^2) = f(r), \tag{10}$$

$$m(2\dot{r}\dot{\theta} + r\ddot{\theta}) = 0,\tag{11}$$

where f(r) is the central force. The second or transverse equation, Eq. (11), gives the result that the angular momentum is constant.

$$r^2\dot{\theta} = \text{constant} = L/m, \tag{12}$$

where L is the angular momentum. The central force equations can be transformed into an orbital equation by the substitution, u = 1/r. The differential equation of the orbit of a particle moving under a central force is

$$\frac{\delta^2 u}{\delta \theta^2} + u = \frac{-1}{mL^2 u^2 / m^2} f(u^{-1}). \tag{13}$$

Because the angular momentum is constant, motion in only one plane need be considered; thus, the orbital equation is given in polar coordinates. The solution of Eq. (13) for an inverse square force

$$f(r) = -\frac{k}{r^2} \tag{14}$$

is

$$r = r_0 \frac{1+e}{1+e\cos\theta},\tag{15}$$

$$e = A \frac{mL^2/m^2}{k},\tag{16}$$

$$r_0 = \frac{mL^2/m^2}{k(1+e)},\tag{17}$$

where e is the eccentricity and A is a constant. The equation of motion due to a central force can also be expressed in terms of the energies of the orbit. The square of the speed in polar coordinates is

$$v^2 = (\dot{r}^2 + r^2 \dot{\theta}^2). \tag{18}$$

Since a central force is conservative, the total energy, E, is equal to the sum of the kinetic, T, and the potential, V, and is constant. The total energy is

$$\frac{1}{2}m(\dot{r}^2 + r^2\dot{\theta}^2) + V(r) = E = \text{constant}.$$
 (19)

Substitution of the variable u = 1/r and Eq. (12) into Eq. (19) gives the orbital energy equation

$$\frac{1}{2}m\frac{L^2}{m^2}\left[\left(\frac{\delta^2 u}{\delta\theta^2}\right) + u^2\right] + V(u^{-1}) = E.$$
 (20)

Because the potential energy function V(r) for an inverse square force field is

$$V(r) = -\frac{k}{r} = -ku,\tag{21}$$

the energy equation of the orbit (Eq. (20)), is

$$\frac{1}{2}m\frac{L^2}{m^2}\left[\left(\frac{\delta^2 u}{\delta\theta^2}\right) + u^2\right] - ku = E,\tag{22}$$

$$\left[\frac{\delta^2 u}{\delta \theta^2} + u^2\right] - \frac{2m}{L^2} [E + ku] = 0, \tag{23}$$

which has the solution

$$r = \frac{m(L^2/m^2)k^{-1}}{1 + [1 + 2Em(L^2/m^2)k^{-2}]^{1/2}\cos\theta},$$
 (24)

where the eccentricity, e is

$$e = \left[1 + 2Em\frac{L^2}{m^2}k^{-2}\right]^{1/2}. (25)$$

Eq. (25) permits the classification of the orbits according to the total energy, E, as follows:

E < 0, e < 1, ellipse,

E < 0, e = 0, circle (special case of ellipse),

E = 0, e = 1, parabolic orbit,

$$E > 0$$
, $e > 1$, hyperbolic orbit. (26)

Since E = T + V and is constant, the closed orbits are those for which T < |V|, and the open orbits are those for which $T \geqslant |V|$. It can be shown that the time average of the kinetic energy, $\langle T \rangle$, for elliptic motion in an inverse square field is 1/2 that of the time average of the potential energy, $\langle V \rangle$. $\langle T \rangle = 1/2 \langle V \rangle$.

Bohr's solution is trivial in that he specified a circular bound orbit which determined that the eccentricity was zero, and he specified the angular momentum as a integer multiple of Planck's constant bar. Eq. (25) in CGS units becomes

$$E = -\frac{1}{2} \frac{me^4}{n^2 \hbar^2} = -\frac{e^2}{2n^2 a_0}.$$
 (27)

2.2. Schrödinger theory of the hydrogen atom

In 1923, de Broglie suggested that the motion of an electron has a wave aspect — $\lambda = h/p$. This was confirmed by Davisson and Germer in 1927 by observing diffraction effects when electrons were reflected from metals. Schrödinger reasoned that if electrons have wave properties, there must be a wave equation that governs their motion. And, in 1926, he proposed the time-independent Schrödinger equation

$$H\Psi = E\Psi, \tag{28}$$

where Ψ is the wave function, H is the wave operator, and E is the energy of the wave. To give the sought three quantum numbers, the Schrödinger equation solutions are three dimensional in space and four dimensional in spacetime

$$\left[\nabla^2 - \frac{1}{v^2} \frac{\delta^2}{\delta t^2}\right] \Psi(r, \theta, \phi, t) = 0, \tag{29}$$

where $\Psi(r, \theta, \phi, t)$ according to quantum theory is the probability density function of the electron as described below. When the time harmonic function is eliminated [3]

$$-\frac{\hbar^2}{2\mu} \left[\frac{1}{r^2} \frac{\delta}{\delta r} \left(r^2 \frac{\delta \Psi}{\delta r} \right) + \frac{1}{r^2 \sin \theta} \frac{\delta}{\delta \theta} \left(\sin \theta \frac{\delta \Psi}{\delta \theta} \right)_{r,\phi} \right]$$

$$+\frac{1}{r^2\sin^2\theta} \left(\frac{\delta^2\Psi}{\delta\phi^2}\right)_{r,\theta} + V(r)\Psi(r,\theta,\phi) = E\Psi(r,\theta,\phi),$$
(30)

where the potential energy V(r) in CGS units is

$$V(r) = -\frac{e^2}{r}. (31)$$

The Schrödinger equation (Eq. (30)) can be transformed into a sum comprising a part that depends only on the radius and a part that is a function of angle only obtained by separation of variables and linear superposition in spherical coordinates. The general form of the solutions for $\psi(r, \theta, \phi)$ are

$$\psi(r,\theta,\phi) = \sum_{l,m} R_{nlm}(r) Y_{lm}(\theta,\phi), \tag{32}$$

where l and m are separation constants. The azimuthal (θ) part of Eq. (30) is the generalized Legendre equation which is derived from the Laplace equation by Jackson (Eq. (3.9) of Jackson [4]). The solutions for the full angular part of Eq. (30), $Y_{lm}(\theta, \phi)$, are the spherical harmonics

$$Y_{lm}(\theta,\phi) = \sqrt{\frac{(2l+1)(l-m)!}{4\pi(l+m)!}} P_l^m(\cos\theta) e^{im\phi}.$$
 (33)

By substitution of the eigenvalues corresponding to the angular part [5], the Schrödinger equation becomes the radial equation, R(r), given by

$$-\frac{\hbar^2}{2mr^2}\frac{d}{dr}\left(r^2\frac{dR}{dr}\right) + \left[\frac{\hbar^2l(l+1)}{2mr^2} + V(r)\right]R(r) = ER(r).$$
(34)

The time-independent Schrödinger equation is similar to Eq. (20) except that the solution is for the distribution of a spatial wavefunction in three dimensions rather than the dynamical motion of a point particle of mass m along a one-dimensional trajectory. Electron motion is implicit in the Schrödinger equation. For wave propagation in three dimensions, the full time-dependent Schrödinger equation is required, whereas the classical case contains time

derivatives. The kinetic energy of rotation is K_{rot} is given classically by

$$K_{\rm rot} = \frac{1}{5}mr^2\omega^2,\tag{35}$$

where m is the mass of the electron. In the time-independent Schrödinger equation, the kinetic energy of rotation K_{rot} is given by

$$K_{\text{rol}} = \frac{\ell(\ell+1)\hbar^2}{2mr^2},\tag{36}$$

where

$$L = \sqrt{\ell(\ell+1)\hbar^2} \tag{37}$$

is the magnitude of the electron angular momentum L for the state $Y_{lm}(\theta, \phi)$.

In the case of the ground state of hydrogen, the Schrödinger equation solution is trivial for an implicit circular bound orbit which determines that the eccentricity is zero, and with the specification that the electron angular momentum is Planck's constant bar. With $k = e^2$, Eq. (25) in CGS units becomes

$$E = -\frac{1}{2} \frac{me^4}{\hbar^2} = -\frac{e^2}{2a_0},\tag{38}$$

which corresponds to n=1 in Eq. (27). Many problems in classical physics give three quantum numbers when three spatial dimensions are considered. In order to obtain three quantum numbers, the Schrödinger equation requires that the solution is for the distribution of a spatial wavefunction in three dimensions with implicit motion rather than a one dimensional trajectory of a point particle as shown below. However, this approach gives rise to predictions about the angular momentum and angular energy which are not consistent with experimental observations as well as a host of other problems which are summarized in Section 10.

The radial equation may be written as

$$\frac{\mathrm{d}}{\mathrm{d}r}\left(r^2\frac{\mathrm{d}R}{\mathrm{d}r}\right) + \frac{2mr^2}{\hbar^2}\left[E - V(r) - \frac{l(l+1)\hbar^2}{2mr^2}\right]R(r) = 0.$$
(39)

Let U(r) = rR(r), then the radial equation reduces to

$$U'' + \frac{2m}{\hbar^2} \left[E - V(r) - \frac{l(l+1)\hbar^2}{2mr^2} \right] U = 0, \tag{40}$$

where

$$\psi = \frac{1}{r} U_{lm}(r) Y_{lm}(\theta, \phi). \tag{41}$$

Substitution of the potential energy given by Eq. (31) into Eq. (40) gives for sufficiently large r

$$U_{\infty}^{"} - \left(\frac{\alpha}{2}\right)^2 U = 0 \tag{42}$$

provided we define

$$\left(\frac{\alpha}{2}\right)^2 = \frac{-2mE}{\hbar^2},\tag{43}$$





where α is the eigenvalue of the eigenfunction solution of the Schrödinger equation given infra having units of reciprocal length and E is the energy levels of the hydrogen atom. To arrive at the solution which represents the electron, a suitable boundary condition must be imposed. Schrödinger postulated a boundary condition: $\Psi \to 0$ as $r \to \infty$, which leads to a purely mathematical model of the electron. This equation is not based on first principles, has no validity as such, and should not be represented as so. The right-hand side of Eq. (43) must be postulated in order that the Rydberg equation is obtained as shown below. The postulate is implicit since Eq. (43) arises from the Schrödinger equation which is postulated. It could be defined arbitrarily, but is justified because it gives the Rydberg formula. That Schrödinger guessed the accepted approach is not surprising since many approaches were contemplated at this time [6], and since none of these approaches were superior, Schrödinger's approach prevailed.

The solution of Eq. (42) that is consistent with the boundary condition is

$$U_{\infty} = c_1 e^{(\alpha/2)r} + c_2 e^{-(\alpha/2)r}. \tag{44}$$

In the case that α is real, the energy of the particle is negative. In this case U_{∞} will not have an integrable square if c_1 fails to vanish wherein the radial integral has the form

$$\int_0^\infty R^2 r^2 \, \mathrm{d}r = \int U_\infty^2 \, \mathrm{d}r. \tag{45}$$

It is shown below that the solution of the Schrödinger corresponds to the case wherein c_1 fails to vanish. Thus, the solutions with sufficiently large r are infinite. The same problem arises in the case of a free electron that is ionized from hydrogen. If α is imaginary, which means that E is positive, Eq. (42) is the equation of a linear harmonic oscillator [7]. U_{∞} shows sinusoidal behavior; thus, the wavefunction for the free electron cannot be normalized and is infinite. In addition, the angular momentum of the free electron is infinite since it is given by $\ell(\ell+1)\hbar^2$ (Eq. (37)) where $\ell \to \infty$. In order to solve the bound electron states, let

$$E = -W \tag{46}$$

so that W is positive. In Eq. (39), let $r = x/\alpha$ where α is given by Eq. (43)

$$x\frac{d^2R}{dx^2} + 2\frac{dR}{dx} + \left[\frac{2me^2}{\hbar^2\alpha} - \frac{x}{4} - \frac{l(l+1)}{x}\right]R = 0.$$
 (47)

Eq. (47) is the differential equation for associated Laguerre functions given in general form by

$$xy'' + 2y' + \left[n^* - \frac{k-1}{2} - \frac{x}{4} - \frac{k^2 - 1}{4x}\right]y = 0, \quad (48)$$

which has a solution possessing an integrable square of the form

$$y = e^{-x/2} x^{(k-1)/2} \frac{d^k}{dx^k} L_{n^*}(x), \tag{49}$$

provided that n^* and k are positive integers. However, n^* does not have to be an integer, it may be any arbitrary constant β . Then the corresponding solution is [8]

$$y = e^{-x/2} x^{(k-1)/2} \frac{d^k}{dx^k} L_{\beta}(x).$$
 (50)

In the case that n^* is chosen to be an integer in order to obtain the Rydberg formula, $n^* - k \ge 0$ since otherwise $L_{n^*}^k(x)$ of Eq. (49) would vanish. By comparing Eqs. (47) and (48),

$$\frac{k^2 - 1}{4} = \ell(\ell + 1). \tag{51}$$

Thus.

$$k = 2\ell + 1 \tag{52}$$

and

$$n^* - \frac{k-1}{2} = n^* - \ell = \frac{me^2}{\hbar} \left(\frac{\alpha}{2}\right)^{-1}$$
 (53)

Substitution of the value of α and solving for W gives

$$W = \frac{1}{2} \frac{me^4}{(n^* - \ell)^2 \hbar^2}. (54)$$

Because of the conditions on n^* and k, the quantity $n^* - \ell$ cannot be zero. It is usually denoted by n and called the principal quantum number. The energy states of the hydrogen atom are

$$W_n = -E_n = \frac{1}{2} \frac{me^4}{n^2 \hbar^2} \tag{55}$$

and the corresponding eigenfunctions from Eq. (49) are

$$R_{n,\ell} = c_{n,\ell} e^{-x/2} x^{\ell} L_{n+\ell}^{2\ell+1}(x), \tag{56}$$

where the variable x is defined by

$$x = \alpha r = \frac{\sqrt{8mW}}{\hbar} r = \frac{2me^2}{n\hbar^2} r. \tag{57}$$

In the Bohr theory of the hydrogen atom, the first orbital has a radius in CGS units given by

$$a_0 = \frac{\hbar^2}{mc^2} = 0.53 \times 10^{-8} \text{ cm.}$$
 (58)

Thus, $\alpha = 2/na_0$ and

$$x = \frac{2}{n} \frac{r}{a_0}.\tag{59}$$

The energy states of the hydrogen atom in CGS units in terms of the Bohr radius are given by Eq. (27). From

Eq. (56), $R_{n,\ell}$ for the hydrogen atom ground state is

$$R_{1,0} = c_{1,0}e^{-r/a_0}L_1^1 = 2a_0^{-3/2}e^{-r/a_0}.$$
 (60)

For this state

$$Y_{00} = cons \tan t = (4\pi)^{-1/2}, \tag{61}$$

when the function is normalized. Thus, the ground state function is

$$\psi_0 = (\pi a_0^3)^{-1/2} e^{-r/a_0}. \tag{62}$$

Immediately further problems arise. Since & must equal zero in the ground state, the predicted angular energy and angular momentum given by Eqs. (36) and (37), respectively, are zero which are experimentally incorrect. In addition, different integer values of ℓ exist in the case of excited electron states. In these cases, the Schrödinger equation solutions (Eqs. (36) and (37)), predict that the excited state rotational energy levels are nondegenerate as a function of the ℓ quantum number even in the absence of an applied magnetic field. Consider the case of the excited state with n=2; $\ell=1$ compared to the experimentally degenerate state n=2; $\ell=0$. According to Eq. (37) the difference in angular energy of these two states is 3.4 eV where the expectation radius, 4a0, is given by the squared integral of Eq. (70) over space. Thus, the predicted rotational energy in the absence of a magnetic field is over six orders of magnitude of the observed nondegenerate energy $(10^{-7}-10^{-6} \text{ eV})$ in the presence of a magnetic field.

Schrödinger realized that his equation was limited. It is not Lorentzian invariant; thus, it violates special relativity. It also does not comply with Maxwell's equations and other first principle laws. Schrödinger sought a resolution of the incompatibility with special relativity for the rest of his life. He was deeply troubled by the physical consequences of his equation and its solutions. His hope was that the resolution would make his equation fully compatible with classical physics and the quantization would arise from first principles.

Quantum mechanics failed to predict the results of the Stern-Gerlach experiment which indicated the need for an additional quantum number. Quantum electrodynamics was proposed by Dirac in 1926 to provide a generalization of quantum mechanics for high energies in conformity with the theory of special relativity and to provide a consistent treatment of the interaction of matter with radiation. From Weisskopf [9], "Dirac's quantum electrodynamics gave a more consistent derivation of the results of the correspondence principle, but it also brought about a number of new and serious difficulties". Quantum electrodynamics: (1) does not explain nonradiation of bound electrons; (2) contains an internal inconsistency with special relativity regarding the classical electron radius — the electron mass corresponding to its electric energy is infinite; (3) it admits solutions of negative rest mass and negative kinetic energy; (4) the interaction of the electron with the predicted zero-point field fluctuations leads to infinite kinetic energy and infinite electron mass; and (5) Dirac used the unacceptable states of negative mass for the description of the vacuum; yet, infinities still arise.

A physical interpretation of Eq. (28) was sought. Schrödinger interpreted $e\Psi^*(x)\Psi(x)$ as the charge-density or the amount of charge between x and x + dx (Ψ^* is the complex conjugate of Ψ). Presumably, then, he pictured the electron to be spread over large regions of space. Three years after Schrödinger's interpretation, Max Born, who was working with scattering theory, found that this interpretation led to logical difficulties, and he replaced the Schrödinger interpretation with the probability of finding the electron between r, θ , ϕ and r + dr, $\theta + d\theta$, $\phi + d\phi$ as

$$\int \Psi(r,\theta,\phi) \Psi^{\bullet}(r,\theta,\phi) \, \mathrm{d}r \, \mathrm{d}\theta \, \mathrm{d}\phi. \tag{63}$$

Born's interpretation is generally accepted. Nonetheless, interpretation of the wave function is a never-ending source of confusion and conflict. Many scientists have solved this problem by conveniently adopting the Schrödinger interpretation for some problems and the Born interpretation for others. This duality allows the electron to be everywhere at one time — yet have no volume. Alternatively, the electron can be viewed as a discrete particle that moves here and there (from r=0 to ∞), and $\Psi\Psi^*$ gives the time average of this motion.

Schrödinger was also troubled by the philosophical consequences of his theory since quantum mechanics leads to certain philosophical interpretations [10] which are not sensible. Some conjure up multitudes of universes including "mind" universes; others require belief in a logic that allows two contradictory statements to be true. The question addressed is whether the universe is determined or influenced by the possibility of our being conscious of it. The meaning of quantum mechanics is debated, but the Copenhagen interpretation is predominant. It asserts that "what we observe is all we can know; any speculation about what a photon, an atom, or even a superconducting quantum interference device (SQUID) really is or what it is doing when we are not looking is just that - speculation" [10]. As shown by Platt [11] in the case of the Stern-Gerlach experiment, "the postulate of quantum measurement (which) asserts that the process of measuring an observable forces the state vector of the system into an eigenvector of that observable, and the value measured will be the eigenvalue of that eigenvector". According to this interpretation every observable exists in a state of superposition of possible states, and observation or the potential for knowledge causes the wavefunction corresponding to the possibilities to collapse into a definite.

According to the quantum mechanical view, a moving particle is regarded as a wave group. To regard a moving particle as a wave group implies that there are fundamental limits to the accuracy with which such "particle" properties as position and momentum can be measured. Quantum predicts that the particle may be located anywhere within its





wave group with a probability $|\Psi|^2$. An isolated wave group is the result of superposing an infinite number of waves with different wavelengths. The narrower the wave group, the greater range of wavelengths involved. A narrow de Broglie wave group thus means a well-defined position (Δx smaller) but a poorly defined wavelength and a large uncertainty Δp in the momentum of the particle the group represents. A wide wave group means a more precise momentum but a less precise position. The infamous Heisenberg uncertainty principle is a formal statement of the standard deviations of properties implicit in the probability model of fundamental particles.

$$\Delta x \, \Delta \mathbf{p} \, \geqslant \, \frac{\hbar}{2}. \tag{64}$$

According to the standard interpretation of quantum mechanics, the act of measuring the position or momentum of a quantum mechanical entity collapses the wave-particle duality because the principle forbids both quantities to be simultaneously known with precision.

3. The wave-particle duality is not due to the uncertainty principle

Quantum entities can behave like particles or waves, depending on how they are observed. They can be diffracted and produce interference patterns (wave behavior) when they are allowed to take different paths from some source to a detector — in the usual example, electrons or photons go through two slits and form an interference pattern on the screen behind. On the other hand, with an appropriate detector put along one of the paths (at a slit, say), the quantum entities can be detected at a particular place and time, as if they are point-like particles. But any attempt to determine which path is taken by a quantum object destroys the interference pattern. Richard Feynman described this as the central mystery of quantum physics.

Bohr called this vague principle 'complementary', and explained it in terms of the uncertainty principle, put forward by Werner Heisenberg, his postdoc at the time. In an attempt to persuade Einstein that wave-particle duality is an essential part of quantum mechanics, Bohr constructed models of quantum measurements that showed the futility of trying to determine which path was taken by a quantum object in an interference experiment. As soon as enough information is acquired for this determination, the quantum interferences must vanish, said Bohr, because any act of observing will impart uncontrollable momentum kicks to the quantum object. This is quantified by Heisenberg's uncertainty principle, which relates uncertainty in positional information to uncertainty in momentum — when the position of an entity is constrained, the momentum must be randomized to a certain degree.

More than 60 years after the famous debate between Niels Bohr and Albert Einstein on the nature of quantum

reality, a question central to their debate — the nature of quantum interference — has resurfaced. The usual textbook explanation of wave-particle duality in terms of unavoidable 'measurement disturbances' is experimentally proven incorrect by an experiment reported by Durr et al. [12]. Durr et al. report on the interference fringes produced when a beam of cold atoms is diffracted by standing waves of light. Their interferometer displayed fringes of high contrast — but when they manipulated the electronic state within the atoms with a microwave field according to which path was taken, the fringes disappeared entirely. The interferometer produced a spatial distribution of electronic populations which were observed via fluorescence. The microwave field canceled the spatial distribution of electronic populations. The key to this new experiment was that although the interferences are destroyed, the initially imposed atomic momentum distribution left an envelope pattern (in which the fringes used to reside) at the detector. A careful analysis of the pattern demonstrated that it had not been measurably distorted by a momentum kick of the type invoked by Bohr, and therefore that any locally realistic momentum kicks imparted by the manipulation of the internal atomic state according to the particular path of the atom are too small to be responsible for destroying interference.

4. The correspondence principle does not hold

Recent experimental results also dispel another doctrine of quantum mechanics [13,14]. Bohr proposed a rule of thumb called the correspondence principle [15]. A form of the principle widely repeated in textbooks and lecture halls states that predictions of quantum mechanics and classical physics should match for the most energetic cases.

Bo Gao [13] calculates possible energy states of any chilled, two-atom molecule, such as sodium, that's vibrating and rotating almost to the breaking point. He performs the calculations via quantum mechanical and the so-called semi-classical methods and compares the results. Instead of the results agreeing better for increasingly energetic states. The opposite happens.

5. Classical solution of the Schrodinger equation

Mills has solved and published a solution of a Schrödinger type equation based on first principles [16]. The central feature of this theory is that all particles (atomic-size and macroscopic particles) obey the same physical laws. Whereas Schrödinger postulated a boundary condition: $\Psi \to 0$ as $r \to \infty$, the boundary condition in Mills' theory was derived from Maxwell's equations [17].

For non-radiative states, the current-density function must not possess space-time Fourier components that are synchronous with waves traveling at the speed of light.

Application of this boundary condition leads to a physical model of particles, atoms, molecules, and, in the final analysis, cosmology. The closed-form mathematical solutions contain fundamental constants *only*, and the calculated values for physical quantities agree with experimental observations. In addition, the theory predicts that Eq. (3), should be replaced by Eq. (65).

$$n = 1, 2, 3, \dots$$
 and $n = \frac{1}{2}, \frac{1}{3}, \frac{1}{4}, \dots$ (65)

Some revisions to standard quantum theory are implied. Quantum mechanics becomes a real physical description as opposed to a purely mathematical model where the old and the revised versions are interchangeable by a Fourier transform operation [16].

The theories of Bohr, Schrödinger, and presently Mills all give the identical equation for the principal energy levels of the one-electron atom.

$$E_{\text{ele}} = -\frac{Z^2 e^2}{8\pi\epsilon_0 n^2 a_{\text{H}}} = -\frac{Z^2}{n^2} 2.1786 \times 10^{-18},$$

$$J = -Z^2 \frac{13.598}{n^2} \text{ eV}.$$
(66)

The Mills theory solves the two-dimensional wave equation for the charge-density function of the electron. And, the Fourier transform of the charge-density function is a solution of the three-dimensional wave equation in frequency (k,ω) space. Whereas, the Schrödinger equation solutions are three dimensional in spacetime. The energy is given by

$$\int_{-\infty}^{\infty} \psi H \psi \, d\nu = E \int_{-\infty}^{\infty} \psi^2 \, d\nu, \tag{67}$$

$$\int_{-\infty}^{\infty} \psi^2 \, \mathrm{d}\nu = 1. \tag{68}$$

Thus,

$$\int_{-\infty}^{\infty} \psi \, H\psi \, \mathrm{d}\nu = E. \tag{69}$$

In the case that the potential energy of the Hamiltonian, H, is a constant times the wavenumber, the Schrödinger equation is the well-known Bessel equation. Then with one of the solutions for ψ , Eq. (69) is equivalent to an inverse Fourier transform. According to the duality and scale change properties of Fourier transforms, the energy equation of the present theory and that of quantum mechanics are identical, the energy of a radial Dirac delta function of radius equal to an integer multiple of the radius of the hydrogen atom (Eq. (66)). Bohr obtained the same energy formula by postulating nonradiative states with angular momentum

$$L_z = m\hbar \tag{70}$$

and solving the energy equation classically.

The mathematics for all three theories converge to Eq. (66). However, the physics is quite different. Only the Mills theory is derived from first principles and holds over a scale of spacetime of 45 orders of magnitude: it correctly predicts the nature of the universe from the scale of the quarks to that of the cosmos.

Mills' revisions transform Schrödinger's and Heisenberg's quantum theory into what may be termed a classical quantum theory. Physical descriptions flow readily from the theory. For example, in the old quantum theory the spin angular momentum of the electron is called the "intrinsic angular momentum". This term arises because it is difficult to provide a physical interpretation for the electron's spin angular momentum. Quantum Electrodynamics provides somewhat of a physical interpretation by proposing that the "vacuum" contains fluctuating electric and magnetic fields. In contrast, in Mills' theory, spin angular momentum results from the motion of negatively charged mass moving systematically, and the equation for angular momentum, $\mathbf{r} \times \mathbf{p}$, can be applied directly to the wave function (a current-density function) that describes the electron, and quantization is carried by the photon, rather than probability waves of the electron.

6. Fractional quantum energy levels of hydrogen

The nonradiative state of atomic hydrogen which is historically called the "ground state" forms the basis of the boundary condition of Mills' theory [16] to solve the wave equation. Mills further predicts [16] that certain atoms or ions serve as catalysts to release energy from hydrogen to produce an increased binding energy hydrogen atom called a hydrino atom having a binding energy of

Binding energy =
$$\frac{13.6 \,\text{eV}}{n^2}$$
, (71)

where

$$n = \frac{1}{2}, \frac{1}{3}, \frac{1}{4}, \dots, \frac{1}{n}$$
 (72)

and p is an integer greater than 1, designated as $H[a_H/p]$ where a_H is the radius of the hydrogen atom. (Although it is purely mathematical, these stable energy levels are also given by both Bohr's and Schrödinger's theories by postulating integer values of the central charge. Justification may be based on notions such virtual particles which are acceptable in other applications of Schrödinger's equation.) Hydrinos are predicted to form by reacting an ordinary hydrogen atom with a catalyst having a net enthalpy of reaction of about

$$m \cdot 27.2 \text{ eV},$$
 (73)

where m is an integer. This catalysis releases energy from the hydrogen atom with a commensurate decrease in size of the hydrogen atom, $r_n = na_H$. For example, the catalysis of H(n=1) to H(n=1/2) releases 40.8 eV, and the hydrogen radius decreases from a_H to $(1/2)a_H$.

It is taught in textbooks that atomic hydrogen cannot go below the ground state. Atomic hydrogen having an experimental ground state of 13.6 eV can only exist in a vacuum or in isolation, and atomic hydrogen cannot go below this ground state in isolation. However, there is no known composition of matter containing hydrogen in the ground state of 13.6 eV. Atomic hydrogen is radical and is very reactive. It may react to form a hydride ion or compositions of matter. It is a chemical intermediate which may be trapped as many chemical intermediates may be by methods such as isolation or cryogenically. A hydrino atom may be considered a chemical intermediate that may be trapped in vacuum or isolation. A hydrino atom may be very reactive to form a hydride ion or a novel composition of matter. Hydrogen at predicted lower energy levels, hydrino atoms, has been identified in the extreme ultraviolet emission spectrum from interstellar medium. In addition, new compositions of matter containing hydrogen at predicted lower energy levels have recently been observed in the laboratory, which energy

The excited energy states of atomic hydrogen are also given by Eq. (71) except that

levels are achieved using the novel catalysts.

$$n=1,2,3,\ldots (74)$$

The n = 1 state is the "ground" state for "pure" photon transitions (the n = 1 state can absorb a photon and go to an excited electronic state, but it cannot release a photon and go to a lower energy electronic state). However, an electron transition from the ground state to a lower energy state is possible by a nonradiative energy transfer such as multipole coupling or a resonant collision mechanism. These lower energy states have fractional quantum numbers, n =1/integer. Processes that occur without photons and that require collisions are common. For example, the exothermic chemical reaction of H + H to form H_2 does not occur with the emission of a photon. Rather, the reaction requires a collision with a third body, M, to remove the bond energy $-H + H + M \rightarrow H_2 + M^*$ [18]. The third body distributes the energy from the exothermic reaction, and the end result is the H2 molecule and an increase in the temperature of the system. Some commercial phosphors are based on nonradiative energy transfer involving multipole coupling [19]. For example, the strong absorption strength of Sb3+ ions along with the efficient nonradiative transfer of excitation from Sb3+ to Mn2+, are responsible for the strong manganese luminescence from phosphors containing these ions. Similarly, the n = 1 state of hydrogen and the n = 1/integer states of hydrogen are nonradiative, but a transition between two nonradiative states is possible via a nonradiative energy transfer, say n = 1 to 1/2. In these cases, during the transition the electron couples to another electron transition, electron transfer reaction, or inelastic scattering reaction which can absorb the exact amount of energy that must be removed from the hydrogen atom. Thus, a catalyst provides a net positive enthalpy of reaction of $m \cdot 27.2$ eV (i.e. it absorbs $m \cdot 27.2$ eV where m is an

integer). Certain atoms or ions serve as catalysts which resonantly accept energy from hydrogen atoms and release the energy to the surroundings to effect electronic transitions to fractional quantum energy levels.

Once formed hydrinos have a binding energy given by Eqs. (71) and (72); thus, they may serve as catalysts which provide a net enthalpy of reaction given by Eq. (73). Also, the simultaneous ionization of two hydrogen atoms may provide a net enthalpy given by Eq. (73). Since the surfaces of stars comprise significant amounts of atomic hydrogen, hydrinos may be formed as a source to interstellar space where further transitions may occur.

A number of experimental observations lead to the conclusion that atomic hydrogen can exist in fractional quantum states that are at lower energies than the traditional "ground" (n=1) state. For example, the existence of fractional quantum states of hydrogen atoms explains the spectral observations of the extreme ultraviolet background emission from interstellar space [20], which may characterize dark matter as demonstrated in Table 2. (In these cases, a hydrogen atom in a fractional quantum state, $H(n_i)$, collides, for example, with a n=1/2 hydrogen atom, H(1/2), and the result is an even lower energy hydrogen atom, $H(n_f)$, and H(1/2) is ionized.

$$H(n_i) + H(\frac{1}{2}) \to H(n_f) + H^+ + e^- + \text{photon.}$$
 (75)

The energy released, as a photon, is the difference between the energies of the initial and final states given by Eqs. (71) and (72) minus the ionization energy of H(1/2), 54.4 eV. The catalysis of an energy state of hydrogen to a lower energy state wherein a different lower energy state atom of hydrogen serves as the catalyst is called disproportionation by Mills [16].

7. Identification of lower energy hydrogen by soft X-rays from dark interstellar medium

The first soft X-ray background was detected and reported [21] about 25 years ago. Quite naturally, it was assumed that these soft X-ray emissions were from ionized atoms within hot gases. In a more recent paper, a grazing incidence spectrometer was designed to measure and record the diffuse extreme ultraviolet background [20]. The instrument was carried aboard a sounding rocket and data were obtained between 80 and 650 Å (data points approximately every 1.5 Å). Here again, the data were interpreted as emissions from hot gases. However, the authors left the door open for some other interpretation with the following statement from their introduction:

It is now generally believed that this diffuse soft X-ray background is produced by a high-temperature component of the interstellar medium. However, evidence of the thermal nature of this emission is indirect in that it is based not on observations of line emission, but on

Table 1 Energies (Eq. (76)) of several fractional-state transitions catalyzed by $H[a_H/2]$

n _i	n_{f}	Δ <i>E</i> (eV)	λ (Å)
1/2	1/3	13.6	912
1/3	1/4	40.80	303.9
1/4	1/5	68.00	182.4
1/5	1/6	95.20	130.2
1/6	1/7	122.4	101.3
1/7	1/8	149.6	82.9

indirect evidence that no plausible non-thermal mechanism has been suggested which does not conflict with some component of the observational evidence.

The authors also state that "if this interpretation is correct, gas at several temperatures is present". Specifically, emissions were attributed to gases in three ranges: $5.5 < \log T < 5.7$; $\log T = 6$; $6.6 < \log T < 6.8$.

The explanation proposed herein of the observed dark interstellar medium spectrum hinges on the possibility of energy states below the n=1 state, as given by Eqs. (71) and (72). Thus, lower energy transitions of the type

$$\Delta E = \left(\frac{1}{n_{\rm f}^2} - \frac{1}{n_{\rm i}^2}\right) \times 13.6 \text{ eV} - 54.4 \text{ eV}$$

$$n = 1, \frac{1}{2}, \frac{1}{3}, \frac{1}{4}, \dots$$
 and $n_i > n_f$. (76)

induced by a disproportionation reaction with $H[a_H/2]$ ought to occur. The wavelength is related to ΔE by

$$\lambda (A) = \frac{1.240 \times 10^4}{\Delta E(\text{eV})}.$$
 (77)

The energies and wavelengths of several of these proposed transitions are shown in Table 1. Note that the lower energy transitions are in the soft X-ray region.

8. The data and its interpretation

In their analysis of the data, Labov and Bowyer [20] established several tests to separate emission features from the background. There were seven features (peaks) that passed their criteria. The wavelengths and other aspects of these peaks are shown in Table 2. Peaks 2 and 5 were interpreted by Labov and Bowyer as instrumental second-order images of peaks 4 and 7, respectively. Peak 3, the strongest feature, is clearly a helium resonance line: $He(1s^12p^1 \rightarrow 1s^2)$. At issue here, is the interpretation of peaks 1, 4, 6, and 7. It is proposed that peaks 4, 6, and 7 arise from the $1/3 \rightarrow 1/4$, $1/4 \rightarrow 1/5$, and $1/6 \rightarrow 1/7$ hydrogen atoms transitions given by Eq. (76). It is also proposed that peak 1 arises from inelastic helium scattering of peak 4. That is, the $1/3 \rightarrow 1/4$ transition yields a 40.8 eV photon (303.9 Å).

When this photon strikes He(1s²), 21.2 eV is absorbed in the excitation to He(1s¹2p¹). This leaves a 19.6 eV photon (632.6 Å), peak 1. For these four peaks, the agreement between the predicted values (Table 1) and the experimental values (Table 2) is remarkable.

One argument against this new interpretation of the data is that the transition $1/5 \rightarrow 1/6$ is missing — predicted at 130.2 Å by Eqs. (76) and (77). This missing peak cannot be explained into existence, but a reasonable rationale can be provided for why it might be missing from these data. The data obtained by Labov and Bowyer are outstanding when the region of the spectrum, the time allotted for data collection, and the logistics are considered. Nonetheless, it is clear that the signal-to-noise ratio is low and that considerable effort had to be expended to differentiate emission features from the background. This particular peak, $1/5 \rightarrow 1/6$, is likely to be only slightly stronger than the $1/6 \rightarrow 1/7$ peak (the intensities, Table 2, appear to decrease as n decreases), which has low intensity. Labov and Bowyer provided their data (wavelength, count, count error, background, and background error). The counts minus background values for the region of interest, 130.2 ± 5 Å, are shown in Table 3 (the confidence limits for the wavelength of about ±5 Å are the single-side 1 confidence levels and include both the uncertainties in the fitting procedure and uncertainties in the wavelength calibration). Note that the largest peak (count - background) is at 129.64 Å and has a counts - background = 8.72. The counts - background for the strongest signal of the other hydrino transitions are: n=1/3-1/4, 20.05; n=1/4-1/5, 11.36; n=1/6-1/7, 10.40. Thus, there is fair agreement with the wavelength and the strength of the signal. This, of course, does not mean that there is a peak at 130.2 Å. However, it is not unreasonable to conclude that a spectrum with a better signal-to-noise ratio might uncover the missing peak.

Another, and more important, argument against this new interpretation is the fact that the proposed fractional-quantum-state hydrogen atoms have not been detected before. There are several explanations. Firstly, the transitions to these fractional states must be forbidden or must have very high activation energies - otherwise, all hydrogen atoms would quickly go to these lower energy states (an estimated transition probability, based on the Labov and Bowyer data, is be between 10-15 and 10⁻¹⁷ s⁻¹). In actuality, a catalyst is required in order to obtain emission. Secondly, the number of hydrogen atoms (n = 1), the hydrogen-atom density, and the presence of an active catalyst under any conditions on Earth is exceeding low. The combination of extremely low population and extremely low transition probability makes the detection of these transitions especially difficult. Thirdly, this is a very troublesome region of the electromagnetic spectrum for detection because these wavelengths do not penetrate even millimeters of the atmosphere (i.e. this region is the vacuum ultraviolet which requires windowless spectroscopy at vacuum for detection). Lastly, no one previously has been





Table 2
Emission features of the LaBov and Bowyer spectrum and their interpretation

Peak	λ (Å)	Confidence limit· (Å)	Intensity (photons cm ⁻² s ⁻¹ sr ⁻¹)	Assignment [20]	Assignment [33]	Predicted λ (Eqs. (76) and (77)) (Å)
1	633.0	-4.7 to +4.7	19,000	O^{4+} ; $\log T = 5.5$	He scattering of 303.9 line (peak 4)	633.0
2	607.5	-4.9 to $+4.9$	Second order	Second order of 302.5 line	Second order of 303.9 line	607.8
3	584	-4.5 to +4.5	70,400	He resonance $(1s^12p^1 \rightarrow 1s^2)$	He resonance $(1s^12p^1 \rightarrow 1s^2)$	584
4	302.5	-6.0 to $+5.9$	2,080	He^+ ; $(2p^1 \rightarrow 1s^1)$	n = 1/3 - 1/4	303.9
5	200.6	-4.4 to + 5.3	Second order	Second order of 101.5 line	Second order of 101.3 line	202.6
6	181.7	-4.6 to $+5.1$	1030	Fe ⁹⁺ and Fe ¹⁰⁺ ; $\log T = 6$	n=1/4-1/5	182.3
7	101.5	-5.3 to $+4.2$	790	Fe ¹⁷⁺ and Fe ¹⁸⁺ ; $\log T = 6.6 - 6.8$	n = 1/6 - 1/7	101.3

Table 3 Data (Labov and Bowyer) near the predicted $1/5 \rightarrow 1/6$ transition (130.2 Å)

/ (Å) Counts		Background	Counts-background
125.82	26	21.58	4.42
127.10	22	21.32	0.68
128.37	18	19.50	-1.50
129.64	29	20.28	8.72
130.90	18	19.76	-1.76
132.15	20	19.50	0.50
133.41	19	19.50	-0.50
134.65	19	20.80	-1.80

actively searching for these transitions. The Chandra X-ray Observatory is scheduled to perform similar experiments with detection at much better signal to noise than obtained by Labov and Bowyer.

9. Novel energy states of hydrogen formed by a catalytic reaction

The catalysis of hydrogen involves the nonradiative transfer of energy from atomic hydrogen to a catalyst which may then release the transferred energy by radiative and nonradiative mechanisms. As a consequence of the nonradiative energy transfer, the hydrogen atom becomes unstable and emits further energy until it achieves a lower energy nonradiative state having a principal energy level given by Eqs. (71) and (72).

Potassium ions can also provide a net enthalpy of a multiple of that of the potential energy of the hydrogen atom. The second ionization energy of potassium is 31.63 eV; and K^+ releases 4.34 eV when it is reduced to K. The combination of reactions K^+ to K^{2+} and K^+ to K, then, has a net enthalpy of reaction of 27.28 eV, which is equivalent to

$$m = 1$$
 in Eq. (73).

27.28 eV + K⁺ + K⁺ +
$$H\left[\frac{a_{\rm H}}{p}\right] \to K + K^{2+} + H\left[\frac{a_{\rm H}}{(p+1)}\right]$$

+[$(p+1)^2 - p^2$]13.6 eV, (78)

$$K + K^{2+} \rightarrow K^{+} + K^{+} + 27.28 \text{ eV}.$$
 (79)

The overall reaction is

$$H\left[\frac{a_{\rm H}}{p}\right] \to H\left[\frac{a_{\rm H}}{(p+1)}\right] + [(p+1)^2 - p^2]13.6 \text{ eV}.$$
 (80)

Typically, the emission of extreme ultraviolet light from hydrogen gas is achieved via a discharge at high voltage, a high-power inductively coupled plasma, or a plasma created and heated to extreme temperatures by RF coupling (e.g. > 10⁶ K) with confinement provided by a toroidal magnetic field. Intense EUV emission was observed by Mills et al. [22-27] at low temperatures (e.g. $< 10^3$ K) from atomic hydrogen and certain atomized pure elements or certain gaseous ions which ionize at integer multiples of the potential energy of atomic hydrogen. The release of energy from hydrogen as evidenced by the EUV emission must result in a lower energy state of hydrogen. The lower energy hydrogen atom called a hydrino atom by Mills [16] would be expected to demonstrate novel chemistry. The formation of novel compounds based on hydrino atoms would be substantial evidence supporting catalysis of hydrogen as the mechanism of the observed EUV emission. A novel hydride ion called a hydrino hydride ion having extraordinary chemical properties given by Mills [16] is predicted to form by the reaction of an electron with a hydrino atom. Compounds containing hydrino hydride ions have been isolated as products of the reaction of atomic hydrogen with atoms and ions identified as catalysts in the Mills et al. EUV study [16,22-33]. The novel hydride compounds were identified analytically by techniques such as time of flight secondary ion mass spectroscopy, X-ray photoelectron spectroscopy, and proton nuclear magnetic resonance spectroscopy. For example, the time of flight secondary ion mass spectroscopy showed a large hydride peak in the negative spectrum. The X-ray photoelectron spectrum showed large metal core level shifts due to binding with the hydride as well as novel hydride peaks. The proton nuclear magnetic resonance spectrum showed significantly upfield shifted peaks which corresponded to and identified novel hydride ions.

10. Discussion

The Schrödinger equation gives the observed spontaneously radiative energy levels and the nonradiative state of hydrogen. On this basis alone, it is justified despite its inconsistency with physicals laws and numerous experimental observations such as

- The appropriate eigenvalue must be postulated and the variables of the Laguerre differential equation must be defined as integers in order to obtain the Rydberg formula.
- The Schrödinger equation is not Lorentzian invariant.
- The Schrödinger equation violates first principles including special relativity and Maxwell's equations [16,34].
- The Schrödinger equation gives no basis why excited states are radiative and the 13.6 eV state is stable [16].
- The Schrödinger equation solutions (Eqs. (36) and (37)), predict that the ground state electron has zero angular energy and zero angular momentum, respectively.
- The Schrödinger equation solution (Eq. (37)) predicts that the ionized electron may have infinite angular momentum.
- The Schrödinger equation solutions (Eqs. (36) and (37)), predict that the excited state rotational energy levels are nondegenerate as a function of the \(\ell\) quantum number even in the absence of an applied magnetic field, and the predicted energy is over six orders of magnitude of the observed nondegenerate energy in the presence of a magnetic field. In the absence of a magnetic field, no preferred direction exists. In this case, the \(\ell\) quantum number is a function of the orientation of the atom with respect to an arbitrary coordinate system. Therefore, the nondegeneracy is nonsensical and violates conservation of angular momentum of the photon.
- The Schrödinger equation predicts that each of the functions that corresponds to a highly excited state electron is not integrable and cannot be normalized; thus, each is infinite.
- The Schrödinger equation predicts that the ionized electron is sinusoidal over all space and cannot be normalized; thus, it is infinite.
- The Heisenberg uncertainty principle arises as the standard deviation in the electron probability wave, but experimentally it is not the basis of wave-particle duality.

- The correspondence principle does not hold experimentally.
- The Schrödinger equation does not predict the electron magnetic moment and misses the spin quantum number all together.
- The Schrödinger equation is not a wave equation since it gives the velocity squared proportional to the frequency.
- The Schrödinger equation is not consistent with conservation of energy in an inverse potential field wherein the binding energy is equal to the kinetic energy and the sum of the binding energy and the kinetic energy is equal to the potential energy [2].
- The Schrödinger equation permits the electron to exist in the nucleus which is a state that is physically nonsensical with infinite potential energy and infinite negative kinetic energy.
- The Schrödinger equation interpreted as a probability wave of a point particle cannot explain neutral scattering of electrons from hydrogen [16].
- The Schrödinger equation interpreted as a probability wave of a point particle gives rise to infinite magnetic and electric energy in the corresponding fields of the electron.
- A modification of the Schrödinger equation was developed by Dirac to explain spin which relies on the unfounded notions of negative energy states of the vacuum, virtual particles, and gamma factors.

The success of quantum mechanics can be attributed to (1) the lack of rigor and unlimited tolerance to ad hoc assumptions in violation of physical laws, (2) fantastical experimentally immeasurable corrections such as virtual particles, vacuum polarizations, effective nuclear charge, shielding, ionic character, compactified dimensions, and renormalization, and (3) curve fitting parameters that are justified solely on the basis that they force the theory to match the data. Quantum mechanics is now in a state of crisis with constantly modified versions of matter represented as undetectable minuscule vibrating strings that exist in many unobservable hyperdimensions, that can travel back and forth between undetectable interconnected parallel universes. And, recent data shows that the expansion of the universe is accelerating. This observation has shattered the long held unquestionable doctrine of the origin of the universe as a big bang [35]. It may be time to reconsider the roots of quantum theory, namely the theory of the hydrogen atom. Especially in light of the demonstration that the hydrogen atom can be solved in closed form from first principles, that new chemistry is predicted, and that the predictions have substantial experimental support.

Billions of dollars have been spent to harness the energy of hydrogen through fusion using plasmas created and heated to extreme temperatures by RF coupling (e.g. > 10⁶ K) with confinement provided by a toroidal magnetic field. Mills et al. [22-27] have demonstrated that energy may be released from hydrogen using a chemical catalyst at relatively low temperatures with an apparatus which is of trivial technological complexity compared to a tokomak. And, rather





than producing radioactive waste, the reaction has the potential to produce compounds having extraordinary properties [28-33]. The implications are that a vast new energy source and a new field of hydrogen chemistry have been discovered.

References

- Beiser A. Concepts of modern physics, 4th ed. New York: McGraw-Hill, 1987. p. 87-117.
- [2] Fowles GR. Analytical mechanics, 3rd ed. New York: Holt, Rinehart, and Winston, 1977. p. 154-6.
- [3] McQuarrie DA. Quantum chemistry. Mill Valley, CA: University Science Books, 1983. p. 78-9.
- [4] Jackson JD. Classical electrodynamics, 2nd ed. New York: Wiley, 1962. p. 84-108.
- [5] McQuarrie DA. Quantum chemistry. Mill Valley, CA: University Science Books, 1983. p. 221-4.
- [6] Moore W. Schrödinger life and thought. Cambridge: Cambridge University Press, 1989. p. 198.
- [7] Fowles GR. Analytical mechanics, 3rd ed. New York: Holt, Rinehart, and Winston, 1977. p. 57-60.
- [8] Margenau H, Murphy GM. The mathematics of chemistry and physics. New York: D. Van Nostrand Company, Inc. 1943. p. 77-8.
- [9] Weisskopf VF. Rev Mod Phys 1949;21(2):305-15.
- [10] Horgan J. Quantum philosophy. Sci Am 1992;267:94-104.
- [11] Platt DE. Am J Phys 1992;60(4):306-8.
- [12] Durr S, Nonn T, Rempe G. Nature 1998;395:33-7.
- [13] Gao B. Phys Rev Lett 1999;83(21):4225-8.
- [14] Weiss P. Physics rule of thumb gets thumbs down: Sci News 1999;156:342.
- [15] Thomsen DE. Going Bohr's way in physics. Sci News 1/11/86. p. 26.
- [16] Mills R. The grand unified theory of classical quantum mechanics, January 1999 ed. Cranbury, NJ: BlackLight Power, Inc. Distributed by Amazon.com.
- [17] Haus HA. On the radiation from point charges. Am J Phys 1986;54:1126-9.
- [18] Sidgwick NV. The chemical elements and their compounds, vol. I. Oxford: Clarendon Press, 1950. p. 17.
- [19] Lamb MD. Luminescence spectroscopy. London: Academic Press, 1978, p. 68.
- [20] Labov S, Bowyer S. Spectral observations of the extreme ultraviolet background. Astrophys J 1991;371:810-9.

- [21] Bower S, Field G, Mack J. Detection of an anisotrophic soft X-ray background flux. Nature 1968;217:32.
- [22] Mills R, Dong J, Lu Y. Observation of extreme ultraviolet hydrogen emission from incandescently heated hydrogen gas with certain catalysts. 1999 Pacific Conference on Chemistry and Spectroscopy and the 35th ACS Western Regional Meeting, Ontario Convention Center, CA, October 6-8, 1999.
- [23] Mills R, Dong J, Lu Y. Observation of extreme ultraviolet hydrogen emission from incandescently heated hydrogen gas with certain catalysts. Int J Hydrogen Energy, 2000;25: 919-43.
- [24] Mills R. Observation of extreme ultraviolet hydrogen and hydrino emission from hydrogen-KI plasmas produced by a hollow cathode discharge. Int J Hydrogen Energy, submitted.
- [25] Mills R. Temporal behavior of light-emission in the visible spectral range from a Ti-K2CO3-H-Cell. Int J Hydrogen Energy, in press.
- [26] Mills R, Lu Y, Onuma T. Formation of a hydrogen plasma from an incandescently heated hydrogen-potassium gas mixture and plasma decay upon removal of heater power. Int J Hydrogen Energy, submitted.
- [27] Mills R, Nansteel M, Lu Y. Observation of extreme ultraviolet hydrogen emission from incandescently heated hydrogen gas with strontium that produced an optically measured power balance that was 4000 times the control. Int J Hydrogen Energy, in press.
- [28] Mills R, Dhandapani B, Greenig N, He J. Synthesis and characterization of potassium iodo hydride. Int J Hydrogen Energy, 2000;25:1185-1203.
- [29] Mills R. Novel hydride compound. Int J Hydrogen Energy, in press.
- [30] Mills R. Novel hydrogen compounds from a potassium carbonate electrolytic cell. Fusion Technol 2000;37(2):
- [31] Mills R, He J, Dhandapani B. Novel hydrogen compounds. 1999 Pacific Conference on Chemistry and Spectroscopy and the 35th ACS Western Regional Meeting, Ontario Convention Center, CA, October 6-8, 1999.
- [32] Mills R, Dhandapani B, Nansteel M, He J. Synthesis and characterization of novel hydride compounds. Int J Hydrogen Energy, in press.
- [33] Mills R. Highly stable novel inorganic hydrides. Int J Inorganic Mater, submitted.
- [34] Fuchs CA, Peres A. Quantum theory needs no 'interpretation'. Phys Today 2000;53(3):70-1.
- [35] Bahcall NA, Ostriker JP, Perlmutter S, Steinhardt PJ. Science 1999;284:1481-8.

THIS PAGE BLANK (USPTO)

THE ASTROPHYSICAL JOURNAL, 371:810–819, 1991 April 20 © 1991. The American Astronomical Society, All rights reserved. Printed in U.S.A.

SPECTRAL OBSERVATIONS OF THE EXTREME ULTRAVIOLET BACKGROUND

SIMON E. LABOV1 AND STUART BOWYER2 Center for Extreme Ultraviolet Astrophysics, University of California, Berkeley, CA 94720 Received 1990 April 16; accepted 1990 October 2

ABSTRACT

A grazing incidence spectrometer was designed to measure the diffuse extreme ultraviolet background. It was flown on a sounding rocket, and data were obtained on the diffuse background between 80 and 650 Å. These are the first spectral measurements of this background below 520 A. Several emission features were detected, including interplanetary He i 584 Å emission and geocoronal He ii 304 Å emission. Other features observed may originate in a hot ionized interstellar gas, but if this interpretation is correct, gas at several different temperatures is present. The strongest of these features is consistent with O v emission at 630 Å. This emission, when combined with upper limits for other lines, restricts the temperature of this component to $5.5 < \log T < 5.7$, in agreement with temperatures derived from O vi absorption studies. A power-law distribution of temperatures is consistent with this feature only if the power-law coefficient is negative, as is predicted for saturated evaporation of clouds in a hot medium. In this case, the O vi absorption data confine the filling factor of the emission to $f \le 4\%$ and the pressure to more than 3.7×10^4 cm⁻³ K, substantially above ambient interstellar pressure. Such a pressure enhancement has been predicted for clouds undergoing saturated evaporation. Alternatively, if the O v emission covers a considerable fraction of the sky, it would be a major source of ionization. A feature centered at about 99 Å is well fitted by a cluster of Fe xvm and Fe xxx lines from gas at $\log T = 6.6-6.8$. These results are consistent with previous soft X-ray observations with lowresolution detectors. A feature found near 178 Å is consistent with Fe x and Fe x1 emission from gas at $\log T = 6$; this result is consistent with results from experiments employing broad-band soft X-ray detectors.

Subject headings: instruments — interstellar: matter — line identifications — ultraviolet: spectra — X-rays: spectra

1. INTRODUCTION

It has been more than 30 years since it was first suggested that hot, million-degree gas exists within our Galaxy (Spitzer 1956), and more than 20 years since the soft X-ray background was first detected (Bowyer, Field, & Mack 1968). It is now generally believed that this diffuse soft X-ray background is produced by a high-temperature component of the interstellar medium. However, evidence of the thermal nature of this emission is indirect in that it is based not on observations of line emission, but on the indirect evidence that no plausible nonthermal mechanism has been suggested which does not conflict with some component of the observational evidence.

The distribution of the soft X-ray background has been observed in detail with proportional counters that have limited energy resolution (McCammon et al. 1983; Marshall & Clark 1984). Measurements with greater resolution have been obtained with a gas scintillation proportional counter (Inoue et al. 1979). These results show an enhancement near 20 Å which has been suggested to be O vii emission from a 106 K plasma. Inoue et al. modeled their spectrum with emission from a 106 K isothermal plasma absorbed by intervening neutral material. The model has a strong O vii line along with other lines that blend together to fit an observed feature at 20 Å. The instrument's resolving power $(\lambda/\Delta\lambda)$ is only about 2 at 44 Å and is not high enough to resolve the individual emission lines of this model.

Measurements of the soft X-ray spectrum have been made by Schnopper et al. (1982) and by Rocchia et al. (1984) with a

¹ Current postal address: Space Sciences Laboratory, University of Califor-

² Also with the Astronomy Department, University of California, Berkeley. nia, Berkeley, CA 94720.

lithium-drifted, silicon solid-state detector. This instrume resolution similar to that of the gas scintillation proportion counter used by Inoue et al. (1979). In addition to detection 20 A feature reported by Inoue et al., Rocchia et al. suggest that lines of C v and C vi at 40 A were detected. tunately, the instrument's long-wavelength cutoff is near and consequently the data show only one side of this enhancement, and there is no indication that the drops at wavelengths larger than 40 Å.

A minimal amount of data on the background extreme ultraviolet (EUV) has been obtained with broad detectors. The diffuse EUV background was first detectors. Berkeley sounding rocket experiment (Cash, Malina, 1976). These measurements covering the 115-155 Alband later confirmed by the data obtained with the Apollo EUV telescope, which performed longer observations different regions of the sky in the same band (Stern 1979). Bloch et al. (1986) used a sounding rocket expense scan a portion of the sky in the 115-155 A band experiments are the only ones to have detected diff background radiation; all other observations have duced upper limits to the background intensity.

Stern and Bowyer found that the emission was with the temperatures inferred from the soft X-12 ments but that some gas must be at cooler temps $T \lesssim 4 \times 10^5$. Bloch et al. (1986) found no evide cooler gas; their analysis is consistent with the perature derived from the X-ray measurements

In addition to the 115-155 A band measurem with the Apollo-Soyuz EUV telescope, data were on the diffuse background in bands covering 500-800 A. Unfortunately, the intensity measure



dominated by the bright, resonantly scattered solar He II at 304 Å and He I at 584 Å, making direct obserof interstellar lines impossible. Stern and Bowyer analyzed the Apollo-Soyuz observations in the antisolar tion, where the scattered 304 A geocoronal line intensity is reduced, to obtain upper limits on the interstellar inten-Paresce & Stern (1981) argued that the residual signal in band is consistent with emission from a single line at 584 they employed a differencing technique to obtain a more pagent upper limit on this intensity. While this approach be valid, such a procedure adds considerable uncertainty

Holberg (1986) analyzed data from 1,508,198 s of observaat high Galactic latitude with the Voyager 2 ultraviolet trometer. The EUV part of this observation is dominated the solar He 1 584 A line intensity that is resonantly scating from neutral helium flowing through the solar system. therg removed this bright He I line from his spectra along th other sources of background to derive upper limits to

erstellar emission between 520 and 1100 Å. If the diffuse EUV background is the product of emission from a hot gas, most of the radiated power will be concentrated remission lines from highly ionized atoms (Kato 1976; Sapiro & Moore 1976; Raymond & Smith 1977; Stern, wang, & Bowyer 1978; Mewe, Gronenschild & van den Oord 1035. Hence spectral measurements will not only provide Africative proof of the existence of a hot component of the ISM, at they will also provide useful diagnostics of this gas. Despite is compelling motivation, spectral measurements have not geviously been made at EUV wavelengths shorter than 520 Å. The reason lies in the difficulty of building grazing incidence affuse spectrometers.

In § 2 we describe our diffuse EUV spectrometer and our abservations obtained on a sounding rocket flight. In § 3 we describe the tests performed on the data to search for emission mes. In § 4 we provide an interpretation of the observation with respect to emission from hot interstellar gas. The implicasons of our findings are discussed in § 5, and a summary of our

esults is provided in § 6.

2. INSTRUMENTATION AND FLIGHT

The spectrometer described here was designed specifically to observe the EUV background radiation. The instrument is an objective grating, grazing incidence spectrometer. A wire grid collimator restricts the field of view in one dimension to 40', bile allowing 15° of sky to enter the instrument in the orthogonal direction. This wedge of light is diffracted by an array of shat, blazed reflection gratings at grazing incidence. Once diffracted, the light is focused in the spectral direction by an array of mirrors through thin film bandpass filters and onto microchannel plate detectors. A schematic of the spectrometer is

shown in Figure 1. The total instrument payload consists of three such specfrometers, each tailored to a specific wavelength range. To obtain higher sensitivity at shorter wavelengths, the spectrom-Feter that covers 80-230 Å has 44 cm² of collecting area, about twice the area of each of the other two spectrometers. The medium-wavelength spectrometer covers 230-430 Å, and the long-wavelength spectrometer covers 430-650 Å. The latter two spectrometers have higher resolution than the shortwavelength system because of the requirement that the bright He 1 and He II solar system lines be separated from the much weaker interstellar lines. The two longer wavelength spec-

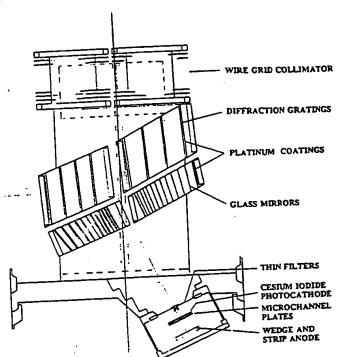


Fig. 1.—Schematic of the diffuse EUV spectrometer.

trometers both focus on different parts of the same imaging detector.

The grasp of the spectrometer, defined as the effective area integrated over the solid angle, is shown in Figure 2. Absolute detector efficiency and absolute effective area were measured relative to either an EUV diode calibrated by the National Bureau of Standards or to a proportional counter with known window transmission and gas efficiency. The spectrometer resolution, shown in Figure 3, was measured with narrow beams of EUV radiation entering the spectrometer at a variety of angles and positions across the instrument. Ray trace analysis of the system shows that the spectrometer resolution varies smoothly with wavelength; therefore, the estimated

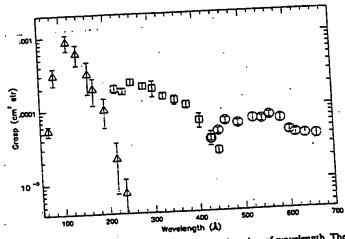


Fig. 2.—The spectrometer grasp $(A_{\rm eff} \, \Omega)$ as a function of wavelength. The short-, medium-, and long-wavelength spectrometer measurements are indicated by the triangles, squares, and circles, respectively.

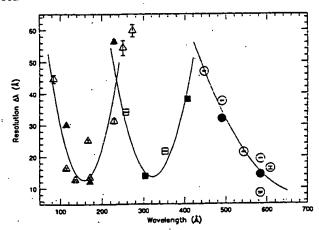


FIG. 3.—The resolution (FWHM in Å) as a function of wavelength. The triangles show the short-wavelength system resolution, and the squares and circles shown the medium- and long-wavelength systems; respectively. The open symbols indicate measurements made prior to launch, and the solid symbols show postflight measurements. The error bars shown are the 80% confidence intervals to the fits of each measurement, and the curves are parabolae that have been fit to the data.

resolution measurements have been fit to parabolic curves, as shown in Figure 3. These curves are taken as a reasonable estimate of the instruments' resolution, and the scatter of the measurements about the curve as an indicator of the total uncertainty of the individual measurements.

The spectrometer was designed to avoid false line problems, and the assembled instrument was tested extensively to check for "ghost lines" and to determine the effects of scattered light and particle infiltration. Intense beams of 170 Å, 304 Å, 584 Å, and 1216 A radiation, and electrons and ions with energies up to 400 eV were scanned across the instrument while aimed directly down the optical axis and at 5° and 10° to either side of the axis. Images accumulated during these tests show no signs of any ghost lines with count rates thousands of times higher than those observed in the brightest line (584 Å) during flight. The tests with low-energy particles and radiation outside a given spectrometer's bandpass showed no measurable increase in count rate over the detector background of that spectrometer. Furthermore, no increase in count rates were seen in any spectrometer when radiation of any wavelength was incident at angles outside the central 40' field of view of the collimator.

If filter pinholes developed before the observation, intense \$216 Å radiation scattering through the instrument could have entered the detector chamber. In this case, the scattered light would appear only as an increased detector background unless there were intrinsic detector nonuniformities that mimicked line emission. Therefore, many points on the detector surface were measured to test for fluctuations in quantum efficiency over different regions of the detector. These measurements showed the detector response to be quite uniform. The entire detector area was also illuminated with a diffuse beam of farultraviolet (FUV) radiation. These flat-field images have been examined for signs of line emission in the exact same manner as the flight data. No lines were found in this flat-field test data.

The diffuse EUV spectrometer was launched from White Sands, New Mexico, at 10 minutes after midnight (MST), 1986 April 22, on a Nike-boosted Black Brant sounding rocket. The rocket reached an apogee of 303.9 km at 283 s after launch. The spectrometer was pointed in the antisolar direction, down

Earth's shadow. This position was held for 160 s and the shifted 1°.5 along the narrow (40°) field of view and held another 160 s. As detailed later, this shift helped to determine the point source contribution to the observed emission. The flight ended with a scan away from Earth's shadow toward the southern horizon. The pointing was centered at the position $l = 325°.0 \pm 0°.5$, $b = 47°.7 \pm 0°.5$, as confirmed by a 35 mm and camera which photographed the sky every 5 s during the first

Postflight calibration of the instrument alignment resolution and a partial throughput test were performed with 1 month of the launch. The alignment was within 4% of 1 preflight values, and the postflight resolution measurement indicated by the solid symbols in Figure 3, were all within (2.3σ) of their preflight values. Unfortunately the aperture door on the optics cavity lost its vacuum seal during reconstructions a rupture of the thin filters and eliminating the postflight of carrying out a complete postflight throughput test with the postflight which we then corrected with the preflight measurement to better than 45% (1.2 σ). The spectrometer system is described further in Labov (1988a, b, 1989).

3. DATA ANALYSIS

A raw spectrum was derived for each spectrometer photons detected while the instrument was pointed in the solar direction and while the detectors were operating stant background levels. The short-wavelength spec (80-230 Å) includes 329 s of data with a detector backer level at 1.0 counts s-1 cm-2. The medium- and long-ways spectra (230-650 Å) include 234 s of data with a detector ground level of 1.6 counts s -1 cm -2. The constant backet of the detectors was about twice the background obser the laboratory, which is common for these detectors altitudes. The resultant spectrum is shown in Figure width of the pixels in Figure 4 is the electronic sampling the minimum spectrometer line width covers five to these electronic pixels. Solar radiation at 584 A scattered by neutral helium flowing through the solar clearly present in this figure, and features near 100

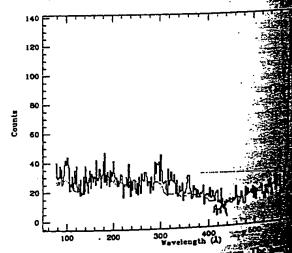


Fig. 4.—Raw spectra from all three spectrometers shows the number of counts accumulated in each waves antisolar pointing. The dotted line shows the detector become or smoothing has been performed.

371 hen

for

ine

Пае

the

ion

itar

ht.

and

hin '

the

nts,

5%

uic

try,

610, and 635 Å are suggested. The dotted curve in Figure 4 indicates the overall shape of the detector background spectrum as measured in the laboratory, scaled by a factor of 2.

3.1. Tests for Emission Features

Since the signal to noise of our measurement was expected 10 be low, three critera were established for a feature to be considered significant. First, the feature must not be due to a transient malfunction of the detector or spectrometer system. The postflight calibration (discussed in § 2) indicates that only the filters were damaged during the flight. The instrument has three independent vacuum pumps, each connected to one of the three chambers that are separated by the two filters. All these pumps were in operation after launch and prior to the observation. The pump voltage and current monitors showed that a pressure differential existed at this time, indicating that the filters were intact after the separation of the payload from the booster engines. At most, only a small pinhole could have been present during the observation. If such a filter pinhole did aist during the observation, or if a detector nonuniformity developed, the flight images would show a small region of mhanced count rate. However, since the spectrometers have so focusing perpendicular to the spectral direction, a true emisson line will evenly illuminate the entire length of the detector. Several tests for uneven detector illumination were performed, and only one of the eight possible emission features detected was unevenly illuminated. That feature, located at 120 Å, was removed from subsequent analysis.

Second, the feature must not be a consequence of the pethod employed in establishing the continuum (or backgound) level. The detector background was established by mining the dark counts accumulated before and after the ght under a variety of conditions. An independent method of mating the background continuum has also been applied. elector images have been artificially created with perfectly dummy " images are then processed in a manner identical to form backgrounds in the active area of the detector. These flight data. This provides a relatively smooth continuum erve that includes the changes in background levels due to the ange in image size as a function of wavelength. The analysis arried out using both methods of continuum estimation; emission line is a consequence of the noise in the backcound estimates, it will not appear in the analysis with the both dummy-image continuum. All the features discussed refler are present regardless of the method used to estimate continuum

hird, the feature must show a statistically significant rise we the continuum level. To find how many significant lines in each spectrum, the raw spectrum was fitted with a composed only of the continuum detector background rum multiplied by a scale factor. The model was fitted to spectrum data by varying the continuum scale factor mimize χ^2 . A line was then added to the model at the largest residual in the fit with the standard probable line was added at the wavelength corresponding largest residual in the fit with one line, and the wavelengths of both lines were varied as well as the largest residual in the fit with one line, and the wavelengths of both lines were varied as well as the largest residual in further improvement in the fit was noted. The wavelengths of the most probable lines were detersonfidence intervals were determined for the strength

and wavelength of each line. Because of the low number of counts per bin in the raw spectra, the likelihood-ratio test described by Cash (1979) was used with the procedure described by Lampton, Margon, & Bowyer (1976) for determining confidence intervals. A similar technique was applied at all wavelengths across the spectra to determine upper limits to line radiation at each wavelength.

3.2. Tests for Noninterstellar Emission

Once an emission feature was established as being significant, all possible solar and stellar origins for this emission were considered. This section describes procedures designed to test different noninterstellar emission mechanisms that might, in principle, have contributed to the observed features.

The field of view in the target direction does not contain any of the FUV point sources listed in the TD-1 catalog (Jamar et al. 1976). This catalog includes all O- through B3-type stars brighter than seventh magnitude and other B stars to about sixth magnitude. With these sensitivity limits, the catalog includes all stars that are hotter than 12,000 K, have little interstellar extinction, and lie within the nearest 100 pc. Any FUV source likely to appear in the EUV is therefore included in this catalog. The diffuse EUV spectrometer field of view does not contain any of the X-ray sources in the HEAO A-2 catalog (Nugent et al. 1983) or the HEAO A-1 catalog (Wood et al. 1984). The A-2 catalog has a limiting sensitivity of 10⁻¹¹ ergs cm⁻² s⁻¹ at 28-69 Å, and the A-1 catalog is complete to 250 μ Jy at 2.5 Å. If an uncataloged object with a flux equal to the limiting sensitivity of the HEAO surveys happened to be in the field of view of the spectrometer, that object would produce only a few counts at 100 Å during a 300 s observation by the diffuse EUV spectrometer.

The point source sensitivity of the diffuse EUV spectrometer is such that only the brightest known EUV sources (such as the hot white dwarf HZ 43) could produce a signal with count rates approaching those observed. No known white dwarfs hotter than 12,000 K are located near the field of view in the target direction (McCook & Sion 1984). Furthermore, white dwarfs are continuum emitters, not line emitters; therefore, if such an object were in the field of view, it could only raise the continuum level, not create lines. Similarly, only the brightest known EUV coronal emitters (such as a Cen) could be detected by the spectrometer. Halfway through the point observation, the instrument was shifted 1.5 in the narrow field of view direction. The flight data in each detected emission line were examined for changes corresponding to this shift. No change greater than 1 σ was observed in any of the lines or in the total count rate for any of the spectrometers. Since the probability of having two bright, unknown, and identical EUV sources separated by only 1.5 in a region that can extend ~ 100 pc is unlikely, we conclude that the emission observed is truly diffuse emission.

A possible noninterstellar source of diffuse EUV emission is resonantly scattered solar radiation. Since we observed in the antisolar direction down Earth's shadow cone, solar photons must be multiply scattered to reach the field of view of the spectrometer. If any of the detected features were geocoronal in origin, they would appear at least 40 times brighter in previous observations that were not confined to Earth's shadow (Weller & Meier 1974a; Chakrabarti et al. 1982). With the exception of He n 304 Å emission, radiation at these intensities is ruled out by the observations of Stern & Bowyer (1979) and Holberg (1986).

Another possible noninterstellar emission source is Earth's atmosphere. Spectra of the dayglow at wavelengths above 400 Å show several O II and N II emission lines, including an N II emission line at 629 Å (Chakrabarti et al. 1983). As atmospheric ions recombine at night, the intensity of the recombination lines will be significantly diminished. For example, the O I line at 989 Å is over 300 times brighter in the day than at night (Chakrabarti et al. 1983; Chakrabarti, Kimble, & Bowyer 1984). If the N II 629 Å dayglow emission is scaled down by this factor, it would be 25 times dimmer than the 635 Å feature reported here. Furthermore, several of the O II dayglow lines are much brighter than the N II 629 Å line, and none of these lines were found in the diffuse EUV spectrometer data. It therefore seems unlikely that the 635 Å feature is atmospheric in origin.

3.3. Line Strengths

The emission features that pass the criteria discussed in § 3.1 are summarized in Table 1. The wavelength and count rate of the line at 609 Å supports the hypothesis that it is 304 Å geocoronal He II emission detected in second order. Similarly, the feature at 200 Å is consistent with a second-order image of the 99 Å feature. The 200 and 609 Å intensities are therefore excluded from Table 1. The confidence intervals for the wavelengths are the single-side $1\ \sigma$ confidence levels. These intervals include both the uncertainties in the fitting procedure and those associated with the wavelength calibration. The observed counts listed in column (2) are the total number of counts in the line after correction for background. The confidence levels here are those found in the fitting procedure. The statistical confidence listed for each line in column (5) includes an estimate of the systematic errors.

The intensities listed in Table 1 have been corrected for atmospheric absorption. This absorption was calculated with the cross sections of Kirby et al. (1979) combined with the MSIS-83 thermospheric composition model atmosphere (Hedin 1983). The atmospheric attenuation was calculated as a function of wavelength, altitude, and zenith angle and then averaged for the conditions encountered during the observation. The maximum average attenuation used was 10%. The confidence levels for the intensities included both statistical and instrumental calibration uncertainties. For convenience the intensities in Table 1 are listed in photons cm⁻² s⁻¹ sr⁻¹ and in rayleighs (1 photon cm⁻² s⁻¹ si⁻¹ = $4\pi/10^6$ rayleighs).

The lines listed in Table 1 are presented in Figure 5 along with the upper limits to line emission. Also shown in Figure 5 is the strength necessary for a single line to produce the broadband upper limits from the Apollo-Soyuz EUV telescope obser-

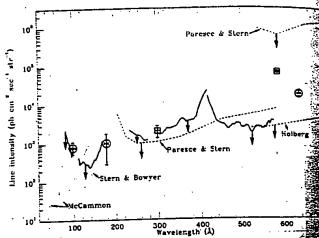


Fig. 5.—The emission features detected are indicated with 1 σ uncertainties in both wavelength and intensity. The uncertainties indicated include calibration and fitting procedure uncertainties. The squares show the non-stellar lines (304 and 584 Å), and the circled points are the lines the believed to be interstellar in origin. The bold lines indicate the upper (90% confidence level) to line radiation interred from this observation dashed lines indicate the upper limits derived from previous observations the dotted lines indicate the previous soft X-ray and EUV observations.

vations (Paresce & Stern 1981) and the upper to line radii found with the *Voyager* instrument (Holberg 1986). In Figure 8, we show the single line strength that would produce the rates observed in the soft X-ray carbon band (C band A), boron band (B band, 66-95 A), and the beryllium band, 115-155 A) (McCammon et al. 1983; Stern & 1979).

As can be seen in Figure 5, the 178 Å line is consistent the previous observations. Bloch et al. (1986) measured band intensity at two locations within 20° of the Posobserved. The 1 σ range in 178 Å intensity listed would produce between 2.5 and 17.7 counts sportional counter of Bloch et al. (1986). At l=35. Bloch et al. observed 7.2 \pm 0.8 counts s⁻¹, and $b=41^{\circ}$, 4.5 ± 0.6 counts s⁻¹ were observed, both with our measurement. Bloch (1988) has analyzed the height information from the Bloch et al. (1986) data cludes that if the emission they observe is dominated by emission at 178 Å or by emission at 178 Å or by emission wavelengths.

TABLE I
OBSERVED EMISSION FEATURES

		INTENSITY				
<i>i</i> .	OBSERVED COUNTS	photons cm ⁻² s ⁻¹ sr ⁻¹	rayleighs	STATISTICAL CONFIDENCE		
(A) 98.7 * \$\frac{1}{2} \tag{2}	191 ± 57 57 ± 32 57 ± 35 99 ± 37 72 ± 23 738 ± 32 87 ± 21 113 ± 17 113 ± 17	790+320 1030+740 1030+740 (Second order) 2080+720 70,400+3600 (Second order) 19,000+3600 19,000+3600	0.0100±0,0034 0.013±0,000 0.013±0,000 0.026±0,000 0.885±0,011 0.238±0,034	>0.99 0.86 0.96 0.99 >0.99 >0.99		

tude both

none

radiation

Figure 3

he count

id, 4437

band (B

Boy

tent

ed lbe

vation. Det anons, and The 99 Å feature is within 2.2 σ of the B band intensity abserved by McCammon et al. (1983). The 635 Å line plotted in figure 5 is significantly above the upper limits of Holberg. If the emission is interstellar in origin, it would be subject to strong absorption by neutral interstellar hydrogen, and the highlightness of the emission would be extremely sensitive to the momenty of the emitting and absorbing regions. Since our view interction was different from that of Holberg, our observations have not be in conflict.

4. INTERPRETATION

The feature observed at about 300 Å is the first spectroscopic beection of diffuse He n 304 A geocoronal background, and the 609 Å feature is consistent with this 304 Å line observed in goond order. The 304 Å intensity listed in Table 1 is consistent with the upper limit to 304 Å emission in the antisolar direcion (0.02 rayleighs) reported by Paresce, Fahr, & Lay (1981). None of the other lines appear to emanate from Earth's geoorona. The 0.9 rayleigh 584 A emission is consistent with solar adiation resonantly scattered by neutral helium flowing brough the solar system; previous 584 Å measurements vary from 0.5 to 10 rayleighs (Weller & Meier 1974b; Freeman et al. 1976, 1977; Broadfoot & Kumar 1978; Weller & Meier 1979; Weiler & Meier 1981; Dalaudier et al. 1984). This leaves three possible features, those at 99, 178, and 635 Å, which may be produced by the hot ISM. Calculations of the emission from a not interstellar plasma show bright lines near these waveengths produced by Si v, Ne vII, Ne vIII, Fe xVIII, or Fe XIX (9) Å); O vi or Fe viii to Fe xi (178 Å); and O v (635 Å) (Stern, Wang, & Bowyer 1978; Raymond & Smith 1984; Mewe, Gronenschild, & van den Oord 1985).

For an analysis of these features we consider the ISM to wassist of an emitting component with no self-absorption and a second component which is purely absorbing. For an optically thin isothermal gas in which the emitting material is homogeneous along the line of sight, the total emission from the emitting region is

$$I^{\circ}_{\lambda} = \frac{1}{4\pi} \frac{\lambda}{hc} \frac{P_{\lambda}(T)}{n_{\epsilon}^{2}} \text{ EM} , \qquad (1)$$

where EM is the emission measure, $P_{\lambda}(T)/n_{z}^{2}$ is the line power, and P_{λ} is in photon units (photons cm⁻² s⁻¹ sr⁻¹).

The ISM models can be extended to include a distribution of imperatures; following Jenkins (1978b) and Paresce & Stern 1981), a power-law temperature distribution defined by

$$\frac{dn_e}{d\ln T} = C_e T^a \tag{2}$$

filing factor and pressure of the ISM. This temperature in the probability of the ISM is the pressure of the ISM. This temperature in the probability of the ISM is the pressure of the ISM. This temperature is the probability of the ISM is t

The observed line intensity I_1 can be calculated by multiving the emitted line intensity I_2 by the effective transmiss of the ISM. The net absorption is affected not only by the amount of absorbing material in the line of sight, but also the geometry of this material and how it is arranged relative emitting material. In the simple slab absorption model, emitting material lies beyond the absorbing material, $I_2 = I_2 e^{-\sigma_2 N_H}$, where σ_1 is the photoelectric cross section hydrogen atom (Cruddace et al. 1974; Morrison & amount 1983). This model does not include the effects due

to clumping of the absorbing material; such effects were first examined by Bowyer & Field (1969) and later refined by Jakobsen & Kahn (1986). Jakobsen and Kahn's generalized "embedded clump" model describes the effect of a statistical distribution of absorbing clouds with a clumping factor η_{λ}^{0} that is multiplied by the photoelectric cross section yielding the effective cross section: $\sigma_{\lambda \text{ eff}} = \eta_{\lambda} \sigma_{\lambda}$. By using a power-law cloud distribution with an exponent of $\xi = -2$ and a maximum cloud size of $N_{\text{H max}} = 1.7 \times 10^{21} \text{ cm}^{-2}$, the clumping factor η_{λ} can be calculated at any wavelength as a function of the minimum cloud size $N_{\text{H min}}$ (Kahn & Jakobsen 1988; Labov 1988b). Jakobsen & Kahn (1986) also define a macrogeometrical parameter R as the ratio of scale heights of the absorbing gas to the emitting gas: $R = \beta_{\sigma}/\beta_{\sigma}$. By varying the two parameters, $N_{\text{H min}}$ and R, this model can encompass a

large variety of geometries and clumping. The most straightforward approach is to consider our line strengths and upper limits directly in terms of the models of the ISM discussed above. In practice this is possible with only one of the three features observed, the feature at 635 A. At long wavelengths the higher resolving power of the spectrometer, coupled with the limited number of strong lines produced at these wavelengths, makes it possible to analyze this feature directly. The most likely origin of this feature is O v emission at 629.7 Å. Within the 3 o confidence interval for the wavelength of this feature, the next strongest line produced by a cosmic composition of gas at temperatures between log T = 5and 7 is more than two orders of magnitude weaker (Stern, Wang, & Bowyer 1978; Raymond & Smith 1984). Two of these other lines are N II lines, including one at 635 Å. This N II line, however, would be accompanied by the N II 533 Å line, which is 16 times stronger. Any absorbing material in the line of sight will attenuate the 635 Å line more than the 533 Å line, making the apparent line ratio even larger. This 533 Å line was not observed. Since the strength of the observed 635 Å feature is 10 times larger than the upper limit at 533 Å, the 635 Å feature cannot be N II. Other lines within 3 σ of the observed 635 Å feature include C m (622.1 Å) and O π (644.2 Å), which can both be ruled out in the same way as the N II line. Additional nearby lines include Mg x (625.3 Å), O v (627.3 Å), N v (628.9 A), and O viii (632.7 A). These are unlikely candidates because the emission measures and temperatures required to produce these lines would also produce bright lines at shorter wavelengths. Such lines were not observed. Another possible source of the observed feature at 635 Å is the [He I] $2^3S \rightarrow 1^1S$ line at 625.6 Å. This line is 2 σ from the recorded 635 Å feature, whereas the O v line is within 1 o of the recorded feature. Therefore, in the following analysis it has been assumed that the seature at 635 Å is the 630 Å O v line.

Our observation places strong constraints on the temperature of the O v emitting gas. The O v 630 Å line is strongest at temperatures of $10^{5.4}$ K. An O IV line at 554 Å can be almost as strong as the O v 630 Å line at its peak emission temperature of $10^{5.3}$ K. This line was not detected. The ratio of the upper limit at 554 Å to the detected O v 630 Å emission is $I_{554}/I_{630} \cong 0.1$. This ratio places a lower limit on the temperature of $\log T \geq 5.4$. A Ne VII line exists at 465 Å that peaks near $\log T = 5.8$. This Ne VII line also was not detected, and the ratio of the upper limit at 465 Å to the detected 630 Å line strength is again about 1/10. This places an upper limit on the temperature of $\log T \leq 5.7$. Absorption, in any geometry, will have a greater effect at 630 Å than at 465 or 554 Å and, therefore, further tightens these temperature constraints.

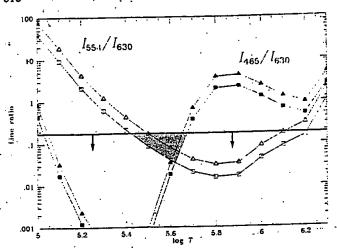


Fig. 6.—The ratio of the O rv 554 Å line to the O v 630 Å line as a function of temperature is shown by open symbols. The solid symbols indicate the Ne vn 465 Å to O v 630 Å line ratios. The predicted line ratios with no interstellar absorption are shown by the squares connected by solid lines, and the triangles show the line ratios predicted by a slab absorption model with a column density of $\log N_{\rm H} = 18$. The solid horizontal line shows the upper limit imposed on both of these line ratios by the data reported here. The temperature of the emitting gas is restricted to the shaded region.

These results are shown in Figure 6. The line ratios with no absorption and with a slab absorption model where $\log N_{\rm H}=18$ are shown. We also show the 90% confidence upper limit for both lines which is provided by our results. The emitting material must produce line ratios which lie below this line and above the solid lines that show the case of emission with no absorption. This leaves only a small range of permitted temperatures: $5.42 \le \log T \le 5.67$. To test the sensitivity of these results to differences in plasma codes, the line ratios were calculated from both the code of Stern, Wang, & Bowyer (1978) and the code of Raymond & Smith (1984); the results were consistent to within 3%, showing that our conclusions are not particularly sensitive to differences in plasma codes.

The nonisothermal emission model defined in equation (2) has little effect on this temperature constraint. With a wide range of temperature exponents, $-2 < \alpha < 3$, the smallest I₅₅₄/I₆₃₀ line ratio this model can produce is 0.4. Only by increasing the lower temperature limit log T_{\min} to 5.5 can a line ratio as small as 0.1 be obtained. The I_{465}/I_{630} limit works with a full range of temperatures, log $T_{\rm min} = 5$ to log $T_{\rm max} = 7$, but the power-law coefficient a must be negative. These results are similar to the conclusion above; the I_{554}/I_{630} ratio is not consistent with a gas at temperatures less than 105.5 K. The $\alpha < 0$ constraint from the I_{465}/I_{630} implies that the gas density decreases as the temperature increases. Therefore a higher temperature component, or a distribution of temperatures higher than 105.5 K, could exist as long as the emission measure of the hotter material does not exceed the emission measure of the log T = 5.5 gas. The hotter material in this gas can coexist with the $10^{5.5}$ K gas because the strongest lines at higher temperatures are only 1/10 as powerful as the O v 630 Å line at 10^{5.5} K.

These line ratio calculations utilized line power calculated under the assumption of ionization equilibrium. If the gas is cooling from a 10⁶ K equilibrium state, the calculations of Shapiro & Moore (1976) show that the ions do not recombine quickly enough to remain in equilibrium, and so each stage of

ionization persists at lower temperatures. This does not however, prevent recombination into O IV at about the same temperature (10^{5.3} K). Similarly, the temperature of the Ne VI peak (10^{5.78} K) is the same in the steady state and time dependent calculations. Nonequilibrium ionization, therefore does not effect the above conclusion that at least one component of the gas must be at a temperature near 10^{5.5} K.

The features centered at 99 and 178 Å, if produced by a bot ISM, will be produced by clusters of lines. The resolution of the spectrometer at these wavelengths is not high enough to idea tify any one emission line in these features. Hence it is necessity sary to generate model spectra and compare them with the spectra observed. To this end we generated synthetic spectra from isothermal models of the ISM with both slab and embed ded clump geometries using line strengths from Raymond Smith (1984) and interstellar absorption from Cruddace et al. (1974) and Morrison & McCammon (1983). The 90% and 993 confidence limits for emission measure and temperature for slab absorption model with NH as a free parameter are show in Figure 7. In this model only values of $\log N_{\rm H}$ less than 113 can fit the data. The results from the embedded clump mode with $N_{H \min}$ and R as free parameters are also shown in Figure 7. Both the slab absorption and the embedded clump isother mal models are dominated by the log T = 5.5 solution. the embedded clump model includes a large range of absorbing geometries, it is consistent with a large range of emission me sures. To determine values of $N_{H \, min}$ and R, at least two sections originating from the same gas are necessary. Since only of the features observed with the diffuse EUV spectrous originates at $\log T = 5.5$, these data cannot substantially. strain the $N_{H_{min}}$ and R parameters, and only solutions $\log N_{\rm H\,min} < 18$ can be rejected. This restriction correspond rejection of any solution with a relatively smooth unclumped absorbing medium.

The results shown in Figure 7 confirm our results de above for the O v 630 Å emission feature. However, thermal model with log T = 5.5 produces no emission or 178 Å. To reproduce the observed 99 and 178 Å \mathbb{R}^{3}

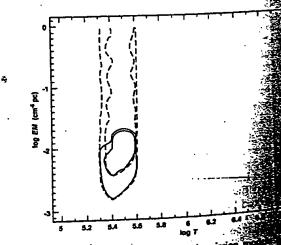


Fig. 7.—Results from fitting isothermal emission in reported here. The solid contours show the 90% and 90 for the slab absorption model including columns of 108 and 21. The dashed contours show the 90% and 90 and 21 to the first to the embedded absorber model. In this is 108 N_{H min} = 17, 18, 19, 20, and 21 are included, with and 10

does not, the same the Ne vn and timetherefore, one com-K.

I by a hot tion of the h to ident is neces ı with the ic spectral id embedymond & dace et al. and 99%类 ture for a are shown than اعد mp mode in Figure p isother ion Since absorbing Sion mea two bines only on ctronacter tially con-tions walks sponds to

ooth sand

the is

model with more than one temperature is required. A multiple temperature slab absorption model with $N_{\rm H}$ a free parameter, one temperature fixed at log T = 5.5, and the Wisconsin B and C band intensities (McCammon et al. 1983) included as upper limits provided an improved fit to the data. This model required a total of three temperatures to reproduce the observed features. In addition to the log T = 5.5 component, a solution near $\log T = 6.8$ and $\log EM = -1.8$ produces several Fe xvII and Fe xIX lines near 99 A. The other solution near log T = 6.0 and log EM = -2.0 produces no lines near 99 Å, but it does produce a cluster of Fe x and Fe x lines near 178 Å. Synthetic spectra were also generated with the plasma emission code of Mewe, Gronenschild, & van den Oord (1985) below 300 Å, and the code of Stern, Wang, & Bowyer (1978) above 300 Å. The model-fitting results were always similar to the results described above which were obtained with the Raymond & Smith (1984) code.

5. DISCUSSION

5.1. The 635 A Line

The 635 Å line is consistent with emission from O v at 630 Å originating in gas at log T=5.5. This gas will not produce emission lines at 99 or 178 Å, nor will it produce the observed soft X-ray intensity. This implies that hot gas exists at $\log T=5.5$, in addition to the gas emitting soft X-rays. In this section we examine other evidence for interstellar gas at $\log T=5.5$ and the implications of the O v emission for the ISM.

We first compare the temperature constraints provided by our observation with temperature constraints from OVI absorption studies. The star α Vir (Spica) is 6.6 away from the position we observed. This spectroscopic binary is at a distance of 84 ± 25 pc, has a hydrogen column of $N_{\rm H} = 1.0 \pm 0.25$ x 10^{19} cm⁻², and an O IV column of $N_{\rm OVI} = 2.69 \times 10^{13}$ cm⁻² (York 1974; Jenkins 1978a; Bohlin, Savage, & Drake 1978; Paresce 1984). The average density of the O VI column to 10^{10} cm⁻² is 3.7 times the global average (Jenkins 1978b).

Absorption from N v was not observed along the line of what to α Vir (York 1974). The upper limit to the N v/O virial constrains the temperature to 5.53 \leq log $T \leq$ 5.75. York malyzed the line widths to make an independent estimate of the upper temperature limit of the absorbing O vi gas. In the fraction of α Vir, he finds $\log T < 5.6$. The temperature containts imposed by our observation of O v emission at 630 Å are explainable by the presence of gas near $10^{5.5}$ K that sorbs O vi radiation and emits O v line radiation.

We next consider the strength of the 635 Å line and the plications of the inferred emission measure. We use the ationship

$$EM = \int n_e^2 ds = f L n_e^2 = f L \left(\frac{p/k}{1.91T} \right)^2,$$
 (3)

For L is the path length, f is the filling factor of the hot gas, P is the pressure. Since the total galactic $N_{\rm H}$ observed in direction of α Vir corresponds to an attenuation of 10^{10} at A, the distance to α Vir, 84 pc, is a good upper limit to L. Setting log T=5.5 and log EM ≥ -2.5 from our results A, and A is a sequence of A in the pressure to A in the pressure in A is a consistent with meathermal pressures in diffuse clouds (Jenkins, Jura, & Loesian 1983) and the pressure inferred from broad-band soft

X-ray measurements (Shapiro & Field 1976; Cox & Snowden 1986; Snowden et al. 1990).

The filling factor can be constrained if one assumes that the gas observed in absorption toward α Vir is typical of what we observed in emission. With this assumption, the O vi column density observed toward α Vir can be combined with our O v emission measure to estimate directly the filling factor and pressure. The electron density in the O vi absorption regions can be estimated by

$$n_e = n_{O \text{ VI}} \left[\frac{O}{O \text{ VI}} \right] \left[\frac{H}{O} \right] \left[\frac{e}{H} \right]. \tag{4}$$

At log T=5.5, the O vi/O ratio is 25% in steady state ionization equilibrium (Raymond & Smith 1984; Shapiro & Moore 1976). With the abundances of Allen (1973), equation (4) reduces to $n_e=7.12\times 10^3 n_{\rm O\,VI}$. The O vi density is related to the average O vi density by the filling factor $f:n_{\rm O\,VI}=\langle n_{\rm O\,VI}\rangle f^{-1}$. Combining this relation with equations (3) and (4) gives $p/k=2.68\times 10^{-4}T$ EM $L^{-1}\langle n_{\rm O\,VI}\rangle^{-1}$ and $f=5.07\times 10^7L\langle n_{\rm O\,VI}\rangle^2$ EM⁻¹. Inserting the lower limit to the observed emission measure and the upper limit to the length of the emission region ($L\leq 84$ pc), we find $p/k\geq 3.0\times 10^4$ cm⁻³ K and $f\leq 1.5\%$. This pressure is larger than the predicted thermal pressure of the local hot gas.

If the gas were not in a steady state situation but had been heated to $\log T = 6$ and is now cooling through $\log T = 5.5$, the ionization balance would be shifted, leaving less gas in both the O v and O vi ionization stages (Shapiro & Moore 1976). However, time-dependent ionization does not change the difference between the emission measure predicted from O vi absorption and the emission measure observed for O v emission, and hence our results would not be altered.

If the observed 630 Å O v emission originates from a nonisothermal gas, an analysis similar to that above can constrain the pressure and filling factor of the emitting region. In § 4 we showed that a power-law temperature distribution (equation (2)) can exist only if the minimum temperature of the gas is 10^{3.5} K and the exponent of the distribution is negative. Such a distribution is not consistent with classical evaporating clouds as described by McKee & Cowie (1977). If the cloud evaporation is saturated, however, a negative exponent of $\alpha = -5/4$ describes the temperature distribution in the saturated zone (McKee & Cowie 1977; Cowie & McKee 1977). If the lower temperature can be held at $\log T = 5.5$, and if the region is saturated, it is possible that the observed emission originates in a dense interface. With $\alpha = -5/4$, log $T_1 = 5.5$, and log $T_2 =$ 6.0, the pressure in the nonisothermal gas is $p/k = 1.23 \times 10^3$ $I_{\lambda}^{0}^{1/2}L^{-1/2}f^{-1/2}$ cm⁻³ K, where L is in parsecs. The lower limit emission measure that is compatible with the data, log EM ≥ -2.5 , corresponds to a minimum line intensity of 3.0×10^3 photons cm⁻² s⁻¹ sr⁻¹, restricting the pressure to $p/k \geq 7.4 \times 10^3 f^{-1/2}$ cm⁻³ K.

As with the isothermal case, the O vi absorption data for α Vir can be used to restrict the filling factor and the pressure independently. Combining equations (2) and (4) yields the average O vi density expected from a given temperature distribution. Using the steady state ionization fractions from Shapiro & Moore (1976) with the maximum emission length and minimum intensity derived from our observation, the filling factor and pressure are found to be restricted to $f \le 4.0\%$ and $p/k \ge 3.7 \times 10^4$. In this case, however, a pressure above the ambient ISM pressure is expected. For highly satu-

Casi

Chal

Chal

Cowi

Cox.

Crud

Dalai 171

Freen

Freezi 197

Hedin.

Holbe

Inoue. 227.

lpoue.

Jakobs

Jamar. Wils-

Jenkins

Jenkins.

Kahn. S

Kato, T Kirby, J

Labov.

Lamptor

Marshall

(Pari

1980

Re

rated evaporation, Cowie & McKee (1977) find a relationship for this enhancement. For the values considered here, a pressure enhancement of 3.7 would be expected for a cloud size just under one parsec.

Regardless of the origin, the 635 Å emission observed could be a major source of ionization. Reynolds (1983, 1984, 1985) has shown that diffuse $H\alpha$ emission is ubiquitous throughout the Galaxy, and widespread sources of flux shortward of 912 Å are required. Pulsar dispersion measures (Reynolds 1989) indicate a high scale height for the associated ionized material. Since the path length for radiation shortward of 912 Å is low, this implies that the ionizing source must also have a large scale height and be widespread. Transient heating appears unlikely, and the steady state ionization rate is more than can be provided by cosmic rays, the soft X-ray background, B stars, or hot white dwarfs (Reynolds 1986; Bruhweiler & Cheng 1988). Sciama (1990) and Salucci & Sciama (1990) have argued that a variety of observations can be explained by the presence of dark matter in the galaxy which decays with the emission of radiation below 912 Å.

The flux of 635 Å radiation required to produce hydrogen ionization is given by $F = \zeta_H/\sigma_\lambda = 4.3 \times 10^4 \zeta_{-13}$ photons cm⁻² s⁻¹, where ζ_{-13} is the ionizing rate in units of 10^{-13} s⁻¹ per H atom. Reynolds (1986) estimates that in the immediate vicinity of the Sun, a steady state ionizing rate of ζ_{-13} between 0.4 and 3.0 is required. To produce this range of ionization, the 635 Å intensity we observe would have to be distributed over 7%-54% of the sky.

5.2. The 99 and 178 A Features

The 178 Å feature can be produced by a group of Fe x and x lines at log T=6. The best-fit emission measure for this gas is log EM = -20, implying a pressure of $p/k = 1.9 \times 10^4/\sqrt{fL_2}$ cm⁻³ K, where L_2 is the path length in units of 100 pc. With L_2 and f near 1, this pressure is only slightly above the overall pressure of the local ISM. Bloch (1988) finds that depleted abundances are required to fit an interstellar emission model to his Be band data. There is too much uncertainty in our 178 Å intensity to determine if the log T=6 gas is depleted.

The 99 Å feature is best fitted by gas at $\log T = 6.6-6.8$, where a complex of Fe xviii and Fe xix lines contribute. At the temperature of $\log T = 6.6-6.8$, the bulk of the emission will be emitted in the 14-25 Å range (Raymond & Smith 1984; Mewe, Gronenschild, & van den Oord 1985). In the direction observed by the diffuse EUV spectrometer, the Wisconsin 13-28 Å M_1 band is 3 times brighter than the average high-latitude intensity, and the 11-20 Å M_2 band is about 2 times brighter than average (McCammon et al. 1983). At $\log T = 6.6-6.8$, the emission measure required to produce the Wisconsin M_1 band count rate is $\log EM = -1.9$ to -1.7 and the M_2 band count rate requires $\log EM = -2.3$ to -2.1 (McCammon et al. 1983). These emission measures are in agreement with the lower limit of $\log EM \ge -2$ derived from the observations reported here.

In regions with similar M band enhancements, Inoue et al. (1980) reported a temperature of $\log T = 6.5$, and Rocchia et al. (1984) found evidence for two temperatures, $\log T = 6$ and $\log T = 6.7$. The high-temperature component found by

Rocchia et al. (1984) has a 90% confidence interval of $6.63 \le \log T \le 6.72$ and an emission measure between $\log EM = -2.0$ and -1.7, which is consistent with our results.

6. SUMMARY

We have designed and built a spectrometer to measure the diffuse EUV astronomical background radiation. Results from our sounding rocket observation reveal five emission-line feat tures, two of which appear in first and second order. The strongest emission line is solar backscattered He I 584 Å radiation. Solar 304 A radiation resonantly scattered by geocoronal He II was observed in both first and second order. Each of the three remaining spectral features is consistent with those expected from hot interstellar gas. Of these features, the strongest is the feature at 635 Å, which we tentatively identify as 630 Å O v emission. This emission, when combined with upper limits for other lines which were not observed, restricts the temperature of this gas to $5.5 < \log T < 5.7$, which is consistent with temperatures derived from O vi absorption studies. A power-law distribution of temperatures is consistent with the data only if the minimum temperature is 105.5 K and the power law of the distribution is negative.

The isothermal models that best fit our O v results have low absorption (log $N_{\rm H}$ < 17.5) and emission measures (of $\log EM = -2.5$. If the O vi absorption data from the nearby star \alpha Vir is taken as typical for the region observed, then filling factor of less than 1.5% and a pressure of more than 3.0 × 10⁴ cm⁻³ K would be required; such a pressure is considerably out of equilibrium with the interstellar environment With a negative power-law temperature distribution such that predicted for saturated evaporation of clouds in a boo medium (McKee & Cowie 1977), the a Vir O vi absorpt data confine the filling factor of the emission to $f \le 4.0\%$ the pressure to more than 3.7 × 10⁴ cm⁻³ K. Such a pressure enhancement has been predicted for clouds undergoing rated evaporation. Alternatively, if the 635 A emission covers considerable fraction of the sky, it would be a major sources ionization.

The 99 Å feature is best fitted by a cluster of Fe Type Fe XIX lines from gas at $\log T = 6.6-6.8$. Gas at the perature, however, is consistent with the 11-28 Å observations of McCammon et al. (1983), and it is compared with results found by low-resolution spectral observation is consistent with these previous observation feature found at 178 Å is consistent with Fe x and Fe sion from gas at $\log T = 6$, which is the same temps derived from 44-77 Å soft X-ray background observations.

We wish to thank Christopher Martin, Anne Jelinsky, Glen Stark, Rick Raffanti, John Bogard Stirling for assistance in developing the instrument acknowledge useful discussions with Carl Heiles Smike Lampton, Richard Link, and Chris McKe assistance was provided by Brenda Hatfield and This work was funded by NASA grant NGR 05 NASA Graduate Student Researchers grant NGR

REFERENCES

al of tween sults.

re the s from ie fea-: The

ı radi-/ geoorder. it with

es, the lentify d with :stricts

is conrption sistent K and

s have ires. of nearby then 🖺 e than is conuch as

% and CSSUTE. 2 53 tu

a bol TOUOU3

Bruhweiler, F. C., & Cheng, K. P. 1988, ApJ, 335, 188

Cash, W. 1979, ApJ, 228, 939

Cash, W., Malina, R., & Stern, R. 1976, ApJ, 204, L7

Chakrabarti, S., Kimble, R., & Bowyer, S. 1984, J. Geophys. Res., 89, 5660

Chakrabarti, S., Paresce, F., Bowyer, S., Chiu, Y., & Aiken, A. 1982, Geophys.

Res. Letters 9 Chakrabarti, S., Paresce, F., Bowyer, S., Kimble, R., & Kumar, S. 1983. J. Geophys. Res., 88, 4898

Cowie, L. L., & McKee, C. F. 1977, ApJ, 211, 135 Cox. D. P., & Snowden, S. L. 1986, Adv. Space Res., 6, 97 Cruddace, R., Paresce, F., Bowyer, S., & Lampton, M. 1974, ApJ, 187, 497 Dalaudier, F., Bertaux, J. L., Kurt, V. G., & Mironova, E. N. 1984, A&A, 134,

171
Freeman, J., Paresce, F., Bowyer, S., & Lampton, M. 1976, ApJ, 208, 747
Freeman, J., Paresce, F., Bowyer, S., Lampton, M., Stern, R., & Margon, B.
1977, ApJ, 215, L83
Hedin, A. E. 1983, J. Geophys. Res., 88, 10170
Holberg, J. B. 1986, ApJ, 311, 969
Inoue, H., Koyama, K., Matsuoka, M., Obashi, T., & Tanaka, Y. 1979, ApJ, 277, L84

Kato, T. 1976, ApJ, 30, 397

McCaramon, D., Burrows, D. N., Sanders, W. T., & Kraushaar, W. L. 1983, ApJ, 269, 107

McCook, G. P., & Sion, E. M. 1984, A Catalogue of Spectroscopically Identified White Dwarfs, 2d ed. (Villanova, PA: Villanova Press)

McKee, C. F., & Cowie, L. L. 1977, ApJ, 215, 213

Meyer P. Gronerschild E. H. P. M. S. van den Oord, G. H. I. 1985, A&AS

Mewe, R., Gronenschild, E. H. B. M., & van den Oord, G. H. J. 1985, A&AS,

Morrison, R. & McCammon, D. 1983, ApJ. 270, 119 Nugent, J. J., et al. 1983, ApJS, 51, 1 Paresce, F. 1984, AJ, 89, 1022

Paresce, F., & Stern, R. 1981, J. Geophys. Res. 86, A12 Paresce, F., & Stern, R. 1981, ApJ, 247, 89 Raymond, J. C., & Smith, B. W. 1977, ApJS, 35, 419

——. 1989, ApJ, 339, L29
Rocchia, R., Arnaud, M., Blondel, C., Cheron, C., Christy, J. C., Rothenflug, R., Schnopper, H. W., & Delvaille, J. P. 1984, A&A, 130, 53
Salucci, P., & Sciama, D. W. 1990, preprint
Schnopper, H. W., et al. 1982, ApJ, 253, 131
Sciama, D. W. 1990, preprint
Shapiro, P. R., & Field, G. F. 1976, ApJ, 205, 762
Shapiro, P. R., & Moore, R. T. 1976, ApJ, 207, 460
Snowden, S. L., Cox. D. P., McCammon, D., & Sanders, W. T. 1990, ApJ, 354.

Snowden, S. L., Cox, D. P., McCammon, D., & Sanders, W. T. 1990, ApJ, 354,





FRACTIONAL QUANTUM ENERGY LEVELS OF HYDROGEN

RANDELL L. MILLS and WILLIAM R. GOOD HydroCatalysis Power Corporation, Great Valley Corporate Center 41 Great Valley Parkway, Malvern, Pennsylvania 19355

Received May 23, 1994 Accepted for Publication December 19, 1994

ELECTROLYTIC DEVICES

KEYWORDS: X-ray photoelectron spectroscopy, lower energy hydrogen, mass spectroscopy

Report is made of the detection of atomic hydrogen in fractional quantum energy levels below the traditional "ground" state—hydrinos—by X-ray photoelectron spectroscopy and by a reinterpretation of soft X-ray emissions from the interstellar medium. Hydrino formation occurs with the release of energy on nickel cathodes during the electrolysis of aqueous potassium carbonate. The detection of a new molecular species—the diatomic hydrino molecule—by high-resolution mass spectroscopy is also reported.

I. INTRODUCTION

J. J. Balmer showed, in 1885, that the frequencies for some of the lines observed in the emission spectrum of atomic hydrogen could be expressed with a completely empirical relationship. This approach was later extended by J. R. Rydberg, who showed that all of the spectral lines of atomic hydrogen were given by the equation

$$\bar{\nu} = R\left(\frac{1}{n_f^2} - \frac{1}{n_i^2}\right) \,, \tag{1}$$

where $R = 109677 \text{ cm}^{-1}$, $n_f = 1, 2, 3, ..., n_i = 2, 3, 4, ..., and <math>n_i > n_f$.

Niels Bohr, in 1913, developed a theory for atomic hydrogen that gave energy levels in agreement with Rydberg's equation. An identical equation, based on a totally different theory for the hydrogen atom, was developed by E. Schrödinger, and independently by W. Heisenberg, in 1926:

$$E_n = -\frac{e^2}{n^2 8\pi\epsilon_0 a_{\rm H}} = -\frac{13.598 \text{ eV}}{n^2}$$
 (2a)

$$n = 1, 2, 3, \dots$$
 (2b)

where $a_{\rm H}$ is the Bohr radius for the hydrogen atom, 52.947 pm, e is the magnitude of the charge of the electron, and ϵ_0 is the vacuum permittivity.

The purpose of this paper is to describe a number of experimental observations that lead to the conclusion that atomic hydrogen can exist in fractional quantum states that are at lower energies than the traditional "ground" (n = 1) state. Explicitly, we propose that the energy-level equation for atomic hydrogen is as given in Eq. (2a), but the restriction on "n," Eq. (2b), should be replaced by Eq. (2c):

$$n = 1, 2, 3, \dots$$
, and $n = \frac{1}{2}, \frac{1}{3}, \frac{1}{4}, \dots$ (2c)

The complete theory is given elsewhere.^{1,2} The central feature of this theory is that all particles (atomic-size particles and macroscopic particles) obey the same physical laws. Whereas Schrödinger postulated a boundary condition: $\Psi \to 0$ as $r \to \infty$, which leads to a purely mathematical model of the electron, the boundary condition in this theory was derived from Maxwell's equations³:

For non-radiative states, the current-density function must not possess space-time Fourier components that are synchronous with waves traveling at the speed of light.

Application of the latter boundary condition leads to an entirely different model of particles, atoms, molecules, and to a very different concept of the nature of the physical universe.^{1,2}

This paper has been organized as follows: Sec. II describes the determination of excess heat release during the electrolysis of aqueous potassium carbonate and how a catalytic reaction of atomic hydrogen from n=1 to fractional quantum energy levels accounts for this excess heat. Section III describes the experimental identification of hydrogen atoms in fractional quantum energy levels — hydrinos — by X-ray photoelectron spectroscopy (XPS) of the electrodes from these electrolytic cells. Section IV describes the experimental identification of hydrinos by emissions of soft X rays from





the dark interstellar medium. Section V describes the experimental identification of hydrogen molecules in fractional quantum energy levels—dihydrino molecules—by high-resolution magnetic sector mass spectroscopy. Section VI gives a summary.

II. EXCESS HEAT RELEASE DURING THE ELECTROLYSIS OF AQUEOUS POTASSIUM CARBONATE

II.A. Calorimetry Methods

Pulsed-current electrolysis of aqueous potassium carbonate at a nickel cathode was performed in a single-cell calorimeter. The cell operated at 50°C and was designed to have primarily conductive and convective heat losses to a water-cooled condenser. The output power was determined by flow calorimetry of the condenser coolant and the input power was measured with a power meter.

The calorimeter/electrolysis cell, Fig. 1, was a 16.5-? vacuum-jacketed dewara with a 4-in. inside diameter (i.d.) opening. A 60-in.-long × 3.9-in. outside diameter (o.d.) glass test tube liner (11.5 l) was placed in the 79.75-in.-long dewar. This inner glass tube liner held the cathode, the anode, and the electrolyte. The calorimeter was sealed with a 3-in.-thick machined Teflon cap with two outer-diameter Vitron O-rings. The cap had perforations fitted with glass sleeves having innerdiameter Vitron O-ring seals for the electrode leads and the condenser. The Graham condenser was a 10-mm-i.d. glass spiral, 35 cm in length, which was sealed in a 5-cm diam cylindrical water jacket. Tygon tubing connected the inlet of the condenser to a peristaltic pump, the outlet of the condenser to a 5-gal reservoir, and the reservoir to the pump inlet. The water coolant reservoir was maintained at ambient temperature by a constant temperature chiller.d The condenserwater flow rate (±0.1 ml/min) was measured from the digital readout of the peristaltic pumpe and confirmed with a stopwatch and volumetric measurements. The condenser-water inlet temperature (±0.1°C) and outlet temperature (±0.1°C) were each recorded with a microprocessor thermometer using a type K thermocouple, which was inserted into the inlet or outlet of the condenser. The temperature (±0.1°C) of the electrolyte was measured with a microprocessor thermometer using a type K thermocouple inserted through the Teflon cap. The resistance heater used during the calibration of the efficiency of heat transfer to the condenser was a 120 V/600 W Incoloy-alloy-coated^g hermetically

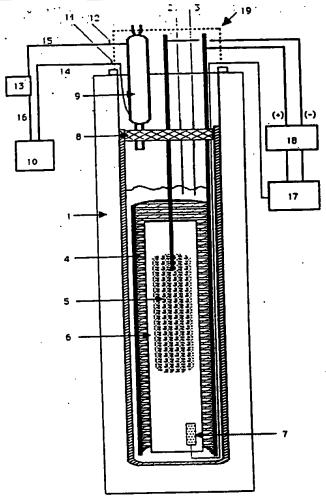


Fig. 1. The calorimeter/electrolysis cell: 1 = vacuum jacketed dewar, 2 = electrolyte thermistor, 3 = conductivity sensor, 4 = nickel anode, 5 = nickel cathode, 6 = Teflon spacer, 7 = resistor heater, 8 = Teflon cap, 9 = condenser, 10 = peristaltic pump, 11 = inlet thermistor, 12 = outlet thermistor, 13 = water reservoir, 14 = condenser inlet tubing, 15 = condenser outlet tubing, 16 = reservoir to pump tubing, 17 = power supply, function generator, power meter, 18 = oscilloscope, 19 = insulated cap.

sealed heater. The power was supplied by a constant power ($\pm 0.1\%$) supply. The voltage ($\pm 0.1\%$) and current ($\pm 0.1\%$) were recorded with a digital multimeter.

The general form of the energy balance equation for the cell in steady state is

$$0 = P_{in} + P_{xx} - P_{loss} , \qquad (3)$$

^{*}International Cryonics, Inc.

bAce Glass 7644.

cAt-Mar Glass.

^dYamato-Komatsu Coolnics Circulator CTE 24A.

^{*}Masterflex Microprocessor Pump Drive, model 7524-00.

Omega HH21.

*INCOLOY is a trademark of the Inco family of companies.

hWatlow G8A53-NT96.

Invar, model #TP 36-18.

Fluke 8600A.



Mills and Good

FRACTIONAL QUANTUM ENERGY LEVELS

where P_{in} is the input power; P_{xx} is the excess power generated (the source of this power is described later in this paper); and P_{lox} is the thermal power loss from the cell. In these experiments, the applied voltage V_{appl} was an intermittent square wave with current I only during the high-voltage interval of the cycle. Thus, the input power is given by

$$P_{in} = (V_{appl}I)Dc , \qquad (4)$$

where Dc is the duty cycle—the pulse length divided by the period.

When an aqueous solution is electrolyzed to liberate hydrogen and oxygen gases, the input power can be partitioned into two terms:

$$P_{in} = P_{ohm} + P_{gas} , \qquad (5)$$

where P_{ohm} is the ohmic power that heats the cell and P_{gas} is the power needed to produce the H_2 and O_2 gases.

$$H_2O(l) \to H_2(g) + \frac{1}{2}O_2(g)$$
 (6)

An expression for P_{ges} (= $V_{ges}I$) is readily obtained from the known enthalpy of formation of water ($\Delta H_f = -286 \text{ kJ/mol}$):

$$V_{gas} = -\frac{\Delta H_f}{\alpha F} = -\frac{-286 \times 10^3 \text{ J/mol}}{2 \times 96484 \text{ C/mol}} = 1.48 \text{ V}, (7)$$

where α is the number of moles of electrons involved in the reaction and F is the faraday constant. The net faraday efficiency of gas evolution is assumed to be unity. Thus, the ohmic power is given by

$$P_{ohm} = (V_{appl} - 1.48)IDc . (8)$$

The thermal power loss from the cell can be partitioned into two terms:

$$P_{loss} = P_{cdr} + P_{other} , (9)$$

where P_{cdr} is the power lost to the condenser and P_{other} is other power losses (e.g., hot gases that escape through the condenser before reaching thermal equilibrium; conductive heat losses from the cell to the room). Power losses to the condenser, P_{cdr} , are given by

$$P_{cdr} = vC_p(T_O - T_I) , \qquad (10)$$

where v is the flow rate of the water through the condenser; C_p is the specific heat of water at constant pressure (4.184 J/g·K); T_I is the temperature of the condenser-water at the inlet; T_O is the temperature of the condenser-water at the outlet.

Power losses other than to the condenser were determined with no electrolysis processes occurring by turning on an internal resistance heater to give a cell temperature of 50°C and inferring the efficiency eff from the ratio of the measured condenser losses to the power dissipated in the heater P_{hir} .

$$P_{htr} = V_{htr} I_{htr} \tag{11}$$

$$eff = \frac{P_{cdr}}{P_{htr}} = \frac{vC_p(T_O - T_I)}{P_{htr}} . \tag{12}$$

This method overestimates the efficiency because there is no electrolysis gas flow (which adds to the heat losses other than to the condenser).

During electrolysis, then, the output power P_{out} is given by

$$P_{out} = \frac{P_{cdr}}{eff} . {13}$$

Data points $(V_{appl}, I, Dc, v, T_O, T_I, V_{hir})$ were taken every two min. The total energy input E_{in} is the summation over n data points of input power \times time intervals Δt_i . The value P_{in} for each data point is given by Eq. (4) for the electrolysis experiments and by Eq. (11) for the resistance heater experiments:

$$E_{in} = \sum_{i}^{n} (P_{in})_i \Delta t_i . \qquad (14)$$

Similarly, the total energy output E_{out} is the summation over n data points of output power \times time intervals Δt_i , where P_{cdr} for each data point is given by Eq. (10):

$$E_{out} = \frac{1}{eff} \sum_{i}^{n} (P_{cdr})_i \Delta t_i . \qquad (15)$$

II.B. Electrolysis Methods

Each cathode was a 30.5-cm-wide \times 122-cm-long 100×100 mesh, 0.0051-cm-diam nickel 200 wire cloth^k that was sewed on one long edge with 0.38-mm-diam nickel wire to a 244-cm-long, 6.35-mm-diam nickel 200 rod¹ that also served as the lead. Each cathode was cleaned by placing it in the glass test tube liner containing 0.57 MX_2 CO₃/3% H_2 O₂, X = K for the K_2 CO₃ experiments and X = Na for the Na_2 CO₃ experiments, for 30 min and then rinsed with distilled water.

Each anode was a 20-cm-wide × 100-cm-long × 0.080-in.-thick nickel fiber mat with 0.80 g of NiO per square inch^m that was sewed on one long edge with 0.38-mm-diam nickel wire to a 244-cm-long, 6.35-mm-diam nickel 200 rod¹ that also served as the lead. The anodes were cleaned as mentioned earlier for the cathodes. The anode sheet was wrapped around the cathode and a 1-mm-thick Teflon mesh sheet was inserted to prevent contact between the cathode and the anode.

As usual in electrochemistry, measures were taken to avoid impurities in the system, especially organic substances. We note here the known problems with the

Belleville Wire Cloth Co., Inc.

Williams.

[&]quot;National Standard 80/20 Fibrex.





reproducibility of the hydrogen overpotential, which can be overcome only by ensuring the lowest possible level of impurities. The following procedures were used in order to reproduce the excess heat effect. Before starting the experiment, the electrolysis dewar liner was cleaned with Alconox and 0.1 M nitric acid and rinsed thoroughly with distilled water to remove all organic contaminants. The nickel cathode and anode were handled with rubber gloves. The electrodes were cut and folded in such a way that no organic substances were transferred to the nickel surfaces. The electrodes were assembled in the glass test tube, which was sealed with the Teflon cap; the leads penetrated the cap. The glass liner containing the electrode assembly was inserted into the dewar, and the condenser was inserted through a perforation in the Teflon cap. The electrode leads were then connected to the power supply, and electrolyte was added under electrolysis voltage. The electrodes were never left in the electrolyte without electrolysis current.

The electrolyte level was maintained to full by additions of distilled water through the condenser (to replace water lost through electrolysis). A drop in the electrolyte level of 50 ml below full was indicated by an open circuit resistance reading of two nickel leads that penetrated the Teflon cap.

A Kepco ATE-100M constant current supply was programmed at 15.0-A peak current (±0.05%) and driven by a function generatorn to produce a square wave. The time average voltage, current, and power were measured with a digital V-A-W meter.º The voltage, current, and power readings of the power meter, as well as the temperature data of the microprocessor thermometers were acquired every 2 min over the duration of the experiment by the data acquisition systeman Apple Mac II SI 5/80 with a NU bus adapter and the following G W Instruments, Inc. hardware: GWI-625 Data Acquisition Board; GWI-J2E Multiplexer; GWI-ABO Analog Breakout System; GWI-34W Ribbon cable. The peak current was determined from the voltage measurement (±0.1%) across an Ohio Semitronics CTA 101 current transducer. The peak voltage, offset voltage, duty cycle, and frequency measurements were made with an oscilloscope.p

For experiment 1, the electrolyte solution was 11 ℓ of 0.57 M aqueous K_2CO_3 (Aldrich $K_2CO_3 * \frac{3}{2}H_2O$ 99+%). The current-voltage parameters were as follows: a periodic square-wave having an offset voltage of 1.51 V (1.51 V was applied at zero current); a peak voltage of 2.10 V; a peak constant current of 15.0 A; a 15.0% duty cycle; a frequency of 1 Hz. Experiment 1 was run for 14 days. Experiment 1A was the calibration of the efficiency of heat transfer to the condenser

for Experiment 1 without electrolysis. Experiment 1A was run for 7 days.

For Experiment 2, the electrolyte solution was 11 ℓ of 0.57 M aqueous Na₂CO₃ (Aldrich Na₂CO₃ A.C.S. primary standard 99.95+%). The current-voltage parameters were as follows: a periodic square-wave having an offset voltage of 1.49 V(1.49 V was applied at zero current); a peak voltage of 2.01 V; a peak constant current of 15.0 A; a 15.0% duty cycle; a frequency of 1 Hz. Experiment 2 was run for 7 days. Experiment 2A was the calibration of the efficiency of heat transfer to the condenser for Experiment 2 without electrolysis. Experiment 2A was run for 7 days.

II.C. Calorimetry and Electrolysis Results

The calorimetry parameters, the electrolysis parameters, and the results of Experiments 1 and 2 are given in Table 1. The calorimetry parameters and the results of the efficiency determinations, Experiments 1A and 2A, are given in Table II.

For Experiment 1, the cell was disassembled and inspected after 14 days of continuous operation. This inspection showed no visible signs of a reaction between the electrodes and the electrolyte. The pH, specific gravity, concentration of K2CO3, and the elemental analysis of the electrolyte sample taken after 14 days of continuous operation were unchanged from that of the values obtained for the electrolyte sample taken before operation, see Table III. Results of elemental analysis of a sample of the nickel cathode taken before operation of the cell and a sample taken immediately after day 14, Table IV, showed that the nickel cathode had not changed chemically. Photomicrographs of a sample of the nickel cathode taken before operation and a sample taken immediately after day 14, Fig. 2, were identical, indicating that the nickel cathode had not changed physically. The water volume added to the cell per 24 h to maintain a constant fill level was 19.1 ml. The volume consumed by faraday losses (conversion to H2 and O2) is calculated to be 18.3 ml. Thus, the maintenance water volume exceeded the faraday losses by 4.4% due to loss by atomization (small water droplets swept out of the system) during electrolysis.

H.D. Discussion

The following can be seen from Tables I and II:

1. Substantial excess power was produced during the electrolysis of the aqueous potassium carbonate. The average output power of 24.6 W exceeded the average ohmic power of 1.40 W by a factor >17. During the electrolysis of the aqueous sodium carbonate, however, the output power and the ohmic power were comparable, 1.08 and 1.19 W, respectively. The excess power in the case of aqueous potassium carbonate cannot be attributed to recombination of the evolved hydrogen and

ⁿBK Precision Dynascan Corporation, model 3011.

[°]Clarke Hess Communications Research Corp., model 259 power meter Dc to 30 kHz with an IEEE-488 bus option and a 50-A shunt for Dc to 1 kHz.

PTektronix 10-MHz storage oscilloscope T912.



Mills and Good

FRACTIONAL QUANTUM ENERGY LEVELS

TABLE I

Input and Output Parameters for the Electrolysis of 0.57 M K₂CO₃ and 0.57 M Na₂CO₃*

	•	Input a	nd Output	Parameter	2 101 the 1						
		G. being	<i>V_{appl}</i> ±0.01 V	<i>P_{in}</i> ±0.10 W	$P_{ohm} \pm 0.04~\mathrm{W}$	Duration (days)	<i>E_{in}</i> ±0.12 MJ	Average P _{cd} (W)	Average Pout (W)	$\frac{P_{out}}{P_{ohm}}$	E _{out} (MJ)
Ex	periment	Solution	±0.01 ·					24.5 ± 0.4	24.6 ± 0.5	17.6	29.8 ± 0.4
	1 2	K ₂ CO ₃ Na ₂ CO ₃	2.10 2.01	4.73 4.52	1.40 1.19	14 7	5.72 2.73	1.08 ± 0.02	1.08 ± 0.02	0.91	1.31 ± 0.02

^{*}Here, $I = 15.0 \pm 0.1$ A, $Dc = 0.150 \pm 0.003$, and $eff = 0.996 \pm 0.012$.

TABLE II

The Power Input and Output Parameters for the Determination of the Efficiency of Heat Transfer from the Electrolyte to the Condenser

	of Heat	Transfer from	n the Electro	lyte to the C			
Colution	<i>V_{kir}</i> +0.01 V	I _{htr} +0.001 A	<i>P_{htr}</i> ±0.01 W	Duration (days)	<i>E_{in}</i> ±0.01 MJ	P_{cdr} ±0.10 W	Efficiency ±0.012
20Inmori	10.01 \				0.05	6.54	0.996
K ₂ CO ₃ Na ₂ CO ₃	12.34 12.34	0.532 0.531	6.56 6.55	7 7	3.96	6.53	0.997
		Solution V_{hir} $\pm 0.01 \text{ V}$ K_2CO_3 12.34	Solution V_{hir} I_{hir} $\pm 0.01 \text{ V}$ $\pm 0.001 \text{ A}$ V_{2}^{2} V_{2}^{2} V_{3}^{2} V_{4}^{2} V_{5}^{2} V_{5}^{2} V_{5}^{2}	Solution V_{hir} I_{hir} $+0.01 \text{ W}$ V_{hir} $+0.001 \text{ A}$ V_{hir} $+0.01 \text{ W}$ V_{2} V_{2} V_{3} V_{4} V_{5} V_{6}	Solution $\begin{array}{c cccc} V_{hir} & I_{hir} & P_{hir} & Duration \\ \pm 0.01 \text{ V} & \pm 0.001 \text{ A} & \pm 0.01 \text{ W} & (days) \\ \hline K_2CO_3 & 12.34 & 0.532 & 6.56 & 7 \\ & & & & & & & & & & & & & & & & &$	Solution $\begin{vmatrix} V_{hir} \\ \pm 0.01 \text{ V} \end{vmatrix} = \begin{vmatrix} I_{hir} \\ \pm 0.001 \text{ A} \end{vmatrix} = \begin{vmatrix} P_{hir} \\ \pm 0.01 \text{ W} \end{vmatrix} = \begin{vmatrix} D_{uration} \\ (days) \end{vmatrix} = \begin{vmatrix} E_{in} \\ \pm 0.01 \text{ MJ} \end{vmatrix}$ K_2CO_3 12.34 0.532 6.56 7 3.97 0.531 6.55 7 3.96	Solution $\begin{array}{c ccccccccccccccccccccccccccccccccccc$

TABLE III

Chemical Analysis of the K₂CO₃ Electrolyte of Experiment 1 Before and After 14 Days of Operation

Flame emission spectrographic analysis

Mainly

Slight trace (100 to 1000 ppm)

Very slight trace (<10 ppm)

Specific gravity = 1.062

Concentration = 0.63 M K₂CO₃

Solution pH = 11.1

TABLE IV

Flame Emission Spectrographic Analysis of the Nickel Cloth Cathode of Experiment 1 Before and After 14 Days of Operation

Mainly Trace (0.1 to 0.5%) Slight trace (100 to 1000 ppm) Very slight trace (10 to 100 ppm) Very, very, slight trace (<10 ppm)	Nickel Magnesium Copper Manganese Titanium, sodium, silver, aluminum, iron, chromium, silicon
--	---

oxygen gases because the average output power greatly exceeded the average input power (by a factor >5).

2. Substantial excess energy was produced during the electrolysis of the aqueous potassium carbonate.

The energy output of 29.8 MJ exceeded the energy input of 5.72 MJ by 24 MJ. For the electrolysis of the aqueous sodium carbonate, however, the energy output was considerably less than the energy input. This is the expected result because most of the input energy is consumed in the conversion of water to H₂ and O₂.

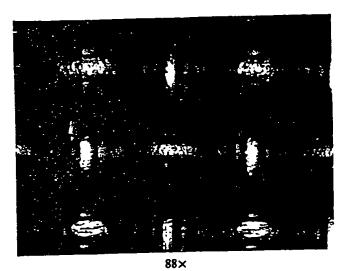
3. The excess power and energy that is produced during the electrolysis of aqueous potassium carbonate cannot be attributed to an error in the measurement of the efficiency, 0.996 (Table II). If anything, this value is too high. During electrolysis the evolving hydrogen and oxygen gases must contribute to heat losses other than to the condenser and the efficiency is, undoubtedly, closer to the ratio P_{cdr}/P_{ohm} in experiment 2; 1.08 W/1.19 W or 0.91.

Given these observations and (a) that the potassium ion and the sodium ion are chemically similar, (b) that the anion in the electrolyte was always constant (always carbonate), (c) that the composition of the nickel cathode used in the aqueous potassium carbonate electrolyte was the same before and after the electrolysis (as determined by elemental analysis), and (d) that chemical analysis for potassium ion, carbonate ion, pH, and specific gravity indicated no change in the electrolyte as a result of the electrolysis — we conclude that excess heat and energy were produced in the electrolysis of aqueous potassium carbonate and that no chemical reaction involving the electrodes or the electrolyte is the source of that excess heat.

Similar excess heat results have been reported by Mills^{4,5} and others.^{6,7}







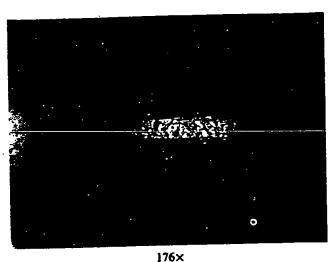


Fig. 2. Photomicrographs of metallurgical samples of the nickel 200 wire cloth (cathode) taken at day 14 of continuous operation.

ILE. Relationship to Fractional Quantum Energy Levels of Atomic Hydrogen

Excess energy during the electrolysis of water in the presence of potassium ions but not in the presence of sodium ions is consistent with an electrocatalytic, exothermic reaction whereby the electrons of hydrogen atoms are induced to undergo transitions to quantized energy levels of lower energy than the conventional "ground state." These lower energy states correspond to fractional quantum numbers as given in Eqs. (2a) and (2c). According to the novel atomic theory, 1.2 transitions of atomic hydrogen (n = 1) to these lower energy states are stimulated by the presence of resonant energy holes (energy sinks or means to remove energy) of 27.2 eV (the potential energy of a hydrogen atom in the n = 1 state; derivation in Refs. 1 and 2). Transitions

to these lower energy states occur with the release of energy and with a commensurate decrease in size of the hydrogen atom, 1,2 $r_n = na_H$. For example: the transition H(n=1) to $H(n=\frac{1}{2})$ releases 40.8 eV, see Eq. (2a), and the hydrogen radius decreases from a_H to $\frac{1}{2}a_H$. An energy hole that is an efficient catalytic system for these atomic hydrogen transitions involves the potassium ion, K^+ . The second ionization energy of potassium is 31.63 eV (vacuum level); this energy hole is too high for resonant absorption of 27.2 eV. However, K^+ releases 4.34 eV (vacuum level) when it is reduced to K. The combination of K^+ to K^{2+} and K^+ to K, then, has a net energy change of 27.28 eV (vacuum level). Thus, the stimulated transition can be written as

27.28 eV + K⁺ + K⁺ + H(
$$n = 1$$
, $r = a_H$)

$$\rightarrow K + K^{2+} + H\left(n = \frac{1}{2}, r = \frac{a_H}{2}\right) + 40.8 \text{ eV} .$$
(16)

The K atom and the K²⁺ ion will transfer an electron with the release of energy:

$$K + K^{2+} \rightarrow K^{+} + K^{+} + 27.28 \text{ eV}$$
 (17)

The overall, catalytic reaction is

$$H(n = 1, r = a_H) \rightarrow H\left(n = \frac{1}{2}, r = \frac{a_H}{2}\right) + 40.8 \text{ eV}$$
 (18)

Thus, each (n = 1) hydrogen atom that undergoes this transition releases a net of 40.8 eV. Additional catalytic transitions are possible: $n = \frac{1}{2} \rightarrow \frac{1}{3}$, $\frac{1}{3} \rightarrow \frac{1}{4}$, $\frac{1}{4} \rightarrow \frac{1}{5}$, and so on.

These transitions are, apparently, taking place on the nickel cathode during the electrolysis of aqueous potassium carbonate. Atomic hydrogen is produced at the cathode surface during the electrolysis (part of the process of reducing H₂O to H₂). The juxtaposition of the hydrogen atoms and potassium ions in the electrolyte is an ideal configuration for the catalytic transition of hydrogen to fractional quantum energy levels. The observed "excess heat" is, we suggest, a consequence of these atomic hydrogen transitions.

Neglect, for the moment that $H(n = \frac{1}{2})$ can form a diatomic molecule (called a dihydrino; Sec. V of this paper). Equation (18) predicts that 40.8 eV is released per H atom transition to the $n = \frac{1}{2}$ quantum state, which corresponds to 8 MJ/mol of H_2 . In contrast, only 286 kJ is consumed by electrolyzing 1 mol of H_2 O to produce 1 mol of H_2 , see Eq. (6). Thus, the excess energy produced in experiment 1 of 24 MJ (which also produces 14.1 mol of H_2) could be accounted for by the conversion of 21% of the hydrogen atoms from the n = 1 state to the $n = \frac{1}{2}$ state.

For sodium ions, no electrocatalytic reaction of ~27.2 eV is possible and the analogous reaction for sodium is not an appropriate catalytic reaction to produce



Mills and Good



lower energy hydrogen atoms. For example, 42.15 eV of energy is absorbed by the reverse of the reaction given in Eq. (17) where Na⁺ replaces K⁺:

$$Na^+ + Na^+ + 42.15 \text{ eV} \rightarrow Na + Na^{2+}$$
 (19)

Almost all electrolysis experiments will be similar to the case of Na₂CO₃, which does not provide an energy hole of ~27.2 eV. Only a few combinations of electrolytes/electrodes, such as the K₂CO₃ case mentioned earlier, provide an energy hole of approximately 27.2 eV, Eqs. (16), (17), and (18), and will yield excess heat.

III. IDENTIFICATION OF HYDRINOS — HYDROGEN ATOMS IN FRACTIONAL QUANTUM ENERGY LEVELS — BY XPS

The X-ray photoelectron spectroscopy (XPS) is capable of measuring the binding energy, E_b , of each electron of an atom. A photon source with energy E_h is used to ionize electrons from the sample. The ionized electrons are emitted with energy $E_{kinetic}$:

$$E_{kinetic} = E_{hr} - E_b - E_r , \qquad (20)$$

where E_r is a negligible recoil energy. The kinetic energies of the emitted electrons are measured by measuring the magnetic field strengths necessary to have them hit a detector. The values $E_{kinetic}$ and E_{hr} are experimentally known and are used to calculate E_b , the binding energy of each atom. Thus, XPS can provide an incontrovertible identification of an atom.

The binding energy of various hydrino states is easily calculated, Eq. (21) and Table V. The technique of XPS was used to search for the $n=\frac{1}{2}$ hydrino, $E_b=54.4$ eV, because it is closest in energy to the n=1 state of hydrogen and, therefore, predicted to be the most abundant:

$$E_b = \frac{1}{n^2} 13.6 \text{ eV} \qquad n = \frac{1}{2}, \frac{1}{3}, \frac{1}{4}, \dots$$
 (21)

III.A. Experimental Method

A series of XPS analyses have been made on (a) nickel cathodes used in electrolysis of aqueous potassium carbonate and aqueous sodium carbonate, (b) precursor (nickel) electrode material, and (c) various standards. The XPS was performed by the Zettlemoyer Center for Surface Studies, Lehigh University.

The instrument conditions were similar for all of the analyses. In all cases a high quality spectrum was obtained over a minimum binding energy range of 80 to 0 eV. This energy region completely covers the Ni 3p region and the region around 55 eV, which is the approximate location of the $H(n = \frac{1}{2})$ binding energy, 54.4 eV.

Each electrode was removed from the cell while maintaining the electrode overvoltage, rinsed immedi-

TABLE V

Binding Energies of the Hydrino Atom as a Function of Principal Quantum Number, Eq. (22)

п	E (eV)
<u> </u>	13.6
1	54.4
2 1	122.4
1	217.6

ately with distilled water, and dried with a N₂ stream. A piece of suitable size was cut from the electrode, mounted on a sample stub, and placed in the vacuum system. Fourteen nickel cathode samples were analyzed by XPS. Each had a slightly different history: two different laboratories ran the electrolyses; nickel foil and nickel wire were used; 99+% and 99.99% K₂CO₃ were used in the electrolyte; 99.95% Na₂CO₃ was used in the electrolyte; some were electrolyzed with simultaneous calorimetric measurements and others were not; some were analyzed immediately after electrolysis and some were stored in liquid N₂ before analysis. A brief description of the preparation conditions for each of the samples discussed in this manuscript is given as follows:

Sample 1: Nickel foil. K₂CO₃ (Alpha 99+%) electrolyte. Platinum anode. No calorimetry performed during electrolysis.

Sample 9: Nickel wire. K₂CO₃ (Puratronic 99.999%) electrolyte. Nickel anode. The K₂CO₃ electrolyte was further purified by preelectrolyzing: the electrolyte was prepared and electrolyzed with a "dummy" nickel cathode for 1 month; the "dummy" nickel electrode was then replaced with the nickel wire (sample 9). Calorimetry was performed during electrolysis. Cell was producing "excess" heat.

Sample 14: Nickel wire. Na₂CO₃ (99.95%) electrolyte. Nickel anode. The Na₂CO₃ electrolyte was further purified by preelectrolyzing as described for sample 9. Calorimetry was performed during electrolysis. Cell was not producing "excess" heat.

Specimens of pure elements and the passivation oxides of these elements that were analyzed to provide standards were not given sample numbers. The preparation conditions for these specimens are listed on the figures or given in the figure captions.



III.B. Results and Discussion

A survey spectrum of sample 1 is shown in Fig. 3. The primary elements are identified on the figure. Most of the unidentified peaks are secondary peaks or loss features associated with the primary elements. Tin is clearly a major contaminant of the surface composition.

Figure 4 shows the low binding energy range for sample 1. Again, tin is seen to be a major surface contaminant. Magnesium and chromium are also present. The broad peak labeled X is the one of most interest because it falls near the predicted binding energy for the hydrino $(n = \frac{1}{2})$, 54.4 eV. It has a full-width at halfmaximum (FWHM) of about 5.1 eV, and it is centered at a binding energy of 54.6 eV. It is important to note that binding energies in XPS are measured relative to the fermi level, not to the vacuum level. Although the agreement is remarkable, it was necessary to eliminate all other possible explanations before assigning the X feature to the hydrino. Elements that potentially could give rise to a peak near 55 eV can be divided into three categories: fine structure or loss features associated with one of the four major surface components-nickel, platinum, tin, zinc; elements that have their primary peaks in the vicinity of 55 eV-lithium; elements that have their secondary peaks in the vicinity of 55 eViron. To examine these possibilities, several experiments were performed.

Nickel. Nickel was the cathode material. Figure 5 shows an expanded scale spectrum of (unused) nickel foil material that has undergone a variety of treatments

ranging from clean metal (scraped in vacuum) to room temperature oxidation in pure O_2 (30 kPa for 15 min at room temperature) to air passivation at room temperature. Examination of this figure shows no evidence for any spectral features in the range of interest. The X feature is not from nickel or nickel oxide.

Platinum. Platinum was the anode material in the electrolysis and was found in the survey spectrum of sample 1. The Pt $5p_{3/2}$ falls at 51.4 eV—close to the 54.6 eV feature and close to the predicted binding energy of the hydrino, 54.4 eV. From a spectrum of pure platinum, it was determined that the area ratio of the Pt $5p_{3/2}$ peak to the total Pt 4f peak is 0.043. In the spectrum of sample 1, the area ratio of the X feature to the Pt 4f peaks is 0.75. The area of X is about 17 times too large to attribute the peak to platinum. Furthermore, Fig. 6 shows that the platinum peak position does not match that of feature X; platinum is eliminated.

Tin. Tin was found in the survey spectrum of sample 1. Figure 6 superimposes four spectra: sample 1, clean tin metal, thick tin oxide, and platinum metal. Clean tin metal has a bulk plasmon peak at \sim 53 eV. However, this plasmon peak is several times weaker than the plasmon at 38.7 eV. The 38.7-eV peak does not appear in the spectrum of sample 1. Thus, the X feature cannot be assigned to tin metal. The thick tin oxide spectrum shows no structure in this energy range. Comparison of the tin peaks in sample 1 and the tin oxide peaks indicate that most of the tin signal is from oxidized tin. Feature X is not from tin or tin oxide.

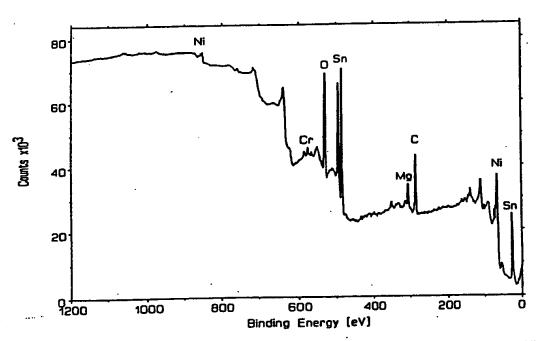


Fig. 3. The XPS survey spectrum of nickel (foil) sample 1. Primary impurity elements are identified.



Mills and Good

FRACTIONAL QUANTUM ENERGY LEVELS

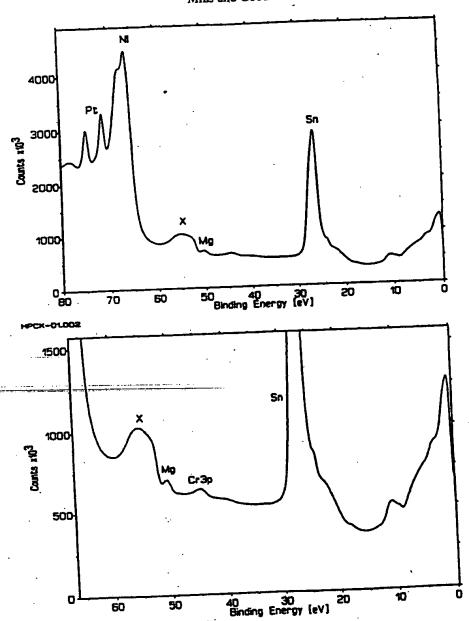


Fig. 4. The XPS spectrum of nickel sample 1 in the low-energy region. It shows feature X centered at 54.6 eV.

Zinc. Zinc was found in the survey spectrum of sample 1. Zinc was eliminated using similar arguments as those used to eliminate tin, see Fig. 7.

Lithium. First, the lithium 1s peak is several eV below that of feature X. Second, if feature X was due to lithium, the lithium would be in the form of lithium oxide and the oxide peak would be off scale. Third, the Li 1s peak is quite narrow whereas feature X is broad. Fourth, a sample of the nickel was analyzed by time-of-flight secondary ion mass spectroscopy (TOF-SIMS), and no lithium was found. Feature X is not from lithium.

Iron. Iron has a 3p peak in this region. The primary iron peak, the 2p levels, are obscured by the very strong nickel Auger lines. Spectra of clean nickel and clean iron suggest that iron concentrations of <5% (relative to nickel) should be discernible in the Fe 2p energy region. The intensity of the X feature is such that if the X feature was assigned as Fe 3p, the iron concentration would be $\sim10\%$ and the Fe 2p would be discernible from the nickel Auger lines—but it is not. Iron can also be eliminated by noting the shift in binding energy of feature X upon heating. Figure 8 overlays three spectra: sample 1, sample 1 heated to ~700 °C, and sample 1 stored in air for 26 days. Note that heating





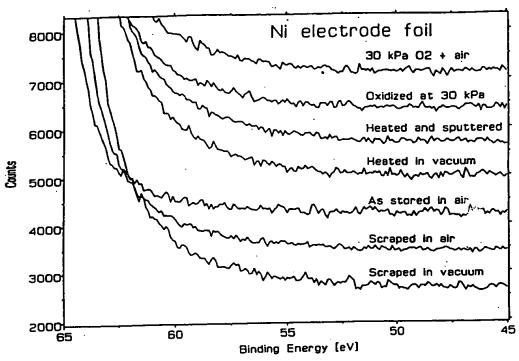


Fig. 5. The XPS spectra of unused nickel foil subjected to various conditioning treatments.

shifts the centroid to a higher binding energy. Heating under ultrahigh vacuum (UHV) conditions tends to reduce oxides and shifts peaks to lower binding energies. This is clearly evident in Fig. 9 which shows the Sn 4d spectrum of sample 1 before and after heating. If feature X is an Fe 3p peak, the expected result would have been a decrease in the binding energy upon heating. Feature X is not from iron.

To further eliminate the possibility that feature X was due to the impurities mentioned, four additional measures were taken for the conditioning of sample 9:

- 1. use of a higher purity nickel wire
- using nickel as the anode (rather than platinum, which was an impurity source in sample. 1)
- 3. use of 99.999% K₂CO₃
- 4. the potassium was preelectrolyzed (see sample 9 description earlier).

In addition, sample 9 was taken from a calorimeter/ electrolysis cell known to be producing more power than the total input power. Only two impurities were found in the survey spectrum of sample 9: potassium, suggesting that the rinsing may not have been complete, and indium at a very low level (undoubtedly from the nickel wire). This sample was also analyzed for iron by electron-dispersive spectroscopy (EDS), Auger, and TOF-SIMS at the Idaho National Engineering Laboratory (INEL)—no iron was found above the detection limit, ~0.1%. The XPS results were confirmed at INEL and Charles Evans & Associates followed by time of flight-secondary ion mass spectroscopy (TOF-SIMS) analysis of the nickel surface at Charles Evans & Associates. The Charles Evans & Associates TOF-SIMS results were negative for iron and negative for lithium. Figure 10 shows the lower binding energy portion of the spectrum for sample 9 (99.999% K₂CO₃). Feature X is closer to 57 eV, but it is very similar in shape to the feature of other nickel samples using aqueous K₂CO₃ as the electrolyte. The spectrum of sample 1 is overlaid for comparison.

As an additional control experiment, nickel from a sodium carbonate cell that was not producing excess heat was examined. Sample 14 is the exact analog of sample 9—except for the difference in electrolyte. The low energy portion of the spectrum of sample 14 (nickel cathode from Na₂CO₃ electrolysis) is shown in Fig. 11. There is only a small trace of magnesium in the region of interest. Feature X is not present and was not found on any spectrum of nickel samples from aqueous Na₂CO₃ electrolysis. Figure 12 is an overlay of the spectra of sample 9 (K₂CO₃) and sample 14 (Na₂CO₃).

In summary:

1. Nickel cathodes used in the electrolysis of aqueous K_2CO_3 (no calorimetry measurements taken) had a broad peak at 54.6 eV—close to the predicted vacuum binding energy of the hydrino $(n = \frac{1}{2})$, 54.4 eV.



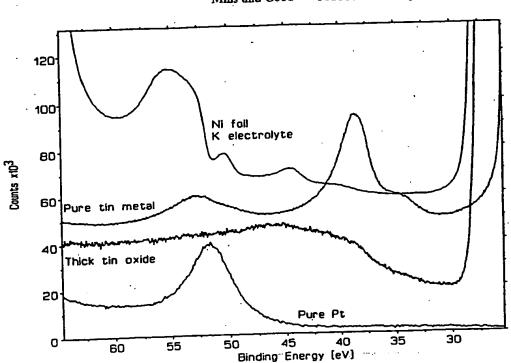


Fig. 6. Overlay of four spectra: sample 1; platinum; tin; tin oxide. These impurities have smaller binding energies than feature X.

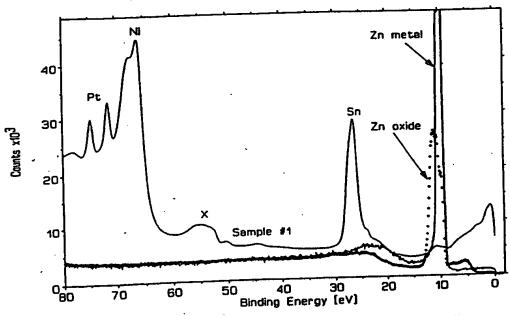


Fig. 7. Overlay of three spectra: sample 1; Zn; ZnO. These binding energies do not match the binding energy of feature X.

- 2. A nickel cathode used in the electrolysis of aqueous K_2CO_3 (99.999%) where calorimetry measurements had shown that the cell was producing more power than the total input power, also had a broad peak close to the predicted binding energy of the hydrino $(n = \frac{1}{2})$, 54.4 eV.
- 3. Clean nickel, heated nickel, and nickel under various oxidizing conditions did not have a peak in this range.
- 4. Nickel cathodes used in the electrolysis of aqueous Na₂CO₃ did not have a peak in this range.



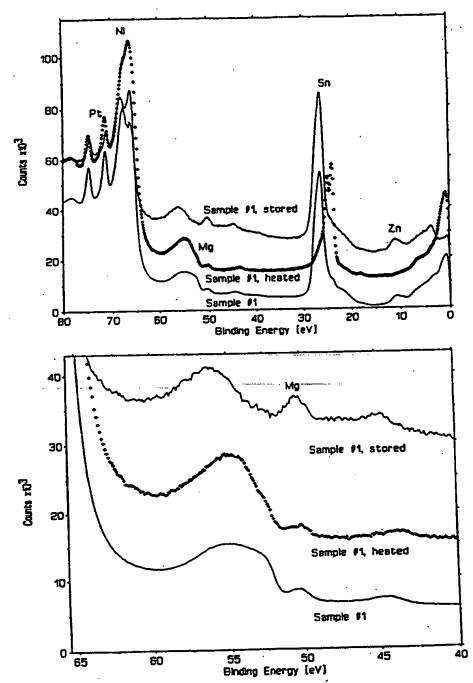


Fig. 8. Overlay spectra: sample 1; sample 1, heated; sample 1, stored. Heating shifts feature X to a higher binding energy.

5. Efforts to identify this peak as one of the surface contaminants or as another element with a primary or secondary peak in this energy range have failed.

The data are consistent with the assignment of the broad 54.6-eV peak to the hydrino, $H(n = \frac{1}{2})$. The abnormal breath of the peak is consistent with the presence of both $H(n = \frac{1}{2})$ and the corresponding molecule described in Sec. V.

IV. IDENTIFICATION OF FRACTIONAL QUANTUM ENERGY LEVELS OF HYDROGEN BY SOFT X RAYS FROM THE DARK INTERSTELLAR MEDIUM

The first soft X-ray background was detected and reported⁸ about 25 yr ago. Quite naturally, it was assumed that these soft X-ray emissions were from ionized atoms within hot gases. In a more recent paper, a grazing incidence spectrometer was designed to measure and



3

Mills and Good FRACTIONAL QUANTUM ENERGY LEVELS

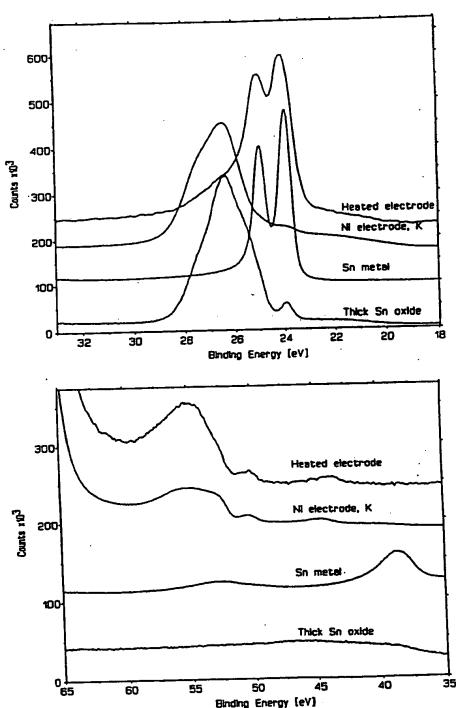


Fig. 9. Overlay spectra showing that heating under UHV tends to reduce metals and shift peaks to lower binding energies.

record the diffuse extreme ultraviolet background.⁹ The instrument was carried aboard a sounding rocket, and data were obtained between 80 and 650 Å (data points approximately every 1.5 Å). Here again, the data were interpreted as emissions from hot gases. However, the authors left the door open for some other

interpretation with the following statement from their introduction:

"It is now generally believed that this diffuse soft X-ray background is produced by a high-temperature component of the interstellar medium. However,



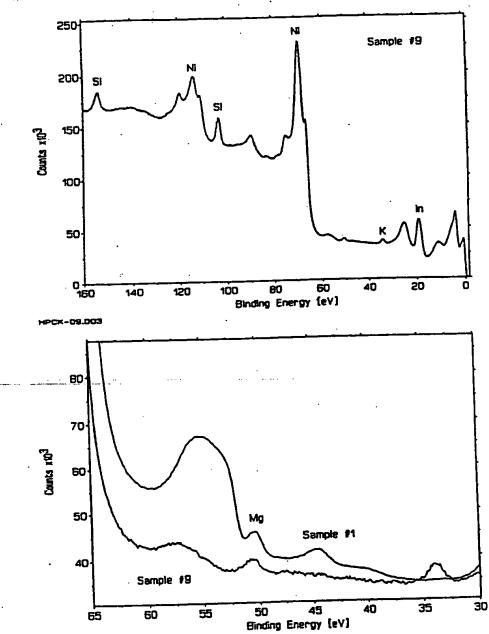


Fig. 10. Survey spectrum of nickel (wire) sample 9 (99.999% K₂CO₃). The sample is much "cleaner" than sample 1.

evidence of the thermal nature of this emission is indirect in that it is based not on observations of line emission, but on indirect evidence that no plausible nonthermal mechanism has been suggested which does not conflict with some component of the observational evidence."

The authors also state that "if this interpretation is correct, gas at several temperatures is present." Specifically, emissions were attributed to gases in three ranges: $5.5 < \log T < 5.7$; $\log T = 6$; $6.6 < \log T < 6.8$.

The explanation proposed herein of the observed dark interstellar medium spectrum hinges on the possibility of energy states below the n = 1 state, as given by Eqs. (2a) and (2c). Thus, transitions of the type,

$$\Delta E = 13.60 \left(\frac{1}{n_f^2} - \frac{1}{n_i^2} \right) \text{eV} \qquad n = 1, \frac{1}{2}, \frac{1}{3}, \frac{1}{4}, \dots$$

$$n_f > n_f \qquad (22)$$

ought to occur. The wavelength is related to ΔE by

FUSION TECHNOLOGY VOL. 28 NOV. 1995



Mills and Good

FRACTIONAL QUANTUM ENERGY LEVELS

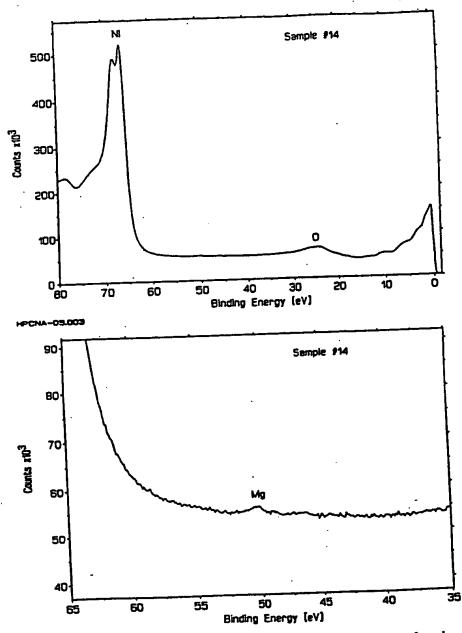


Fig. 11. The XPS spectrum of sample 14 (Na₂CO₃). Feature X is not found.

$$\lambda \text{ (in Å)} = \frac{1.240 \times 10^4}{\Delta E \text{ (in eV)}}$$
 (23)

The energies and wavelengths of several of these proposed transitions are shown in Table VI. Note that the lower energy transitions are in the soft X-ray region.

IV.A. The Data and Data Interpretation

In their analysis of the data, Labov and Bowyer⁹ established several tests to separate emission features from the background. There were seven features (peaks)

that passed their criteria. The wavelengths and other aspects of these peaks are shown in Table VII. Peaks 2 and 5 were interpreted by Labov and Bowyer as instrumental second-order images of peaks 4 and 7, respectively. Peak 3, the strongest feature, is clearly a helium resonance line: He(1s¹2p¹ \rightarrow 1s²). At issue here, is the interpretation of peaks 1, 4, 6, and 7. We suggest that peaks 4, 6, and 7 arise from the $1 \rightarrow \frac{1}{2}, \frac{1}{2} \rightarrow \frac{1}{3}$, and $\frac{1}{4} \rightarrow \frac{1}{3}$ hydrogen atoms transitions given by Eq. (22). We also suggest that peak 1 arises from helium scattering of peak 4. That is, the $1 \rightarrow \frac{1}{2}$ transition yields a 40.8 eV photon (303.9 Å). When this photon strikes He





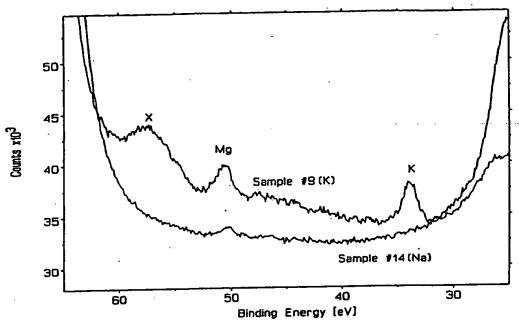


Fig. 12. Overlay of spectra of sample 9 (K₂CO₃) and sample 14 (Na₂CO₃) in the region of interest. Feature X is found only in the nickel from the K₂CO₃ electrolysis.

(1s2), 21.2 eV is absorbed in the excitation to He (1s¹2p¹). This leaves a 19.6 eV photon (632.6 Å), peak 1. For these four peaks, the agreement between the predicted values, Table VII, and the experimental values is remarkable.

One argument against this new interpretation of the data is that the transition $\frac{1}{3} \rightarrow \frac{1}{4}$ is missing—predicted at 130.2 A by Eqs. (22) and (23). This missing peak cannot be explained into existence, but a reasonable rationale can be provided for why it might be missing from these data. The data obtained by Labov and Bowyer are outstanding when the region of the spectrum, the time allotted for data collection, and the logistics are considered. Nonetheless, it is clear that the signal-tonoise ratio is low and that considerable effort had to be expended to differentiate emission features from the background. This particular peak, $\frac{1}{3} \rightarrow \frac{1}{4}$, is likely to be

TABLE VI **Energies of Several Fractional-State Transitions**

n _i	ng	Δ <i>E</i> (eV)	λ (Å)
1	1	40.80	303.9
į	li	68.00	182.4
į	į	95.20	130.2
į	li	122.4	101.3
į	į	149.6	82.9

only slightly stronger than the $\frac{1}{4} \rightarrow \frac{1}{3}$ peak (the intensities, Table VII, appear to decrease as n decreases), which has low intensity. Labov and Bowyer supplied their data to us (wavelength, count, count error, background, and background error). The counts minus background values for the region of interest, 130.2 \pm 5 A, are shown in Table VIII (the confidence limits for the wavelength of about ±5 Å are the single-side 1 confidence levels and include both the uncertainties in the fitting procedure and uncertainties in the wavelength calibration). Note that the largest peak (count minus background) is at 129.64 Å and has a counts minus background = 8.72. The counts minus background for the strongest signal of the other hydrino transitions are: n = 1 to $n = \frac{1}{2}$, 20.05; $n = \frac{1}{2}$ to $n = \frac{1}{3}$, 11.36; $n = \frac{1}{4}$ to $n = \frac{1}{3}$, 10.40. Thus, there is fair agreement with the wavelength and the strength of the signal. This, of course, does not mean that there is a peak at 130.2 A. However, it is not unreasonable to conclude that a spectrum with a better signal-to-noise ratio might uncover the missing peak.

Another, and more important, argument against this new interpretation is the fact that the proposed fractional-quantum-state hydrogen atoms have not been detected before. There are several explanations. First, the transitions to these fractional states must be forbidden or must have very high activation energies otherwise all hydrogen atoms would quickly go to these lower energy states (we estimate the transition probability, based on the Labov and Bowyer data, to be between 10^{-15} and 10^{-17} s⁻¹). Second, the number of hydrogen atoms (n = 1) and the hydrogen-atom density





Mills and Good FRACTIONAL QUANTUM ENERGY LEVELS

TABLE VII

Emission Features of the LaBov and Bowyer Spectrum and Peak Assignments

						Predicted λ
Peak	λ (Å)	Confidence Limit (Å)	Intensity (photon/cm ² ·s·sr)	Assignment ⁹	Assignment ⁵	(Ref. 5)
1	- 634.7	-4.7 to +4.7	19 000	O^{4+} ; $\log T = 5.5$	Helium scattering of 303.9 line (peak 4)	632.6
2	609.1	-4.9 to +4.9	Second order	Second order of 299.7	Second order of 303.9 line	607.8
3	582.1	-4.5 to +4.5	70 400	Helium resonance $(1s^12p^1 \rightarrow 1s^2)$	Helium resonance $(1s^12p^1 \rightarrow 1s^2)$	584
4 5 6	299.7 200.4 - 178.1	-6.0 to +5.9 -4.4 to +5.3 -4.6 to +5.1	2 080 Second order i 030	He ⁺ ; (2p ¹ to 1s ¹) Second order of 98.7 line Fe ⁹⁺ and Fe ¹⁰⁺ ; log $T = 6$	$n = 1$ to $n = \frac{1}{2}$ Second order of 101.3 line $n = \frac{1}{2}$ to $n = \frac{1}{3}$	- 303.9 202.6 - 182.4
7	_ 98.7	-5.3 to +4.2	790	Fe ¹⁷⁺ and Fe ¹³⁺ ; $\log T = 6.6 \text{ to } 6.8$	$n=\frac{1}{4} \text{ to } n=\frac{1}{3}$	_ 101.3

under any conditions on Earth is exceeding low. The combination of extremely low population and extremely low transition probability makes the detection of these transitions especially difficult. Third—hydrogen atoms in these lower energy states would be very stable, diffuse readily, and have higher (thermal) velocities than helium, which readily escapes from the planet. Fourth, this is a very troublesome region of the electromagnetic spectrum for detection because these wavelengths are significantly attenuated by the atmosphere. Last, no one previously has been actively searching for these transitions.

IV.R. Discussion

mn-

We have given an alternative explanation for the soft X-ray emissions of the dark interstellar medium observed by Labov and Bowyer⁹ based on the proposed existence of fractional-quantum-energy-level hy-

TABLE VIII

Data⁹ Near the Predicted ¼ → ¼ Transition⁴

λ (Å)	Counts	Background	Counts — Background
125.82	26	21.58	4.42
127.10	22	21.32	0.68
128.37	18	19.50	-1.50
129.64	29	20.28	8.72
130.90	18	19.76	-1.76
132.15	20	19.50	0.50
133.41	19	19.50	-0.50
134.65	19	20.80	-1.80

*130.2 Å.

drogen atoms, hydrinos. The agreement between the experimental data and the values predicted for the proposed transitions is remarkable. These results and the interpretation presented herein are consistent with the data and interpretations presented in the other sections of this manuscript—XPS spectrum of the $n=\frac{1}{2}$ hydrino; excess heat from the electrolysis of aqueous potassium carbonate; and mass spectral data for the dihydrino molecule, Sec. V, which follows.

V. IDENTIFICATION OF THE DIHYDRINO MOLECULE

When hydrogen atoms bind to metals, they demonstrate a high degree of mobility, as shown by electron energy loss spectroscopy (EELS) (Ref. 10). A mobile hydrogen atom can bind with a neighboring hydrogen atom to form a diatomic molecule, H_2 ; this happens routinely in the electrolysis of aqueous solutions. We have shown earlier that the $n=\frac{1}{2}$ hydrino is produced with the release of energy (Sec. II) during the electrolysis of aqueous potassium carbonate and that the $n=\frac{1}{2}$ hydrino is found on the nickel surface (Sec. III). Thus, it is reasonable to predict that dihydrino molecules should be produced from these $n=\frac{1}{2}$ hydrinos.

Specifically, it is known that two hydrogen atoms, H(n = 1), can react to form a diatomic molecule, $H_2(n = 1)$, with a bond energy of 4.75 eV:

$$2H(n = 1; r = a_H) \rightarrow H_2[n = 1; r_e = \sqrt{2}a_H]$$
, (24)

where r_e is the internuclear distance. Here, we assert that two $n = \frac{1}{2}$ hydrino atoms can similarly react to form a dihydrino molecule²:

$$2H\left(n=\frac{1}{2}; r=\frac{a_{H}}{2}\right) \rightarrow H_{2}\left[n=\frac{1}{2}; r_{e}=\frac{\sqrt{2}}{2} a_{H}\right].$$
 (25)





The bond energy for the dihydrino molecule should be much larger than the bond energy for the dihydrogen molecule-certainly more than twice as large.

Furthermore, dihydrogen molecules form dihydrogen molecular ions when they are singly ionized. The ionization energy is 15.46 eV.

$$H_2[n=1; r_e = \sqrt{2}a_H] \rightarrow H_2^+[n=1; r_e = 2a_H] + e^-$$
 (26)

Similarly, dihydrino molecules should form dihydrino molecular ions when they are singly ionized2:

$$H_{2}\left[n = \frac{1}{2}; r_{e} = \frac{\sqrt{2}}{2} a_{H}\right]$$

$$\rightarrow H_{2}^{+}\left[n = \frac{1}{2}; r_{e} = \frac{2a_{H}}{2}\right] + e^{-}. \tag{27}$$

The ionization energy for the dihydrino molecule should be much larger than the ionization energy for the dihydrogen molecule (certainly more than the ionization of the $n = \frac{1}{2}$ hydrino, 54.4 eV).

Thus, we explored the possibility of using mass spectroscopy to discriminate $H_2(n=1)$ from $H_2(n=\frac{1}{2})$ on the basis of the large difference between the ionization energies of the two species.

V.A. Sample Collection and Preparation

One liter of electrolytic gases was collected from a potassium carbonate electrolysis cell producing excess power (experiment 14 of Ref. 5) in a high-vacuum gas collection bulb. One litre of electrolytic gases from an identical sodium carbonate electrolysis cell that showed no excess heat was collected similarly. These electrolysis gases were cryofiltered according to the method of Bush¹¹ and collected in two-port 250-ml high-vacuum sample bulbs. A schematic of the cryofiltration apparatus appears in Fig. 13. There were three additional control samples:

- 1. a sample bulb filled with molecular hydrogen (not cryofiltered)
- 2. a sample bulb filled with molecular hydrogen which had been cryofiltered
- 3. for a background comparison, a bulb with gases collected from the cryofilter in the absence of any sample introduction (referred to as cryofiltered alone in the following discussion).

The (predicted) dihydrino molecules were also enriched in the electrolytic gases by partial combustion. About 1650 ml of the electrolysis gases was collected in a mylar balloon from a potassium carbonate electrolysis cell producing excess power (experiment 14 of Ref. 5). The gas was transferred into an elastomer bladder in three aliquots. The bladder contained a wetted spark plug, which was activated after the transfer of each aliquot causing an explosion of the gas contents and combustion of most of the gaseous contents. The volume of the bladder following three combustions was 70 ml. These gases were not cryofiltered and are referred to as postcombustion gases in the following discussion.

V.B. Mass Spectroscopy

The mass spectroscopy was performed by Schrader Analytical and Consulting Laboratories, Inc. using an AEI MS 30 with a VG 7070 source set at a sensitivity

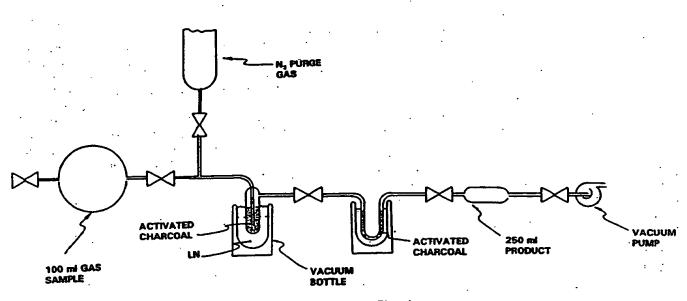


Fig. 13. Schematic of the cryofiltration apparatus.





Mills and Good

FRACTIONAL QUANTUM ENERGY LEVELS

of 700. The ionization energy was calibrated to within ± 1 eV.

Mass spectra of the following (a) cryofiltered gases from potassium carbonate electrolysis cells, (b) cryofiltered gases from sodium carbonate electrolysis cells, (c) uncryofiltered molecular hydrogen, (d) cryofiltered molecular hydrogen, and (e) gases from the cryofilter alone were taken. The intensity of the m/e = 1 and m/e = 2 peaks was recorded while varying the ionization potential (IP) of the mass spectrometer. The volume of sample gas injected into the mass spectrometer at each IP setting was made identical by evacuating the connection between the sample and the stopcock of the spectrometer, opening the evacuated volume to the sample vessel, closing the sample stopcock, and then opening the stopcock to the spectrometer. The entire range of masses through m/e = 70 was measured following the determinations at m/e = 1 and m/e = 2.

Mass spectra of the postcombustion gases were taken at IP = 70 eV for the entire range of masses through m/e = 70. Then, high resolution [0.001 atomic mass unit (AMU)] magnetic sector mass spectroscopy was performed on the postcombustion gas sample and the uncryofiltered molecular hydrogen at a nominal mass to charge ratio of 2 at 25 eV [above the ionization energy of molecular hydrogen yet below the expected ionization energy of $H_2(n = \frac{1}{2})$] and at 70 eV [above the expected ionization energy of $H_2(n = \frac{1}{2})$]. The data were displayed on an oscilloscope (see footnote p on p. 1700). The scan speed and oscilloscope sweep speed were adjusted so that mass differences of 0.001 AMU would give distinctly separate peaks, resolved nearly to baseline. The gas sample pressure was adjusted to provide peaks of essentially the same intensity of ~0.5 V from the baseline to the peak. Photographs of the oscilloscope traces of the m/e = 2 ion were made under the following conditions: resolution, 2000; energy, 25 and 70 eV; scan speed, 30 s/decade; scope speed, 5 ms/division; scope voltage setting, 0.2 V/division.

V.C. Results and Discussion

In all samples, the only peaks detected in the mass range m/e = 3 to 70 were consistent with trace air contamination (argon, nitrogen, oxygen, water vapor).

The results of the mass spectroscopic analysis (m/e = 2) with varying ionization potential of molecular hydrogen and various cryofiltered gases are given in Table IX. For molecular hydrogen, not cryofiltered, there is no signal intensity at IP = 13 eV (less than the ionization energy of H2, 15.46 eV) and there is a significant signal intensity at 28 eV. Above 28 eV the signal intensity increases (roughly) linearly with IP. In independent experiments, it was determined that the relative signal intensity [for example, the ratio (signal intensity at IP = 79 eV)/(signal intensity at IP = 23 eV)] of molecular hydrogen was independent of mass spectrometer sensitivity and sample pressure. The signal intensity for the uncryofiltered molecular hydrogen was much greater than the signal intensity for all of the cryofiltered samples because, as expected, the number of molecules successfully passing through the cryofilter was quite small. Note, for example, that the cryofilter removes essentially all of the molecular hydrogen (Table IX, H2 cryofiltered). The cryofilter itself does not release any unusual species with a mass to charge ratio of 2 (Table IX, cryofilter alone).

The greatest signal intensity for any of the cryofiltered samples occurs with the gases from the K_2CO_3 cell at IP = 79 eV. There is also a slightly elevated signal with the gases from the Na_2CO_3 cell at IP = 79 eV. Both of these samples had a significant m/e = 18 water peak. The base peak for water vapor is at m/e = 18, but water vapor also gives peaks at m/e = 1 and m/e = 2. Independent experiments show that the ratio (at 79 eV) (signal intensity m/e = 1)/(signal intensity m/e = 2) is 6 for water vapor. The data in Table X show that the ratio of the signal intensities (at 79 eV), m/e = 1 to m/e = 2, is 0.150/0.025 or 6.0 for the gases from the

TABLE IX

Mass Spectroscopic Analysis of Molecular Hydrogen and Cryofiltered Samples with Varying Ionization Potential at m/e = 2

	,		Intensity of Signal		<u> </u>
Ionization Potential (eV)	H ₂ Not Cryofiltered	H ₂ Cryofiltered	Gases from Cryofilter Alone	Gases from Na ₂ CO ₃ Cell	Gases from K ₂ CO ₃ Cell
13 23 45 79	0.0 2.5 5.4 6.8	0.000 0.000 0.005 0.005	0 0 0	0.000 0.004 0.000 0.025	0.000 0.025 0.020 0.24



 Na_2CO_3 cell. Thus, the signal intensity at m/e = 1 and m/e = 2 (1P = 79) with the Na₂CO₃ gases is from residual water vapor in the vacuum system. Note, however, that this ratio for the gases from the K2CO3 cell is 0.060/0.24 or 0.25-much too low to be from water vapor. Assuming that all of the signal intensity at m/e = 1 is from water vapor, the contribution of water vapor to the m/e = 2 peak should be 0.060/6 or 0.01 - negligible in comparison to the observed signal of 0.24. Thus, the large increase in signal intensity at m/e = 2 between IP = 45 eV and IP = 79 (0.020 to 0.24, a factor of 12) for cryofiltered gases from the potassium carbonate electrolysis does not appear to be caused by molecular hydrogen or water vapor. A species with a much higher ionization potential than molecular hydrogen, somewhere between 45 to 79 eV, is present. Systematic scans while varying the IP show that the onset of the ionization of this species is at 63 eV:

Photographs of the high resolution magnetic sector mass spectra of the uncryofiltered molecular hydrogen sample (m/e = 2) at 25 eV and at 70 eV are given in Fig. 14. Both peaks have a typical shape. Photographs of the high resolution magnetic sector mass spectra of the postcombustion gases (m/e = 2) at 25 eV and 70 eV are given in Fig. 15. Notice that there is one peak at 25 eV and that this peak has a typical shape. However, there are two peaks at 70 eV. Only a limited number of "traditional" m/e = 2 peaks are possible – H₂⁺, D⁺, He²⁺ – and only one of these could cause a peak at m/e = 2 in these samples:

- 1. $H_2^+(n=1)$ causes one of the peaks.
- 2. Deuterium D+ is eliminated because (a) light water, not heavy water, was used and (b) no $HD^+(g)$, m/e = 3, peak was observed.
- 3. He^{2+} was eliminated because no He^{+} , m/e = 4, peak was observed.

Thus, some other species is causing the second peak at 70 eV. It is likely that $H_2^+(n=\frac{1}{2})$ would be ionized at 70 eV and that it would not be ionized at 25 eV, but the mass of $H_2^+(n=\frac{1}{2})$ would only be ~100 eV (or 1 × 10^{-7} AMU) less than $H_2^+(n=1)$ – not distinguishable on the basis of mass even with high resolution mass spectroscopy. We note, however, that the magnetic moment of the $H_2^+(n=\frac{1}{2})$ ion has been predicted to have a larger magnetic moment than the $H_2^+(n=1)$ ion.² It is likely, then, that the two molecules would have different flights in the magnetic sector (MS). We assert, therefore, that the partial combustion of the evolved gases from the electrolysis of aqueous K2CO3 yields unreacted, molecular hydrogen molecules and unreacted, dihydrino molecules. In the mass spectrum, the $H_2^+(n=1)$ peak is present at 25 eV and at 70 eV. The harder-to-ionize dihydrino molecule, however, is not present at 25 eV and $H_2^+(n=\frac{1}{2})$ appears only at the higher IP, 70 eV. The possibility of artifact was

Mass Spectroscopic Analysis of Cryofiltered Gases from Na₂CO₃ and K₂CO₃ Cells with Varying Ionization Potential at m/e = 1 and 2

	Intensity of Signal					
Ionization	Na ₂ CO at Ma Charge	from O3 Cell ass to e Ratio (e)	Gases from K ₂ CO ₃ Cell at Mass to Charge Ratio (m/e)			
Potential (eV)	1	2	1	2		
13 23 45 79	0.000 0.014 0.040 0.150	0.000 0.004 0.000 0.025	0.000 0.010 0.024 0.060	0.000 0.025 0.020 0.24		

ruled out by studying normal hydrogen over a range of pressures and ionization energies. No double peaks (m/e = 2) were observed.

We conclude that hydrinos are produced on or near the cathode surface as hydrogen atoms are stimulated to relax to quantized potential energy levels below that of the "ground state" (see Sec. II.E) and that two hydrinos, $H(n = \frac{1}{2})$, react to form the lower energy dihydrino molecule.

V.D. Alternative Explanations of Related Experiments by Other Researchers

The internuclear distance of the dihydrino molecule is a factor of 2 shorter than the internuclear distance of the normal hydrogen molecule.2 The same ratio applies when deuterium nuclei replace the protons. In accordance with the predictions of Fukai 12 relating fusion reaction rates to internuclear separation, production of the dideutrino molecule (hydrino molecule with the protons replaced by deuterons) could account for the observation of detectable levels of tritium over long duration electrolysis experiments. 1,13,14

We have reported previously our interpretation⁵ that Miles 11,15-17 observed the dideutrino molecule as a species with a mass to charge ratio of four and having a higher ionization potential than normal molecular deuterium. Miles was using mass spectroscopy to analyze the cryofiltered gases evolved from excess power producing electrolysis cells (palladium cathode and a LiOD/D2O electrolyte; a catalytic couple of 27.54 eV). And, we have previously reported our interpretation5 that Yamaguchi 18,19 observed the dideutrino molecule as a large shoulder on the D_2 peak and a split D_2 peak during the high resolution (0.001 AMU) quadrupole mass spectroscopic analysis of the gases released from



Mills and Good

FRACTIONAL QUANTUM ENERGY LEVELS

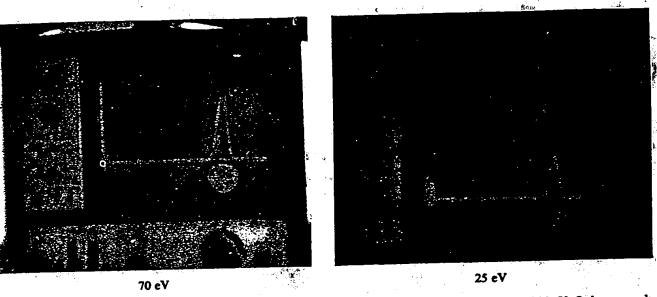


Fig. 14. The high resolution magnetic sector mass spectra at m/e = 2 of molecular hydrogen at 25 and 70 eV. Only one peak is found: $H_2(n = 1)$ ionization.

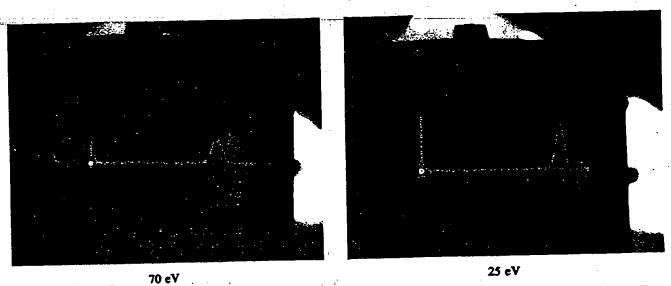


Fig. 15. The high resolution magnetic sector mass spectra at m/e = 2 of the postcombustion gases at 25 and 70 eV. Two peaks are found at the higher IP: $H_2(n = 1)$ ionization and $H_2(n = \frac{1}{2})$ ionization. The two peaks were about of the same intensity in this sample. In other (similarly prepared) samples, however, the two peaks had different intensities.

excess heat producing, deuterium-loaded, oxide-coated palladium sheets (a catalytic couple of 27.2 eV).

VL SUMMARY

The complete theory which predicts fractional quantum energy levels of hydrogen and the exothermic reaction whereby lower-energy hydrogen is produced is given elsewhere.^{1,2}

Excess power and heat were observed during the electrolysis of aqueous potassium carbonate. Flow calorimetry of pulsed current electrolysis of aqueous potassium carbonate at a nickel cathode was performed in a single-cell dewar. The average power out of 24.6 W exceeded the average input power (voltage times current) of 4.73 W by a factor >5. The total input energy (integration of voltage times current) over the entire duration of the experiment was 5.72 MJ; whereas, the total output energy was 29.8 MJ. No excess heat was





observed when the electrolyte was changed from potassium carbonate to sodium carbonate. The source of heat is assigned to the electrocatalytic, exothermic reaction whereby the electrons of hydrogen atoms are induced to undergo transitions to quantized energy levels below the conventional "ground state." These lower energy states correspond to fractional quantum numbers: $n = \frac{1}{2}, \frac{1}{3}, \frac{1}{4}, \dots$ Transitions to these lower energy states are stimulated in the presence of pairs of potassium ions (K+/K+ electrocatalytic couple) which provide 27.2-eV energy sinks.

We report the identification of the $n = \frac{1}{2}$ hydrogen atom, $H(n = \frac{1}{2})$. Samples of the nickel cathodes of aqueous potassium carbonate electrolytic cells and aqueous sodium carbonate electrolytic cells were analyzed by XPS. A broad peak centered at 54.6 eV was present only in the cases of the potassium carbonate cells. The binding energy (in vacuum) of $H(n = \frac{1}{2})$ is 54.4 eV. Thus, the theoretical and measured binding energies for $H(n = \frac{1}{2})$ are in excellent agreement.

Further experimental identification of hydrinos—down to $H(n=\frac{1}{2})$ —can be found in our alternative explanation for the soft X-ray emissions of the dark interstellar medium observed by Labov and Bowyer. We believe that the agreement between the experimental spectrum and the energy values predicted for the proposed transitions is remarkable.

We have identified the reaction product of two $H(n=\frac{1}{2})$ atoms, the dihydrino molecule, by mass spectroscopy. The mass spectrum of the cryofiltered gases evolved during the electrolysis of a light water K2CO3 electrolyte with a nickel cathode demonstrated that the dihydrino molecule, $H_2(n = \frac{1}{2})$, has a higher ionization energy, about 63 eV, than normal molecular hydrogen, $H_2(n = 1)$, 15.46 eV. The high resolution (0.001 AMU) magnetic sector mass spectroscopic analysis of the postcombustion gases indicated the presence of two peaks of nominal mass, two at 70 eV, and one peak at 25 eV. The same analysis of molecular hydrogen indicates only one peak at 25 eV and one peak at 70 eV. In the case of the postcombustion sample at 70 eV, one peak was assigned as the hydrogen molecular ion peak, $H_2^+(n=1)$, and one peak was assigned as the dihydrino molecular peak, $H_2^+(n = \frac{1}{2})$.

Based on our analysis⁵ of the raw data of Miles^{11,15-17} and Yamaguchi, ^{18,19} we interpret their results as evidence of the dideutrino, $D_2(n = \frac{1}{2})$; heavy hydrogen, ²H, was used in their experiments, not ¹H.

ACKNOWLEDGMENTS

Special thanks to the following: G. Simmons and A. Miller of Lehigh University who performed the XPS analysis; J. DeFever of Schrader Analytical and Consulting Laboratories, Inc., who performed the mass spectroscopy; S. LaBov and S. Bowyer for providing spectral data; J. Farrell, Department of Chemistry, Franklin & Marshall College, for assistance in preparing this manuscript; D. Backman, De-

partment of Physics and Astronomy, Franklin & Marshall College, for his many suggestions and, in particular, for his help in deriving the transition probability from the Labov and Bowyer data.

REFERENCES

- 1. R. MILLS, Unification of Spacetime, the Forces, Matter, and Energy, Technomics Publishing Company, Lancaster, Pennsylvania (1992).
- 2. R. MILLS, "Energy/Matter Conversion Methods and Structures," U.S. Patent Application (Aug. 16, 1993).
- 3. H. A. HAUS, Am. J. Phys., 54, 1126 (1986).
- 4. R. L. MILLS and S. P. KNEIZYS, "Excess Heat Production by the Electrolysis of an Aqueous Potassium Carbonate Electrolyte and the Implications for Cold Fusion," Fusion Technol., 20, 65 (1991).
- 5. R. MILLS, W. GOOD, and R. SHAUBACH, "Dihydrino Molecule Identification," Fusion Technol., 25, 103 (1994).
- 6. V. NONINSKI, "Excess Heat During the Electrolysis of a Light Water Solution of K₂CO₃ with a Nickel Cathode," Fusion Technol., 21, 163 (1992).
- 7. R. NOTOYA and M. ENYO, *Proc. 3rd Annual Conf. Cold Fusion*, Nagoya, Japan, October 21-25, 1992, p. 421, H. IKEGAMI, Ed., Universal Academy Press, Inc., Tokyo (1992).
- 8. S. BOWYER, G. FIELD, and J. MACK, Nature, 217, 32 (1968).
- 9. S. LABOV and S. BOWYER, Ap. J., 371, 810 (1991).
- 10. R. NIEMINEN, Nature, 365, 289 (1992).
- B. F. BUSH, J. J. LAGOWSKI, M. H. MILES, and G. S. OSTROM, J. Electroanal. Chem., 304, 271 (1991).
- 12. Y. FUKAI, "The ABC's of the Hydrogen-Metal System," Proc. 3rd Annual Conf. Cold Fusion, Nagoya, Japan, October 21-25, 1992, p. 265, H. IKEGAMI, Ed., Universal Academy Press, Inc., Tokyo (1992).
- 13. M. FLEISCHMANN, S. PONS, W. ANDERSON, L. JUN LI, and M. HAWKINGS, J. Electroanal. Chem., 287, 293 (1990).
- 14. E. STORMS and C. TALCOTT, "Electrolytic Tritium Production," Fusion Technol., 17, 680 (1990).
- 15. M. H. MILES, B. F. BUSH, G. S. OSTROM, and J. J. LAGOWSKI, *The Science of Cold Fusion: Proc. 2nd Annual Conf. Cold Fusion*, Como, Italy, June 29-July 4, 1991, T. BRESSANI, E. DEL GIUDICE, and G. PREPARATA,





Mills and Good

FRACTIONAL QUANTUM ENERGY LEVELS

Eds., Vol. 33, p. 363, in Conf. Proc. Italian Physical Society, Bologna (1992).

16. M. H. MILES, R. A. HOLLINS, B. F. BUSH, J. J. LAGOWSKI, and R. E. J. MILES, J. Electroanal. Chem., 346, 99 (1993).

17. M. H. MILES and B. F. BUSH, Proc. 3rd Annual Conf. Cold Fusion, Nagoya, Japan, October 21-25, 1992, p. 189, H. IKEGAMI, Ed., Universal Academy Press, Inc., Tokyo (1992).

18. E. YAMAGUCHI and T. NISHIOKA, "Direct Evidence for Nuclear Fusion Reactions in Deuterated Palladium," *Proc. 3rd Annual Conf. Cold Fusion*, Nagoya, Japan, October 21-25, 1992, p. 179, H. IKEGAMI, Ed., Universal Academy Press, Inc., Tokyo (1992).

19. E. YAMAGUCHI and T. NISHIOKA, Personal Communication regarding helium-4 production from deuterated palladium at low energies, Nipon Telegraph & Telephone Basic Research Laboratories (1992).

Randell L. Mills (BA, chemistry, Franklin and Marshall College, 1982; MD, Harvard University, 1986) developed magnetic susceptibility imaging for high-resolution internal vascular images, the MIRAGE cancer therapy, and the Luminide drug delivery molecule. He is founder of Mills Technology, HydroCatalysis Power Corporation, and Luminide Pharmaceutical Corporation.

William R. Good (BS, chemistry, Franklin and Marshall College) has been studying hydrogen emission by catalytic thermal electronic relaxation. He is currently research director at HydroCatalysis Power Corporation.

THIS PAGE BLANK (USPTO)

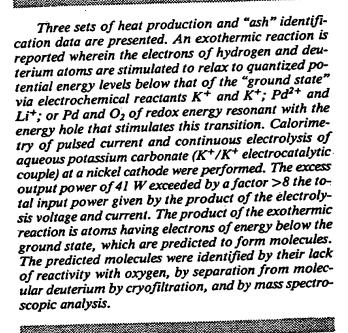


DIHYDRINO MOLECULE IDENTIFICATION

RANDELL L. MILLS and WILLIAM R. GOOD HydroCatalysis Power Corporation, Greenfield Corporate Center 1860 Charter Lane, Lancaster, Pennsylvania 17601

ROBERT M. SHAUBACH Thermacore, Inc. 780 Eden Road, Lancaster, Pennsylvania 17601

Received June 16, 1993
Accepted for Publication July 27, 1993



HYDROCATALYSIS POWER CORPORATION THEORY

Quantum mechanics based on the Schrödinger equation assumes that atomic-sized particles obey different physical laws than macroscopic objects, which behave classically. To overcome the shortcomings of quantum mechanics, physical laws that are exact on all scales were sought. Rather than endowing the electron with a wave nature as suggested by the Davisson-Germer experiment and fabricating a set of associated postulates and mathematical rules for wave operators, we derived a new theory from first principles. In both theories, solutions to the classical wave equation were sought, and the solution of the equation of the electron is time harmonic. But, the novel theory departs from the usual theory in the solutions of the spatial func-



NUCLEAR REACTIONS IN SOLIDS

KEYWORDS: calorimetry, mass spectroscopy, new hydrogen molecule

tions. Rather than invoking a postulated boundary condition, $\psi \to 0$ as $r \to \infty$, which leads to a purely mathematical model, we derived the boundary condition from Maxwell's equations¹: For nonradiative states, the charge-density function must not possess space-time Fourier components that are synchronous with waves traveling at the speed of light.

Application of this physical boundary condition leads to a physical model that is consistent with classical physics. The novel theory2 unifies Maxwell's equations, Newton's laws, and Einstein's general and special relativity. Theoretical predictions conform with experimental observations. The closed-form calculations of a broad spectrum of fundamental phenomena contain fundamental constants only. Equations of the oneelectron atom are derived that give four quantum numbers, the Rydberg constant, the ionization energies, the results of the Stern-Gerlach experiment, the electron g factor, the spin angular momentum energies, the excited states, the results of the Davisson-Germer experiment, the parameters of pair production, and the hyperfine structure interval of positronium. Ionization energies of two- and three-electron atoms are given as well as the bond energies, vibrational energies, and bond distances of molecular hydrogen and the molecular hydrogen ion. From the closed-form solution of the helium atom, the predicted electron scattering intensity is derived. The closed-form scattering equation matches the experimental data, whereas calculations based on the Born model of the atom "utterly fail" at small scattering angles. The implications for the invalidity of the Schrödinger and Born models of the atom and the dependent Heisenberg uncertainty principle are discussed. The atomic equations of gravitation are derived from which the gravitational constant and the masses of the leptons and the neutron and proton are derived. The magnetic moments of the nucleons are derived. The beta decay energy of the neutron and the binding energy of deuterium are calculated. Also, the theory predicts exactly the spectral observations of the extreme ultraviolet background emission from interstellar matter, which characterizes dark matter; it provides a resolution of the solar neutrino paradox, and it provides a basis to produce heat in electrolytic cells that represents an endless supply of cheap, clean energy.

A novel model of the electron² describes a bound electron by a charge-density (mass-density) function that is the product of a radial delta function [f(r) = $d(r-r_n)$], two angular functions (spherical harmonic functions), and a time-harmonic function. Thus, an electron is a spinning, two-dimensional spherical surface, called an electron orbitsphere, that can exist in a bound state only at specified distances from the nucleus.

PHOTON-INDUCED STATES OF THE ONE-ELECTRON ATOM

It is well known that resonator cavities can trap electromagnetic radiation of discrete resonant frequencies. A bound electron is a resonator cavity and can trap photons of discrete frequencies. The relationship between an allowed radius and the electron wavelength is

$$2\pi (nr_1) = 2\pi r_n = n\lambda_1 = \lambda_n , \qquad (1)$$

where

$$n = 1$$

 $n = 2, 3, 4, \dots$
 $n = \frac{1}{2}, \frac{1}{3}, \frac{1}{4}, \dots$

 λ_1 = allowed wavelength for n = 1

 r_1 = allowed radius for n = 1.

Higher and lower energy states are equally valid. The photon standing wave in both cases is given as a solution of Laplace's equation in harmonic coordinates:

excited-state photon:

$$\epsilon \hat{t}_{r\,photon\,n,l,m} = \frac{e\,(na_0)^l}{4\pi\epsilon_0} \frac{1}{r^{(l+2)}}$$

$$\times \left(-1 + \frac{1}{r}\operatorname{Re}\{i\,[Y_l^m(\phi,\theta) + Y_s^{m_s}(\phi,\theta)]\}\right), \qquad (2)$$

for

$$n = 2, 3, 4, \ldots,$$

 $l = 1, 2, \ldots, n - 1$,

and

$$m_l = -l, -l+1, \ldots, 0, \ldots, +l;$$

below-ground-state photon:

$$\epsilon \hat{l}_{r\,photon\,n,l,m} = \frac{e}{4\pi\epsilon_0} \frac{\left(\frac{a_0}{n}\right)^l}{r^{(l+2)}} \times \left\{-1 + n[Y_l^m(\phi,\theta) + Y_s^{m_s}]\right\}, \quad (3)$$



for

$$n=2,3,4,\ldots,$$

$$l=1,2,\ldots,n-1,$$

and

$$m_l = -l, -l+1, \ldots, 0, \ldots, +l$$
.

From energy conservation, the resonance energy hole of a hydrogen atom that excites resonator modes of radial dimensions $a_0/(m+1)$ is

$$m \times 27.2 \text{ eV}$$
,

where

$$m=1,2,3,4,\ldots.$$

After resonant absorption of the hole, the radius of the orbitsphere a_0 shrinks to $a_0/(m+1)$. After p cycles of resonant shrinkage, the radius is $a_0/(mp+1)$.

In other words, the radial ground-state field can be considered as the superposition of Fourier components. The removal of negative Fourier components of energy $m \times 27.2$ eV, where m is an integer, increases the positive electric field inside the spherical shell by m times the charge of a proton. The resultant electric field is a time-harmonic solution of LaPlace's equations in spherical coordinates. In this case, the radius at which force balance and nonradiation are achieved is $a_0/(m+1)$, where m is an integer. In the decay to this radius from the ground state, a total energy of $[(m+1)^2 - 1^2] \times$ 13.6 eV is released. The potential energy well of the hydrogen or deuterium atom is shown in Fig. 1. The exothermic reaction is referred to as hydrogen emission by catalytic thermal electronic relaxation.

An efficient catalytic system that hinges on the coupling of three resonator cavities involves potassium. For example, the second ionization energy of potassium is 31.63 eV. This energy hole is obviously too high for resonant absorption. However, K+ releases 4.34 eV when it is reduced to K. The combination of K+ to K2+ and K+ to K, then, has a net energy change of 27.28 eV:

27.28 eV + K⁺ + K⁺ + H
$$\left(\frac{a_0}{p}\right)$$
 \rightarrow K + K²⁺
+ H $\left[\frac{a_0}{(p+1)}\right]$ + $[(p+1)^2 - p^2] \times 13.6$ eV, (4)

$$K + K^{2+} \rightarrow K^{+} + K^{+} + 27.28 \text{ eV}$$
 (5)

And, the overall reaction is

$$H\left(\frac{a_0}{p}\right) \to H\left[\frac{a_0}{(p+1)}\right] + [(p+1)^2 - p^2]$$

$$\times 13.6 \text{ eV} . \tag{6}$$



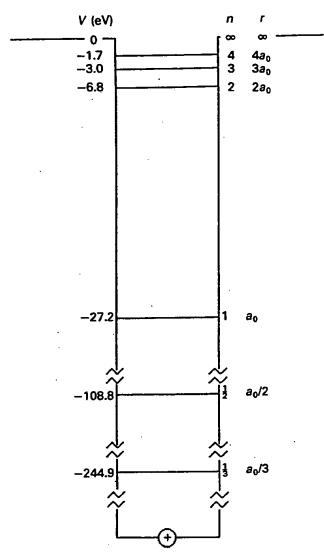


Fig. 1. Potential energy well of a hydrogen atom.

Other less efficient catalytic systems that hinge on the coupling of three resonator cavities exist. For example, the third ionization energy of palladium is 32.93 eV. This energy hole is obviously too high for resonant absorption. However, Li⁺ releases 5.392 eV when it is reduced to Li. The combination of Pd²⁺ to Pd³⁺ and Li⁺ to Li, then, has a net energy change of 27.54 eV:

27.54 eV + Li⁺ + Pd²⁺ + H
$$\left(\frac{a_0}{p}\right)$$

 \rightarrow Li + Pd³⁺ + H $\left[\frac{a_0}{(p+1)}\right]$
+ $[(p+1)^2 - p^2] \times 13.6 \text{ eV}$, (7)
Li + Pd³⁺ = Li⁺ + Pd²⁺ + 27.54 eV. (8)



And, the overall reaction is

$$H\left(\frac{a_0}{p}\right) \to H\left[\frac{a_0}{(p+1)}\right] + [(p+1)^2 - p^2] \times 13.6 \text{ eV} . \tag{9}$$

A catalytic system that hinges on the transfer of two electrons from an atom to a molecule involves palladium and oxygen. For example, the first and second ionization energies of palladium are 8.34 and 19.43 eV, respectively, and the first and second electron affinities of the oxygen molecule are 0.45 and 0.11 eV, respectively. The energy hole resulting from a two-electron transfer is appropriate for resonant absorption. The combination of Pd to Pd²⁺ and O₂ to O₂²⁻, then, has a net energy change of 27.21 eV:

27.21 eV + Pd + O₂ + H
$$\left(\frac{a_0}{p}\right)$$

 $\rightarrow Pd^{2+} + O_2^{2-} + H\left[\frac{a_0}{(p+1)}\right]$
+ $[(p+1)^2 - p^2] \times 13.6 \text{ eV}$, (10)
 $Pd^{2+} + O_2^{2-} \rightarrow Pd + O_2 + 27.21 \text{ eV}$, (11)

And, the overall reaction is

$$H\left(\frac{a_0}{p}\right) \to H\left[\frac{a_0}{(p+1)}\right] + [(p+1)^2 - p^2] \times 13.6 \text{ eV} . \quad (12)$$

Additional atoms, molecules, or compounds that could be substituted for O_2 are those with first and second electron affinities of -0.45 and 0.11 eV, respectively, such as a mixed oxide (MnO_x, AlO_x, or SiO_x) containing oxygen to form O_2^{2-} or O_2 to form O_2^{2-} .

For sodium or sodium ions, no electrocatalytic reaction of ~27.21 eV is possible. For example, 42.15 eV of energy is absorbed by the reverse of the reaction given in Eq. (5) where Na⁺ replaces K⁺:

$$Na^+ + Na^+ + 42.15 \text{ eV} \rightarrow Na + Na^{2+}$$
 (13)

NEW HYDROGEN MOLECULE

According to HydroCatalysis Power Company (HPC) theory, a hydrino atom, a hydrogen atom with its electron in a lower-than-ground-state energy level corresponding to a fractional quantum number, has an unpaired electron and would bind to the nickel cathode. Bound hydrogen atoms demonstrate a high degree of mobility as shown by electron energy loss spectroscopy. Hydrino atoms are predicted to possess high mobility that permits the possibility of subsequent shrinkage reactions and dihydrino-molecule-forming reactions. The hydrino must form muon-like molecules, as indicated by the trace tritium production during the electrolysis of a K₂CO₃ heavy water electrolyte with a



nickel cathode.2 Dihydrino molecules are evolved from the cathode and are found in the effluent electrolysis gas.

A preferred method to identify the dihydrino molecule is via cryofiltration followed by a search for mass spectroscopic anomalies.

EXISTING EVIDENCE FOR HYDRINO ATOMS AND DIHYDRINO MOLECULES

Hydrogen transitions to electronic energy levels below the n = 1 state have been found in the spectral lines of the extreme ultraviolet background of interstellar space. This assignment resolves the paradox of the identity of dark matter. It also accounts for other celestial observations such as the facts that diffuse $H\alpha$ emission is ubiquitous throughout the galaxy and widespread sources of flux shortward of 912 A are required to account for this emission.2,4

The dihydrino molecule can be identified by mass spectroscopy. Miles and coworkers⁵⁻⁸ and Chien et al.⁹ report ⁴He production as identified by mass spectroscopy of the cryofiltered gases evolved from an electrolysis cell comprising a palladium cathode and a LiOD/ D₂O electrolyte. According to Miles et al., ⁷ the intensity of the helium peak maintained an approximate correspondence to the amount of excess power or heat observed in electrochemical calorimetric cells. The samples for helium analysis were analyzed "blindly" by mass spectroscopy. That is, the spectroscopist did not know whether a given sample produced excess heat or not. 10 According to Miles et al., 7 "ignoring the helium/heat relationship (Table I of Ref. 7), the simple yes/no detection of helium in 7/7 experiments producing excess heat and the absence of helium in 6/6 experiments not producing excess heat (1 in D2O, 5 in H2O) implies a chance probability of $(\frac{1}{2})^{13} = \frac{1}{8192}$ or 0.012%." The fusion reaction proposed by the authors is as follows:

$$D + D \rightarrow {}^{4}He + \gamma(23.8 \text{ MeV})$$
 . (14)

Miles et al.8 report the production of ⁴He at a rate of ~10¹¹ ⁴He/s. The associated gamma emission from this proposed fusion corresponds to a 10-Ci 23.8-MeV source. Secondary X rays must also be present as well as neutrons and charged particles in the correct ratios.11 No neutrons were observed, and no significant radiation above background was observed. 12 Numerous identical heat-producing experiments failed to produce fusion products within 13 orders of magnitude of that necessary to account for the heat. 13 According to Rees, 13 "even if a new fusion process were occurring, there ought to be x-rays produced. It is hard to believe that you could lose over 20 MeV in a single event and see nothing at all coming out."

We feel that the data are not consistent with a fusion reaction as the source of the excess heat or the mass 4 peak. The mass 4 peak is incorrectly assigned as ⁴He.

The correct assignment is D₂, the dideutrino molecule. These molecules form from deutrino atoms on the surface of the palladium cathode. The deutrino atoms form according to the exothermic reaction given by Eqs. (7), (8), and (9), which is the source of the observed excess heat.

The dideutrino molecule is predicted to be spin paired, to be of comparable size to the helium atom, and to have a higher ionization energy and a lower liquefaction temperature than D2. Thus, cryofiltration of the gases of an electrolytic cell having an electrolyte of one or more electrocatalytic couples that induce transitions of deuterium atoms to energy levels below the ground state to release excess heat energy followed by mass spectroscopic analysis would appear to be producing 4He. In fact, the mass spectroscopic separation of ⁴He and D₂ would be difficult. And, Miles et al. ¹⁰ used the higher ionization potential of the mass 4 peak as a criterion to make its assignment as ⁴He rather than D₂.

The dideutrino molecule can also be identified by high-resolution quadrupole mass spectroscopy. Yamaguchi and Nishioka¹⁴ reported high-resolution (0.001 amu) quadrupole mass spectroscopic data of the gases released from deuterium- or hydrogen-loaded palladium sheets coated on one side with a hydrogen-impermeable gold layer and coated on the other surface with an oxide coat (MnO_x, AlO_x, or SiO_x). Heat was observed from light and heavy hydrogen only when the mixed oxide coat was present. The mass spectroscopic data of the gases released when a current was applied to a deuterium-loaded (99.9%), MnO_x-coated palladium sheet indicate the presence of a large shoulder on the

 D_2 peak.

Yamaguchi and Nishioka's¹⁴ control D₂ peak is shown in Fig. 2. A shoulder on the D2 peak is shown in Figs. 3 (Ref. 14) and 4 (Ref. 15). The anomalous peak of Fig. 3 was assigned to HT (1H-3H) by Yamaguchi and Nishioka. Tritium is produced by nuclear fusion, and this (HT) peak grows with time as heat evolves. However, no such peak is possible because no ¹H was present, as demonstrated in the control spectrum, and the proposed HT peak was larger than the D₂ peak. The observed heat, including that observed from light hydrogen, is inexplicable from the proposed observed nuclear products. We assert that the data are not consistent with a fusion reaction or with the assignment of the anomalous mass 4 peak as HT. The correct assignment is D₂*, the dideutrino molecule. These molecules form from deutrino atoms on the surface of the palladium sheet, and the deutrino atoms form according to the exothermic reaction given by Eqs. (10), (11), and (12), which is the source of the observed excess heat.

After cryofiltration or combustion, the dihydrino molecule can be distinguished from normal molecular hydrogen by mass spectroscopy. The branching ratio to form m/e = 1 relative to m/e = 2 that is observed for the dihydrino molecule is different than the ratio that



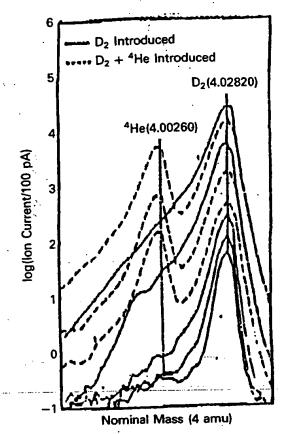


Fig. 2. Yamaguchi and Nishioka's 14 control high-resolution mass spectrum of helium and hydrogen.

is observed for normal molecular hydrogen. Mass spectroscopy will further distinguish a sample containing dihydrino molecules from a sample containing H_2 by showing a different ion production efficiency as a function of ionization potential and a different ion production efficiency at a given ionization potential for the two samples.

LIGHT WATER CALORIMETRY EXPERIMENTS

Methods

A search for excess heat during the electrolysis of aqueous potassium carbonate (K⁺/K⁺ electrocatalytic couple) was conducted by using single-cell, silver-coated, vacuum-jacketed dewars and noninsulated plastic vessels. To simplify the calibration of these cells, they were constructed to have primarily conductive heat losses. Thus, a linear calibration curve was obtained. Two methods of differential calorimetry were used to determine the cell constant that was used to calculate the excess enthalpy. First, we calculated the cell constant during the experiment (on-the-fly calibration) by turning an internal resistance heater off and on and infer-



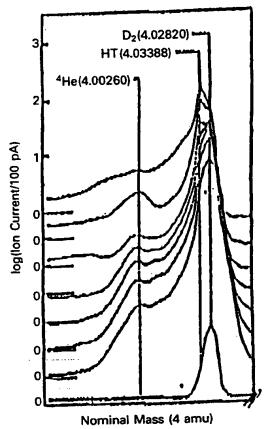


Fig. 3. Yamaguchi and Nishioka's¹⁴ high-resolution mass spectroscopic data of the gases released when a current was applied to a deuterium-loaded (99.9%), MnO_x-coated palladium sheet, indicating the presence of a large shoulder on the D₂ peak that increases with time.

ring the cell constant from the difference between the losses with and without the heater. Second, we determined the cell constant with no electrolysis processes occurring by turning an internal resistance heater off and on for a well-stirred cell and inferring the cell constant from the difference between the losses with and without the heater. This method overestimates the cell constant because there is no gas flow (which adds to the heat losses).

The general form of the energy balance equation for the cell in steady state is

$$0 = P_{appl} + Q_{htr} + Q_{xs} - P_{gas} - Q_{loss} , \qquad (15)$$

where

 P_{appl} = electrolysis power

 Q_{htr} = power input to the heater

 Q_{xx} = excess heat power generated by the hydrogen "shrinkage" process

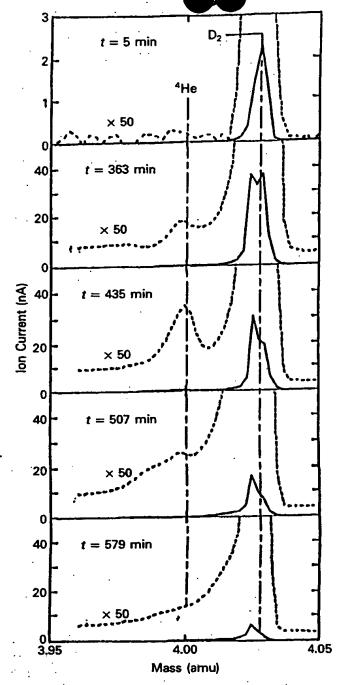


Fig. 4. Yamaguchi and Nishioka's 15 high-resolution mass spectroscopic data of the gases released when a current was applied to a deuterium-loaded (99.9%), MnO_x-coated palladium sheet, indicating the presence of a large shoulder on the D₂ peak that increases with time.

 P_{gas} = power removed as a result of evolution of H_2 and O_2 gases

 Q_{loss} = thermal power loss from the cell.

When an aqueous solution is electrolyzed to liberate hydrogen and oxygen gases, the electrolysis power P_{appl} (= $E_{appl}I$) can be partitioned into two terms:

$$P_{appl} = E_{appl}I = P_{cell} + P_{gas} . {16}$$

An expression for P_{gas} (= $E_{gas}I$) is readily obtained from the known enthalpy of formation of water from its elements:

$$E_{gas} = \frac{-\Delta H_{form}}{\alpha F} \tag{17}$$

(F is Faraday's constant), which yields $E_{gas} = 1.48 \text{ V}$ for the reaction

$$H_2O \rightarrow H_2 + \frac{1}{2}O_2$$
 (18)

The net faradaic efficiency of gas evolution is assumed to be unity; thus, Eq. (16) becomes

$$P_{cell} = (E_{appl} - 1.48V)I$$
 (19)

We calibrated the cell for heat losses by turning an internal resistance heater off and on while maintaining constant electrolysis and by inferring the cell conductive constant from the difference between the losses with and without the heater where heat losses were primarily conductive losses through the top of the dewar or through the surfaces of the plastic vessel. When the heater was off, the losses were given by

$$c(T_c - T_b) = P_{appl} + 0 + Q_{xx} - P_{gat}$$
, (20)

where

c = conductive heat loss coefficient'

 $T_b =$ ambient temperature

 $T_c = \text{cell temperature}.$

When a new steady state is established with the heater on, the losses change to

$$c(T'_c - T_b) = P'_{appl} + Q_{htr} + Q'_{xx} - P'_{xxx}$$
, (21)

where the primes indicate values that changed when the heater was on. When we assume

$$Q_{xx} = Q'_{xx}$$
, $P_{appl} = P'_{appl}$, and $P_{gax} = P'_{gax}$, (22)

the cell constant or heating coefficient a, the reciprocal of the conductive loss coefficient c, is given by the result

$$a = \frac{T_c' - T_c}{Q_{htr}} . (23)$$

In all heater power calculations, we used the following equation:

$$Q_{htr} = E_{htr} I_{htr} . (24)$$



In the case of intermittent square-wave electrolysis with current only during the high-voltage interval of the cycle, the P_{appl} value of Eq. (16) is calculated as the product of the peak voltage, the peak current, and the duty cycle Dc, which is the pulse length divided by the period:

$$P_{appl} = (E_{appl}I)Dc = (P_{cell} + P_{gas})Dc . (25)$$

In the case of intermittent square-wave electrolysis with current only during the high-voltage interval of the cycle and where the net faradaic efficiency of gas evolution is assumed to be unity, P_{cell} of Eq. (19) becomes

$$P_{cell} = [(E_{appl} - 1.48V)I]Dc$$
 (26)

HPC Experiments 1, 2, and 3

These experiments were carried out by observing and comparing the temperature differences, $\Delta T_1 =$ $T(\text{electrolysis only}) - T(\text{blank}) \text{ and } \Delta T_2 = T(\text{resistor})$ heating only) -T(blank) referred to unit input power, between two identical cells. Each cell consisted of a 350-ml silver-coated, vacuum-jacketed dewar (Cole Palmer model 8600) with a 7-cm opening covered with a 0.75-in.-thick Styrofoam stopper lined with Parafilm. One calorimeter dewar of the same configuration, containing the same amount of electrolyte and the same electrodes (nickel cathode and platinum anode), resistorheater, and thermistor, stirred at the same speed, was used as the blank. In this dewar, neither electrolysis nor heating by the resistor was carried out. Experiments were also carried out by using the blank dewar from a previous experiment as the working dewar and vice versa. This exchange was done to ensure that the effect is not due to any difference in the thermal properties of the two specific dewars used. The experimental apparatus for the differential calorimetry used for these studies is shown in Fig. 5.

The heating coefficients were calculated from

$$a = \Delta T_1 / P_{cell} \tag{27}$$

and

$$a = \Delta T_2 / Q_{htr} . (28)$$

The outsides of the cells were maintained at ambient air temperature, which was monitored. Ambient temperature fluctuations over 24 h were typically <0.5°C.

The cathode was 24 m of 0.127-mm-diam nickel wire (99% Alfa 10249, cold drawn) that was coiled about the central platinum anode. We cleaned the cathode by placing it in a beaker of 0.57 $M \, \text{K}_2\text{CO}_3/3\%$ $H_2\text{O}_2$ for 30 min and then rinsing it with distilled water. The leads were inserted into Teflon tubes to ensure that no recombination of the evolving gases occurred.

The anode was a 10-cm × 1-mm-diam spiraled plat-



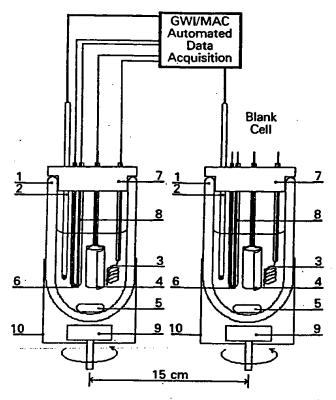


Fig. 5. Experimental calorimeter setup: (1) vacuum-jacketed dewar, (2) thermistor, (3) platinum anode, (4) nickel cathode, (5) magnetic stirring bar, (6) resistor-heater, (7) Styrofoam stopper lined with Parafilm, (8) Teflon tubing, (9) magnetic stirrer, and (10) aluminum cylinder.

inum wire (Johnson-Matthey) with a 0.127-mm platinum lead wire. The leads were inserted into Teflon tubes to prevent recombination, if any, of the evolving gases. The cathode-anode separation distance was 1 cm.

As usual in electrochemistry, measures were taken to avoid impurities in the system, especially organic substances. We note here the known problems with the reproducibility of the hydrogen overpotential that can be overcome only by ensuring the lowest possible level of impurities. The following procedures were applied in order to reproduce the excess heat effect. Before starting the experiment, the electrolysis dewar was cleaned with Alconox and 0.1 M nitric acid and rinsed thoroughly with distilled water to remove all organic contaminants. The platinum anode was mechanically scoured with steel wool, soaked overnight in concentrated HNO3, and rinsed with distilled water. The nickel cathode was removed from its container with rubber gloves, and cut and folded in such a way that no organic substances were transferred to the nickel surface. The nickel cathode was dipped into the working

solution under electrolysis current and was never left in the working solution without electrolysis current.

In experiments 1 and 2, the electrolyte solution was 200 ml of 0.57 M aqueous K_2CO_3 (Aldrich $K_2CO_3 * \frac{3}{2}H_2O$ 99+%); in experiment 3, the electrolyte solution was 200 ml of 0.57 M aqueous Na_2CO_3 (Aldrich Na_2CO_3 ACS primary standard 99.95+%).

The resistance heater used during calibration and operation was a $10-\Omega$, 1% precision metal oxide resistor in a 2-mm-o.d. Teflon tube. The heater was powered by a variable direct current voltage power source ($\pm 0.5\%$). The heating power was calculated by Eq. (24).

The electrolyte solution was stirred with a 7-mm × 2-cm prolate spheroid magnetic stirring bar that was spun by a 6-cm-long open magnet mounted on an open shaft revolving at 750 rpm under the dewar. The shaft was that of an open mixing motor (Fisher Flexa-Mix model 76).

Erroneous attribution of the effect to temperature gradients was prevented by testing for minute spatial variations of the temperature over time. Three thermistors were positioned ~ 2.5 cm apart from each other at the bottom, middle, and upper parts of the electrolyte. No difference was observed (within the limit of detection, $\pm 0.01^{\circ}$ C).

Voltage ($\pm 0.5\%$), current ($\pm 1\%$), and temperature ($\pm 0.1^{\circ}$ C) data were acquired by a data acquisition system consisting of an Apple Mac II SI 5/80 with an NU bus adapter and the following GW Instruments hardware: GWI-625 data acquisition board, GWI-J2E multiplexer, GWI-ABO analog breakout system, and GWI-4W ribbon cable. The value of P_{appl} was given by Eq. (16) as the product of the voltage and the constant current, and P_{cell} was given by Eq. (19).

The current voltage parameters for experiment 2 were a periodic square wave having an offset voltage of 1.60 V, a peak voltage of 1.90 V, a peak constant current of 47.3 mA, a 36.0% duty cycle, and a frequency of 600 Hz. Peak voltage measurements were made with an oscilloscope (BK model 2120), and the time-average current was determined from a multimeter voltage measurement ($\pm 0.5\%$) across a calibrated resistor (1 Ω) in series with the lead to the cathode. The waveform of the pulsed cell was a square wave. Since there was current only during the peak voltage interval of the cycle, P_{appl} was given by Eq. (25), and P_{cell} was given by Eq. (26).

The faradaic efficiency of gas production by a potassium cell was studied. Comparing this result with the sodium system allows the accuracy of the analysis to be seen. A closed cell was fashioned from a 150-ml round-bottom flask, a 2-cm × 2-mm prolate spheroid stir bar, a glass "Y" adapter, glass tubing bent into the shape of one cycle of a square wave, a 150-ml beaker, and a 0.01-ml graduated buret. The cell was set up to mimic the calorimetry tests as closely as possible. A constant current (±0.1%) supply was used to supply the power for the electrolysis. Current measurement was



done with a Heathly multimeter $(\pm 0.1\%)$. Gas was collected and measured in the buret. Several experiments were run to ensure that the cell was sealed tightly.

Thermacore Experiment 4

The cell was a 10-gal (33- \times 15-in.) Nalgene tank (model 54100-0010). Two 4-in.-long $\times \frac{1}{2}$ -in.-diam terminal bolts were secured in the lid, and a cord for a calibration heater was inserted through the lid.

The cathode was a 5-gal polyethylene bucket with $\frac{1}{2}$ -in. holes drilled over all surfaces at $\frac{3}{4}$ -in. spacings of the hole centers, which served as a perforated (mesh) support structure, and 5000 m of 0.5-mm-diam clean. cold-drawn nickel wire (NI 200, 0.0197-in., HTN36-NOAG1, A1 Wire Tech). The wire was wound uniformly around the outside of the mesh support as 150 sections of 33-m length. The ends of each of the 150 sections were spun to form three cables of 50 sections per cable. The cables were pressed in a terminal connector that was bolted to the cathode terminal post. The connection was covered with epoxy to prevent corrosion. A central cathode was made from 5000 m of the 0.5-mm-diam nickel wire. The wire was wound in a toroidal shape with three cables, each pressed into a terminal connector that was bolted to the cathode terminal post and coated with epoxy. The central cathode was inserted into an cylindrical perforated polyethylene container that was placed inside the outer cathode with the anode array between the central and outer cathodes.

The anode was an array of 15 platinized titanium anodes (ten of Engelhard platinum-titanium mesh, 1.6×8 in., with a $\frac{3}{4} \times 7$ -in. stem attached to the 1.6-in. side plated with 100 U series 3000; and five of Engelhard 1-in.-diam × 8-in.-long titanium tubes with a $\frac{3}{4}$ - × 7-in. stem affixed to the interior of one end and plated with 100 U platinum series 3000). A 3-in.-wide tab was made at the end of the stem of each anode by bending it at a right angle to the anode. A 1-in. hole was drilled in the center of each tab. The tabs were bolted to a 12.25-in.-diam polyethylene disk (Rubbermaid JN2-2669) equidistantly around the circumference. Thus, an array was fabricated that had 15 anodes suspended from the disk. The anodes were bolted with 1/4-in. polyethylene bolts. Sandwiched between each anode tab and the disk was a flattened nickel cylinder also bolted to the tab and the disk. The cylinder was made from a 7.5- \times 9-cm-long \times 0.125-mm-thick nickel foil. The cylinder traversed the disk, and the other end of each was pressed about a 10 AWG/600 V copper wire. The connection was sealed with shrink tubing and epoxy. The wires were pressed into two terminal connectors and bolted to the anode terminal. The connection was covered with epoxy to prevent corrosion.

Before assembly, the anode array was cleaned in 3 M HCl for 5 min and rinsed with distilled water. The cathode was placed in a tank of 0.57 M K₂CO₃/3% H₂O₂ for 6 h and then rinsed with distilled water. The anode was placed in the support between the central



Milis e DIHYDRINO MOLECULE

and outer cathodes, and the electrode assembly was placed in the tank containing 28 ℓ of 0.57 M K₂CO₃ (Alfa K₂CO₃ 99%). The power supply was connected to the terminals with battery cables.

The cell assembly is shown in Fig. 6.

The heater was a 57.6- Ω , 1000-W Incoloy 800-jacketed Nichrome heater that was suspended from the polyethylene disk of the anode array. It was powered by a constant power ($\pm 0.1\%$) supply (Invar model TP 36-18). The voltage ($\pm 0.1\%$) and current ($\pm 0.1\%$) were recorded with a digital multimeter (Fluke 8600A). The current ($\pm 0.5\%$) was read from an Ohio Semitronics CTA 101 current transducer. The heating power was calculated by using Eq. (24).

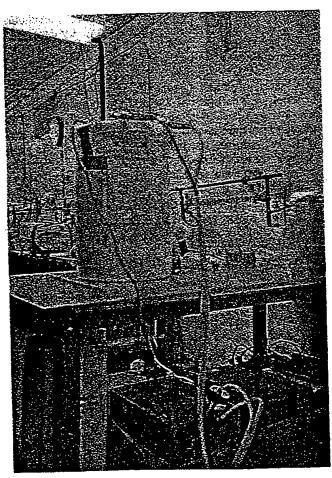
Electrolysis was performed at 50-A constant current with a constant current ($\pm 0.02\%$) power supply (Kepco model ATE6-100M). The value of P_{appl} was given by Eq. (16) as the product of the voltage and the constant current, and P_{cell} was given by Eq. (19).

The temperature $(\pm 0.1^{\circ}\text{C})$ was recorded with a microprocessor thermometer (Omega HH21) using a type K thermocouple that was inserted through a $\frac{1}{4}$ -in.

hole in the tank lid and anode array disk. To eliminate the possibility of temperature gradients, the temperature was measured throughout the tank. No position variation was found to within the detection of the thermocouple $(\pm 0.1^{\circ}\text{C})$.

The temperature rise above ambient $[\Delta T = T(\text{electrolysis only}) - T(\text{blank})]$ and electrolysis power were recorded daily. The heating coefficient was determined on the fly by the addition of 20 W of heater power to the electrolytic cell every 72 h; 24 h was allowed for steady state to be achieved. The temperature rise above ambient $[\Delta T_2 = T(\text{electrolysis} + \text{heater}) - T(\text{blank})]$ was recorded as were the electrolysis power and heater power.

In all temperature measurements, the blank consisted of 28 ℓ of water in a 10-gal (33- \times 15-in.) Nalgene tank with lid (model 54100-0010). The stirrer was a 1-cm-diam \times 43-cm-long glass rod to which an 0.8- \times 2.5-cm Teflon half-moon paddle was fastened at one end; the other end was connected to a variable-speed stirring motor (Talboys Instrument model 1075C). The stirring rod was rotated at 250 rpm.



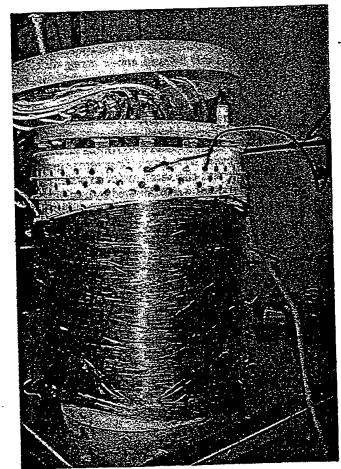


Fig. 6. Cell assembly of experiments 4 through 14.

The blank (nonelectrolysis cell) was stirred to simulate stirring in the electrolytic cell by gas sparging. The 1 W of heat from stirring resulted in the blank cell operating at 0.2°C above ambient.

The temperature $(\pm 0.1^{\circ}\text{C})$ of the blank was recorded with a microprocessor thermometer (Omega HH21) that was inserted through a $\frac{1}{4}$ -in. hole in the tank lid.

Thermacore Experiments 5 Through 13

The electrolytic cell was the same as in experiment 4. Intermittent square-wave electrolysis was performed at 2 Hz at the duty cycles listed in Table I. A constant current supply (Kepco ATE-100M) was programmed at 101-A peak current ($\pm 0.05\%$) and driven by a function generator (BK Precision Dynascan model 3011). Duty cycle measurements were made with an oscilloscope (BK model 2120), and the peak current was determined from the voltage measurement ($\pm 0.1\%$) across an Ohio Semitronics CTA 101 current transducer. The waveform of the pulsed cell current was a square wave. Since there was current only during the peak voltage interval of the cycle, P_{appl} was given by Eq. (25), and P_{cell} was given by Eq. (26).

The peak voltage $(\pm 0.1\%)$ was recorded with a digital multimeter (Fluke 8600A). The temperature $(\pm 0.1^{\circ}\text{C})$ was recorded with a microprocessor thermometer (Omega HH21) that was inserted through a $\frac{1}{4}$ -in. hole in the tank lid and anode array disk. To eliminate the possibility of temperature gradients, the temperature was measured throughout the tank. No position variation was found to within the detection limit of the thermocouple $(\pm 0.1^{\circ}\text{C})$.

The temperature rise above ambient $[\Delta T = T(\text{electrolysis only}) - T(\text{blank})]$ and electrolysis power were recorded at least every 24 h. In all temperature measurements, the blank was the same as for experiment 4.

The electrolytic cell was calibrated by applying electrical power to the 1000-W heater with electrolysis

TABLE I

Duty Cycles for Experiments 5 Through 13

Experiment	Duty Cycle (%)
5	. 3
6	4
7 ·	5
8 ·	6
9	7
10	10
· 11	15
12	20
13	25

power set to near zero. He cell temperature rise above ambient $[\Delta T = T(\text{heater only}) - T(\text{blank})]$ and heater power were recorded daily. The heating coefficient was determined on the fly by the addition of 40 W of heater power every 72 h; at least 24 h was allowed for steady state to be achieved. The heating power was calculated by Eq. (24).

Thermacore Experiment 14

The electrolytic cell was the same as in experiments 5 through 13. Intermittent square-wave electrolysis was performed at 1 Hz, 20% duty cycle, by programming a constant current supply (Kepco ATE-50M) at 10-A peak ($\pm 0.5\%$) driven by a function generator (BK Precision Dynascan model 3011). Data were recorded by the apparatus described for experiments 5 through 13. Since there was current only during the peak voltage interval of the cycle, P_{appl} was given by Eq. (25), and P_{cell} was given by Eq. (26).

LIGHT WATER CALORIMETRY RESULTS

Mills's theory² predicts that the exothermic catalytic reaction whereby the electrons of hydrogen atoms are each stimulated to relax to a lower energy level corresponding to a fractional quantum state by providing an energy hole resonant with this transition will occur during the electrolysis of K₂CO₃/light water solutions but will not occur during the electrolysis of Na₂CO₃/light water solutions. The results of the electrolysis with a nickel wire cathode at 83-mA constant current and heater run of K₂CO₃ appear in Fig. 7 and Table II. The heating coefficient of the heater run (calibration) was 41°C/W, whereas the heating coefficient of the electrolysis run was 87°C/W. The production of excess enthalpy is observed. The higher the heating coefficient is, the more heat is released in the process.

The results of the electrolysis of a K₂CO₃ electrolyte with a nickel cathode and a periodic square-wave having an offset voltage of 1.60 V, a peak voltage of 1.90 V, a peak constant current of 47.3 mA, a 36.0% duty cycle, and a frequency of 600 Hz appear in Fig. 8 and Table II. The output power was 16 times the ohmic input power.

The results of the electrolysis at 81-mA constant current and heater run of Na₂CO₃ appear in Fig. 9 and Table II. The heating coefficient of the electrolysis run was 47°C/W, whereas the heating coefficient of the heater run (calibration) was 46°C/W. The production of excess heat is not observed.

The data of the faradaic efficiency of the production of gas by a potassium cell and a control sodium cell appear in Table III.

Almost all electrolysis experiments will be similar to the case of Na₂CO₃. Only a few combinations of electrolytes and electrodes, such as the K₂CO₃ case, will yield excess heat.



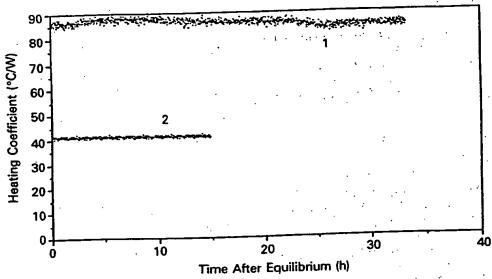


Fig. 7. Experiment 2: plot of the heating coefficients over time: (1) electrolysis with a nickel wire cathode at 0.083 A in K₂CO₃ and (2) resistor working in K₂CO₃.

TABLE II

Power Input and Output Parameters of Experiments 1 Through 14

Experiment Number	ν (V)	Duty Cycle (%)	<i>I</i> (A)	VI Power (W)	(V - 1.48)I Input Power (W)	Output Power (W)	Excess Power (W)	Output Input (%)
1 2* 3 4 5* 6* 7* 8* 9* 10* 11* 12* 13* 14*	3.05 1.90 3.51 3.25 4.13 4.04 4.00 3.95 3.89 3.88 3.85 3.83 2.37	100 36 100 100 3 4 5 6 7 10 15 20 25 20	0.083 0.0473 0.081 49.9 101 102 102 101 102 101 101 101	0.253 0.032 0.284 162 12.5 16.3 20.4 24.2 27.5 39.6 58.8 77.8 96.7 4.98	0.130 0.007 0.164 88.3 8.03 10.3 12.9 15.1 17.0 24.5 36.4 47.9 59.3 1.87	0.275 0.114 0.167 137 31.0 43.5 54.7 63.2 70.0 58.3 105.5 118.1 135 41.0	0.145 0.107 0.003 48.2 21.5 33.2 41.8 48.1 53.0 60.8 69.1 70.2 75.7 39.1	212 1630 102 155 386 422 424 419 412 348 290 247 228 2193

^{*}Output is greater than VI.

TABLE III

Faradaic Efficiency of Gas Production by a K₂CO₃ Cell and a Na₂CO₃ Control Cell

	Faraday's Gas (mmol)	Calculated Volume (ml)	Measured Volume (ml)	Efficiency (%)
Electrolyte		49.91	51.30	102.8
0.57 M K ₂ CO ₃ 0.57 M Na ₂ CO ₃	1.961 1.955	49.69	49.86	100.3



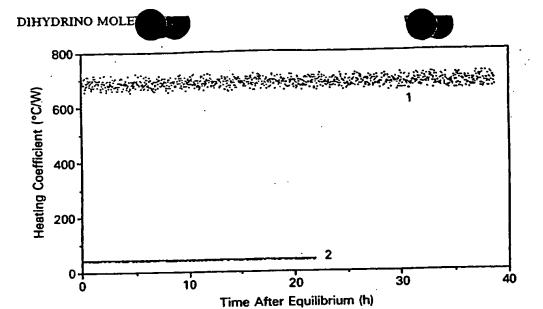


Fig. 8. Experiment 2: plot of the heating coefficients over time: (1) electrolysis with a nickel cathode and a periodic square wave having an offset voltage of 1.60 V, a peak voltage of 1.90 V, a peak constant current of 47.3 mA, a 36.0% duty cycle, and a frequency of 600 Hz in K₂CO₃ and (2) resistor working in K₂CO₃.

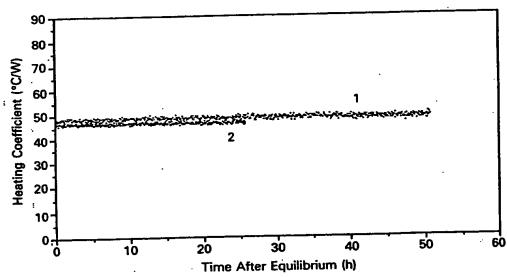


Fig. 9. Experiment 3: plot of the heating coefficients over time: (1) electrolysis at 0.081 A in Na₂CO₃ and (2) resistor working in Na₂CO₃.

Data from experiment 4 were recorded over a 29-day period. The voltage remained relatively constant at 2.35 V, and the electrolyte temperature was ~23°C above the temperature of the blank. The parameters at day 27 are given in Table II. The on-the-fly calibration curve of experiment 4 as well as the integral calibration curve for the matched blank cell are shown in Fig. 10.

The on-the-fly heating coefficient of the electrolytic cell was $(0.17 \pm 0.01$ °C/W). The intercept at zero in-

put power for the integrally calibrated electrolytic cell was 8.2°C, which indicates 48.2 W of excess heat.

It was observed that gas sparging in the electrolytic cell provides sufficient mixing in the absence of stirring so that temperature gradients were not observed to within their detection limit ($\pm 0.1^{\circ}$ C). The calibration (nonelectrolysis cell) was stirred at 250 rpm to compensate for the lack of stirring by gas sparging. It was determined that the stirring power increased the blank



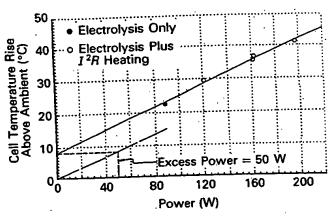


Fig. 10. A graphical determination of the excess power of experiment 4.

temperature 0.20°C above the ambient temperature, and this power was not subtracted from the blank temperature in the temperature measurements. Accounting for this temperature rise would increase the experimentally determined electrolytic cell excess energy by ~1.2 W.

From the condensed evolving water vapor, the evaporative losses from experiment 4 were measured to be 6.5 ml per 24 h, and 402 ml of water was added to the cell per 24 h to maintain a constant fill level. The volume consumed by Faraday losses is calculated to be 403 ml. Thus, the evaporative and Faraday losses equaled the maintenance water volume to within 1%.

Elemental analysis and scanning electron microscopy of metallurgical samples of the nickel cathode taken before operation and at day 56 of continuous operation were identical, indicating that the nickel cathode had not changed chemically or physically. Elemental analysis data of a sample of the nickel cathode taken at day 56 of continuous operation are shown in Table IV. Photomicrographs of a sample of the nickel cathode taken at day 56 of continuous operation are shown in Fig. 11.

The cell was disassembled and inspected after 23

TABLE IV

Chemical Analysis of the Nickel Wire of Experiment 4
After 56 Days of Operation

Mainly nickel
Trace (0.1 to 1.0%) copper
Slight trace (100 to 1000 ppm) magnesium
Very slight trace (10 to 100 ppm) aluminum and
manganese
Very, very slight trace (<10 ppm) chromium, titanium,
silver, tin, iron, silicon, boron, and phosphorus



TABLE V

Chemical Analysis of the Potassium Carbonate Electrolytic Solution of Experiment 4 After 42 Days of Operation

Flame emission spectrographic analysis
Mainly potassium
Slight trace (100 to 1000 ppm) sodium
Very slight trace (<10 ppm) magnesium
Specific gravity = 1.072
Concentration = 0.63 M K₂CO₃
Solution pH = 11.5

days of continuous operation. This inspection showed no visible signs of a reaction between the electrodes and the electrolyte. The cell was reassembled, and it continued to operate with an excess power production of ~50 W for an additional 19 days, after which time the voltage and current parameters of experiment 5 were initiated.

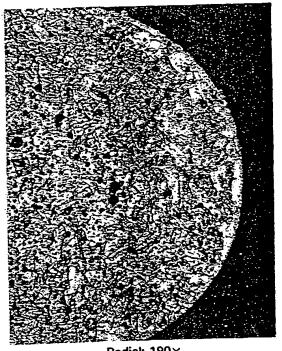
The pH, specific gravity, concentration of K₂CO₃, and elemental analysis of the electrolyte sample taken after 42 days of continuous operation were unchanged from the values obtained for the electrolyte sample before operation. These data are shown in Table V.

The results of the gas chromatographic analysis of the evolving electrolytic gases showed two-thirds hydrogen, one-third oxygen, and trace amounts of nitrogen. No significant quantities of CO or CO₂ were found, confirming that the K₂CO₃ electrolyte was not degraded during operation.

Measurements of neutrons were considered unnecessary since light water was used rather than deuterium oxide. Scintillation counter and photographic film measurements show no radiation above background was detected, indicating that nuclear reactions did not occur.

Data from experiments 5 through 13 were recorded over a 135-day period as the duty cycle was increased from 3 to 25%. The input and output powers are listed in Table II as a function of duty cycle. A comparison of cell temperature rise above ambient and power with the calibration curve is shown in Fig. 12. The comparison for experiment 9 shows ~53 W of excess energy at a 7% duty cycle. This corresponds to an output over input power ratio of ~4.12:1.

Data from experiment 14 were recorded over a 240-day period at an operating condition of 1 Hz, 10 A, and 20% duty cycle. Data for day 120 are recorded in Table II and show 41 W of output with an output-to-input ratio of ~22 assuming 100% Faraday efficiency. Actual Faraday efficiency at these low-current levels (2 A on average) has not been established. If the Faraday efficiency were zero (100% recombination), then the output-to-input ratio would be 8.2:1.



Axial: 95×

Radial: 190×

Fig. 11. Photomicrographs of metallurgical samples of the nickel cathode taken at day 56 of continuous operation.

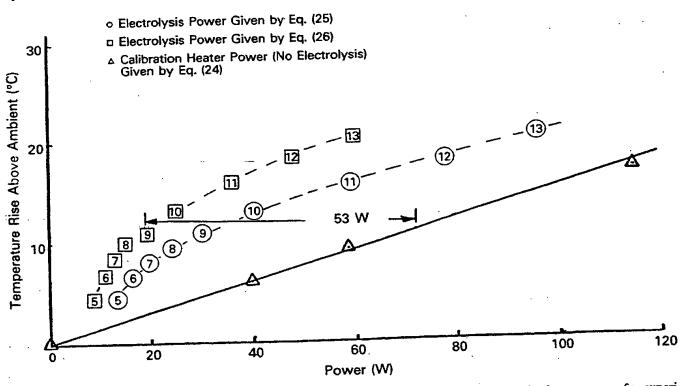


Fig. 12. Comparison between cell temperature rise above ambient for electrolysis power and for heater power for experiments 5 through 13.



EXPERIMENTAL IDENTIFICATION OF THE DIHYDRINO MOLECULE

The dihydrino molecules would be stable to combustion relative to molecular hydrogen, and the dihydrino molecule could be detected by mass spectroscopy with the presence of a m/e = 2 peak with a different branching ratio to form m/e = 1 relative to m/e = 2. To test this premise, we collected in an elastomer bladder 1650 ml of the electrolysis gases from experiment 14, which produced 39.1 W of excess power according to the exothermic reaction given by Eqs. (4), (5), and (6). The bladder contained a spark plug that was activated, causing an explosion of the gas contents. The volume of the bladder following combustion was 70 ml. Samples of the pre- and postcombustion electrolysis gases as well as hydrogen and water-saturated air were analyzed by mass spectroscopy.

The dihydrino molecule, H_2^* , has a higher ionization energy than H_2 . Mass spectroscopy of the post-combustion electrolysis gas sample was performed whereby the intensity of the m/e = 1 and m/e = 2 peaks was recorded while the ionization potential of the mass spectrometer was varied.

The results of the mass spectroscopic analysis of gases evolved from experiment 14 before and after combustion are given in Table VI; of room air saturated with water, in Table VII; of the standard hydrogen sample, in Table VIII; and of the postcombustion electrolysis gas sample whereby the intensity of the m/e = 1 and m/e = 2 peaks was recorded while the ionization potential of the mass spectrometer was varied, in Table IX.

DISCUSSION

From Table VI, the m/e = 18 and m/e = 32 peak intensities, respectively, demonstrate that both the pre-

TABLE VI

Mass Spectroscopic Analysis of Gases Evolved from the Cell of Experiment 14 Before and After Combustion (IP = 70 eV)

Mass/Charge (m/e)	Intensity of Precombustion Electrolysis Gases	Intensity of Postcombustion Electrolysis Gases
1	1.2×10^{-7}	0.40×10^{-7}
2	1.55×10^{-5}	0.55×10^{-7}
3	0.30×10^{-7}	<u> </u>
18	0.57×10^{-5}	0.55×10^{-5}
28	0.37 × 10 ⁻⁴	0.90 × 10 ⁻⁴
28 32	0.69 × 10 ⁻⁴	0.65 × 10 ⁻⁴
	0.90 × 10 ⁻⁶	0.40×10^{-5}
40 44	0.70 × 10 ⁻⁶	0.12×10^{-5}



and postcombustion electrolysis gas samples contained the same percentage of water vapor and of O_2 . The predicted percentage for the precombustion electrolysis gas sample is one-third, as given by Faraday's law for the electrolysis of water. The oxygen signal for the postcombustion electrolysis gases is higher than can be due to atmospheric contamination.

From Table VI, the m/e = 28 peak intensity demonstrates that the pre- and postcombustion electrolysis gas samples contained the same percentage of nitrogen. The nitrogen was present in trace amounts in both gas samples as demonstrated by the m/e = 28 peak intensities from Table VI and the volume change with combustion. From the volume change, nitrogen represented <4% of the precombustion gas sample, and the m/e = 28 peak intensity of the postcombustion gas

TABLE VII

Mass Spectroscopic Analysis of Room Air
Saturated with Water
(IP = 70 eV)

Mass/Charge (m/e)	Intensity (× 10 ⁻⁷)
1	0.24
2	0.040
18	43.0

TABLE VIII

Mass Spectroscopic Analysis of Hydrogen
(IP = 70 eV)

Mass/Charge (m/e)	Intensity (× 10 ⁻⁷)
1	2.0
2	300.0
3 HD	0.12
3 H ₃	2.0

TABLE IX

Mass Spectroscopic Analysis with Varying Ionization
Potential of Gases Evolved from the Cell of
Experiment 14 Following Combustion

Ionization Potential (eV)	Intensity of Signal Mass-to-Charge Ratio	
	(m/e=1)	(m/e=2)
20 70	$0.007 \times 10^{-8} \\ 1.8 \times 10^{-8}$	$0.03 \times 10^{-8} \\ 1.8 \times 10^{-8}$

OLE OF

sample was only a factor of 2.4 of that of the precombustion electrolysis gas sample. No hydrogen is anticipated following combustion.

The data are consistent with the remaining two-thirds of the postcombustion electrolysis gases comprising the dihydrino molecule, H_2^* , which does not undergo combustion with oxygen. The stoichiometric ratio of two-thirds H_2^* to one-third O_2 gives the correct mass balance. The m/e=2 peak for the postcombustion electrolysis gases is ten times the intensity of the peak from water [given by the product of the ratio of m/e=2 to m/e=18 of the water-saturated air mass spectrum times the intensity of the m/e=18 peak (H_2O) of the postcombustion electrolysis gas sample]. Thus, the m/e=2 peak is assignable to H_2 or to H_2^* .

The assignment to H2 is made as follows. The m/e = 1 peak of the postcombustion electrolysis gas sample is significantly more intense than that predicted by production from water [given by the product of the ratio of m/e = 1 to m/e = 18 of the water-saturated air mass spectrum times the intensity of the m/e = 18 peak (H₂O) of the postcombustion gas sample]. The additional contribution to the m/e = 1 peak predicted with the assignment of the m/e = 2 peak to hydrogen (given by the product of the ratio of m/e = 1 to m/e = 2 of the hydrogen mass spectrum times the intensity of the m/e = 2 peak of the postcombustion electrolysis gas sample) is insufficient to explain the intensity of the m/e = 1 peak. Thus, the species giving rise to the m/e = 2 peak must have a different m/e = 1 to m/e = 2production efficiency than H_2 . Therefore, the m/e=2peak is assigned to H2.

The dihydrino molecule, H_2^* , has a higher ionization energy than H_2 . This was observed by measuring the intensity of the m/e = 1 and m/e = 2 peaks while the ionization potential of the mass spectrometer was varied. The ionization reaction of H_2 is

$$H_2(g) \to H_2(g)^+ + e^- IE = 15.46 \text{ eV}$$
 (29)

The ionization energies of water are 12.61, 14.8, 18.8, and 32 eV. The data of Table IX demonstrate that no m/e = 2 peak is present at an ionization potential above the threshold for the ionization of molecular hydrogen, but a m/e = 2 peak that is too intense to be attributed to water ionization is present at a significantly higher ionization potential. The data are consistent with the assignment of m/e = 2 to H_2^* , the dihydrino molecule.

CONCLUSION

We review and present three sets of heat production and product identification data including the work of HydroCatalysis Power Corporation (experiments 1, 2, and 3) and Thermacore, Inc. (experiments 4 through 14). We report here experimental evidence supporting the HPC theory that an exothermic reaction occurs wherein the electrons of hydrogen and deuterium atoms

are each stimulated to relax to a quantized potential energy level below that of the ground state via electrochemical reactants K+ and K+; Pd2+ and Li+; or Pd and O2 of redox energy resonant with the energy hole that stimulates this transition. Calorimetry of pulsed current and continuous electrolysis of aqueous potassium carbonate (K+/K+ electrocatalytic couple) at a nickel cathode was performed. The excess output power of 41 W exceeded the total input power given by the product of the electrolysis voltage and current by a factor of >8. The product of the exothermic reaction is atoms having electrons each of energy below the ground state, and they are predicted to form molecules. The predicted molecules were identified by their lack of reactivity with oxygen, by separation from molecular deuterium by cryofiltration, and by mass spectroscopic analysis.

The combustion of the gases evolved during the electrolysis of a K_2CO_3 /light water electrolyte (K^+/K^+ electrocatalytic couple) with a nickel cathode was incomplete. The mass spectroscopic analysis of uncombusted gases demonstrated that the species predominantly giving rise to the m/e = 2 peak must have a different m/e = 1 to m/e = 2 production efficiency than hydrogen. The further mass spectroscopic analysis of the m/e = 2 peak of the uncombusted gas demonstrated that the dihydrino molecule, H_2^* , has a higher ionization energy than H_2 .

The mass spectroscopic analysis of the cryofiltered gases evolved during the electrolysis of a heavy water LiOD electrolyte (Pd²⁺/Li⁺ electrocatalytic couple) with a palladium cathode demonstrated that the dideutrino molecule, D₂, has a higher ionization energy than D₂.

Palladium sheets coated on one side with a hydrogenimpermeable gold layer and on the other surface with an oxide coat (MnO_x, AlO_x) , or SiO_x were loaded with deuterium or hydrogen. Heat was observed from light and heavy hydrogen only when the mixed oxide coat was present (Pd/O_2) electrocatalytic couple). The high-resolution (0.001) amu quadrupole mass spectroscopic analysis of the gases released when a current was applied to a deuterium-loaded (99.9%), MnO_x -coated palladium sheet indicate the presence of a large shoulder on the D_2 peak that is due to the dideutrino molecule, D_2^* .

Further experiments are planned to demonstrate that this lower energy form of hydrogen is the product of heat-producing cells. Following cryofiltration of the electrolysis gases, the dihydrino molecule is distinguished from normal molecular hydrogen by mass spectroscopy. The branching ratio to form m/e = 1 relative to m/e = 2 that is observed for the dihydrino molecule is different from the ratio that is observed for normal molecular hydrogen. Mass spectroscopy further distinguishes a sample containing dihydrino molecules from a sample containing H_2 by showing a different ion production efficiency as a function of ionization potential and a different ion production efficiency at a



given ionization potential for the two samples. Highresolution mass spectroscopy shows two peaks for a mixture of H_2 and H_2^* .

ACKNOWLEDGMENTS

Special thanks to J. Farrell for technical support, papers, discussions, and review of this manuscript and to D. Parees, of Air Products Corporation, who performed the mass spectroscopy.

REFERENCES

- 1. H. A. HAUS, "On the Radiation from Point Charges," Am. J. Phys., 54, 1126 (1986).
- 2. R. MILLS, Unification of Spacetime, the Forces, Matter; and Energy, Technomics Publishing Company, Lancaster, Pennsylvania (1992).
- 3. R. NIEMINEN, "Atoms Band Together," Nature, 365, 289 (1992).
- 4. J. FARRELL, W. GOOD, and R. MILLS, "An Alternative Explanation of Extreme Ultraviolet Emissions from Dark Matter," submitted to Astrophys. Lett. Communications (1993).
- 5. M. H. MILES, B. F. BUSH, G. S. OSTROM, and J. J. LAGOWSKI, "Helium Production During the Electrolysis of D₂O in Cold Fusion Experiments," J. Electroanal. Chem., 304, 271 (1991).
- 6. R. DAGANL, "New Evidence Claimed for Nuclear Process in Cold Fusion," Chem. Eng. News, 31 (Apr. 1, 1991).
- 7. M. H. MILES, B. F. BUSH, G. S. OSTROM, and J. J. LAGOWSKI, "Heat and Helium Production in Cold Fusion



Experiments," Proc. Conf. The Science of Cold Fusion, Como, Italy, June 29-July 4, 1991, p. 363, T. BRESSANI, E. DEL GIUDICE, and G. PREPARATA, Eds., SIF (1991).

- 8. M. H. MILES, R. A. HOLLINS, B. F. BUSH, J. J. LAGOWSKI, and R. E. MILES, "Correlation of Excess Power and Helium Production During D₂O and H₂O Electrolysis Using Palladium Cathodes," J. Electroanal. Chem., 346, 99 (1993).
- 9. C. C. CHIEN, D. HODKO, Z. MINEVSKI, and J. BOCKRIS, "On an Electrode Producing Massive Quantities of Tritium and Helium," J. Electrognal. Chem., 338, 189 (1992).
- 10. B. F. BUSH, Department of Chemistry, University of Texas, Austin, Personal Communication (1993).
- 11. S. JONES, Newsgroups: sci.physics.fusion (Mar. 3, 1993).
- 12. M. H. MILES and B. F. BUSH, "Search for Anomalous Effects Involving Excess Power and Helium During D₂O Electrolysis Using Palladium Cathodes," *Proc. 3rd Int. Conf. Cold Fusion*, Nagoya, Japan, October 21-25, 1992, p. 189.
- 13. B. REES, "Cold Fusion: What Do We Know? What Do We Think?" J. Fusion Energy, 10, 1, 111 (1991).
- 14. E. YAMAGUCHI and T. NISHIOKA, "Direct Evidence for Nuclear Fusion Reactions in Deuterated Palladium," *Proc. 3rd Int. Conf. Cold Fusion*, Nagoya, Japan, October 21-25, 1992.
- 15. E. YAMAGUCHI and T. NISHIOKA, "Helium-4 Production from Deuterated Palladium at Low Energies," NTT Basic Research Laboratories and IMRA Europe S.A., Personal Communication (1992).

THIS PAGE BLANK (USPTO)





EXCESS HEAT PRODUCTION BY THE ELECTROLYSIS OF AN AQUEOUS POTASSIUM CARBONATE ELECTROLYTE AND THE IMPLICATIONS FOR COLD FUSION

RANDELL L. MILLS Mills Technologies, The Griest Building Suite 700 I, 8 North Queen Street, Lancaster, Pennsylvania 17603

STEVEN P. KNEIZYS Ursinus College, Academic Computing Collegeville, Pennsylvania 19426

Received February 20, 1991 Accepted for Publication April 1, 1991

COLD FUSION

TECHNICAL NOTE

KEYWORDS: cold fusion, calorimetry, electrolysis

According to a novel atomic model, the predominant source of heat of the phenomenon called cold fusion is the electrocatalytically induced reaction whereby hydrogen atoms undergo transitions to quantized energy levels of lower energy than the conventional ground state. These lower energy states correspond to fractional quantum numbers. The hydrogen electronic transition requires the presence of an energy hole of ~27.21 eV provided by electrocatalytic reactants (such as Pd²+/Li+, Ti²+, or K+/K+) and results in "shrunken atoms" analogous to muonic atoms. In the case of deuterium, fusion reactions of shrunken atoms predominantly yielding tritium are possible. Calorimetry of pulsed current and continuous electrolysis of aqueous potassium carbonate (K+/K+ electrocatalytic couple) at a nickel cathode is performed in single-cell dewar calorimetry cells. Excess power out exceeded input power by a factor of >37.

L INTRODUCTION

As a result of the de facto assumptions of quantum mechanics and the incomplete or erroneous models that often follow, the prediction and development of useful or functional systems and structures requiring an accurate understanding of atomic structure and energy transfer have been limited. The Schrödinger equation, for example, does not explain the phenomenon referred to as "cold" nuclear fusion: large anomalous heat release and trace tritium production of certain heavy water electrolytic cells having a palladium cathode and a lithium electrolyte. Thus, advances in this field are largely limited to laboratory discoveries that have limited or suboptimal utility. To remedy the shortcomings and inconsistencies of quantum mechanics, Mills and Farrell¹ developed a novel theory for which the fundamental laws of nature are shown to be applicable on all scales. Maxwell's equations, Einstein's general and special relativity, Newtonian mechanics, and the strong and weak forces are unified. Their theory is a quantum theory in which the four quantum numbers of the electron of the one-electron atom arise naturally without gamma factors and provide an explanation for the seemingly contradictory and inconsistent observations of cold fusion. A summary of the development of the theory pertinent to cold fusion follows.

IL THE ONE-ELECTRON ATOM

One-electron atoms include the hydrogen atom, He(I), Li(II), Be(III), and so on. In each case, the nucleus contains Z protons and the atom has a net positive charge of (Z-1)e. All forces are central. The mass-energy and angular momentum of the electron are constant; this requires that the equation of motion of the electron be temporally and spatially harmonic. Thus, Laplace's equation applies and

$$\left(\nabla^2 + \frac{1\delta^2}{v^2 \delta t^2}\right) V = 0 .$$
(1)

ILA. The Boundary Condition

The condition for radiation by a moving charge is derived from Maxwell's equations. To radiate, the space-time Fourier transform of the charge density function must possess components that are synchronous with waves traveling at the speed of light.² Alternatively, for nonradiative states, the charge density function must *not* possess space-time Fourier components that are synchronous with waves traveling at the speed of light.

II.B. The Radial Function

Mills and Farrell¹ do not solve for the radial function from Laplace's equation. Rather, they treat this as a boundary value problem and assume a delta function for the radial function:

$$f(r) = \delta(r - r_n) , \qquad (2)$$





where r_n is an allowed radius. [Note that the boundary condition for solution of the radial function of the hydrogen atom with the Schrödinger equation is $\Psi \to 0$ as $r \to 0$. Here, however, the boundary condition is embodied in Eq. (2).] Thus, this trial function implies that the allowed states are two-dimensional spherical shells (zero thickness) of charge density (and mass density) at specific radii r_n . These shells are referred to as electron orbit spheres. When the form of the charge density function is known, the boundary condition (for nonradiation) can be applied to determine specific conditions for r_n . Here, the results of Mills and Farrell are given:

$$2\pi(nr_1) = 2\pi r_n = n\lambda_1 = \lambda_n , \qquad (3)$$

where

 $n = 1, 2, 3, 4, \dots$

 $n = \frac{1}{2}, \frac{1}{4}, \frac{1}{4}, \dots$

 λ_1 = allowed wavelength for n = 1

 r_1 = allowed radius for n = 1.

There are several noteworthy features of Eq. (3):

- 1. Values of n other than the traditional 1,2,3,..., are allowed.
- 2. The potential energy is a constant (at a given n) because the electron is at a fixed distance r_n from the nucleus:

$$V_n = \frac{-Ze^2}{4\pi\epsilon_0 r_n} , \qquad (4)$$

where ϵ_0 is the permittivity of free space.

3. The kinetic energy and velocity squared are constant because the atom does not radiate at r_n and the potential energy is constant:

$$T_n = \frac{1}{2} m_e v_n^2 \quad . \tag{5}$$

4. The linear momentum must be constant:

$$p_n = \pm m_e v_n \ . \tag{6}$$

The wavelength must be constant. Using the de Broglie relationship,

$$\lambda_n = \frac{h}{p_n} = \frac{h}{m_e v_n} \ . \tag{7}$$

ILC. The Angular Function

The radial function for the electron indicates that the electron is two-dimensional. Therefore, the angular mass density function $A(\theta, \phi, t)$ of the electron must be a solution of the Laplace equation in two dimensions (plus time):

$$\left(\nabla^2 + \frac{1}{v^2} \frac{\delta^2}{\delta t^2}\right) A(\theta, \phi, t) = 0$$
 (8)

OL

$$\left[\frac{1}{r^2 \sin \theta} \frac{\delta}{\delta \theta} \left(\sin \theta \frac{\delta}{\delta \theta} \right)_{r\phi} + \frac{1}{r^2 \sin^2 \theta} \left(\frac{\delta^2}{\delta \phi^2} \right)_{r\theta} + \frac{1}{v^2} \frac{\delta^2}{\delta t^2} \right] \times A(\theta, \phi, t) = 0 , \qquad (9)$$

where v is the linear velocity of the electron.

Conservation of momentum and energy allows the angular functions and time functions to be separated:

$$A(\theta,\phi,t) = Y(\theta,\phi)K(t) . \tag{10}$$

Charge is conserved as well, and the charge of an electron can be superimposed on its mass. That is, the angular mass density function $A(\theta, \phi, t)$ is also the angular charge density function.

The electron orbit sphere experiences a constant potential energy because it is fixed at $r = r_n$. To avoid being pulled into the nucleus, the orbit sphere must rotate. It is the rotation of the orbit sphere that causes angular momentum. The rotational energy of a rotating body is

$$E_{rotational} = \frac{1}{2}I\omega^2 , \qquad (11)$$

where

I = moment of inertia

 $\omega = \text{angular velocity}.$

The angular velocity must be constant (at a given n) because r is constant, and the energy and angular momentum are constant. The allowed angular velocities are related to the allowed frequencies by

$$\omega_n = 2\pi \nu_n . (12)$$

The allowed frequencies are related to the allowed velocities by

$$v_n = \nu_n \lambda_n \tag{13}$$

The allowed velocities and angular frequencies are related to r_n by

$$v_n = r_n \omega_n , \qquad (14)$$

$$\omega_n = \frac{\hbar}{m.r^2} , \qquad (15)$$

and

$$v_n = \frac{\hbar}{m_e r_n} . {16}$$

The magnitude of the angular momentum |L| must be constant. The constant is \hbar :

$$|L_n| = m_e v_n r_n = m_e \frac{\hbar}{m_e r_n} r_n = \hbar$$
 (17)

Thus, Eq. (9) becomes

$$-\frac{\hbar^{2}}{2I} \left[\frac{1}{\sin \theta} \frac{\delta}{\delta \theta} \left(\sin \theta \frac{\delta}{\delta \theta} \right)_{r\phi} + \frac{1}{\sin^{2} \theta} \left(\frac{\delta^{2}}{\delta \phi^{2}} \right)_{r\theta} \right] \times A(\theta, \phi, t) = EA(\theta, \phi, t) . \tag{18}$$

The space-time angular function $A(\theta, \phi, t)$ is separated into an angular function and a time function, $Y(\theta, \phi)K(t)$. The time-harmonic function $K(t) = \exp(i\omega_n t)$ is a solution. [Here, again, the boundary condition (for nonradiation) determines the specific conditions for ω_n .] When the time-harmonic function is eliminated,

$$-\frac{\hbar^2}{2I} \left[\frac{1}{\sin \theta} \frac{\delta}{\delta \theta} \left(\sin \theta \frac{\delta}{\delta \theta} \right)_{r\phi} + \frac{1}{\sin^2 \theta} \left(\frac{\delta^2}{\delta \phi^2} \right)_{r\theta} \right] \times Y(\theta, \phi) = EY(\theta, \phi) . \tag{19}$$

Equation (19) is the equation for the rigid rotor. The angular function can be separated into a function of Θ and a function of Φ , and the solutions are well known.³ The energies are given by

$$E_{rotational} = \frac{\hbar^2 l(l+1)}{2I}$$
 , $l = 0,1,2,3,...$ (20)

FUSION TECHNOLOGY VOL. 20 AUG. 1991



Mills and Kneizys

The angular functions are the spherical harmonics $Y_i^m(\phi,\theta)$. The spherical harmonic $Y_s(\phi,\theta) = 1$, $s = \frac{1}{2}$, is also a solution. The spherical harmonics can be positive or negative (depending on θ); the most negative value is -1. But the mass of the electron cannot be negative, and the charge cannot be positive. Thus, to ensure that the function is always positive or zero, the form of the angular solution must be

$$Y_{S}(\phi,\theta) + Y_{I}^{m}(\phi,\theta) , \qquad (21)$$

where $Y_S(\phi, \theta)$ is called the angular spin function and $Y_I^m(\phi,\theta)$ is called the angular orbital function. The function $Y_I^m(\phi,\theta)$ can be thought of as a modulation function. Thus, the angular momentum can be thought of as arising from a spin component and an orbital component that have corresponding energies. One result of this model for l = 0 [uniform charge (mass) density] is that some of the angular momentum (kinetic energy) is not counted in the spin angular momentum · (rotational energy). That is, for any spin axis, there is an infinite number of great circles with planes passing through that axis with angles other than 90 deg. All points on any one of these great circles are moving, but not all of that motion is part of the spin angular momentum (rotational energy); only that motion perpendicular to the spin axis is part of the spin angular momentum (rotational energy). Thus, the spin angular momentum (rotational energy) is always less than the total angular momentum (kinetic energy). The following relationships must hold:

$$E_{rotational} = \frac{1}{2}I\omega^2 \le \frac{1}{2}mv^2 , \qquad (22)$$

$$I_{(i)} < h \tag{23}$$

and

$$I \le mr^2 . (24)$$

Furthermore, it is known from the Stern-Gerlach experiment that a beam of silver atoms splits into two components when passed through an inhomogeneous magnetic field. The measured spin angular momentum is $\sqrt{\frac{1}{4}}\hbar$, and the angular momentum in the direction of the applied field is $\pm \hbar/2$. Given a uniform density of points traveling on great circles with a total angular momentum of \hbar , it can be shown that the projection of the total angular momentum onto the spin axis is $\sqrt{\frac{1}{4}}\hbar$. The Stern-Gerlach experiment implies a magnetic moment of one Bohr magneton and an associated angular momentum quantum number of $\frac{1}{2}$. Historically, this quantum number is called the spin quantum number m_s , and that designation is maintained.

II.D. The Magnetic Field from the Spinning Orbit Sphere

The orbit sphere is a spinning shell of negative charge. For l = 0, the orbit sphere gives rise to a magnetic moment of one Bohr magneton,³

$$\beta = \frac{e\hbar}{2m} = 9.274 \times 10^{-24} \text{ J/T} ,$$
 (25)

and a magnetic field,1

$$H = \begin{cases} \frac{e\hbar}{m_e r_n^3} \left(\hat{i}_r \cos \theta - \hat{i}_{\theta} \sin \theta \right) , & \text{for } r < r_n \\ \frac{e\hbar}{2m_e r^3} \left(\hat{i}_r 2 \cos \theta - \hat{i}_{\theta} \sin \theta \right) , & \text{for } r > r_n \end{cases}$$
 (26)

Note that the magnetic field is a constant for $r < r_n$.

AQUEOUS POTASSIUM CARBONATE ELECTROLYTE

It can be shown that the energy stored in the magnetic field of the electron orbit sphere is

$$E_{mag} = \frac{\pi \mu_0 e^2 \hbar^2}{m_e^2 r_o^3} . {28}$$

II.E. Determination of r.

The one-electron orbit sphere is a spherical shell of negative charge (total charge = -e) of zero thickness at a distance r_n from the nucleus (charge = +Ze). For the ground state (n = 1), the centrifugal force of the electron is given by

$$f_{centrifugal} = \frac{m_e v_1^2}{r_1} . (29)$$

The centripetal force is the Coulombic force f_{Coul} between the electron and the nucleus:

$$f_{Coul} = \frac{Z_{eff}e^2}{4\pi\epsilon_0 r_1^2} , \qquad (30)$$

where ϵ_0 is the permittivity of free space. Thus,

$$\frac{m_e v_1^2}{r_1} = \frac{Ze^2}{4\pi\epsilon_0 r_1^2} \ . \tag{31}$$

Using Eq. (16),

$$r_1 = \frac{4\pi\epsilon_0\hbar^2}{Ze^2m_e} {.} {(32)}$$

The Bohr radius is substituted into Eq. (32):

$$a_0 = \frac{4\pi\epsilon_0 h^2}{e^2 m_e} \tag{33}$$

and

$$r_1 = \frac{a_0}{7} . {34}$$

ILF. Energy Calculations

The potential energy V can be calculated from the force between the electron and the nucleus [Eq. (30)] and the radius r_1 :

$$V = \frac{-Ze^2}{4\pi\epsilon_0 r_1} = \frac{-Z^2e^2}{4\pi\epsilon_0 a_0} = -Z^2 \times 4.3675 \times 10^{-18} \text{ J}$$
$$= -Z^2 \times 27.2 \text{ eV} . \tag{35}$$

Because this is a central force problem, the kinetic energy T is $-\frac{1}{2}V$:

$$T = \frac{Z^2 e^2}{8\pi\epsilon_0 a_0} = Z^2 \times 13.159 \text{ eV} . \tag{36}$$

The same result can be obtained from $T = \frac{1}{2}m_e v_1^2$ and Eq. (16).

Alternatively, the kinetic energy, which is equal to the stored electric energy E_{ele} , can be calculated from⁴

$$T = E_{ele} = -\frac{1}{2} \epsilon_0 \int_{-\infty}^{r_1} \epsilon^2 dv , \qquad (37)$$

where

$$\epsilon = \frac{Ze}{4\pi\epsilon_0 r^2} .$$





Thus, as the orbit sphere shrinks from ∞ to r_1 ,

$$E_{ele} = -\frac{1}{2} \epsilon_0 \int_0^{2\pi} \int_0^{\pi} \int_{-\infty}^{\pi} \epsilon^2 r^2 \sin\theta \, dr \, d\theta \, d\Phi \qquad (38)$$

$$= -\frac{Z^2 e^2}{8\pi\epsilon_0} \int_{\infty}^{r_1} \frac{1}{r^2} dr$$
 (39)

$$= \frac{Z^2 e^2}{8\pi\epsilon_0 a_0} = Z^2 \times 2.1837 \times 10^{-18} \text{ J}$$
$$= Z^2 \times 13.589 \text{ eV} . \tag{40}$$

III. EXCITED STATES OF THE ONE-ELECTRON ATOM

It is well known that resonator cavities can trap electromagnetic radiation of discrete resonant frequencies. The orbit sphere is a resonator cavity and can trap photons of discrete frequencies. Thus, photon absorption occurs as an excitation of a resonator mode.

An electron in the ground state (n = 1) is in force balance:

$$\frac{m_e v_1^2}{r_1} = \frac{Ze^2}{4\pi\epsilon_0 r_1^2} . \tag{41}$$

When an electron in the ground state absorbs a photon of sufficient energy to take it to a new nonradiative state (n = 2,3,4,...), force balance must be maintained. This is possible only if $Z_{eff} = Z/n$; therefore,

$$\frac{m_e v_n^2}{r_n} = \frac{Z_{eff} e^2}{4\pi \epsilon_0 r_n^2} . {(42)}$$

The reduction of the charge from Ze to Ze/n is caused by trapping a photon in the orbit sphere cavity—a spherical cavity. The photon's electric field creates standing waves in the cavity with an effective charge of (-1 + 1/n)Ze (at r_n). The total charge experienced by the electron is the sum of the proton and photon charge components. The equation for these trapped photons can be solved as a boundary value problem of Laplace's equation.

For the hydrogen atom, the boundary conditions are that the radial electric field of the photon at r_n is

$$\epsilon \hat{i}_{rphoton} = \left(-1 + \frac{1}{n}\right) \frac{e}{4\pi\epsilon_0 (r_n)^2}$$
, $n = 2, 3, 4, \dots$, (43)

The general form of the solution to Laplace's equation in spherical coordinates is

$$\Phi(r,\theta,\phi) = \sum_{l=0}^{\infty} \sum_{m=-l}^{l} [A_{l,m}r^{l} + B_{l,m}r^{-(l+1)}]
\times [Y_{l,m}(\theta,\phi) + Y_{s}(\theta,\phi)] .$$
(44)

All $A_{l,m}$ are zero because the electric field given by the potential must be inversely proportional to the radius to obtain force balance. The electric field is the gradient of the potential:

$$\epsilon = -\nabla \Phi \tag{45}$$

and

$$\epsilon \hat{i}_r = -\frac{\delta \Phi}{\delta r} \hat{i}_r \ . \tag{46}$$

Thus,

$$\epsilon \hat{i}_r = \sum_{l=0}^{\infty} \sum_{m=-l}^{l} B_{l,m} (l+1) r^{-(l+2)} [Y_l^m(\phi,\theta) + Y_S^{m_S}(\phi,\theta)] . \tag{47}$$

Given that $\epsilon(proton) = +e/4\pi\epsilon_0 r_n^2$ and that the electric fields of the proton and photon must superimpose to yield a field equivalent to a central point charge of +Ze/n, the photon electric field for each mode is determined as follows. The angular part of the charge density function of the orbit sphere at force balance must be in phase with the electric field of the orbit sphere because the relationship between the total electric field equation and the photon charge density function is given by Maxwell's equation in two dimensions:

$$n \cdot (\epsilon_1 - \epsilon_2) = \frac{\sigma}{\epsilon_0} , \qquad (48)$$

where

 $n = \text{normal unit vector } (\hat{i}_r)$

 $\epsilon_1 = 0$ = electric field outside of the orbit sphere

 ϵ_2 = total electric field at $r_n = na_0$

 σ = surface charge density.

Thus,

$$\hat{\epsilon_{i_{r}photon}}_{i_{r_{a}mn_{0}}}^{i_{r_{a}mn_{0}}} = \frac{e^{2}}{4\pi\epsilon_{0}(na_{0})^{2}} \left(-1 + \frac{1}{n} \operatorname{Re}\{i[Y_{l}^{m}(\phi,\theta) + Y_{s}^{m_{s}}(\phi,\theta)]\}\right) \tag{49}$$

$$= \sum_{l=0}^{\infty} \sum_{m=-l}^{l} -B_{l,m}(l+1)(na_0)^{-(l+2)} \times \text{Re}\{i[Y_l^m(\phi,\theta) + Y_s^{ms}(\phi,\theta)]\}, \qquad (50)$$

·for

$$n = 2,3,4,...$$

 $l = 1,2,...,n-1$
 $m = -l,-l+1,...,0,...,+l$,

and

$$= \frac{e^2}{4\pi\epsilon_0 (na_0)^2} \left(-1 + \frac{1}{n} \operatorname{Re}\{i[Y_i^m(\phi, \theta) + Y_z^{m_z}(\phi, \theta)]\} \right).$$
(51)

Therefore,

$$\sum_{l=0}^{\infty} \sum_{m=-l}^{l} B_{l,m} = \frac{e(na_0)^l}{4\pi\epsilon_0(l+1)} \left(-1 + \frac{1}{n}\right)$$
 (52)

ลกด

$$\epsilon \hat{i}_{rphoton\,n,l,m} = \frac{e \left(na_0\right)^l}{4\pi\epsilon_0} \frac{1}{r^{(l+2)}} \times \left(-1 + \frac{1}{n} \operatorname{Re}\left[i\left[Y_l^m(\phi,\theta) + Y_s^{m_s}(\phi,\theta)\right]\right]\right),$$
(53)



Mills and Kneizys

AQUEOUS POTASSIUM CARBONATE ELECTROLYTE

where

 $\epsilon \hat{i}_{r total} = \text{sum of the photon and proton electric fields:}$

$$\epsilon \hat{i}_{r total} = \frac{e}{4\pi\epsilon_0 r^2} + \frac{e (na_0)^l}{4\pi\epsilon_0} \frac{1}{r^{(l+2)}}$$

$$\times \left(-1 + \frac{1}{n} \operatorname{Re} \{ i [Y_l^m(\phi, \theta) + Y_s^{m_s}(\phi, \theta)] \} \right). \tag{54}$$

For $r = na_0$, the magnitude of the total radial electric field is

$$\epsilon \hat{i}_{r total} = \left[\frac{e}{4\pi\epsilon_0 (na_0)^2} + \frac{e}{4\pi\epsilon_0 (na_0)^2} \right] \left(-1 + \frac{1}{n} \right) \quad (55)$$

and

$$\epsilon \hat{i}_{rtotal} = \frac{1}{n} \frac{e}{4\pi\epsilon_0 (na_0)^2}$$
 (56)

For quantum numbers n, l, and m, the potential functions are solutions to Laplace's equation. All boundary conditions are met for the corresponding electric fields. Thus, Eq. (54) is the solution of the excited modes of the resonator cavity (orbit sphere). And, the quantum numbers of the electron are n, l, $m(m_l)$, and m_s , as described in Sec. II.

The energy of the photon that excites a mode in a stationary spherical resonator cavity from radius a_0 to radius na_0 is

$$E_{photon} = \frac{e^2}{4\pi\epsilon_0 a_0} \left(1 - \frac{1}{n^2} \right) = h\nu = \hbar\omega$$
 (57)

After multiplying Eq. (57) by

$$\frac{a_0}{a_0} = \frac{4\pi\epsilon_0\hbar^2}{e^2m_ea_0} ,$$

where a_0 is given by Eq. (33), ω_{photon} is

$$\omega_{photon} = \frac{\hbar}{m_e a_0^2} \left(1 - \frac{1}{n^2} \right) . \tag{58}$$

In the case of an electron orbit sphere, the resonator possesses kinetic energy before and after the excitation. The kinetic energy is always one-half of the potential energy. As a result, the energy and angular frequency to excite an electron orbit sphere is only one-half of the values in Eqs. (57) and (58).

The angular velocity of an electron orbit sphere of radius na_0 is

$$\omega_n = \frac{\hbar}{m_e (na_0)^2} . \tag{59}$$

The change in angular velocity of the orbit sphere for an excitation from n = 1 to n = n is

$$\Delta\omega = \frac{\hbar}{m_e(a_0)^2} - \frac{\hbar}{m_e(na_0)^2} = \frac{\hbar}{m_e(a_0)^2} \left(1 - \frac{1}{n^2}\right) . \quad (60)$$

The kinetic energy change of the transition is

$$\frac{1}{2} m_e (\Delta v)^2 = \frac{1}{2} \frac{e^2}{4\pi\epsilon_0 a_0} \left(1 - \frac{1}{n^2} \right) = \frac{1}{2} \hbar \omega . \tag{61}$$

The change in angular velocity of the electron orbit sphere [Eq. (60)] is identical to the angular velocity of the photon necessary for the excitation ω_{photon} [Eq. (58)]. The energy of the photon to excite the equivalent transition in an electron

orbit sphere is one-half of the excitation energy of the stationary cavity because the change in kinetic energy of the electron orbit sphere supplies one-half of the necessary energy. The photon can carry zero or $\pm \hbar$ units of angular momentum [Eq. (17)]. Thus, during excitation, the spin, orbital, or total angular momentum of the orbit sphere can change by zero or $\pm \hbar$. The electron transition rules arise from conservation of angular momentum. The radius of an orbit sphere increases with the absorption of electromagnetic energy. On ionization, the orbit sphere radius goes to infinity, and the electron is a plane wave (consistent with double-slit experiments) with a de Broglie wavelength of $\lambda = \hbar/p$.

IV. PAIR PRODUCTION

Matter and energy are interconvertible and are, in essence, different states of the same entity. The state, matter or energy, is determined by the laws of nature and the properties of space-time. A photon propagates according to Maxwell's equations at the speed of light in space-time with intrinsic impedance η . Matter as a fundamental particle is created in space-time from a photon. Matter obeys the laws of special relativity, the relationship of motion to space-time, and space-time is curved by matter according to the laws of general relativity. Relationships must exist between these laws and the implicit fundamental constants. The conversion of energy into matter requires a transition state in which the identification of the entity as matter or energy is impossible. From the properties of the entity, as matter or energy, and from the physical laws and the properties of space-time, the transition state hereafter called a virtual orbit sphere is derived.

For example, a photon of energy 1.02 MeV becomes a positron and an electron in the presence of charge. This phenomenon, called pair production, involves the conservation of mass/energy, charge, and angular momentum. Pair production occurs as an event in space-time where all boundary conditions are met according to the physical laws: Maxwell's equations, Newton's laws, and Einstein's special and general relativity, where matter and energy are indistinguishable by any physical property. Matter exists as orbit spheres; thus, the conversion of energy to matter must involve the orbit sphere equations derived earlier. It must also depend on the equations of electromagnetic radiation and the properties of spacetime because matter is created from electromagnetic radiation as an event in space-time.

Matter and light obey the wave equation relationship:

$$v = \lambda \frac{\omega}{2\pi} . ag{62}$$

The boundary condition for nonradiation by a virtual orbit sphere is

$$2\pi(r_n^*) = 2\pi(nr_1^*) = n\lambda_1^* = \lambda_n^*$$
, (63)

where

$$n=1,2,3,4,\ldots$$

OI

$$n=\frac{1}{2},\frac{1}{3},\frac{1}{4},\cdots,$$

and where r^* and λ^* are the allowed radii and wavelengths for the virtual matter in question.

The relationship between the potential energy of an



electron orbit sphere and the angular velocity of the orbit sphere is

$$V = \hbar \omega^* = \frac{1}{n} \frac{e^2}{4\pi \epsilon_0 n a_0} . \tag{64}$$

It can be demonstrated that the velocity of the electron orbit sphere satisfies the relationship for the velocity of a wave by substitution of Eqs. (3) and (15) into Eq. (62), which gives Eq. (16). Similarly, the relationship among the velocity of light in free space c, frequency ω , and wavelength λ is

$$c = \lambda \frac{\omega}{2\pi} , \qquad (65)$$

and the energy of a photon of frequency ω is

$$E = \hbar\omega . (66)$$

Recall from Sec. III that a photon of discrete frequency ω can be trapped in the orbit sphere of an electron that serves as a resonator cavity of radius r_n where the resonance excitation energy of the cavity is given by Eq. (64).

The angular velocities of the orbit sphere and trapped photon are the same, and the ratio of their linear velocities is

$$\frac{v_n}{c_{photon}} = \frac{\lambda_n \frac{\omega_n}{2\pi}}{\lambda_{photon} \frac{\omega_{photon}}{2\pi}} = \frac{\lambda_n}{\lambda_{photon}},$$
 (67)

where the subscripts n refer to orbit sphere quantities.

Consider a virtual electron orbit sphere, which is defined as the transition state between light and matter where light and matter are indistinguishable. For this case, the velocity of the electron virtual orbit sphere is the speed of light in the inertial reference frame of the photon that formed the virtual orbit sphere. Substituting c for v_n in Eq. (62), λ_n given by Eq. (3) [where r_1 is given by Eqs. (32) and (33)] for λ , and of ω_n given by Eq. (15) for ω results in

$$c = 2\pi n a_0 \frac{h}{m_e (n a_0)^2} . ag{68}$$

Maxwell's equations provide that

$$c = \left(\frac{1}{\epsilon_0 \mu_0}\right)^{1/2} . \tag{69}$$

The result of substituting Eqs. (33) and (69) into Eq. (68) is

$$\frac{1}{n} = \frac{\hbar}{m_e c a_0} = \frac{\hbar (\epsilon_0 \mu_0)^{1/2}}{m_e} \frac{e^2 m_e}{4\pi \epsilon_0 \hbar^2} = \frac{1}{4\pi} \left(\frac{\mu_0}{\epsilon_0}\right)^{1/2} \frac{e^2}{\hbar} = \alpha^{-1} . \tag{70}$$

In fact, α is the fine-structure constant (a dimensionless constant for pair production). The experimental value is $\frac{1}{137.03604}$. However, by the boundary condition for nonradiation [Eqs. (3) and (63)] 1/n must be 1 divided by an integer. That integer is exactly 137.

The permeability μ_0 of free space is defined as $4\pi \times 10^{-7}$ N/A⁻². The experimental permittivity ϵ_0 of free space is extremely close to $1/36\pi \times 10^{-9}$ F/m, and the experimental value of e^2/\hbar is extremely close to $\frac{1}{410}$.

To match the boundary condition [Eq. (3)], $\hbar/e^2 = 4110 = (30)(137)$ exactly, and $\epsilon_0 = 1/36\pi \times 10^{-9}$ F/m exactly.

In a similar fashion, the intrinsic impedance of free space can be calculated as

$$\eta = \left(\frac{\mu_0}{\epsilon_0}\right)^{1/2} = \left(\frac{4\pi \times 10^{-7}}{\frac{1}{36\pi} \times 10^{-9}}\right)^{1/2} = 120\pi\Omega , \quad (71)$$

and the speed of light is determined to be exactly

$$c = \frac{1}{(\mu_0 \epsilon_0)^{1/2}} = 3 \times 10^8 \text{ m/s}$$
 (72)

The result that c is exactly 3×10^8 m/s may appear counterintuitive given the arbitrary nature of the definitions of metres and seconds. However, mks units are not arbitrary. They are defined according to mutually dependent relationships between the constants and the electric and magnetic force laws. The units take on significance by the definition of μ_0 in terms of Newtons per square ampere. It can be demonstrated that this definition fixes the exact value of the constants and gives rise to an exact definition of the second, metre, and kilogram.

The radius of the virtual electron orbit sphere is $a_0/137$, and the potential energy V is given by Eq. (64), where n is $\frac{1}{137}$:

$$V = -\frac{(137)^2 e^2}{4\pi\epsilon_0 a_0} \ . \tag{73}$$

Substituting

$$a_0 = \frac{4\pi\epsilon_0 \hbar^2}{m_e e^2} ,$$

$$\frac{\hbar}{e^2} = (30)(137) ,$$

$$\eta = \left(\frac{\mu_0}{\epsilon_0}\right)^{1/2} = 120\pi ,$$

and

$$c = \left(\frac{1}{\epsilon_0 \mu_0}\right)^{1/2}$$

into Eq. (73) results in

$$V = m_e c^2 . (74)$$

Furthermore, the result of the multiplication of both sides of Eq. (15) by \hbar , $r_n = na_0$, and substituting

$$a_0 = \frac{4\pi\epsilon_0 h^2}{m_e e^2} ,$$

$$\frac{h}{e^2} = (30)(137) ,$$

$$\eta = \left(\frac{\mu_0}{\epsilon_0}\right)^{1/2} = 120\pi ,$$

and

$$c = \left(\frac{1}{\epsilon_0 \mu_0}\right)^{1/2}$$

yields

$$\hbar\omega_{1/137}^* = m_e c^2 \ . \tag{75}$$

FUSION TECHNOLOGY VOL. 20 AUG. 1991



The relativistic factor,

$$\dot{\gamma} = \frac{1}{\left[1 - \left(\frac{v}{c}\right)^2\right]^{1/2}} \quad ,$$

for an orbit sphere at radius $r^*/137$ ($a_0/137$ for the electron) is 2π . The energy stored in the magnetic field of the electron orbit sphere is

$$E_{max} = \frac{\pi \mu_0 e^2 h^2}{(m_e)^2 r_n^3} . \tag{76}$$

As a result of substituting $a_0/137$ for r_n , 137 for Z_{eff} (recall that $r_n = a_0/Z_{eff}$), the relativistic mass $2\pi m_e$ for m_e ,

$$a_0 = \frac{4\pi\epsilon_0 \hbar^2}{m_e e^2} ,$$

$$\frac{\hbar}{e^2} = (30)(137) ,$$

$$\eta = \left(\frac{\mu_0}{\epsilon_0}\right)^{1/2} = 120\pi ,$$

and

$$c = \left(\frac{1}{\epsilon_0 \mu_0}\right)^{1/2}$$

 $E_{max} = m_e c^2 . ag{77}$

Thus, the energy stored in the magnetic field of the virtual electron orbit sphere equals the electrical potential energy of the virtual orbit sphere. The magnetic field is a relativistic effect of the electrical field; thus, equivalence of the potential and magnetic energies when v = c is given by special relativity where these energies are calculated using Maxwell's equations. The energy stored in the electric and magnetic fields of a photon are equivalent. The corresponding equivalent energies of the virtual orbit sphere are the electrical potential energy and the energy stored in the magnetic field of the orbit sphere.

Space-time is an electrical LC circuit with an intrinsic impedance of exactly

$$\eta = \left(\frac{\mu_0}{\epsilon_0}\right)^{1/2} = \left(\frac{4\pi \times 10^{-7}}{\frac{1}{36\pi} \times 10^{-9}}\right)^{1/2} = 120\pi . \tag{78}$$

The circumference of the virtual electron orbit sphere is $2\pi a_0/137$. The relativistic factor for the radius of $a_0/137$ is 2π ; thus, due to relativistic length contraction, the total capacitance of free space of the virtual orbit sphere of radius $a_0/137$ is

$$C = \frac{2\pi \frac{a_0}{137} \epsilon_0}{2\pi} = \epsilon_0 \frac{a_0}{137} , \qquad (79)$$

where ϵ_0 is the capacitance of space-time per unit length (farad per metre). Similarly, the inductance is

$$L = \frac{2\pi \frac{a_0}{137} \mu_0}{2\pi} = \mu_0 \frac{a_0}{137} , \qquad (80)$$

where μ_0 is the inductance per unit length (henry per metre).

AQUEOUS POTASS. CARBONATE ELECTROLYTE

Thus, the resonance frequency of a virtual electron orbit sphere is

$$\omega^* = \frac{1}{(LC)^{1/2}} = \frac{1}{\left(\epsilon_0 \frac{a_0}{137} \mu_0 \frac{a_0}{137}\right)^{1/2}} . \tag{81}$$

Using

$$a_0 = \frac{4\pi\epsilon_0 \hbar^2}{m_e e^2} ,$$

$$\frac{\hbar}{e^2} = (30)(137) ,$$

$$\eta = \left(\frac{\mu_0}{\epsilon_0}\right)^{1/2} = 120\pi ,$$

and

$$c = \left(\frac{1}{\epsilon_0 \mu_0}\right)^{1/2}.$$

then

$$\omega^* = \frac{m_e c^2}{h} . \tag{82}$$

Thus, the LC resonance frequency of free space for a virtual electron orbit sphere equals the angular frequency of the photon that forms the virtual orbit sphere.

The impedance of any LC circuit goes to infinity when it is excited at the resonance frequency. Thus, the electron virtual orbit sphere is an LC circuit excited at the corresponding resonance frequency of free space. The impedance of free space becomes infinite, and electromagnetic radiation cannot propagate. At this event, the frequency, wavelength, velocity, and energy of the virtual orbit sphere are equal to that of the photon. The mass/energy of the electron virtual orbit sphere is exactly the rest mass at infinity. Thus, a real orbit sphere electron is formed at infinity (with zero velocity) from the electron virtual orbit sphere in the presence of a central electric field of

$$\epsilon = \frac{+e}{4\pi\epsilon_0 r^2} , \qquad (83)$$

where all of the electron virtual orbit sphere equations developed herein apply to this central field.

Actually, due to conservation of charge, a positron and an electron are formed of two photons of energy equal to the rest mass/energy of the electron. (Photons superimpose; thus, pair production occurs with a single photon of energy equal to twice the rest mass of an electron.)

For pair production, angular momentum is conserved. All photons carry h angular momentum, and the angular momentum of all matter as orbit spheres is h [see Eq. (17)]. The radius of particle creation is $r_1^*/137$. This radius is equal to the Compton wavelength bar λ_c , where $\lambda_c = h/\text{mc}$. It arises naturally from the boundary condition of no radiation [Eqs. (3) and (63)], (where $n = \frac{1}{137}$), the de Broglie relationship [Eq. (7)], and the fact that the velocity of the virtual orbit sphere equals c:

$$r_{1/137}^{\bullet} = \frac{\hbar}{mc} = \lambda_c . \tag{84}$$

The correct prediction of electron and positron creation (pair production) having a dimensionless cross section of $\frac{1}{12}$ establishes the validity of electron states corresponding to fractional quantum numbers. In Sec. V, it is demonstrated that

the transition to fractional quantum states and the resulting "shrunken" atoms account for the phenomenon called cold fusion.

V. HECTER AND COULOMBIC ANNIHILATION FUSION (COLD FUSION)

For the hydrogen atom, the radius of the ground-state orbit sphere is a_0 . This orbit sphere contains no photonic waves, and the centripetal force and the Coulombic force balance. Thus,

$$\frac{m_e v_1^2}{a_0} = \frac{e^2}{4\pi\epsilon_0 a_0^2} \ . \tag{85}$$

It is shown in Sec. III that the electron orbit sphere is a resonator cavity that can trap electromagnetic radiation of discrete frequencies. The photon potential functions are solutions of Laplace's equation. The photons decrease the nuclear charge to 1/n and increase the radius of the orbit sphere to na_0 . The new configuration is also in force balance:

$$\frac{m_e v_n^2}{n a_0} = \frac{e^2/n}{4\pi \epsilon_0 (n a_0)^2}$$
 (86)

Mills and Farrell¹ propose, however, that the orbit sphere resonator can trap photons that increase the nuclear charge and decrease the radius of the orbit sphere. This occurs, for example, when the orbit sphere couples to another resonator cavity that can absorb energy—this is the absorption of an energy hole. The absorption of an energy hole destroys the balance between the centrifugal force and the increased central Coulombic force. As a result, the electron is pulled toward the nucleus. If another allowed state that obeys the boundary conditions is not available, the electron plunges into the nucleus.

Now, recall that, for the He⁺ ion (Z=2, a one-electron atom), an allowed state exists at $0.5a_0$. It can be shown that if a ground-state hydrogen atom emits a photon of -27 eV, two photons are created—one is ejected and one remains in the orbit sphere. The photonic wave in the orbit sphere creates an effective charge at the orbit sphere such that the electron experiences an effective charge of +2e and establishes a new centripetal/Coulombic equilibrium at $r_{1/2}=0.5a_0$. That is, the orbit sphere shrinks from $r_1=a_0$ to $r_{1/2}=a_0/2$:

$$V = -\frac{Z_{eff}e^2}{4\pi\epsilon_0 r_{1/2}} = -\frac{2\times 2e^2}{4\pi\epsilon_0 a_0}$$
$$= -4\times 27.178 \text{ eV} = -108.70 \text{ eV} . \tag{87}$$

The kinetic energy of the shrunken orbit sphere is $-\frac{1}{2}V$ or T=54.35 eV. The ground-state hydrogen atom has a net energy of -13.59 eV, and the final hydrogen atom has a net energy of -54.42 eV (the same as He⁺), and $\Delta E=-40.83$ eV for the reaction

$$H(Z_{eff} = 1; r_1 = a_0) \rightarrow H(Z_{eff} = 2; r_{1/2} = 0.5a_0)$$
 (88)

That is, -27 eV is lost with the absorption of the energy hole, and -14 eV is given off after absorption of the energy hole. It is shown later that the resonance energy hole of a hy-

drogen atom that excites resonator modes of radial dimensions $a_0/(m+1)$ is

$$m \times 27.2 \text{ eV}$$
 , (89)

where

$$m = 1, 2, 3, 4, \dots$$

After resonant absorption of the hole, the radius a_0 of the orbit sphere shrinks to $a_0/(m+1)$, and after p cycles of resonant shrinkage, the radius is $a_0/(mp+1)$.

In other words, the radial ground-state field can be considered as the superimposition of Fourier components. The removal of negative Fourier components of energy $m \times 27.2$ eV, where m is an integer, gives rise to a larger positive electric field inside the spherical shell, which is a time-harmonic solution of Laplace's equations in spherical coordinates. In this case, the radius at which force balance and nonradiation are achieved is $a_0/(m+1)$, where m is an integer. In decaying to this radius from the ground state, a total energy of $[(m+1)^2-1^2]\times 13.6$ eV is released. The process is hereafter referred to as hydrogen emission by catalytic thermal electronic relaxation (HECTER).

The electric field of a hydrogen atom, or a deuterium atom, is zero for $r > r_n$, where r_n is the radius of the orbit sphere of the electron. Thus, as the orbit sphere shrinks, approaching nuclei experience a smaller Coulombic barrier, and the internuclear distance (between two deuterium atoms, for example) shrinks as well. As the internuclear separation decreases, fusion is more probable. In muon-catalyzed fusion, for example, the internuclear separation is reduced by ~200 (the muon-to-electron mass ratio), and the fusion rate increases by ~80 orders of magnitude. In a catalytic system that produces energy holes of 27.21 eV, deuterium atoms can be repeatedly shrunk, and the internuclear separation can be much smaller than the muon reduction. These smaller internuclear distances yield much higher fusion rates. Mills and Farrell call this fusion process Coulombic annihilation fusion (CAF).

It is important to note that the products of CAF are tritium, ³H, and protons, ¹H. In hot fusion, deuterium nuclei collide randomly and produce -50% ³H plus ¹H and -50% ³He plus a neutron. In CAF, however, the nuclei are moving slowly and will collide in the most favored Coulombic arrangement – with the two protons as far from each other as possible. Thus, for CAF, significantly more ³H will be produced than ³He.

Titanium(II) is one of the catalysts that can cause resonant shrinkage because the third ionization energy is 27.49 eV [m=1 in Eq. (89)]. Thus, the shrinkage cascade for the p'th cycle is

27.491 eV + Ti²⁺ + ²H
$$\left(\frac{a_0}{p}\right)$$
 \rightarrow Ti³⁺ + e⁻ + ²H $\left[\frac{a_0}{(p+1)}\right]$
+ $[(p+1)^2 - p^2] \times 13.6$ eV (90)

and

$$Ti^{3+} + e^- \rightarrow Ti^{2+} + 27.491 \text{ eV}$$
 (91)

The overall reaction is

$${}^{2}H\left(\frac{a_{0}}{p}\right) \rightarrow {}^{2}H\left[\frac{a_{0}}{(p+1)}\right] + [(p+1)^{2} - p^{2}] \times 13.6 \text{ eV} .$$
(92)



Mills and Kneizys

AQUEOUS POTASSIUM CARBONATE ELECTROLYTE

Note that the energy given off as the atom shrinks is much greater than the energy lost to the energy hole, and the energy released is large compared to conventional chemical reactions.

Rubidium(1) is also a potential catalyst. The second ionization energy is 27.28 eV:

27.28 eV + Rb⁺ + ²H
$$\left(\frac{a_0}{p}\right)$$
 \rightarrow Rb²⁺ + e^- + ²H $\left[\frac{a_0}{(p+1)}\right]$
+ $[(p+1)^2 - p^2] \times 13.6$ eV (93)

and

$$Rh^{2+} + e^- \rightarrow Rb^+ + 27.28 \text{ eV}$$
 (94)

The overall reaction is the same as Eq. (92).

Less efficient catalytic systems hinge on the coupling of three resonator cavities. For example, the third ionization energy of palladium is 32.93 eV. This energy hole is obviously too high for resonant absorption. However, Li(I) releases 5.392 eV when it is reduced to Li. The combination of Pd(II) to Pd(III) and Li(I) to Li, then, has a net energy change of 27.54 eV:

27.54 eV + Li⁺ + Pd²⁺ + ²H
$$\left(\frac{a_0}{p}\right)$$

 \rightarrow Li + Pd³⁺ + ²H $\left[\frac{a_0}{(p+1)}\right]$
+ $[(p+1)^2 - n^2] \times 13.6$ eV (95)

and

$$Li + Pd^{3+} \rightarrow Li^{+} + Pd^{2+} + 27.54 \text{ eV}$$
 (96)

The overall reaction is the same as Eq. (92).

An efficient catalytic system that hinges on the coupling of three resonator cavities involves potassium. For example, the second ionization energy of potassium is 31.63 eV. This energy hole is obviously too high for resonant absorption. However, K(I) releases 4.34 eV when it is reduced to K. The combination of K(I) to K(II) and K(I) to K, then, has a net energy change of 27.28 eV.

27.28 eV + K⁺ + K⁺ + ²H
$$\left(\frac{a_0}{p}\right)$$

$$\rightarrow K + K^{2+} + ^2H\left[\frac{a_0}{(p+1)}\right]$$
+ $[(p+1)^2 - n^2] \times 13.6$ eV (97)

and

$$K + K^{2+} \rightarrow K^{+} + K^{+} + 27.28 \text{ eV}$$
 (98)

The overall reaction is the same as Eq. (92).

In general, absorption of an energy hole causes the orbit sphere to undergo a transition from one stable nonradiative radius to another stable nonradiative radius. The Coulombic force is attractive; thus, the orbit sphere shrinks when the effective nuclear charge increases. The orbit sphere has an initial radius r_n , initial effective nuclear charge Z_{eff} , and initial velocity v_n given by the condition for nonradiation:

$$2\pi(nr_1) = n\lambda_1$$
, $n = 1, \frac{1}{2}, \frac{1}{3}, \frac{1}{4}, \dots$, (99)

and

$$v_n = \frac{\hbar}{m_e n a_0} . ag{100}$$

At force balance,

$$\frac{\hbar^2}{m_e(r_n)^3} = \frac{Z_{eff}e^2}{4\pi\epsilon_0(r_n)^2} . \tag{101}$$

Shrinkage occurs because the effective nuclear charge increases by an integer m when Eqs. (99), (100), and (101) are satisfied by the introduction of an energy sink of a coupled resonator, such as an electron orbit sphere resonator cavity comprising an electrochemical couple. The coupled resonator provides energy holes and affects the shrinkage transition from the initial radius $a_0/(mp+1)$ and a nuclear charge of (mp + 1) to the second radius $\{a_0/[m(p + 1) + 1]\}$ and a nuclear charge of m(p+1) + 1. Energy conservation and the boundary condition that trapped photons must be a solution to Laplace's equation determine that the energy hole to cause a shrinkage is given by Eq. (89). As a result of coupling, the deuterium atom emits a photon of $m \times 27.21$ eV, and this photon is absorbed by the coupled resonator. Stated another way, the deuterium atom absorbs an energy hole of $m \times$ 27.21 eV. The energy hole absorption causes a second photon to be trapped in the deuterium atom electron orbit sphere. Recall from Sec. III that electromagnetic radiation of discrete energy can be trapped in a resonator cavity. As shown previously, the photonic equation must be a solution of Laplace's equation in spherical coordinates. The photon field comprises an electric field that provides force balance and a nonradiative orbit sphere. The solution to this boundary value problem of the radial photon electric field is given by

$$\epsilon \hat{i}_{rphotonj,l,m} = \frac{e}{4\pi\epsilon_0} \frac{(na_0)^l}{r^{(l+2)}} \left\{ -1 + n[Y_l^m(\phi,\theta) + Y_s^{m_s}] \right\} . \tag{102}$$

It is apparent from this equation that, for l = 0 and given an initial radius of $[a_0/(mp+1)]$ and a final radius of ${a_0/[m(p+1)+1]}$, the nuclear charge is increased by m with the absorption of an energy hole of $m \times 27.2$ eV. The potential energy decreases by this energy; thus, energy is conserved. However, the force balance equation is not initially satisfied as the effective nuclear charge increases by m. Further energy is emitted as force balance is achieved at the final radius. By replacing the initial radius with the final radius and by increasing the charge by m in Eq. (101),

$$[m(p+1)+1]^{3} \frac{\hbar^{2}}{m_{e}a_{0}^{3}}$$

$$= [m(p+1)+1]^{2} \frac{\{[m(p+1)+1]e\}e}{4\pi\epsilon_{0}a_{0}^{2}}, \quad (103)$$

force balance is achieved and the orbit sphere is nonradiative. The energy balance for m = 1 is as follows. An initial en-

ergy of 27.21 eV is emitted as the energy hole absorption event. This increases the effective nuclear charge by one and decreases the potential by 27.21 eV. More energy is emitted until the total energy released is $[(p+1)^2 - p^2] \times 13.6$ eV.

In general, the resonance energy to cause shrinkage of the radius from a_0 to $a_0/(m+1)$ is $m \times 27.21$ eV, where m=1,2,3,4. The resonant absorption of this energy hole causes the effective nuclear charge to increase by m. And, the energy released in going from infinity to $a_0/(m+1)$ is $(m+1) \times$ $(m+1) \times 13.6 \text{ eV} \text{ or } (m+1)^2 \times 13.6 \text{ eV}.$

Energy holes add. The corresponding effective charges resulting from the absorption of energy holes also add. Thus, any combination of energy holes that sums to $m \times 27.21$ eV,





where m is the same as the m for the final radius $(a_0/m + 1)$ leads to shrinkage to the same final radius of the orbit sphere.

VI. METHODS

A search for excess heat during the electrolysis of aqueous potassium carbonate (K+/K+ electrocatalytic couple) was investigated using single-cell, silvered, vacuum-jacketed dewars. To simplify the calibration of these cells, they were constructed to have primarily conductive heat losses. Thus, a linear calibration curve was obtained. Three methods of differential calorimetry were used to determine the cell constant, which was used to calculate the excess enthalpy:

- 1. The cell constant was calculated during the experiment (on-the-fly-calibration) by turning an internal resistance heater off and on and inferring the cell constant from the difference between the losses with and without the heater.
- 2. The cell constant was determined with no electrolysis processes occurring by turning an internal resistance heater off and on for a well-stirred dewar cell and inferring the cell constant from the difference between the losses with and without the heater. This method overestimates the cell constant because there is no gas flow (which adds to the heat
- 3. In the third method, rather than keeping the ambient temperature constant while raising the cell temperature with heater power input, the ambient temperature was lowered and heater power was applied to maintain a constant cell temperature. This method caused the least perturbation to temperature-dependent electrochemical processes.

The general form of the energy balance equation for the cell in steady state is

$$0 = P_{appl} + Q_{hir} + Q_{xs} - P_{gas} - Q_{loss} , \qquad (104)$$

where

 P_{appl} = electrolysis power

 Q_{htr} = power input to the heater

 Q_{xx} = excess heat power generated by an unknown

 $P_{\text{gas}} = \text{power removed as a result of evolution of } H_2$ and O2 gases

 Q_{loss} = thermal power loss from the cell.

When an aqueous solution is electrolyzed to liberate hydrogen and oxygen gases, the electrolysis power P_{appl} (= $E_{appl}I$) can be partitioned into two terms:

$$P_{appl} = E_{appl}I = P_{cell} + P_{gas} . ag{105}$$

An expression for P_{ges} (= $E_{ges}I$) is readily obtained from the known enthalpy of formation of water from its elements:

$$E_{zas} = \frac{-\Delta H_{form}}{\alpha F} ,$$

where F is Faraday's constant, which yields $E_{pos} = 1.48 \text{ V}$ for the reaction

$$H_2O \rightarrow H_2 + \frac{1}{2}O_2$$
.

The net Faradaic efficiency of gas evolution is assumed to be unity; thus, Eq. (105) becomes

$$P_{ceil} = (E_{appl} - 1.48V)I$$
 (106)

The cell was calibrated for heat losses by turning an internal resistance heater off and on while maintaining constant electrolysis and by inferring the cell conductive constant from the difference between the losses with and without the heater, where heat losses were primarily conductive losses through the top of the dewar. When the heater was off, the losses were given by

$$c(T_c - T_b) = P_{appl} + 0 + Q_{xx} - P_{zax}$$
, (107)

where

c =conductive heat loss coefficient

 $T_b =$ ambient temperature

 $T_c = \text{cell temperature}.$

When a new steady state is established with the heater on, the losses change to

$$c(T'_c - T_b) = P'_{appl} + Q_{htr} + Q'_{xs} - P'_{gas}$$
, (108)

where a superscript prime indicates a changed value when the heater was on. When the following assumptions apply,

$$Q_{xz} = Q'_{xz}$$
 , $P_{appl} = P'_{appl}$,

and

$$P_{gas} = P'_{gas}$$
 ,

the cell constant a, the reciprocal of the conductive loss coefficient c, is given by

$$a = \frac{T_c' - T_c}{O_{br}} \quad . \tag{109}$$

Also, the slope of the plot of $\Delta T = T_c - T_B$ versus $P_T =$ $Q_{hir} + P_{cell}$ is the cell constant:

$$a = \frac{\Delta T' - \Delta T}{\Delta P_T} \ . \tag{110}$$

VII. EXPERIMENTAL

An electrolytic cell was assembled comprising a 500-ml, silvered, vacuum-jacketed dewar with a 5-cm opening covered with a 0.75-in.-thick tapered rubber stopper (vessel A) fitting 0.25 in. into the dewar mouth or a 200-ml, silvered, vacuumjacketed dewar with a 3-cm-diam opening covered with Parafilm (vessel B).

The cathode was a 7.5-cm-wide \times 5-cm-long \times 0.125mm-thick nickel foil (Aldrich 99.9+%) spiral with a 9-mm diameter and 2-mm pitch with a nickel lead strip (cathode A) or a 5-cm-long × 0.75-cm-diam graphite rod with a 0.127-mm platinum lead (cathode B). The nickel cathode was prepared by tightly rolling the nickel foil about a 9-mm rod. The rod was removed, and the spiral was formed by partially unrolling the foil.

The anode was a 10-cm × 1-mm-diam spiraled platinum wire (Johnson-Matthey) with a 0.127-mm platinum lead wire (anode A) or a 2.5-cm-diam × 7.5-cm-high platinum basket with a 1-mm-diam platinum lead wire (anode B). When anode A was utilized, the cathode/anode separation distance was 1 cm. When anode B was used, the cathode/anode separation distance was 1.2 cm.

The electrolyte solution was 100 ml of 0.57 M aqueous K_2CO_3 (Aldrich $K_2CO_3 * \frac{3}{2}H_2O$ 99+%) (solution A) or



Mills and Kneizys

AQUEOUS POTASSIUM CARBONATE ELECTROLYTE

100 ml of 0.57 M aqueous Na₂CO₃ (Aldrich Na₂CO₃ American Chemical Society primary standard 99.95+%) (solution B).

The resistance heater used during calibration and operation comprised a 100 or 10.5 Ω , 1% precision metal oxide resistor in a 2-mm-o.d. Teflon tubing powered by a variable direct current (dc) voltage power source $(\pm 0.5\%)$.

A constant dc current $(\pm 0.1\%)$ was provided by the circuit shown in Fig. 1 (mode C). A constant dc voltage power supply $(\pm 0.5\%)$ was used directly in the continuous current mode (mode B). A power controller with the circuit shown in Fig. 2 was used to provide intermittent current (mode A). The current voltage parameters were an intermittent square-wave with an offset voltage of -2.2 V, a peak voltage of -2.75 V, a peak current of -175 mA, an -35% duty cycle, and a fre-

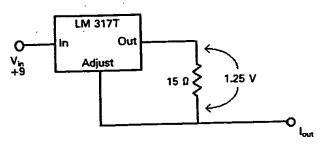


Fig. 1. Schematic of the circuit used to provide constant do current.

quency of -500 Hz. The voltage and current waveforms are shown in Figs. 3 and 4, respectively.

In stirring mode A, the electrolyte solution was stirred with a 7-mm × 2-cm spheroidal ellipse magnetic stirring bar that was spun by a 6-cm-long open magnet mounted on an open shaft revolving at 750 rpm under the dewar. The shaft was that of an open mixing motor (Flexa-Mix model 76, Fisher). The temperature correction for the Joule heating of stirring was determined from an identical experimental apparatus that was only stirred.

In stirring mode B, the electrolyte solution was stirred by a 2-cm-wide × 1-cm-high glass paddle connected to a 40-cm-long × 5-mm-o.d. glass rod that entered the dewar vertically through a 6-mm-i.d. vacuum greased glass tube implanted through the rubber stopper covering the dewar. The rod was rotated at 380 rpm by a mixing motor (Lightnin model L, Mixing Equipment Company) controlled by a variable auto-transformer (Powerstat model 116B). The temperature correction for the Joule heating of stirring was determined by stirring the electrolyte and measuring its temperature relative to the temperature of an unstirred matched cell before initiating an experiment. Otherwise, the experiments were stirred by gas sparging from the gases produced during electrolysis.

Nickel cathodes were initially operated in reverse polarity with a continuous or time-averaged current of 80 mA for 30 min to break in a new cathode. This operation conditions the electrode and makes the electrolysis more surface uniform. Following any change in heater power, an intentional ambient temperature change, or commencement of electrolysis, time was allowed for the cell temperature to establish a

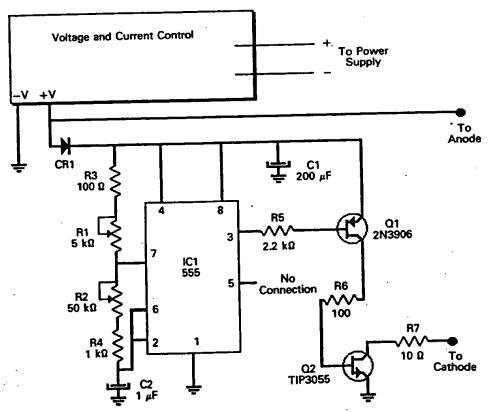


Fig. 2. Schematic of the circuit used to provide intermittent (on/off) dc voltage.



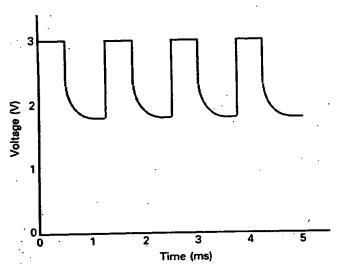


Fig. 3. Voltage versus time oscilloscope trace of the circuit of Fig. 2.

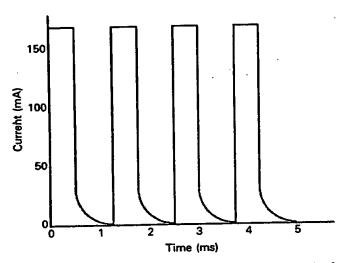


Fig. 4. The current versus time oscilloscope trace of the circuit of Fig. 2.

new steady state before data were recorded. The time for the temperature to stabilize following the commencement of electrolysis was typically 12 h. The time for the temperature to stabilize following an increase of heater power of ~ 0.3 W was ~ 4 h for cells with no electrolysis and for electrolytic cells operating for > 12 h. The dewar was agitated prior to a temperature reading to ensure thorough thermal mixing.

The outside of the vessel was maintained at ambient air temperature, which was monitored, and the difference between cell and a matched nonoperative cell was determined with a thermometer (±0.1°C). Ambient temperature fluctuations per 24 h were typically <0.5°C. (The matched nonoperative cell was structurally and chemically identical, but the electrolysis current was zero and the heater power was zero. In the case of stirring mode A, the matched nonoperative cell was stirred identically.)

For another method, rather than keeping the ambient temperature constant while raising the cell temperature with

heater power input, the ambient temperature was lowered by adjusting the thermostatic control of the room temperature, and heater power was applied to maintain an approximately constant cell temperature. The room temperature and heater power were adjusted until the excess heat before and after the change in ambient temperature were equal. The ambient temperature reached a steady-state temperature (±0.1°C) in 8 h, and the cell reached a steady-state temperature (±0.1°C) 4 h later. The temperature difference between the cell and a matched nonoperative cell was determined with a thermometer (±0.1°C).

For circuit A, peak voltage measurements were made with an oscilloscope (BK model 2120), and the time-averaged current was determined from a multimeter voltage measurement $(\pm 0.2\%)$ across a calibrated resistor (1 Ω) in series with the lead to the cathode. The waveform of the pulsed cell was a square wave. Since there was current only during the peak voltage interval of the cycle, P_{appl} [Eq. (105)] is given by the product of the peak voltage and the peak current and the duty cycle, which is the product of the peak voltage and the time-averaged current. In circuit B, voltage across the cell was measured with the multimeter, and the current was determined from the multimeter voltage measurement across a calibrated resistor (1 Ω) in series with the lead to the cathode. For this mode, P_{appl} [Eq. (105)] is given by the product of the constant voltage and the constant current.

VIII. RESULTS

A summary of the results of the excess enthalpy released during the electrolysis of potassium carbonate (K⁺/K⁺ electrocatalytic couple) as well as the results for the control (sodium carbonate, for which no electrocatalytic reaction of ~27.21 eV is possible) are given in Table I, which also lists the experiment number. Experiments designated with a number followed by an "A" had heat added to the experiment designated by the same number.

Figures 5 through 9 show the difference between experimental cell temperature and the temperature of a matched

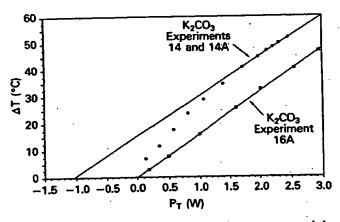


Fig. 5. Plots of the differences between cell temperature and the temperature of a matched nonoperative cell (ΔT) as a function of total power P_T for (a) K₂CO₃ experiments 14 and 14A in which the electrolysis current was maintained at ~85 mA and (b) K₂CO₃ experiment 16A in which electrolysis current was zero. Increasing temperatures were recorded as the calibration resistor was stepped in power. The curves are fit to the solid symbols.



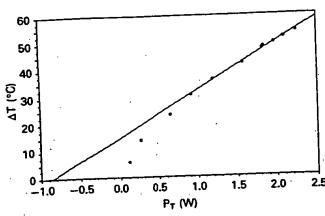


Fig. 6. Plot of the difference between cell temperature and the temperature of a matched nonoperative cell (ΔT) as a function of total power P_T for K_2CO_3 experiments 15 and 15A, in which the electrolysis current was maintained at 82 mA. Increasing temperatures were recorded as the calibration resistor was stepped in power. The curve was fit to the solid circles.

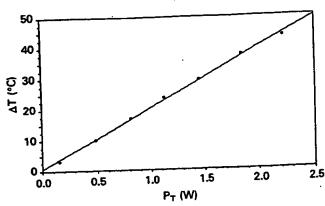
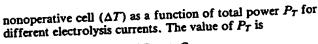


Fig. 7. Plot of the difference between cell temperature and the temperature of a matched nonoperative cell (ΔT) as a function of total power P_T for K_2CO_3 experiment 17A. The electrolysis current was zero. Increasing temperatures were recorded as the calibration resistor was stepped in power.



$$P_T = P_{cell} + Q_{htr}$$
,

where P_{cell} is calculated using Eq. (106). Increasing temperatures were recorded as the calibration resistor was stepped in power.

In K_2CO_3 experiment 16A, there was no hydrogen to react, and this experiment is a control of differential calorimetry for K_2CO_3 experiments 14 and 14A. The plot for K_2CO_3 experiment 16A (see Fig. 5) is linear with an x intercept and a y intercept of zero, which indicates no excess heat. However, the plot for K_2CO_3 experiments 14 and 14A (K+/K+ electrocatalytic couple) (see Fig. 5) is highly nonlinear in the 25 to 50°C temperature range and approximately linear thereafter. Interpolation of the linear data to the y intercept indi-

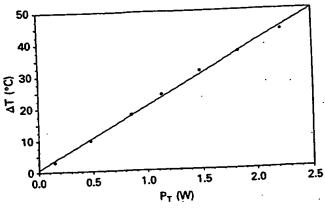


Fig. 8. Plot of the difference between cell temperature and the temperature of a matched nonoperative cell (ΔT) as a function of total power P_T for Na₂CO₃ experiments 18 and 18A. The electrolysis current was maintained at 79.7 mA. Increasing temperatures were recorded as the calibration resistor was stepped in power.

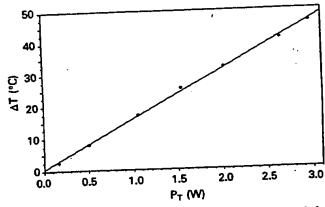


Fig. 9. Plot of the difference between cell temperature and the temperature of a matched nonoperative cell (ΔT) as a function of total power P_T for Na₂CO₃ experiments 19 and 19A. The electrolysis current was maintained at 79.7 mA. Increasing temperatures were recorded as the calibration resistor was stepped in power.

cates an excess temperature of -15° C. Interpolation of the linear data to the x intercept indicates an excess power of -10 times the input power.

The plot of ΔT versus P_T for Na₂CO₃ experiments 18 and 18A and 19 and 19A are shown in Figs. 8 and 9, respectively. No electrocatalytic reaction of -27.21 eV is possible for sodium; thus, these experiments represent controls that are essentially chemically identical but lack an electrocatalytic couple to induce the electrons of hydrogen atoms to relax to a quantized potential energy level below that of the ground state by providing a redox energy-energy hole (27.28 eV) resonant with this transition. These plots are linear with an x intercept and a y intercept of zero, which indicates no excess heat. However, the plots for K_2 CO₃ experiments 14, 14A, 15, and 15A (K⁺/K⁺ electrocatalytic couple), shown in Figs. 5 and 6, respectively, are highly nonlinear in the 25 to 50°C



TABLE

Percentage Excess Enthalpy Where the Cell Constant

	•	rescentage Excess Emmapy							
Experiment	Solution	Cathode	Anode	Vessel	Stirring Mode	Mode	Duty Cycle (%)	Frequency (Hz)	
K ₂ CO ₃ 1 1A 1AA 2 2A 3 3A 4 4A 5 5A 6 6A 7 7A 8 8A 9 9A 10 10A 11A 12A 13 13A 14 14A 15	A A A A A A A A A A A A A A A A A A A	AAAAAAAAAAAAAAAAAAAAAAAAAAAAAAAAAAAAAA	Anode A A A A A A A A A A A A A A A A A A A	Vessel A A A A A A A A A A A A A A A A A B B	A B B	Mode AAAAAAAAABAAABBAAABBCC	40 40 40 40 35 35 35 35 35 35 35 35 35 35 35 35 35	500 500 500 500 500 500 500 500 500 500	
15A 16A 17A	A A A	A A A	A A	A	A A				
Na ₂ CO ₃ 18 19	B B	A A	A A	A	A A	C C			

*See Sec. VII for an explanation of the experimental configurations.

temperature range and approximately linear thereafter. Interpolation of the linear data to the y intercept indicates an excess temperature of ~15°C. Interpolation of the linear data to the x intercept indicates an excess power of -10 times the input power. For each experiment, the upper limit of the cell parameter a was determined from the slope at ~55°C.

Linear plots of ΔT versus P_T for heater alone (no electrolysis) K₂CO₃ control experiments 16A (Fig. 5) and 17A (Fig. 7), which go through zero at the origin, validate the original assumptions that the losses were conductive. The upper

limit of the cell parameter a was determined from the slope. The cell parameter was slightly lower for electrolytic cells compared to matched nonelectrolytic cells, as shown in Fig. 5. This is attributed to the additional heat loss due to gas flow in the electrolytic cells.

The results of the determination of the cell constant, Q_{∞} , and Q'_{∞} at an operating temperature of -32°C appear in Table II. For calibration runs (K2CO3 experiments 20A1, 20A2, 20A3, and 20A4), the ambient temperature was ~2 to 5°C lower than in the reference cell (K2CO3 experiment 20),

^aQ_{hir} = heater watts added to raise the temperature of the cell during operation.

 $^{{}^{\}mathbf{b}}\widetilde{\Delta}\widetilde{T}=T_{c}-T_{b}.$

 $^{^{}c}\Delta T_{htr} = aQ_{htr} =$ temperature change in the cell due to the heater. $^{d}\Delta\Delta T = \Delta T - \Delta T_{htr}$.

 $^{^{}c}\Delta T_{cell} = aP_{cell}$.





I Was Determined by On-the-Fly-Calibration*

Offset Voltage (V)	Peak Voltage (V)	Peak Current (mA)	Cell Constant (°C/W)	Q _{htr} a (W)	Δ <i>T</i> ^b (°C)	ΔT _{htr} °	ΔΔT ^d (°C)	ΔT _{cell} e (°C)	Excess Heat ^f (%)
	 ``							0.00	328
	2.42	180	14.8	0	8.9			2.08	1234
2.73	3.43	112	15	1.044	29	15.67	13.33	1	557
2.36	2.96		14.8	2.196	47.2	32.9	14.3	2.17	
2.32	3.22	212	14.8	0	4.2			1.56	169
2.19	2.79	231		2.196	45	32.9	12.1	1.88	544
2.55	3.15	217	14.8	2.170			l '	2.42	156
	3.63	163	14.8	0	6.2			2.17	662
2.93		231	14.8	2.196	49.5	32.94	16.56		183
2.795	3.295	254	14.8	0	4.5	ì	l <u>.</u> .	1.58	
2.185	2.685		14.8	2.21	46.5	33.17	13.33	1.19	1016
2.02	2.42	245	14.8	0	4.8	1	1	1.45	231
2.12	2.72	225	14.0	1	1		9.7	1.32	634
2.01	2.51	248	14.8	2.22	43	33.3	9.7	1.71	215
2.01	3.125	205	14.5	0	5.4	·	1	1.57	612
2.425		208	14.5	2.22	44.5	· 33.3	11.2		147
2.47	2.97	246	15.7	0	4.3		i	1.74	
2.17	2.77		15.7	0.911	25	14.3	10.7	1.33	705
2.04	2.54	228	15.7	0.511	1	1	I	1.19	252
	2.42	75	16.9	0	4.2		1122	1.08	953
	2.28	80	16.9	0.99	28.1	16.73	11.37	0.626	395
١.,		131	14.8	10	3.1		1	0.367	3766
2.1	2.4	114	14.8	0.778	25.7	11.51	14.19		408
2	2.1	117	14.6	0	2.8	1	1	0.551	1
2.1	2.4	117			L .	28.65	12.5	0.461	2621
2	2.25	117	14.6	1.96	41.2	13.68	8.91	0.95	838
2.5	2.8	114	18	0.76	22.6		11.7	1.036	1027
2	2.31	80	15.6	0.771	23.7	12	1 11.7	1.39	217
ا ،	2.55	243	15.25	0	4.4	1 4	15.5	1.3	1094
2 2.1	2.6	217	15.25	1.537	38.9	23.4	15.5	L	1
2.1	1	1	l l	١ ,	6.9	!	<u> </u>	2.01	243
1	3.08	85	14.8	0	40.9	23.5	17.4	1.87	830
1	2.9	89	14.8	1.59	5.7	1 23.3	1	1.82	213
1	2.748	82	17.5	0		35.5	16.01	1.01	1355
1	2.247	82	17.5	2.028	51.5	1	1	1	1
1	- === ·	I	15.9		1	1	1	l.	ı
]	1	15.5	1	1		1	Ì	
1	1	i		1		1	i	1	1
1	.		10.7	0	3.2		ì	3.14	1.9
l	3.48	79.7	19.7	Ö	3	1	\ `	2.95	1.6
	3.37	79.7	19.6	۱ ۲		<u> </u>			

f
Excess heat =
$$\begin{cases} \frac{\Delta T - \Delta T_{cell}}{\Delta T_{cell}} \times 100, & \text{when heater was off} \\ \frac{\Delta \Delta T - \Delta T_{cell}}{\Delta T_{cell}} \times 100, & \text{when heater was on} \end{cases}$$

and heater power was added to make the temperature of each calibration cell approximately equal to the cell temperature of the reference cell. The cell constant was determined by subtracting Eq. (107) with the parameters of the reference run from Eq. (108) with the parameters of each calibration run, and Eq. (106) was used to determine P_{cell} for each equation. It was assumed that the losses were conductive and that $Q_{cc} = Q_{cc}'$. The assumption that the losses Q_{loss} were conductive for these silvered dewars is supported by the data of Figs. 8 and 9. The assumption that $Q_{cc} = Q_{cc}'$ was verified by

calculating these parameters from the cell constant determined.

IX. DISCUSSION

The data clearly indicate that excess heat was generated. Once the technique was perfected, each experiment using potassium carbonate produced excess heat. Some experiments were permitted to operate for weeks, and the excess heat remained relatively constant. What is the source of this excess



TABLE Determination of the Cell Constant by Lowering the Ambient Temperature

Experiment	Solution	Cathode	Anode	Vessel	Stirring Mode	Mode	Voltage (V)
K ₂ CO ₃ 20 20A1 20A2 20A3 20A4	A A A A	A A A A	A A A A	A A A A	B B B B	B B B B	2.38 3.08 3.11 3.11 3.2

enthalpy? Electrochemical reactions that consume the electrolyte can be ruled out because any proposed electrochemical reactant would be completely consumed over the duration of these experiments. Nickel forms a hydride during cathodic electrolysis, but this process is endothermic.6 The weight of the nickel cathode was unchanged by use in a heat-producing cell to within 0.00001 g (the cathode was rinsed after 36 h of operation, then dried and degassed in vacuum before the final weight was determined). The only remaining candidates are heat-releasing reactions involving the electrolytically generated hydrogen or oxygen atoms or molecules. Because the excess enthalpy exceeds that which can be accounted for due to complete recombination, new processes must be sought.

The results are consistent with the release of heat energy from hydrogen atoms where the K+/K+ electrocatalytic couple induces the electrons of hydrogen atoms to relax to a quantized potential energy level below that of the ground state by providing a redox energy-energy hole (27.28 eV) resonant with this transition. The balanced reaction is given by Eqs. (92), (97), and (98). Excess heat was also measured when K₂CO₃ was replaced by Rb₂CO₃. The Rb⁺ ion (energy hole from the second ionization is 27.28 eV) alone is electrocatalytic according to the reaction given by Eqs. (92), (93), and (94). No excess heat was observed when K2CO3 was replaced by Na₂CO₃ as demonstrated with Na₂CO₃ experiments 18 and 18A and 19 and 19A, shown in Figs. 8 and 9, respectively. For sodium or sodium ions, no electrocatalytic reaction of -27.21 eV is possible. For example, 42.15 eV of energy is absorbed by the reverse of the reaction given in Eq. (98), where Na⁺ replaces K⁺:

$$Na^+ + Na^+ + 42.15 \text{ eV} \rightarrow Na + Na^{2+}$$
.

It has not been overlooked that other researchers have reported anomalous heat,7 tritium,7,8 and neutron production7 during electrolysis of heavy water using a lithium salt electrolyte and a palladium cathode. The excess enthalpy is reported to be substantially larger than can be accounted for by nuclear reactions that produce tritium or neutrons.7 In these cases, the couple is Pd2+/Li+ (27.54 eV). The balanced reaction is given by Eqs. (92), (95), and (96). The excess heat arises from the HECTER process, and the trace nuclear reactions are due to CAF as described in Sec. V. The HECTER process produces much greater quantities of heat energy than typical chemical reactions.

Neutron^{9,10} and tritium¹⁰ emissions from heavy water electrolytic cells using a titanium cathode and deuterium gas cells with titanium shavings have been reported. The tritiumto-neutron ratio is reported to be 108 (Ref. 10) as opposed to the 1:1 branching ratio of ³H to ³He observed for hot fu-

sion. This result is anticipated for CAF. In the case of titanium, Ti2+ (27.49 eV) is electrocatalytic according to the reaction given by Eqs. (90), (91), and (92).

The data indicate that the shrinkage reaction is temperature dependent. This is clearly demonstrated by the nonlinear curves in Figs. 5 and 6 and by comparing the heated experiments (Table I) and the experiment of the same number for which heater power was zero. Most chemical reactions double their rates for each 10°C rise in temperature. Increasing temperature increases the collision rate between the hydrogen atoms and the electrocatalytic couple, which increases the shrinkage reaction rate. With large temperature excursions from room temperature, the kinetic energy distribution of the reactants can be sufficiently altered to cause the energy effecting the hydrogen shrinkage transition and the electrocatalytic redox reaction to conform to a greater or lesser extent. The rate is proportional to the extent of conformation or resonance of these energies.

The source of reactant hydrogen atoms is aqueous electrolytic production on the surface of the nickel cathode. Electrolysis and the associated ohmic losses consume (i.e., require) input power. The losses obviously rise with a rise in current. However, increased current increases the concentration of reactant hydrogen atoms. A trade-off exists between total excess power and percentage excess power. It was found that increasing the current with a concomitant increase in the concentration of reactant hydrogen atoms increases the total excess power but decreases the percentage excess power. During continuous electrolysis, much of the reactant hydrogen is lost as evolved gas. It was anticipated that more efficient production of reactant hydrogen could be provided by an electrolysis circuit that periodically generates reactant hydrogen atoms and allows them to react in the absence of further power dissipation. Comparing the experiments of Table I with pulsed peak current of ~115 mA with those with continuous ~80-mA current electrolysis, it can be appreciated that the efficiency of heat generation is correlated with the efficiency of hydrogen atom generation. For example, the input power of K2CO3 experiment 9A, which was pulsed, is one-third that of K2CO3 experiment 8A, which was operated with continuous current. The ratio of the percentage excess power of K2CO3 experiment 9A to K2CO3 experiment 8A is 3. An intermittent current (i.e., on-off) electrolysis circuit increases the percentage of excess heat by providing an optimal concentration of hydrogen atoms (reactants) while minimizing ohmic and electrolysis power losses. The frequency, duty cycle, peak voltage, step waveform, peak current, and offset voltage were adjusted to achieve the optimal shrinkage reaction rate and concomitant power while minimizing ohmic and.





П

While Maintaining Constant Cell Temperature by Addition of Heat

While Maintainin	P _{cell}	Qhir	P_T	ΔΤ	Cell	<i>Qx</i> s (W)	Ο'χς (W)
Current (mA)	(W)	(W)	(W)	(°C)	Constant	(")	<u>`</u>
79 90 85 81 100	0.0711 0.144 0.1386 0.132 0.172	0 0.3249 0.1681 0.2621 0.2621	0.0711 0.4689 0.3067 0.3942 0.4341	3.2 9.6 7 8.4 9	16.09 16.13 16.095 15.98	0.128 0.127 0.128 0.129	0.128 0.127 0.128 0.129

electrolysis power losses. When the K⁺/K⁺ electrocatalytic couple was used with carbonate as the counterion, nickel as the cathode, and platinum as the anode, an intermittent square-wave with an offset voltage of ~2.2 V, a peak voltage of ~2.75 V, a peak current of ~120 mA, an ~35% duty cycle, and a frequency of ~500 Hz optimized the percentage excess power.

Although only the results for carbonate are reported, a strong dependence of the excess enthalpy on the structure and charge of the counterion was found. For carbonate, the transition state to the fractional quantized state of the hydrogen atom likely involves a neutral complex of carbonate with two juxtaposed potassium ions. The counterion of the electrocatalytic couple of the electrolytic solution can affect the shrinkage reaction rate by altering the energy of the transition state. For example, the transition state complex of the K+/K+ electrocatalytic couple with the hydrogen atom has a +2 charge and involves a three-body collision, which is unfavorable. A -2 charged oxyanion can bind the two potassium ions; thus, it provides a neutral transition-state complex of lower energy, whose formation depends on a binary collision, which is greatly favored. The rate depends on the separation distance of the potassium ions as part of the complex with the oxyanion. The greater the separation distance, the less favorable is the transfer of an electron between them. A close juxtaposition of the potassium ions increases the rate.

Further work to enhance the power, to search for chemical species with shrunken hydrogen atoms, and to search for products of predicted subsequent nuclear processes (CAF) following the shrinkage reaction are in progress. Preliminary data indicate that the electrolysis of a heavy water potassium carbonate electrolyte at a nickel cathode produces significant

quantities of tritium, but the amount is much less than can account for the heat observed.

REFERENCES

- 1. R. L. MILLS and J. J. FARRELL, The Grand Unified Theory, Science Press (1989).
- 2. H. A. HAUS, "On the Radiation from Point Charges," Am. J. Phys., 54, 1126 (1986).
- 3. D. A. McQUARRIE, Quantum Chemistry, University Science Books, Mill Valley, California (1983).
- 4. E. M. PURCELL, Electricity and Magnetism, McGraw-Hill Book Company, New York (1965).
- 5. I. S. HUGHES, *Elementary Particles*, Cambridge University Press (1972).
- 6. G. ALEFELD and J. VOLKL, Eds., Hydrogen in Metals II, p. 176, Springer Verlag (1967).
- 7. M. FLEISCHMANN, S. PONS, W. ANDERSON, L. J. LI, and M. HAWKINGS, "Calorimetry of the Palladium-Deuterium-Heavy Water System," J. Electroanal. Chem., 287, 293 (1990).
- 8. E. STORMS and C. TALCOTT, in Proc. Workshop on Cold Fusion Phenomena, Santa Fe, New Mexico, May 23-25, 1989.
- 9. S. JONES et al., "Observation of Cold Nuclear Fusion in Condensed Matter," Nature, 338, 737 (1989).
- P. IYENGAR et al., "Bhabha Atomic Research Centre Studies on Cold Fusion," Fusion Technol., 18, 32 (1990).

THIS PAGE BLANK (USPTO)





EXCESS HEAT DURING THE ELECTROLYSIS OF A LIGHT WATER SOLUTION OF K₂CO₃ WITH A NICKEL CATHODE

V. C. NONINSKI[®] Laboratory for Electrochemistry of Renewed Electrode-Solution Interface (LEPGER), P.O. Box 9, Sofia 1504, Bulgaria

Received July 5, 1991 Accepted for Publication August 19, 1991

COLD FUSION

TECHNICAL NOTE

KEYWORDS: excess energy. electrolysis of H₂O, nickel cathode

Experimental results of differential heat loss calorimetry measurements during the electrolysis of light water solutions of K_2CO_3 and Na_2CO_3 with a nickel cathode are presented. A significant increase in temperature with every watt input, compared with the calibration experiment, is observed during the electrolysis of K_2CO_3 . This effect is not observed when Na_2CO_3 is electrolyzed. No trivial explanation (in terms of chemical reactions, change in heat transfer properties, etc.) of this effect has been found so far. If the nontriviality of the observed overcoming of the energy breakeven barrier is further confirmed, this phenomenon may find application as an important new energy source.

INTRODUCTION

The studies in this paper follow the general lines of the work of Fleischmann and Pons, although electrolysis of D2O is usually considered when excess energy is claimed. Observation of excess energy production during the electrolysis of H2O was first mentioned by Pons and later rejected. Pons et al., however, explicitly state the possibility of obtaining excess energy during electrolysis of ordinary water (using nickel as a cathode, among other proposed metals) in Ref. 2. Unexplained excess heat in light water is also claimed in a paper by Bush et al.3 Mills and Kneizys4 claim to have obtained excess energy above the amount spent during the electrolysis of a K2CO3 ordinary water solution with a nickel cathode. The excess energy effect, according to these authors, is not observed when Na2CO3 is electrolyzed. Furthermore, unusual effects during the electrolysis of light water have also been reported by Maisumoto.5

This paper compares the heating coefficients for a nickel/platinum (Ni/Pt) circuit with those for a resistor heater in vacuum-jacketed dewar electrolytic cells containing K_2CO_3 or Na_2CO_3 . Note that the excess energy effect from an electrochemical system containing K^+ (Li⁺ is usually used in these studies) in D_2O is reported in Ref. 6.

EXPERIMENTAL DETAILS

The experiments were carried out by observing and comparing the temperature difference, $\Delta T_1 = T_{electrolrim}$ only T_{blenk} and $\Delta T_2 = T_{resistor}$, heating only $-T_{blenk}$ referred to unit input power, between two identical 200-ml silver-coated vacing the silver-coated vacing num-jacketed dewars. A calorimeter dewar having the same configuration and containing the same amount of electrolyte, same type of electrodes (nickel cathode and platinum anode), resistor heater, and thermistor (thermometer) and stirred at the same speed was used as a blank; neither electrolysis nor heating by the resistor was carried out in this dewar. Experiments were also carried out by using as a blank a dewar used in a previous experiment and vice versa. This exchange was done to ensure that the effect was not due to any difference in the thermal properties of the two specific dewars used. Each dewar had a 3-cm opening, and a 2-cm-thick tapered rubber stopper was placed I cm into the dewar. The experimental apparatus for the differential calorimetry used in these studies is shown in Fig. 1. Unlike the studies in Ref. 4, the resistor and the electrolytic circuit were not run simultaneously in this study; the effects of heating by the resistor and by the electrolysis circuit were studied in separate runs.

As is usual in electrochemistry, measures were taken to avoid impurities in the system, especially organic substances. While it is unclear at this point what the relationship is, if any, between the contamination effect on the hydrogen overpotential and that on the eventual excess heat, one should recall the known problems with the reproducibility of the hydrogen overpotential, which can be overcome only by ensuring the lowest possible level of impurities. Certain procedures should be applied to reproduce the excess heat effect. For instance, before starting the experiment, mechanically scour the platinum anode with steel wool, soak overnight in concentrated HNO3, and then rinse with distilled water. Remove the nickel cathode from its container with rubber gloves, and cut and bend it in such a way such that no organic substances are transferred to the nickel surface. Preferably, dip the nickel cathode into the working solution under an electrolysis current, and avoid leaving the nickel cathode in the working solution in the absence of an electrolysis current. Clean the electrolysis dewar, and free it of organic contam-

After assembling the experimental setup, the nickel cathode was subjected to anodizing by a constant electrolysis current of 0.083 A for 1 h. Then, the direction of the electrolysis

Visiting scholar at Franklin and Marshall College, Chemistry Department, Lancaster, Pennsylvania.





Noninski EXCESS HEAT WITH LIGHT WATER SOLUTION

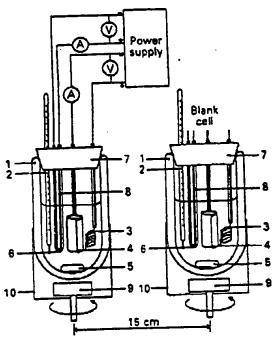


Fig. 1. Experimental setup: (1) vacuum-jacketed dewar. (2) thermometer. (3) platinum anode. (4) nickel cathode. (5) magnetic stirring bar. (6) resistor heater. (7) rubber stopper. (8) Teflon tubing. (9) magnetic stirrer, and (10) aluminum cylinder.

current was reversed (platinum anode and nickel cathode), and the electrolysis was carried out for 14 to 16 h.

The electrolysis heating power was calculated as $P_{el} = (E_{el} - 1.48)I_{el}$, where E_{el} is the applied electrolysis voltage, I_{el} is the electrolysis current (the term "electrolysis power" is used here for convenience, denoting only the power contributing to the joule heating effect during the electrolysis), and 1.48 V is the isoenthalpic voltage, which at the temperatures studied practically coincides with the thermoneutral voltage. The rasistor heater power was calculated as $P_{el} = I_{el} E_{el}$, where I_{el} denotes the resistor current and E_{el} denotes the resistor voltage.

The cathode was a 7.5-cm-long × 4-cm-wide × 0.0125cm-thick nickel foil (Aldrich 99.9+%) spiralled into a cylindrical form. The anode was a 0.1-cm-diam × 10-cm-long platinum wire (Johnson-Matthey). The spiral anode and the cylindrical cathode were parallel to each other. The leads were inserted into Teflon tubes to prevent any recombination of the evolving gases. The electrolyte solution in both dewars was 153 ml of 0.57 M K2CO3 or 0.57 M Na2CO3 in H2O. The distilled water was from the common distiller of the Chemistry Department of Franklin and Marshall College. The power was delivered by a Zenith SP-2718 power supply (alternating current component < 0.1%). The resistance heater was a 100-0, 1% precision, metal oxide resistor in a 2-mm-o.d. Teflon tube. The electrolyte solution in both dewars was stirred slmultaneously (synchronized for the two dewars) by two identical spheroidal ellipse magnetic bars rotated by two magnetic stirrers at -300 rpm. Electrolysis voltage and current were measured by two Keithley 169 multimeters, and the resistor voltage and current were measured by Extech 380198 and

Micronta 22-185 A multimeters with 0.01-V and 0.001-A accuracy, respectively. The use of vacuum-jacketed dewars, rather than air-jacketed dewars or simple flasks, made the measurements more sensitive (higher heating coefficient). In a vacuum-jacketed dewar unit, input power leads to a greater steady-state temperature, thus enabling differences in steady-state temperatures (for the same configuration) to be more pronounced. The temperatures in this study were monitored continuously using the capability of the standard calorimeters (Parr P-318) to record the temperature continuously (with 0.01°C accuracy) on their strip-chart recorder (Fisher Recordall Series 5000).

RESULTS AND DISCUSSION

The results of the study are shown in Figs. 2 through 5. Figure 4 is based on the data presented in Figs. 2 and 3. Figure 2 shows the absolute change in the measured temperatures of the dewars at different conditions, while Fig. 3 shows the input powers in each case. It can be seen from Fig. 3 that while the input power with the resistors working was constant as expected, the input electrolysis power was not, and there is a time lag between the application of power and the temperature response. We compensated for this by selecting appropriste power values when calculating the heating coefficients plotted in Fig. 4 (more precisely, the term "heating coefficient" refers only to the steady-state values of the quantities in Fig. 4; the last parts of the curves in Fig. 4 can be considered to represent steady state). The heating coefficients plotted in Fig. 4 were calculated using the average power plotted in Fig. 3. Note that other reasonable ways of referring the observed ΔT to the applied power are possible; however, even the most conservative approach gives the same qualitative effect as that seen in Fig. 4. Studies currently in progress, using a data acquisition system, show sustained steady-state production of excess heat for many days. Results from these studies are presented elsewhere.

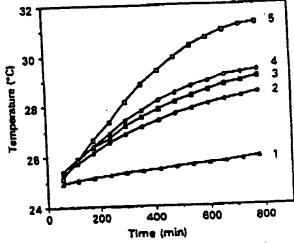


Fig. 2. Time history of temperatures: (1) blank cell (this curve is used as the blank for computing the heating coefficients of Fig. 4); (2) K₁CO₂ calibration cell (with only resistor heater working); (3) Na₂CO₂ calibration cell; (4) K₂CO₃ electrolysis cell (with only electrolysis working); and (5) Na₂CO₃ electrolysis cell.



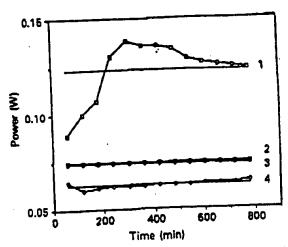


Fig. 3. Time history of the applied power: heating power with (1) electrolysis in the Na₁CO₁ cell, (2) the resistor in the Na2CO3 cell, (3) the resistor in the K2CO3 cell, and (4) electrolysis of the K₂CO₃ cell. The thermoneutral voltage is 1.48 V. For the calculations presented in this paper, mean values of the electrolysis powers in the Na₂CO₃ and K₂CO₃ cells are used, shown as solid lines in curves 1 and 4.

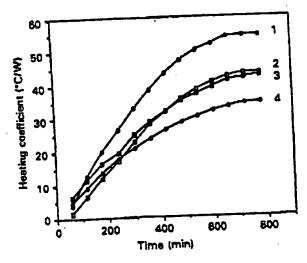


Fig. 4. Plot of the heating coefficients over time: (1) electrolysis at 0.083 A in K2CO3, (2) resistor working in Na2CO3, (3) electrolysis at 0.083 A in Na₂CO₃, and (4) resistor working in K₂CO₂.

The heating coefficient of the Na₂CO₃ cell is plotted in-Fig. 4. The heating coefficient for the resistor heater only and that for the electrolysis circuit only are essentially identical. This is to be expected for a given dewar and a given electrolyte when steady state is reached: The ΔT corresponding to a unit heating power has a strictly defined value, determined by the properties of the materials through which heat is being lost. The properties of the cell are unaltered during operation. Specifically, the volume of electrolyte remains practically constant: -0.2% of the solution volume is being electrolyzed during the 12-h operation of the Ni/Pt cell.

In contrast, the calorimeter containing K2CO3 showed very different behavior. The heating coefficient of the K2CO3 cell is plotted over time in Fig. 4. The heating coefficient-time curve of the working electrolysis cell is clearly above the curve of the dewar in which only a resistor is working. The value of the heating coefficient with the Ni/Pt circult working is -50°C/W, while the heating coefficient with only the resistor working is -30°C/W. Therefore, the output power obtained through the Ni/Pt circuit is -160% of the input power. The time-integrated power (i.e., energy) input into the system during the course of the experiment in Fig. 4 is -4800 J compared with the output power of -8000 J. Thus, Fig. 4 shows a significant difference in the thermal behavior of two identical systems that differ only in the positive ions of the salt.

A trivial explanation for this behavior of the K2CO3 cell is not straightforward. In fact, the electrolysis should be expected to lead to a decrease in the heating coefficients compared with those of the cells in which only the resistor is working ". . . consistent with additional heat losses caused by gas evolution . . . , "? which is currently observed only in

the Na₂CO₃ cell. The erroneous attribution of the effect to temperature gradients was eliminated by testing for minute spatial variations of the temperature over time. Three thermistors were positioned ~2.5 cm apart at the bottom, middle, and upper part of the electrolyte. The results, shown in Fig. 5, clearly demonstrate that no difference is observed (within the limit of detection, 0.01°C).

Note that the electrolysis is always started with a newly manufactured cathode from the batch of 99.9%+ purity nickel. The use of new nickel excludes any possibility that the effect is due to the decomposition of species formed before the beginning of the electrolysis. The reaction of hydride formation is exothermic with a standard enthalpy of formation of $-8.79 \pm 0.59 \text{ kJ} \cdot \text{mol}^{-1} \text{ H}_2$. However, if all of the hydrogen evolved during the run became hydride, an energy contribution would result that is more than one order of magnitude less than the excess heat that is observed according to Fig. 4. This can easily be calculated based on the amount of hydrogen evolved over ~12 to 14 h at a rate of 0.083 A. Although the overall amount of energy produced in the experiment is relatively low, it is clear that the observed effect is outside the error limit of the experiment, which is of the order of ±1°C/W, calculated from the accuracies of the measured parameters at the respective ranges.

It is not known what trivial chemical reaction might be triggered by the applied electrolysis that would be capable of producing the observed amount of excess heat. Some exotic farfetched possibilities for explaining the difference in electrochemical behavior between K2CO3 and Na2CO3 can be postulated. One such example is the formation of formic acid, e.g., by the reaction HCO; + 2H2O - HCOOH + 30H, or methane if KHCO; is present in the electrolyte. However, even if such possibilities are invoked, it should not be forgotten that energy is also being spent for these electrochemical reactions, which will again result in an isoenthalpic (or thermoneutral) voltage. In most cases, the value of this thermoneutral voltage may exceed 1.48 V, which will cause cooling rather than heating of the solution. This is indicative of even higher excess energy values. A reaction that readily comes to mind is oxygen reduction. It is well known, however, that nickel is a poor catalyst of oxygen reduction, and the current density of this reaction is negligibly small compared with the current density applied here (-1 mA/cm2).



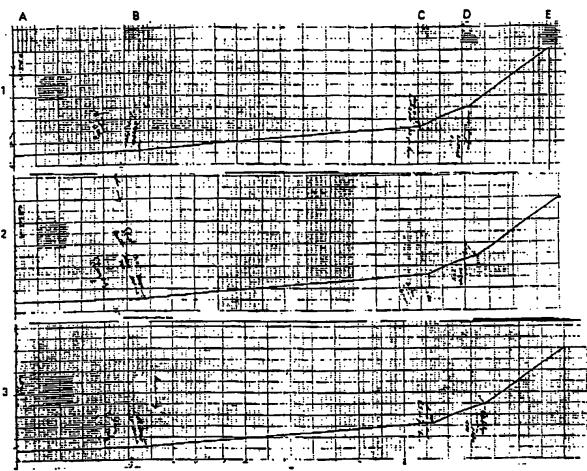


Fig. 5. Temperature changes at three points within the solution: (1) at the top. (2) in the middle, and (3) at the bottom. The setup used for this study is similar to that presented in Fig. 1, but in the working cell there are three thermistors instead of one. Section A-B: x axis scale = 30 division/h, y axis scale = 0.2°C/division, stirring only; section B-C: x axis scale = 30 division/h, y axis scale = 0.2°C/division, resistor only; section C-D: x axis scale = 5 division/h, y axis scale = 0.2°C/division, resistor only; and section D-E: x axis scale = 5 division/h, y axis scale = 0.2°C/division, electrolysis only.

These possibilities were rejected after study of the correspondence of the Faraday efficiency of the evolved H_3 and O_2 gases. This was done in a separate experiment by collecting the evolved gases and comparing the measured volume of the gases with the volume corresponding to the quantity of electricity that had passed through the cell over a given time. Note also that the absence of appreciable $H_2(D_2) + O_2$ recombination has been noted by a number of investigators, even in systems that contain metals (e.g., palladium) that are known to be good catalysts of that reaction (e.g., Refs. 9 through 14). Other preliminary studies (mass spectroscopy, pH measurements, titration) before and after the experiment showed no unexpected species or pH change. These studies should be continued further.

The problem of recombination is a crucial one in this study (note again that the excess heat here is calculated after subtracting 1.48 V), however, and it deserves special attention in any further experiments. On the other hand, as we have noted, the problem of recombination (and the other connected calorimetric problems) preferably should not be solved by studying the effect in a closed cell with a recombiner. The recombiner adds new unknowns since the kinet-

ics of the recombination of H_2 and O_2 to H_2O should be well understood through studies such as those in Ref. 15. On the other hand, since the claimed excess energy itself is a newly found, unstudied phenomenon, no additional conditions should be imposed because their eventual effect on the reproducibility of the excess energy is unknown. For instance, it is not clear whether the ability of the recombiner to recombine not only the H_2 and O_3 evolving through electrolysis but also all other quantities of H_2 and O_3 existing in the gas and the liquid phase, thus creating concentration gradients, will be a hindering factor for the appearance of excess energy.

An explanation for the increase in the heating coefficient for a Ni/Pt circuit might be that an additional source of energy of unknown nature is acting from within that adds to the energy input to the cell from without. If this nontrivial possibility is confirmed, this effect will be of great importance as an alternative energy source. Further calorimetric sophistication is necessary to further confirm the reality of the observed effect and to obtain a quantitative assessment of its magnitude. For instance, to avoid errors of a subjective nature, a data acquisition and processing system is necessary. The measurements should be carried out at constant input



717 898 0648;# 6

Noninski

EXCESS HEAT WITH LIGHT WATER SOLUTION

power and for longer periods of time so that curves like curve 1 of Fig. 2 reach a clear and sustained steady state. Maintaining a constant ambient temperature is also a requirement in these studies. Such studies are now in progress. To fully avoid concerns connected with the peculiarities of heat transfer during bubble evolution, it is necessary, together with heat loss calorimetry measurements (including Seebeck), that this effect be observed in an adiabatic-type calorimeter (bomb calorimeter) similar to the one used in Ref. 6. Note, however, that despite the opinions of some researchers, if careful studies are carried out, calorimetric techniques are not only capable but are the only ones that can decisively prove (or disprove) the reality of the effect in question. There is also no reason to expect that time spans of tens of hours will be insufficient to definitely rule out (or conclusively confirm) & trivial explanation of the observed effect if the studies are conducted carefully. It seems, however, that the reality of the effect can qualitatively be established with the described procedure. It seems also that the reported effect is reproducible and can easily be demonstrated.

It is the author's understanding that speculations (invoking reactions of nuclear or any other origin) as to why overcoming the energy breakeven barrier might come about should be carried out only after firmly establishing the reality of the claimed effect through experiments. This circumstance is not new for science. One may recall the experimental findings of Davison and Germer, Einstein, Wien, Compton, and others, which were unexplainable at the level of knowledge at their time. These experimental findings virtually caused the birth of 20th century physics, especially quantum mechanics. Even one of the most recent scientific discoveries high-temperature superconductivity - whose reality is undeniable, still remains unexplained, which does not make this experimentally found effect less important.

Since the problem of the reality (nontriviality) of the excess energy reported here is of primary concern, we leave open the questions for the theoretical explanation of the phenomenon.

CONCLUSIONS

The experimental results presented here show that there is more evidence than usually considered for the eventual production of excess energy during the electrolysis of water. Therefore, further efforts seem to be justified for verifying the claim of Fleischmann and Pons for overcoming the energy breakeven barrier through electrolysis.

Contrary to the opinion expressed in Refs. 16 and 17, it does not seem plausible that light water should be used as a "control" when excess energy is being sought during the electrolysis of heavy water.

ACKNOWLEDOMENTS

The author wishes to thank J. J. Farrell, Franklin and Marshall College, for his kind invitation to use his laboratory for these studles. Thanks are also due to James McBreen, Brookhaven National Laboratory; David Worledge, Electric Power Research Institute; and M. H. Miles, Naval Weapons Center, for useful discussions. The author would like to thank also W. R. Good for technical help.

The author also wishes to thank the two referees for their careful reading of the manuscript and for their useful remarks.

REFERENCES

- 1. M. FLEISCHMANN and S. PONS, "Electrochemically Induced Nuclear Fusion of Deuterium, J. Electroanal. Chent., 262, 301 (1989); see also Errata, J. Electroanal. Chem., 263, 187 (1989).
- 2. S. PONS, M. FLEISCHMANN, C. WALLING, and J. SI-MONS, "Method and Apparatus for Power Generation," International Application Published Under Patent Cooperation Treaty (PCT/US90/01328: International Publication Number WO 90/10935) (Mar. 13, 1989).
- 3. B. F. BUSH, J. J. LAGOWSKI, M. H. MILES, and G. S. OS-TROM, "Helium Peoduction During the Electrolysis of D2O in Cold Fusion Experiments," J. Electroanal. Chem., 304, 271 (1991).
- 4. R. L. MILLS and S. P. KNEIZYS, "Excess Heat Production by the Electrolysis of an Aqueous Potassium Carbonate Electrolyte and the Implications for Cold Fusion." Fusion Technol., 20, 65
- 5. T. MATSUMOTO, "Cold Fusion Observed with Ordinary Water." Fusion Technol., 17, 490 (1990).
- 6. V. C. NONINSKI and C. I. NONINSKI, "Determination of the Excess Energy Obtained During the Electrolysis of Heavy Water," Fusion Technol., 19, 364 (1991).
- 7. G. M. MISKELLY, M. J. HEBEN, A. KUMAR, R. M. PEN-NER, M. J. SAILOR, and N. S. LEWIS, "Analysis of the Published Calorimetric Evidence for Electrochemical Fusion of Deuterium in Palladium." Science, 246, 793 (1989).
- 8. G. ALEFELD and J. VOLKL, Eds., Hydrogen in Metals II. p. 173, Springer-Verlag (1967).
- 9. V. J. CUNNANE, R. A. SCANNELL, and D. J. SCHIFFRIN, *H₃ + O₂ Recombination in Non-Isothermal, Non-Adiabatic Electrochemical Calorimetry of Water Electrolysis in an Undivided Cell," J. Electroanal. Chem., 269, 163 (1989).
- 10. R. C. KAINTHLA et al., "Sporadic Observation of the Fletchmann-Pons Heat Effect," Electrochim. Acta, 34, 1315 (1989).
- 11. D. E. WILLIAMS et al., "Upper Bounds on 'Cold Fusion' in Electrolysis Cells," Nature, 342, 375 (1989).
- 12. T. R. JOW, E. PLICHTA, C. WALKER, S. SLANE, and S. GILMAN, "Calorimetric Studies of Deutrated Pd Electrodes." J. Electrochem. Soc., 137, 2473 (1990).
- 13. D. ALBAGLI et al., "Measurement and Analysis of Neutron and Gamma-Ray Emission Rates, Other Fusion Products, and Power in Electrochemical Cells Having Pd Cathodes," J. Fusion Ener<u>k</u>y, 9, 133 (1990).
- 14. J. DIVISEK, L. FURST, and J. BALEJ, "Energy Balance of DrO Electrolysis with a Palladium Cathode. Part II. Experimental Results," J. Electroanal. Chem., 278, 99 (1990).
- 15. M. J. JONCICH and N. J. HACKERMAN, "The Reaction of Hydrogen and Oxygen on Submerged Platinum Electrode Catalysts. 1. Effect of Stirring, Temperature and Electric Polarization, J. Phys. Chem., 57, 674 (1953).
- 16. H. FURST, cited after "Hopes for Nuclear Fusion Continue to Turn Cool," Nature, 338, 691 (1989).
- 17. J. MADDOX, "What to Say About Cold Fusion," Nature, 338, 701 (1989).

THIS PAGE BLANK (USPTO)





NASA Technical Memorandum 107167

Replication of the Apparent Excess Heat Effect in a Light Water—Potassium Carbonate— Nickel Electrolytic Cell

Janis M. Niedra NYMA, Inc. Cleveland, Ohio

Ira T. Myers, Gustave C. Fralick, and Richard S. Baldwin Lewis Research Center Cleveland, Ohio

February 1996



THIS PAGE BLANK (USPTO)





REPLICATION OF THE APPARENT EXCESS HEAT EFFECT IN A LIGHT WATER - POTASSIUM CARBONATE - NICKEL ELECTROLYTIC CELL

Janis M. Niedra NYMA, Inc. NASA Lewis Research Center Group Cleveland, Ohio 44135 Ira T. Myers
Gustave C. Fralick
Richard S. Baldwin
NASA Lewis Research Center
Cleveland, Ohio 44135

ABSTRACT

Replication of experiments claiming to demonstrate excess heat production in light water-Ni-K2CO3 electrolytic cells was found to produce an apparent excess heat of 11 W maximum, for 60 W electrical power into the cell. Power gains ranged from 1.06 to 1.68. The cell was operated at four different de current levels plus one pulsed current run at 1 Hz, 10% duty cycle. The 28 liter cell used in these verification tests was on loan from a private corporation whose own tests with similar cells are documented to produce 50 W steady excess heat for a continuous period exceeding hundreds of days. The apparent excess heat can not be readily explained either in terms of nonlinearity of the cell's thermal conductance at a low temperature differential or by thermoelectric heat pumping. However, the present data do admit efficient recombination of dissolved hydrogen-oxygen as an ordinary explanation. Calorimetry methods and heat balance calculations for the verification tests are described. Considering the large magnitude of benefit if this effect is found to be a genuine new energy source, a more thorough investigation of evolved heat in the nickel-hydrogen system in both electrolytic and gaseous loading cells remains warranted.

BACKGROUND

Motivated by the possibility of a new and practical source of abundant energy, a growing flurry of activity continues around the world to replicate, control and understand the source of anomalous heat in the so-called 'cold fusion' effect, first reported in March, 1989 by Fleischman, Pons and Hawkins(1) and also by Jones et al.(2) in electrochemical cells that load deuterium into metallic palladium or titanium. The initial disappointment at lack of experimental reproducibility has by now been compensated to a fair degree by the realization that special and usually difficult to achieve conditions(3) are necessary before the Pons-Fleischman effect can be observed. For example, it is now known that a high D/Pd loading ratio is one such difficult necessary condition and that likely there are others. Thus in the EPRI program⁽⁴⁾ on deuterated metals, McKubre et al. report⁽⁵⁾ that in a batch of Pons-Fleischman type cells, carefully prepared for precision calorimetry, every cell achieving a D/Pd≥0.95 showed excess heat, whereas none did that had a D/Pd<0.90. This and other effects, such as the frequently

long time delay to onset of excess heat, were not fully appreciated at the time of the initial high profile, negative follow-up reports from Harwell⁽⁶⁾, Caltech^(7,8) and M.I.T.⁽⁹⁾; moreover, some of this work was done in haste and under great pressure of public scrutiny. These early follow-up reports may now be mostly of historical interest, as controversy regarding their calorimetric⁽¹⁰⁾ and data reduction⁽¹¹⁾ methods has been raised.

Modern cells of various types have been reported to produce 50 W or more of excess power for hundreds of days, to have power multiplication factors over 10, and to achieve specific powers as high as -4 kW/cm³ (12). If true, such data clearly exclude by orders of magnitude an ordinary chemistry explanation and force one to consider various lattice assisted nuclear channels, or exotic quantum chemistry (electron transitions catalyzed to unusual, deep atomic levels (13,14,15,16) and also the subsequent fusing of the "shrunken" atoms), or the even more exotic possibility that somehow space energy, such as effects of the electromagnetic zero-point fluctuations, is involved.

It seems fair to say, however, that many still doubt the quality of evidence for the existence of consistent anomalous heat, citing the sporadic reproducibility and paucity of compelling evidence. Nevertheless, current experimental emphasis is shifting away from mere replication of the basic effect to developing it in diverse embodiments such as cells based on gas phase interactions with certain metals, light water-K₂CO₃-Ni, molten salt electrolytes, proton conductors, etc.. Such alternatives may offer specific advantages for the generation of power and understanding of the underlying mechanisms. For an overview of the latest experiments and the diverse contending theories, the reader may peruse the series of Proceedings of the nth International Conference on Cold Fusion (lately ICCF4 and ICCF5).

THE LIGHT-WATER CELL TESTED AT NASA

If the anomalous heat effect is found to be genuine, then it may be useful as a power source to replace radio isotope thermal generators for planetary spacecraft or other applications. An opportunity arouse in 1994 to obtain, on loan from the Hydrocatalysis Power Corporation, a lightwater cell for verification testing. The relative simplicity and reliability of the light water-Ni-K₂CO₃ electrolytic cell



made it particularly attractive for startup experimentation into this anomalous heat effect.

The existence of an excess heat effect in electrolytic cells based on a platinum (coated) anode and a nickel cathode immersed in a light-water solution of K_2CO_3 was first reported by R.L. Mills and S.P. Kneizys⁽¹⁶⁾, although the possibility was stated earlier by S. Pons et al. in a patent application⁽¹⁷⁾. The effect was soon verified by V.C. Noninski⁽¹⁸⁾ and continues as an active topic of research at numerous laboratories.

Prevailing experience has it that only rarely do the light-water cells using either K_2CO_3 or Rb_2CO_3 fail to produce at least some apparent excess heat immediately upon electrolysis, although full power may take months to develop. In contrast, cells based on Pd and D_2O often remain inactive for many days and require very careful selection and loading of the Pd.

The cell obtained was a rather large sized demonstrator, operating with 28 1 of 0.57 M K₂CO₃ solution in deionized, but otherwise ordinary, water in a 10-gal. polyethylene tank (Nalge 54100-0010). Its anode was a set of 10 platinized 1.6"x10" titanium strips and 5 platinized 1"Dx8" titanium tubes. And the cathode consisted of 5000 m of 0.5 mm D cold drawn nickel wire, wound as 150 sections, each 33 m long, on a perforated, 5 gal. polyethylene bucket. The 15 anode sections were suspended in a circular array close to the inner wall of this bucket from a 1214 " D polyethylene disk covering the top of the bucket and located several inches above the liquid level. Cathode and anode connections were brought out from the air space between the disk and the outer lid by means of two 1/2"Dx4" plated steel carriage bolts. Small holes were available in the outer lid and in the disk for insertion of the rod of a stirring paddle and thermocouples into the volume of the inner bucket. This cell came equipped with a 57.6 Ω , 1000 W, incoloy cased and teflon jacketed heating rod for on-the-fly calorimetric calibration.

Another cell, identical except for a missing anode structure, was obtained to provide a stable ambient temperature reference by averaging the short-term air temperature fluctuations.

The cell tested at NASA is thus nearly the same as the one pictured and described in more detail under "Thermacore Experiment 4" in Reference 15, except that the Thermacore cell used an additional, inner cathode wound from 5000 m of nickel wire.

EXPERIMENTAL SETUP AND PROCEDURES

The two cells, the active one on the left and blank reference on the right, were placed side by side in a hood, as shown in Figure 1, with their centers about 48 cm apart and 33 cm behind the draw window. Both cells sat on top of identical, 1" thick, closed cell, plastic foam pads placed



in plastic trays; pad compression over the weeks of operation was minor. During operation, the bottom edge of the hood draw window was kept at a fixed mark, level with the tops of the cells. In this way the cells were equally cooled by a steady, 0.7 m/s breeze driven by the hood fan, reducing the vagaries of air convection and variation of cell thermal conductivity with cell temperature. Room temperature variations were moderated only by the basement location, as no thermostatic control was available. Although room air temperature variations up to a few degrees C were experienced during some days, their effect appeared to be well canceled by referencing the active cell temperature rise with respect to the thermally matched blank cell. This room temperature instability unfortunately did make it difficult to obtain reliable data of cell thermal conductivity directly with respect to the ambient air at heater powers below 50 W. No experiments were performed involving electrolysis action in both cells simultaneously (such as comparing the action of K2CO3 and Na2CO3 solutions in the two cells operated in series) because our blank had no anode.

During steady dc electrolysis, all data was recorded on a Yokogawa model HR2300 multichannel stripchart recorder. This instrument can resolve 0.1 °C using type T thermocouples on any channel programmed for temperature. The actual thermocouple wire used was type T duplex, teflon covered and of enhanced accuracy, obtained from Omega Engineering, Inc. and labeled as "special limits of error." With this wire, the 3 thermocouples used to measure the electrolyte temperature near its center, top and bottom were found to track each other within 0.1 °C from room temperature to 72 °C. In all, 5 temperature probes were monitored: air temperature at hood entrance, active cell electrolyte temperature at three depths and blank cell water temperature at mid depth. The average of the 3 electrolyte temperatures was computed by the HR2300 and also recorded, as was the difference between this average and the blank cell temperature. All immersed thermocouples were electrically isolated from the electrolyte by 6 mm OD (3.5 mm ID) glass tubing, fused shut at one end.

The dc voltages of interest, i.e. at the cell and heating rod terminals as well as from current shunts, were routed to the HR2300 and recorded individually. Electrolysis current was sensed by a 1 $\ensuremath{m\Omega}$ precision shunt and the dc powered heating rod current was sensed by a 66.67 $m\Omega$ precision shunt. Power computations were done by multiplication and scaling internal to the HR2300 and the results were recorded. A check with a Racal-Dana Series 6000 digital multimeter revealed that the voltage and power values displayed digitally by the HR2300 were accurate to at least ±0.1%. All the HR2300 input channels were operated floating differential. Also, the output of the 6 V, 50 A electrolysis power supply, a Kepco model ATE6-50M, was entirely dc isolated. With these precantions, the chance of any significant ground loop induced error was minimal





Since the thermal time constant of the cell in the setup was observed to be 5.5 hours, uncontrolled drift of environmentally sensitive parameters could waste many hours of running time and create errors. Primarily this involves control of the heater and electrolysis powers. In the case of electrolysis power, it seemed best for two reasons to fix the cell current and let the voltage drift with the cell temperature. First, at a normal operating point, the cell differential resistance is low, meaning that the current will be very sensitive to small changes in cell voltage or temperature, making control by voltage difficult. Second, one expects any excess heat to basically depend on the current, because the rate of delivery of hydrogen ions to the nickel surface is proportional to the current.

The heater rod in the active cell was used to develop the curve of temperature rise ΔT , as referenced to the unheated blank cell, versus ohmic power dissipated in the active cell by observing the steady state ΔT at selected heater powers. The slope of this line is just the thermal resistance of the cell and the process of generating such a line during electrolysis is called calibration on-the-fly 15,10 . An on-the-fly calibration is necessary, for as will be shown, the effects of electrolysis can significantly affect the cell thermal resistance.

To keep heater power constant, even as the heater resistance or supply voltage varies, we used a precision constant power controller. This was a circuit based on analog multiplication and feedback techniques controlling a series-pass power MOSFET and similar to load controllers described by J.M. Niedra⁽¹⁹⁾. Using a 100 V dc supply, any preset power up to 120 W and stable to within ±0.5% could easily be delivered to the heater.

During the regular runs, the active cell was stirred continuously by means of a small teflon half-moon attached to the end of a glass rod rotating at a constant 250 rpm, but the blank cell was stirred only intermittently to eliminate the 0.5 °C or so temperature stratification that could be seen in the water if left undisturbed for a day. Preliminary experiments with the unheated blank cell had shown that in an undisturbed cell suddenly so stirred, any small temperature nonuniformity returned to within 0.1 °C in a minute or two. Further, even after 27 hours of stirring at 315 rpm and with the hood fan off, no clear temperature rise above ambient could be resolved (0.1 to 0.2 °C). Hence the paddle arrangement and its 250 rpm speed was judged entirely satisfactory, producing a negligible contribution to the steady ΔT.

Pulse mode control of the electrolysis current has been claimed to increase the ratio of excess heat to input power, both in D₂O-Pd⁽²⁰⁾ and H₂O-Ni cells⁽¹⁵⁾. We tested this mode, as time permitted, for at least a 1 Hz pulse repetition rate at 10% duty cycle. The above mentioned power supply was found to be a good source of sharply rectangular current pulses, when operated in its voltage programmed current mode, with peak current set by the current limiter. Current-to-voltage conversion was done by

a $0.010~\Omega$ shunt, whose performance with pulses was verified by comparison to a high speed current probe. To simultaneously record the rectangular cell current pulses and associated terminal voltage, we used two Tektronix type 11A33 differential comparators in a DSA602A digitizing oscilloscope mainframe. The instantaneous product of cell current and voltage was recorded as well. Also, null input recordings were taken immediately after a data recording in order to correct for dc offsets in the 11A33s, which were observed at times to be as much as several percent of the signal amplitude. Null recording provided the only means of baseline correction for the cell voltage waveform record, because the cell voltage did not decay to zero during the cycle. As a check on the digitized data, time-averaged cell current and voltage, formed by 100 s time constant RC networks, were recorded with the HR2300.

ANALYSIS OF DATA

Blank cell thermal conductance

One expects to observe some differences in the steady state heat loss characteristics, or thermal conductance K, of the blank cell and the active cell during electrolysis. Additional water vapor being carried away in the evolved H₂ and O₂ gas bubbles may well contribute an extra heat loss during electrolysis. And as the electrolysis current is increased, the evolving gases may conceivably contribute to a decrease in k due to their insulating effect. The heat loss contribution to κ arising from the specific heats of the H₂ and O₂ seems negligible, however, being only about 2.16x10⁻⁴ WA⁻¹°K⁻¹ I, where I is the electrolysis current. Thus for I=10 A, this additional loss is only a few milliwatts per °K. This heat loss has been estimated using the gas specific heats c, of 28.7 and 26.0 Joule/(mole °K) for H_2 and O_2 , (21) respectively, and assuming 100% Faradaic efficiency. Finally, the welding cables clamped the electrolysis electrode terminals may have contributed a slight additional, temperature dependent heat loss to the active cell. This effect too seemed to be minor, as the temperature rise of the top of the cell was always much less than that of the liquid contained below. In any case, all heat losses for the active cell are automatically included by the on-the-fly calibration.

A number of heat loss calibration runs were performed with the blank cell, loaded with 28.0 liters of deionized water. This amount of water contributes 1.17x10⁵ J/°K to the heat capacity, whereas the 8.75 kg of Ni wire contributes only 3.88x10³ J/°K, with contributions from the other cell hardware being negligible. At least 24 hours were allotted for the cell to reach equilibrium temperature at each of the heater powers set by the precision controller.

The result of the first 4 blank cell heat loss calibration runs is represented by the lower line in Figure 2, which has a reciprocal slope of κ_{bl} =6.13 W/K. The 3 lower

power points are seen to be very well aligned with the origin, but the 125 W point droops slightly. The reason for this droop was thought to be the onset of more rapid water vaporization at the 43 °C temperature of the 125 W point. Therefore a straight line through the origin was fitted to the 3 lower points only. No points below 50 W were taken because of lack of time and the observation that the 1/4 inch thick, plastic underpad used initially had compressed to an unacceptably thin 1/8 inch under the weight of the cell. Thereafter a 1 inch thick plastic foam underpad was substituted, which suffered only minor relative compression. The upper straight line through the origin in Figure 2 represents the new characteristic, again ignoring the 125 W point. Now the reciprocal slope is a slightly lower K_{bi}=5.85 W/°K, which is the same as the 0.17 °C/W on-the-fly coefficient at L=50 A given for the Thermacore experiment no. 4. Unfortunately the 75 W point turned out to be the lowest power data obtained with the thicker pad, because lack of time and an unstable room temperature caused by weather made it impossible to take accurate low power points.

In spite of the lack of lower power calibration points, the good alignment with the origin of the points obtained (except for the highest power ones) is evidence that κ is a constant for ΔT below about 17 °C. The purpose of setting the cells in a vigorously and uniformly flowing airstream was of course to reduce any temperature dependence of κ . As seen below, a highly temperature sensitive κ invalidates, or at least complicates, the usual regressive extrapolation toward the origin in order to find the excess heat.

The presence of additional heat loss channels induced by electrolysis necessitates on-the-fly thermal characterization of the active cell. However, this method has a lower limit on power for a given electrolysis current, because this current dissipates ohmic heat in the electrolyte. Nevertheless, lower ohmic heat points were obtained in some electrolysis runs and these support the constancy of κ with ΔT . The active cell runs also exhibited quite clearly a small, but not insignificant, dependence of κ on the electrolysis current. The blank cell calibration line serves merely as a limiting low current check on the active cell thermal behavior.

Heat balance and the excess heat effect

Figure 3 defines the various input and output powers to the cell viewed as a box enclosing unknown and certainly complex processes. There are only two unquestionably significant power inputs, namely the cell terminal power $P_c=V_c$ I_c and the heater power P_h . Note that resistive drops in connections internal to the cell might make the power delivered to the electrolyte slightly less than P_c . Thermoelectric pumping of heat through the electrolysis terminals by the Peltier effect is a consideration that has been drawn as an input power P_{tc} . The experimentally negligible Joule heat input P_{st} due to stirring is drawn

there also.

The temperature rise dependent heat losses consisting of convection, water vaporization and various conductions are lumped into a thermal loss P_{tb} , which is just $\kappa\Delta T$ if the process is linear over the ΔT range of interest here. The remaining loss is the energy carried away by the H_2 and O_2 gases escaping the cell. This loss amounts to the energy 4.75×10^{-19} J/molecule of H_2O that could be retrieved if the gases were recombined and condensed to liquid H_2O at the same temperature. When calculated in terms of I_c , this energy corresponds to the thermoneutral voltage of 1.48 V and the 'gas power' is written as 1.48 ηI_c , where the Faradaic efficiency η may be less than 1 to cover the case of a partial recombination of the H_2 and O_2 within the cell.

The excess heat P_{exc}, if any, is simply the difference between the total output and input powers and can be written as

$$P_{exc} = (P_{th} + 1.48 \eta I_c) - (P_c + P_h + P_{tc} + P_{st}).$$
 (1)

To be useful for computing P_{exc} , Eq. 1 must be put into a form that relates closer to what is measured. First we note that the thermal heat loss $P_{th} = P_{th}(I_c, \Delta T)$ is an unknown function, but with the property that $P_{th}(I_c, 0) = 0$. The simplest such admissible form is $P_{th} = \kappa(I_c) \Delta T$. Information about this function must be gleaned experimentally, say by varying P_{th} , with I_c fixed. P_c will then vary also, since the V_c versus I_c characteristic is temperature sensitive. Nevertheless, one can combine some of these variables into a single term

$$P_o = P_c + P_h + P_{te} + P_{st} - 1.48 \eta I_c,$$
 (2)

representing the part of the total input power that is dissipated as heat in the electrolyte. For a fixed L, P_h =0 gives the least possible P_e . Even if P_{te} and P_{st} are negligible, the possibility that η <1 can not be ignored. Therefore it is convenient for plotting purposes to define a 'reduced' dissipated power

$$\bar{P}_{c} = P_{b} + P_{c} - 1.48 I_{c} \tag{3}$$

that underestimates the true dissipation, but is completely determined once $P_{\rm h}$ and $I_{\rm c}$ are set. With this definition,

$$P_o = \bar{P}_o + P_{te} + P_{st} + 1.48 \, \eta_{rec} \, I_c,$$
 (4)

where

$$\eta_{\text{rec}} = 1 - \eta$$
(5)

is a recombination efficiency. With these definitions, Eq. 1 becomes

$$P_{exc} = P_{tb} - P_{o}$$

$$= P_{tb} - \tilde{P}_{o} - (P_{tc} + P_{st} + 1.48 \eta_{rec} I_{c}).$$
 (6)





One can curve fit experimental data of steady state (\bar{P}_o , ΔT), obtained by varying P_b at fixed I_c . This plot can then be extrapolated to ΔT =0 to obtain $\bar{P}_o|_{\Delta T=0}$; the confidence one can place in this extrapolation depends on the scatter of the data, the nature of the fitted curve and the closeness of the data to the origin. As mentioned, $P_{cb}|_{\Delta T=0}$ =0, regardless of the particular dependence of P_{cb} on ΔT . Thus from Eq. 6 and this property of P_{cb} , it follows immediately that the true excess heat is

$$P_{exc} = (-\bar{P}_{o \mid \Delta T=0}) - (P_{te} + P_{st} + 1.48 \eta_{rec} I_{s}),$$
 (7)

A summary of the steady state ΔT versus \bar{P}_o data obtained at fixed L=5, 10, 20 and 40 A is presented in Figure 4; this data was obtained by varying P_h , as stated under Eq. 6 above. Straight lines gave excellent least squares fits to the data and their extrapolated \bar{P}_o -axis intercepts are $\bar{P}_o|_{\Delta T=0}=-7.20$, -8.57, -11.4 and -8.41 W, corresponding respectively to the above L. If the terms P_{te} , P_{st} and 1.48 $\eta_{re}L_c$ are negligible (P_{st} certainly is; see EXPERIMENTAL SETUP AND PROCEDURES), then, according to Eq. 7, these ($\bar{P}_o|_{\Delta T=0}$) are the positive excess powers corresponding to the above 4 dc L; however, the P_{te} and 1.48 $\eta_{re}L_c$ contributions will be discussed. In general, we shall call ($\bar{P}_o|_{\Delta T=0}$) the apparent excess power or heat.

Along with each data line in Figure 4, also the blank cell calibration line is redrawn to provide a comparison of their slopes. This comparison shows that $\kappa(I_c) \succ \kappa_{cd}$ in all 4 cases and that $\kappa(I_c)$ tends to increase slightly with I_c . A summary of this behavior of $\kappa(I_c)$ is presented as a scatter plot in Figure 5, that also includes the κ_{cd} data point as well as κ from a pulse I_c run plotted at its average current $I_c=3.10$ A.

Due to time constraints on laboratory space, the only pulse I_c data taken was with 30 A rectangular pulses at a 10% duty cycle and 1 Hz repetition rate, giving the mentioned average I_c =3.10 A. Values for the on-the-fly calibration plot were obtained by time averaging Eq. 3, etc.. From the corresponding line fitted in Figure 6, the apparent excess heat is found to be only 2.66 W. And the thermal conductance is seen to be very close to that of the blank cell, as already indicated in Figure 5. A sampling of the I_c , I_c and I_c waveforms recorded at thermal equilibrium and I_c is presented along side to show the cell polarization effect. The time averages I_c and I_c noted in Figure 6 include small corrections for baseline offsets in the DSA602A.

Internal recombination and water addition

Reliable data on water loss during electrolysis from cells operating without a recombiner is essential to the correct interpretation of the apparent excess heat, especially in low power cases having $-\bar{P}_{0|\Delta T=0}<1.48I_c$. In such cases a sufficiently high recombination efficiency η_{rec} can imply that $P_{exc}=0$, even if P_{te} and P_{st} are negligible, as inspection of Eq. 7 shows.

Unfortunately, the run time allotted to each constant heater power P_h was limited to at most a day or two, which precluded the taking of accurate water loss data in our setup. In efforts to compensate for data inaccuracies, a loss rate was calculated for each selected I_c by adding the loss amounts for all the corresponding runs of fixed P_h and dividing by their total time. This procedure reduces the data scatter at the cost of lumping together temperature dependent evaporation rates. Water loss rates so processed are plotted against I_c in Figure 8 and fitted by a straight line. 100% efficient $(\eta=1)$ electrolysis would generate the loss rate αI_c , where $\alpha=9.34\times10^{-5}$ g s⁻¹A⁻¹, which too is plotted in Figure 8.

The total water loss rate is the sum of evaporation and electrolysis losses, or

$$\underline{\alpha} = \underline{\alpha}_{xx} + \eta \alpha \underline{I}_{c} , \qquad (8)$$

where \mathfrak{L}_{ev} depends on T_e , and hence on I_e and P_h . However, only the I_e dependence of \mathfrak{L}_{ev} will be considered below, because for each I_e the P_h dependence has been 'averaged out' in the data of Figure 8. Evaporation dominates recombination in Figure 8, for the data fact that $\mathfrak{D} > \alpha I_e$ is the same as

$$g_{ev} > \eta_{rec} \alpha I_c$$
 (9)

Although our data is insufficient to place a hard upper bound on $\eta_{\rm rec}$, a bound tighter than Eq. 9 can be had by substituting the experimental fit

$$\mathbf{g} = \beta \mathbf{I}_{c} + \mathbf{g}_{cv}(0) , \qquad (10)$$

where $\beta=9.03\times10^{-5}$ g s⁻¹A⁻¹ and $\Omega_{cv}(0)=3.78\times10^{-4}$ g s⁻¹, into

$$\mathfrak{Q} - \alpha I_{c} = \mathfrak{Q}_{cv} + (\eta - 1)\alpha I_{c}
= \mathfrak{Q}_{cv} - \eta_{rec}\alpha I_{c}$$
(11)

to obtain

$$\eta_{\text{rec}} \alpha I_{\text{c}} = \mathcal{G}_{\text{ev}}(I_{\text{c}}) - \mathcal{G}_{\text{ev}}(0) + (\alpha - \beta)I_{\text{c}}. \tag{12}$$

This formula is useful, because at the lower I_c of the runs the contribution of the I_c to ohmic heating was small as compared to the upper P_h values over which the water loss data was averaged to obtain the points in Figure 8. Thus $\mathfrak{L}_{cv}(I_c)$ can not be much greater than $\mathfrak{L}_{cv}(0)$ in the present case.



DISCUSSION

To claim the reality of excess heat in the presence of other comparable heat transfer processes, one must support the validity of the extrapolation to get the apparent excess heat (-PolAT=0). Both the blank and active cell thermal conductance data shows that these cells in the environment described are well characterized by a thermal conductance κ that depends slightly on the cell current I_e , but not at all on the temperature rise AT, at least for 0≤AT≤17°C. The blank cell runs showed in particular that the lower ΔT versus heater power Ph points are well in line with the origin. This eliminates the possibility that the (ΔT , P_b) locus could curve into (0, 0) from above; multiple curvature inflections seem quite unlikely. Further, the active cell constant L runs show in Figures 4 and 6 that the thermal conductance characteristic is very linear down to total ohmic heatings of only a few watts, assuming negligible hydrogen-oxygen recombination. Hence there is good evidence for the validity of the linear extrapolation to ∆T=0 of our data.

Accepting the rationale for the apparent excess heat extrapolated from the on-the-fly thermal data, the burden is shifted to showing that the heat additions P_{te} , P_{st} and $1.48\eta_{re}I_{c}$ can not account for the apparent excess. These heats will be discussed below. Worthy of mention is also the possibility of corrections whose omission leads to an underestimate of the excess heat. Ohmic heat is generated in the wires and connections inside the cell, but above the electrolyte. This heat is included in P_{c} , even though it is not wholly delivered to the electrolyte. Thus in the cell tested, some warming of the external anode terminal was evident for $I_c>20$ A, while the external cathode terminal remained at about the cell top temperature. Finally, any unrecognized mechanism of electrochemical energy storage is an error on the conservative side.

The stirring power P_{st} is not a contender in accounting for the observed apparent excess heat, because stirring induced ΔT was at the resolution limit, 0.1 °C, of the recorder. This implies a P_{st} below a watt on the blank cell calibration slope $\kappa=5.85$ W/°C.

Handel(22) has recently proposed that the thermoelectric power Pte into an electrolytic cell may in some cases account for the claimed excess, mainly citing experiments exhibiting a proportionality between steady I_e and excess power. He justifies the required very high (for pure metals) effective differential Peltier coefficient ΔΠ=400 mV by pointing to cases where the excess heat was observed for only a small fraction of the time. We contend, however, that several circumstances greatly reduce the likelihood of, if not entirely eliminating heat pumping as the cause in our case. First, the apparent excess power at L=5 A was a steady 1.44 W/A at essentially room temperature, requiring an effective differential Seebeck coefficient $\Delta S=5.27 \times 10^{-3} \text{ V/K}$; recall that Π =ST and $P_{te}=I_{c}\Delta\Pi=I_{c}T_{c}\Delta S$. This value of ΔS is several times that observed even in semiconductors.

Second, a proportionality of excess power to I_c is not supported by the data plot in Figure 7. In contrast, this plot suggests onset of saturation or even interference with rising I_c. Our last, weaker comment is that in our case the P_{te} into the cell vessel is theoretically zero because the electrolysis electrodes exiting the lid are identical. This reduces the problem to one of heat pumping between the junctions in the air space below the lid and the effectively Pt-Ni junction in the electrolyte below. However, no cooling of the exiting electrodes was ever discerned.

To account for all of the observed excess heat by hydrogen-oxygen recombination within the cell requires a recombination efficiency of quite a high magnitude in our case. This efficiency,

$$\eta_{\rm rec} = -\tilde{P}_{\rm o \, | \, \Delta T = 0} / (1.48 I_{\rm c}) ,$$
(13)

follows from Eq. 7 by setting Perc to zero and neglecting P_{te} and P_{st} . The plot of this η_{rec} in Figure 9, based on the previously derived values of $P_{o|AT=0}$ at the selected I_c , shows that in the dc case for I_c below 10 A the η_{rec} exceeds 0.55 and grows rapidly to unity at L near 5 A. However, our data does marginally admit such an explanation. First, any recombination heat released in the air space between the electrolyte and the leaky lid, where the most active exposed catalyst was nickel wire connecting to the cathode, could hardly be well transmitted to the liquid below. Hence the recombination would have to be within the electrolyte. Using $\mathfrak{L}_{ev}(L)=\mathfrak{L}_{ev}(0)$, as argued below Eq. 12 for low L, and the experimental data in Figure 8, the loose upper bound on η_{rec} imposed by Eq. 9 falls somewhat below the plot of Eq. 13 in Figure 9. Presumably Eq. 12 restricts η_{rec} even more. Our sparse water addition data thus seems not to entirely favor the recombination explanation, but fails to be decisive either way for lack of accurate 2 data.

In a recent paper (23) applicable to water-based electrolytic cells, J.E. Jones et al. point out the well known (24) effectiveness of Ni, Pt and Pd to catalyze the recombination of oxygen and hydrogen. They present electrolytic cell experiments demonstrating the quenching of apparent excess heat in configurations that inhibit the transport of dissolved oxygen to the cathode and hydrogen to the anode. And they further demonstrate the achievement of $\eta_{rec} > 0.95$ when O_2 was bubbled through an operating cell. Accepting these results, our data are then generally consistent with the recombination explanation and the behavior of the apparent excess heat with cell current that it predicts.

The fact that the initial slope of the apparent excess heat versus I_c data shown in Figure 7 is comparable to the slope (1.48 W/A) of the maximum gas power line is as predicted at low current density by the recombination hypothesis; the solution of gas becomes more effective at low evolution rates. Related to this, the few reported dc tests of cells nearly identical to the present one, except for the nickel, also suggest a similar slope, even though they





produced up to 50 W excess¹⁵⁾. Only the pulse mode, not systematically explored here, seems to have produced significantly more energy per coulomb throughput. Therefore, given an equal area of nickel wire, the indications now are that the metallurgy of the nickel greatly affects the saturation $P_{\rm exc}$, but probably less so the initial $P_{\rm exc}/I_{\rm c}$ slope. In fact, subsequent testing of the present cell by the Hydrocatalysis Power Corp. has verified our observations of its low saturation $P_{\rm exc}$ under the same conditions that produced 50 W excess from cells differing only in the source of the nickel wire. For the cell we examined, evidently there was an unfortunate choice of nickel wire from an untested source.

No conclusions can be drawn here regarding exothermal chemical reactions involving the electrodes, because the run times at each cell current and heater power were usually restricted to the minimum needed to establish thermal equilibrium - about 24 hours. However, no ordinary chemical reactions involving nickel are known that could account for the total excess energy from similar Mills type cells claimed to produce 50 W excess for months. And no report of a chemical or metallurgical change of the nickel cathode is known to us.

SUMMARY AND CONCLUSIONS

The light water-Ni-K₂CO₃ electrolytic cell on loan from the Hydrocatalysis Power Corporation clearly exhibited the phenomenon of apparent excess heat when tested at 4 selected dc currents and one pulse mode current. Data was collected using simple 'on-the-fly' calorimetric calibration in the thermal steady state and was reduced to give the apparent excess heat by extrapolation methods that are accepted practice in the field of anomalous heat cell ('cold fusion') research.

Our main findings regarding cell voltages, currents and powers are summarized in Table I. The apparent power gains ranged from 1.06 to 1.68. The apparent excess power of this particular cell saturated at a rather low 11.4 W, at an electrical input power of 59.6 W, using a cell current of 20 A dc, as compared to about 50 W apparent excess reported by other workers for essentially the same cell. We attribute this shortfall to an unfortunate choice of untested nickel from an alternate source.

The power gain given in Table I and plotted in Figure 10 is based on the apparent excess power $(-F_{o|\Delta T=0})$ and is the most optimistic possible, since gas recombination, stirring power and any thermoelectric heat injection are then neglected (see Eq. 7). The maximum possible gas power (1.48L) is included as part of the output power. The plot of the gain $(P_{exc,apparent}+P_o)/P_e$ in Figure 10 appears of a form decreasing asymptotically to unity for large I_e , as expected for a saturating $P_{exc,apparent}$.

Although our data admits the existence of an unusual source of heat within the cell, it falls far short of being

compelling. To delimit the alternatives, we have examined the following factors considered in the literature as potential ordinary causes of multiwatt level, steady state, apparent excess heat in the present type of cell:

- Unrecognized nonlinearity in the cell thermal conductivity (κ) at low temperature differential (ΔT), leading to erroneous extrapolation for the excess heat.
- 2. Injection of heat into the cell by thermoelectric pumping (Seebeck effect).
- 3. Exothermic chemical reactions involving the nickel cathode.
- Heat from hydrogen-oxygen recombination within the cell.

And we have come to terms with these possibilities as follows:

- Nonlinearity in k is contraindicated by the good alignment of our high power thermal calibration points with a straight line through the origin and also by the linear alignment of our 'on-the-fly' calibration points reaching down below 10 W. This linearity was achieved by forced convective cooling.
- 2. For thermoelectric heat pumping to account for the apparent excess heat would require differential Seebeck coefficients several times those of even semiconductors. Also, such heat pumping through the lid of our cell is zero in first order because the two exiting electrodes were identical.
- 3. The apparent energy evolved in the present experiments was inadequate to eliminate chemical reactions - runs too short for the power observed. However, this possibility has been examined and rejected by other workers operating very similar cells at 50 W apparent excess heat for months.
- 4. Our inadequate water accounting data are at least marginally consistent with the recombination explanation of the source of the apparent excess heat, even though this requires recombination efficiencies exceeding 0.55 at 10 A and rising to near unity at 5 A of cell current (Figure 9). Nevertheless, J.E. Jones et al. (23) have claimed to show that light water cells with nickel and platinum electrodes can indeed achieve such high recombination of dissolved oxygen and hydrogen. Also, our Figure 7 suggests this possibility.

Following the principle of simplest explanation that fits the data on hand, recombination becomes the explanation of choice. But even perfect recombination can not account for all of the apparent excess heat in those Mills cells usually operated in a pulsed current mode and reported to produce a thermal output solidly exceeding the VI power



input to the cell. These cases at least leave the door open to more interesting possibilities. Considering the potential value of a new energy source, it seems worth while to restudy the Mills type cell in configurations allowing an accurate account for recombination and water loss.

Insufficient resources prevented us from proceeding with a more careful study of the excess heat effect in cell types adapted to bear on specific questions. For example, certain gaseous loading types, such as the D₂-Pd transient pressurizing experiment⁽²⁵⁾ at NASA or the H₂-Ni heating experiment⁽²⁶⁾ at the University of Siena, could avoid the complications of electrolytic cells, while exploring possibilities of high temperature operation and radiation emission⁽²⁷⁾.

ACKNOWLEDGMENTS

The authors gratefully acknowledge both the loan of equipment and technical assistance from the Hydrocatalysis Power Corporation and the support for this work from the Directors Discretionary Fund of the NASA Lewis Research Center.

REFERENCES

- M. Fleischmann, S. Pons and M. Hawkins, "Electrochemically Induced Nuclear Fusion of Deuterium", J. Electroanalytical Chem. 261, 1989, pp. 301 - 308.
- S.E. Jones et al., Observation of Cold Nuclear Fusion in Condensed Matter", Nature 338, 1989, p. 737.
- D. Cravens, "Factors Affecting the Success Rate of Heat Generation in CF Cells", Proc. of ICCF4, Vol. 2, Maui, Hawaii, December 6-9, 1993, pp. 18-1 to 18-14.
- T.O. Passell, "Overview and Status of the EPRI Program on Deuterated Metals", ASME Joint International Power Conference, Phoenix, Arizona, October 2-6, 1994.
- M. McKubre et al., "Nuclear Processes in Deuterated Metals", EPRI Report TR-104195, August 1994. See also M. McKubre et al., "Loading, Calorimetric and Nuclear Investigation of the D/Pd System", Proc. of ICCF4, Vol. 1, Mani, Hawaii, December 6-9, 1993, pp. 5-1 to 5-28.
- D.E. Williams et al., "Upper Bounds on 'Cold Fusion' in Electrolysis Cells", Nature 342, 1989, p. 375.
- N.S. Lewis et al., "Searches for Low Temperature Nuclear Fusion of Deuterium in Palladium", Nature 340, 1989, p. 525.

- G.M. Miskelly et al., "Analysis of the Published Calorimetric Evidence for Electrochemical Fusion of Deuterium in Palladium", Science <u>246</u>, 1989, p. 793.
- D. Albagli et al., "Measurement and Analysis of Neutron and Gamma-Ray Emission Rates, Other Fusion Products, and Power in Electrochemical Cells Having Pd Cathodes", J. Fusion Energy 9, 1990, p. 133.
- M.H. Miles et al., "Calorimetric Principles and Problems in Measurement of Excess Power during Pd-D₂O Electrolysis", J. Phys. Chem. <u>98</u>, no. 7, 1994, pp. 1948-1952.
- 11. M.R. Swartz, "Some Lessons from Optical Examination of the PFC Phase-II Calorimetric Curves", Proc. of ICCF4, Vol. 2, Maui, Hawaii, December 6-9, 1993, pp. 19-1 to 19-14.
- M. Fleischmann and S. Pons, "Calorimetry of the Pd-D₂O system: from simplicity via complications to simplicity", Phys. Lett. A <u>176</u>, 1993, p. 118.
- J.A. Maly and J. Vavra, "Electron Transitions on Deep Dirac Levels I", Fusion Technology <u>24</u>, November 1993, pp. 307 - 318.
- J.-P. Vigier, "New Hydrogen (Deuterium) Bohr Orbits in Quantum Chemistry and "Cold Fusion" Processes", Proc. of ICCF4, Vol. 4, Maui, Hawaii, December 6-9, 1993, pp. 7-1 to 7-25.
- R.L. Mills, W.R. Good and R.M. Shaubach, "Dihydrino Molecule Identification", Fusion Technology <u>25</u>, January 1994, pp. 103 - 119.
- R.L. Mills and S.P. Kneizys, "Excess Heat Production by the Electrolysis of an Aqueous Potassium Carbonate Electrolyte and the Implications for Cold Fusion", Fusion Technology 20, August 1991, pp. 65-81.
- S. Pons, M. Fleischmann, C. Walling and J. Simons, "Method and Apparatus for Power Generation," International application published under Paten Cooperation Treaty (PCT/US90/01328; International Publication No. WO90/10935), 13 March 1989.
- V.C. Noninski, "Excess Heat During the Electrolysis of a Light Water Solution of K₂CO₃ With a Nickel Cathode", Fusion Technology <u>21</u>, March 1992, pp. 163-167.
- J.M. Niedra, "Analog Synthesized Fast-Variable Linear Load," Proc. of the 26th IECEC, Boston, Massachusetts, August 1991. Also NASA CR-187155.
- A. Takahashi et al., "Windows of Cold Nuclear Fusion and Pulsed Electrolysis Experiments", Fusion





Technology 19, 1991, pp. 380-390.

- CRC Handbook of Chemistry and Physics, 69th Edition, CRC Press, Boca Raton, 1988-1989, p. D-44.
- P.H. Handel, "Subtraction of a New Thermo-Electrochemical Effect from the Excess Heat, and the Emerging Avenues to Cold Fusion", Proc. of ICCF4, Vol. 2, Mani, Hawaii, December 6-9, 1993, pp. 7-1 to 7-8.
- J.E. Jones et al., "Faradaic Efficiencies Less Than 100% During Electrolysis of Water Can Account for Reports of Excess Heat in "Cold Fusion" Cells", J. Phys. Chem. 99, no. 18, 1995, pp. 6973-6979.
- A. McDougall, Fuel Cells, Energy Alternatives Series, John Wiley, New York, 1976, p. 54.
- 25. G.C. Fralick, A.J. Decker and J.W. Blue, "Results of an Attempt to Measure Increased Rates of the Reaction ²D+²D→³He+n in a Nonelectrochemical Cold Fusion Experiment," NASA TM-102430, December 1989.
- S. Focardi, R. Habel and F. Piantelli, "Anomalous Heat Production in Ni-H Systems," Il Nuovo Cimento 107A, N.1, January 1994, pp. 163-167.
- C. Manduchi et al., "Anomalous Effects During the Interaction of Subatmospheric D₂ (H₂) with Pd from 900 °C to Room Temperature," Il Nuovo Cimento 107A, N.2, February 1994, pp. 171-183.

Table I. Operating characteristics of Hydrocatalysis Power Corporation's demonstration light water-Ni-K₂CO₃ electrolytic cell.

I _e	V _c	Duty Cycle	V _e I _e	P _{exc} , apparent	Apparent Power
(A)	(V)	(%)	(W)	(W)	Gain ⁽³⁾
5.0	2.12	100	10.6	7.20	1.68
10.0	2.55	100	25.5	8.57	1.34
20.0	-2.98	100	59.5	11.4	1.19
40.0	3.36	100	134.5	8.41	1.06
31.0(1)	1.72 ⁽²⁾	10	8.58 ⁽²⁾	2.66	1.31

- (1) Peak current of rectangular pulse
- (2) Time average
- (3) Apparent Power Gain $\equiv (P_{exc, apparent} + V_c I_c)/(V_c I_c)$

Note: usual test duration was about 24 hours at each fixed I and heater power





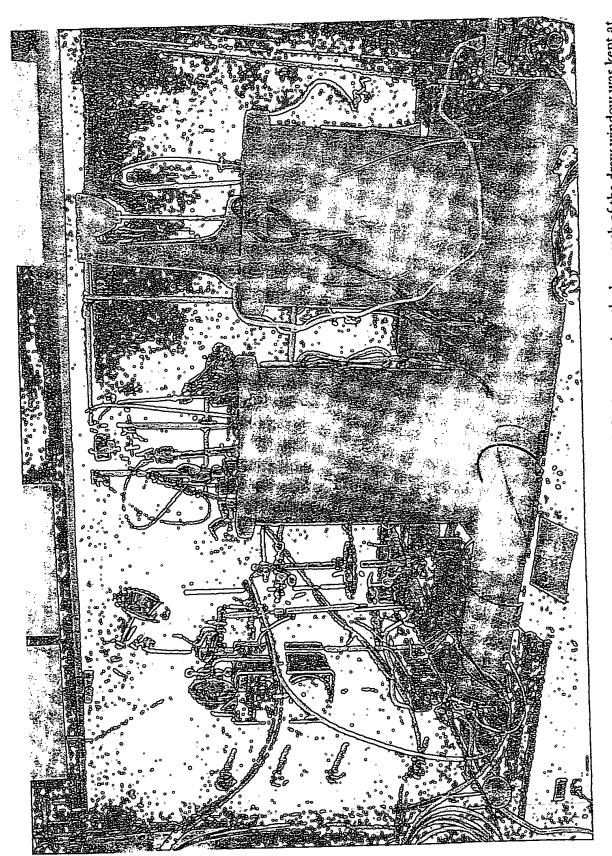
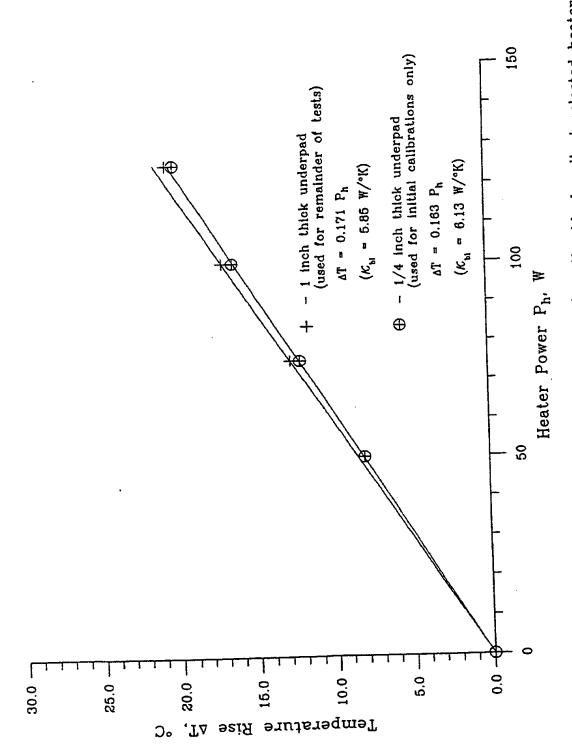


Figure 1. Active (left) and reference cells on the floor of a hood. During operation, the lower sash of the draw window was kept at a height even with the tops of the cells, giving a window airflow of 0.7 m/s.

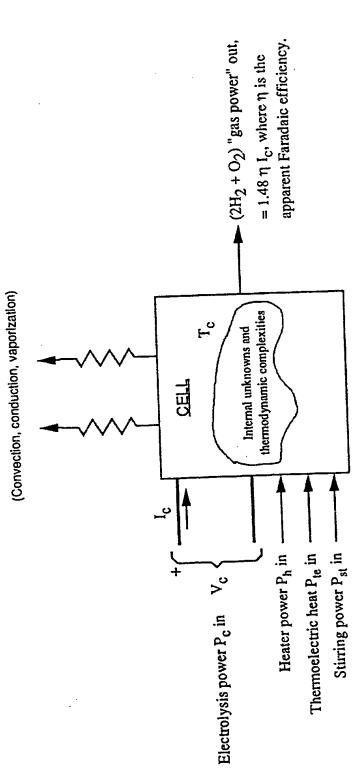


powers. Fits are least squares straight lines through the origin, ignoring the 125 W points, which appeared to be drooping due to the increased water vaporization at their temperature (~43 °C). Figure 2. Temperature rise above ambient air (~23 °C) of the blank cell at selected heater



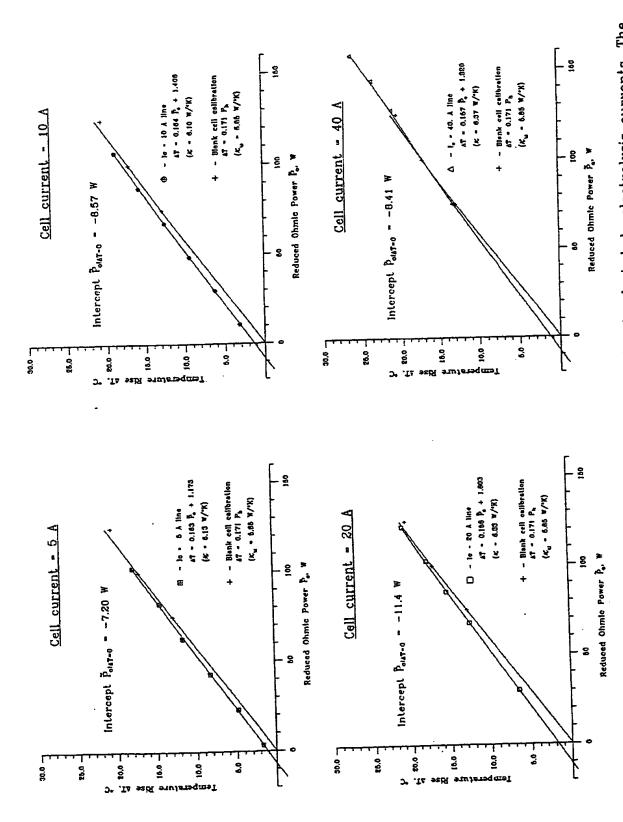






Ambient temperature Ta

Figure 3. Identification of the cell input and output powers considered in the analysis of excess heat.



The blank cell calibration line is repeated in each plot for comparison of thermal conduction. Figure 4. On-the-fly thermal calibration of the active cell for 4 selected dc electrolysis currents. The apparent excess heat is the negative intercept $-\tilde{P}_{olaT=0}$ of the fitted line with the \tilde{P}_o-axis .





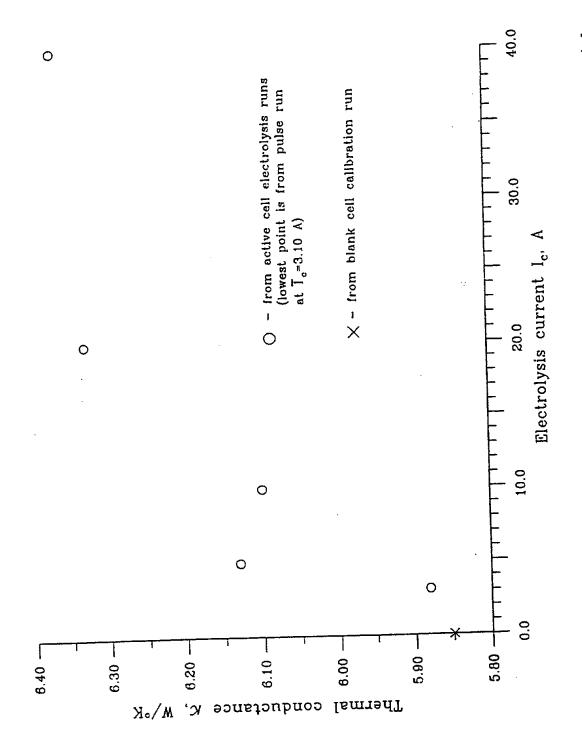
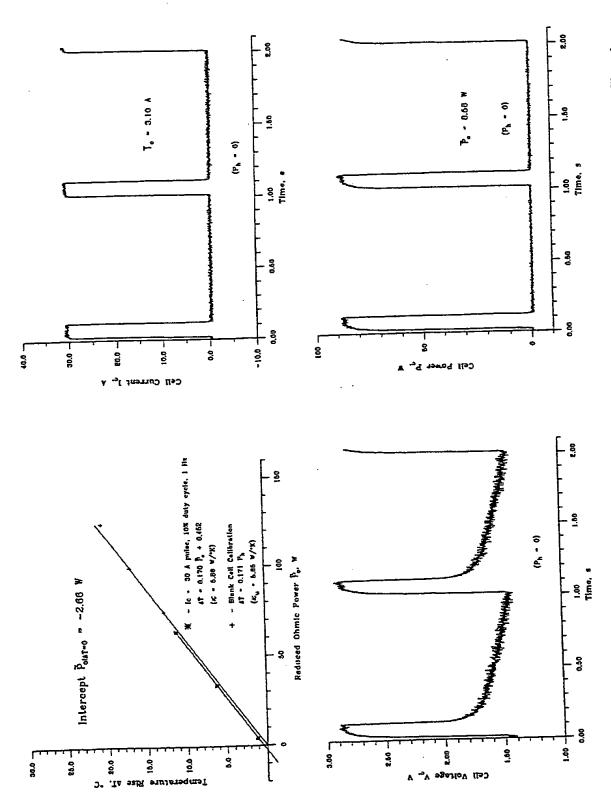


Figure 5. Scatter plot of cell thermal conductance κ versus electrolysis current I_{c} , showing 6 for the blank cell and all active cell runs.



of cell current, terminal voltage and power are shown at thermal equilibrium for zero heater power. Note near equality of active and blank cell thermal conductances. Figure 6. On—the—fly thermal calibration of the active cell for a pulsed electrolysis current. Waveforms





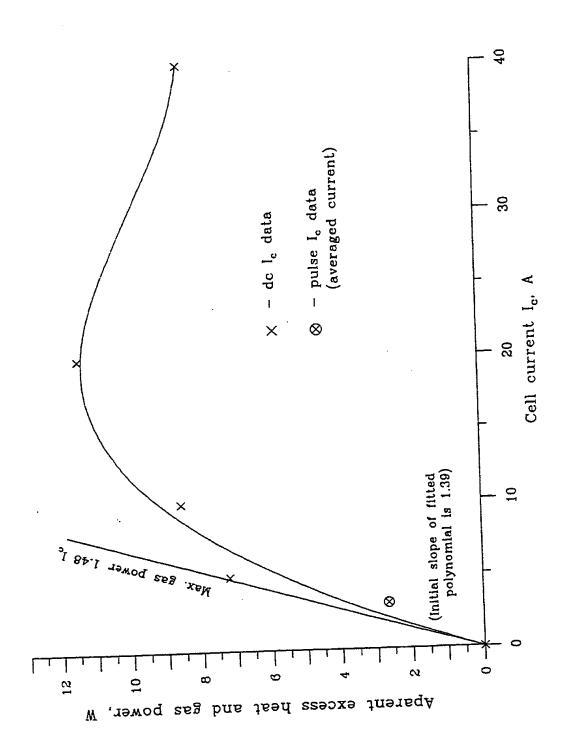


Figure 7. Plot of apparent excess power $(-\tilde{P}_{oldr*0})$ versus cell current I_o for all electrolysis runs. The fitted curve is a cubic polynomial through the origin, but has no special significance. The maximum gas power line is shown for comparison.



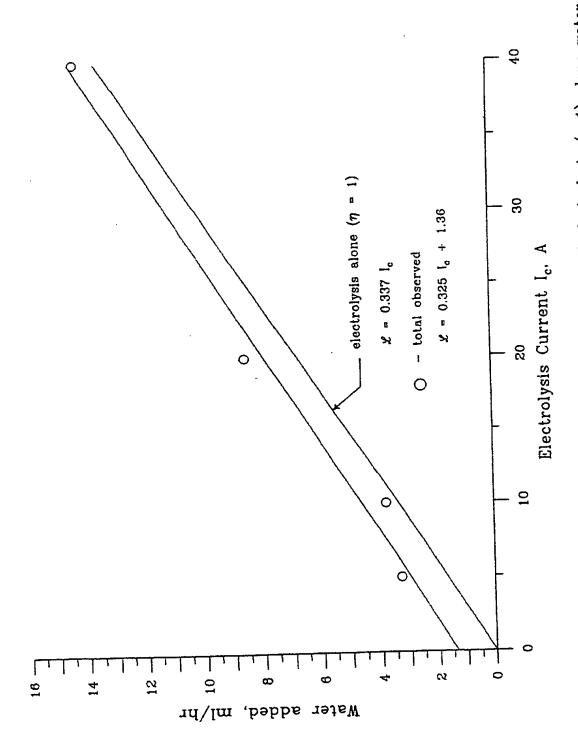
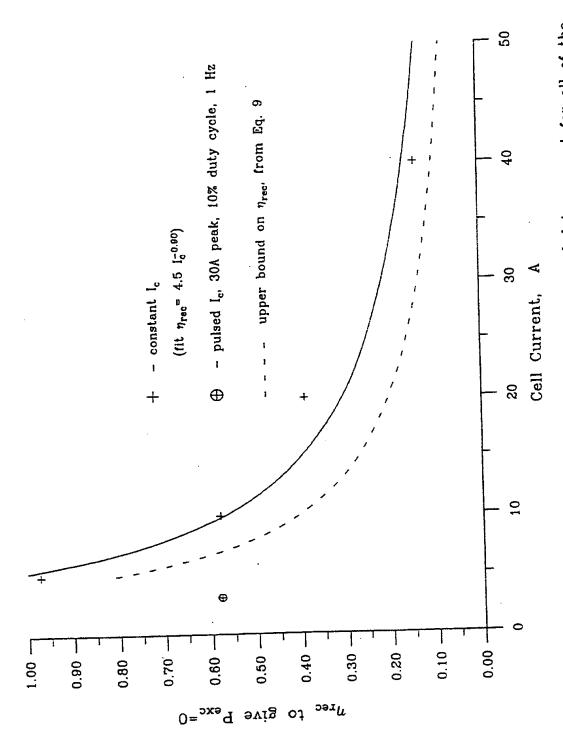


Figure 8. Comparison of the total observed and calculated electrolysis $(\eta=1)$ alone water losses from the active cell at the four selected cell currents Ic. At each Ic. the losses have been averaged over the selected heater powers.







apparent excess heat at each of the experimental runs. Dashed curve shows the upper bound on η_{roc} imposed by Eq. 9 and experimental data of Fig. 8. Figure 9. Oxygen-hydrogen recombination efficiency needed to account for all of the

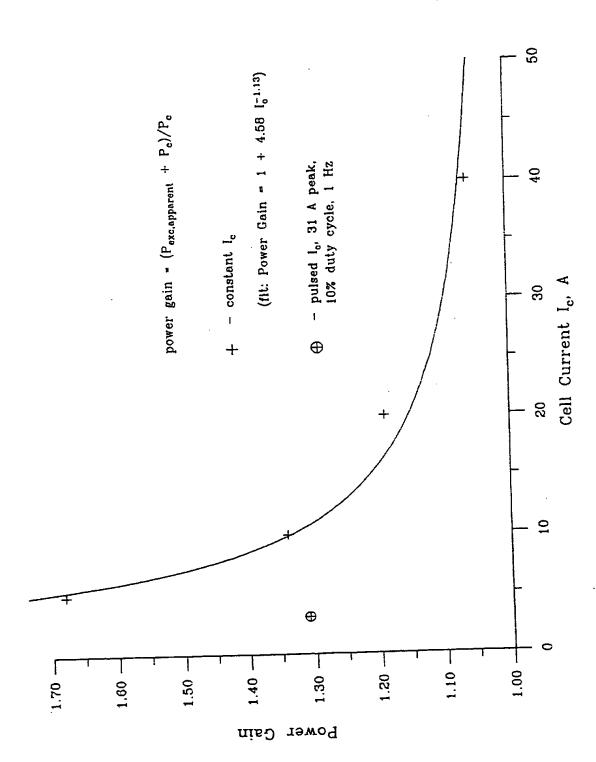


Figure 10. Power gain based on the apparent excess power observed at the selected cell currents $\mathbf{I_c}$. All chemically stored energy is considered as part of the output.



REPORT DOCUMENTATION PAGE

Form Approved OMB No. 0704-0188

Public reporting burden for this collection of information is estimated to average 1 hour per response, including the time for reviewing instructions, searching existing data sources, gathering and maintaining the data needed, and completing and reviewing the collection of information. Send comments regarding this burden estimate or any other aspect of this collection of information, including suggestions for reducing this burden, to Washington Headquarters Services, Directorate for Information Operations and Reports, 1215 Jetterson collection of information, including suggestions for reducing this burden, to Washington Headquarters Services, Directorate for Information Operations and Reports, 1215 Jetterson Collection of Information, Including suggestions for reducing this burden, to Washington Project (0704-0188), Washington, DC 20503.

Davis Highway, Suite 1204, Arlington, VA 22202-43	12 SE DISCONT DATE	3. REPORT TYPE AND	DATES COVERED		
1. AGENCY USE ONLY (Leave blank)	2. REPORT DATE		Technical Memorandum		
	February 1996	•	5. FUNDING NUMBERS		
4. TITLE AND SUBTITLE Replication of the Apparent Excess Heat Effect in a Light Water—Potassium Carbonate—Nickel Electrolytic Cell			₩U-307-51-00		
6. AUTHOR(S)					
Janis M. Niedra, Ira T. Myers, Gustave C. Fralick, and Richard S. Baldwin					
7. PERFORMING ORGANIZATION NAME	8. PERFORMING ORGANIZATION REPORT NUMBER				
National Aeronautics and Space Lewis Research Center Cleveland, Ohio 44135-3191	E-10118				
9. SPONSORING/MONITORING AGENCY	(NAME(S) AND ADDRESS(ES)		10. SPONSORING/MONITORING AGENCY REPORT NUMBER		
9. SPONSORING/MONITORING AGENC		;	AGENC) NEPON NO.		
National Aeronautics and Space Administration Washington, D.C. 20546-0001			NASA TM-107167		
TARREST OF THE TARREST OF THE STATE OF THE S	HOTAVE (FIZHER, BIG TOOLS		(work funded by NASA Contract Lewis Research Center, Responsible		
person, Gustave C. Fralick, or	ganization code 2010, (210)	35 30 0	12b. DISTRIBUTION CODE		
12a DISTRIBUTIONAVAILABILITY STA	TEMENT				
Unclassified - Unlimited Subject Categories 44 and 70					
This publication is available from t	he NASA Center for Aerospace Inf	formation, (301) 621–0390			
13. ABSTRACT (Maximum 200 words) Replication of experiments clifound to produce an apparent from 1.06 to 1.68. The cell we cycle. The 28 liter cell used i similar cells are documented. The apparent excess heat can low temperature differential cripn of dissolved hydrogen-or	aiming to demonstrate excess excess heat of 11 W maximum as operated at four different don these verification tests was to produce 50 W steady excess not be readily explained either by thermoelectric heat pump aygen as an ordinary explanate.	heat production in light m, for 60 W electrical place current levels plus of on loan from a private is heat for a continuous er in terms of nonlinear ping. However, the pro-	nt water-Ni-K ₂ CO ₃ electrolytic cells was power into the cell. Power gains range me pulsed current run at 1 Hz, 10% duty corporation whose own tests with period exceeding hundreds of days. The cell's thermal conductance at a esent data do admit efficient recombinations and heat balance calculations for the seffect is found to be a genuine new gen system in both electrolytic and		

14. SUBJECT TERMS Anomalous heat cell; Energine fusion; Light water cell	15. NUMBER OF PAGES 22 16. PRICE CODE A03 20. LIMITATION OF ABSTRACT		
17. SECURITY CLASSIFICATION OF REPORT Unclassified	18. SECURITY CLASSIFICATION OF THIS PAGE Unclassified	19. SECURITY CLASSIFICATION OF ABSTRACT Unclassified	Standard Form 298 (Rev. 2-69)

gaseous loading cells remains warranted.

•		·		
			·	
	·			





National Aeronautics and Space Administration

Lewis Research Center
21000 Brookpark Rd.
Cleveland, OH 44135-3191

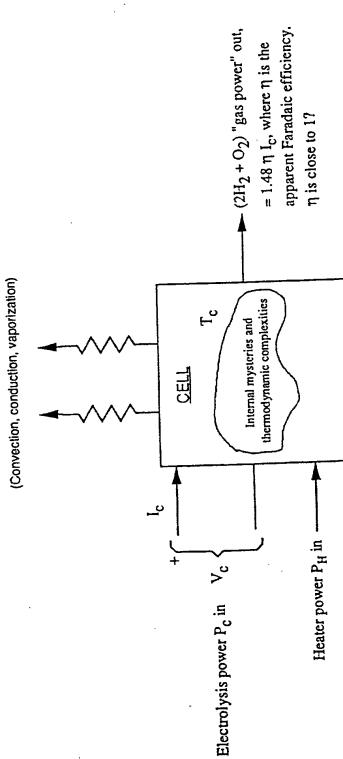
Official Business Penalty for Private Use \$300 POSTMASTER: If Undeliverable — Do Not Return



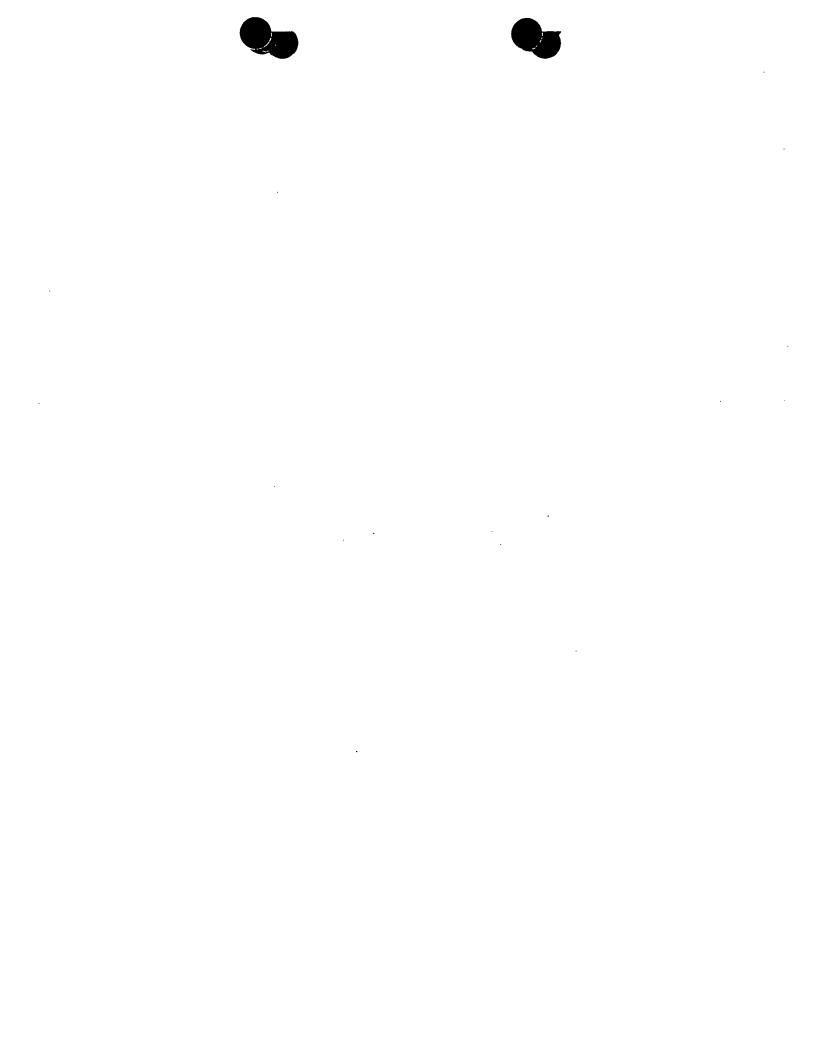




Heat out, P_T



Ambient temperature Ta



AND REVIEW OF HYDROCAT CELL EXPERIMENTS AT NASA LEWIS ANOMALOUS HEAT CELL METHODS

"CALIBRATE CELL" MODE MEASURES THE 'THERMAL CONDUCTIVITY' K OF THE CELL THIS TEST SETS V., I.=0 AND DETERMINES STEADY STATE TEMPERATURE RISE $\Delta T = T_e - T_a AS$ A FUNCTION OF TOTAL OHMIC HEAT (P_H in this case, since P_c=0)

OUR RESULT OF k=0.171 °C/W SEEMS IN GENERAL AGREEMENT WITH HYDROCAT/THERMACORE (Why should it?)

THIS RESULT USED MOSTLY JUST FOR REFERENCE





A BLANK CELL SITS WITH Po, PH=0 TO SERVE AS AN 'INTEGRATOR' OF AIR TEMPERATURE

ITS THERMAL ENVIRONMENT IS AS CLOSE AS POSSIBLE TO THAT OF THE ACTIVE CELL IT PROVIDES A STABLE (at most slowly varying) REFERENCE TEMPERATURE Tblenk

VARIATIONS DOWN TO 0.1 °C CAN BE RESOLVED (Yokogawa HR2300 recorder)

ACTIVE CELL RUNS IN A CONSTANT (OR CONTROLLED PULSE) CURRENT MODE

 $\Delta T = T_c - T_{blank}$

FOR FIXED I, THE P, IS VARIED TO DEVELOP THE AT VS. TOTAL OHMIC HEAT LINE

3. CALCULATION OF OHMIC HEAT P., AND EXCESS HEAT Pgen, ASSUMING n=1:

COULD USE EXCESS HEAT = (POWER OUT) - (POWER IN)

$$= (1.48 l_c + P_T) - (P_c + P_H)$$

AND JUST VARY I, WITH PH=0.

HOWEVER, THIS LEADS TO A SYSTEMATIC ERROR (will be shown), BECAUSE ACTIVE OPERATION (I ≠0) INTRODUCES ADDITIONAL HEAT LOSS, WHICH ALTERS THE SLOPE OF THE ORIGINAL AT VS. PT CALIBRATION LINE.

.: BETTER TO USE THE "CAL. ON THE FLY" METHOD:

FIND THE TOTAL POWER THAT GOES INTO OHMIC HEATING OF THE CELL:

$$P_o = P_H + P_c - 1.48 l_c$$

FOR FIXED I,, MEASURE P, AND ΔT AT A NUMBER OF SELECTED P $_{\rm H}$

PLOT A AT vs. P, LINE FOR THIS FIXED Ic:

$$: \Delta T = k P_{total \, heat} = k P_{o_1} + k P_{gen},$$

ONE CAN EXTRAPOLATETO AT = 0 TO FIND Pgm FOR THIS 12.





4. INTERNAL 2H₂+O₂ RECOMBINATION REDUCES APPARENT FARADAIC η AND GIVES INFLATED Pgen

LOW OUTPUT CELLS, i.e. HAVING APPARENT Pgm < 1.48 Ic. CAN BE VULNERABLE TO THIS

OBJECTION IS REMOVABLE BY OPERATING AN INTERNAL CATALYTIC RECOMBINER:

1.48 I, THEN ABSENT FROM INPUT/OUTPUT CONSIDERATIONS

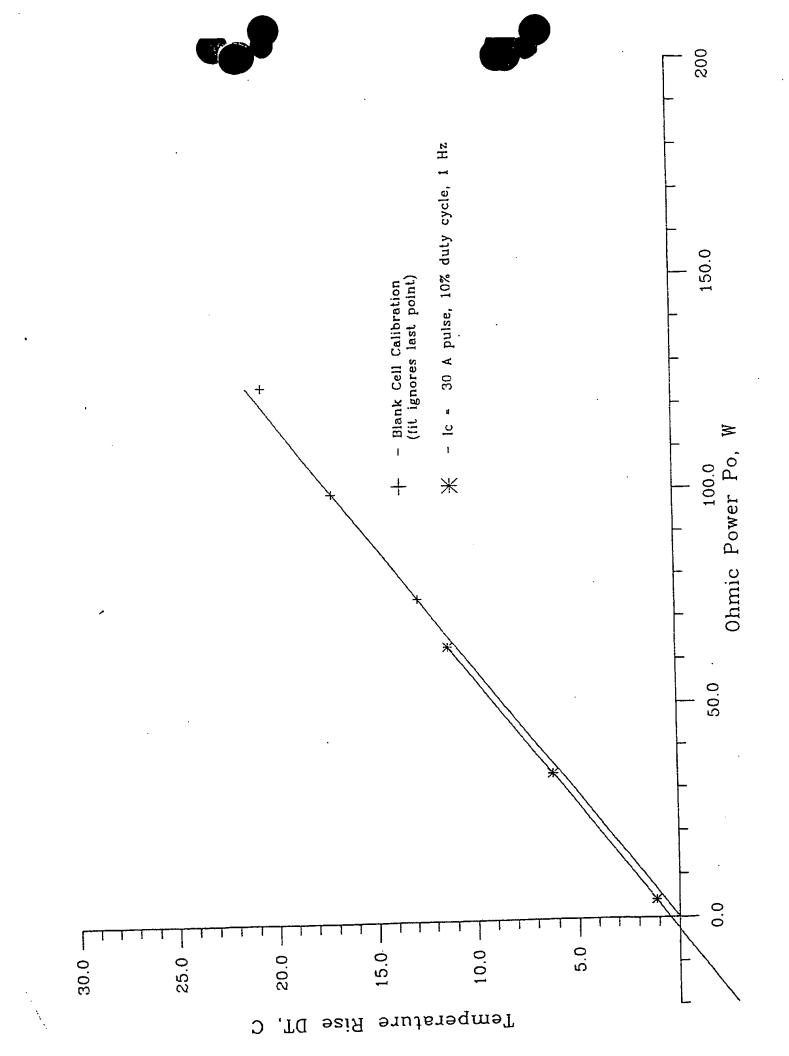
DETAILS:

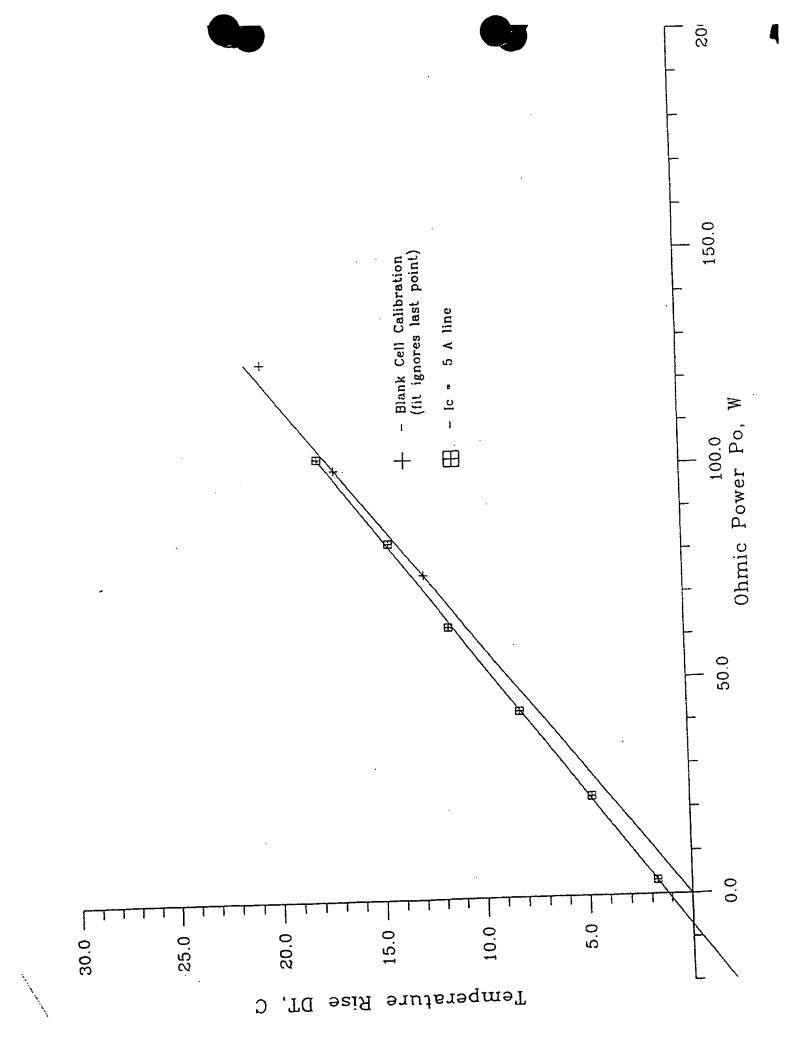
LET APPARENT FARADAIC EFFICIENCY $\eta \equiv 1 - \eta_{\rm inc.}$ THEN PREVIOUS P. BECOMES ONLY. AN APPARENT, UNDERESTIMATED, OHMIC HEAT AND

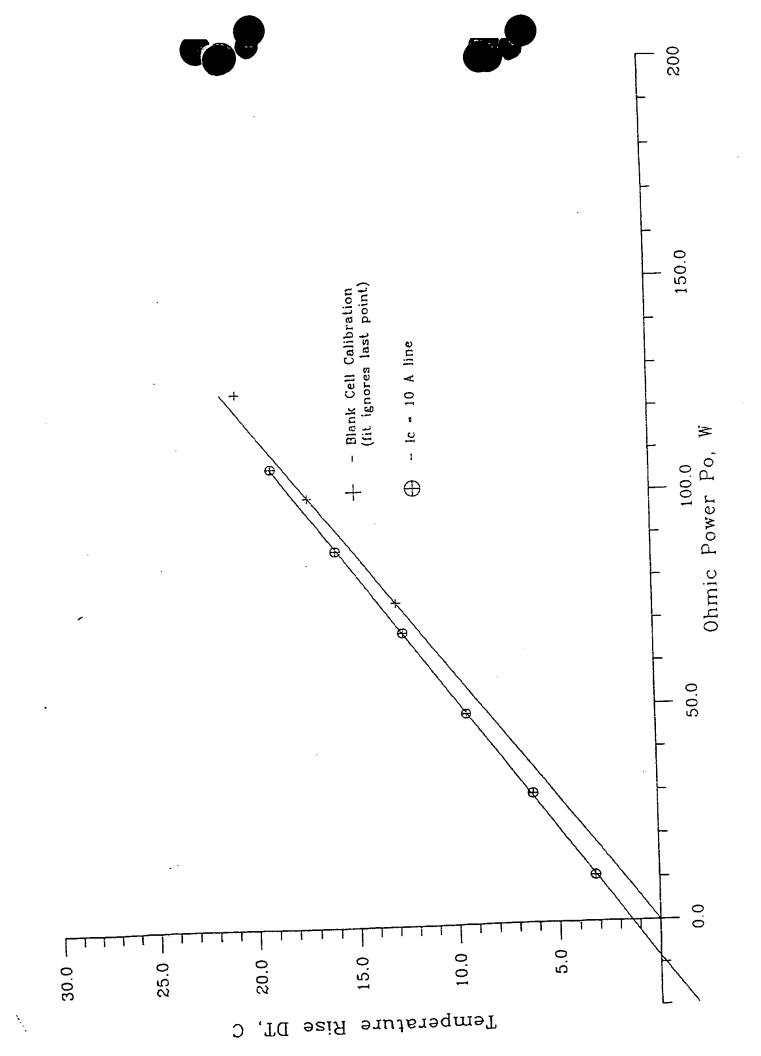
$$\Delta T/K = (P_H + P_c - 1.48 \, l_o) + 1.48 \, \eta_{rec} \, l_c + P_{gen}$$

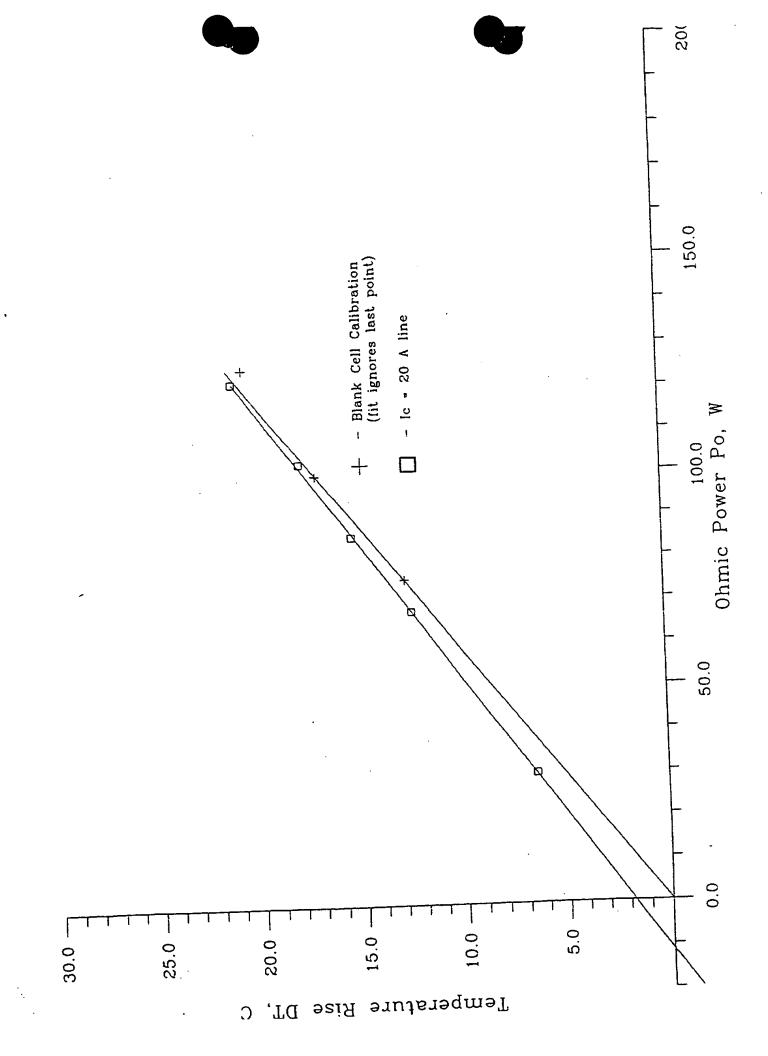
OBSERVATION: HOW LOW MUST APPARENT 11 BE TO ACCOUNT FOR ALL OF Pgm ?

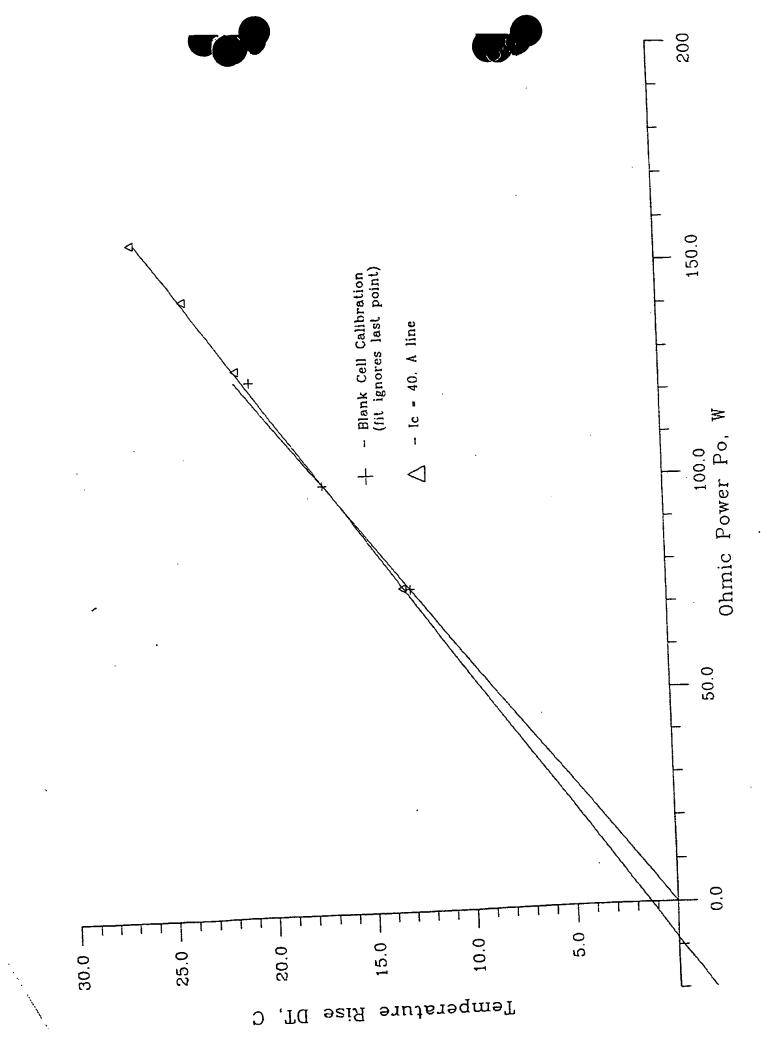
$$(P_{gen} = 0) \Leftrightarrow [\eta = 1 + P_{o,o}/(1.48 \, I_c)]$$

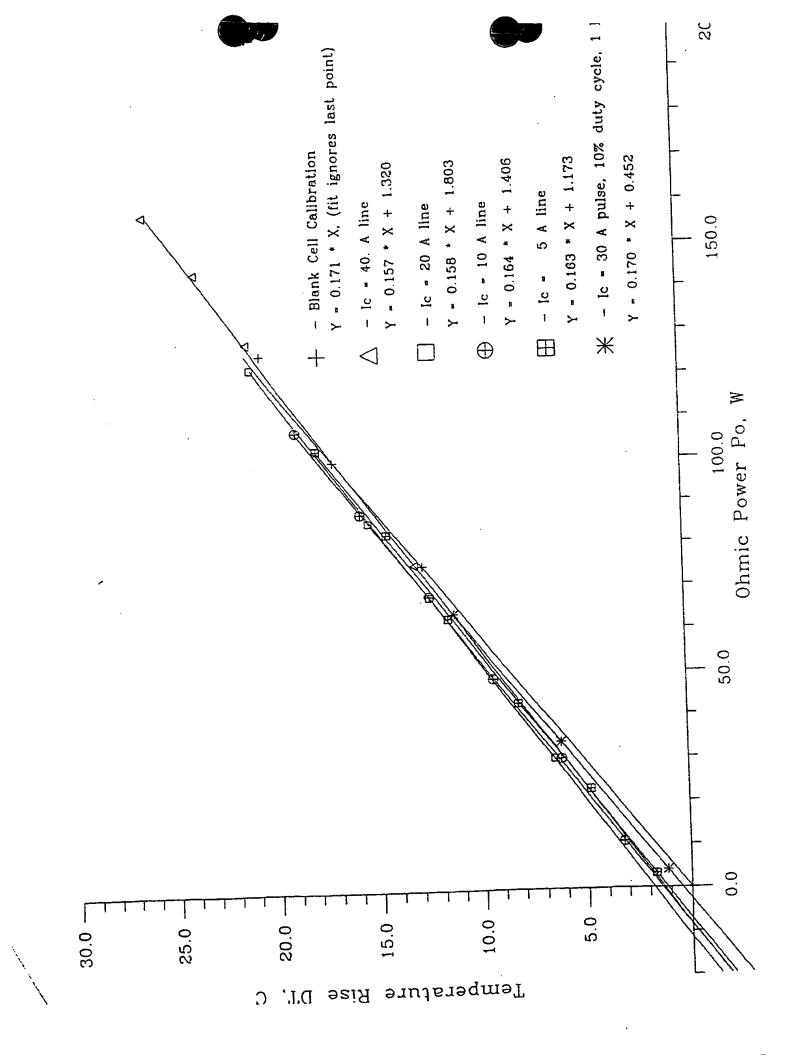


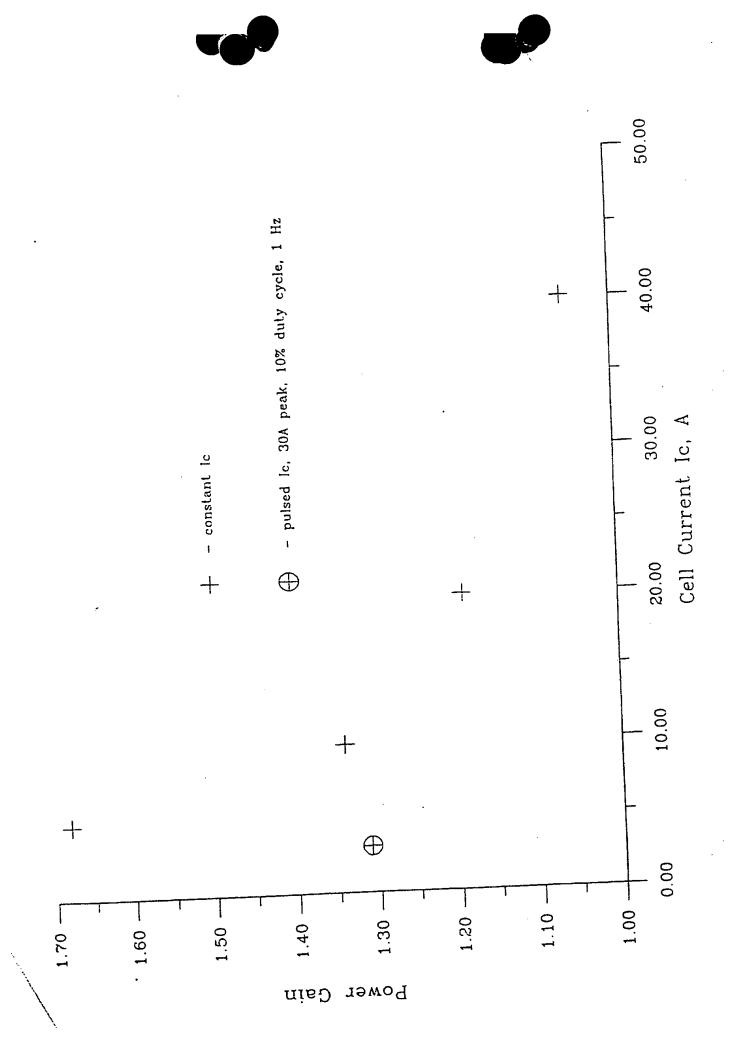


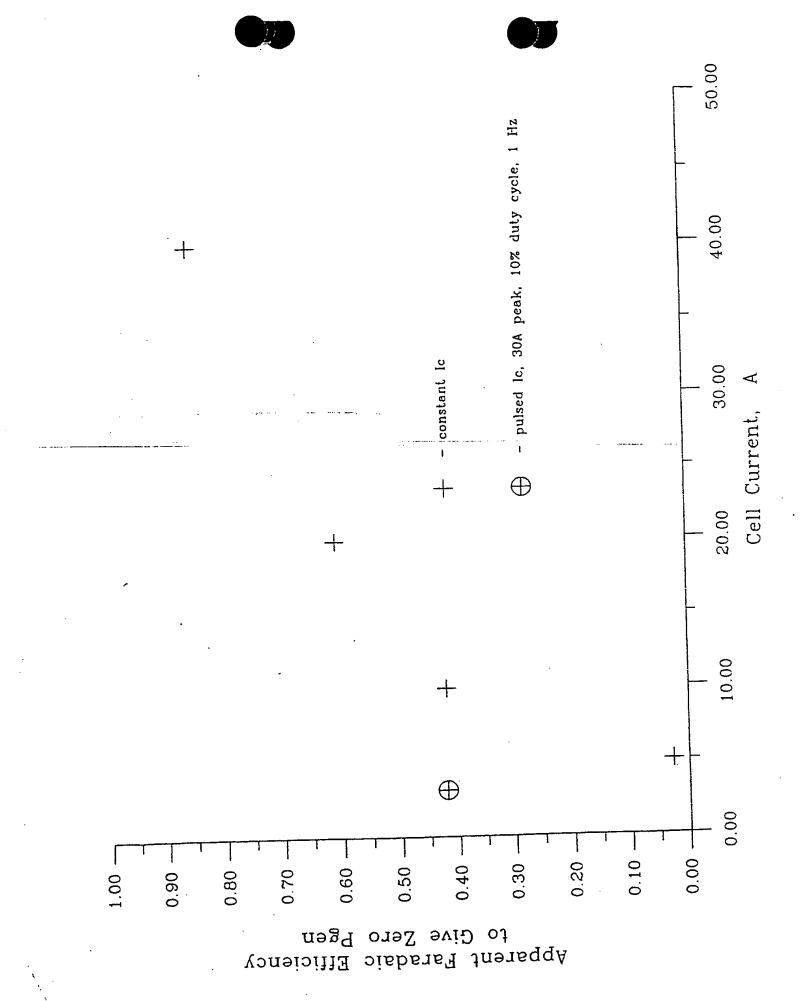


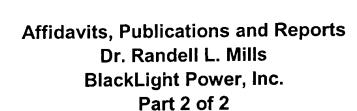












30. N. Popov, "Electrochemical Characterization of BlackLight Power, Inc. MH as Electrodes for Li-ion Batteries, Dept. of Chemical Engineering, University of South Carolina, February 6, 2000.

Electrochemical characterization of MHX (SrHBr, CaHBr, CaHCl, KHBr, and KHI) as electrodes for a Li-ion battery system was carried out in Swagelok three electrode cells (T cells). The anode and the reference electrodes were discs of lithium foil, and the separator was a sheet of Whatman glass fiber filter paper. The cathode consisted of a mixture of the BL/MHX, carbon black and poly(tetrafluoroethylene) which was pressed into a thin film 50-60 mm thick. The electrolyte used was 1 M LiPF₆ in a 1:1:3 mixture of propylene carbonate, ethylene carbonate and dimethyl carbonate (EM Industries). Handling of materials and cell assembling was carried out in an Ar-filled glove box with water content less than 5 ppm (Vacuum Atmospheres). The rest potential of all tested materials was 3.1 V vs. Li/Li+ reference electrode. To fingerprint the potentials at which the redox reactions occurred and to determine their electrochemical reversibility, the cyclic voltammograms were obtained for all materials at the potential range from their rest potential in the cathodic direction to 0.5 V vs. Li/Li⁺. Next, the potential was reversed in the anodic direction to 3.5 V and 4.2 V vs. Li/Li+ reference electrode. The scan rate was 0.1 mV/s for all cases. A cathodic peak was observed in the cyclic voltammogram of CaHBr, CaHCl, and KHI indicating reduction of the electrode active material. CaHBr and CaHCl could be cycled. CaHBr, CaHCl, and KHI have potential as primary batteries. CaHBr also shows promise an electrode active material for a secondary battery.

31. Technology Insights, 6540 Lusk Boulevard, Suite C-102, San Diego, CA 92121, "HydroCatalysis Technical Assessment Prepared for PacifiCorp", August 2, 1996.

This report documents a technical assessment of a novel source of hydrogen energy advanced by HydroCatalysis Power Corporation now BlackLight Power, Inc. (BLP). The assessment was conducted as part of the due diligence performed for PacifiCorp. It was conducted by a literature search and review, site visits to BLP and collaborating organizations, and telephone interviews with others active in the general

area. A description of concept is provided in Section 3. Section 4 presents an assessment of the concept background, supporting theory, laboratory prototypes, projected initial products, and economic and environmental aspects. Section 5 documents the results of telephone interviews and site visits. An overall summary and conclusions are presented in the following section.

32. Kline-Anderson, Inc., 8926 Kirby Drive, Houston, TX 77054, "Review of Schedule and Resource Requirements to Develop a HydroCatalysis Functional Prototype Unit Final Report for Technology Insights", October 23, 1996.

This report documents a technical assessment of a novel source of hydrogen energy advanced by HydroCatalysis Power Corporation now BlackLight Power, Inc. (BLP). The report is based on fact finding trips to BLP and NovaTech and written documentation provided by BLP and Technology Insights. The assessment was conducted as part of the due diligence performed for PacifiCorp under guidance of Technology Insights. The work scope was to assess and formulate a plan to commercial the BLP technology by a new commercialization company COMCO with a considerable investment by PacifiCorp. Plans for development of a functional prototype unit and comments and recommendations regarding planned tasks, resource requirements, and project schedule are given.

33. P. M. Jansson, "HydroCatalysis: A New Energy Paradigm for the 21st Century", Thesis Submitted in partial fulfillment of the requirements of the Masters of Science in Engineering Degree in the Graduate Division of Rowan University, May 1997, Thesis Advisors: Dr. J. L. Schmalzel, Dr. T. R. Chandrupatla, and Dr. A. J. Marchese, External Advisors: Dr. J. Phillips, Pennsylvania State University, Dr. R. L. Mills, BlackLight Power, Inc., W. R. Good, BlackLight Power, Inc.

This thesis reviews the problems of worldwide energy supply, describes the current technologies that meet the energy needs of our industrial societies, summarizes the environmental impacts of those fuels and technologies and their increased use by a growing global and increasing technical economy. The work also describes and advances the technology being developed by BlackLight Power, Inc. (BLP) a scientific company located in Princeton, New Jersey. BLP's technology proports to offer commercially viable and useful heat generation via a previously unrecognized natural phenomenon - the catalytic reduction of the hydrogen atom to a

lower energy state. Laboratory tests obtained as original research of this thesis as well as the review of the data of others substantiate the fact that replication of the experimental conditions which are favorable to initiating and sustaining the new energy release process will generate controllable, reproducible, sustainable and commercial meaningful heat. For example, Jansson has determined heat production associated with hydrino formation with a Calvet calorimeter which yielded exceptional results. Specifically, the results are completely consistent with Mills hydrino formation hypothesis. Approximately 10-3 moles of hydrogen was admitted to a 20 cm3 Calvet cell containing a heated platinum filament and KNO3 powder. In the three separate trials with a platinum filament hydrogen dissociator which was varied in length of 10 cm, 20 cm, and 30 cm, a mean power of 0.581, 0.818, and 1.572 watts was observed, receptively. The closed experiments were run to completion. The energy observed was 622, 369, and 747 kJ, respectively. This is equivalent to the generation of $6.2 \times 10^8 \text{ J/mole}$, $3.7 \times 10^8 \text{ J/mole}$, and $7.5 \times 10^8 \text{ J/mole}$ of hydrogen, respectively, as compared to $2.5 \times 10^5 \text{ J/mole}$ of hydrogen anticipated for standard hydrogen combustion. Thus, the total heats generated appear to be at least 1000 times too large to be explained by conventional chemistry, but the results are completely consistent with Mills model. Convincing evidence is presented to lead to the conclusion that BLP technology has tremendous potential to achieve commercialization and become an energy paradigm for the next century. The research was also conducted as part of the due diligence performed for Atlantic Energy now Conectiv.

34. Phillips, J., Smith, J., Kurtz, S., "Report On Calorimetric Investigations Of Gas-Phase Catalyzed Hydrino Formation" Final report for Period October-December 1996", January 1, 1997, A Confidential Report submitted to BlackLight Power, Inc. provided by BlackLight Power, Inc., Great Valley Corporate Center, 41 Great Valley Parkway, Malvern, PA 19355.

Pennsylvania State University Chemical Engineering Department has determined heat production associated with hydrino formation with a Calvet calorimeter which yielded exceptional results. Specifically, the results are completely consistent with Mills hydrino formation hypothesis. In three separate trials, between 10 and 20 K Joules were generated at a rate of 0.5 Watts, upon admission of approximately 10^{-3} moles of hydrogen to the $20\ cm^3$ Calvet cell containing a heated platinum filament and KNO_3 powder. This is equivalent to the generation of $10^7\ J/mole$ of hydrogen, as compared to $2.5\ X10^3\ J/mole$ of hydrogen anticipated for standard hydrogen combustion. Thus, the total heats generated appear to be 100 times too

large to be explained by conventional chemistry, but the results are completely consistent with Mills model.

35. Phillips, J., Shim, H., "Additional Calorimetric Examples of Anomalous Heat from Physical Mixtures of K/Carbon and Pd/Carbon", January 1, 1996, A Confidential Report submitted to HydroCatalysis Power Corporation provided by HydroCatalysis Power Corporation, Great Valley Corporate Center, 41 Great Valley Parkway, Malvern, PA 19355.

Pennsylvania State University Chemical Engineering Department has determined excess heat release from flowing hydrogen in the presence of ionic hydrogen spillover catalytic material: 40% by weight potassium nitrate (KNO₃) on graphitic carbon powder with 5% by weight 1%-Pd-on-graphitic carbon (K⁺/K⁺ electrocatalytic couple) by the very accurate and reliable method of heat measurement, thermopile conversion of heat into an electrical output signal. Excess power and heat were observed with flowing hydrogen over the catalyst. However, no excess power was observed with flowing helium over the catalyst mixture. Rates of heat production were reproducibly observed which were higher than that expected from the conversion of all the hydrogen entering the cell to water, and the total energy observed was over four times larger than that expected if all the catalytic material in the cell were converted to the lowest energy state by "known" chemical reactions. Thus, "anomalous" heat, heat of a magnitude and duration which could not be explained by conventional chemistry, was reproducibly observed.

36. Bradford, M. C., Phillips, J., "A Calorimetric Investigation of the Reaction of Hydrogen with Sample PSU #1", September 11, 1994, A Confidential Report submitted to HydroCatalysis Power Corporation provided by HydroCatalysis Power Corporation, Great Valley Corporate Center, 41 Great Valley Parkway, Malvern, PA 19355.

Pennsylvania State University Chemical Engineering Department has determined excess heat release from flowing hydrogen in the presence of nickel oxide powder containing strontium niobium oxide (Nb³⁺/Sr²⁺ electrocatalytic couple) by the very accurate and reliable method of heat measurement, thermopile conversion of heat into an electrical output signal. Excess power and heat were observed with flowing hydrogen over the catalyst which increased with increasing flow rate. However, no excess power was observed with flowing helium over the catalyst/nickel oxide mixture or flowing hydrogen over nickel oxide alone. Approximately 10 cc of

nickel oxide powder containing strontium niobium oxide immediately produced 0.55 W of steady state output power at 523 ¡K. When the gas was switched from hydrogen to helium, the power immediately dropped. The switch back to hydrogen restored the excess power output which continued to increase until the hydrogen source cylinder emptied at about the 40,000 second time point. With no hydrogen flow the output power fell to zero.

The source of heat is assigned to the electrocatalytic, exothermic reaction whereby the electrons of hydrogen atoms are induced to undergo transitions to quantized energy levels below the conventional "ground state". These lower energy states correspond to fractional quantum numbers: n = 1/2, 1/3, 1/4, ... Transitions to these lower energy states are stimulated in the presence of pairs of niobium and strontium ions (Nb³⁺/Sr²⁺ electrocatalytic couple) which provide 27.2 eV energy sinks.

37. Jacox, M. G., Watts, K. D., "The Search for Excess Heat in the Mills Electrolytic Cell", Idaho National Engineering Laboratory, EG&G Idaho, Inc., Idaho Falls, Idaho, 83415, January 7, 1993.

Idaho National Engineering Laboratory (INEL) operated a cell identical to that of Thermacore [16] except that it was minus the central cathode and that the cell was wrapped in a one-inch layer of urethane foam insulation about the cylindrical surface. The cell was operated in a pulsed power mode. A current of 10 amperes was passed through the cell for 0.2 seconds followed by 0.8 seconds of zero current for the current cycle. The cell voltage was about 2.4 volts, for an average input power of 4.8 W. The electrolysis power average was 1.84 W, and the stirrer power was measured to be 0.3 W. Thus, the total average net input power was 2.14 W. The cell was operated at various resistance heater settings, and the temperature difference between the cell and the ambient as well as the heater power were measured. The results of the excess power as a function of cell temperature with the cell operating in the pulsed power mode at 1 Hz with a cell voltage of 2.4 volts, a peak current of 10 amperes, and a duty cycle of 20 % showed that the excess power is temperature dependent for pulsed power operation, and the maximum excess power was 18 W for an input electrolysis joule heating power of 2.14 W. Thus, the ratio of excess power to input electrolysis joule heating power was 850 %. INEL scientists constructed an electrolytic cell comprising a nickel cathode, a platinized titanium anode, and a 0.57 M K2CO3 electrolyte. The cell design appears in Appendix 1. The cell was operated in the environmental chamber in the INEL Battery Test Laboratory at constant current,



P

and the heat was removed by forced air convection in two cases. In the first case, the air was circulated by the environmental chamber circulatory system alone. In the second case, an additional forced air fan was directed onto the cell. The cell was equipped with a water condenser, and the water addition to the cell due to electrolysis losses was measured. The data of the forced convection heat loss calorimetry experiments during the electrolysis of a 0.57 M K₂CO₃ electrolyte with the INEL cell showed that 13 W of excess power was produced. This excess power could not be attributed to recombination of the hydrogen and oxygen as indicated by the equivalence of the calculated and measured water balance.

38. Peterson, S., H., Evaluation of Heat Production from Light Water Electrolysis Cells of HydroCatalysis Power Corporation, Report from Westinghouse STC, 1310 Beulah Road, Pittsburgh, PA, February 25, 1994.

Westinghouse Electric Corporation reports that excess heat was observed during the electrolysis of aqueous potassium carbonate (K+/K+ electrocatalytic couple) where the electrolysis of aqueous sodium carbonate served as the control. The data of the temperature of the cell minus the ambient temperature shows that when potassium carbonate replaced sodium carbonate in the same cell with the same input electrolysis power, the potassium experiment was twice as hot as the sodium carbonate experiment for the duration of the experiment, one month. The net faraday efficiency of gas evolution was experimentally measured to be unity by weighing the experiment to determine that the expected rate of water consumption was observed. The output power exceeded the total input power. The data was analyzed by HydroCatalysis Power Corporation [29].

39. Mills, R., Analysis by HydroCatalysis Power Corporation of Westinghouse Report Entitled "Evaluation of Heat Production from Light Water Electrolysis Cells of HydroCatalysis Power Corporation, Report from Westinghouse STC", February 25, 1994.

The data from the Westinghouse Report [28] was analyzed by HydroCatalysis Power Corporation now BlackLight Power, Inc. Westinghouse scientists report that excess heat was observed during the electrolysis of aqueous potassium carbonate (K+/K+ catalysts); whereas, no excess heat was observed during the electrolysis of aqueous sodium carbonate. The data of the temperature of the cell minus the ambient temperature showed that when potassium carbonate replaced sodium carbonate in the same cell with the same input electrolysis power, the potassium

experiment was twice as hot as the sodium carbonate experiment for the duration of the experiment, one month. The present experimental results are consistent with the release of heat energy from hydrogen atoms where pairs of potassium ions (K⁺/K⁺ electrocatalytic couple) induce the electrons of hydrogen atoms to relax to quantized energy levels below that of the "ground state" by providing a net enthalpy equal to an integer multiple of $27.2\,eV$ which stimulate these transitions. Excess heat was observed only when Na₂CO₃ was replaced by K₂CO₃. For two sodium ions, no comparable reaction with a net enthalpy equal to an integer multiple of ______ is possible. The excess energy could not be explained by recombination or known chemistry.

40. Haldeman, C. W., Savoye, G. W., Iseler, G. W., Clark, H. R., MIT Lincoln Laboratories Excess Energy Cell Final report ACC Project 174 (3), April 25, 1995.

During the electrolysis of aqueous potassium carbonate, researchers working at MIT Lincoln Laboratories observed long duration excess power of 1-5 watts with output/input ratios over 10 in some cases with respect to the cell input power reduced by the enthalpy of the generated gas. In these cases, the output was 1.5 to 4 times the integrated volt-ampere power input. Faraday efficiency was measured volumetrically by direct water displacement.

41. Craw-Ivanco, M. T.; Tremblay, R. P.; Boniface, H. A.; Hilborn, J. W.; "Calorimetry for a Ni/K₂CO₃ Cell", Atomic Energy Canada Limited, Chemical Engineering Branch, Chalk River Laboratories, Chalk River, Ontario, June 1994.

Atomic Energy Canada Limited, Chalk River Laboratories, report that 128 % and 138% excess heat were observed in separate experiments by flow calorimetry during the electrolysis of aqueous potassium carbonate (K+/K+ electrocatalytic couple) in a closed cell, and that 138% was observed in an open cell.

42. Shaubach, R. M., Gernert, N. J., "Anomalous Heat From Hydrogen in Contact with Potassium Carbonate", Thermacore Report, March 1994.

A high temperature/high pressure/high power density industrial prototype gas cell power generator which produced 50 watts of power at 300 °C having a nickel surface area of only 300 cm² was successfully developed. A sample of the nickel tubing of the aqueous potassium carbonate permeation cell was analyzed by XPS at the Zettlemoyer Center for Surface Studies, Sinclair Laboratory, Lehigh University. A

broad peak centered at 54.6 eV was present; whereas, the control nickel tube showed no feature. The binding energy (in vacuum) of H(n = 1/2) is 54.4 eV. Thus, the theoretical and measured binding energies for H(n = 1/2) are in excellent agreement. No excess energy or 54.6 eV feature were observed when sodium carbonate replaced potassium carbonate.

43. Gernert, N., Shaubach, R. M., Mills, R., Good, W., "Nascent Hydrogen: An Energy Source," Final Report prepared by Thermacore, Inc., for the Aero Propulsion and Power Directorate, Wright Laboratory, Air Force Material Command (ASC), Wright-Patterson Air Force Base, Contract Number F33615-93-C-2326, May, (1994).

In a report prepared for the <u>Aero Propulsion and Power Directorate, Wright Laboratory, Air Force Material Command (ASC), Wright-Patterson Air Force Base, Thermacore reports, "anomalous heat was observed from a reaction of atomic hydrogen in contact with potassium carbonate on a nickel surface. The nickel surface consisted of 500 feet of 0.0625 inch diameter tubing wrapped in a coil. The coil was inserted into a pressure vessel containing a light water solution of potassium carbonate. The tubing and solution were heated to a steady state temperature of 249 °C using an I²R heater. Hydrogen at 1100 psig was applied to the inside of the tubing. After the application of hydrogen, a 32 °C increase in temperature of the cell was measured which corresponds to 25 watts of heat. Heat production under these conditions is predicted by the theory of Mills where a new species of hydrogen is produced that has a lower energy state than normal hydrogen. ESCA analysis, done independently by Lehigh University, have found the predicted 55 eV signature of this new species of hydrogen."</u>

44. Wiesmann, H., Brookhaven National Laboratory, Department of Applied Science, Letter to Dr. Walter Polansky of the Department of Energy Regarding Excess Energy Verification at Brookhaven National Laboratory, October 16, 1991.

Calorimetry of continuous electrolysis of aqueous potassium carbonate (K+/K+ electrocatalytic couple) at a nickel cathode was performed in single cell dewar calorimetry cell by Noninski at <u>Brookhaven National Laboratory</u>. Dr. Weismann observed the experiment and reported the results to Dr. Walter Polansky of the U. S. Department of Energy. Dr. Weismann reports, "The claim is as follows. The temperature rise in the dewar is greater in the case of electrolysis as compared to

using a resistor, even though the power dissipated is equal in both cases. According to Dr. Mills' theory, this apparent "excess power" is due to the fact that the electron in a hydrogen atom can "decay" to stable subinterger quantum levels. **Dr. Noninski demonstrated this thermal effect at BNL.**" The observed rise in temperature for a given input power was twice as high comparing electrolysis versus heater power.

45. Nesterov, S. B., Kryukov, A. P., Moscow Power Engineering Institute Affidavit, February, 26,1993.

The Moscow Power Engineering Institute experiments showed 0.75 watts of heat output with only 0.3 watts of total power input (power=VI) during the electrolysis of an aqueous potassium carbonate electrolyte with a nickel foil cathode and a platinized titanium anode. Excess power over the total input on the order of 0.45 watts was produced reliably and continuously over a period of three months. Evaluation of the electrolyte after three months of operation showed no significant change in its density or molar concentration. The cell was disassembled and inspected after over one month of operation at 0.1 amperes. This inspection showed no visible signs of a reaction between the electrodes and the electrolyte. The cell was re-assembled and operated as before. Excess energy was produced for the three month duration of the experiment. Scintillation counter measurements showed no signs of radiation external to the cell.

46. Miller, A., Simmons, G., Lehigh X-Ray Photoelectron Spectroscopy Report, Zettlemoyer Center for Surface Studies, Sinclair Laboratory, Lehigh University Bethlehem, PA, November 1993.

Samples of the nickel cathodes of aqueous potassium carbonate electrolytic cells and aqueous sodium carbonate electrolytic cells were analyzed by XPS by Miller and Simmons of the Zettlemoyer Center for Surface Studies, Sinclair Laboratory, Lehigh University. A broad peak centered at 54.6 eV was present only in the cases of the potassium carbonate cells. The binding energy (in vacuum) of H(n = 1/2) is 54.4 eV. Thus, the theoretical and measured binding energies for H(n = 1/2) are in excellent agreement. Lehigh University has conducted an extensive investigation of the cathodes from heat producing as well as those from control cells. Miller concludes that "I was unable to find any other elements on the surface that cause the feature. The persistent appearance of a spectral feature near the predicted binding energy for many of the electrodes used with a K electrolyte is an encouraging piece of evidence for the existence of the reduced energy state hydrogen".

47. Jacox, M. G., Watts, K. D., "INEL XPS Report", Idaho National Engineering Laboratory, EG&G Idaho, Inc., Idaho Falls, Idaho, 83415, November 1993.

The Lehigh XPS results of a broad peak centered at 54.6 eV present only in the cases of the potassium carbonate cells [36] were confirmed at Idaho National Engineering Laboratory (INEL). Samples which demonstrated the feature as well as control electrodes were tested for the presence of trace amounts of impurities of the elements iron and lithium at a sensitivity level of greater than 1000 times that of XPS. TOF-SIMS (Time of Flight-Secondary Ion Mass Spectroscopy) and XPS analysis of the nickel surface was performed by Charles Evans & Associates [38]. The 54.6 eV feature was also observed by Charles Evans & Associates in the case of cathodes of potassium carbonate electrolytic cells [39]. Iron and lithium were the only remaining atoms which were in question by Lehigh University and INEL as the source of the 54.6 eV XPS peak. The Charles Evans TOF-SIMS results demonstrate that iron and lithium were not the source of this peak.

48. Lee, Jang-Jung, Charles Evans & Associates Time-Of-Flight Secondary Ion Mass Spectroscopy (TOF-SIMS) Surface Analysis Report, CE&A Number 40150, March 18, 1994.

The Lehigh XPS results of a broad peak centered at 54.6 eV present only in the cases of the potassium carbonate cells [36] were confirmed at Idaho National Engineering Laboratory (INEL) [37]. Samples which demonstrated the feature as well as control electrodes were tested for the presence of trace amounts of impurities of the elements iron and lithium at a sensitivity level of greater than 1000 times that of XPS. TOF-SIMS (Time of Flight-Secondary Ion Mass Spectroscopy) and XPS analysis of the nickel surface was performed by Charles Evans & Associates. The 54.6 eV feature was also observed by Charles Evans & Associates in the case of cathodes of potassium carbonate electrolytic cells [39]. Iron and lithium were the only remaining atoms which were in question by Lehigh University and INEL as the source of the 54.6 eV XPS peak. The Charles Evans TOF-SIMS results demonstrate that iron and lithium were not the source of this peak.

49. Craig, A., Y., Charles Evans & Associates XPS/ESCA Results, CE&A Number 44545, November 3, 1994.

The Lehigh XPS results of a broad peak centered at 54.6 eV present only in the cases of the potassium carbonate cells [36] were confirmed at Idaho National

Engineering Laboratory (INEL) [37]. Samples which demonstrated the feature as well as control electrodes were tested for the presence of trace amounts of impurities of the elements iron and lithium at a sensitivity level of greater than 1000 times that of XPS. TOF-SIMS (Time of Flight-Secondary Ion Mass Spectroscopy) and XPS analysis of the nickel surface was performed by Charles Evans & Associates [38]. The 54.6 eV feature was also observed by Charles Evans & Associates in the case of cathodes of potassium carbonate electrolytic cells. Iron and lithium were the only remaining atoms which were in question by Lehigh University and INEL as the source of the 54.6 eV XPS peak. The Charles Evans TOF-SIMS results demonstrate that iron and lithium were not the source of this peak.

50. Gary L. Turner, Ph.D., Rule 132 Declaration; Bala Dhandapani, Ph.D., Rule 132 Declaration.

Dr. Turner has been conducting NMR scans for over 20 years. He conducted scans on about 100 blind samples of compounds provided by BlackLight Power, Inc. Dr. Turner observed signals at –4 to –5 ppm. Dr. Turner states that he has never before observed signals in this range.

Dr. Dhandapani is a research scientist at BlackLight Power, Inc. His declaration identifies the samples sent to Dr. Turner NMR analysis. Dr. Dhandapani states that the upfield shifts to -4 to -5 ppm demonstrates the existence of lower energy states in which the electron is closer to the nucleous in the hydrogen atoms of the compounds.

51. Jonathan Phillips, Ph.D., Rule 132 Declaration.

Dr. Phillips conducted an experiment using an electrolytic cell and a potassium catalyst according to Dr. Mills invention. Dr. Phillips observed an excess of heat that could not be explained by any conventional chemical process.





Report Entitled:

Electrochemical Characterization of BlackLight Power, Inc. MH as Electrodes for Li-ion Batteries

Branko N. Popov*

Department of Chemical Engineering University of South Carolina, Columbia, SC 29208

> *Tel: (803) 777-7314 Fax: (803) 777-8265

Email: popov@engr.sc.edu

Submitted to: Mr. William Good BlackLight POWER, Inc 493 Old Trenton Road Granbury, NJ 08512

February 6, 2000



Electrochemical Characterization of BlackLight Power, Inc MH as Electrode for Li-ion Batteries

Experimental:

The following materials were tested as received from BlackLight Inc: (i) SrH_xBr_y , (ii) CaH_xBr_y , (iii) CaH_xCl_y , (iv) KH_xBr_y (v) KH_xI_y . Electrochemical characterization of the above materials as electrode for Li-ion battery system was carried out in Swagelok three electrode cells (T cells) presented in Fig. 1A. The anode and the reference electrodes were discs of lithium foil, and the separator was a sheet of Whathman glass fiber filter paper. The cathode consisted of a mixture of the BL/MH, carbon black and poly(tetrafluoroethylene) which was pressed into a thin film 50-60 μ m thick. The electrolyte used was 1 M LiPF₆ in a 1:1:3 mixture of propylene carbonate, ethylene carbonate and dimethyl carbonate (EM Industries). Handling of materials and cell assembling was carried out in an Ar-filled glove box with water content less than 5 ppm (Vaccum Atmospheres).

The rest potential of all tested materials was 3.1 V vs. Li/Li⁺ reference electrode. To fingerprint the potentials at which the redox reactions occur and to determine their electrochemical reversibility, the cyclic volatmmograms were obtained for all materials at potential range from their rest potential in the cathodic direction to 0.5 V vs. Li/Li⁺ Next, the potential was reversed in the anodic direction to 3.5V and 4.2 V vs. Li/Li⁺ reference electrode. The scan rate was 0.1 mV/s for all cases.

Results and Discussion:

Fig. 1 presents cyclic voltammograms obtained for sample A (KH_xI_y 990630 MWNA). The cathode was cycled between 0.5 V and 4.2 V vs Li/Li⁺ reference electrode using a scan rate of 0.1 mV/s. As shown in Fig. 1 a small peak with a peak current less than 0.07 A/g is observed at 1.95 V vs Li/Li⁺ reference electrode indicating reduction of the electrode active material. Anodically, there is a current plateau of 0.002 A/g from 1.6 V up to 3.95 V when a large increase of the current was observed. At this potential gassing of the electrode occurred, indicating that the observed current may be due to the irreversible oxidation of the active material through a gas





evolution reaction. As shown in Fig. 1, after the scanned potential passes through 4.2 V and returns in a negative direction, larger currents are observed at less positive potentials due to the parasitic gas reaction. In the second cycle almost identical redox behavior was observed. To understand better the processes occurring at 4.2V, an attempt was made to charge the cathode under constant current (CC) mode until the electrode potential reaches 4.2 V and by keeping the electrode potential constant at 4.2 V, the material was charged under constant voltage mode (CV). The objective of this study was: (i) to determine the amount of charge/g necessary for a complete charge of the material (CC mode) and (ii) to determine the presence of any diffusion of the electractive species (H) in bulk of the active material (CV mode). To test the cells, charge - discharge studies were done using currents of $50\,\mu\,\text{A}$.

Under the CC mode, it took only several seconds with a total charge of 4 to 5 mA/g to charge the electrode to 4.2 V vs Li/Li⁺ reference electrode. However, when the polarization was stopped, the potential dropped immediately from 4.2 V to its open circuit potential value of 3.1V indicating that the material cannot be charged above 3.2 V. Thus, the open circuit potential observed initially at 3.2 V was actually a potential at which the materials was in its oxidized form.

The CV data obtained analyzing the sample A (KH_xI_y 990630 mwnA) in the region between 0.5 V and 3.2 V vs Li/Li⁺ reference electrode indicated that the cathode material is not reversible over the entire intercalation range. Anodic peak was not observed when the electrode was cycled in the positive direction indicating that the active material cannot be oxidized back reversibly to its initial oxidation state.

Fig. 2 presents cyclic voltammograms obtained for the sample B(CaH_xCl_y 990723 mwnA). The voltage was varied between 0.5 V and 4.2 V (Fig. 2B) and between 0.5 V and 3.0 V vs Li/Li⁺ reference electrode. The scan between 0.5 V and 3.0 V was used to avoid any possible structural breakdown of the active material at high overpotentials (4.2 V).

Fig. 2 B shows a very well developed cathodic peak at 2.0 V vs Li/Li⁺ reference electrode with a very high peak current of 45 mA/g. The anodic peak observed in the reverse scan, Fig. 2A was smaller 10 mA/g. However, this material shows better reversibility than A(KH_xI_y 990630 mwnA). The initial studies indicated that B (CaH_xCl_y 990723 mwnA) may be used to construct a primary battery. To utilize this material as a cathode material for secondary batteries, further studies will be necessary with an objective to improve its electrochemical reversibility.



Fig. 3 presents cyclic voltammograms obtained for the sample C(CaH_xBr_y 990812mwnA). The voltage was varied between 0.5 V and 4.2 V vs Li/Li⁺ reference electrode using a scan rate of 0.1 mV/sec.

Sample C(CaH_xBr_y 990812mwnA) exhibits almost the same electrochemical characteristics as sample B(CaH_xCl_y 990723 mwnA). As shown in Fig.3 a very well developed cathodic peak is observed at 2.0 V vs Li/Li⁺ reference electrode with a very high peak current of approxiametlly 50 mA/g. The anodic peak was absent in the reverse scan, until the electrode reaches an anodic potential of 3.2 V. The nature of the current observed at potentials higher than 3.2 V was discussed in details in Fig. 1.

The initial studies indicated that the material B(CaH_xCl_y 990723 mwnA) can be used to construct a primary battery. To utilize this material as a cathode material for secondary batteries, further studies should have an objective to improve its electrochemical reversibility.

Fig. 4 presents cyclic voltammograms obtained for the sample D(CaH_xBr_y 990819mwnA). The voltage was varied between 0.5 V and 3.6 V V vs Li/Li⁺ reference electrode using a scan rate of 0.1 mV/sec. The electrode was scanned to only 3.6 V to avoid any possible structural breakdown of the active material at higher overpotentials.

Sample D(CaH_xBr_y 990819mwnA) exhibits similar electrochemical characteristics when compared with the other samples. As shown in Fig.4, the cathodic peak is shifted in cathodic direction (1.2 V vs Li/Li⁺ reference electrode). Two anodic peaks are observed in the positive direction. One is almost reversible to the cathodic peak at 1.2 V and the other was observed at 1.8 V. The peak current (5 mA/g) observed in the first cycle is almost 10 times smaller than in the case of sample C. In the second cycle the peak current decreases to a value of 2mA/g and then in the third and the fourth cycle stabilizes to a value of 1.5 mA/g.

Both anodic peaks are stable with anodic peak current of 1mA/g. Further studies should have an objective to increase (i) the electrochemical reversibility and (ii) capacity of this material.

Fig. 5 presents cyclic voltammograms obtained for the sample E(SrH_xBr_y 990812mwnA). The voltage was varied between 0.5 V and 4.2 V vs Li/Li⁺ reference electrode using a scan rate of 0.1 mV/sec. This sample was not stable in the electrolyte. Several T cells were constructed in a glove box using this material. However, it was not possible to obtain any current response from





the electrode/electrolyte (1 M LiPF₆ in a 1:1:3 mixture of propylene carbonate, ethylene carbonate and dimethyl carbonate) interface.

Figures 6 and 7 show the charge-discharge curves obtained for samples A and D, respectively. Similar results were obtained for the other samples. The electrode was cycled between 0.5 and 4.2 V at the rate of 50 μ A. All materials showed low reversible capacity of approximately 5 mA/g. To use these materials as cathodes in Li-ion secondary batteries it will necessary to improve the stability in the electrolyte and their reversible capacity.

The samples A, B and C show large initial irreversible capacity which can be use to power primary Li batteries.

References

- 1. P. Yu, B. N. Popov, J. A. Ritter and R. E. White, "Determination of the Lithium Ion Diffusion Coefficient in Graphite," J. Electrochem. Soc., 146, (1), 8-14 (1999).
- Dong Zhang, Branko Popov, Pankaj Arora and Ralph E. White, "Cobalt Doped Chromium Oxides as Cathode Materials for Secondary Batteries," J. of Power Sources, 83, 121 (1999).
- 3. B. N. Popov, Battery Work at University of South Carolina, *Automotive Technology Development*, 1, 371-397 (1997) DOE, Energy Efficiency and Renewable Energy, Office of Transportation Technologies, Washington, DC. (1997).
- P. Arora, B. N. Popov and R. E. White, Electrochemical Investigation of Cobalt-Doped LiMn₂O₄ as Cathode Material for Li-ion Batteries. J. Electochem. Soc. 145, 807 (1998).

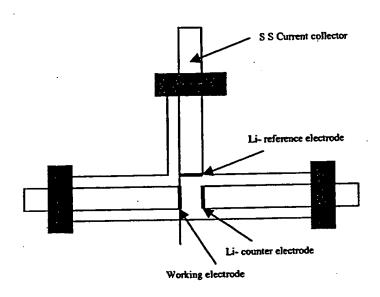


Fig. 1A Schematic of Swagelok type three electrode cell (T - cell)



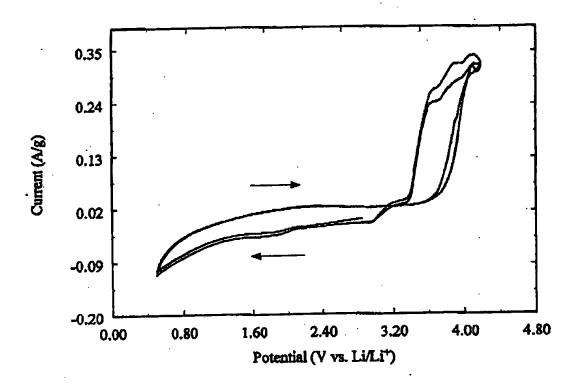


Figure 1

Cyclic voltammograms of sample A

Weight of Cathode - 30 mg

Scan Rate - 0.1 mV/sec

Potential window - 0.5 V to 4.2 V

Index

A - 990630MWNA B - 990723MWNE C - 990812MWNA

D - 990819MWNA



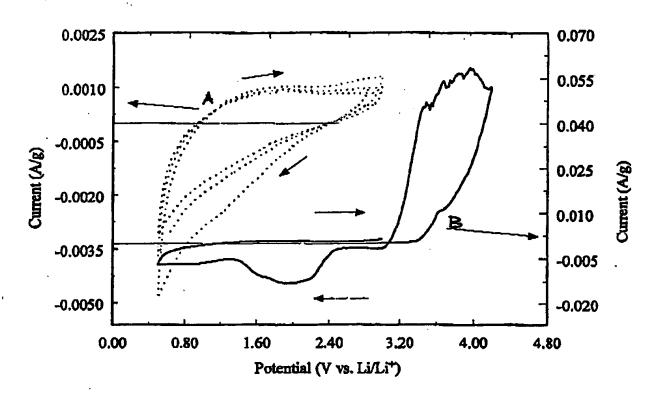


Figure 2

Cyclic voltammogram of sample B

Weight of Cathode - 30 mg

Scan Rate - 0.1 mV/sec

Potential window

(A) - 3.0 V - 0.5 V

(B) - 4.2 V - 0.5 V

Index

A - 990630MWNA

B - 990723MWNE

6 C-990812MWNA

D - 990819MWNA

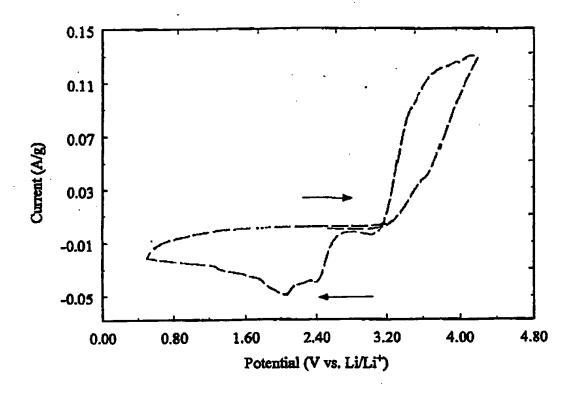


Figure 3

Cyclic voltammogram of sample C

Weight of Cathode - 30 mg

Scan Rate - 0.1 mV/sec

Potential window - 4.2 V - 0.5 V

Index

A - 990630MWNA B - 990723MWNE

C - 990812MWNA

D - 990819MWNA



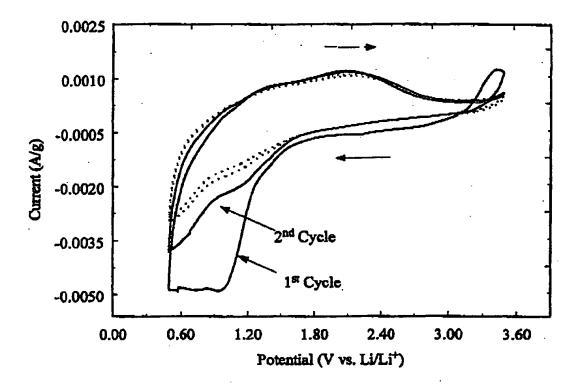


Figure 4 Cyclic voltammograms of sample D Weight of Cathode - 30 mg Scan Rate - 0.1 mV/sec

Potential window - 4.2 V - 0.5 V

Index

A - 990630MWNA

B - 990723MWNE

C - 990812MWNA

D-990819MWNA



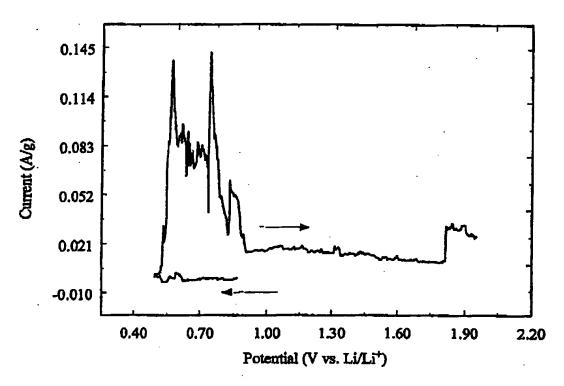


Figure 5

Cyclic Voltammogram of Sample E
Reference/Counter Electrode - Li
Weight of active material - 30 mg (10% binder)
Scan Rate - 0.1 mV/sec

Potential window - 4.2 V - 0.5 V

Index

A - 990630MWNA

B - 990723MWNE

C - 990812MWNA

D - 990819MWNA



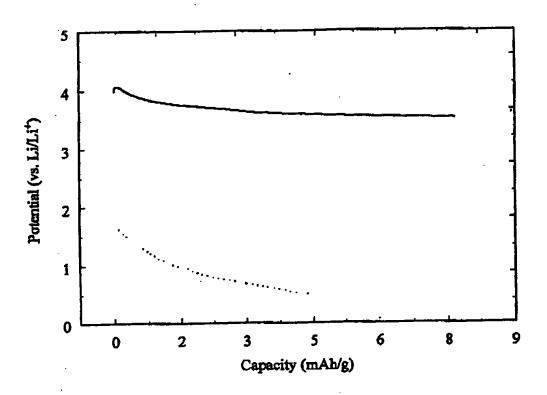


Figure 6 Charge Discharge characteristics of sample A Weight of Cathode - 30 mg Charge - Discharge current - 50 µA

Index

A - 990630MWNA

B - 990723MWNB

C-990812MWNA

D - 990819MWNA

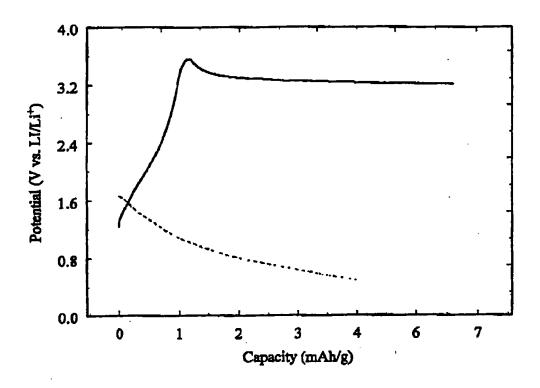


Figure 7

Charge Discharge characteristics of sample D

Weight of Cathode - 30 mg

Charge - Discharge current - 50 µA

Index

A - 990630MWNA

B - 990723MWNE

C-990812MWNA

D-990819MWNA







TECHNOLOGY INSIGHTS

DRAFI

HydroCatalysis Technical Assessment

Prepared for PACIFICORP

Any further distribution of this confidential report must have the expressed consent of PacifiCorp

Prepared by

TECHNOLOGY INSIGHTS

6540 Lusk Boulevard Suite C-102 San Diego, CA 92121 619-455-9500

August 2, 1996







TECHNOLOGY INSIGHTS

Copy No	
R.L. Mills	
Recipient	

DRAFE

HydroCatalysis Technical Assessment

Prepared for PACIFICORP

Any further distribution of this confidential report must have the expressed consent of PacifiCorp

Prepared by

TECHNOLOGY INSIGHTS

6540 Lusk Boulevard Suite C-102 San Diego, CA 92121 619-455-9500

August 2, 1996





DRAFT

TABLE OF CONTENTS

		Title	<u>Page</u>	È			
<u>Item</u>							
_			j	ii			
Table	Table of Contentsiii List of Tables						
List of Tables							
1.0	Intro	duction		1			
2.0	Sum	mary and Conclusions	'	4			
3.0	Cond	mary and Conclusions		4			
	3.1	Background/Ineory		6			
	3.2	Evolution of Laboratory Prototypes		6			
		2 2 1 Water Based Electrolyte Cell (Low Temperature)		8			
	•	3.2.2 Gas Cell		9			
	3.3	Basic Features and Penormance of Vapor Flase College	1	0			
		3.3.1 At-Mar Glass Lamp	1	1			
		3.3.2 Isothermal Calorimeter	1	2			
		3.3.3 Calvet Calorimeter Cell	1	3			
		3.3.4 Metal Hydride Hydrogen Source Cell	1	4			
		3.3.5 Tungsten Powder Cell	1	15			
	3.4	Applications and Projected Products	1	15			
4.0	Con	cept Assessment	1	15			
•••	4.1	Theory	'	16			
		4.1.1 Hydrino - Laboratory Observations	2	20			
		4.1.2 Hydrinos - Environmental Observations		22			
	4.2	4.1.2 Hydrinos - Environmental Observations Prototype Performance		22			
		4.2.1 Water Based Electrolyte Cell (Low Tomportus)		24			
		4.2.2 Gas Cells		27			
		4.2.3 Vapor Phase Cell Development Status and Issues	:	30			
	4.3	Applications and Projected Products Economics and Environmental Considerations		32			
	4.4	Economics and Environmental Considerations 111		32			
	•	4.4.1 Economics		34			
5.0	Tel	4.4.2 Environmental Considerationsephone Interviews and Site Visits		36			
	5.1	Telephone Interviews		36			
		5.1.1 General Background		38			
		5.1.2 Theory and Hydrino Validation		40			
		5.1.3 Excess Power Evidence		41			
	5.2	5.1.3 Excess Power Evidence		41			
		5.2.1 HydroCatalysis Power Corporation		42			
		5.2.1 HydroCatalysis Power Corporation		43			
		5.2.3 Pennsylvania State University		44			
		5.2.4 Lehigh University		45			
		5.2.5 Franklin and Marshall College		46			
6.0	Re	5.2.5 Franklin and Marshall College					

.35()





LIST OF FIGURES

	Title	<u>Page</u>
Fig. 3-2 Fig. 3-3 Fig. 3-4 Fig. 3-5 Fig. 3-6 Fig. 3-7	Thermacore Experiment At-Mar Glass Lamp Schematic At-Mar Glass Lamp Test Results Isothermal Calorimeter Isothermal Calorimeter Test Results Isothermal Calorimeter Test Results Penn State Calvet Calorimeter Cell Nickel Hydride Hydrogen Source Cell Tungsten Powder Cell Isothermal Calorimeter Test Results	10 11 12 13 13
	LIST OF TABLES	
	Title	Page
Table 4	-1 Power Density Estimate Comparisons	34
Table 4	-3 Revised Comparative Cost Projections	3





DRAFT

1.0 Introduction

This report documents a technical assessment of a novel source of energy from hydrogen advanced by HydroCatalysis Power Corporation (HPC) (Ref. 1). It is an extension, drawing from HPC confidential data, of an earlier report based on publicly available information (Ref. 2). HPC represents that energy can be generated by a catalytic reaction allowing hydrogen atoms to achieve more stable states below the ground state established by generally accepted atomic theory, resulting in the release of energy and formation of a new form of low energy hydrogen, labeled hydrino (the term hydrino refers to both individual low energy hydrogen atoms and low energy hydrogen gas). The theory behind this concept, developed by Dr. Randell Mills of HPC in collaboration with Dr. John Farrell of Franklin and Marshall College (Ref. 3), remains controversial and has not received broad acceptance within the scientific community. Given the complexity, and the profound and comprehensive nature of Mills' theoretical work, immediate acceptance would not be expected even if the theory is absolutely correct.

The assessment was conducted by a literature search and review, site visits to HPC and collaborating organizations, and telephone interviews with others active in the general area. A description of the concept is provided in Section 3. Section 4 presents an assessment of the concept background, supporting theory, laboratory prototypes and projected initial products, economic and environmental aspects. Section 5 documents the results of telephone interviews and site visits. An overall summary and conclusions are presented in the following section.

2.0 Summary and Conclusions

It would be difficult to overstate the potential significance of either the theory or the practical applications arising from the theory advanced by HPC. If validated, the theory would represent one of the most fundamental advances in the history of science, revising models of matter and energy from the subatomic level to the history and structure of the universe. If reduced to practice as a new energy source as projected by HPC, the concept will have a profound effect on the world economic, political and social structure. It would seem unlikely that a discovery of such magnitude would arise from such obscure beginnings. However, the results of this assessment indicate that while it may be unlikely, it may also be true. The following observations are noted:

 The theoretical basis for the HPC concept was originally published in 1989, and has remained essentially constant in its fundamental elements since that time. It has languished in obscurity for the most part, with a few informed supporters substantially outnumbered by detractors. However, it appears to be gaining respect and attention of late fueled by an increasing number of validating observations at the atomic and astrophysical level. Some limitations and contradictions were noted by an informed supporter, and



DRAFT

significant revisions and extensions could be expected if the major elements become generally accepted and the subject of widespread research.

- HPC has used the theory to guide the development of energy cells based around the release of energy from hydrogen by a catalytic reaction which allows hydrogen to achieve energy levels below the observed "ground state".
 Experimental devices have evolved from a water based electrolytic cell operating at low temperatures and power densities to hydrogen gas cells operating at increasing temperatures and power densities. HPC's success in applying the theory for this purpose is a significant factor supporting its general validity.
- A majority view among technically qualified individuals that have worked with the electrolysis cells evolved by HPC is that some form of excess heat has been produced which is not explainable by conventional chemical processes. This view is not unanimous, and the degree of acceptance decreases with decreasing proximity to and understanding of the experiments. The conclusion of this assessment is that data from experiments on the electrolytic cells are sufficient to demonstrate the production of excess heat. However, consistent with the conclusion of HPC and others, electrolytic cell performance is not sufficient to support commercial applications for energy generation.
- HPC began working on hydrogen gas based cells about two years ago and has recently (beginning in January, 1996) developed a relatively simple vapor phase concept. Analysis of data obtained from HPC indicate power densities in the range of 1-4 Watts/cc, and possibly as high as 30 Watts/cc have been obtained. The progress achieved by HPC on the vapor phase concept over the past seven months has been impressive and provides a basis for optimism regarding the commercial potential of this concept.
- HPC has developed and refined procedures for identification of low energy hydrogen atoms, called hydrinos, and lower energy hydrogen molecules, called dihydrinos, produced during operation of their cells. Evidence supporting the existence of hydrinos and dihydrinos has been developed by HPC and by independent laboratories. Indications consistent with projected characteristics of hydrinos have been obtained from three independent procedures. Two additional tests which could provide definitive evidence of hydrinos have been identified and one or both may be conducted in the near future.
- Westinghouse has been following HPC's work for several years, conducting
 independent testing of electrolytic cells in 1993/94 through their Science and
 Technology Center (STC). They currently have an internally funded project
 to review the supporting information on the HPC concept and to support
 experiments at Penn State directed toward identification and characterization





of hydrino. STC has a commitment to reach a definitive conclusion and recommendation regarding the HPC concept by the end of 1996.

- The HPC theory and the projected characteristics of hydrino have been used to explain solar and deep space spectral observations in the soft X-ray and ultraviolet regions. HPC is working with the National Radio Astronomy Laboratory (NRAO) to conduct an experiment later this fall which could provide more conclusive results regarding the existence of hydrino, and in the process may contribute to a fundamental revision in the accepted model of the universe. However, discussions with a participant from the NRAO indicate that the experiment has not yet been approved, is challenging, and may not lead to conclusive results.
- Assuming the HPC concept is successful, the energy content of hydrogen is nominally estimated to be increased by at least a factor of 70 over hydrogen combustion. By another form of comparison, the resulting energy content of water would be at least 30 times that of gasoline.
- Assuming the process can be adapted to a gas turbine application, a net economic advantage of 1 to 2.5¢/kWh relative to a natural gas fired combined cycle gas turbine is projected. With a market share of 33% of current world electricity consumption, 2¢/kWh would translate to \$66 Billion/year.
- The environmental releases associated with the HPC process would be far below fossil generation options that represent the majority of existing generating capacity and new capacity additions. In fact, oxygen release is likely to be considered a benefit, offsetting some of the reduced oxygen production arising from a reduction in tropical rain forests. A possible environmental concern could arise from the fact that water used to produce hydrino will be permanently lost from the planet. However, it was estimated to take 370,000 years to consume an inch of the ocean while supplying 33% of the current world electricity consumption.

On the whole, a significant and growing body of data supporting the validity of the HPC theory and hydrogen energy concept was identified. Some uncertainty remains regarding the identification and characterization of hydrino. A greater level of uncertainty is associated with the reduction of the energy concept to practice in the projected applications, but recent progress provides a strong basis for optimism regarding ultimate success. Key issues to be addressed in conjunction with developing the concept into a commercial product are increasing the reaction power density and establishing an energy cell and supporting auxiliaries design that provides the necessary degree of controllability for integration with a power conversion system. Telephone interviews and site visits to HPC and collaborating organizations covered the full range of functions from validating research through concept optimization and energy cell engineering. In all cases, the individuals involved were found to be



exceptionally capable and professionally qualified to address the challenging tasks that remain to bring the concept to the point of integration with commercial power conversion or heat utilization systems.

3.0 Concept Description

The HPC concept is based on modifications to existing theory which, if proven correct, would represent a major advance in the understanding of matter and energy. The theory was developed by Dr. Randell Mills, the founder of HPC, in collaboration with Dr. John Farrell of Franklin and Marshall College. One of the predictions of the theory is the existence of nonradiative states of the hydrogen atom below the "ground state" defined by existing theory. Dr. Mills believes he has developed a means of achieving these lower level energy states, liberating energy in much larger amounts than are obtained from the combustion of hydrogen. The theory behind the concept, existing laboratory prototypes, and projected initial products are summarized in the following subsections.

3.1 Background/Theory

The HPC concept originated in the same time frame as the "cold fusion" concepts, which came to public and general scientific attention in 1989 (Ref. 4, 5, 6). As attempts to explain the excess heat apparent in the experiments proliferated, possible phenomena beyond fusion have been introduced. Because of its widespread use in earlier years, the term "cold fusion" has evolved to encompass broader theories and processes for excess energy generation. While the Mills theory does not involve nuclear fusion, the theoretical basis for the HPC concept originated in parallel with the "cold fusion" experiments, and the initial HPC experimental procedure was similar to those used in the early "cold fusion" experiments, thus the concept has often been viewed within the general framework of "cold fusion". Since the HPC concept does not involve fusion, and given the negative perceptions and controversy associated with cold fusion, HPC has attempted to distance itself from the cold fusion community.

The energy released in the HPC process is postulated to be released by a catalytic reaction which allows hydrogen atoms to achieve a lower energy than their naturally occurring "ground state". Because of its simplicity relative to other elements, hydrogen was the subject of a great deal of scientific attention in the late nineteenth and early twentieth centuries. Experimental observations of hydrogen behavior were used to gain a more detailed understanding of the nature of matter at the submicroscopic level. A primary piece of evidence was the discrete bands of light emitted by hydrogen gas during combustion and other forms of excitation. These data were used to construct a model of the atom consisting of discrete energy levels associated with allowed orbits of the electron about the nucleus, with the observed radiation emissions associated with changes in energy levels arising from transitions among these orbits. Quantum numbers were assigned to the orbits beginning with the





lowest observed energy state, which was assigned the quantum number n=1. Additional theoretical refinements resulted in the development of models treating matter as having both particle and wave properties. The evolving understanding was given mathematical formalism through the Schrödinger equation, which was used with various assumptions and boundary conditions to make further explanations of experimental observations.

Dr. Randell Mills, the founder of HPC, in collaboration with Professor John Farrell of Franklin and Marshall College, developed the theory on which the HPC concept is based, and initially published their results and conclusions in 1989 (Ref. 3). The Mills theory represents a modification and extension of the fundamental representation of matter and energy developed primarily in the early twentieth century. One result of the theory is a prediction that additional lower energy states are possible for the hydrogen atom, but are not normally achieved because transition to these states is not directly associated with the emission of radiation, thus the hydrogen atom as well as lower energy hydrogen atoms (hydrinos) are stable in isolation. It is postulated that hydrogen atoms (and other single electron atoms, e.g., He ion) can achieve these states by a "resonant collision" with a nearby atom or combination of atoms having the capability to absorb the energy required to effect the transition. The following summary of the process is taken from Ref. 7:

"The quantum number n=1 is routinely used to describe the "ground" electronic state of the hydrogen atom. Dr. Mills shows that the n=1 state is the "ground" state for "pure" photon transitions (the n=1 state can absorb a photon and go to an excited electronic state, but it cannot release a photon and go to a lowerenergy electronic state). However, an electron transition from the ground state to a lower-energy state is possible by a "resonant collision" mechanism. These lower-energy states have fractional quantum numbers, n=1/integer. Processes that occur without photons and that require collisions are common. For example, the exothermic chemical reaction of H + H to form H_2 does not occur with the emission of a photon (Ref. 8). Rather, the reaction requires a collision with a third body, M, to remove the bond energy - $H + H + M - H_2 + M$. The third body distributes the energy from the exothermic reaction, and the end result is the H_2 molecule and an increase in the temperature of the system. Similarly, the n=1state of hydrogen and the n=1/integer states of hydrogen are nonradiative, but a transition between two nonradiative states is possible via a resonant collision, say n=1 to n=1. In these cases, during the collision the electron couples to another electron transition or electron transfer reaction which can absorb the exact amount of energy that must be removed from the hydrogen atom, a resonant energy sink. The end result is a lower-energy state for the hydrogen and an increase in the temperature of the system. The reaction of hydrogen to lower-energy states is referred to as a transition reaction. Certain inorganic ions which are proprietary to the Company serve as transition catalysts which resonantly accept energy from hydrogen atoms and release the energy to the surroundings. The transition catalyst should not be consumed in the reaction. It accepts energy from hydrogen and releases the energy to the surroundings.



Thus the transition catalyst returns to the original state. And, the energy released from hydrogen atoms is very large compared to conventional chemical reactions including the combustion of hydrogen. Multiple cycles of catalysis are possible with increasing amounts of energy with successive cycles of transitions."

Potassium (K*) is identified as having a transition energy level that matches with the calculated hydrogen atom energy exchange (27.2 ev) needed to effect a transition from the generally accepted "ground state" associated with quantum number n=1 to a lower energy state associated with n=1, and to other lower level fractional states. Thus potassium is considered a potential catalyst for releasing the hydrogen energy. The n=1-n=1 reaction involves a hydrogen atom and two potassium atoms which undergo changes in ionization state, resulting in a net release of energy (40.8 ev) and a shrunken hydrogen atom, identified by Mills as a "hydrino". Subsequent additional lower level transitions are predicted to occur, increasing the energy release per atom by the process. These postulated reactions form the basis for the HPC concept, which for the purposes of this assessment is assumed to result in an average energy release of 100 ev/atom. In comparison, the combustion of hydrogen in a conventional chemical reaction releases about 1.5 ev/atom.

3.2 Evolution of Laboratory Prototypes

Dr. Mills has been developing reaction cells to test the theory and demonstrate the release of energy and formation of hydrinos since 1989. The initial cells used water based electrolyte, and several variants have been described in the open literature. More recently, higher temperature cells have been developed using hydrogen gas.

3.2.1 Water Based Electrolyte Cell (Low Temperature)

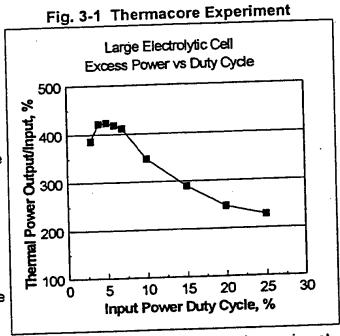
Construction and operation of an early (1990) version of a water based electrolyte cell was described in Ref. 9. The cells used were relatively small, containing 100 ml of electrolyte. The base case cell was constructed using a nickel foil cathode and a platinum wire anode, with a potassium carbonate (K2CO3) electrolyte for most of the runs performed. Electrolysis of the electrolyte by passing a current through the electrodes was postulated to allow hydrogen and potassium atoms at the surface of the cathode to interact, resulting in the release of energy. Control cases used a sodium carbonate (Na₂CO₃) electrolyte, which was not expected to produce excess heat according to Mills' theory. Variables studied included electrode and vessel configurations, cell stirring and power application (square wave vs. dc). Power generation in the cell was calculated from cell temperature, based on a calibrated conductive heat loss path to ambient. A total of 29 cases using K2CO3 electrolyte with voltage applied to the electrodes were reported. Excess power represented to be coming from the hydrogen reaction was reported in all cases, ranging from 1.5 to 40 times the net input power (total power to the electrodes minus the water electrolysis power).





Additional electrolytic cell results were reported by HPC and Thermacore in Ref. 10, as summarized below.

- HPC reported results from three experiments in a cell somewhat larger (350 ml) than the earlier cell noted above. Excess power was reported in the experiments conducted using a potassium carbonate electrolyte (output/input of 200% for continuous, 1600% for pulsed input). No excess power was reported for the control experiment using sodium carbonate, consistent with the Mills theory.
 - Thermacore reported results from 11 experiments conducted in a much larger (10 gallon) cell. It had been observed that higher excess power was obtained in a pulsed input power mode, using a low frequency (1-2 Hz) square wave. Nine of the Thermacore experiments consisted of varying the duty cycle (percent of time the voltage was applied) of the input square wave while holding other variables constant, with results shown in Fig. 1. The results indicate a well behaved process producing excess power



beyond what could be explained by measurement errors. A final experiment conducted at a lower input power with a duty cycle of 20% was operated for 240 days with an output/net input power ratio in excess of 2000%.

A later, more advanced cell was operated in 1994, as described in Ref. 11. This cell was much larger than the earlier HPC cells, containing 11 liters of electrolyte. The cathode was constructed of nickel wire cloth and the anode of a nickel fiber mat, providing a large reaction surface area for each. The cell was placed in a dewar to minimize uncontrolled heat loss, and heat removal was through a controlled and instrumented condenser. Cases were run using K_2CO_3 electrolyte, expected to produce excess power via catalysis of the hydrogen energy release by the potassium in accordance with Mills' theory, and Na_2CO_3 , which was not expected to produce excess power. A calibration run (no voltage applied to the electrodes, while an internal resistance heater was operated) was performed for each electrolyte. Both Na_2CO_3 cases and the K_2CO_3 calibration run were operated for 7 days, while the K_2CO_3 electrolysis run was operated for 14 days. Excess power in the K_2CO_3 electrolysis run was measured at 17.6 times the net input power.



3.2.2 Gas Cell

A new approach using hydrogen gas in a reaction cell was begun in 1993 and has advanced considerably over the past year. Recognizing the limitations in temperature and power density capabilities of the electrolytic cells that had served to provide evidence of the production of excess heat and the existence of hydrino, HPC proceeded to develop new concepts based on using hydrogen gas as an input to the cell rather than producing it in the cell through electrolysis. This concept provides the potential for achieving much higher temperatures and power densities than have been achieved in the electrolytic cells discussed above. The evolution of the gas cell concept is summarized below, followed by additional discussion of the most recent and most promising concept, the vapor phase cell in the following section.

The gas cell concepts introduce hydrogen into the cell in gaseous form rather than generating hydrogen by electrolysis of an aqueous solution in the cell, as is done in the electrolytic cells. Guided by Mills' theory, the objective of all of the concepts is to produce a local mixture of hydrogen atoms and catalyst ions, thus allowing the catalytic reaction to produce low energy hydrogen. An initial concept added hydrogen to a potassium carbonate solution via a coil of nickel tubing. Subsequent concepts moved toward introducing hydrogen gas directly in the cell, using initially a sintered catalyst, then a spillover catalyst, and most recently a vapor phase cell. The characteristics of these concepts are summarized below.

- Hydrogen Diffusion/Aqueous Solution This concept was developed by Thermacore, working in collaboration with HPC. Hydrogen was introduced into the cell through a coil of thin-walled nickel tubing placed inside a pressurized vessel containing a solution of K₂CO₃. Hydrogen atoms could then diffuse through the nickel and react with the potassium on the outer surface of the tubing. By using a pressurized vessel, higher temperatures and pressures (relative to atmospheric pressure aqueous solution electrolytic cells) were achieved. Excess power was observed in these cells as reported in Ref. 12, proving that excess power could be produced without electrolysis. However, Thermacore was unable to achieve sufficient power densities to support commercial applications.
- Solid State Catalyst Seeking to develop a concept with more economic potential, HPC began to investigate cells which would involve the direct interaction of hydrogen gas and a solid state catalyst. Initial concepts were based on a sintered metal oxide compound mixed with a catalyst material to induce the low energy hydrogen reaction. Tests at Penn State showed indications of excess power (Ref. 13) interpreted by HPC to be produced by transition of hydrogen to lower levels (hydrino). The solid state catalyst approach was further evolved through the development of hydrogen spillover catalysts consisting of mixtures of hydrogen dissociation materials and catalytic materials on graphitic carbon powder. Tests at Penn State also





demonstrated the production of excess power from spillover catalyst cells (Ref. 14, 15). In evaluating the results of the testing on the spillover catalyst cells, HPC concluded that excess power was being produced, but recognized that the catalyst was being neutralized after a period of time, eventually terminating the reaction, thus this concept would require catalyst replenishment for sustained operation.

Vapor Phase Cell - In reviewing the results of the spillover catalyst cell testing, HPC concluded that the reaction may have been taking place in the vapor phase, leading to the development of a vapor phase cell as the current leading concept for energy production. The vapor phase cell consists of a means for establishing catalyst atoms in a gaseous state along with hydrogen atoms, thus supporting a catalytic reaction in the vapor phase. This evolution reduces the device to the basic elements predicted by the theory to produce low energy hydrogen: atomic hydrogen and catalyst ions to provide the required energy hole. The theory also predicts that optimum performance will be obtained at a low pressure (less than 1/1000th of an atmosphere. The prediction of optimum pressure is based on the development of the disproportionation reaction concept based on observation of solar reactions. With disproportionation, a hydrino atom can catalyze further collapse of another hydrino atom. At lower pressures recombination of hydrogen and hydrino atoms into molecules via collision with other atoms is less likely, thus the reaction can be more effectively sustained. The concept is discussed in more detail in the following section.

3.3 Basic Features and Performance of Vapor Phase Cells

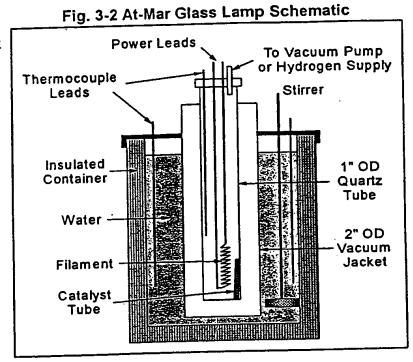
HPC began work on their first vapor phase cell concepts in January, 1996, constructing small tabletop systems with one running at a time. Based on early successes, a priority effort was begun in the spring of 1996. As of July, 1996, several variants of vapor phase cells have been constructed and operated at HPC and most recently at Pennsylvania State University. In most cases, they have consisted of a vessel containing a powered metal filament to dissociate hydrogen molecules, a compound to produce catalyst atoms at the desired vapor pressure and operating temperature, an attached vacuum pump to provide for initial purging of contaminants and to achieve and maintain the desired operating pressure, and a source of hydrogen gas. For control experiments, provisions may also be included for a non-dissociating heat source (e.g., cartridge heater) in addition to a metal filament, and provision for introducing neutral gas (e.g., helium) and non-catalytic compounds (e.g., sodium compounds). A recent variant utilizes a metal powder for dissociation of hydrogen molecules in conjunction with an external heater to achieve desired operating conditions. HPC reports that excess power is being observed in all of the vapor phase variants. A brief description of the devices and a summary of recent results is provided in the following subsections.



3.3.1 At-Mar Glass Lamp

A small gas vapor cell referred to by HPC as an "At-Mar Glass Lamp" is shown

in Fig. 3-2. In this device, a vacuum pump is used to evacuate the cell and bake out impurities, then the cell is filled with hydrogen at a low pressure (~1 torr). Hydrogen atoms are produced by dissociation of hydrogen molecules by the high temperature filament (typically tungsten). A small tube of a catalyst compound (e.g., KNO₃) is placed alongside the filament to serve as a source of catalyst atoms. The device is placed in an insulated container partially filled with water kept at a uniform temperature by a stirring device and brought to an initial equilibrium temperature.



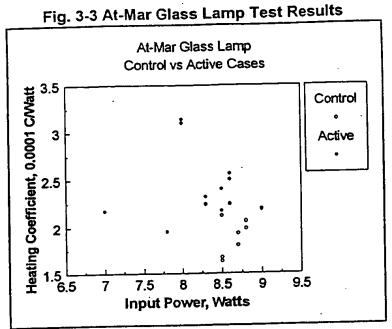
Power is applied to the filament and the temperature of the water is monitored by two thermocouples to determine the rate of increase of water temperature at a constant, measured level of input power. The cell heating coefficient ($\Delta T/\Delta t/P$ ower, °C/Wattsecond) is determined for a set of control cases for comparison with cases where conditions supporting low energy hydrogen production are present. For some of the runs, the internal surface of the quartz tube was plated with silver to reduce radiant heat loss and thus increase the operating temperature of the cell.

HPC has conducted a series of experiments using the At-Mar Glass Lamp device to investigate the production of excess energy. A set of control cases were





operated with hydrogen and power to the filament, and compared with a set of active cases in which a potassium catalyst compound was added. The results are shown in Fig. 3-3. A considerable scatter in the results is present, with average values for the Heating Coefficient (10-4 °C/Watt-second) of 1.91± 0.19 for the control cases and 2.37 ± 0.35 for the active cases. Calculating the excess power ratio as the ratio of the heating coefficient for the active cases over the control



3.3.2 Isothermal Calorimeter

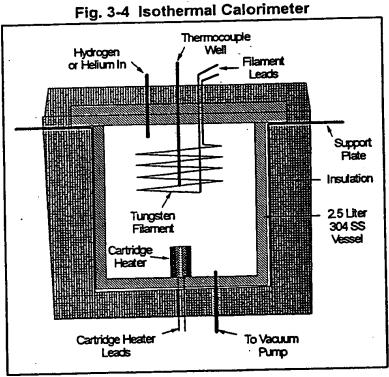
cases, excess power would be

about 20% of input, or about 2

watts on average.

A schematic diagram for a larger (2.5 liter volume) HPC vapor phase cell

operating on the same principle as the At-Mar Glass lamp, and designated the Isothermal Calorimeter is shown in Figure 3-4. The Isothermal Calorimeter Cell has been operated in a combination of control and active experiments to study the effect of key parameters (i.e., presence of catalyst and: hydrogen gas, means for dissociation of hydrogen molecules). In a typical experiment, the vessel is pumped down and baked out to remove contaminants, then the desired conditions are established and the temperature is monitored until equilibrium is reached. For example, a control experiment





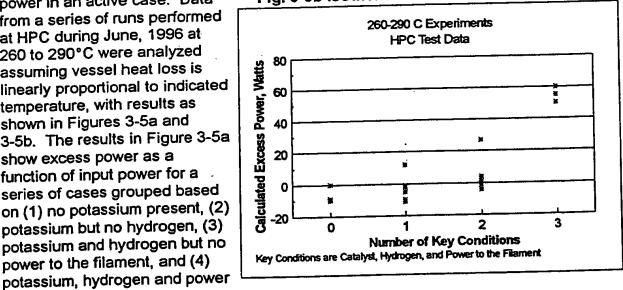


might use the cartridge heater instead of the filament to heat the vessel without dissociation of hydrogen gas. A series of experiments reaching equilibrium at about the same temperature was conducted with various combinations of the key parameters, while noting the input power required to achieve the target temperature. Assuming the heat loss from the cell is the same in all cases, the excess power generated in the cell would be the difference between the input power in the control cases and the input power in an active case. Data from a series of runs performed at HPC during June, 1996 at 260 to 290°C were analyzed assuming vessel heat loss is linearly proportional to indicated temperature, with results as shown in Figures 3-5a and 3-5b. The results in Figure 3-5a show excess power as a function of input power for a series of cases grouped based on (1) no potassium present, (2) potassium but no hydrogen, (3) potassium and hydrogen but no

Fig. 3-5a Isothermal Calorimeter Test Results 260-290 C Experiments **HPC Test Data** No K Excess Power, Watts 60 No H 40 No Pfil 20 0 K+H+Pfil 0 -20 <u>-</u> 20 100 120 80 60 40 Input Power (Cartridge Heater+Filament), Watts

Fig. 3-5b Isothermal Calorimeter Test Results

Sequential Inclusion of Key Parameters



to the filament. Figure 3-5b shows the same excess power results plotted as a function of the number of key conditions present during the test. The data indicate a large amount of excess power for the cases where all of the conditions for the HydroCatalysis reaction are present.

3.3.3 Calvet Calorimeter Cell

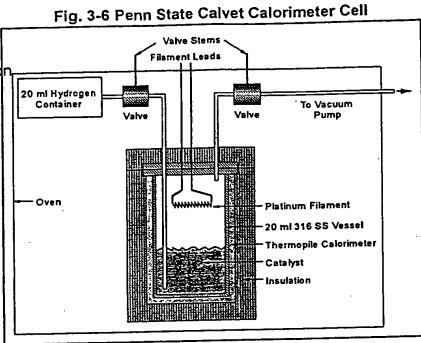
power to the filament, and (4)

Another cell variant based on the same principle as the At-Mar Glass lamp is a small metal vessel cell operated within an oven to establish a well controlled operating temperature. These cells have been operated in multiples with simultaneous operation





of control and active cells to investigate excess power generation, and in combination with a precisidr thermopile based calorimeter, called a Calvet Calorimeter. Independent testing of a Calvet Calorimeter Cell began at Penn State in mid-July, as noted in the summary of a visit to Penn State provided in Section 5.2.3. A schematic of the device constructed at Penn State, which is similar to



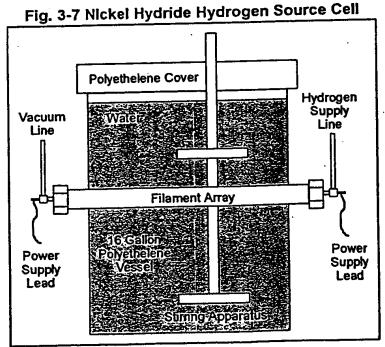
shown in Figure 3-6. As, discussed in Section 5.2.3, the cell was operated at near atmospheric pressure at an input power of 5 Watts, with preliminary analysis indicating the production of excess power in the range of 0.01 to 0.05 Watts over several days for a total energy corresponding to about 20 times the amount which would result from combustion of all of the hydrogen present in the cell and hydrogen reservoir. HPC reported excess power of 0.3 to 0.7 watts for a similar cell operating at a hydrogen pressure of about 200 millitorr and an input power

of about 4 Watts.

corresponding cells operated at HPC, is

3.3.4 Metal Hydride **Hydrogen Source** Cell

Another concept pursued by HPC involves the use of hydrided metal as a hydrogen source (Figure 3-7). In these devices, nickel wire which had been used as a cathode in an electrolytic cell is used as a filament in a gas cell. The nickel wire is wrapped around a quartz tube or mandrel, electrical leads are attached, and the assembly is placed inside a larger quartz





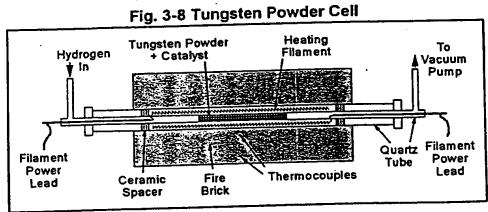
tube. The larger tube is epoxied into a large water container, the ends are sealed, the larger tube is evacuated, and power is applied to the filament. As the filament temperature increases, hydrogen stored in the nickel during earlier electrolytic cell operation is released along with potassium which had plated out on the surface. The released potassium serves as the catalyst in some experiments, while others include additional catalyst compound which is vaporized as the cell reaches operating temperature. The water in the container is stirred as power is applied to the cell, and energy input to the water (output power from the cell) is determined from the rate of temperature rise. Additional control experiments have been conducted to improve the accuracy of the determination of cell output power.

HPC reported that early tests which relied on potassium plated out on the nickel wire as the source of catalyst atoms were erratic in their performance, and it was concluded that a separate source of catalyst should be added to the cell. Thus a quartz capillary containing a catalyst compound was placed inside the inner quartz tube for subsequent tests. Testing of the nickel hydride gas cell concept was conducted by varying input power over a range of approximately 400 to 800 watts. For these runs measured excess power ranged from 40 to 120 watts (6 to 17% of input power). A test in late July was reported to have produced approximately 250 watts of excess power with an input power of 170 watts. HPC believes the increased power may be a result of a disproportionation reaction supported by hydrino atoms released from the nickel wire. HPC also believes their earlier gas cells were limited by the hydrogen atom densities in the cells, and have evolved their devices to provide adequate hydrogen atom density. They feel that current results are being limited by catalyst atom density, and are directing device design and operation to address this limit.

3.3.5 Tungsten Powder Cell

Another gas cell concept being pursued by HPC is the use of tungsten powder rather than a tungsten filament for hydrogen dissociation. In this concept, as depicted

in schematic form in Fig. 3-8, the reaction chamber is a quartz tube containing tungsten powder and a catalyst compound. The tube is surrounded by a heating filament to achieve the required temperatures to



dissociate hydrogen on the tungsten. Results from a series of tests initiated in July are reported to indicate about 10 watts excess power. This concept is in the early stage of



development, and can be expected to undergo significant refinement as a result of initial testing.

3.4 Applications and Projected Products

HPC has begun to explore concepts for application of the technology for electricity generation. These concepts, currently in a very early stage of development, are based on using the heat energy developed by the hydrogen transition reaction in conjunction with conventional power conversion equipment. Applications envisioned include:

- 10 kW units for heat and electricity in residential applications
- Industrial cogeneration and distributed generation applications in the 100 kW to multi-megawatt range
- Large central station applications, including units for retrofitting fossil boilers and repowering nuclear plants

The initial products are at a very early conceptual stage, with no evidence of detailed conceptual design development and review. The thinking to date has been based on using the gas reactor in a heat exchanger configuration to generate steam or integrated into a gas turbine. Other applications are envisioned including motive power for automobiles, trucks, etc.

4.0 Concept Assessment

This section discusses the results of the concept assessment. Subsections 4.1 and 4.2 address the validity of the theory and the experimental basis for the generation of excess heat from the HPC process. Subsections 4.3 and 4.4 address potential initial products and their projected economic and environmental characteristics, assuming the HPC process is proven and commercially viable.

4.1 Theory

The generally accepted theory of the hydrogen atom and the broader quantum mechanics models upon which it is based are supported by a long standing body of analytical models and empirical observations. The mathematics and empirical data involved are of sufficient complexity and magnitude to support years of study and controversy before acceptance of major new developments or changes in accepted interpretations. The Mills theory proposes changes in interpretation of quantum mechanical phenomena relative to the hydrogen atom and other physical phenomena on a scale not seen since early in this century. Thus it is not surprising that the theory



is controversial and not readily accepted by the scientific community. However, it appears that a small but expanding number of scientists are beginning to take the Mills theory seriously.

The Mills theory has been documented in a series of publications, beginning with Ref. 3, with the most recent revision provided in Ref. 16. A review of one of the publications, Ref. 17, was documented by Dr. Reinhart Engelmann of the Oregon Graduate Institute of Science & Technology, Ref. 18. In summary, Dr. Engelmann stated "I am confident that the soundness of your basic, though unusual, approach to quantum theory, combined with convincing experimental results, should eventually convince a broader scientific community". As evidence is accumulating in support of the existence of hydrino, it appears that this broader acceptance is beginning to happen.

Given the time and resource limitations of this assessment, it was not considered productive to attempt an in-depth review of the theory. However, discussions with Dr. Stewart Kurtz (Section 5.1) of Penn State indicate that the theory has received considerable review by reputable physicists over the past several years, resulting in extensions of the phenomena addressed by Mills, but no fundamental flaws in the theory have been identified. Dr. Reinhard Engelmann of the Oregon Graduate Institute of Science & Technology has also spent considerable effort reviewing the theory and its mathematical derivation (interview summary, Section 5.1). Dr. Engelmann indicated a strong belief in the general validity and importance of Mills' theory, but expressed concern regarding some inconsistencies in the theoretical framework which he was unable to resolve. He feels that what is needed is for others to become interested and begin working on the mathematical development of the theory, and believes that the best way to make that happen is to advance an energy generation device and expand the empirical evidence supporting the theory. Consistent with this view, attention was focused on the case for the existence of the postulated results - the hydrino - and the degree of confidence in the observation of excess energy in the cell experiments conducted by HPC and others. The cell experiments are addressed in Section 4.2, and the case for the existence of hydrino is addressed below.

4.1.1 Hydrino - Laboratory Observations

If the theory is valid, hydrino could be expected to be found as a residual product from the operation of the HPC cells, but hydrino would not be easily detected because of its predicted high degree of stability, making it relatively inert, and its expected tendency to diffuse readily. Two methods for detecting hydrino as a byproduct of the reactions in the cells have been presented in the open literature, and a third has been recently advanced by HPC as summarized below:

X-ray Photoelectron Spectroscopy (XPS) - XPS was used to search for evidence of the presence of hydrinos on the surface of the cathode material from





electrolytic cells. The XPS procedure utilizes an X-ray photon source to ionize atoms and measure the kinetic energy of the emitted electron. The binding energy of the emitted electrons can be determined from their kinetic energy and the known photon energy. The procedure results in a spectrum of binding energy peaks for materials present in the specimen. The binding energy for a n=1/2 hydrino would be 54.4 ev according to Mills' model. XPS data were developed for HPC specimens by the Zettlemoyer Center for Surface Studies, Lehigh University, with independent confirming data produced by the Idaho National Engineering Laboratory and Charles Evans & Associates. Ref. 11 reported XPS data for the following specimens:

- Nickel foil from a cathode which had been operated with K₂CO₃ electrolyte (no calorimetry)
- Nickel wire from a cathode which had been operated with K₂CO₃ electrolyte in a cell measured to be producing excess heat
- Nickel wire from a cathode which had been operated with Na₂CO₃ electrolyte
- Precursor nickel electrode material (pure, heated, and oxidized specimens)

A broad peak was observed in the vicinity of the predicted 54.4 ev binding energy of the hydrino for the first two cases and not for the remaining samples. Other nearby peaks were identified as being associated with nickel and known impurities in the samples. Mills & Good concluded that the observed broad peak was produced by hydrinos present on the samples which had been operated as cathodes in cells with K₂CO₃ electrolyte. The data presented in Ref. 11 are generally supportive of this conclusion, but are not totally convincing, in that apparently significant variations in the average energy of the observed peak are not explained in the paper. In subsequent discussions, Mills stated that the broadening of the peak is caused by Compton scattering, and that some drift in the measured energy levels can be expected for XPS measurements.

Recent unpublished XPS data associated with identification of hydrino were made available by HPC during the course of this assessment (Ref. 19, 20). Additional XPS testing has been conducted at Lehigh University on glassy carbon electrode materials taken from an electrolytic cell. The use of carbon electrodes eliminates the large peaks associated with nickel which were present with the nickel electrodes and thus reduces the potential for secondary peaks in the energy regions where hydrino would be expected. HPC has identified features in these data which they associate with the presence of n=1/2, 1/3, and 1/4hydrinos. However, as noted in Section 5.2.4, Dr. Miller of Lehigh, who performed the XPS work, does not feel the data developed to date provides conclusive evidence of hydrino. Miller is concerned about the very small X-ray cross-section of hydrogen (0.0002 relative to a carbon baseline) and of hydrino by extension, implying a requirement for a very high density of hydrino on the specimen surface to generate a signal. In addition there is the possibility of a second order potassium peak associated with lower energy potassium peaks





which are present in the data. Miller believes that definitive results could be obtained by a gas phase experiment where the only material present is the gas from an HPC cell. He estimates that such an experiment would take between three and six months and cost between \$100,000 and \$200,000.

Mass Spectroscopy - Mills projects that if hydrinos are present on the cathode metal surface, they would bind together to form "dihydrinos", the equivalent of hydrogen molecules. These dihydrinos would be expected to be present in the electrolysis gases along with molecular hydrogen and oxygen. Mass spectroscopy was performed on electrolysis gas samples from K2CO3 and Na₂CO₃ cells along with control hydrogen samples by Schrader Analytical and Consulting Laboratories. An additional gas sample from a K2CO3 cell was ignited with the objective of increasing the dihydrino fraction through combustion of much of the hydrogen and oxygen, thus increasing the hydrino fraction (termed postcombustion gases). The following tests and observations were reported:

- It was postulated that the dihydrinos would have considerably higher ionization energy than molecular hydrogen. Ionization potential was varied to identify thresholds for ionization of the molecules present, resulting in identification of a species with an ionization potential of 63 ev in the gases from the K₂CO₃ cell, well above the hydrogen molecule ionization potential of 15.46 ev. This species was not present in the gases from the Na₂CO₃ cell or the control samples.
- It was also postulated that while the mass/charge ratio for dihydrinos and hydrogen molecules would be indistinguishible, there would be a detectable difference in the magnetic moments of the two molecular ions. A double peak in the high resolution magnetic sector mass spectra at m/e=2 was observed for postcombustion gases at an ionization potential of 70 ev. The feature was not present for the gases at 25 ev or for a control hydrogen gas sample at 25 or 70 ev.

It was concluded that both observations are supportive of the presence of a species with the expected characteristics of dihydrino molecules in the gases from the K₂CO₃ cell.

Additional mass spectroscopy data have been developed by HPC utilizing offgas from a vapor cell utilizing a Calvet calorimeter and gas collected from an electrolysis cell as discussed in Ref. 19 and summarized below.

Gases were collected from a small (20 ml) gas vapor cell connected to a Calvet calorimeter for on-line detection of excess power production and passed through a mass spectrometer. Cell operating conditions were adjusted to obtain production of excess power in one case (as verified by the calorimeter) and to preclude production of excess power in a control case. The ionization potential of the mass spectrometer was varied back and forth





from 30 to 70 ev as the cell was operating. For the control case, the mass spectrometer was adjusted so that the signal remained relatively constant for the mass=2 species during the change in ionization potential. With the same mass spectrometer settings for the excess energy case, a large increase in signal was observed as a result of the change of ionization potential.

Gases were collected from an evacuated hollow nickel cathode of an aqueous potassium carbonate electrolytic cell and an aqueous sodium carbonate electrolytic cell (control case). Each cathode was sealed at one end and was on-line to a mass spectrometer at the other end, allowing some of the gas produced during electrolysis to diffuse through the wall of the nickel tubing and flow to the mass spectrometer. The ionization potential of the mass spectrometer was varied between 30 and 70 ev and the response for mass=2 species was observed. Data from the control case (sodium carbonate electrolyte) indicated an approximately constant signal during the change in ionization potential (average ratio for 70 ev signal vs 30 ev signal = 0.9). Data from the potassium carbonate electrolyte case showed a significant increase in the signal in all cases (average ratio = 4.1).

Gas Chromatography - Gas chromatography was used to search for evidence of dihydrinos due to differences in magnetic energies relative to hydrogen molecules. As stated by HPC (Ref. 19): "Lower-energy hydrogen has an internuclear distance which is fractional compared with that of normal hydrogen. Thus, nuclear hyperfine structure interactions are greater. Also orbital magnetic hyhyperfine interactions are possible for lower-energy hydrogen. The ortho and para forms of molecular hydrogen can readily be separated by chromatography at low temperatures. Thus, we explored the possibility of using gas chromatography at cryogenic temperatures to discriminate hydrogen molecules from dihydrinos on the basis of the difference between magnetic energies of the two species."

Gas chromatography was performed on two sources: (1) A control sample of hydrogen gas produced by reacting NaOH with aluminum chips, and (2) a sample expected to contain lower energy hydrogen molecules (dihydrinos). The second sample was produced from a 60 meter section of nickel wire which had been used as an electrode in a potassium carbonate electrolytic cell. The wire was placed in an evacuated quartz tube and heated to 800°C, resulting in the outgassing of potassium and hydrogen loaded into the wire during electrolysis. The gas chromatography results showed the expected twin peaks associated with para and ortho hydrogen molecules for the control sample. For the sample from the quartz tube, the normal peaks were present along with additional intermediate lower level peaks, which were attributed by HPC to the presence of lower level hydrogen molecules. The gas chromatography results are relatively recent, and HPC is still developing the technique for this application, thus external review of the procedure and results has been limited to date. Nonetheless, these data lend additional weight to the evidence for the existence





of hydrino developed by XPS and mass spectroscopy.

As HPC has gained experience with procedures to detect the presence of hydrinos, the case for their presence on electrodes from the electrolytic cells, and in off-gases from both electrolytic and gas cells is gathering strength. HPC is working to expand the number of reputable scientific institutions working with the cells and conducting and refining procedures for hydrino identification as a means of developing widespread acceptance. Another procedure currently under consideration is to perform extreme ultraviolet/soft X-ray spectroscopy of emissions from an operating gas vapor cell. An established procedure for conducting spectroscopy under conditions and configurations similar to a gas vapor cell is said to be available, and is being investigated for use in conjunction with the vapor cell work currently under way at Penn State. If clear spectral lines consistent with hydrino transition energies are observed and found to correlate with the production of excess power, this procedure would provide definitive confirmation of the low energy hydrogen concept.

4.1.2 Hydrinos - Environmental Observations

Another argument for the existence of hydrino is based on observations of radiation spectra from space. Extremely large quantities of hydrogen are known to be present in interstellar space. Thus if the Mills theory is correct, evidence of hydrino formation in the form of soft X-ray emissions at wavelengths corresponding to the transition energies could be expected. However, to explain the quantities of hydrogen remaining in the universe given generally accepted values for the age of the universe, the transition probabilities must be low. This results in a relatively low strength signal for hydrino transitions. In addition, atmospheric attenuation is large in this region of the spectrum and background levels are high relative to expected signal strengths. Other potential sources of evidence of hydrino arising from more subtle effects, such as transitions in rotational energy among dihydrino molecules, would be found in other parts of the spectrum. HPC has been reviewing radiation data and seeking independent review and collaboration with astrophysicists with regard to evidence of the existence of hydrino.

In Ref. 16, spectral data taken by a sounding rocket, as reported in Ref. 21, were evaluated by HPC for indications of hydrino. Ref. 21 reported seven observed emission features in the wavelength range of 80 to 650 Å as shown in Table 4-1. In HPC's initial review of Ref. 21, peaks with wavelengths corresponding to transitions $n=1-\frac{1}{2}$, $\frac{1}{2}-\frac{1}{3}$ and $\frac{1}{4}-\frac{1}{5}$ were identified and assigned (Ref. 11), and the low signal-tonoise ratio of the data was stated as likely to have obscured the $\frac{1}{3}$ - $\frac{1}{4}$ transition peak. HPC also reported in Ref. 11 that a review of the raw data obtained from the authors identified a possible additional peak which could be associated with the $\frac{1}{3}$ - $\frac{1}{4}$ transition. Following external review and comment, and subsequent extension of the Mills model, including the development of the disproportionation reaction model, the emission energy from transitions was shifted by 54.4 ev, resulting in a reassignment of the lines to $n=\frac{1}{3}-\frac{1}{4}$, $\frac{1}{4}-\frac{1}{5}$ and $\frac{1}{6}-\frac{1}{7}$ transitions. The final assignments, as



documented in Ref. 16 are shown in Table 4-1. Several additional lines were identified in Ref. 16 from a review of the raw data and were assigned to other low energy hydrogen transitions plus related scattering and second order peaks.

	Table 4-1 Extre	me UV Interstell	ar Spectral Data		
Observed Peak Wavelength, Ź	Labov & Bowyer Assignment ¹	Labov & Bowyer Wavelength, Å ¹	Mills Assignment ²	Mills Wavelength ²	
-5.3 98.7* ^{4.2}	Fe XVII, Fe XIX Log T=6.8	~99 1/6 - 1/7 Transition		101.3	
_{4,6} 178.1 ^{+5.1}	Fe X, FeXI Log T=6.0	~178	1/4 - 1/5 Transition	182.3	
_{-1,4} 200.4*5.3	Second Order 98.7 Line	~198	Second Order 1/6 - 1/7 Line	202.6	
-6.0 299.7*5.9	He II	304	1/3 - 1/4 Transition	303.9	
4.5 582.1 ^{4.5}	He Scattering of Solar Radiation	584	He Resonance Scattered Emission	584	
49 609,1 ^{44,9}	Second Order He II Line	609	Second Order 1/3 - 1/4 Line	607.8	
4.7 634.7*4.7	O V 5.4 <log t<5.7<="" td=""><td>629.7</td><td>He Scattered 1/3 - 1/4 Line</td><td>633.0</td></log>	629.7	He Scattered 1/3 - 1/4 Line	633.0	

Peak wavelengths determined from raw data by astrophysicists Labov and Bowyer, who conducted the
experiment (Ref. 21), shown with 10 confidence limits. These are the only peaks identified within the statistical
experiment (Ref. 21), shown with 10 confidence limits. These are the only peaks identified within the statistical
experiment (Ref. 21), shown with 10 confidence limits. These are the only peaks identified within the statistical
experiment of the confidence limits.

 Assignment of peaks identified in Ref. 21 by Mills based on transition energies for low energy hydrogen, (Ref. 16). Additional analysis of raw data obtained from Labov and Bowyer by Mills resulted in the conclusion that additional peaks were discernable that were associated with low energy hydrogen transitions.

It was concluded by HPC that the data were consistent with the presence of the lower energy hydrogen states predicted by the Mills theory, and that use of the Mills theory provides a more satisfactory explanation for the observed data than existing models. The comparison with the Labov and Bowyer peaks as assigned in their paper was identified by John Farrell (Section 5.2.5) as the strongest case for the existence of hydrino based on astrophysical evidence. The HPC interpretation of the data has been disputed by Bowyer, and the paper on the HPC interpretation submitted by Farrell, Mills and Good (Ref. 22) to Astrophysical Letters and Communications was not accepted for publication. Thus the low energy hydrogen concept and its implications regarding data interpretation has not received general review or acceptance by the astrophysics community.

More recent work by Mills has identified additional evidence of the existence of hydrino in astrophysics data. Spectral lines and characteristics of the sun have been associated with calculated hydrino transition energy levels, including dihydrino

×





molecule rotational transitions. The success of hydrino models in explaining observations heretofore not rationalized has begun to attract attention from astrophysicists. A proposed joint research project with the National Radio Astronomy Observatory is directed toward further exploring the validity of the Mills model in predicting radiation phenomena in space, as noted in the summary of a phone conversation with Dr. Barry Turner of the National Radio Astronomy Observatory in Section 5.1. It thus appears that the application of Mills theory to the explanation of observed phenomena in space is gaining some acceptance and credibility. However, as indicated by lack of acceptance of an earlier proposal (Ref. 23), the astrophysics community remains generally resistant to serious consideration of Mills' theory.

The correlation of the Labov and Bowyer extreme ultraviolet radiation study results with hydrino transition energies derived from Mills' theory is indeed striking. It is particularly noteworthy that the original identification of the spectral lines was conducted independently with no awareness of the Mills theory and its predictions regarding emission spectra. However, the complexity of interpretation of radiation data from space, in conjunction with the resistance in the astrophysics community noted above makes use of these data for assessing the validity of Mills' theory difficult. The absence of generally accepted support for the existence of low energy hydrogen among the astrophysical community is understandable given the revolutionary nature of the theory and the major revisions to longstanding interpretations of existing data which could result. For example, solar flare spectral observations proposed to be indications of a new element by Norman Lockyer in 1870 was not accepted as evidence of the existence of helium until 1895 (Ref. 24). If the low energy hydrogen reactions projected by Mills become proven and widely accepted, it can be expected that considerable attention will be given to reinterpretation of astrophysics data, and association of observed data with hydrino appears likely. However, in the current circumstances, and for the purposes of this assessment, the evidence for hydrino and excess power developed in the laboratory experiments is considered of greater value.

4.2 Prototype Performance

This section addresses the laboratory performances of cells constructed and operated in accordance with the HPC concept with regard to the case for the production of excess power (power beyond that which could be explained by conventional processes).

4.2.1 Water Based Electrolyte Cell (Low Temperature)

The 1990 cell reported in Ref. 9 was a small unit, utilizing a half liter container and 100 ml of electrolyte. The cell calorimetry was based on calibrating the thermal resistance for heat loss through what was designed to be a predominately conduction based heat transfer path to ambient. A resistance heater was included in the cell to support determination of the thermal resistance for cell heat loss, and the heater was also operated in conjunction with power to the electrodes in many of the cases.





"Excess power" was calculated by subtracting the difference between the cell energy iosses:

- Heat transfer losses to ambient
- Water electrolysis energy

and the known cell energy inputs:

- Resistance heater power
- Power to cell electrodes

The quantities of energy losses and power input were small, ranging from a fraction of a watt to a few watts. Since the "excess power" was calculated as the difference among these quantities, the potential for measurement error or omitted or inadequately modeled phenomena resulting in misinterpretation of results is significant. This is common to all of the experiments of this nature, and provides the primary basis for controversy regarding the outcome of the experiments. A careful review of the cell description and results in Ref. 9 did not provide sufficient basis for a clear conclusion that excess power had in fact been observed.

The 1994 cell reported in Ref. 11 represented a considerable advance over the earlier cell. The larger size and increased power levels reduced measurement uncertainties, while the instrumented condenser provided for a direct measurement of cell heat loss. Thus the calibration runs constituted a check on the effectiveness of isolating the condenser as the dominant heat removal path, showing agreement between the input power and heat removal through the condenser. It was noted that during the electrolysis runs, an additional heat removal path was provided via vapor carryover and sensible heat loss from the effluent gases. This would result in an underestimate of the energy production in the cell and a corresponding underestimate in the cell excess power. The results from this experiment appear to provide a convincing case for excess power generation.

Independent confirmation of excess heat from electrolytic cells over long periods of time has been documented, including the following:

- V.C. Noninsky of the Laboratory for Electrochemistry of Renewed Electrode-Solution Interface, Sophia, Bulgaria, conducted H₂O/K₂CO₃ electrolyte/nickel electrode cell experiments as a visiting scholar at Franklin and Marshall College. He reported evidence of excess heat production in Ref. 25.
- Work was conducted at the Hokkaido University Catalysis Research Center in Japan to measure excess heat in H₂O/K₂CO₃ and H₂O/Na₂CO₃ cells using nickel, gold, silver and tin electrodes. Excess heat was reported for the H₂O/K₂CO₃ electrolyte/nickel electrode cell along with some of the other cells operated at the Center (Ref. 26 and 27).



- Additional measurements of excess heat in H₂O/K₂CO₃ electrolyte/nickel electrode cells has been reported (Ref. 28 and 29). However, while the experimenters reported excess heat, they believed that it was being generated by a fusion reaction with the alkali metals rather than the mechanism proposed by Mills.
- Engineers at the Moscow Power Engineering Institute reported excess energy produced "reliably and continuously over the last three months" (Ref. 30).
- In a report to Wright Laboratory of the Air Force Materials Command, Thermacore reported anomalous heat in a pressurized H₂O/K₂CO₃ cell with hydrogen gas introduced via a coil of nickel tubing (Ref. 31).
- A study at NASA Lewis Research Center (Ref. 32) identified apparent excess heat, but noted that the observations could be explained by recombination of electrolysis gases in the cell.
- Additional unpublished work at INEL, Westinghouse, and MIT Lincoln Laboratories (Ref. 33, 34, 35) indicate production of excess power.

While there has been a number of independent confirmations of excess power generation in the $\rm H_2O/K_2CO_3$ electrolyte/nickel electrode cells, there has also been controversy regarding the source of the excess power. Other scientists continue to challenge the validity of the excess heat observations, most recently in Ref. 36. While the debate continues, the evidence of excess power generation in electrolytic cells based on the HPC concept identified in this assessment is convincing. Meanwhile, HPC has concluded that the electrolytic cells offer little commercial potential, and has moved on to gas cells as discussed below.

4.2.2 Gas Cells

As illustrated in Sections 3.2, the gas cells are a recent development and have been undergoing rapid evolution from hydrogen diffusion/aqueous solution cells to solid state (sintered and spillover) catalyst cells to the most recent concepts, the vapor phase cells. Excess power production in the hydrogen diffusion/aqueous solution cell concept has been measured by Thermacore, as reported in Ref. 31. As noted in Section 3.2.2, testing of HPC cells at Penn State indicated excess power production by HPC sintered catalyst and spillover catalyst cells. Papers documenting these results were reviewed and the bases for the conclusions regarding the production of excess power were confirmed. However, most of the excess power review effort was directed toward the vapor phase cells, since they hold the most promise and are the focus of current HPC efforts to develop a commercially viable product.

The data obtained from HPC were reviewed and used to calculate the excess power values provided in Section 3.3 for the At-Mar Glass Lamp (Fig. 3-3) and the Isothermal Calorimeter cells (Fig. 3-5a,b). These tests are of limited accuracy and repeatability, as evidenced by the scatter in the data among the cases reported. For

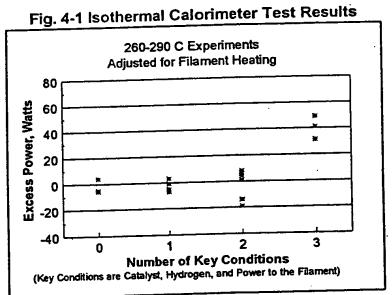




the At-Mar Glass Lamp, heat losses out the top and by radiation to the water in the container are relatively uncontrolled. The silver plating on the internal surface of the inner quartz tube was a key factor in limiting radiant heat losses, and HPC noted that the silver appeared to be redistributing during the series of tests. Measurement of temperature inside the cell was difficult because the low pressure and predominance of radiant heat transfer made indicated temperature a strong function of thermocouple location relative to the filament. Thus cell temperature in the reaction zone, a key variable, was not well known or controlled. HPC addressed these limitations by conducting control tests with conditions as close to the active tests as possible. On balance, the overall results for the At-Mar Glass Lamp are considered to provide a statistically significant indication of excess power production.

The Isothermal Calorimeter is a relatively simple device where heat loss is assumed to be proportional to temperature, and the amount of input power required to bring the device to a given temperature is measured under various operating conditions. A reduction in the amount of input power required is an indication of excess power production. In reviewing the design of the Isothermal Calorimeter cell, a concern was identified regarding the measurement of temperature within the cell and its use to indicate heat loss from the cell. As illustrated in Figure 3-4, the thermocouple well was

placed within the tungsten filament element. Under low pressure conditions with. predominantly radiant heat transfer, heating of the thermocouple well by the filament could establish a significant temperature difference between the thermocouple well and the vessel wall. Since heat loss to ambient is a function of vessel wall temperature, this could result in a significant overestimate of heat loss to ambient and the corresponding excess power for cases where the filament is powered in



comparison with cases where heat input to the cell is provided by the cartridge heater at the bottom. Data from HPC regarding the operation of the Isothermal Calorimeter provided support for the expectation that the thermocouple well would be hotter than the vessel wall when the filament was powered, and a basis for estimating the magnitude of the effect. These data were used to adjust the data for the filament heating effect, with results as shown in Fig. 4-1. In discussing this adjustment with HPC staff, it was agreed that this problem could be eliminated by placing thermocouples on the outside of the vessel, an approach HPC plans to take for future testing. While this adjustment reduces the excess power from about 60 Watts as





indicated in Fig. 3-5b to about 40 Watts, there is still a clear indication of excess power production that correlates with the conditions required for excess power according to the HPC theory.

The Calvet Calorimeter cell is a much smaller device than the Isothermal Calorimeter cell, both in terms of physical size and range of input power. However, when placed inside an oven, it provides for better control of operating temperature and a much more accurate determination of thermal power production in the cell. It also provides a time dependent signal, indicating the time varying characteristics of the experiments, although short term variations in the reaction would not be detectable due to the long thermal time constant of the externally insulated thermopile. Since a continuous electrical output proportional to heat flow is generated by the thermopile, the signal can be used in conjunction with an input power signal from the power supply to calibrate the cell under control conditions. In the Penn State experiments, the filament power is produced by a highly accurate and stable constant power supply and the thermopile signal is zeroed out against the input power once steady state is reached in the absence of hydrogen. The input power is then held constant as hydrogen is introduced into the cell, allowing for a precise determination of the change in power production in the cell following the introduction of hydrogen. In the Penn State experiment in progress during the site visit, a fixed amount of hydrogen (the amount in the hydrogen container of Fig. 3-6) was available to the cell following opening of the valve to the hydrogen container. The indicated excess power slowly declined from an initial value of about 0.05 Watts to less than 0.01 Watts over a period of several days. This characteristic was consistent with a depletion of the hydrogen in the cell during the experiment. Initial analyses of the results are indicating excess power production on the order of 20 times that which would be generated by the hypothetical combustion of the hydrogen in the test cell. While the power level in the initial Penn State experiment was about a factor of 10 less than the power levels observed at HPC with operation at about 200 millitorr hydrogen pressure, the results could be quite significant from the standpoint of validation of the low energy hydrogen reaction. Atmospheric pressure operation of a vapor phase cell may be an effective way to produce sufficient quantities of gas to support more definitive experiments on the detection and characterization of hydrino. The vapor cell Calvet Calorimeter data being produced by HPC and Penn State provide strong support for the validity of the HPC concept, particularly in combination with earlier data produced by Penn State using sintered catalyst and spillover catalyst Calvet Calorimeter cells.

The Metal Hydride Cell has produced the highest power and the highest power density of any of the approaches to date. Measurements of cell pressure response as power is applied to the filament has confirmed the effectiveness of the hydrided wire as a source of hydrogen. This approach is an effective means for obtaining adequate hydrogen atom concentrations for testing and also for improving the understanding of the reaction process. It would not be a preferred process for general commercial application because of limits on the amount of hydrogen that can be stored and the resulting need to periodically replace metal hydride components as opposed to a continuous feed of hydrogen gas, and it could also exhibit performance degradation as







the stored hydrogen is depleted. However, it could have commercial potential in limited operation situations such as backup power applications. In the near term, it could serve an important role as a means of providing a convincing demonstration of excess power production.

The Tungsten Powder Cell is being developed as a means of obtaining high hydrogen atom concentration throughout the reaction cell volume. The tungsten powder provides a large surface area which can serve to dissociate hydrogen molecules when operating at elevated temperatures. Initial results were reported by HPC as indicating about 10 watts of excess power (about 10% of input power) from the device illustrated in Fig. 3-8 using 2.1 cubic centimeters of tungsten powder and operating at about 550°C. This concept is at a very early stage of development, and significant refinements and revisions to the device can be expected. For example, the initial device allowed communication between the outer region containing the heating element and the inner region containing the tungsten powder and catalyst compound. This raises a question as to where the reaction is taking place, since hydrogen around the filament will be dissociating and catalyst atoms could be present in the outer region. The device is being modified to seal off the inner region and provide a hydrogen and catalyst supply directly to the tungsten powder section of the inner region. With vibratory compacted powder as currently used, diffusion of hydrogen molecules and atoms, and of catalyst atoms through the powder may limit the power density. However, the use of a dispersed high surface area matrix of material which supports hydrogen dissociation when operated at elevated temperature is a likely avenue for development of an energy cell which could operate at sufficient power density and without electrical input to support commercial applications.

4.2.3 Vapor Phase Cell Development Status and Issues

HPC began working on the vapor phase cell concept in January, 1996. The vapor phase cell concepts are considerably simpler in their construction and operation than the earlier electrolytic cells, providing less room for errors and oversights as a basis for explanation of observed excess power. In addition, the amount of excess power production is increasing to a level that precludes instrument error as a possible explanation. Thus the vapor phase cells have the potential for providing a much more convincing case for the HPC concept than the earlier cells. Recent vapor cell results produced at HPC indicate a rapid advance in cell performance and production of excess power in each of several device configurations. Given these advances, HPC is concentrating on the gas vapor cell concept for testing and concept development.

Performance of HPC vapor phase cells, based on data obtained in the course of this assessment, is summarized in Table 4-1. Calculation of power density is relatively arbitrary because of the expected but not well characterized strong variation of reaction rates as a function of position within the cells. Thus three values for power density are given in the table. The first two assume a primary reaction zone within 1 or 2 mm of the hydrogen dissociation surface (filament) and calculate a power density based on the





HydroCatalysis Technical Assessment

DRAFT

resulting reaction volume. This approach is of more significance with regard to the development potential of the concept because devices can be designed such that the primary reaction zone encompasses most or all of the reaction chamber. The third value is an average power density based on the total volume of the test article, which is of less significance since it is a function of the design features of the test article rather than of the characteristics of the process.

Table	4-1 Power De	nsity Estimat	e Comparis	sons		
	Volume, cc	Power, W	Power Density, W/cc*			
			Reaction Zone		· 	
Cell Type			1 mm	2 mm	Cell	
At-Mar Lamp	150	2	4	1	0.013	
Isothermal Calorimeter	2500	40	6.4	1.6	0.016	
Calvet Calorimeter	20	0.5	1.6	0.4	0.025	
Metal Hydride	30	120	15	7	4	

The temperature is known to vary substantially within the cell, affecting the catalyst atom density distribution due to localized production on hotter surfaces and plateout on colder surfaces, and the hydrogen atom distribution varies strongly with distance from the dissociation surface (e.g., filament) due to recombination to form molecules, thus reaction rate (power density) will be a strong function of location. The power densities shown are calculated assuming a primary reaction zone within 1 or 2mm from the dissociation surface, and a relatively arbitrary value assuming the entire cell volume as a reaction zone.

The progress achieved by HPC on the vapor phase cells, which have only been under development for seven months, is remarkable and indicative of the potential for advancement of this concept. Performance levels achieved at HPC during the past several months, if validated by the Calvet calorimetry work underway at Penn State, should be sufficient to provide a convincing case for excess power production. The primary thrust of current work at HPC is on advancing the concept toward devices that have commercial application potential.

The primary technical issues with regard to commercial application of the HydroCatalysis process are achieving adequate power density and controllability of the process. These issues are discussed below within the framework of the likely characteristics of the HPC process as understood from the information obtained. The HydroCatalysis device which would produce energy and transfer heat to an energy conversion system working fluid or heat exchange surface is referred to as the energy cell. Supporting auxiliary systems (e.g., hydrogen and catalyst feed systems) would have to be designed to support the steady state and dynamic requirements of the energy cell.





- Power Density The power density achieved in the reaction section of the energy cells will drive the size of the cells as a function of output power. If high temperature operation is required, the material costs per unit volume of the energy cell may be considerable. The cost of fuel storage, handling and combustion equipment plus emission control systems of a fossil fueled system would be replaced with the cost of hydrogen production or storage systems plus the energy cell and supporting auxiliaries. The low to negligible fuel costs of the HydroCatalysis concept will support a premium in capital costs while remaining economically competitive, but energy cell reaction section power density will be a key factor in economic viability. As illustrated in Table 4-1, the power density obtained in cells operated to date is not well known because the spatial distribution of the reaction rate is not well characterized. From the overall data, power density in the range of 1 to 10 W/cc appears to have been achieved. Ideally, power densities in the range of other current energy systems (e.g., light water reactors, combustion turbines), on the order of 100 W/cc (see following section) would be desireable, but economic viability could probably be achieved at lower power densities. HPC projects a theoretical upper limit of power density of 55,000 W/cc, well beyond what is necessary or practically manageable. The disproportionation reaction mechanism postulated by HPC would enable multiple collapse of hydrogen atoms and a major increase in the energy production per atom, providing a plausible means of achieving the desired power density. A series of tests based on a preferred cell design and varying key parameters (e.g., hydrogen and catalyst atom density, temperature) to map out performance is needed to assess potential power densities and means of achieving them. The results to date are encouraging, given the limited time and resources expended on the vapor phase cell concept, but considerable work remains before a preferred cell design can be established and the needed tests conducted. In the interim, power density will remain a significant uncertainty.
 - Controllability The following discussion is based on an electric generation application, similar considerations would apply to heat or motive power applications.
 - Startup The first aspect of controllability to consider is starting a system and achieving a stable initial operating mode for power operation. As currently envisioned, the energy cell reaction zone would have to be brought to an elevated temperature and the reaction process would be initiated and stabilized at a minimum self sustaining level by the introduction and control of hydrogen and catalyst atom densities. This would have to be achieved by the energy cell in coordination with the operation of the power conversion equipment, since some degree of heat removal from the energy cell will be required at minimum power to establish a stable operating temperature.

HydroCatalysis Technical Assessment

DRAFT

- Power Operation Power operation would require the ability to achieve and maintain stable operation at any power level in the operating range, and to increase or decrease energy cell output power level with response characteristics as required by the energy conversion system for a range of normal operation and transient conditions (e.g., step load changes, component failures).
- Shutdown Shutdown would include a range of conditions from slow decreases in power level to unit trips. The characteristics and requirements of the energy cell and supporting auxiliaries for decreasing or terminating power generation and cooling down would have to be integrated with the corresponding characteristics and requirements of the power conversion equipment.

If the energy cell is required to operate at high temperatures with ceramic components (e.g., thermal insulation), controlling cyclical thermal stresses to support an adequate design life may be a primary requirement driving system design. The dynamic response of the HydroCatalysis reaction and the thermal response of the energy cell will need to be well characterized to support modeling for control system design and system operation.

4.3 Applications and Projected Products

A systematic technology and market development process is needed to evolve HydroCatalysis technology to commercial practice. Such a process matches technology attributes with market opportunities to identify target markets for the mature technology, as well as with chances for early market penetration. A brief survey of energy industry applications was conducted to gain an initial impression of the market profile.

In a broad sense, HydroCatalysis offers a new fuel option to the energy industry. Its market acceptance will be enhanced if it can be utilized without a major re-tooling of power generation equipment. Ideally, the HydroCatalysis reactor (or a secondary heat transfer loop) would fit within the envelop currently required for the heat generation and transfer function. For example, a gas turbine combustor is the zone in which the fuel/air mixture is ignited and combusted before expansion through the power turbine. A potential HydroCatalysis reactor application is to replace the fuel combustor function. The space envelope for the combustor, expressed as power density, for commercial gas turbines is estimated to be in the range of 50 to 150 kilowatts per liter. As a further point of comparison, the power density of a boiling water reactor (ratio of reactor power to the volume of material inside the fuel cladding) was calculated to be about 200 kilowatts per liter. On this basis, a HydroCatalysis reactor power density in the vicinity of 100 kilowatts per liter is desirable, although a factor of 2 or so in either direction is probably acceptable.





Based on currently perceived HydroCatalysis reactor attributes, a likely initial target application is to replace the fuel combustor for powering gas turbines. For the past several years, gas turbine technology has been the focus of government and industry sponsored efforts to reduce pollutants and improve the utilization of coal and natural gas. In addition, several innovative small turbine concepts have recently been introduced in an anticipation of a new market in distributed generation assets. The merits of this application include:

- Gas turbines comprise over half of new generation sales and are proliferating rapidly in the global market.
- In the current cost and environmentally sensitive market, gas turbine concepts
 provide the lowest capital costs, and thermal efficiencies approaching 60% in
 combined cycle applications.
- The relative sophistication and temperature regime of advanced turbine systems appear to be compatible with the HydroCatalysis reactor interface, i.e., high temperature (in the vicinity of 1400°C) heat exchanger technology.
- Sizable markets exist for units in the range of a few hundred kW to a few MW,
 i.e., units sufficiently large to realize credits for pollution control advantages and
 to economically support auxiliary systems (e.g., hydrogen generation, reactor
 preheat and vacuum systems), yet within the range of a practical multiple unit
 beta testing program.

General Electric, Westinghouse, Allison Engine, and Caterpillar's Solar Turbines are all participants in separate DOE cost-shared (25%) advanced turbine development projects for natural gas-fired systems. In addition, Hague International is participating in an innovative concept called an "indirectly fired cycle" for coal-fired systems that employs a ceramic heat exchanger to protect the turbine from combustion gases. Such heat exchanger technology may be relevant to the HydroCatalysis reactor interface. Hague is constructing a 2-megawatt industrial-scale facility for testing the ceramic heat exchanger. Results will form the basis for a Clean Coal Technology project at Pennsylvania Electric Company's Warren Station.

Two other recent innovations in gas turbine technology are the Capstone Turbogenerator and the Solar Turbines' T-300 Gas Turbine Generator Set. Both are relatively efficient (30 and 40%), small (24 and 300 kWe), high speed (96,000 and 37,000 rpm, respectively) that employ directly coupled permanent magnet generators and state-of-the-art electronic power conversion technology. These attributes provide exceptionally compact machines, well suited to the distributed generation/cogeneration market. Their somewhat lower turbine inlet temperatures (~800°C) may offer a less demanding initial interface requirement for incorporation of a HydroCatalysis reactor.

Stirling engine applications were also briefly reviewed and several innovative concepts may eventually be enabled by successful development of the HydroCatalysis reactor. For example, the Stirling Technology Company (STC) has produced a 350







watt prototype device labeled the RG-350 RemoteGen™ and is developing 1 and 3 kWe devices. Their target market is remote telecommunications installations, off-grid homes and cogeneration applications. The reference design couples a free piston Stirling engine with a linear alternator to continuously supply 120 VAC or 12 VDC power. STC claims a 60,000-hour maintenance free life for their machines and have completed 23,000 hours of endurance testing on small functional prototypes. Although advanced energy storage or HydroCatalysis may someday enable such devices to be used in broad applications independent of a utility grid, such as in developing countries, they are relatively inefficient (~20%) and markets are not yet developed.

Of course, a wide spectrum of other potential applications exists and range from the Rankine cycle for electricity generation to the direct use of heat, and it is quite possible that further investigation will reveal premium niche applications for which HydroCatalysis is ideally qualified. Given its potential to bring about profound changes in the energy industry, a market for very early consideration is "functional demonstration units". Small units that can be used to display elementary heat generation from the HydroCatalysis process will be of interest to industrial product developers. A potential use of such devices is to acquaint the OEMs of industrial equipment with HydroCatalysis technology so that they can develop strategies for adapting product lines as a prelude to licensing agreements. Such devices may be in the size range of a few watts, need not be prototypic of a commercial product, and have minimal reliability and equipment interface requirements. They will command a substantial price premium, and the interactions with OEMs can be a source of early feedback to the HydroCatalysis reactor development program.

It is recommended that the HydroCatalysis development program proceed from the outset with the means to acquire and assimilate market information. In addition to identifying target markets to guide technical work and niche markets as a source of early revenue streams, knowledge of end-user needs relevant to process control and O&M is an essential aspect of defining technical design requirements and establishing cost/price targets.

4.4 Economics and Environmental Considerations

At a conceptual level, a process which obtains many times more energy per unit volume from water than is available from oil would be expected to have a major economic advantage over existing energy sources. Likewise, the absence of combustion products or other typical waste byproducts would be expected to represent a major environmental advantage. These prospects are addressed briefly in the following subsections.

4.4.1 Economics

The ability to extract considerably larger amounts of energy from hydrogen via the HPC process relative to conventional chemical processes is fundamental to the





economics. By illustration, assuming an average energy release of 100 electron-volts per hydrogen atom, the energy content of a standard cubic foot of hydrogen would be about 23,000 Btu/ft³, in comparison with hydrogen energy content from the combustion process of about 340 Btu/ft³. As another comparison, the net energy content of water would be about 30 times the energy content of gasoline. Thus the fuel costs for this concept would not contribute significantly to electricity generation costs, which would be determined by capital and operation and maintenance costs.

In their Business Summary (Ref. 7, pg. 55), HPC provided the following data on comparative electricity generation costs:

Table 4-2 HPC Comparative Cost Projections			
Energy Source	Cost (¢/kWh)		
Coal	4-5		
Natural Gas	4-5		
Oil	4-5		
Nuclear	5-6		
Hydroelectric	4-7		
HydroCatalysis	<1		

EPRI was cited as the source of the cost of competing energy sources, noting that the cost estimates did not include externalities. For the purposes of this study, a detailed review of these costs was not conducted; however, levelized life-cycle cost data from a recent Energy Information Administration paper (Ref. 37) were used for an approximate cost comparison. Only coal and natural gas were considered in the comparison since these options represent the dominant fuel forms of new generation capacity additions for the near future. Using the projections of levelized cost for the year 2000 in 1994 dollars for a capacity factor range of 60-100% and regional variations, the ranges shown in Table 4-2 were developed for coal and gas fired generation with fuel costs of about \$1.25/MMBtu for steam coal and \$2.20/MMBtu for natural gas. For the HydroCatalysis process, a combined cycle gas turbine configuration was assumed, consistent with the discussion in Section 4.3, with allowances for parasitic losses associated with electrolytic hydrogen generation (~5% of gross generation) and a reduction in cycle efficiency (due to reaction chamber material temperature limits) relative to a combustion turbine. These results are also shown in Table 4-2. In practice, steam methane reforming may be a more economic means of producing the hydrogen (Ref. 38) than the electrolysis process assumed above, but the difference in cost would not significantly affect the above results.





Table 4-3 Revised Comparative (Year 2000 Levelized Co	e Cost Projections ost, 1994 \$)
Energy Source	Cost (¢/kWh)
Coal	4-5.5
Natural Gas	3-4
HydroCatalysis	1.5-2

In summary, while the cost advantage for the HPC process is likely to be less than projected by HPC, it is still substantial. Given the current total world electricity consumption, approaching 10¹³ kWh/year (Ref. 39), a projected market share of 33%, and a differential cost advantage of 2¢/kWh, a total of \$66 Billion/year is obtained. This is considered to represent a reasonable projection of the potential value of the worldwide application of the HPC concept to the electrical sector. The preceding analysis does not consider the cost advantage of the HPC concept associated with externalities such as the environmental considerations discussed in the following section. Policy development efforts to quantify and assess the costs of these externalities are continuing (Ref. 40), and could result in an additional cost advantage approaching the 2¢/kWh noted above.

4.4.2 Environmental Considerations

The quantities of water consumption, and oxygen and hydrino production for a 1000 MWe HydroCatalysis based multi unit combined cycle gas turbine plant were estimated, with assumptions and results as shown in Table 4-3 below.

Table 4-4 HPC CCGT P	lant Characterization
Description	Value
Plant Capacity	1000 MWe
Net Thermal Efficiency	45 %
H ₂ Energy Release, Avg	100 ev/H atom
Water Consumption	47,500 gallons/day
Oxygen Production	176 tons/day

The above values are based on multiple fractional quantum state hydrogen transitions taking place in the reactor such that on average 100 ev of energy is released per hydrogen atom produced for fuel. The actual average amount of energy per hydrogen atom is not known at present, since it is a function of the degree of collapse before the





reaction is terminated by the formation of a dihydrino molecule. The disproportionation mechanism could drive the reaction to lower levels of collapse, and much larger energy releases. Hydrogen production by electrolysis with an 80% efficiency of energy usage is assumed, with 5% of the gross generation being used in the electrolysis process. The net thermal efficiency of 45% includes this 5% loss, along with an allowance for a lower efficiency for the gas turbine relative to the best combined cycle units being deployed today because the temperatures are assumed to be lower than combustion turbine temperatures due to the need for a heat exchange surface between the HPC reaction gas and the air.

The environmental factors associated with coal-fired, gas-fired, and projected HydroCatalysis based generation are compared in Table 4-4 below.

Table 4-5 E	lectricity Genera	tion E	Environmental	Releas	e Comparison	
	Fuel Production		Fuel Transportation		Generation	
Coal	NO _x , CO _x , SO _x , particulates, hydrocarbons		NO _x , CO _x , SO _x , particulates, hydrocarbons		NO _x , CO _x , SO _x , particulates, hydrocarbons	
Natural Gas	hydrocarbons		NO _x , CO _x , hydrocarbons		NO _x , CO _x , hydrocarbons;	
HydroCatalysis	oxygen				NO _x , hydrino	

The shaded columns of the above table are intended to indicate the degree of significance of the release, with darker shading indicating greater significance. The releases from the coal and natural gas fueled generation noted are generally understood and will not be discussed further here. The HPC gas cell requires hydrogen as a fuel, resulting in the release of oxygen during the production of hydrogen from water feedstock. Oxygen is currently a marketable commodity, however, the quantities produced by a substantial penetration of the electricity generation market by HydroCatalysis would be expected to greatly exceed demand, resulting in release to the environment. The release of oxygen could be a net environmental benefit, replacing some of the oxygen source lost by the depletion of the tropical rain forests, although the magnitude of the release from the HydroCatalysis would be considerably smaller. For the gas turbine configuration, No. production is expected to occur in the high temperature zone around and downstream of the HydroCatalysis heat exchanger. As indicated in the above table, the effluents from the HydroCatalysis process would be much less detrimental to the environment than the primary existing options for power generation.

Despite the apparently benign characteristics of the HPC process, it is conceivable that some opposition could arise due to the permanent consumption of water in the production of hydrogen. An estimate was made of the water consumption assuming the HPC process was producing 33% of the current total world electricity



consumption with operating parameters consistent with Table 4-3. This resulted in an annual water consumption of 6.6x10^s gallons of water consumed per year. While this appears to be a significant quantity, it would take 370,000 years at this rate to consume an inch of water from the oceans.

5.0 Telephone Interviews and Site Visits

A number of telephone interviews and site visits were conducted in the course of this assessment. The perspectives and information gained through these discussions are reflected in the information and assessment provided in the earlier sections. The individuals and organizations contacted and the information obtained is summarized in the following sections.

5.1 Telephone Interviews

Telephone interviews are grouped in the following areas: (1) General Background, (2) Theory and Hydrino Validation, and (3) Excess Power Evidence. The interviews are summarized in the following subsections.

5.1.1 General Background

 Tom Passell, EPRI (Ref. 41) - As Manager, Deuterated Metals Research Program, Passell has managed EPRI research involving cold fusion and other related areas. Passell noted that EPRI had spent about \$10 million in cold fusion related research, and has confirmed that excess heat is present in some cases, but hasn't confirmed the source of the heat. EPRI's primary contractor, SRI, has not seen any positive results from light water, but they had not expected to see anything so they have not done much in that area. Passell had visited HPC and Thermacore (where an HPC cell was operating) in 1992, and felt there were considerable uncertainties in the cell configuration they were operating at the time. EPRI had funded an attempt to replicate the Mills process at AECL's Chalk River Laboratories, which was unsuccessful in demonstrating excess energy in Passell's view. He noted that HPC and Chalk River were involved in litigation regarding the content and distribution of the final report. Overall, Passell felt there remains a possibility that the HPC process is generating excess energy, but expressed reservations about HPC's strong convictions regarding the validity of the theory, which he felt could be affecting the interpretation of their data. The EPRI program budget for 1996 is \$200 K, including Passell's labor and expenses (Passell is now working half time), leaving about \$100 K for outside work. Their current focus is on identification of nuclear species from cell electrodes using neutron activation analysis, assuming some sort of fusion reaction is responsible for the excess heat. Passell noted that Ernest Criddle





of Ottawa University had been studying the HPC cell and would be a good source of additional information.

- Ernest E. Criddle, formerly Ottawa University (Ref. 42) As noted above, Dr. Criddle was recommended as a reference by Tom Passell of EPRI. Dr. Criddle has retired from Ottawa University, but has maintained an interest and involvement in HPC type electrolytic cells through his work with ESCO Energy Inc., a spinoff of the university. He noted that he believes something is going on with the cells, but he hasn't been able to figure it out, and has had trouble getting repeatability. He also noted that he was visited several years ago by Randy Mills and Bill Good of HPC, and that they have techniques about preparing and filling the cell which are critical to performance, and are not related to "textbook chemistry". He was unaware that HPC is now focusing on a gas cell, but said he is convinced that a gas cell is the way to go with the process, because it eliminates the chemical complexities of the electrolysis process in the liquid cell.
- George H. East, Stone & Webster Engineering Corp. (Ref. 43) Dr. East's name was provided by Mills as a reference for current interactions between HPC and SWEC. He said SWEC involvement began last fall with a visit to SWEC by Mills, followed by a SWEC visit to HPC. He said they have executed a confidentiality agreement with HPC, but that their work was on a minor level, having reviewed published papers and documentation obtained from HPC, but not having seen HPC's recent gas cells or audited their performance, and having limited knowledge of the details. They have been working with HPC on an unfunded basis to provide support regarding boiler options and energy conversion equipment. At this point, SWEC is interested in the concept, but are not sure how it's going to go, noting that the theory is controversial and that they would like to see more independent confirming results.
- Dick Mulik, Westinghouse (Ref. 44) Dr. Mulik is coordinating an assessment of HPC for the Westinghouse Science & Technology Center (STC). Mulik noted that Westinghouse "has been putting in some real money" into a program at STC this year, which is intended to reach a definitive conclusion regarding the HPC theory and low energy hydrogen. Westinghouse has been dealing with HPC on and off for the past several years, having done an in-house experiment several years ago which they considered to be inconclusive. No experimental work related to HPC is currently being performed within Westinghouse, but the current assessment is looking at both the theoretical and experimental aspects of HPC's work. Mulik noted that if they find the theory to be incorrect, they're going to have to come up with some other explanation for the experimental results (implying a conviction that something unusual is occurring). He said it would be premature to make any comment regarding Westinghouse's view of the technology at this point.



Mulik, along with Art Beyers of Westinghouse STC and Rex Ramsier of Westinghouse Bettis Atomic Power Laboratory visited Penn State on the same day as the TI visit (addressed in Section 5.2.3). Mulik stated that there is high level interest at Westinghouse, and that STC has until the end of the year to reach a definitive position regarding the HPC process. Ramsier said that the head of Naval Reactors had received a letter regarding the HPC process, which was the basis for Ramsier's participation in the review. He noted that he had attended a seminar at STC given by Mills in 1994, and that his trip report had raised some interest at Bettis at the time and caused him to be identified with the subject. All of the Westinghouse reviewers were skeptical of the Mills theory and unconvinced of the existence of hydrino from their review of the data. They were interested in measuring the thermal conductivity of the off-gas from a cell, expecting that hydrino would have higher thermal conductivity than hydrogen. They intend to work with Mills and Phillips of Penn State to plan and conduct thermal conductivity measurements (Mills had earlier expressed skepticism that this approach will be successful because of the quantities of hydrino gas required). Phillips agreed to collaborate with Westinghouse on performing the measurements, with the understanding that the work would be done in close collaboration with HPC.

5.1.2 Theory and Hydrino Validation

 Stewart Kurtz, Pennsylvania State University (Ref. 45) - Dr. Kurtz is Professor of Electrical Engineering and Vice Chair of the Materials Research Institute at Penn State. He has an industrial research background, having worked at Bell Laboratories for 10 years, served as Director of Research at Philips Electronics, and as VP, Engineering at Bristol Meyers before joining the faculty at Penn State. He became involved with the HPC concept about five years ago, when he met with Mills in Lancaster, PA as Assistant Director of the Materials Research Institute. He has been working to understand and challenge Mills' theoretical work since that time. He has involved a number of physicists in his review of the theory, and each of them have raised objections which have been addressed by further development of the theory. These challenges have resulted in substantial growth in Mills' book from the earlier versions to the current version. He also contacted H. A. Haus of MIT, who developed much of the mathematical formalism underlying Mills' theory (Ref. 46) and requested that he review the theory. Haus said the mathematics were correct, but he could not support the physics because it is not adequately supported by data. At this point, Kurtz believes HPC has demonstrated excess heat with reproducibility, and they need to develop more data regarding the presence of hydrino to provide complete confirmation. He has been talking with Mills and Jonathan Phillips about experimental procedures that could provide sufficient proof of the existence of hydrino.





Kurtz also said that he had followed the Thermacore involvement with HPC in the development of the concept. He had high regard for Yale Eastman, the founder of Thermacore, and for his company, noting that Eastman had invested several hundred thousand dollars in independent confirmation of the excess heat and development of potential commercial applications. Thermacore had demonstrated excess heat, but were unable to identify a commercial application for the devices they were working on.

Barry Turner, National Radio Astronomy Observatory (Ref. 47) - Dr. Turner has been working with HPC regarding the potential for confirmation of the existence of hydrino via astrophysical data. He has been working with HPC on the development of a proposal to search for evidence of hydrino using an NRAO radio telescope (Ref. 48). Turner said that Mills has a case for looking further for astrophysical evidence, but not a compelling one. He said that some of the spectral lines have been "flat out misidentified" in earlier HPC documents, but there are enough questions left over to be of interest. A search of the type being proposed is very difficult because the frequency region to be scanned has to be identified accurately. Due to the high resolution required, a small frequency range has to be identified to limit the telescope time required. On the whole, Turner believes it is unlikely that the search will shed new light because they can't calculate the energies of hydrino hyperfine splitting accurately. In addition, the kind of gas that would be detectable as containing hydrino would also emit recombination lines. Although the recombination lines could be calculated precisely, they would take up about 15% of the spectrum in the region of interest (~29 GHz) and thus would require extensive calculations to assure that lines that might be assigned to hydrino were not recombination lines. A failure to confirm the existence of hydrino by the experiment would not be very significant because it would be very difficult to obtain a strong positive result. However, the range of spectrum being considered has never been searched, and given the importance of a positive outcome, he thinks it should be done.

Turner said that an earlier proposal (Ref. 48) based on part on the HPC interpretation of the Labov and Bowyer paper (Ref. 21) had not been successful. In the review of the proposal, the referees had focused on the proposal's interpretation of the Labov and Bowyer data, and concluded that the original interpretation of the data by Labov and Bowyer is correct. From his review of the communications and the paper, Turner said he agrees with the referees, and believes that a revised proposal with fewer lines cited would have a better chance. He noted that diffuse X-ray spectroscopy is not an easy thing to do, and he would not be surprised if not all of the lines expected from hydrino transitions are present. He hopes to get additional support from Mills in the form of calculation of hydrino collision probabilities as input to preparation of a revised proposal in August for telescope time during the coming winter. He noted that the telescope to be used will be shut





down after one more year, so this would be the last chance at conducting the experiment as proposed.

Reinhart Engelmann, Oregon Graduate Institute of Science & Technology (OGI) (Ref. 49) - Dr. Engelmann is a member of the faculty of the Department of Electrical Engineering and Applied Physics at OGI, currently on a leave of absence. He received a degree in Nuclear Physics from the Technical University in Munich, Germany in 1961, and his current research interests include modeling and design of solid-state photonic devices: quantum well lasers and optical waveguides. Engelmann documented a review of Mills' second book, Unification of Spacetime, the Forces, Matter, and Energy (Ref. 50), and has been following Mills' progress for several years (he is a member of the HPC Science Advisory Board). Engelmann's perception is that Mills works on a highly intuitive scale, then once he has an intuitive picture, he tries to wrap it into a mathematical description.

Engelmann said he has a very strong feeling that Mills has proper ideas, particularly regarding the low energy forms of hydrogen. However, he is not completely in agreement with everything that Mills had done in developing the theory from a mathematic point of view. He said one of the problems is that Mills presents information in a form physicists are not used to, and that although he has worked closely with Mills, he cannot follow everything. He believes there are some inconsistencies in the theoretical framework, noting treatment of the Dirac δ function in spherical coordinates, and conclusions regarding the Heisenberg Uncertainty Principle as examples of his concerns. He feels that what is needed is for others to become interested and begin working on it, and believes that the best way to make that happen is to advance an energy generation device and expand the empirical evidence supporting the theory. He noted that he had visited Mills at HPC in early 1995 and again in April, 1996, and was very impressed with what had been accomplished in advancing the cells during that period.

5.1.3 Excess Power Evidence

Michael G. Jacox, INEL (Ref. 51) - Michael Jacox was identified in a list of references provided by HPC in conjunction with work done at INEL in 1992 with regard to independent confirmation of excess heat from an HPC cell. He was contacted as an audit check on the list of references. Jacox was located in Albuquerque, where he is currently on assignment with the Air Force on an unrelated project. He was surprised that I was asking him about the results of his work, in that the paper describing the results was never approved for release by INEL management. However, he said he stands by the results of the work, and believes that he did get positive results regarding the release of excess heat in the cell.

į



- Bob Shaubach, formerly Thermacore (Ref. 52) Shaubach left Thermacore in 1995, having worked on the HPC theory and technology since 1992. On of the first experiments performed by Thermacore was the operation of an electrolytic cell obtained from HPC that was reported by HPC to have produced 50 watts of excess power. Thermacore did observe 50 watts of excess power from the cell, in one case with only 5 watts of input power in a pulsed mode. Shaubach was also involved in the conduct of experiments using hydrogen permeation through nickel tubing and nickel powder permeated with hydrogen. All the experiments demonstrated excess power, but did not provide a basis for a commercial application. Shaubach has not kept up with the evolution of the HPC cells, so was unaware of recent developments.
- Nelson Gernert, Thermacore (Ref. 53) Gernert was the project engineer on the experiments conducted by Thermacore relative to Mills' theory. He noted that they had conducted experiments with electrolytic cells, hydrogen diffusion through nickel tubing, and hydrogen permeated metal powder, and they saw excess power in all cases. He said they didn't see anything that would be inconsistent with Mills' theory, and he is convinced that they were seeing excess power. However, after several years of trying different approaches, they were unable to get the power density up to a level which would be sufficient for commercial applications. Thermacore is currently putting a high priority on developing volume manufacturing capability for heat pipe cooling devices for laptop computers, and hasn't been actively pursuing the HPC concept for several months. Some of their cells have been loaned to HPC for interim use. Thermacore expects to get the cells back, and would be interested in taking another look if HPC makes progress on increasing the power density.

5.2 Site Visits

5.2.1 HydroCatalysis Power Corporation

A visit to the HydroCatalysis Power Corporation offices was conducted on June 17-18, 1996. Prior to the visit, Technology Insights executed a confidentiality agreement with HPC to allow access to recent data and internal HPC documents. Much of the visit was spent in discussions with Mills regarding the theoretical basis for their concept and the experimental evidence for excess heat and hydrino. These discussions served to strengthen TI's understanding of these areas, and are reflected in the respective sections of this report. A tour of the laboratory area of the HPC offices was conducted by Bill Good, and included operating cells representing the most recent gas cell concept. A particularly striking element of the current cells is their simplicity as indicated by the relatively small number of connections (tubing, instrument and power leads) to the cells and by drawings of the cell internals. This characteristic





should be of significant value both in demonstrating the validity of the concept and in translating the concept into practical applications.

HPC was visited again on July 2-3, 1996 in conjunction with a meeting to discuss the results of TI's initial review and arrive at an agreement for a standstill period for further due diligence review and venture development. Prior to the meeting, the current experimental work being conducted in the HPC lab was reviewed with Bill Good, and data produced by recent vapor cell experiments were obtained. The initial results of a TI review of these data was discussed with Bill Good at HPC on July 17, 1996 in conjunction with a round of visits to supporting university laboratories. Activities in the HPC laboratory were again observed, including initial operation of a higher temperature cell utilizing a tungsten powder concept. The results of the HPC visits are reflected in the discussions of the technology provided in other sections of this report.

5.2.2 NovaTech

NovaTech is a small (currently 7 professional employees) engineering and technical services company located in Lynchburg, Virginia, and made up primarily of former Babcock & Wilcox engineers. NovaTech has been identified by HPC as a potential engineering arm to provide design, fabrication and testing services for the development of an energy cell to be used in a prototype unit. Since several key NovaTech personnel are currently on assignment in California, a meeting was held in the Los Angeles area to discuss NovaTech capabilities and interests relevant to the HPC concept. NovaTech representatives at the meeting included Richard Rochow, President; Lew Walton, Director of Business Development; and Barry Miller.

NovaTech has experience that is directly applicable to the HPC gas cell concept, and appears well qualified to support the evolution of the cell design. As an engineering contractor on the Air Force Space Nuclear Thermal Propulsion (SNTP) project, they provided design and testing support services for high temperature, high power devices utilizing hydrogen. Design capabilities include mechanical design, structural analysis, thermo-hydraulic analysis, materiels and systems engineering. They also have fabrication and testing experience with devices at temperatures and with system complexities that would envelope the anticipated HPC cell development.

NovaTech has had interactions with HPC going back several years, and has a good understanding of the concept and its primary characteristics. In 1994 they developed and presented a proposal to HPC for a systematic exploration of the variables associated with the electrolytic cells to achieve an economically viable level of performance. That proposal was not funded, but in 1996 NovaTech has performed internally funded work pursuing the gas vapor cell concept. The work was conducted under limited funding and time constraints, and has not succeeded in producing measureable excess power. They believe the negative results may have been due to shortcomings in their procedures, but have suspended further work to address other





commitments. (Subsequent telephone discussions with NovaTech personnel indicated that they may have seen a small (~1.5% of input power) amount of excess power in an experiment conducted in early July.) NovaTech recently submitted a proposal to HPC to design, fabricate and operate a vapor cell which could provide for a systematic and controlled variation in key parameters (e.g., temperature, hydrogen pressure, catalyst pressure). They expressed reservations about the validity of Mills' theory, particularly with regard to modeling of the universe. However, they are confident that excess power has been produced in HPC cells, and are motivated to participate in the development of the concept.

5.2.3 Pennsylvania State University

Dr. Jonathan Phillips of the Penn State Chemical Engineering Department has been conducting calorimetry experiments on HPC cells utilizing a catalyst and flowing hydrogen. TI met with Dr. Phillips on July 15-16, 1996. Representatives from Westinghouse were also visiting Dr. Phillips' lab on July 16, and participated in the lab tour and subsequent discussions. The Westinghouse participants and their intended future actions are discussed in Section 5.1 in the context of an earlier phone conversation with Dick Mulik of Westinghouse.

Phillips has been developing and working with precision micro calorimeters and developing catalytic processes for the past four years in areas unrelated to HPC, and is increasingly recognized as an authority in the field. His work with the HPC cells utilizes thermopile based calorimeters capable of accurately measuring changes in power of less than 0.01 watt relative to an established baseline. He has filed declarations in support of HPC patents based on early work with HPC cells (Ref. 54). Recent results from spillover catalyst cells designed and fabricated in collaboration with HPC and operated by Phillips demonstrated energy releases well in excess of known chemical processes (Ref. 15).

Dr. Phillips is well qualified for performing work on the HPC cells directed toward identifying and quantifying excess power generation. He has a strong personal interest in the technology, and has contributed significant amounts of time and discretionary resources to studying cell performance. However, he has taken a low key approach to working with HPC in light of the negative environment within the academic community surrounding any work which could be perceived as "cold fusion" related. A brief tour of the Chemical Engineering Laboratory and review of other experiments being conducted by Phillips and supported graduate students was confirming of positive impressions regarding his capabilities gained from initial discussions.

Testing of the HPC vapor cell concept is at the very early stages, having begun in mid-July, 1996. The first test was underway during the site visit, with initial results indicating excess power was being produced. In a phone conversation subsequent to the visit, Phillips said that their initial analysis indicated total energy generation in the cell equivalent to about 20 times that which would result from combustion of hydrogen





given the hypothetical presence of oxygen (confirmed by TI based on observations made during the visit). This first test was operated at near atmospheric pressure, far above the approximately 1 torr (1/760th of an atmosphere) of primary interest to HPC. While this was the result of a miscommunication between Phillips and the graduate student conducting the work, Phillips noted that he likes to approach the early runs in an experiment in a somewhat random fashion because the results aren't always as expected, and information can be gained by not focusing the testing too early. Operating the cell at near atmospheric pressure has produced results which indicate energy generation at a level detectable by the highly sensitive calorimeter developed by Phillips. While these results may not be very useful in the optimization of an energy production device, they may point to a means of efficiently producing hydrino gas predominately composed of n=1/2 atoms. This may significantly accelerate the process of obtaining results which will support the broad acceptance of the existence of low energy hydrogen.

5.2.4 Lehigh University

Dr. Albert Miller of the Zettlemoyer Center for Surface Studies at Lehigh University has been conducting X-ray Photoelectron Scattering (XPS) measurements on nickel cathodes from electrolysis cells provided by HPC, and a carbon cathode from a cell operated at Lehigh. As noted earlier, the XPS data are considered by HPC to be important evidence of the existence of hydrino. Miller discussed the difficulty of using XPS for identification of hydrogen or any material similar to hydrogen because of the small cross section for photon interaction (on a normalized scale where the cross section of carbon is 1.0, the cross section of hydrogen is 0.0002). Assuming hydrino has a cross section similar to or less than hydrogen, substantial quantities would be required to obtain a signal, and very small fractional quantities of impurities, or secondary peaks from other materials present (i.e., potassium), could produce a signal which would mask or be mistaken for hydrino. HPC maintains that iron is the primary impurity which could produce a peak in the region of 55 ev, where a hydrino peak would be expected, and since iron has been shown not to be present by other means (TOF-SIMS), the observed peaks are assigned to hydrino. Miller believes the results of experiments to date neither prove nor disprove the existence of hydrino, because low level impurities in the electrode or the electrolyte which could be concentrated at the cathode surface during the electrolysis process, or secondary peaks of potassium could produce the feature assigned to hydrino by HPC.

Dr. Miller believes that definitive results regarding the existence of hydrino could be obtained from a gas phase XPS experiment. This experiment would flow off-gas from an HPC cell, which would be expected to contain hydrino and may be processed to enrich the hydrino content, through an XPS instrument. Miller expects that such an experiment would require about a half liter of gas (~ 10% or greater hydrino). The total scope of the experiment, including producing baseline results on pure hydrogen and other samples as appropriate, is estimated to take between three and six months and cost between \$100,000 and \$200,000.





5.2.5 Franklin and Marshall College

As noted previously, Dr. John Farrell of the Chemistry Department of Franklin and Marshall College was an early collaborator with Mills in the development of the theoretical basis for the HPC concept (Ref. 3). Franklin and Marshall is a small (~1800 students), private liberal arts college located in Lancaster, PA. Mills attended Franklin and Marshall, receiving a BA in Chemistry in 1982. Farrell said Mills was widely recognized as an exceptional student, and typically presented a strong intellectual challenge to the faculty in the courses he took, asking difficult questions based on an in-depth fundamental understanding. After obtaining a M.D. from Harvard in 1986, Mills received support from Franklin and Marshall in the form of equipment and laboratory space to pursue development of medical technology devices. The initial development of Mills' quantum mechanics theory took place during this time, leading to publication of the initial book (Ref. 3) on the subject.

In the course of discussions at HPC in conjunction with this review, Mills had identified Farrell for follow-up regarding the astrophysics data supporting the existence of hydrino. Farrell said he believes the strongest evidence from astrophysics comes from the paper by Labov and Bowyer (Ref. 21). The paper was found by Bill Good in a literature search for astrophysics evidence of the existence of hydrino. In this case, the spectral lines had been identified from the raw data by the authors, and were in excellent agreement with the expected lines from hydrino transitions (see Table 4-1). Farrell said that a paper documenting the matching of the Labov and Bowyer results with low energy hydrogen emission spectra was submitted to Astrophysical Letters and Communications (Ref. 22), a companion publication to the Astrophysics Journal which published the Labov and Bowyer results, but the paper was not accepted for publication. Farrell expressed frustration at the unwillingness of the leaders of the astrophysics community to consider alternative interpretations of observed data. However, Farrell felt the other astrophysical data comparisons (e.g., solar flare data) were based on direct interpretation of the raw data, which requires a sophisticated level of understanding of statistical applications in astrophysics, and thus are of lesser confidence than using the original Labov and Bowyer data interpretation.

Farrell is a member of the HPC Science Advisory Board as well as a shareholder in HPC. Some of the early confirmatory work replicating HPC electrolytic cells was performed at Franklin and Marshall (Ref. 25), but no work is being conducted at present in support of HPC. Farrell noted that two other members of the Chemistry Department at F&M hold HPC shares, indicating the degree of support for the concept. Farrell also noted that two members of the F&M Physics Department have been following the development and validation of Mills' theory.

6.0 References

- FAX: C. N. Winningstad to Fred Buckman, "RE: New Paradigm for Utilities", May 13, 1996.
- 2. Technology Insights, "HydroCatalysis Power Corp. Assessment", July, 1996.
- 3. R. L. Mills and J. J. Farrell, <u>The Grand Unified Theory</u>, Science Press (1989).
- E. Storms and C. Talcott, <u>Proceedings of Workshop on Cold Fusion</u> <u>Phenomena, Santa Fe, NM</u>, May 23-25, 1989.
- 5. S. Jones, et. al., "Observation of Cold Nuclear Fusion in Condensed Matter", Nature, 338, 737, (1989).
- M. Fleischmann, S. Pons and M. Hawkings, "Electrochemically Induced Nuclear Fusion of Deuterium", J. Electroanalytical Chem., 261, 301 (1989).
- HydroCatalysis Power Corporation, "Business Summary" (1996).
- N. V. Sidgwick, <u>The Chemical Elements and Their Compounds</u>, Volume I, Oxford, Clarendon Press, (1950), p. 17.
- 9. R. L. Mills and S. P. Kneizys, "Excess Heat Production by the Electrolysis of an Aqueous Potassium Carbonate Electrolyte and the Implications for Cold Fusion", Fusion Technol., 20, 65-81, (1991).
- R. L. Mills, W. R. Good and R. M. Shaubach, "Dihydrino Molecule Identification", Fusion Technology, 25, 103, (1994).
- 11. R. L. Mills and W. R. Good, "Fractional Quantum Energy Levels of Hydrogen", Fusion Technol., 28, 1697-1719, (1995).
- N. J. Gernert, R. M. Shaubach, "Nascent Hydrogen: an Energy Source", SBIR Phase I Project, Sponsored by Wright-Patterson AFB, Report 11-1124, March, 1994.
- Bradford, M.C.; Phillips, J.; "A Calorimetric Investigation of the Reaction of Hydrogen with Sample PSU #1", Report to HPC, (1994).
- 14. Phillips, Jonathan; Shim, Hyunsip; "Additional Calorimetric Examples of Anomalous Heat from Physical Mixture of K/Carbon and Pd/Carbon", Report to HPC (1996).
- 15. Phillips, Jonathan, "Additional Examples of Anomalous Heat: Hydrogen Mass Balance", Report to HPC (1996).





- 16. R. L. Mills, The Grand Unified Theory of Classical Quantum Mechanics, (1995)
- 17. R. L. Mills, <u>Unification of Spacetime</u>, the Forces, Matter, and Energy, Science Press (1992).
- 18. Letter, R. Engelmann to R. Mills, Review of <u>Unification of spacetime, the Forces, Matter, and Energy</u>, June 3, 1994.
- 19. Mills, R., et.al., "Fractional Quantum Energy Levels of Hydrogen, Representative Recent Results, Prepared for PacifiCorp 7/3/96", (1996)
- Mills, R. "Identification of Hydrinos--Hydrogen Atoms in Fractional Quantum Energy Levels--by XPS (X-ray Photoelectron Spectroscopy)", (1996)
- S. Labov and S. Bowyer, "Spectral Observations of the Extreme Ultraviolet Background", The Astrophysics Journal, 371, 810, (1991).
- 22. Farrell, J.; Mills, R.; Good W.; "An Alternative Explanation of Extreme Ultraviolet Emissions from Dark Matter", Submitted for Publication to Astrophysical Letters and Communications (1993).
- 23. Mills, R.; Kurtz, S.; Turner, B.; "A Search for Hydrino A New Form of Hydrogen". (1995)
- 24. New Scientist Forum, "Happy Birthday, Helium", April, 1995.
- V. C. Noninski, "Excess Heat During the Electrolysis of a Light Water Solution of K₂CO₃ with a Nickel Cathode", Fusion Technology, 21, 163 (1992).
- 26. R. Notoya, "Cold Fusion by Electrolysis in a Light Water-Potassium Carbonate Solution with a Nickel Electrode", Fusion Technology, 24, 202 (1993).
- T. Ohmori, M. Enyo, "Excess Heat Evolution During Electrolysis of H₂O with Nickel, Gold, Silver, and Tin Cathodes", Fusion Technology, 24, 293 (1993).
- R. T. Bush, "A Light Water Excess Heat Reaction Suggests that 'Cold Fusion' May Be 'Alkali-Hydrogen' Fusion", Fusion Technology, 21, 163 (1992).
- 29. M. Shrinvasan, et.al., "Tritium and Excess Heat Generation During Electrolysis of Aqueous Solutions of Alkali Salts with Nickel Cathode", 3rd Annual Conference on Cold Fusion (1992).
- 30. S. B. Nesterov, A. P. Kryukov, Supporting declaration in support of Mills patent application No. 07/825, 845, "Energy/Matter Conversion Methods and Structures".



- N. J. Gernert, R. M. Shauback, "Nascent Hydrogen: An Energy Source", Final 31. Report 11-1124 to Wright Laboratory, Air Force Material Command (1993).
- J. M. Niedra, I. T. Myers, "Replication of the Apparent Excess Heat Effect in a 32. Light Water--Potassium Carbonate--Nickel Electrolytic Cell*, NASA Technical Memorandum 107167 (1996).
- HPC writeup with INEL raw data, "Experimental Verification by Idaho National 33. Engineering Laboratory*, (1993).
- Westinghouse STC Report, "Evaluation of Heat Production from Light Water 34. Electrolysis Cells of HydroCatalysis Power Corporation" (1994).
- Haldeman, C., et.al., "Excess Energy Cell Final Report", MIT Lincoln Laboratory 35. meeting viewgraphs (1995)
- J. E. Jones, et.al., "Faradaic Efficiencies Less Than 100% During Electrolysis of 36. Water Can Account for Reports of Excess Heat in "Cold Fusion" Cells", J. Phys. Chem., 99, 6973 (1995).
- Beamon, J. A., Wade, S. H., "Energy Equipment Choices: Fuel Costs and Other 37. Determinants", U. S. Energy Information Administration/Monthly Energy Review, April, 1996.
- D. Morgan, F. Sissine, "Hydrogen: Technology and Policy", Congressional 38. Research Service Report for Congress, April, 1995.
- U. S. Energy Information Administration, International Energy Outlook 1996. 39.
- J. Carlin, "Environmental Externalities in Electric Power Markets: Acid Rain, 40. Urban Ozone, and Climate Change*, Energy Information Administration Renewable Energy Annual (1995).
- Personal Communication, Dr. Thomas O. Passell, Manager, Deuterated Metals 41. Research, Nuclear Power Group, EPRI, June 4, 1996.
- Personal Communication, Ernest E. Criddle, University of Ottawa (retired), June, 42. 1996.
- Personal Communication, George H. East, Mechanical Equipment Group 43. Manager, Senior Principal Engineer, Stone & Webster Engineering Corp., June, 1996.
- Personal Communication, Dick Mulik, Westinghouse Science and Technology 44. Center, July, 1996.





- Personal Communication, Stewart Kurtz, Pennsylvania State University,
 Electrical Engineering Department and Materials Research Institute, July, 1996.
- 46. Haus, H. A., "On the Radiation from Point Charges", American Journal of Physics, **54**, 1126-1129 (1986).
- 47. Personal Communication, Barry Turner, National Radio Astronomy Observatory, NRAO Headquarters, July, 1996.
- 48. Mills, Randell; Kurtz, Stewart; Turner, Barry; "A search for Hydrino A New Form of Hydrogen", 1996.
- 49. Personal Communication, Reinhart Engelmann, Professor, Electrical Engineering and Applied Physics Department, Oregon Graduate Institute (currently on leave in Munich, Germany), July, 1996.
- 50. Engelmann, Reinhart, "Book Review, <u>Unification of Spacetime, the Forces, Matter, and Energy</u>", (1994)
- 51. Personal Communication, Michael G. Jacox, Lockheed Martin Idaho Technologies Company (currently on loan to Air Force), June, 1996.
- 52. Personal Communication, Bob Shaubach, formerly Thermacore, Inc., July, 1996.
- 53. Personal Communication, Nelson Gernert, Project Engineer, Thermacore, Inc., July, 1996.
- 54. Phillips, Johathan, Declaration in support of HPC patent for "Energy/Matter Conversion Methods and Structures", December 14, 1995.

THIS PAGE BLANK (USPTO)





Kline-Anderson, Inc.

Review of Schedule and Resource Requirements to Develop a HydroCatalysis Functional Prototype Unit

Final Report for Technology Insights

October 23, 1996

Confidential and Proprietary

8926 Kirby Drive, Houston, Texas 77054 Fax: 713-665-5934 713-660-8414

Copy of 8 : Assigned to BLACKLIGHT POWER





.

.





Apparently there is color, apparently sweetness, apparently bitterness; actually there are only atoms and the void.

Democritus 420 BC







Table of Contents

Section Title			age	
1,	Introduction	·····································	1	
2.	Review Background Material	(Subtask 1)	2	
3.	Visit to NovaTech and HPC	(Subtask 2)	2	
4.	Regarding Resource Requirements	(Subtask 3)	7	
	Viability of Projected Schedule	(Subtask 4)	13	
6.	Conclusions of a Technical Nature		14	
7 .	Off-Task Observations		15	

Attachment A

Commitment to Commercialization Investment Phases I - IV. (Technology Insights)

Attachment B

HydroCatalysis Project Phase I Schedule dated 9/24/96. (Technology Insights)

Attachment C

Definition of Phase I Test Cell Milestones (Technology Insights, assisted by Kline-Anderson).

Attachment D

List of Documents received by Kline-Anderson Inc. as background material from HPC and Technology Insights.

Attachment E

"Conceptual characterization of HydroCatalysis Turbine Application Options" (Technology Insights).

Attachment F

"S-1 Radiant Recirculating Boiler" (Technology Insights).





THIS PAGE BLANK (USPIC





1. Introduction

Objective:

The scope of work for this technical evaluation contract consists of the following:

"Review the current status of the HydroCatalysis process development and plans for development of the functional prototype unit, and provide comments and recommendations regarding the planned tasks, resource requirements and projected schedule."

The subtasks for completing the review were broken down into four areas, that are addressed below. COMCO has defined four stages in the "Commercialization Investment" of Dr. Mills's new hydrogen energy source (Attachment A). Kline-Anderson has been asked to provide a "reality check" or a "sanity check" on the Phase I development program, and "red line" the schedule that comprises the first of the four stages (Attachment B). The descriptions of the Test Cells 1, 2 and 3 which were initially given to me were outdated, and needed additional work and recasting. Clarification of what these milestones are was necessarily an integral part of my task. The resultant redefinition of these milestones was finalized by Jim Kendall and is included as Attachment C.

As part of a Due Diligence process that has a bearing on funding levels and timing (staged funding). We (Kline-Anderson) take a conservative view of the technical aspects of this project. I have based my report strictly on my fact finding trip with Jim Kendall to HydroCatalysis Power Corporation (HPC) and the NovaTech labs, and the written information provided to me. In this role, I have been mindful that considerable investment funds are contemplated, and the planning that describes how these funds will be utilized is key to ensuring that resources will be used effectively and efficiently and towards the absolute success of COMCO. We have deemed it wise to err towards the conservative, allowing Technology Insights and PacifiCorp to make up their own minds about how much optimism to inject. Where I did not see a clear process underway, I have pointed that out so that Technology Insights, who has access to many more documents relevant to this technology, and who have months of study behind them about this technology, can incorporate my comments into the total picture.

Most importantly, the alterations in the revised schedule result in a planning document that represents the most likely outcome of the work to date at any given time in the progress of the work. Milestones have been revised to be natural breakpoints in the progress of work, so that now slips or advances in the work schedule may be easily accommodated. This schedule will continue to serve as a working document for tracking results of the investment, and can form the basis for allocation and reallocation of resources along the way. The intention is to provide COMCO management with additional information and working tools to ensure the overall success of this venture.





2. Review Background Material (Subtask 1)

A list of the documents I received and reviewed is in Attachment D.

My study was a technical evaluation of the process to commercialize this invention only, and I have not done a technical review of Dr. Mills's Hydrino Theory, or of the experiments that lead to the design of the vapor-phase reactor. For the purpose of this study, I have assumed that excess heat is evolved by these energy cells, that this result has been verified by independent laboratories, and that the phenomena is explained by Dr. Mills's Hydrino Theory. I reviewed all items in Attachment D only, thus, I have not reviewed the data or experimental methods from this previous work, which goes back several years. Neither have I attempted a review of Dr. Mills's Theory. Therefore I am not opining on the experimental history, or the theory in this report.

However, I saw nothing during my fact-finding trip that contradicted the assertions and representations made by HPC about any of their work, or about Dr. Mills's theory.

3. Visit to NovaTech and HPC Facilities to review the current status of activities relevant to the integrated schedule for development of a functional prototype unit. (Subtask 2)

As explained to me in my visits to HPC and NovaTech, by their personnel, and in conversations with Jim Kendall of Technology Insights, the HPC/NovaTech current plan as outlined is the following (points A through D):

(A) The most long-lived excess heat cell experiments were completed at Thermacore. Multiple experiments at Thermacore demonstrated excess power, but the work was abandoned because the results did not provide a basis for a commercial application.

The electrolytic cells were rejected as a design basis for a commercial unit due to the limitations in power density that they could achieve. In seeking economically viable power densities, the concept of the hydrino transition reaction was re-examined and a new energy cell design was invented from first principles. HPC asserts that the transition reaction can occur in the gas phase, as well as in aqueous solutions. If this assertion is proven true, this enables a new generation of hydrino energy cells to be built that take advantage of traditional chemical process ideas; such as continuous feed of reactants, high operating temperature, and continuous operation.

(B) It is the transition to this new type of cell that is the focus of Test Cell 1 work that is in progress at HPC and NovaTech. The objective of this Task is to demonstrate a cell that will operate repeatedly and controllably. The operating parameters have been defined as:





Operating Parameters

- Catalyst vapor pressure (catalyst concentration)
- Choice of catalyst
- Choice of hydrogen dissociation surface: filament or foam
- Molecular hydrogen gas pressure
- Atomic hydrogen gas pressure
- Filament operating temperature (current supplied to the filament)
- Cell hydrogen flow rate

Optimal operating parameters are expected to be 2 Torr of potassium, 200 milliTorr of molecular hydrogen, and as high a filament temperature as possible to atomize as much hydrogen as possible. (1 atmosphere of pressure = 760 Torr). This information was based on the results of the quartz cell, and calculations by Dr. Mills.

- (C) The design goals are listed in Attachment C. Most importantly, catalyst vapor pressure can be varied by controlling the temperature to the potassium iodide oven with an external heater. Previous designs have used heat from the filament to vaporize the potassium. The addition of this degree of freedom will permit the best operating vapor pressure for potassium to be documented. Secondly, hydrogen can be flowed through the cell continually, the first step in going towards a continuously working cell.
- (D) Fabrication of a test bed, which I recommend be expanded to a conventional Test Fixture is underway at NovaTech. A Test Fixture will allow experimentation with different operating scenarios, by serving as a standard testing device for different designs of the energy cell. (See Section 4).

HPC Site Visit:

The current activity centers around a dramatic change in energy cell design. In changing design from the aqueous cells to vapor phase cells, the problem of getting atomic hydrogen and catalyst ions in the gas phase had to be solved. Bill Good, HPC's research director, has stated that potassium and rubidium both are active catalysts for the transition reaction process. Further he states that alkali halogens are the best chemical forms to utilize and that several salts were tested, and iodides were determined to be the best choice. According to Mr. Good, an operating temperature of greater than 730 C to keep the ions from condensing out on the walls of the vessel is required. He also presented the following information:

Initial testing was done with a quartz tube reaction vessel. Data from this tube indicate that optimal operating conditions will be 2 Torr of potassium ions, 200 milliTorr of molecular hydrogen with a filament temperature (reaction surface temperature) as high as possible (limit on the tungsten is 2000 C).





Tungsten was chosen as the filament material due to its good high temperature properties. However, tungsten reacts with oxygen, thinning the filament and leading to failure. Thus a good vacuum must be established prior to powering up the filament and introducing the reactants. The reaction vessel should be evacuated to below the milliTorr levels that are achieved now, and an upgrade from the current mechanical pumping system is required to ensure a clean vacuum free of contaminants.

Evolved heat is measured by differential calorimetry. HPC and NovaTech have invented a new high temperature calorimeter for this purpose. It is constructed from firebrick, and the energy evolved is measured as a changing heat gradient between two points located radially outward from the energy cell's center. As excess heat is evolved from the energy cell, the rise in temperature differential between the two points is measured. No experimental runs were attempted with any cells until calibration curves for the new calorimeter were stable and reproducible. It is critical to be meticulously careful with these calibrations, since the observable of excess heat will be the chief experimental result that will guide the optimization of these energy cells. Meticulous thermal isolation and calorimetry that is above question is key to this process. It is the single most important issue for the overall success of the development plan.

Recommendations:

Because the energy cell is not totally enclosed in the firebrick, but the ends of the cell protrude from it, there are two heat paths out of the cylindrical energy cell: Radially out through the firebrick, and axially out the ends of the cell. Since conduction and convection dominate over radiation for heat transfer mechanisms, it is reasonable to assume that the proportion of heat that flows via each path remains constant throughout any heat generating operation of the cell. If this proportionality does stay constant, then the measurement of excess heat recorded by the thermocouples located radially out from the center of the cell will indicate data accurately. This assumption may or may not hold up with the addition of the tungsten foam as well as it holds up for a simple tungsten filament. Final resolution of this issue will require construction of a "test bed calorimeter" that completely encloses and isolates the apparatus, like the conventional bomb calorimeter.

This test-bed standard calorimeter should be specified with multiple thermocouples, ten or twelve, that are monitored and recorded by a data acquisition system. Design and construction of this device will require additional materials and instrumentation beyond what is presently in place at HPC. This could be incorporated as part of the Test Fixture. Because the thermal measurements are key to this project, the firebrick calorimeter must be fully characterized and calibrated to a standard calorimeter if possible. If a commercial calorimeter cannot be brought in for standardization against a well known instrument, an acknowledged calorimetry expert can be brought in to independently study and confirm that the calorimeter is fully functioning appropriately. This expert can certify that the calorimeter is functioning properly, and that it is the best way to handle this high temperature situation.





An inherent limitation of this energy cell is the temperature limit of the stainless steel vacuum vessel. The vapor pressure of KI at 710 C is 1 Torr. To achieve 2 Torr, the temperature must be raised to 730 C. For the grade of stainless steel used, a temperature limit of 760 C has been specified, but Matt Ales at NovaTech is willing to push the limit up to 800 C. Certainly commercial energy cell units will require an advanced materials solution, and the test cell development program must reflect this.

Two test cells are slated for operation by HPC (TC1B and TC1C) to improve the understanding of the process by variation of key operational parameters. I have listed these parameters in the box above. To map the multiple parameter-space of the performance of this energy cell, each parameter must be varied independently and systematically. This data guides test cell design and will form the basis for understanding the dynamic characteristics of the prototype energy cell, and indicate requirements for process control instrumentation.

In addition to an upgrade of the vacuum system and test-bed calorimeter, additional testing equipment is required. A high quality stable power supply for the filament, additional thermocouples, and a hydrogen flow meter to measure molecular hydrogen delivered to the reaction vessel is a minimum equipment list for this task. At least two professionals full time should be devoted to this effort. A data acquisition system to monitor and record pressures, temperatures, current to the filament, and current to the potassium heater must be incorporated with these testing cells. This is an important step in the development and understanding of this technology and constitutes a conventional lab Test Fixture.

NovaTech Site Visit

The NovaTech team present included Richard (Hawk) Rochow, Matt Ales, and Lewis Walton. They have expanded their space to house this experiment. In our discussion with NovaTech a quartz energy cell encased in fire brick was described. This work was internally funded by NovaTech and designed to be a "quick and dirty" attempt at independent verification of the evolution of excess heat. It was a static system, capable of no gas recharge. Catalysts used were potassium nitrite and potassium iodide, with heat to the catalyst from the filament only: no independent control. Zirconia and alumina were used as insulators in this cell, with a marginal vacuum system. The calorimeter, which was originally constructed of calcium silicate (failure mode: warping), was replaced with the firebrick insulation that forms the basis for the current calorimeter. Here the simple firebrick delta-T method for measuring heat flow was developed. Results indicated 3% excess heat was evolved, with an estimated 2% uncertainty in the measurement.

In designing Test Cell 1, they described numerous significant design changes that were made based on their experience with the quartz cell. The quartz tube was replaced with a stainless steel vessel with an external catalyst reservoir. Internal aluminum oxide insulation was added to protect the stainless steel wall from thermal damage. A tungsten foam core for dissociation of hydrogen was installed to maximize tungsten surface area. Expected maximum centerline operating temperature is 1500 K, with an absolute

4





maximum at 1800 K, where the alumina will start dissociation. A flowing hydrogen gas system was installed.

Experimentation up to Oct. 16th had not resulted in a statistically significant observation of excess heat. NovaTech proposed several reasons for the failure of the cell to evolve heat. Among them are the following:

- Control of the catalyst location and partial pressure was not sufficient to deliver catalyst to the reaction volume at appropriate concentrations, and at the right moment in the experimental "run" of the cell.
- Large time constant of the calorimeter may be obscuring results.
- Failure of tungsten filament at high temperature and flow conditions.
- Possible contamination of the tungsten foam rendering it inactive for hydrogen dissociation.
- Contamination due to inadequate vacuum.
- Persistent contamination due to alumina insulators.

Recommendations:

To address these issues, they plan to run at higher centerline temperature to achieve greater dissociation of hydrogen gas to atomic hydrogen. They may run with the filament and without the foam. A turbomolecular vacuum pump has been acquired by NovaTech to be fitted to the energy cell. This addition will solve the problems of impurities to a large degree by improving the ultimate vacuum the system can reach, but cannot totally ameliorate the oxygen and water contamination that is the product of the slow outgassing of the thick, hot, alumina insulators. This is seriously problematic and progress will be faster once the alumina is eliminated.

A lengthy discussion of the alumina insulation highlighted the fact that it is a source of oxygen and water in vacuo, and due to the size of the insulators, will take a long, long time to bake out completely. These insulators will also retard heat flow to the surface of the cell for heat transfer in a heat exchanger. Several other choices for insulation were discussed and molybdenum foil emerged as the early favorite, due to its relatively cheap cost (compared to other advanced materials). I recommend that this change be effected immediately, in the multi-layer geometry that NovaTech suggested. It will give their cell a higher temperature capability immediately, and speed progress.





4. Provide comments and recommendations regarding resource requirements for planned tasks leading to the fabrication and initial operation of a functional prototype unit. (Subtask 3)

Test Cell 1

Performance milestone goals require demonstration of excess power over the noise level of the calorimeter (estimated at 2% in the delta T measurement by NovaTech), repeatably and sustained over hours.

Test Cell 1 is currently being modified at NovaTech. Several important issues have been identified that need work-arounds. The most fundamental is the vacuum quality.

While "perfect" mechanical pumps can achieve an ultimate vacuum of 40 milliTorr, this is usually right after a rebuild or general overhaul has been finished, and most pumps only get to 80 or 100 milliTorr, as both NovaTech and HPC have experienced. NovaTech has tried to stretch the quality of the vacuum they get by using the conventional fix: cyclic pumpouts and flushes with an inert gas. This is sound lab practice, and might be good enough if it weren't for the alumina insulators, which present a lengthy outgassing problem due to their thickness. Even after a reasonable "bake-out" period, oxygen and water due to the alumina may persist. The NovaTech solution, to go to greater pumping capacity is a right choice. If they continue to flush with an inert gas, they might try dry nitrogen instead of helium, because it is cheaper.

Thermal isolation of the energy cell and the firebrick calorimeter has been discussed above. I recommend that the firebrick calorimeter be redesigned for complete encasement of the energy cell, and calibrated to a known standard. This will be involved, but will pay off with increased accuracy in measurements. The time constant of the calorimeter (response time) must also be clearly demonstrated, so we will know if results are being obscured. NovaTech is already considering this problem by comparing the centerline temperature excursions to the delta-T measurement. The uncertainty in the delta-T measurement must clearly be established at 2%. This can be accommodated within the Test Fixture.

A significant materials problem has become evident in the operation of this test cell: The entire reaction vessel must be kept above the condensation temperature of potassium iodide (melting point 682 C). The operating temperature selected to achieve the desired vapor pressure of potassium ions in the cell is 710 to 730 C. Inorganic salts are not known for their reflux tendency back into a furnace, and it is unlikely that a substantial liquid phase of KI is resident in the cell. If the potassium ions or KI molecules were condensing out on any surface below 682 C no positive results in excess heat will be observed due to the absence of the reactant. Further, the potassium must be a lone ion to participate in the hydrino transition reaction. The clear indication is that the entire reaction vessel must be operated at temperatures of at least 730 C, and probably higher. In a commercial energy cell, higher operating temperatures (at the surface of the cell) are desirable, as this gives the cell superior heat transfer efficiency, so solving this problem sooner rather than later is wise.





The alumina insulators can probably be run at the desired temperature - however, due to their mass and geometry, it will lengthen the time for the cell to achieve thermal equilibrium at the operating temperature. Further, the problem of oxygen and water contamination from the alumina remains. Direct lab experience in scaleup operations requiring alumina material as pass through insulators or internal static separation units, underscores the need for lengthy bakeouts. The porosity of this material allows outside atmosphere to permeate it each time the vacuum is vented. In this case the problem is critical enough that we recommend replacing it as soon as possible to ensure accurate results in testing.

The proposed solution from NovaTech is to fashion a multiple foil insulator to protect the stainless steel walls from excess heat. This is a good solution for Test Cell 1 and should be implemented now. Not only is the thermal problem solved, but the contamination problem is eliminated, and the design for the cell is simplified. In the commercial cell, the vacuum wall itself must be fabricated from an advanced material. It is prudent to begin testing and evaluation of materials now, as heat shields, in preparation for selecting the final reactor vessel material. This is a serious problem and will take some time to address fully. It comprises a significant modification to the cell, therefore after its implementation the cell must be recalibrated with control runs. NovaTech estimated the cost for molybdenum foil to effect this change at about \$15,000 for one cell. This may be underestimated, and this will be a one-time purchase, but if this solves the problem a much larger purchase of it will be needed.

Test Cell 1	Objective: To achieve a design of a cell that will operate repeatedly and controllably, and use as a basis to formulate a strategy for subsequent cell development
Design Goals:	Status:
Independently control catalyst vapor partial pressure (utilize an externally heated reservoir, no	An external heater has been fitted to the catalyst reservoir, converting it into an oven.
high temperature seals). Utilize a flowing hydrogen cell (prevent "fuel" starvation).	Hydrogen flows in to the reactor through the catalyst furnace.
Overcome the thermal limitations of previous vessels & insulation (keep stainless steel vessel sufficiently cool, but keep stainless steel vessel hot enough so potassium iodide catalyst precipitation is reduced).	Undergoing redesign and modification now, see above. Ultimately will require fabrication from advanced refractory materials.
Design and fabricate a relatively inexpensive test bed (allow for high surface area tungsten foams or powders, allow for various catalysts, investigate other materials, investigate different operating scenarios (T, P, flow, etc.)).	The initial model is in place at NovaTech, but requires a higher quality vacuum system and instrumentation linked to a data acquisition system to record results of different operating scenarios. See "Fabrication and Operation of Test Fixture" below.





To operate at these elevated temperatures all viton seals must be replaced with metal seals. This will require machining new flanges, and may require machining a new stainless steel reactor tube.

The best control protocol must be agreed upon and used consistently. A nondissociating heat source should be considered for control runs of the calorimeter.

After the above modifications are completed and the energy cell is operating, it is reasonable to presume that one or more iterations of design and modification will be required. This will slip the schedule for Test Cell one considerably.

Other technical additions that NovaTech proposed and I also recommend are the following:

- Data acquisition system: to track thermocouples, gas flow, and current supplied to filament.
- Improved catalyst pressure control
- Attempt to eliminate catalyst losses to cool spots.
- Delta-T thermocouples at faster responding locations (and more than two)
- Greater range in power supply/controllable constant power source.

I estimate minimum personnel requirements for the NovaTech team at 4 people full time. This is significantly higher than their current level of effort.

Fabrication and Operation of the Test Fixture, TC1A and TC1B:

The concept of the Test Bed is important and should be expanded to be a conventional Test Fixture. The last design goal for the Test Cell 1 is to fabricate a test fixture to investigate operating scenarios (parameters). Instrumentation needed for optimization of the process will include the following: A constant power - power supply, additional pressure gauges, pumping system upgrade to improve the vacuum (impacts impurity level in the cell), and metering to monitor hydrogen gas flow into the cell. Acquisition of a residual gas analyzer to determine content of the reaction cell should be seriously considered.

This test fixture, instead of being an operating model, serves as a standard testing device for different designs of the prototype energy cell. It will support the development of auxiliary control systems to service the steady state and dynamic requirements of the energy cell (Test Cell 2 performance goals).

It will generate comparable test data all the way along the program, for each change in the energy cell. An automatic data acquisition system run by a dedicated computer is integral to this fixture. It measures all important operating parameters, including amount of reactants delivered over time to the cell, pressures, heat signatures from thermocouples from digital meters, etc. This is all saved to disc for every test run. A graphic paper printout of the data portrays different variables over time. This record-keeping provides a record that documents progress and shows whether milestones are being achieved. It





records a complete data set for analysis and troubleshooting of problems. This test fixture is common lab practice and requires standard instruments.

It is unwise and ill-advised to use a test cell that is incrementally modified and integrated into its own data gathering system for this purpose because any problem that may have occurred that was overlooked can skew results. A test fixture is a work station that, for example, has a multi-lead cable that is plugged into the energy cell under test. It is advisable that the firebrick calorimeter be a permanent part of the test fixture itself. The test fixture houses the metering devices and data acquisition system.

The redesign of TC1A and TC1B as independent test fixtures, with calorimeters that are calibrated to a standard, creates a data acquisition system that records all experimental events, and the results are kept in lab notebooks. This is useful for a number of reasons, among them financial and experimental, and for demonstration purposes. For demonstration to third parties, who will eventually want to see this data (OEM's), it provides a standard lab unit where all cells have been evaluated with results that are easily compared to each other. This issue takes on even more significance since Test Cell 1 hasn't produced a positive result yet, in terms of excess heat. As soon as the cells start generating excess heat, baselines for operations and outcomes will be automatically recorded in the test fixture, facilitating the optimization, and design/modification cycle.

This level of documentation - at each step - increases the overall probability of success of the Phase I program, and lays a foundation for interaction later with OEMs. A person with extensive laboratory experimental experience (advanced degree), and extensive management experience should be put in place to provide strong leadership to the design and testing teams. This leader will keep teams on task, and get them the materials/resources they need for quick work-arounds in between milestone reviews with management.

Conclusions:

The level of professionalism and care displayed by the NovaTech personnel is high and consistent. They appear organized, thorough, thoughtful and prepared to go forward. They have made a business based on prototyping hardware for space applications, which makes them experienced not only in hardware design and methods development, but in working with extreme operating conditions. In the case of space systems, hardware must withstand extremes of temperatures and pressure along with the possibility of frequent thermal cycles. This group is very well-qualified to lead the Test Cell development team and engineer these cells for scientific accuracy as well as functional reliability with a continual awareness of the requirements of the eventual commercial unit. They are a key resource for this project, and the depth, scope and experience that they bring to their work substantially increases the likelihood of the absolute success of this entire Phase I development program.

Their team would be more effective if it were augmented in several ways. They need an expert calorimetrist available to them for quick consultation concerning the operation and calibration of the new firebrick calorimeter. This would be a senior, perhaps retired





person who would be available for occasional discussions. They also need available to them an advanced materials expert, who they have already identified. As the program proceeds, this person will become more and more central to the effort, and should be brought in as soon as possible. Other additions will probably become necessary as the project evolves, and NovaTech has indicated an awareness of this and is ready to recruit expertise as it is required. Their demonstrated ability to identify quickly and solve problems that emerge throughout the course of this project, and assign appropriate personnel to work tasks is critical. This team should head the design team meetings for further clarification of performance goals and design issues for work in progress. They are best qualified to lead the Phase I Test Cell effort.

Another recommended addition to personnel is a veteran government-trained configuration management person who would be utilized at 1/2 or 3/4 time to provide tight configuration and release control for procurement records, non-design drawings, and design drawings. Scientists and engineers typically rely on files for this activity, and do not record this information systematically or completely in their lab notebooks. Files can be lost, or accidentally destroyed.

Test Cell 2

The resource requirements for accomplishing the design and performance goals of Test Cell 2 present a slightly different kind of problem. As the basis for this task, there will already exist an energy cell that produces excess heat over hours of operation. Meeting the goal of 24 hours of continuous operation will require that the auxiliary process controllers be functional and can feed reactants to the energy reaction volume of the cell reliably and steadily. It remains to be discovered if the performance goal of 1 watt per cubic centimeter in the steady state is enough for self-sustaining operation.

At this stage, the power that is generated will now include the heat necessary to sustain the reaction. As a development device, there is no provision for extraction of useful energy, its entire energy production is going in to sustaining its operating temperature, or to ambient losses. The power generated will balance the heat loss to ambient in steady state operation. In later work, when the energy extraction/utilization device (such as an operating field system) is introduced, all the excess power won't be devoted to running the energy utilization device. Some power will be pulled back to sustain the transition reaction in the energy cell, and other energy will be put into electrical feedback for hydrolysis of water to generate hydrogen. In a commercial device, the system will be optimized for these factors. This fraction of energy used to sustain the cell and generate hydrogen may be interpreted as a fuel cost.

Personnel requirements may need to be adjusted for this task, based on the experienced gained in completing Test Cell 1, and this decision should be incorporated in the final Test Cell 1 design review.





Test Cell 3 and the Functional Prototype Energy Cell

Continually during these tasks the COMCO Commercialization Team must stay in contact with the Test Cell Design team concerning issues related to manufacturabilty: scaleup considerations/constraints and market information. During these stages, the Phase I development program must become increasingly interactive. Monthly design reviews are recommended to facilitate this process.

Also a continual dialogue between the engineers who are building the test cells and the COMCO person responsible for future interaction with OEMs must center around the expectations and requirements that must be met for a functional prototype energy cell. A first step in this direction is Jim Kendall's "Conceptual Characterization of HydroCatalysis Turbine Application Options" (Attachment E), and the detailed description of one of the ten options, "S-1 Radiant Recirculating Boiler" (Attachment F). Interaction and dialogue must be ongoing to ensure that the Phase I development work is focused on the requirements of the field prototype, and aligned with the constraints of the energy utilization device that it will be integrated into. This dialogue must be continual, although it may require only a low level of effort to maintain. This should be part of the "initial product options" line 62.

Already this activity has indicated that the commercial energy cell must be small to accommodate high power density on the inside and good heat transfer on the outside of the cell. Initial dimensional estimates are two to four cm in diameter and as long as possible (constrained by the kinetics of the transition reaction). The cells must operate at high temperatures (above 730 C), must maintain a vacuum inside, hold up to pressurized air or water outside (for some options), and have good heat conduction to the walls of the cell to facilitate its role in a heat exchanger. This activity is already generating intellectual property for COMCO. These integrated designs must be carefully documented and treated as sensitive trade secrets. Patentability of these designs for devices must be explored.

Feedback from this team must be factored into the Test Cell 2 and Test Cell 3 design objectives. In particular the startup method for initiating the transition reaction in the test cells, once they are operating as part of a heat exchanger must be considered and planned for by Test Cell 3. For example, initial heating of the energy cells might require that the pressure wall incorporate selective surface reflection capability. Other design requirements will develop in the course of this Phase I program. Frequent interaction and discussion between the Test Cell Design teams and the commercialization team at COMCO will ensure that these issues are dealt with early on in the process and efficiently.

At the Test Cell 3 / Functional Prototype Energy Cell demonstration stage, a cohesive life cycle operation paradigm needs to be outlined. The analysis can be concluded regarding what redesigns may be necessary to demonstrate number of cycles, number of closedowns and restarts will be necessary and expected. Early marketing studies would help identify these constraints such as how often an operator can afford to shutdown and restart the unit. This life cycle analysis is part of the continual comparison of design





specifications and customer needs that goes on for the entire Phase 1 effort as a background activity. The design after this one will generate a demonstrable shut-down and startup system for the energy cell, that occurs without human intervention. Also an estimate of how many cycles the unit will be required to execute, and its operating cost parameters can be determined towards the end of the Phase I planning period.

5. Provide comments regarding the viability of the projected schedule and recommendations for adjustments as appropriate. (Subtask 4)

COMCO has created an aggressive schedule, clearly so that commercialization can proceed as rapidly as possible. When it was determined that there was no cogent listing of performance goals for the test cells (milestone definition), I drafted a set that Jim Kendall and I worked on so they could be included in this report. As a result, the milestones were designed to be natural breaks in the course of work (slip/advance points). Kline-Anderson's independent calculation of the time required to reach each milestone matches up well with the original estimates in the COMCO schedule (Attachment B) after the Test Cell 1 milestone. We have recommended that personnel be augmented in several areas to meet the time goals. Once this performance milestone has been reached, the remainder of the schedule should be reviewed.

In Phase I development programs, such as this one, timeline milestones are often difficult to predict and to achieve owing to the uncertainties in the nature of development work. In this case, a radical design change to the energy cell has been adopted (aqueous phase to vapor phase). Until Test Cell I operates successfully, no one can say how much the schedule may slip, because there isn't a test cell that works yet. Given that the delivery date for the Test Cell 1 report is 12/3, the design team for this is in a very tough spot. This means the work must be completed by Thanksgiving. Even with augmenting the design team as discussed above, it would be reasonable to add 8 weeks to this task, to provide for procurement and implementation of the moly foil, calibration of the calorimeter, and enough process control ability to sustain the reaction for several hours. At least two more complete design/modification iterations are recommended. It could be approximately December 15 before NovaTech has a cell that they can begin to optimize for power density and duration of run time. During this period, they will have addressed several performance goals: 4, 5, 6 (see box). But will only be in a position to begin on 1, 2 and 3. Allowing an additional eight weeks for looking at 1, 2, and 3, puts the milestone for Test Cell 1 at Feb. 15. This is a best case scenario and assumes no new fundamental design problems emerge.





Performance Goals Test Cell 1

1. Show excess power operating over the noise level of the calorimeter (2% in the delta T measurement). Target excess power generation is 10%

2. Sustainable over hours (limit condensation/precipitation of catalyst and oxidation of tungsten filament)

3. Repeatable demonstration of excess power.

4. Controllable (controlled approach to excess power operating conditions and stable operation while generating target level of excess power)

5. Operating temperature 1000 to 1400 degrees C in the "hot zone" reaction volume as measured by the type C thermocouple.

Better understanding of cell insulation and refractory materials requirements.

This is all non-trivial laboratory work that has to be done when changing a basic apparatus, and even with augmenting the NovaTech staff, people who are accustomed to this sort of problem, it will take time. This is a significant schedule slip that is not avoidable.

Another likely place for a schedule slip to occur is if the redesign, management review and go-ahead takes more than the one day that is allocated for this task. To address this issue, and ensure that management is prepared, before the milestone date, for possible reallocation of resources, monthly design reviews are strongly recommended. These reviews should be on site, and conducted by COMCO's project manager and consultants that are selected for this purpose.

Because of the unavoidable uncertainty in the timeline for the milestones, it is important to create a concrete and clear understanding of the work in progress so that adjustments can be made prior to the milestone reviews. Monthly meetings are not too frequent at this stage. This uncertainty cannot be avoided, but its impact has been minimized by the formulation of specific design and performance goals for each step of the way, so that COMCO management can track work closely. This is a conventional way to handle the risk elements involved in Phase I development

As the degrees of risk are removed, it becomes more possible to make a concrete schedule that the COMCO team can stick to. But this actually is not realistic to expect before the first testing of the functional prototype unit itself. After that point, it is Kline-Anderson's experience that total schedule slippage approaches about 6% per year (this will be in Phase II).

Conclusions of a Technical Nature

For successful commercialization of this device, three goals must be met:

1. Increase in the power density that the cell will evolve: A reasonable goal for this is 100 to 150 kW/liter reaction volume. This is the comparable figure for boilers (reference Jim's report). It is estimated that a figure as low as 50 kW/liter will be economically viable





in a commercial unit. The economic viability cutoff power density depends on the features, benefits and costs of the final system.

- 2. Controllability of the process: An increased understanding of the interdependence of the operating parameters, their interdependence (degree of coupling), and instrumentation to control each must be put in place. This will result, ultimately in the basis for process control at the industrial (field test unit) level. Initially, this will be a simple on/off switch, or, ideally, a dial-type control that will vary the energy output of the cell.
- 3. Prolonged operating duration at a self-sustaining power level: The cells must continue to evolve energy after a starting procedure has been executed, and all energy input into the cell withdrawn.

The program is silent about several important concerns: Safety issues, such as storage and disposal of hydrogen gas have not been addressed. Possible rate limiting steps that may prevent the technology from being scaled to economic viability have not been questioned. For example, what chemical kinetics and process dynamics can be anticipated and provided for early in this program? Is the input current in a linear relationship with power evolved, and does that impact scaleup? Are there hidden dynamic characteristics of the process that will preclude scaleup? Does this reaction have a self-limiting aspect, and is there a competing quench reaction.

7. Off-Task Unsolicited Observations

Early marketing studies need to identify how many times in a week or month an operator can afford to restart his unit, and later cell designs must address this. This is the type of commercialization and scaleup issue that will come up more and more often throughout this work. Commercialization of this technology will be highly interactive owing to the nature of the process. Design reviews each month at all labs, are critical to this effort, and the report from the review should have the same intensity and focus that I have given one.

The unit first shown to outsiders, must operate without human intervention. It should be as easy to turn on as throwing one switch, and all safety gating should be in place. A self-sustaining run mode with appropriate shut off is required. To get the maximum financial return from a third party, this unit should not be shown to anyone before it is ready. COMCO cannot show a unit that doesn't work well and then claim to be able to fix it later.

I am concerned about the lack of formal peer review throughout the years Dr. Mills's theory has been published. There has been some peer review of an informal unpublished nature on Dr. Mills's theory. I am aware of Englemann's book review (noted in Technology Insights Technical Assessment). It is surprising that there is not one independently published paper that reports on the fundamental work in his theory, since it





was first published in 1989. It is provocative in its use of the Maxwell non-radiative boundary condition, and the use of the 3-dimensional Dirac delta function. For example, the interpretation of the Planck constant and the particle behavior of the electron is very interesting, and these ideas would seem to attract comment and dialogue from others. However, there seems to be a high threshold for serious consideration of the theory by the physics community. This may be due, in part, to the fact that the theory is contrary and revolutionary, and developed by an individual with unorthodox credentials.

COMCO is already generating intellectual property now.

In all aspects of the technology, but particularly in the scaleup into the commercialization of the technology, constant attention must be paid to intellectual property protection. This activity includes accurate documentation of trade secrets, filing of patents, international PCT filings, and all other aspects of intellectual property regime maintenance.

A COMCO Technical Advisory Board should be formed.

OEMs

An important part of the Phase I schedule involves discussions with OEMs. A focus of the Phase I work should be to prepare for these interactions from the beginning of the Test Cell work. We have expanded on the idea of a Test-Bed in the discussion of the Test Fixture above. The value of the Test Fixture, and the documentation that it creates about the energy generating process, is in these interactions with OEMs. It is our opinion that work should continue in secret until an appropriate Demonstration Unit exists to show OEMs. This is not equivalent to Test Cell 2.

The Demonstration Unit needs will be the first unit that anyone outside of COMCO, PacificCorp, HPC, or NovaTech is shown. This unit must operate without human intervention. It should be as easy to turn on as throwing a switch. All safety gating and release valves need to be in place, and it must start itself up independently, and convert itself over to the self-sustaining running mode automatically. This process should be evidenced to observers by easy to read meters. By throwing the "Off" switch, it must shut down in an appropriate and safe way. It is certainly acceptable to still have some engineering issues left, such as materials issues, and some scaleup. However, it is unwise to show a unit that doesn't work well (every time it is turned on), and add the assurance that it can be made reliable later.

Until this demonstration unit exists, we urge COMCO not to show intermediate results to anyone. Any disclosure of technology and progress contains risk for COMCO, and the potential benefit of the disclosure must be weighed against the risk. To get maximum return and involvement from an OEM, or other third party, an advanced level of development is advised. Our opinion of the "Conventional Wisdom" for return on investment during the commercialization stage is in the graph below. The amount an OEM will be willing to pay to get involved rises dramatically between a Sustainable Unit to a Stand Alone Functional Prototype. Return scales inversely with risk. On the graph





an idea, or "Notion", is worth "x" dollars at its inception; all the risk for getting the product based on that idea to the market remains at 100%. As commercialization proceeds and risk is removed from the investment, the number of dollars that an investor is willing to pay increases. We have depicted this by scaling the value (x) that the original notion was worth. For example, once a Free-Standing Lab Unit exists, an investor would be expected to pay 10 times the amount of the value of the invention at the "Notion" or idea stage. As risk is removed from the venture due to the progress of the commercialization work (move right along the x-axis), then at the stage of a Commercial Unit in Beta Test the only risk remaining is the financial risk of the final step to the market (labeled <10%). There is a dramatic increase in value from the One-Off Lab Unit, to the Scaled-up Free Standing Model. COMCO can maximize its investment value by progressing as far along the commercialization phase as possible.

Dr. Mills's desire to talk to OEMs too early is a risky approach and in fact goes against the conventional wisdom that you keep people away as long as you possibly can, and reduce the risks as far as you can, to realize the maximum financial return from your investment. If OEMs see a unit that is not working well, sustainably, consistently, or can't be turned on remotely with a safe shut-down, financial possibilities will be diminished.

COMCO Leadership

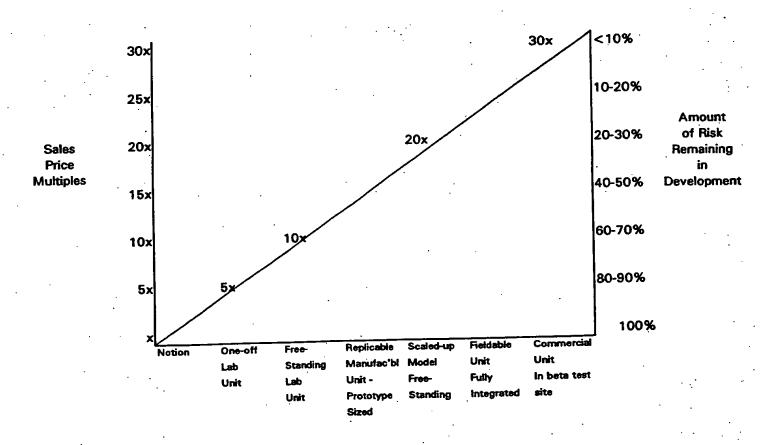
Finally, the role of strong leadership provided by COMCO cannot be overstated. The success of this Phase I effort depends on a high level of interactively, communication, and cooperation between PacifiCorp, COMCO, HPC and NovaTech. This can be achieved through regularly scheduled conference calls, e-mail, and monthly design review meetings at each site conducted by COMCO's project manager and select consultants selects. To perform on this aggressive schedule, no delays due to miscommunication can be permitted.

• !





"Conventional Wisdom" Regarding Sales Price of An Opportunity (SP) to an OEM.







Attachment A

Commitment to Commercialization Investment
Phases I - IV. (Technology Insights)





THIS PAGE BLANK (USPTO)



A

10. Phase Structure/Commitment to Commercialization Investment

The following phases will overlap in time:

Phase I - Functional Prototype (~2 years)

Development and evolution of energy cells to address identified initial device application(s). Integration of hydrocatalysis energy cells with one or more energy utilization devices (e.g., gas turbine) for operation in a shop environment. Unit operation and modifications to identify and resolve resulting technical issues.

Phase II - Commercial Prototype Engineering/Fabrication (~1-2 years)

Design, supporting subcomponent testing (as necessary and practical), fabrication and factory acceptance testing of energy utilization devices for field operation in demonstration projects.

Phase III - Demonstration/Commercial Unit Engineering (~1-2 years)

Operation of prototypes, analysis of operating data, revisions to prototype design to establish final commercial design plus unit cost and reliability projections.

Phase IV - Commercial Production Infrastructure (~1-2 years)

Manufacturing engineering, retooling, quality assurance program, and production and factory acceptance testing of initial production units.





THIS PAGE BLANK (USPIC)





Attachment B HydroCatalysis Project Phase I Schedule dated 9/24/96. (Technology Insights)

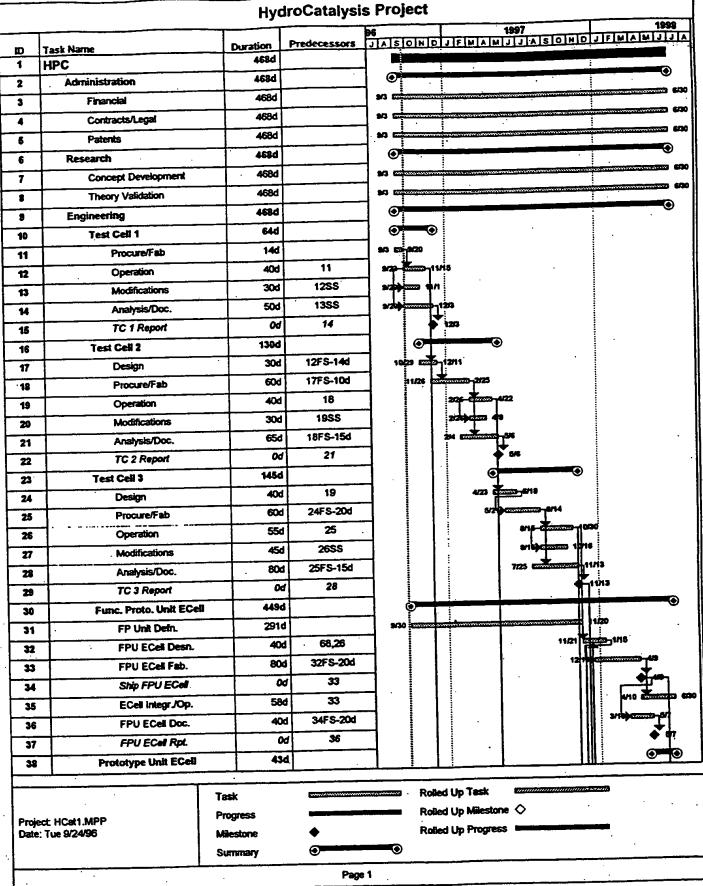


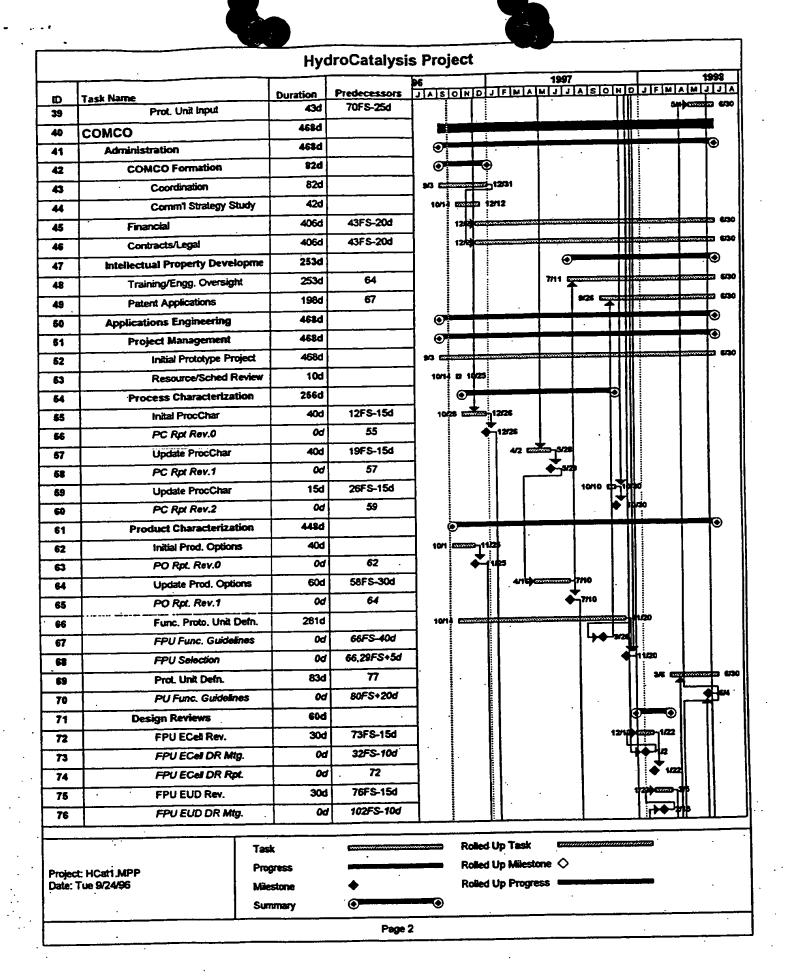


THIS PAGE BLANK (USPTO)













				96	2016	. Ielaila	1997	ASOND	JEMIA	м
ID_	Task Name	Duration Od	Predecessors 75	11/12	SIMINI SIMINI	1 1010	1-1212		15	
77	FPU EUD DR Rpt.		73			i			, b	_
78	Readiness Reviews	30d				1				
79	FPU Opni RR	. 30d	80FS-15d			1	;	}	477	****
80	FPU ORR Mtg.	00	109FS-10d			1	*	1		•
81	FPU ORR Rpt.	Od	79							•
82	New Concepts	158d				1		o l		
83	Concept Development	158d	68					11/21 00	913.41.25.71	er en
84	Marketing	3894			•					
85	Vendor/OEM Interactions	383d				·				
86	Vendor/OEM Contacts	383d			177		**************************************	01/110010010000000000000000000000000000		YAY.
87	Select Lead V/OEM	Od	86SS+60d,65FS			+		7/17		
88	End User Interactions	384d		1		2				
89	Prospective Participants	384d			1,6	r enemicronics	verneurones ve	201211111111111111111111111111111111111	***************************************	0000
50	Business Plans	361d			€					•
91	Initial Bans Plan	90d	56,63]	12/27	-	2755			
92	Bsns Plan Rev.0	Od	91]			♦ 545]		
83	Update Bsns Plan	604	87]			7/18 · E	100		
94	Bsns Plan Rev.1	Od	93					1079		
95	Update Bsns Plan	604	102						77	
96	Bsns Plan Rev.2	06	95	1						•
97]				1		
98	LEAD VENDOR/OEM	248d		1						_
99	Engineering	248d		}			€			_
100	Func. Proto. Unit	248d								
101	Func. Proto. Unit Input	90d	87	7			jus t	***************************************	1/20	
102	FPU EUD Design	70d	68					1121		
103	FPU Design Report	Od	102]					_ 	£
104	FPU Fab/Op Support	108d	103FS-20d			: :	ě	•		
105	Prototype Unit	43d] .						•
106	Prot. Unit Input	436	70FS-25d						4)
107	Manufacturing	108d]					•	_
108	Func. Proto. Unit	108d					•		0	
109	FPU Fab/Installation	60 d	102FS-20d,34FF		•				1/24)	-
110	FPU Operating Manual	00	109FS-10d					•	. 4	*
111	FPU Operation	280	109		Ī					22

·					
•	Task	***************************************	Rolled Up Task,	annamananamanana.	
Project: HCat1,MPP	Progress		Rolled Up Milestone	\Diamond	
Date: Tue 9/24/96	Milestone	•	Rolled Up Progress		
	Summary	⊙			
	1	Page 3			

:





HydroCatalysis Project

- 9 Engineering
 The task groups labeled Test Cell 1, 2 and 3 each represent a series of tests conducted with one or more devices of similar construction. The design The task groups labeled Test Cell 1, 2 and 3 each represent a series of tests conducted with one or more devices of similar construction. The tasks of the test cell series include design of auxiliary, control, and data gathering and analysis systems as needed to conduct the full scope of the test. The procurement/fabrication tasks include the assembly, calibration and initial shakedown operation of the equipment. The analysis/documentation tasks include initial definition and necessary adjustments of the test matrix, as well as data collection, integration, analysis and documentation in a test report.
- 10 Test Cell 1 A device whose design and fabrication is currently in progress at NovaTech under contract to HPC. Quartz tube in fire brick, designed to operate at 700 C,
- 16 Test Celt 2 A device currently envisioned to utilize a stainless steel outer container with internal ceramic insulation and designed to operate at 2000 C in the reaction zone.
- 23 Test Cell 3 A scaleup of the test cell 2 device designed for comparable operating temperature with a geometry evolving toward a heat exhanger configuration for the functional prototype unit energy cell.
- Func. Proto. Unit ECell
 The functional prototype unit includes an energy cell plus its auditaries and controls, in conjunction with an energy utilization device, as well as
 The functional prototype unit includes an energy cell plus its auditaries and controls, in conjunction with an energy utilization device as well as
 necessary instrumentation, data gathering and analysis equipment. The unit would be designed for operation in a controlled shop environment, with
 necessary instrumentation, data gathering and analysis equipment. The unit would be designed for operation in a controlled shop environment, with
 emphasis on understanding and resolving issues associated with the integration of an energy cell and energy utilization device with those of the
 expected operating conditions. Auditary and control systems for the energy cell would not necessarily be physically integrated with those of the
 energy utilization device.
- Process Characterization
 Interactions with HPC/NovaTech regarding cell design and operating experience to characterize the process as it relates to selection of an energy interactions with HPC/NovaTech regarding cell design and operating experience to characterize the process as it relates to selection of an energy interactions with HPC/NovaTech regarding cell design and operating experience to characterize the process as it relates to selection of an energy interaction with HPC/NovaTech regarding cell design and operating experience to characterize the process as it relates to selection of an energy interaction with HPC/NovaTech regarding cell design and operating experience to characterize the process as it relates to selection of an energy interaction.
- 51 Product Characterization Integrating results from the process characterization and product options identification activities to develop functional guidelines for the initial unit, leading to selection of an initial unit concept for detailed design, fabrication and operation as a functional prototype. Subsequent integration of data from energy cell development and functional prototype experience to guide the development of a prototype unit.
- 82 New Concepts Identification and development of new application concepts tailored to the characteristics of the HydroCatalysis process.
- 85 Vendor/OEM Interactions Contacts with vendor/OEM organizations considered candidates for the lead vendor/OEM, leading to establishment of a contractual relationship to design, fabricate and operate the functional prototype unit.
- 88 End User Interactions Support of PHI and/or HPC initiatives to involve additional end users (e.g., utilities, IPP companies) in COMCO, communications with COMCO owners, and coordination of the participation of representatives from COMCO owners in design reviews, operational readiness reviews, etc.
- 80 Business Plans Development and documentation of long term plans and strategies for COMCO structure and operations.
- Func. Proto. Unit

 The functional prototype unit includes an energy cell plus its auxiliaries and controls, in conjunction with an energy utilization device, as well as
 The functional prototype unit includes an energy cell plus its auxiliaries and controls, in conjunction with an energy utilization device and energy utilization device over the range of
 emphasis on understanding and resolving issues associated with the integration of an energy cell and energy utilization device over the range of
 expected operating conditions. Auxiliary and control systems for the energy cell would not necessarily be physically integrated with those of the
 energy utilization device.
- 102 FPU EUD Design
 EUD is energy utilization device (e.g., gas turbine, process heat supply), assumed to be a modification of an existing design to accommodate the HydroCatalysis energy cell.
- 105 Prototype Unit
 The prototype unit would draw upon earlier experience to produce an integrated unit for field operation in one or more demonstration projects.





Attachment C

HydroCatalysis Project Phase I - Functional Prototype Energy Cell Development

The following material provides a definition of the design and performance objectives of an evolving series of HydroCatalysis energy cells leading to an energy cell unit to be integrated with an energy utilization device for the functional prototype unit. Titles refer to task summary entries in the HydroCatalysis project integrated schedule.

Engineering:

The task groups labeled Test Cell 1, 2 and 3 each represent a series of hardware and process design and engineering tests conducted with the vapor phase hydrino power cell (energy cell) that has been developed in collaboration at the HPC and NovaTech labs (note - current expectations are that NovaTech personnel performing the work will move within HPC or COMCO). The milestone reports for each test cell represent design evolution and engineering performance milestones in the evolution of this concept, not different concepts for the embodiment (physical implementation) of the hydrino power cell invention itself.

The design tasks of the test cell series include design of auxiliary, control, and data gathering and analysis systems as needed to conduct the full scope of the test. The procurement/fabrication tasks include the assembly, calibration and initial shakedown operation of the equipment. The analysis/documentation tasks include initial definition and necessary adjustments of the test matrix, as well as data collection, integration, analysis and documentation in a test report.

Test Cell 1

Objective: To achieve a design of a cell that will operate repeatedly and controllably, and use as a basis to formulate a strategy for subsequent cell development.

Design Goals:

- Independently control catalyst vapor partial pressure (utilize an externally heated reservoir, no high temperature seals)
- Utilize a flowing hydrogen cell (prevent "fuel" starvation)





 Overcome the thermal limitations of previous vessels & insulation (keep stainless steel vessel sufficiently cool, but keep stainless steel vessel hot enough so catalyst precipitation is reduced)

 Design and fabricate a relatively inexpensive test bed (allow for high surface area tungsten foams or powders, allow for various catalysts, investigate other materials, investigate different operating scenarios (T, P, flow, etc.))

Performance Goals:

- Show excess power operating over the noise level of the calorimeter (2% in the delta T measurement). Target excess power generation is
- Sustainable over hours (limit condensation/precipitation of catalyst and oxidation of tungsten filament)
- Repeatable demonstration of excess power
- Controllable (controlled approach to excess power operating conditions and stable operation while generating target level of excess power)
- Operating temperature (other than the filament) 1000 to 1400 degrees C in the "hot zone" reaction volume as measured by the type C thermocouple
- Better understanding of cell insulation and refractory materials requirements

Optimal operating parameters expected to be: reaction zone partial pressures of 2 torr potassium iodode or 0.2 torr Rubidium iodide, 200 millitorr hydrogen, as high an operating temperature as possible, power density will be optimized by adjustment of partial pressures and temperatures within the limits of the device. Three Test Cell 1 devices have been fabricated: TC1A for operation by NovaTech directed toward the above objectives, TC1B and TC1C for operation by HPC to improve the understanding of the process by variation of key parameters. Test Cells TC1B and TC1C will have a partial Data Acquisition System.

Test Cell 2

Objective: Self-Sustained Operation (Long term (24 hour) operation without electrical input to the filament while maintaining reaction zone temperatures sufficient to support molecular hydrogen dissociation).

Design Goals:

 Higher temperature capability (eliminate oxide insulation through use of multi-layer insulation)





- Better vacuum system (reduce bake-out times required, improve quality of bake-out)
- Automated Data Acquisition System (DAS)
- Improved catalyst pressure control
- Attempt to eliminate catalyst "loss"
- Instrumentation for optimization of operating parameters (prep for scaleup)
- Delta-T thermocouples at faster responding locations
- Greater range in power supply/controllable constant power source
- Design and fabricate a relatively inexpensive test bed for operation at higher temperatures than Test Cell 1 (allow for high surface area tungsten foams or powders, allow for various catalysts, investigate other materials, investigate different operating scenarios (T, P, flow, etc.))

Performance Goals:

- Reliable and repeatable startup and operation in a self-sustained mode for periods in excess of 24 hours
- Quantitative understanding of power production as a function of key operating parameters
- Average power density in the reaction zone volume greater than 1 watt per cubic centimeter in steady state
- Reliable operation of supporting auxiliary systems
- Centerline temperature operation in the range 1300 2000 °°C

Test Cell 3:

Objective: An engineering redesign of the self-sustaining Test Cell 2 device, designed for comparable operating temperature with a geometry evolving toward a heat exchanger configuration for the functional prototype unit energy cell.

Design Goals

- Designed with advanced refractory materials, where required, from the outset
- Designed to eliminate net catalyst loss during normal operation, including slow reactions of catalyst with cell contents and vessel
- Provision for fabrication of multiple devices of varying length to investigate fuel and catalyst transport limits, with provision for axial data on performance for longer cells
- Provision for cell heat loss characteristics to support both initial heatup power requirements and heat transfer requirements of steady state operation beyond goal power densities
- Provision for parallel operation of two energy cell units serviced by a common power supply, hydrogen supply, catalyst supply and vacuum system





- The materials and design of this cell will provide the basis for study of commercial scaleup in terms of materials choice for function and price of the Functional Prototype Unit Energy Cell
- Analytical projection of sufficient operating lifetime for key materials
- Provision for removal of reaction products or foreign gases during long term operation

Performance Goals

- Reliable and repeatable startup and operation in a self-sustained mode
- Operation of an energy cell in a self-sustained mode for a period in excess of one week
- Average power density in the reaction zone volume greater than 10 watts per cubic centimeter in steady state
- Stable startup and operation of two or more energy cells supported by a common power supply, hydrogen supply, catalyst supply and vacuum system
- Quantitative data on the effect of energy cell length on performance
- Quantitative data supporting the key materials design lifetime analysis

Functional Prototype Unit Energy Cell

Objective: Parallel energy cells, as well as necessary instrumentation, data gathering and analysis equipment designed and fabricated for operation in conjunction with an energy utilization device. The resulting functional prototype unit (combination of hydrocatalysis energy cell unit and energy utilization device) will be designed for operation in a controlled shop environment, with emphasis on understanding and resolving issues associated with the integration of an energy cell and energy utilization device over the range of expected operating conditions. This program may be under the auspices and largely funded by an OEM.

Design Goals:

- An energy cell unit comprised of multiple energy cells operating in parallel and serviced by a common power supply, hydrogen supply, catalyst supply and vacuum system
- Provisions for automated startup and operation of the energy cell unit
 meeting the environmental and control requirements of the energy utilization
 device while operating in a controlled shop environment (Auxiliary and
 control systems for the energy cell would not necessarily be physically
 integrated with those of the energy utilization device)
- Energy cell unit capability (startup, dynamic response, power production, lifetime) as required to support the energy utilization device over a range of conditions covering the planned test matrix
- OEM input





Performance Goals:

- Reliable and repeatable startup and operation
- Power production consistent with the design operating range of the energy utilization device
- Stable operation and dynamic response characteristics consistent with the requirements of the energy utilization device
- Satisfactory operation over the conditions of the planned test matrix
- OEM input

THIS PAGE BLANK (USPTO)





Attachment D

List of Documents received by Kline-Anderson Inc. as background material from HPC and Technology Insights.

HPC:

Confidential Business Summary

Confidential Short Business Summary

"Fractional Quantum Energy Levels of Hydrogen" Fusion Technology, Nov. 1995.

Confidential Paper "Fractional Quantum Energy Levels of Hydrogen Representative

Recent Results Prepared For Kline Anderson

Book review by Dr. Reinhart Engelmann

Confidential Company Presentation

Confidential Protocols:

Search For the Mills Hydrino: An Extreme UV Spectroscopy Proposal

Measurement of Excess Heat From Hydrino Production

Protocol For the Synthesis of Dihydrino Molecules

Protocol For Heat Measurements With the High Temperature Vapor Phase Cell

Protocol for Heat Measurements With the AtMar Glass Lamp

Protocol for Calvet Measurements of the High Temperature Vapor Phase Cell

Carbon XPS Protocol

Gas Phase Hydrocatalysis: Proof of Principal Potassium Carbonate Coated Nickel

Hydride Experiments

One Kilowatt Electric Prototype Proposal

Technology Insights:

HydroCatalysis Technical Assessment, August 30, 1996







Attachment E

"Conceptual characterization of HydroCatalysis Turbine Application Options" (Technology Insights).





THIS PAGE BLANK (USPTO)





COMCO Technical Support Workscope

Conceptual Characterization of HydroCatalysis Turbine Application Options

1.0 Objective

Identify steam and gas turbine options for power generation using the HydroCatalysis process and characterize each option in terms of conceptual configuration, environmental conditions imposed on a HydroCatalysis energy cell, existing experience and precedence, and system design and development issues. Select one or more preferred options for continued evolution in concert with the ongoing development of the energy cells.

2.0 Background

The initial application of the HydroCatalysis process, to be developed jointly by COMCO and BlackLight Power, is anticipated to be for power generation utilizing either a steam or gas turbine. Since the fuel cost of the HydroCatalysis process is anticipated to be small, corresponding to the amortized capital and operation costs associated with production of hydrogen from water, achieving high efficiency is of lesser importance than for conventional power generation technologies. This will reduce the importance of efficiency in the optimization of the overall unit design primarily to its effect on capital cost. The options identified for further definition are intended to span the range of likely approaches for power generation, with expected significant variations in demands on the development of the HydroCatalysis energy cell, in design and development requirements for the power conversion equipment, and in projected commercial unit capital costs. The overall objective is to narrow the field of options being considered with the intent of arriving at one or more functional prototype units for near term development.

3.0 Options to be Addressed

The system configuration options listed below will be considered along with additional options which may be identified in the course of the work. Initial conceptual information is provided in an appendix to this document as a starting point for each configuration and to illustrate the approach to be taken and the information to be developed.

3.1 Steam Turbine

For the steam turbine options, the interface with the energy cell will be either directly or indirectly with a steam boiler. In light of the decreased importance of efficiency, lower pressure saturated or moderately superheated steam, similar to the



steam conditions in commercial water reactor power plants may be appropriate. The following steam turbine options, as defined in the appendix, will be considered.

- S-1 Radiant Recirculating Boiler
- S-2 Radiant Once-Through Boiler
- S-3 Natural Convection Recirculating Boiler
- S-4 Forced Convection Once-Through Boiler
- S-5 Forced Convection Intermediate Loop Boiler

3.2 Gas Turbine

Gas turbine options will include open and closed cycles, with cycle efficiency to be addressed in a manner consistent with the approach for the steam cycles. The following gas turbine options, as defined in the appendix, will be considered.

- G-1 Radiant Open Cycle
- G-2 Forced Convection Open Cycle
- G-3 Forced Convection Intermediate Loop Open Cycle
- G-4 Radiant Closed Cycle
- G-5 Forced Convection Closed Cycle

4.0 Scope of Activities

This effort will encompass the activities defined below.

4.1 Option Characterization

Using the material in the appendix as a starting point, characterize the options in sufficient detail to support the selection of one or more preferred options for further development as candidate(s) for a functional prototype. The following information will be developed for each option:

- Concept Strengths Expand and quantify the list of positive attributes identified in the appendix
- Design Issues Expand and quantify the list of design issues identified in the appendix
- Energy Cell Environment Quantify the energy cell environmental parameters identified in the appendix (with additional parameters if appropriate)



- Development Requirements Identify the scope of activities for development of the functional prototype and commercialization of the concept
- Market Potential Identify the range of products (size range, applications) and estimate the unit costs for volume production

The degree of detail and level of confidence in the results will be consistent among the options addressed and sufficient to support a comparison for the purpose of narrowing the field of options under consideration. The results will be documented in a product options report in a format consistent with the information in the appendix, with additional considerations noted above included.

4.2 Preferred Option(s) Selection

Using the results developed by the work defined in the previous section, a meeting will be held to select the preferred option or options for further definition and iteration with energy cell development as a basis for the functional prototype unit.

4.3 Preferred Option(s) Development

Continue the design and characterization of the selected option(s) in support of the functional prototype unit development and COMCO commercialization plans.



THIS PAGE BLANK (USPTG)



Appendix - Turbine Application Options Conceptual Summary

develop and characterize the options, leading to the selection of one or more preferred concepts for further development. defined in summary form on the following pages. This information is provided as a starting point for an effort to further Steam and gas turbine power conversion system options for the application of the HydroCatalysis process are The options as defined here may be modified or more attractive options developed in the course of the work. The following options are identified:

- Radiant Recirculating Boiler
- Radiant Once-Through Boiler
- Natural Convection Recirculating Boiler
- Forced Convection Once-Through Boiler
- Forced Convection Intermediate Loop Boiler
- Radiant Open Cycle
- Forced Convection Open Cycle
- Forced Convection Intermediate Loop Open Cycle
- Radiant Closed Cycle
- Forced Convection Closed Cycle Q 52

based on a self-sustaining energy cell design (i.e., no electric power input required in the power operation range). Based on current understanding of the HydroCatalysis process, this is further assumed to require the achievement of elevated The concept strengths and design issues are intended to address considerations external to the energy cells as temperature conditions (e.g., > 1500°C) in the reaction zone of the energy cell. Thus the need for high temperature well as demands placed on the design and operation of the energy cells. It is assumed that all of the options will be materials and the resulting design issues for the energy cells is considered applicable for all of the options





Radiant Recirculating Boiler **Option S-1**

Precedents

ABB/Combustion Engineering, Foster Wheeler oil, gas and coal fired steam boilers.

Summary Description

convection recirculating loop with a steam drum containing steam separation equipment to meet the minimum inlet steam insulated container with a reflective inner surface. A movable mirror lattice between the energy cells and boiler tubes is used to control heat transfer from the energy cells during startup and power operation. The boller circuit is a natural A bank of cylindrical HydroCatalysis energy cells is positioned adjacent to a bank of boiler tubes inside an quality requirements of the turbine.

Concept Strengths

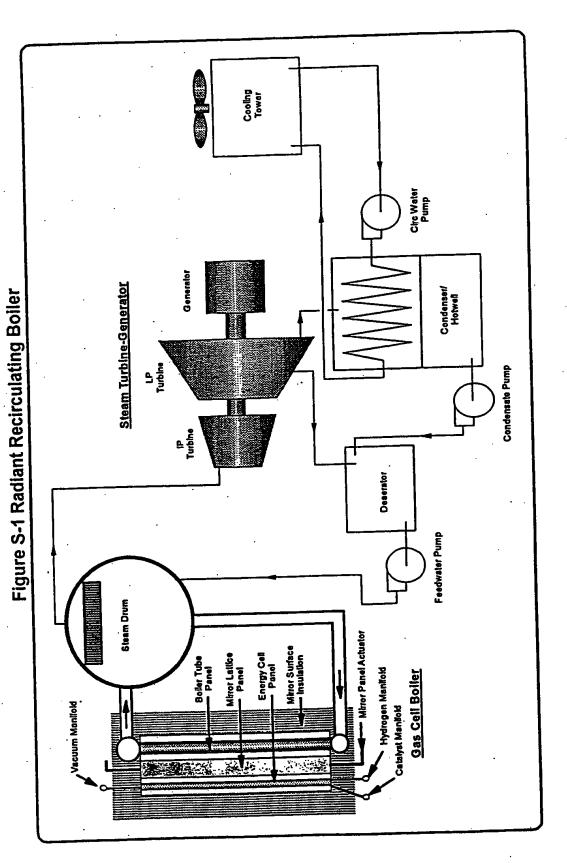
- 1. Low external pressure on energy cells
- 2. No flow induced structural loads on energy cells
- 3. Control of energy cell heat losses during startup
- 4. Boiler tube temperature relatively constant over the tube length and over the load range

Design Issues

- 1. Accommodation of thermal expansion
- 2. Energy cell temperature variation characteristics over the load range
- 3. Radiant panel heat flux size requirements

- 1. Temperature distribution and operating range
- Startup and control requirements





Option S-2 Radiant Once-Through Boiler

Precedents

Babcock & Wilcox oil, gas and coal fired steam boilers.

Summary Description

insulated container with a reflective inner surface. A movable mirror lattice between the energy cells and boiler tubes is used to control heat transfer from the energy cells during startup and power operation. The boiler circuit is a forced A bank of cylindrical HydroCatalysis energy cells is positioned adjacent to a bank of boiler tubes inside an convection once-through system producing superheated steam.

Concept Strengths

- 1. Low external pressure on energy cells
- 2. No flow induced structural loads on energy cells
- 3. Control of energy cell heat losses during startup

Design Issues

- 1. Accommodation of thermal expansion
- Energy cell temperature variation characteristics axially and over the load range
- 3. Radiant panel heat flux size requirements
- 4. Boiler tube stability
- 5. Boiler startup and dynamic control requirements

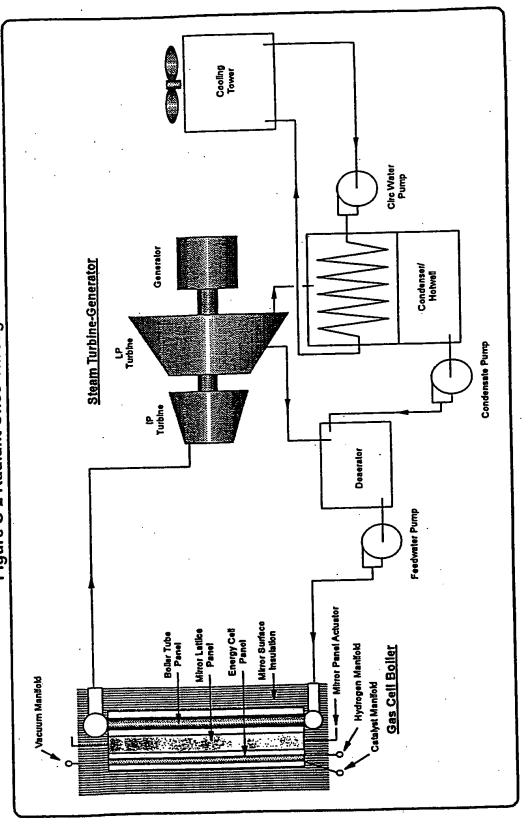
- 1. Temperature distribution and operating range
- 2. Startup and control requirements







Figure S-2 Radiant Once-Through Boiler





Natural Convection Recirculating Boiler Option S-3

Precedents

General Electric Boiling Water Reactors, U-tube steam generators for Westinghouse and ABB/Combustion Engineering Pressurized Water Reactors.

Summary Description

support grids. Recirculating water from the swirl vane separator and steam dryer mix with incoming feedwater, resulting in moderate subcooling at the bottom. The energy cell surface conditions are liquid convection in the bottom region, The energy cells are placed in tubes projecting into the boiler vessel in a bayonet configuration with external changing to nucleate boiling over the majority of the cell length.

Concept Strengths

- 1. High energy cell surface heat flux capability
- Stable cell surface temperature and heat removal characteristics
- Energy cell surface temperature relatively constant over the tube length and over the load range

Design Issues

- 1. Achieving self-sustaining energy cell temperature conditions during startup
 - 2. Accommodation of energy cell internal thermal expansion
- Single-ended access for hydrogen, catalyst and vacuum manifolds რ

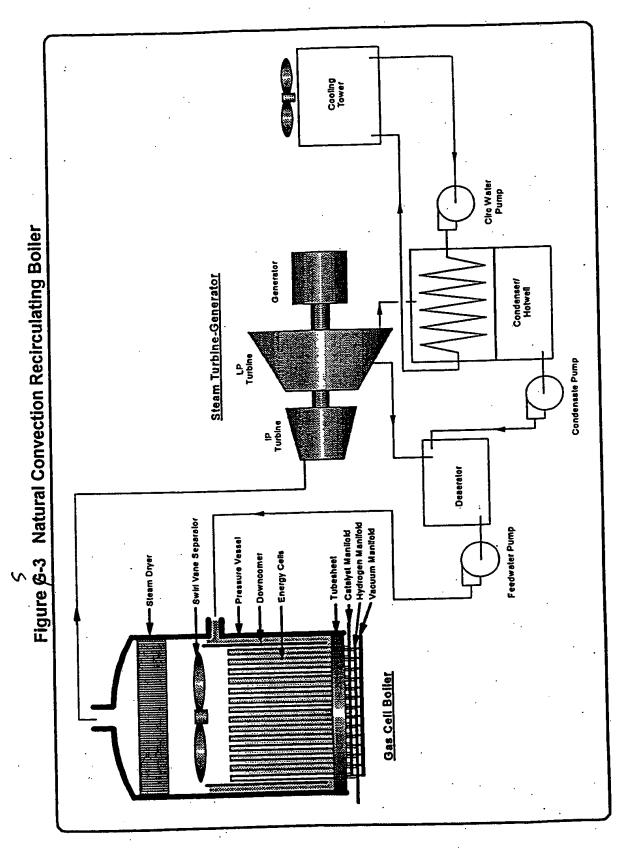
- External pressure range
- Temperature distribution and operating range
- Flowrates and flow induced loads
- Startup and control requirements



Technical Support Workscope







Option S-4 Forced Convection Once-Through Boiler

Precedents

Babcock & Wilcox steam generators for Pressurized Water Reactors.

Summary Description

The energy cells are placed in tubes projecting through the boiler yessel tubesheets with tube support grids on the (sufficient to preclude moisture carryover from dynamic variations or nonuniform spatial effects. The energy cell surface conditions are single phase liquid convection in the bottom region, changing sequentially to nucleate boiling, film boiling shell side. Feedwater enters the bottom of the vessel on the shell side and exits as moderately superheated steam and single phase vapor convection at the top.

Concept Strengths

- 1. Simplicity of boiler internals
- 2. High energy cell surface heat flux capability in the single phase liquid and nucleate boiling zones

Design Issues

- 1. Accommodation of thermal expansion in energy cells and between tube bundle and vessel (may require bellows or sliding seals)
 - 2. Achieving self-sustaining energy cell temperature conditions during startup
 - 2. Energy cell temperature response characteristics over the load range
 - 3. Axial movement of heat transfer zones during load changes

- 1. External pressure range
- 2. Temperature distribution and operating range
- 3. Flowrates and flow induced loads
- 4. Startup and control requirements



PH CONFIDENTIAL*





Cooling Cho Water Pump Figure S-4 Forced Convection Once-Through Boiler Generator Steam Turbine-Generator Condenser/ Hotwell Turbine Deserator Hydrogen Manifold - Catalyst Menifold Vacuum Manifold - Energy Cells Feedwater Pump - Tubesheel - Tubesheet Gas Cell Boller

• PHI Confidential Information - Work Product for Hire Property of PHI

Condensale Pump



Option S-5 Forced Convection Intermediate Loop Boiler

Precedents

Helium cooled reactor (Peach Bottom, Fort St. Vrain, AVR), or carbon dioxide cooled reactor (Magnox, AGR) primary loop/steam generator.

Summary Description

HydroCatalysis energy cells are placed in tubes penetrating a heat exchanger vessel containing a pressurized gas (e.g., He, CO₂) heat transfer fluid. A gas circulator provides forced convection heat transfer on the shell sides of the heat exchanger and a steam generator. A helical coil once-through steam generator providing superheated steam is shown, but variations could include straight tube units as well as recirculating units providing saturated steam.

Concept Strengths

- Independent control of energy cell environment (pressure, temperature, flow) over the startup and power operation range
- Independent design of energy cell heat exchanger to accommodate power density and dynamic characteristics of the HydroCatalysis process

Design Issues

- 1. Development, capital and operating cost
- 2. Flow induced static and dynamic loads
- Achieving self-sustaining energy cell temperature conditions during startup
- High temperature design of energy cell heat exchanger and steam generator vessel and internals, and accommodation of thermal expansion 4

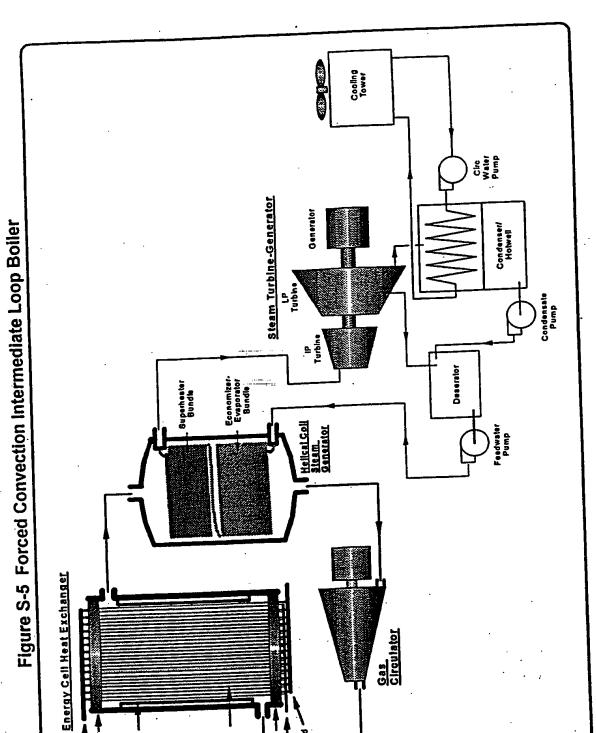
- 1. External pressure range
- 2. Temperature distribution and operating range
 - 3. Flowrates and flow induced loads
- 4. Startup and control requirements



Page A-11

Vacuum Manifold --

Shroud



Tubesheet — Catalyst Menifold — Hydrogen Manifold

Energy Cells -

• PHI Confidential information - Work Product for Hire Property of PHI

Option G-1 Radiant Open Cycle

Precedents

To be identified.

Summary Description

A bank of cylindrical HydroCatalysis energy cells is positioned adjacent to a bank of heat exchanger tubes inside exchanger tubes is used to control heat transfer from the energy cells during startup and power operation. The heat an insulated container with a reflective inner surface. A movable mirror lattice between the energy cells and heat exchanger tubes contain pressurized air, with pressures determined by the characteristics of the gas turbine.

Concept Strengths

- 1. Low external pressure on energy cells
- 2. No flow induced structural loads on energy cells
- 3. Control of energy cell heat losses during startup
- 4. Simple flow circuit

Design Issues

- 1. Radiant energy cell panel and heat exchanger tube panel heat flux size requirements
 - 2. Axial variation in heat exchanger tube temperature/heat transfer from energy cells
- 3. Accommodation of thermal expansion

- 1. Temperature distribution and operating range
- 2. Startup and control requirements

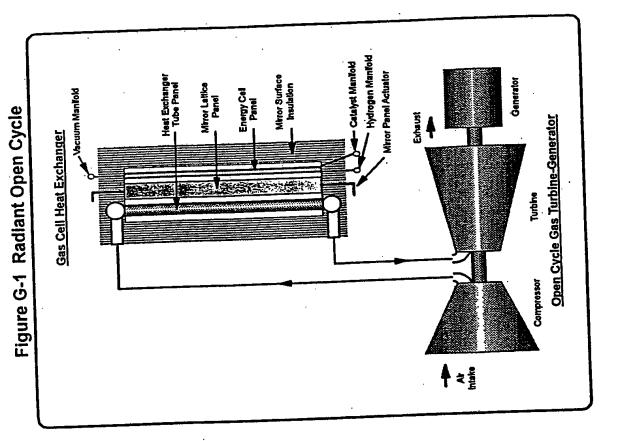






PH CONFIDENTIAL*

Technical Support Workscope





Forced Convection Open Cycle Option G-2

Precedents

To be identified.

Summary Description

HydroCatalysis energy cells in tubes penetrate a heat exchanger pressure vessel, with pressurized air in crossflow the inlet of the power turbine, with pressures determined by the characteristics of the gas turbine. Self-sustaining energy over the tubes. Air from a gas turbine compressor flows to the vessel inlet, and heated air from the vessel outlet flows to cell temperature conditions are achieved during startup by combustion of hydrogen on the shell side of the heat exchanger, analogous to operation of conventional combustion turbines.

Concept Strengths

- 1. Potential for rapid startup using combustion bootstrap
- 2. Effective energy cell heat removal relatively compact design
- 3. Simple flow circuit

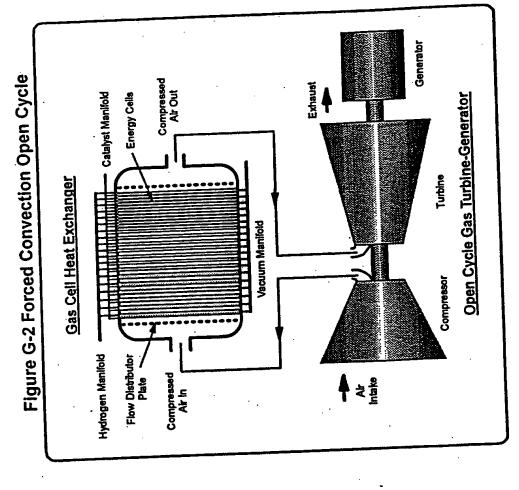
Design Issues

- 1. Flow induced static and dynamic loads on energy cell tubes
- 2. Accommodation of thermal expansion and air temperature rise across heat exchanger
 - 3. Energy cell dynamic response requirements
- 4. High temperature design of gas cell heat exchanger vessel and internals

- 1. External pressure range
- 2. Temperature distribution and operating range
- Flowrates and flow induced loads
- Startup and control requirements







Page A-15



Forced Convection Intermediate Loop Open Cycle Option G-3

Precedents

developed by Hague International in cooperation with Black & Veatch, Foster Wheeler, and Allison Engine Company. Externally Fired Combined Cycle demonstration project at Pennsylvania Electric Company Warren Station,

Summary Description

HydroCatalysis energy cells are placed in tubes penetrating a heat exchanger vessel containing a pressurized gas compressor flows to the shelf side of the gas/air heat exchanger and heated air returns to the inlet of the power turbine. (e.g., He, CO₂) heat transfer fluid. A gas circulator provides forced convection heat transfer on the shell side of the energy cell heat exchanger and the tube side of a gas/air heat exchanger. Pressurized air from a gas turbine

Concept Strengths

- Independent control of energy cell environment (pressure; temperature, flow) over the startup and power operation range
- Independent design of energy cell heat exchanger to accommodate power density and dynamic characteristics of the HydroCatalysis process 'n

Design Issues

- Capital and operating cost
- . Flow induced static and dynamic loads
- Achieving self-sustaining energy cell temperature conditions during startup
- High temperature design of energy cell heat exchanger and gas/air heat exchanger vessel and internals, and accommodation of thermal expansion 4

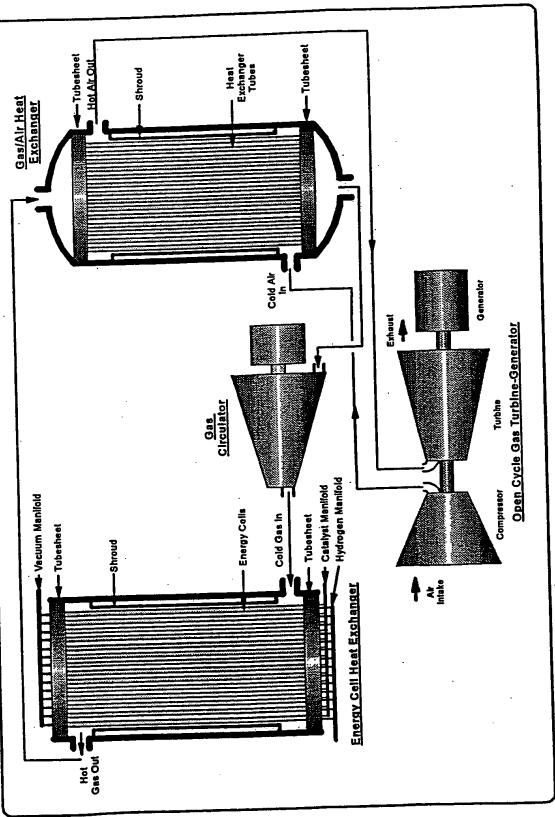
- 1. External pressure range
- Temperature distribution and operating range
- 3. Flowrates and flow induced loads
- 4. Startup and control requirements



Turbine Application Options



Figure G-3 Forced Convection Intermediate Loop Open cycle





Radiant Closed Cycle Option G-4

Precedents

Oberhausen II helium turbine plant, HHV gas turbine test facility (Germany).

Summary Description

A bank of cylindrical HydroCatalysis energy cells is positioned adjacent to a bank of heat exchanger tubes inside exchanger tubes is used to control heat transfer from the energy cells during startup and power operation. The heat exchanger tubes contain pressurized gas (e.g., helium), with pressures determined by the characteristics of the gas an insulated container with a reflective inner surface. A movable mirror lattice between the energy cells and heat turbine cycle.

Concept Strengths

- 1. Low external pressure on energy cells
- No flow induced structural loads on energy cells
- 3. Control of energy cell heat losses during startup
- Controlled pressure, chemistry environment of turbine blades and heat exchanger tubes

Design Issues

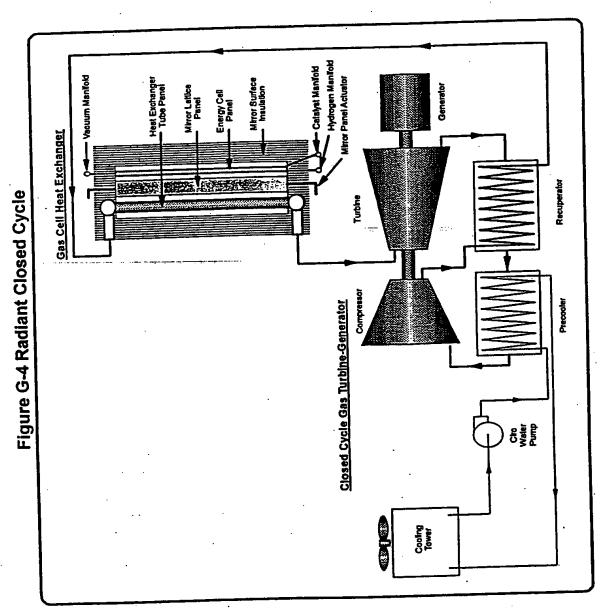
- 1. Development, capital and operating costs
- Radiant energy cell panel and heat exchanger tube panel heat flux size requirements
- 3. Axial variation in heat exchanger tube temperature/heat transfer from energy cells
- 4. Accommodation of thermal expansion

- 1. Temperature distribution and operating range
- 2. Startup and control requirements









Forced Convection Closed Cycle Option G-5

Precedents

Oberhausen II helium turbine plant, HHV gas turbine test facility (Germany).

Summary Description

helium) in crossflow over the tubes. Gas from a gas turbine compressor flows through a recuperator heat exchanger to HydroCatalysis energy cells in tubes penetrate a heat exchanger pressure vessel, with pressurized gas (e.g., the vessel inlet, and heated gas from the vessel outlet flows to the inlet of the power turbine. The gas pressure is determined by the characteristics of the gas turbine cycle.

Concept. Strengths

- 1. Effective energy cell heat removal relatively compact heat exchanger design
- 2. Controlled pressure, chemistry environment of turbine blades and heat exchanger tubes

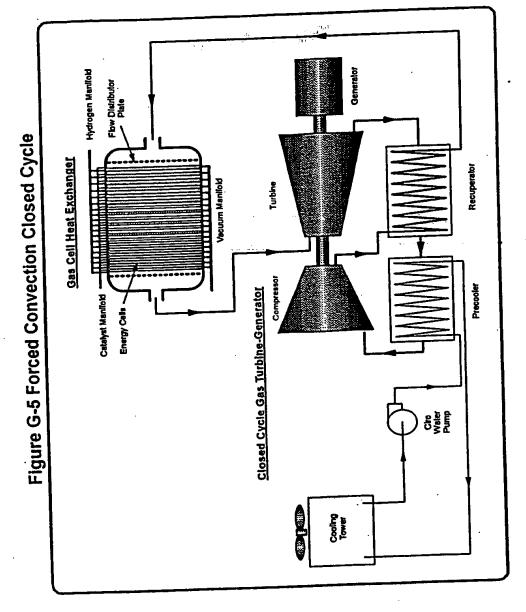
Design Issues

- 1. Development, capital and operating costs
- 2. Achieving self-sustaining energy cell temperature conditions during startup
 - Flow induced static and dynamic loads on energy cell tubes
- 4. Accommodation of thermal expansion and gas temperature rise across heat exchanger
 - 5. High temperature design of gas cell heat exchanger vessel and internals
 - 6. Energy cell dynamic response requirements

- 1. External pressure range
- 2. Temperature distribution and operating range
 - Flowrates and flow induced loads
- Startup and control requirements 4.







PHI Confidential Information - Work Product for Hire Property of PHI





THIS PAGE BLANK (USP)





Attachment F

"S-1 Radiant Recirculating Boiler" (Technology Insights).



S-1 Radiant Recirculating Boiler

S-1.0 Summary

Precedents

ABB/Combustion Engineering, Foster Wheeler oil, gas and coal fired steam boilers.

Summary Description

convection recirculating loop with a steam drum containing steam separation equipment to meet the minimum inlet steam insulated container with a reflective inner surface. A movable mirror lattice between the energy cells and boiler tubes is used to control heat transfer from the energy cells during startup and power operation. The boiler circuit is a natural A bank of cylindrical HydroCatalysis energy cells is positioned adjacent to a bank of boiler tubes inside an quality requirements of the turbine.

Concept Strengths

- Low external pressure on energy cells
- . No flow induced structural loads on energy cells
- Control of energy cell heat losses during startup
- Boller tube temperature relatively constant over the tube length and over the load range

Design Issues

- Accommodation of thermal expansion
- 2. Energy cell temperature variation characteristics over the load range
- Radiant panel heat flux size requirements

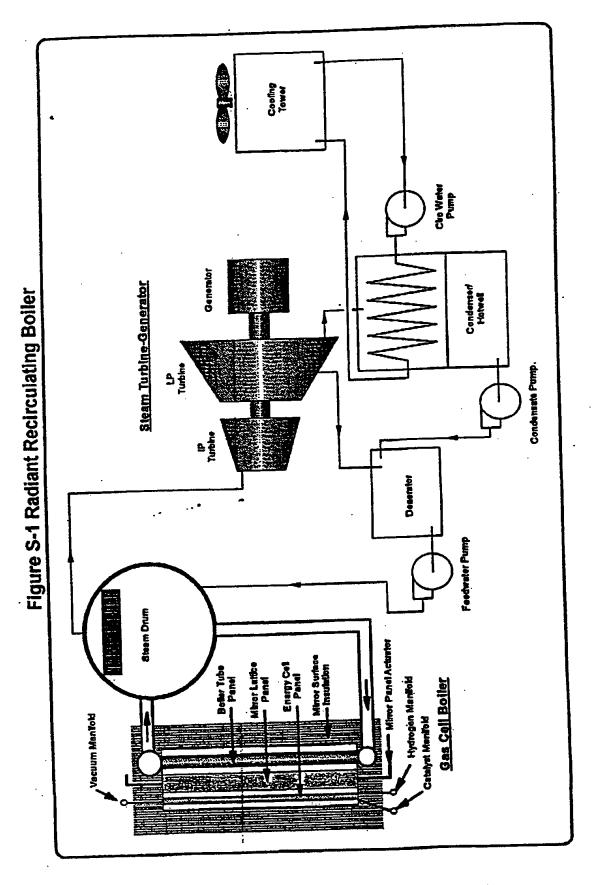
- Temperature distribution and operating range
- Startup and control requirements



Turbine Application Options

Initial Concepts Definition







S-1.1 Thermal Analysis

Heat transfer for the radiant concept can be approximated by neglecting convection and treating the energy cell and boiler tube panels as gray bodies. This results in radiation from the energy cell surface given by the expression:

$$E_g = e_g \, \sigma T^4$$
, where

E_g = Gray body emissive power, watts/cm²

$$\varepsilon_{\rm g} = {\rm Surface\ emissivity}$$

(divisain,⊡ Figure S-1.2 Energy Cell Thermal Radiation Flux ф 60 0.8 0.7 1,000 1,200 1,400 1,800 1,800 Surface Heat Flux as Function of Temp, Emissivity Temperature, C 800 දි) g \$ 2 8 8 Heat Flux, wicm?

energy cell panels, the resulting thermal radiation flux as a function of surface temperature and emissivity is shown in For the temperature range likely to be of interest for the Surface Temperature, "K # |-Figure S-1.2.

requiring detailed descriptions of the energy cell and boiler tube panels, the mirror lattice and chamber walls. However, to a first approximation the heat transfer can be estimated by treating the system as a 1 dimensional configuration with equivalent surface area corresponding to the frontal surface of the energy cell and boiler tube panels. Under these Calculating the exact net radiation heat transfer between the two surfaces is a complex geometric problem assumptions, the net heat transfer per unit panel frontal surface area is given by

$$E_{net} = (E_{g,1} - E_{g,2}) F_{t-2} = oF_{t-2} (e_{g,1} T_1^4 - e_{g,2} T_2^4)$$
, where

 $F_{1-2} = \text{Géometric shape factor for radiation between surfaces 1 and 2 (<math>F_{1-2} = F_{2-1}$ since the areas are equal) Subscripts 1 and 2 refer to the energy cell and boiler tube panel surfaces respectively

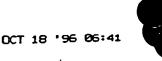
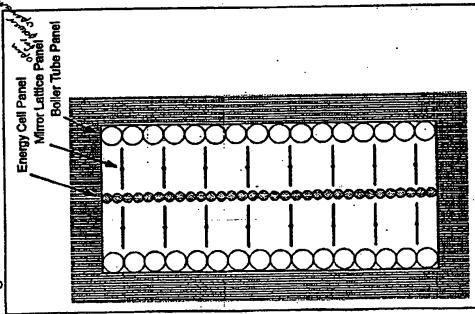




Figure S-1.3 Horizontal Cross Section



panel temperature for a

representative set of

conditions was

function of energy cell

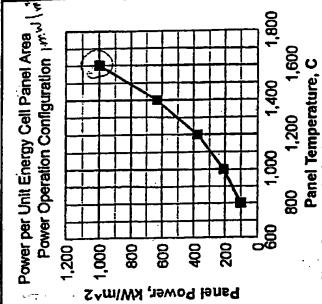
performance as a

selected as practical, achievable values. An equivalent linear shape surface temperature range, with a maximum value of approximately 1 representation of the configuration. The results show a factor of 10 factor of 0.8 was selected as a reasonable and likely conservative variation in heat transfer over the 800-1600°C energy cell panel

as shown in the figure. Larger units may consist of alternating energy cell Figure S-1.3. In this diagram, the energy cells are assumed to be vertical tubes aligned in the center of an insulated chamber with a reflective inner surface. The boiler tubes are placed along the two walls of the chamber A horizontal cross section of a radiant recirculating boiler concept cells and boiler tubes would be in the open position for power operation and boiler tube panels, with interior boiler tube panels receiving radiant opposite the energy cell panel. A lattice of mirrors between the energy consistent with the system diagram shown in Figure S-1.1 is shown in heat from energy cell panels on both sides.



The heat transfer



,000 psig was selected

assumptions discussed

estimated using the

on the previous page.

A steam pressure of

lower pressures having

as a reference, with

the results. Energy cel

and boiler pane

a negligible effect on

Steam Pressure - 1000 pslg

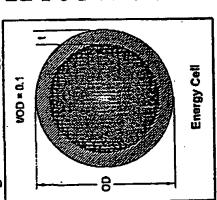
emissivilies of 0.9 were

48 P22

- Energy cell, boller emissivities 0.9
- Equivalent finear shape factor 0.8 **6**



Figure S-1.5 Energy Cell



megawatt per square meter of energy cell panel frontal surface area. The HydroCatalysis cell energy density requirements for this concept are determined by the cell interior volume per unit frontal surface area. This was estimated assuming the energy cells are in the form of cylindrical tubes with a wall thickness equal to 10% of the tube outside diameter and the reaction zone encompassing the entire interior volume, as shown in Figure S-1.5. In this configuration, the energy cell reaction zone volume per unit panel frontal area is

proportional to the tube diameter. The required power density to produce the heat transfer performance shown in Figure S-1.4 was calculated as a function of energy cell tube outside diameter, with results as shown in Figure S-1.6. The heat exchanger performance and energy cell power densities shown in Figures S-1.4 and S-1.6 illustrate the inherent response characteristics of this concept. As

power were used, the energy cell panel would be brought to a temperature of approximately 1,000°C (as Indicated by would result in increasing cell temperatures, reaching a maximum operating cell temperature of 1,600 °C at full rated Figure S-1.4) to establish stable power operation at the low end of the range. Increasing the energy cell power level such, they illustrate how the unit may operate over the load range. For example, if a minimum load of 20% of rated power. Under full power conditions, the maximum surface heat flux at the boiler tubes would be approximately 500 kW/m² (half the bidirectional frontal area power of the cell panel), compared to a burnout heat flux (transition from annular to mist flow) estimated to be well in excess of 3,000 kW/m²

S-1.2 Operational Considerations

are expected to require an elevated temperature in the reaction zone (i.e., ~1,000°C) to achieve self-sustaining energy A primary operational consideration is the startup of the unit. As currently understood, the HydroCatalysis cells

ECell OD, cm Energy Cell Power Density vs. Temperature, Figure S-1.6 Cell Power Density 1,800 Energy Cell Tube Diameter, cm 1,600 Panel Temperature, C 400 Equivalent linear view factor - 0.8 1,200 Panel, boller emissivites - 0.9 Steam Pressure - 1000 psig . 60. 800 8 8 8 ECAII Power Density, kWilter

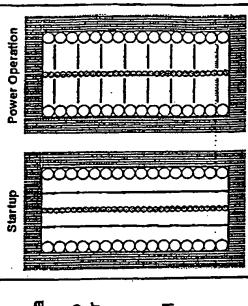
from the heat sink (boller tubes) for heatup to minimum initial temperatures.

The approach, as illustrated in Figure S-1.7, is

production. The concept provides for thermal isolation of the energy cells



18



to rotate the mirror lattice panel for startup to isolate the energy cell panel in a equired to bring the energy cells to initial operating temperature. Heating up the energy cells to self-sustaining temperatures could be accomplished either would be clean, but would present design problems with connecting electrical temperatures could be controlled by a combination of hydrogen and catalyst eads. Once the HydroCatalysis conditions are achieved, energy cell panel concentrations and positioning of the mirror panels. In the power operation heating of the energy cell panel. Combustion could be faster and cheaper, by combustion of hydrogen in the region around the boiler, or resistance but may pose problems with fouling the mirrors, while resistance heating reflective enclosure. This will substantially reduce the amount of energy range the mirror panels would likely be in a full open position.

lemperature. Thus the controls for the reaction process and the boller would be effectively independent, with supervisory The relatively small thermal mass of the energy cell panel may make for more challenging control requirements on power large margins to boiling limits will simplify the boiler control requirements with regard to meeting turbine load demands. level control to maintain the balance of heat generation and removal. The stability of the recirculating boiler, resulting from the large water thermal mass and mixing of incoming feedwater with recirculating saturated liquid, and expected would be essentially decoupled, with the heat losses from the energy cell panel insensitive to the boiler panel generation to maintain the panel within temperature limits, depending on the dynamic characteristics of the The thermal analysis shows that the energy cell panel and the boiler

S-1.3 Development Requirements

HydroCatalysis process.

conventional engineering design issues or modifications of existing designs. The boller tube panel would be very similar of the HydroCatalysis process, much of the work to be done to develop this concept would be expected to be addressing Outside the technology development required to determine the static and dynamic characteristics and limitations environmental conditions. Boiler controls and the balance of the power conversion system should be commercially to the economizer/evaporator section of a conventional recirculating water wall fossil boiler, with less challenging



issues such as accommodation of high temperatures and thermal expansion; routing and valving of the hydrogen and vacuum manifolds; and routing, valving, heat tracing and partial pressure control of the catalyst manifolds. Design of the vacuum energy cell controls will need to address batancing the cells for uniform power production as well as providing stable equipment and controls for heating the energy cell panel to minimum power operating conditions on startup will also available. The energy cell panel would require considerable design development and component testing to address dynamic response as required by the supervisory control system and material limits of the panels. Design of the require unique new design development.

S-1.4 Economic Assessment





THIS PAGE BLANK (USPTO)